How RhoGEFs drive triple negative breast cancer cell invasion through the activation of YAP and TAZ

Patricia Pascual Vargas

A thesis submitted for the degree of Doctor of Philosophy

PhD Supervisor: Professor Chris Bakal

The Institute of Cancer Research

The University of London

October 2019

Declaration

I, Patricia Pascual Vargas declare that the content presented in this thesis is my own. Where work has been derived from other sources, or where work has been performed by, or with the assistance of others, I confirm that it has been indicated in this thesis.

Acknowledgements

Writing this thesis has given me the chance to reflect over the past four years of my PhD and I have many people to thank for its completion. Firstly, I would like to thank my supervisor Chris Bakal for hiring me all those years ago to do my undergrad project in his lab, and which led to me carry out this PhD. Thank you for your support throughout these years, for thinking up this project, for imparting your knowledge on me, for always being encouraging of trying new experiments, for philosophical conversations, and last but not least, for making science fun.

Further thank you Bakalites. Firstly, thank you Mar Arias-Garcia for all that you have taught me, for being such a good friend, and for experiments performed in this thesis. Thank you Alexis Barr for always being so helpful, sharing your cell cycle and cloning knowledge, and thank you and Frankie Butera for showing me how to CRISPR-tag cell lines. Thank you Sam Cooper, Vicky Bousgouni, and Julia Sero for your contributions to my first paper and for making it possible. I would also like to thank Miguel Sanchez-Garcia for all the knowledge imparted on me during my year in research and for still answering my questions. Thank you Chloe Simpson for showing me how to navigate Jupyter notebooks. Thank you Ian Jones for your patience in showing me how to perform PLSR and answering my stats questions. Thank you Scott Stacey for performing supporting experiments which although not present in this thesis, will be useful in the future, and for always being so helpful. Thank you Theo Issitt for showing me how to do western blots and making them less tedious. Thank you also Harry Woods, Ollie Inge, Becky Rickman, Tanne van der Waal, Henriette Stoy, Lucas Dent, Tomo

Higo, and Hansa Shree for helpful discussions and for making the lab a friendly and fun environment to work in.

Thank you also to other members of the ICR who have made my time here enjoyable and helped out throughout my thesis. Further I must thank Theo Roumeliottis and Jyoti Choudhary for performing the proteomics experiments, Nicola Ferrari for providing me with the CAAX-GFP tag, David Robertson and Innes Clatworthy for scanning electron microscopy, as well as Steen Hansen (Boston Children's Hospital) for kindly providing me with the DOCK5 antibody.

I would like to thank my examiners Rafael Carazo-Salas and Vicky Sanz-Moreno for their time and expertise, and for comments on this thesis.

Importantly, I would also like to thank my family and friends. In particular my parents Pedro Pascual and Teresa Vargas, who have provided and continue to provide endless support, for always believing in me, for all their love, and without whom I would not be where I am today. Thank you to the Keane/Tomkins for being my family here, for providing me with a home in this country (literally), and for your support throughout this PhD, especially Joe Keane – thank you for keeping me sane and always believing in me. Also, thank you for everything Nacho Medina Fernández.

Lastly, thank you Cancer Research UK and Stand up to Cancer for funding this project, and all those who continue to raise money for this charity and make projects like this possible.

Abstract

Dynamical remodelling of the cytoskeleton is essential for triple negative breast cancer metastasis (TNBC). Cell shape is regulated by RhoGEFs which activate Rho GTPases resulting in changes in actin polymerisation, contractility, and adhesion. The transcriptional coactivators YAP/TAZ are key effectors of RhoGEF-Rho signalling, which regulate the transcription of genes underpinning invasion. However which RhoGEFs are dysregulated in TNBC, and how they couple TNBC cell shape to YAP/TAZ activity driving invasion is unclear.

To identify RhoGEF/GAPs essential for the cell shape changes driving TNBC, and those that do so by regulating YAP/TAZ, we performed high-throughput RNAi screens of 142 siRNAs targeting human RhoGEF/GAPs. We identified RhoGEF/GAPs which regulate cell shape specifically in the highly metastatic cell line LM2, its less metastatic parental counterpart MDA-MB-231, and in both cell lines. We found that the shape space that LM2 cells explore is very distinct to that of MDA-MB-231. Further, we identified RhoGEFs which regulate YAP/TAZ in LM2, and whether they do so in shape-dependent or independent ways. We also found that more spindly-like TNBC cell lines have high levels of YAP/TAZ activation compared to more spread-like TNBC cell lines. We propose that LM2 cells' ability to dynamically change shape is mediated by a specific set of RhoGEF/GAPs, coupled to their ability to downregulate predominantly active YAP/TAZ in response to their environment, underlies their metastatic nature.

We identified the RhoGEF DOCK5, as a regulator of invasion via YAP/TAZ in LM2 cells. We propose that DOCK5 coordinates leading edge with microtubule dynamics and adhesions, driving invasion through YAP/TAZ, and therefore is an attractive therapeutic target.

Abbreviations

APC	Adenomatous polyposis coli
BL1	Basal-like1
BL2	Basal-like 2
BSA	Bovine Serum Albumin
CAF	Cancer associated fibroblasts
CDC42	Cell division control protein homolog 42
CRB	Apical Crumbs Complex
DHR1	DOCK Homology Region 1
DHR2	DOCK Homology Region 2
DOCK	Dedicatory of cytokinesis
DH	Dbl Homology
DMEM	Dulbecco's Modified Eagle Medium
DMSO	Dimethyl Sulfoxide
DNA	Deoxyribonucleic acid
ECM	Extracellular Matrix
ELMO	Engulfment and motility
EMT	Epithelial to Mesenchymal Transition
FA	Focal Adhesion
FAAS	Focal Adhesion Analysis Server
FAAI	Focal Adhesion Alignment Index
FAK	Focal adhesion kinase
FN	Fibronectin
GAPDH	Glyceraldehyde 3-phosphate dehydrogenase
GDI	Guanine nucleotide dissociation inhibitor
GDP	Guanosine Diphosphate
GFP	Green Fluorescent Protein
GTP	Guanosine Triphosphate
GSK3β	Glycogen synthase kinase 3 beta
HER-2	Human Epidermal Growth Factor Receptor Type 2
HPLC	High Performance Liquid Chromatography
IAA	Iodoacetamide
IM	Immunomodulatory
KIF5B	Kinesin-1 heavy chain
LATS1/2	Large tumour suppressor 1/2
LC-MS/MS	Liquid Chromatography Mass spectrometry
LiCl	Lithium Chloride
LINC	Linker of nucleoskeleton and cytoskeleton
M	Mesenchymal
MAL	Myocardin-related
MAPK2	Mitogen activated protein kinase kinase
MAPK4	Mitogen activated protein kinase 4
MSL	Mesenchymal Stem-like
MST1/2	Mammalian STE20-like kinase 1/2
NF2	Neurofibromatosis type 2
OTP	OnTARGET*Plus*
PAK	p21-activated kinase
PARP	Poly ADP-ribose polymerase
PCNA	Proliferating cell nuclear antigen

PH	Pleckstrin Homology
PHH3	Phospho histone H3
PI3K	phosphatidylinositol 4,5-bisphosphate 3-kinase
qRTPCR	quantitative Real Time Polymerase Chain Reaction
RAC	Ras-related C3 botulinum toxin substrate 1
RHO	Ras homolog gene family
ROCK	Rho-associated Kinase
RhoGAP	Rho GTPase associated proteins
RhoGDI	Rho GDP-dissoaciation inhibitor
RhoGEF	Rho Guanine Nucleotide Exchange Factor
Rho GTPase	Rho Guanine Triphosphatase
ROCK	Rho-associated coiled-coil forming kinases
RPMI	Roswell Park Memorial Institute
RNA	Ribonucleic Acid
RNAi	Ribonucleic Acid Interference
SAV	Salvador
SDC	Sodium deoxycholate
SEM	Scanning electron microscopy
siRNA	Small interfering Ribonucleic Acid
SoRa	Super-Resolution via Optical-Reassignment
SRF	Serum response factor
TAZ	Transcriptional co-activator with PDZ-binding motif
TB	TEAD transcription factor-binding domain
TEAB	Triethylammonium bicarbonate
TEAD	Transcriptional enhancer activator DNA-binding
TCEP	Tris-2-carboxyethyl phosphine
TIRF	Total Internal Reflection Fluorescence
TGF-β	Transforming growth factor-beta
TNBC	Triple Negative Breast Cancer
TMT	Tandem Mass Tag
WWTR1	WW domain containing transcription regulator 1
YAP	Yes-associated protein

Table of contents

Chapter 1 Introduction *13*

1.1 Triple negative breast cancer and the metastatic process **13**

1.1.1 Overview of triple negative breast cancer 13

1.1.2 The metastatic process 14

1.1.3 Triple negative breast cancer subtype characterisation 16

1.2 Rho GTPase signalling pathways **18**

1.2.1 Rho-family of GTPases 18

1.2.2 RhoGEFs 19

1.2.3 RhoGEFs and Rho GTPases in cancer 23

1.3 YAP/TAZ signalling and cancer **31**

1.3.1 Hippo-mediated regulation of YAP/TAZ 32

1.3.2 YAP/TAZ are mechanotransducers 33

1.3.3 RhoGEF-Rho signalling control of YAP/TAZ 34

1.3.4 YAP/TAZ regulation in cancer. 36

1.4 Aims of thesis: **40**

2.1. Cell culture **42**

2.1.1 Cell lines 42

2.1.2 Transfections 43

2.1.3 Generation of CAAX-GFP tagged cell lines via lentiviral transduction 46

2.1.4 Drug treatments 46

2.2 High throughput RNA interference screening **48**

2.2.1 Overview of RNAi screening methodology 48

2.2.3 Plating siRNAs and reverse transfections 50

2.2.4 Immunofluorescence staining and confocal imaging 51

2.2.5 Data collection and analysis 52

2.3 Nucleic acid manipulations **57**

2.3.1 Quantitative Real-Time PCR (qRTPCR) 57

2.4 Protein manipulations **58**

2.4.1 Western blotting 58

2.4.2 Subcellular fractionation 59

2.4.3 Mass spectrometry 61

2.5 Microscopy 64

2.5.1 Immunofluorescence and confocal microscopy 64

2.5.2 Focal adhesion dynamics and Total Internal Reflection Fluorescence Imaging (TIRF) 67

2.5.3 Spreading assay and Super-Resolution via Optical-Reassignment (SoRa) microscopy 68

2.5.3 Scanning Electron Microscopy (SEM) 69

2.6 *In vitro* functional assays 69

2.6.1 3D collagen invasion assay 69

2.6.2. Spheroid invasion assay 71

2.6.3 Wound heal assay 72

2.6.4 Growth curve assay 72

2.6.5 Viability assay 73

2.7 Statistical analyses 73

Chapter 3 RNAi screens for regulators of cell shape and YAP/TAZ localisation in MDA-MB-231 and LM2 75

3.1 Introduction 75

3.2 Results 77

3.2.1 Overview of RNAi screens and automated single-cell analysis workflow in 2D 77

3.2.2 Quantification of YAP/TAZ ratio. 78

3.2.3 Technical validation of screens. 83

3.2.4 Linear classification of shapes 89

3.2.5 Filtering and shape hit identification 91

3.2.6 Analysis of hits across screens 96

3.2.7 Clustering of high-dimensional quantitative morphological signatures based on the effect of RhoGEF/GAPs and Rho GTPase siRNAs on the TNBC cell line LM2. 106

3.2.8 Conserved versus non conserved interactions in MDA-MB-231 and LM2. 112

3.3 Discussion 117

Chapter 4 RhoGEF regulation of YAP/TAZ in TNBC cell lines 123

4.1 Introduction 124

4.2 Results 129

4.2.1 Comparison of basal YAP/TAZ localisation in panel of breast cancer cell lines 129

4.2.2 RhoGEFs which regulate YAP/TAZ localisation 132

4.2.3 Clustering of YAP/TAZ ratios as a result of RhoGEF/GAPs and RhoGTPase siRNAs on the TNBC cell lines LM2, MDA-MB-231, SUM159, and hs587t. 138

4.2.4 Identifying how cell shape varies across cell lines and predicting YAP/TAZ ratio from cell shape. 143

4.2.5 Understanding the phenotype of RhoGEFs that were hits for YAP/TAZ ratio hits in LM2 150

4.3 Discussion 157

Chapter 5 DOCK5 coordinates leading edge with microtubule dynamics and adhesions, driving invasion through YAP/TAZ 163

5.1 Introduction 164

5.2 Results 166

5.2.1 DOCK5 regulates TNBC cell shape and YAP/TAZ localisation 166
5.2.2 *DOCK5* depletion reduces single cell invasion in 3D collagen assays 170
size, and we hypothesise that this decrease in invasion could be due to a lack of front rear polarity and consequent decreased YAP/TAZ ratio. 173
5.2.3 *DOCK5* depletion reduces invasion in Matrigel spheroid assays 173
5.2.4 *DOCK5* depletion reduces wound closure migration rates and affects Golgi orientation 175
5.2.5 *DOCK5* depletion alters focal adhesion dynamics 177
5.2.6 DOCK5 depletion alters protein levels of regulators of front rear polarity and of the cell cycle 181
5.2.7 DOCK5 regulation of focal adhesion dynamics is not RAC1 dependent 198
5.2.9 Inhibiting focal adhesion turnover, and contractility, further reduces YAP/TAZ ratio in si*DOCK5* background 200
5.2.10 *DOCK5* depletion effect on growth 205
5.2.11 Inhibition of mutant KRAS (G13D) signalling and knockdown of *DOCK5* in TNBC cells is synthetic lethal. 209
5.2.12 *DOCK5* depletion results in nucleus uncoupling from cytoskeleton 211

5.3 Discussion 216

Chapter 6 Discussion 222

6.1 Key contributions of this thesis 223

6.2 Limitations of this thesis 225

6.2.1 RNAi screens for regulators of cell shape and YAP/TAZ localisation in MDA-MB-231 and LM2 225
6.2.2 Regulation of YAP/TAZ in TNBC cell lines 228
6.2.3 DOCK5 coordinates leading edge with microtubule dynamics and adhesions, driving invasion through YAP/TAZ 228

6.3 Future directions 231

Bibliography 237

Appendices 262

Appendix 1: Software and equipment 263

Appendix 2 Validation that YAP/TAZ antibody binds both to YAP and TAZ via western blotting 264

Appendix 3 siRNAs do not decrease viability in LM2, MDA-MB-231, siGENOME or OTP screens. 265

Appendix 4: RhoGEF/GAP hits for LM2 and MDA-MB-231 266

Appendix 5: Averaged percentage Z-scores for LM2 and MDA-MB-231 OTP and siGENOME screens 274

Appendix 6 YAP/TAZ ratio versus density in SUM159 and hs578t screens 291

Appendix 7: YAP/TAZ ratio Z-scores for LM2 and MDA-MB-231. 334

Appendix 8 Observed-predicted scores for YAP/TAZ ratio for SUM159 and hs578t screens. 335

Appendix 9 Shape filtering in SUM159 346

Appendix 10 Shape filtering in hs578t 347

Appendix 11 Validation of DOCK5 siRNA knockdown 348

Appendix 12 Beta catenin increase in response to LiCl treatment 349

Appendix 13 Hegde's g values for Figure 5.7 DOCK5 regulation of focal adhesion dynamics is not RAC1 dependent Chapter 5 350

Appendix 14 siGENOME RhoGEF/GAP siRNA catalogue numbers and sequences 351

Appendix 15 ONTARGETPlus RhoGEF/GAP and Rho GTPase siRNA catalogue numbers and sequences.....361

Appendix 16 Automated segmentation for collagen invasion quantification 389

Chapter 1 Introduction

Chapter 1 Introduction

1.1 Triple negative breast cancer and the metastatic process

1.1.1 Overview of triple negative breast cancer

Breast cancer is the most commonly diagnosed cancer and the 4th most common cause of cancer-related death in the UK. In the UK, around 55,200 new breast cancer cases are diagnosed and 11,400 breast cancer deaths are reported per year (Cancer Research UK, 2015). Triple negative breast cancer (TNBC) encompasses 15-20% of all breast cancer types (Anders and Carey, 2009; Lehmann et al., 2011). TNBC has a higher prevalence among young premenopausal African American (Carey et al., 2006) and Hispanic women of low socioeconomic status (Bauer et al., 2007; Cancello et al., 2010). TNBCs are diagnosed at later stages, are generally larger in size and of a higher grade, and are biologically very aggressive (Bauer et al., 2007; Haffty et al., 2006). TNBC patients have shorter, relapse-free survival times (Perou et al., 2000), and they have a shorter median time from relapse to death (Dent et al., 2007). However, if TNBC patients have been disease free for 5 years, their risk of recurrence decreases over the subsequent 10 years (Reddy et al., 2018).

TNBC is characterised by a lack of progesterone, estrogen receptor expression, as well as human epidermal growth factor receptor type 2 (HER-2) amplification (Foulkes et al., 2010; Hudis and Gianni, 2011). These characteristics make TNBC clinically challenging to treat as it does not respond to endocrine therapies or available targeted therapies, making chemotherapy the mainstay option for treatment (Hudis and Gianni, 2011). One of the first molecular insights into TNBC

was that they are likely to arise in patients with mutations in the DNA damage repair gene *BRCA1* (D'Andrea and Grompe, 2003), and that TNBCs have gene expression profiles similar to those of *BRCA1*-deficient tumours (Haffty et al., 2006). Current treatments include neoadjuvant chemotherapy, Poly ADP-ribose polymerase (PARP) inhibitors for patients with *BRCA1* or *BRCA2* mutations, and immunotherapy (atezolizumab) combined with chemotherapy for patients expressing immune checkpoint protein PD-L1 (Marra et al., 2019).

1.1.2 The metastatic process

TNBCs are highly metastatic, spreading primarily to the lungs (40%), brain (30%), liver (20%), and bone (10%) (Foulkes et al., 2010). Metastasis is a complex process characterised by the spreading of cells from a primary tumour to secondary sites (Lambert et al., 2017; Talmadge and Fidler, 2010). The metastatic process involves a series of steps beginning with the degradation of the extracellular matrix (ECM) and invasion of surrounding tissues, followed by intravasation and spreading through the blood and lymphatic systems, and ending with extravasation and colonisation of secondary sites (Chaffer and Weinberg, 2011; Vial et al., 2003). Cancer cells need to remodel their cytoskeleton to metastasise (Fife et al., 2014; Kass et al., 2007; Wirtz et al., 2011).

One classic example of the dramatic cytoskeletal rearrangements cells can perform during the metastatic process, is when cells undergo the epithelial to mesenchymal transition (EMT) to drive tissue invasion. During EMT, epithelial

cells lose their cuboidal appearance, become more elongated and mesenchymal-like (Dongre and Weinberg, 2019; Polyak and Weinberg, 2009). Following EMT tumour cells are more motile, can detach from the primary tumour, and invade the surrounding tissue (Thiery and Sleeman, 2006).

During intravasation and extravasation, cells have been shown to remodel their cytoskeleton: first so as to be able to squeeze between endothelial cells to enter the blood vessels by generating invadopodia which are specialised actin-rich protrusions required for invasion and migration (Gligorijevic et al., 2012), and then to extravasate where they must arrest and adhere via focal adhesions to the endothelial layer and generate invadopodia to exit the vasculature and enter the matrix of another tissue (Leong et al., 2014; Williams et al., 2019). The latter of which also requires cells to remodel their cytoskeleton to adhere to their environment requiring focal adhesion and integrin engagement for survival (Shibue et al., 2012; Shibue and Weinberg, 2009). Changes in cytoskeletal organisation also drive invasion in cell types that do not undergo an obvious EMT. In some cell types, such as melanoma cells, metastasis is in part due to the ability of these cells to convert between amoeboid and mesenchymal forms of migration; characterised by rounded cells with blebs and elongated cells dependent on proteases respectively (Cooper et al., 2015; Sahai and Marshall, 2003; Sanz-Moreno et al., 2008; Sanz-Moreno and Marshall, 2010; Tozluoğlu et al., 2013; Wolf et al., 2013).

Although a great deal of progress has been made in the characterisation of metastasis, it remains poorly understood. For example, it is unclear whether

different genes become dysregulated during the metastatic cascade, or whether metastasis is driven by oncogenes and tumour suppressor genes activated earlier on in tumourigenesis (Bernards and Weinberg, 2002; Lambert et al., 2017; Talmadge and Fidler, 2010; Vial et al., 2003).

Metastasis is the leading cause of death of breast cancer patients (Lambert et al., 2017; Vanharanta and Massagué, 2013; Weigelt et al., 2005). Therefore, uncovering the signalling pathways that govern the cell shape changes required for metastasis will open up therapeutic avenues to prevent cancer cells from changing shape, preventing metastasis and consequently reducing the number of patient deaths.

1.1.3 Triple negative breast cancer subtype characterisation

By analysing gene expression profiles of 21 breast cancer data sets Lehmann et al., 2011 classified TNBC into 6 subtypes based on their different gene expression and ontologies: basal-like (BL1 and BL2), immunomodulatory (IM), mesenchymal (M), mesenchymal stem-like (MSL) and luminal androgen receptor (LAR) subtype (Lehmann et al., 2011). BL1 and BL2 are characterised by upregulated expression of cell cycle and cell division pathways, IM by upregulation of immune cell signalling pathways, and LAR by upregulation of hormone-regulated pathways. Both the M and the MSL subtypes are characterised by upregulation of genes involved in the regulation of the actin cytoskeleton by Rho GTPases, ERK, TGFβ, and Wnt signalling, as well as EMT-associated genes, TAZ, and focal adhesion components.

Patients with the M and MSL subtypes have decreased 5-year distant metastasis-free survival (Lehmann et al., 2011). We hypothesise that it is the upregulation of Rho GTPase signalling that confers M and MSL subtypes' invasive capabilities via regulation of cell shape. Therefore, Rho GTPase signalling components could be attractive therapeutic targets for TNBC.

To identify genes that mediate lung metastasis, Minn et al., 2005 performed a transcriptomic microarray analysis of the highly metastatic LM2 population and its less metastatic parental cell line MDA-MB-231, to generate a gene-expression signature associated with lung metastasis. To obtain the highly metastatic LM2 population, Minn et al., 2005 injected an *in vivo* isolate sub-line (1834) of MDA-MB-231, with no enhancement in bone metastatic behaviour and limited metastatic ability, into the tail vein of immunocompromised mice. Then they and reinoculated expanded 1843-derived lung lesions in cell culture (LM0) into mice, obtaining the highly metastatic second-generation population LM2 after two more rounds of *in vivo* selection. The metastatic lung signature was composed of 54 genes specifically upregulated or downregulated in LM2 compared to MDA-MB-231, which encode extracellular growth and survival factors, chemokines, cell adhesion receptors, extracellular proteases, intracellular enzymes and transcriptional regulators. Minn et al., 2005 confirmed that the signature they identified correlates with the development of lung metastasis in primary breast cancers which are clinically aggressive, estrogen and progesterone receptor negative, and of a basal subtype (Minn et al., 2005). Therefore, MDA-MB-231

and LM2 are ideal cell lines to study morphological changes required for metastasis.

1.2 Rho GTPase signalling pathways

1.2.1 Rho-family of GTPases

Rho GTPases are the master regulators of cell shape in all eukaryotic cells, and their dysregulation has been linked to metastasis (Amin et al., 2013; Sahai and Marshall, 2002; Vega and Ridley, 2008). However, there is little understanding as to how dysregulated Rho GTPase activity leads to metastasis.

Twenty-two mammalian Rho GTPase family members have been identified (Jaffe and Hall, 2002). One of the main cellular functions of Rho GTPases is the regulation of the cytoskeleton and adhesion dynamics during cell migration (Jaffe and Hall, 2005, 2002; Sadok and Marshall, 2014). The most well-studied Rho GTPases are RHOA, RAC1, and CDC42, which both cooperate with or antagonise each other to control cellular behaviours. Studies have shown that RAC1 drives lamellipodium formation at the leading edge of migrating cells; RHOA controls actomyosin contractility and stress fibre formation; while CDC42 establishes front-rear polarity and promotes formation of filopodia, as well as regulating contractility (Calvo et al., 2013; Etienne-Manneville and Hall, 2003; Gadea et al., 2008; Hall, 1998; Pertz et al., 2006; Ridley, 2012, 2004; Calvo et al., 2011)

Rho GTPases act as molecular switches, cycling between an inactive guanosine diphosphate (GDP)- bound state, and an active guanosine triphosphate (GTP)-

bound state (Ridley, 2012). These states are regulated by Rho Guanine Nucleotide Exchange Factors (RhoGEFs), which catalyse the exchange of GDP for GTP, and Rho Guanine Activating Proteins (RhoGAPs), which induce GTP hydrolysis (Figure 1.1). Rho GTPases are also regulated by Rho guanine nucleotide-dissociation inhibitors (GDIs) which promote cytosolic sequestration of Rho GTPases and inhibit nucleotide exchange (Burridge and Wennerberg, 2004). Multiple GEFs and GAPs can regulate each Rho GTPase, and many GEFs and GAPs display activity towards more than one Rho GTPase (Jaffe and Hall, 2005). When bound to GTP, Rho GTPases interact with downstream targets, inducing a variety of cellular responses which include regulation of the cytoskeleton, front-rear polarity, vesicle trafficking, transcription, and migration (Ridley, 2012).

1.2.2 RhoGEFs

There are 82 RhoGEFs in the human genome, which are encoded by two unrelated gene families: the Dbl family and the dedicator of cytokinesis (DOCK) family. Dbl-family RhoGEFs are characterised by a catalytic Dbl homology (DH) domain immediately adjacent to a regulatory C-terminal pleckstrin homology (PH) domain (Rossman et al., 2005). DH domains are responsible for the catalytic exchange of GDP for GTP *in vivo*, while DH-associated PH domains can bind to phosphoinositides or other phospholipids thereby localising RhoGEFs to plasma membranes. Most DH-PH domains are flanked by various protein-protein and protein-lipid interaction domains, which help regulate RhoGEFs' catalytic activity, intracellular localisation, and interaction with other proteins (Goicoechea et al., 2014; Rossman et al., 2005). Both Dbl and DOCK family of RhoGEFs contain

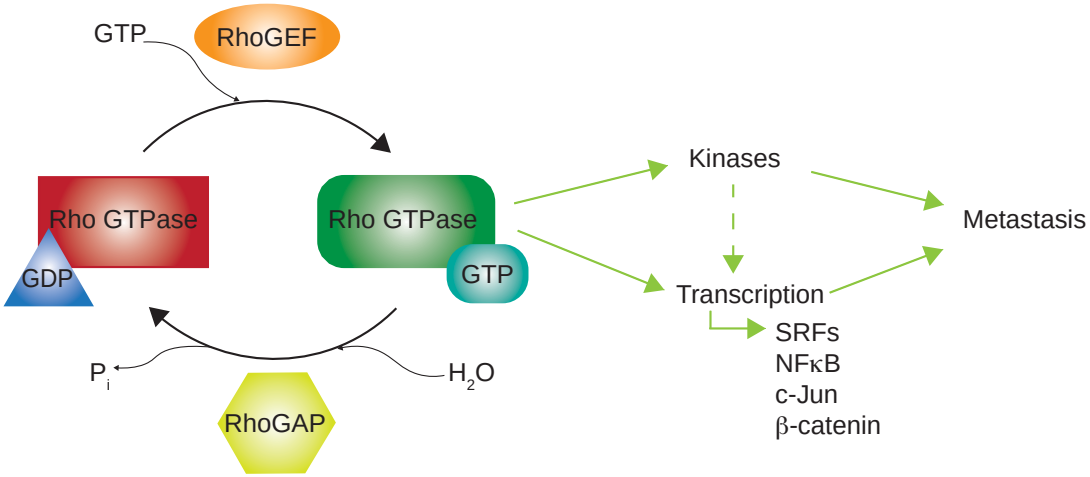

Figure 1.1: Rho GTPases are key regulators of cell shape.

Schematic representation of Rho GTPases cycling between an inactive GDP-bound state and an active GTP-bound state. RhoGEFs catalyse the exchange of GDP for GTP, while RhoGAPs induce GTP hydrolysis. Rho GTPases can regulate the cytoskeleton to promote metastasis by activation of effector kinases or by inducing transcription.

additional domains such as SH2 and/or SH3 which allow them to mediate interaction with membranes or proteins (Bos et al., 2007; Fort and Blangy, 2017; Rossman et al., 2005).

RhoGEFs act downstream of cell surface receptors such as growth factor receptors, integrins, cytokine receptors, and cadherins to stimulate the exchange of GDP for GTP in Rho GTPases in response to fluctuations in the extracellular environment, such as changes in growth factors, or changes in extracellular matrix stiffness (Fife et al., 2014; Rossman et al., 2005). Rho GTPase effector molecules can be kinases or scaffold proteins, whose activation results in remodelling of the cytoskeleton (Sahai and Marshall, 2002). The best described effector kinases are the p21-activated kinases (PAKs), which are effectors of CDC42 and RAC, and Rho-associated coiled-coil forming kinases (ROCKs), effectors of RHOA (Sahai and Marshall, 2002).

1.2.2.1 DOCK family of RhoGEFs

DOCK proteins are structurally unrelated to the Dbl-family. They are characterised by two regions of high sequence conservation: DHR1, a 200-250 amino acid phospholipid binding domain which can target DOCK GEFs to the plasma membrane; and DOCK Homology Region 2 (DHR2), a 450-550 amino acid long domain with catalytic GEF activity (Gadea and Blangy, 2014; Rossman et al., 2005). Of note, DHR2 and DH domains share no primary sequence homology and they catalyse nucleotide exchange in mechanistically different ways (Gadea and Blangy, 2014; Goicoechea et al., 2014). Further, all DOCK

proteins dimerise through their DHR2 domain (Yang et al., 2009). DOCK family GEFs have GEF activity towards RAC-type GTPases and CDC42, but not RHOA (Côté and Vuori, 2002; Gadea and Blangy, 2014).

DOCK proteins can be classified into four subgroups based on their sequence similarity and domain organisation. The DOCK-A subgroup is formed by DOCK1, DOCK2, and DOCK5; DOCK-B subgroup contains DOCK3 and DOCK4; DOCK-C contains DOCK6, DOCK7, and DOCK8; and DOCK-D Subgroup is formed by DOCK9, DOCK10, and DOCK11 (Gadea and Blangy, 2014). DOCK-A and DOCK-B subgroups are characterised by containing an amino-terminal SH3 domain which can bind ELMO (engulfment and motility) adaptor proteins, as well as a proline rich carboxy-terminal domain to bind Crk proteins; while those in DOCK-D subgroup contain a PH domain. DOCK-A and DOCK-B proteins are exchange factors for RAC-type GTPases, while DOCK-D proteins are exchange factors for CDC42, and DOCK-C proteins are exchange factors for both (Brugnera et al., 2002; Côté and Vuori, 2002; Gadea et al., 2008; Hiramoto-Yamaki et al., 2010; Meller et al., 2002; Miyamoto et al., 2007; Vives et al., 2011; Xiao et al., 2013).

DOCK5, a member of the DOCK-A subgroup (Gadea and Blangy, 2014), was first described to be required for establishment of the sealing zone and osteoclast resorbing activity by activating RAC1 (Vives et al., 2011) (Figure 1.2B). Further, the same group identified an inhibitor for DOCK5, C21, which blocks the DHR2 catalytic domain of DOCK5, specifically hindering the interaction between DOCK5 and RAC1 (Ferrandez et al., 2017) (Vives et al., 2015) (Figure 1.2B i).

DOCK5 has also been described to regulate mast cell degranulation in a GEF-independent manner, by associating with NCK2 and AKT, whereby this association results in the phosphorylation and inactivation of GSK3β, promoting microtubule assembly (Ogawa el at., 2014) (Figure 1.2A). Interestingly, DOCK5 has very recently been shown to regulate microtubule dynamic instability in osteoclasts through RAC1-dependent (Figure 1.2Bi, ii) and RAC1-independent pathways, the latter being downstream of AKT (Guimbal et al., 2019) (Figure 1.2Biii). In addition DOCK5 has been shown to promote myoblast fusion (Laurin et al., 2008) and neutrophil chemotaxis (Watanabe et al., 2014). Lastly, DOCK5 has been shown to localise to focal adhesions (Müller et al., 2018), where GIT2 suppresses the activity of Crk-p130Cas-DOCK5 pathway which activates RAC1 mediated lamellipodial protrusion and focal adhesion turnover driving invasion in MDA-MB-231 cells (Frank et al., 2017) (Figure 1.2C).

1.2.3 RhoGEFs and Rho GTPases in cancer

Unlike Ras-type GTPases, where activating mutations drive oncogenesis, activation of Rho GTPases does not appear to underpin cancer progression. Large scale sequencing has revealed some sporadic mutations in all 20 Rho GTPases across various cancers. Such as for example *RAC1* has been shown to have mutations resulting in increased spontaneous release of GDP allowing rapid GDP/GTP cycling increasing signal output (Kawazu et al., 2013) in colorectal, breast, lung, thyroid, and pancreatic cancers (Olson, 2018). On the other hand, inactivating mutations have been observed in *RHOA* (Palomero et al., 2014), suggesting an interplay between decreased RHOA activity and an

increase in RAC1 activity driving tumourigenesis (Olson, 2018). Although in melanoma for example, a RAC1P29S mutation present in 4% of patients which leads to a fast cycling mutant inducing a mesenchymal phenotypic switch via SRF has not biochemically been shown to inhibit RHOA activity (Lionarons et al., 2019)."At the same time, gain of function mutations in RHOA have been observed such as that in *RHOA Y42C* in diffuse gastric cancer which results in impaired GTP hydrolysis and enhanced interaction with its effector ROCK and consequent activation of FAK (Zhang et al., 2019). Further, the RHOA G17V mutation has been shown to drive proliferation promoting lymphomagenesis by inducing specification of T cells (Cortes et al., 2018).

Rho GTPases are most commonly activated aberrantly by indirect mechanisms in cancer, which include increased RhoGEF activity, decreased RhoGAP activity, altered gene expression of Rho GTPases, RhoGEFs, RhoGAPs, RhoGDIs, and alternative splicing which generate constitutively active Rho GTPase isoforms (such as RAC1B) (Cook et al., 2014; Jordan et al., 1999; Schnelzer et al., 2000). Indeed, the mRNA and/or protein levels of Rho GTPases such as RHOA, RHOC, RAC1-3, CDC42, RHOV, and RHOF, are often upregulated in cancer (Aronheim et al., 1998; Gouw et al., 2005; Pulgar et al., 2005; Vega and Ridley, 2008). Although RHOA, RHOB and RHOC are closely related, they have been shown to be activated by different stimuli and effect differential functions on migration and invasion (Ridley, 2013). For example, RHOA activity has been shown to be required for migration and invasion (Carr et al., 2013; Jaffe and Hall, 2002), and overexpression has been observed in breast, lung, colon, testicular germ cell, and head and neck squamous-cell carcinoma (Sahai and Marshall, 2002). On the

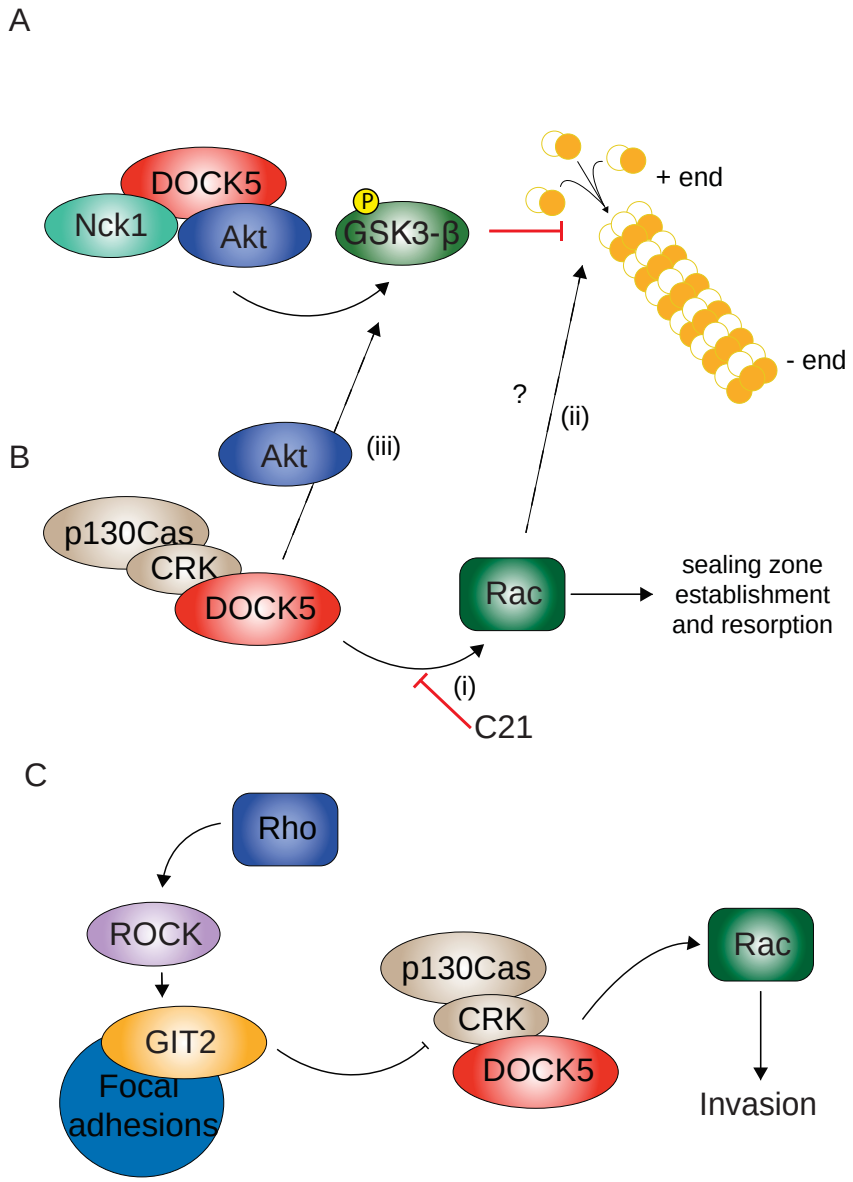

Figure 1.2: DOCK5 signalling pathways.
(A) Schematic representation of DOCK5 regulating mast cell degranulation in a GEF-independent manner by associating with NCK2 and AKT, resulting in the phosphorylation and inactivation of GSK3β, releasing GSK3β's inhibition on microtubule polymerisation (Ogawa el at., 2014). (B) Schematic representation of DOCK5 regulating establishment of the sealing zone and osteoclast resorbing activity in RAC and p130-Crk-dependent manner (Vives et al., 2011). (i) C21 inhibits the interaction between DOCK5 and RAC1 (Ferrandez et al., 2017), preventing bone degradation (Vives et al., 2011). (ii) DOCK5 regulation of microtubule dynamic instability in osteoclasts through RAC1-dependent and (iii) RAC1-independent pathway downstream of AKT (Guimbal et al., 2019). Question mark indicates that the mechanism is not fully described. (C) Rho-dependent activation of ROCK targets GIT2 to focal adhesions where it suppresses the activity of Crk-p130Cas-DOCK5 pathway required to activate RAC1-mediated lamellipodial protrusion and focal adhesion turnover, and mammary epithelial cell invasion (Frank et al., 2017).

other hand RHOB has been shown to regulate cancer cell migration by regulating focal adhesion dynamics by altering β1 integrin expression (Alfano et al., 2012; Vega et al., 2012). Interestingly, RHOA and RHOB have been shown to increase invasion in some cancer types and decrease invasion in others (Simpson et al 2004, Ridley, 2013). Further RHOC has been shown to be required for metastasis (Hakem et al., 2005). RHOC mRNA and protein expression is increased during EMT in ovarian carcinoma cells (Gou et al., 2014) and in a colon cancer model (Bellovin et al., 2006). In breast cancer, overexpression of RHOC is linked to poor prognosis and has been especially linked to highly metastatic inflammatory breast cancers (Kleer et al., 2005; Lang et al., 2017; van Golen et al., 2002, 2000).

Upregulation of RhoGEF expression has also been observed in various cancers. Specifically, breast tumour tissue has been shown to have significantly higher mRNA and/or protein levels of the RhoGEFs TIAM1, TRIO, VAV1, PREX1, and DOCK1 than normal breast tissue, and is associated with poor prognosis (Adamowicz et al., 2006; Cook et al., 2014; Gatza et al., 2014; Lane et al., 2008; Laurin et al., 2013; Sosa et al., 2010). For example DOCK1 interacts with HER2 and promotes HER2-induced RAC1 activation and cell migration essential for HER2-mediated breast cancer progression and metastasis (Laurin et al., 2013). In addition, other RhoGEFs have been shown to play roles in breast cancer such as ARHGEF18 (Terry et al., 2012), ARHGEF7 (Heidary Arash et al., 2014; Kutys and Yamada, 2014) and ARHGEF2 (Liao et al., 2012). Where, for example ARHGEF18 has been shown to be required for efficient migration, driving

invasion through RHOA in breast cancer cell lines in 3D matrices (Terry et al., 2012).

TIAM1, TRIO, VAV1, and PREX1 have also been found to be mutated in some cancers (Cook et al., 2014; Rossman et al., 2005). Other examples of mutated RhoGEFs include BCR, LARG (ARHGEF12), MCF2, ECT2, PREX2, ARHGEF5, OSCN, and FGD5 (Cook et al., 2014; Debily et al., 2004; Rossman et al., 2005). For example, mutations in *OBSCN* have been identified in breast and colon cancers by exome sequencing (Sjöblom et al., 2006), and loss of *OBSCN* in the breast epithelium has been shown to lead to tumours, EMT, and metastasis (Shriver et al., 2015). Further, *FGD5* has been found to be uniquely amplified in patients with highly proliferative luminal breast tumours (Gatza et al., 2014).

RhoGEFs are attractive therapeutic targets for TNBC because they are important context-specific regulators of Rho GTPase activity (Bouquier et al., 2009; Cook et al., 2014), and therefore of metastatic processes upregulated specifically in the M and MSL TNBC subtypes (Figure 1.3). Although the development of RhoGEF inhibitors has been largely unexplored, the fact that the natural ARFGEF inhibitor brefeldin A inhibits ArfGEF's catalytic domain for GDP to GTP exchange (Cook et al., 2014; Peyroche et al., 1999; Robineau et al., 2000) suggests that RhoGEFs can be directly targeted. Indeed, some small molecule inhibitors that target Rho GTPases at the RhoGEF interacting site, thus blocking the interaction, have been developed (Gao et al., 2004; Hocker et al., 2013; Maurer et al., 2012; Shang et al., 2013, 2012; Sun et al., 2012). For instance, the chemical compound NSC23766 was identified to block RAC-specific activation by the RhoGEFs TRIO

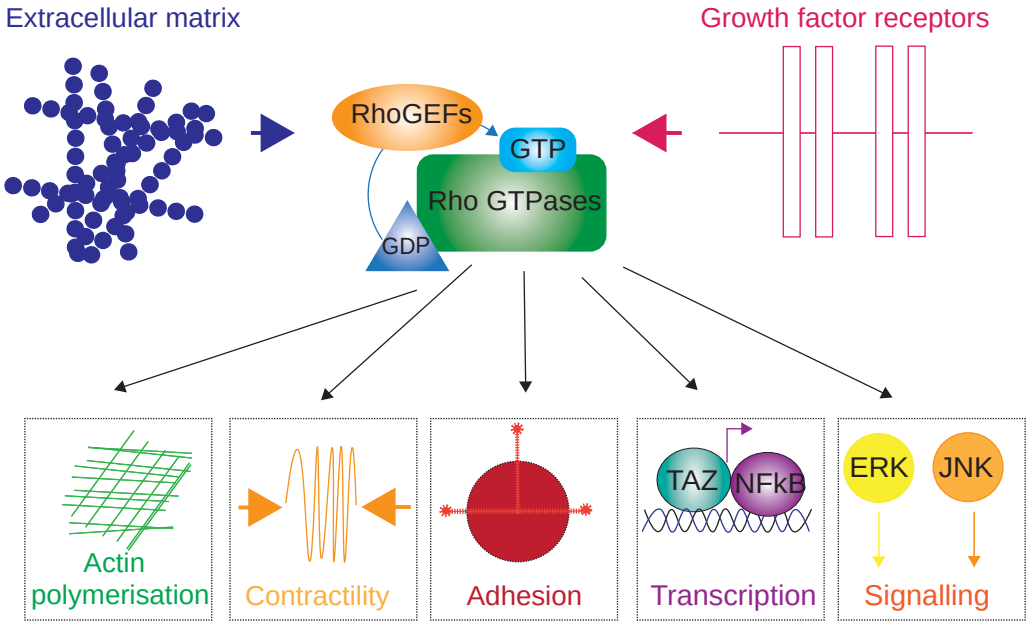

Figure 1.3: RhoGEFs are attractive therapeutic targets for TNBC because they are important context-specific regulators of Rho GTPase activity
Schematic representation of RhoGEF activation of Rho GTPases in response to fluctuations in the microenvironment resulting in the regulation of actin polymerisation, contractility, adhesion, transcription and signalling pathways, upregulated in the M and MSL TNBC subtypes.

and TIAM1 in a dose-dependent manner (Gao et al., 2004). However, RhoGEFs are a large family of signalling enzymes (82 members) (Hall, 2009) and which RhoGEFs should be targeted in TNBC is still unclear.

1.2.3.1 RhoGEFs and Rho GTPases regulate transcription

RhoGEF-Rho GTPase signalling can lead to cell shape changes by regulating the cytoskeleton and by regulating transcription (Bos et al., 2007; Jaffe and Hall, 2002; Vega and Ridley, 2008). RHOA, RAC1 and CDC42 have been shown to stimulate the activity of Jun transcription factors and serum response factor (SRF), the latter of which is the best characterised pathway between Rho GTPases and transcription (Ridley, 1996; Vega and Ridley, 2008). Rho GTPases decrease the levels of actin monomers, which are required to bind to an inhibitory nuclear import of the SRF cofactor myocardin-related MAL, leading to nuclear translocation of MAL and consequent increased SRF-mediated transcription of *FOS* (Miralles et al., 2003), leading to cytoskeletal reorganisation (Jaffe and Hall, 2002) and invasion (Medjkane et al., 2009). Further, RHOA, RAC1, and CDC42 have been shown to regulate *c-jun* NH2-terminal kinase (JNK) and p38 mitogen activated pathways resulting in *c-JUN* transcriptional activity (Bishop and Hall, 2000; Coso et al., 1995; Marinissen et al., 2001; Minden et al., 1995). For example, RAC1 activation of JNK2 kinase can result in the phosphorylation of β-catenin, driving it into the nucleus and promoting β-catenin transcription (Jamieson et al., 2015; Schlessinger et al., 2009; Wu et al., 2008). In addition, Rho GTPases have also been shown to regulate transcription of NF-kB (Gastonguay et al., 2012; Sero et al., 2015).

Because RhoGEFs activate the signalling pathways whose components are upregulated in the M and MSL TNBC subtypes, we hypothesise that it is dysregulated RhoGEF activity that drives invasion in these cancers.

1.3 YAP/TAZ signalling and cancer

YAP and TAZ are two transcriptional coactivators which are regulated by geometrical and mechanical cues from the tumour microenvironment (Piccolo et al., 2014). YAP and TAZ share 46% sequence homology and display similar domain organisation (Hong and Guan, 2012). YAP and TAZ both have a TEAD transcription factor-binding domain (TB), a transactivation domain (TAD), a coiled-coil domain, and a C-terminal PDZ binding motif (Chen et al., 2019; Dobrokhotov et al., 2018; Halder et al., 2012). They differ in the number of conserved and consistently-positioned tryptophan residues domain (WW domain), which confer signalling specificity: YAP has two WW domains, while TAZ only has one (Varelas et al., 2010). The WW domain is a binding domain for PPXY motifs present in some transcription factors (Makita et al., 2008). Further, specific to YAP are an SH3-binding motif and an N-terminal proline-rich domain (Chen et al., 2019). While they show genetic redundancy in a variety of biological functions, individual knockouts in mice result in different phenotypes (Hong and Guan, 2012; Hossain et al., 2007; Kang et al., 2009; Morin-Kensicki et al., 2006; Tian et al., 2007), and it is unclear how they differ in function.

1.3.1 Hippo-mediated regulation of YAP/TAZ

YAP/TAZ are the principal effectors of the Hippo signalling pathway, an evolutionarily conserved kinase cascade first discovered in *Drosophila* (Justice et al., 1995; Tapon et al., 2002; Wu et al., 2003; Xu et al., 1995), which controls organ size, proliferation, tissue homeostasis, and tumourigenesis (Bao et al., 2011; Moroishi et al., 2015; Pan, 2010; Zhao et al., 2010). The Hippo pathway is composed of a tumour suppressor serine/threonine kinase module, LATS1/2; and an oncogenic transcriptional module, YAP/TAZ. When the Hippo pathway is on, activated LATS1/2 phosphorylate YAP/TAZ which inhibits their activity through cytoplasmic retention by protein 14-3-3, and protein degradation (Moroishi et al., 2015; Ren et al., 2010). Contrary to YAP, TAZ is a very unstable protein with a half-life of under 2 hours, suggesting that degradation is the main form of TAZ inhibition (Piccolo et al., 2014). On the other hand, hypophosphorylated YAP/TAZ shuttle into the nucleus and induce target gene expression. YAP/TAZ primarily interact with transcription factors TEAD1-4 (TEADs) and activate expression of target genes which drive proliferation, growth, and survival (Galli et al., 2015; Stein et al., 2015; Zanconato et al., 2015).

LATS1/2 are phosphorylated and activated by the kinases MST1 and MST2 in cooperation with their binding partner SAV1. LATS1/2 can also be phosphorylated and activated by members of the MAPK4 family of mitogen-activated protein kinases (Li et al., 2014; Meng et al., 2015). NF2 is a potent inhibitor of the Hippo pathway in epithelial cells, where it serves as scaffold for MST1/2 and LATS1/2 kinases at cell-cell junctions (Lallemand et al., 2003; Yin et al., 2013). Further apical-basal polarity is a strong regulator of the Hippo pathway,

where primarily polarity protein Scribble acts as a scaffold for MST-LATS-TAZ complex, favouring YAP/TAZ inhibition (Cordenonsi et al., 2011). Another example is the apical crumbs complex (CRB), which binds to YAP/TAZ promoting their cytoplasmic retention (Varelas et al., 2010).

While the Hippo pathway and apical-basal polarity are the most well described regulators of YAP/TAZ signalling, other signalling pathways including Wnt and GPCR signalling, metabolic pathways, and growth factors and inflammatory signalling also regulate YAP/TAZ (Totaro et al., 2018).

1.3.2 YAP/TAZ are mechanotransducers

YAP/TAZ are mechanotransducers which are regulated by changes in cell shape conveyed by different conformation and tension of the F-actin cytoskeleton (Dupont et al., 2011; Piccolo et al., 2014; Totaro et al., 2018). By experimentally manipulating cell shape and the extracellular matrix, YAP/TAZ have been shown to be nuclear and active when intracellular contractile forces are high, displayed by high ROCK- and non-muscle-myosin-II-driven cytoskeletal tension, such as when cells are allowed to spread, when they are on a stiff ECM, and when they are in matrices they can remodel (Dupont et al., 2011; Halder et al., 2012). In these conditions, YAP/TAZ favour proliferation and osteoblast differentiation (Halder et al., 2012). Conversely, YAP/TAZ have been shown to be cytoplasmic and inactive when overall contractile forces are down such as when they are confined to small adhesive spaces, and when they are on soft matrices (Dupont et al., 2011; Halder et al., 2012). Cytoplasmic YAP/TAZ in these cases leads to apoptosis, growth arrest and differentiation of cells which require soft matrices

such as for example adipocyte differentiation (Halder et al., 2012). Further, cell crowding results in reduced adhesion size resulting in cytoplasmic YAP/TAZ, which explains contact inhibition of proliferation (CIP), where cells stop growing when they reach a critical density (Aragona et al., 2013; Zhao et al., 2007). Overall YAP/TAZ regulation is guided by F-actin subcellular organisation and tension exerted by the cytoskeleton and the nucleus, rather than on total levels of F-actin (Totaro et al., 2018).

In addition, nuclear mechanics also regulate YAP/TAZ. The F-actin cytoskeleton affects nuclear mechanics by connecting through the linker of nucleoskeleton and cytoskeleton (LINC) complex. A recent study has shown that ECM-nuclear mechanical coupling results in YAP nuclear translocation due to increased substrate stiffness resulting in increased nuclear pore permeability (Elosegui-Artola et al., 2017). Furthermore, studies have shown that force application to the nucleus is sufficient for YAP translocation, and that it is perinuclear forces originating from stress fibres around the nucleus, rather than forces acting on peripheral adhesions, that are required for YAP nuclear translocation (Elosegui-Artola et al., 2017; Shiu et al., 2018).

1.3.3 RhoGEF-Rho signalling control of YAP/TAZ

Because the structure and dynamics of the actin cytoskeleton are regulated by Rho GTPases, their activity can regulate YAP/TAZ nuclear translocation, and thus YAP/TAZ transcriptional activity.

Indeed, studies have described Rho GTPase control of YAP/TAZ localisation via LATS-dependent and LATS-independent pathways. For example, CDC42 has

been shown to be required for nuclear YAP in mouse kidney development, most likely in a LATS-independent manner via actin cytoskeletal rearrangement (Reginensi et al., 2013). Further, CDC42 has been described to promote nuclear YAP/TAZ downstream of integrin α3 and FAK in stem cells (Hu et al., 2017). Another example would be increased mevalonic acid in tumour cells resulting in activation of YAP/TAZ required for proliferation and self-renewal of breast cancer cells. Here, geranylgeranyl pyrophosphate produced by the mevalonate cascade in tumour cells, activates Rho GTPases which, in turn activate YAP/TAZ in a LATS and cytoskeletal rearrangement independent manner, by preventing YAP/TAZ phosphorylation and promoting nuclear accumulation (Sorrentino et al., 2014).

On the other hand, integrin-dependent focal adhesion formation where RAC1 activation of its effector PAK1 results in YAP dephosphorylation, triggered by cell adhesion, has been shown to be Hippo-pathway dependent (Sabra et al., 2017). Further, fibronectin has been shown to negatively regulate the Hippo pathway inducing YAP nuclear accumulation via focal adhesion kinase (FAK)-SRC-phosphatidylinositol 4,5-bisphosphate 3-kinase (PI3K) signalling pathway resulting in LATS1/2 phosphorylation and inactivation (Kim and Gumbiner, 2015).

Although little is known regarding RhoGEF-dependent regulation of YAP/TAZ, a few RhoGEFs have been described to regulate YAP/TAZ. One such RhoGEF is ARHGEF7 otherwise known as β-Pix, which regulates YAP/TAZ in a LATS-independent manner (Heidary Arash et al., 2014; Sero and Bakal, 2017). More specifically, β-Pix has been shown to be recruited to focal contacts via association

with Git1/2 and paxillin, and is phosphorylated by Src. At focal contacts β-Pix activates CDC42 promoting a negative feedback cycle of adhesion disassembly and FAK dependent nuclear translocation of YAP in mammary epithelial cells (Sero and Bakal, 2017).

The RhoGEF TRIO has been shown to regulate YAP/TAZ in uveal melanoma. An activating mutation of upstream regulators of Rho GTPases Gαq G proteins results in the activation of TRIO which, by activating RHO and RAC1 results in YAP translocation to the nucleus both by inhibiting LATS and by promoting F-actin rearrangement (Feng et al., 2019, 2014). On the other hand, TIAM1 has been shown to directly block YAP/TAZ-TEAD interaction in the nucleus downstream of Wnt signalling (Diamantopoulou et al., 2017); while ARHGEF17 has been suggested to activate RHOA, promoting contractility via its effector ROCK, downstream of YAP (Lin et al., 2017).

1.3.4 YAP/TAZ regulation in cancer.

As described, YAP/TAZ are regulated by the Hippo pathway, Rho GTPase signalling, apical-basal polarity, Wnt and GPCR signalling, metabolic pathways, growth factors and inflammatory pathways (Totaro et al., 2018). Alterations in these pathways converge to induce YAP/TAZ activity in cancer (Zanconato et al., 2016) (Figure 1.4).

With the exception of inherited disorders associated with the upstream regulator *NF2*, somatic mutations in the core Hippo members are extremely rare in human tumours (Harvey et al., 2013; Piccolo et al., 2014; Wang et al., 2018; Zanconato et al., 2016). Studies have shown YAP amplification in liver (Zender et al., 2006) and breast tumours (Overholtzer et al., 2006), and most recently YAP and TAZ have been shown to have the highest amplification frequency in squamous carcinomas (Wang et al., 2018). Further, TAZ is overexpressed in approximately 85% of high-grade human breast cancers, with gene amplification in 15-20% of cases (Cordenonsi et al., 2011).

Activating mutations in the upstream regulators of Rho GTPases Gαq G proteins, have been shown to activate YAP-dependent cell growth independently of the Hippo pathway (Feng et al., 2019, 2014; Yu et al., 2014). Further, *NF2* loss cooperates with oncogenic RAS to activate YAP in thyroid cancers to promote YAP/TEAD-driven transcription of oncogenic and wild-type RAS (Garcia-Rendueles et al., 2015). On the other hand, YAP and mutant RAS have been shown to converge to regulate EMT and tumour survival, bypassing RAS oncogenic addictions in various cancers, driving drug resistance (Calses et al., 2019; Fisher et al., 2017; Kapoor et al., 2014; Kim et al., 2016; Lin et al., 2015; Shao et al., 2014). Further, genetic alterations and methylation in LATS1/2 have been observed in several cancers (Sanchez-Vega et al., 2018).

YAP/TAZ have also been shown to be activated by cancer metabolic pathways, where for example mevalonic acid activates Rho GTPases which prevent YAP/TAZ phosphorylation, promoting their nuclear accumulation (Sorrentino et al., 2014). In a range of cancer cell lines, TEAD-AP1 cooperation are upstream

regulators of DOCK-RAC/CDC42 component to drive reorganisation of the cytoskeleton, motility and invasion (Liu et al., 2016). In addition, the association of YAP/TAZ-TEAD and API has been shown to drive oncogenic growth (Zanconato et al., 2015).

Loss of polarity is frequently seen in cancer, and is associated with EMT, which can result in the activation of YAP/TAZ and consequently tumourigenesis by disrupting the inhibitory association between TAZ and apical-basal cell-polarity determinant Scribble (Cordenonsi et al., 2011; Diepenbruck et al., 2014; Zanconato et al., 2015). Loss of CIP is displayed in many cancers (Abercrombie, 1979; McClatchey and Yap, 2012), where Hippo is no longer activated by cell to cell contacts, releasing the sequestration of YAP/TAZ by LATS, and allowing YAP/TAZ to enter the nucleus driving proliferation, tumour growth, and metastasis (McClatchey and Yap, 2012). Further, TAZ has been shown to sustain its own activity in breast cancer stem cells by promoting the expression of the laminin the laminin LM511 which results in a matrix niche which in turn activates TAZ (Chang et al., 2015), and ectopic expression of TAZ has been shown to promote EMT (Lei et al., 2008). Another example of a mechanical input which

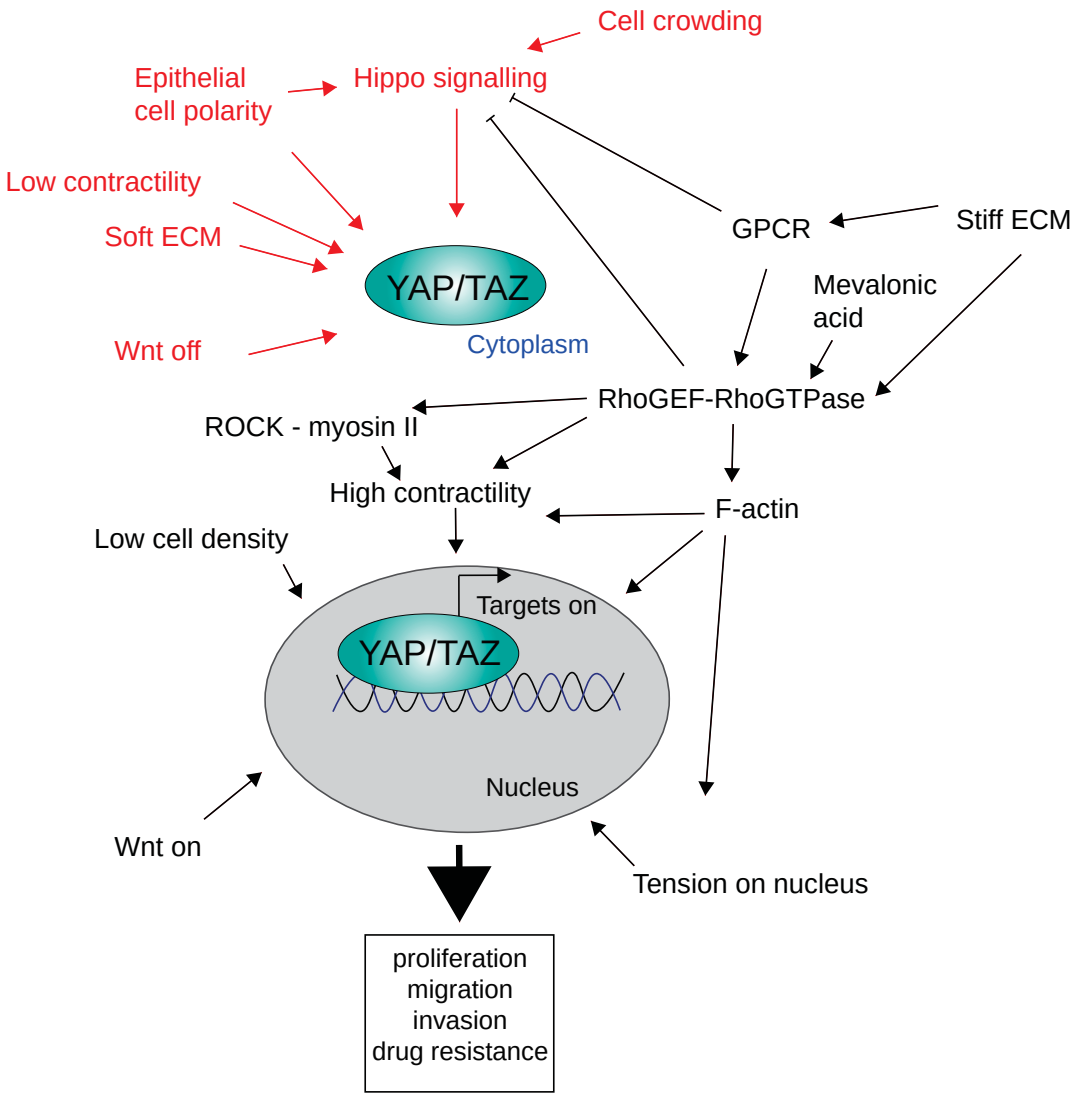

Figure 1.4: Regulatory inputs on YAP/TAZ.
Schematic showing inputs which promote cytoplasmic and inactive YAP/TAZ (in red), and those which promote nuclear and active YAP/TAZ (in black). Nuclear and active YAP/TAZ result in proliferation, migration, invasion, and drug resistance. RhoGEF-Rho GTPase and GPCR inhibitory arrows indicate Hippo signalling inactivation, which promotes nuclear YAP/TAZ.

regulates YAP/TAZ is influenced by altered ECM tissue mechanics in cancer, where, for example, in cancer associated fibroblasts (CAFs), a positive feedback loop has been described where YAP/TAZ directly promote the expression of F-actin modulators, which in turn result in increased contractility, and a stiffer matrix as a result of more collagen deposition (Calvo et al., 2013). This increased matrix stiffness results in more nuclear YAP/TAZ and more expression of F-actin contractility, thus sustaining YAP/TAZ activity in both CAFs and epithelial cells.

Overall, although it is clear that YAP/TAZ play instrumental roles in cancer (Totaro et al., 2018), much remains to be understood about their regulation. The focus of this thesis is on the regulation of RhoGEF-Rho GTPase signalling axis.

1.4 Aims of thesis:

Metastasis is the leading cause of death of TNBC patients. RhoGEFs regulate the cell shape changes which drive metastasis and present attractive therapeutic targets. YAP/TAZ are both sensor and mediators of mechanical signals dictated by the microenvironment and cell shape. However, which RhoGEFs are dysregulated in TNBC, and how they couple TNBC cell shape to YAP/TAZ is unknown. Therefore, in this thesis I aim to understand which RhoGEFs regulate TNBC invasion by regulating cell shape, and which do so by regulating YAP/TAZ using high-throughput RNAi screening. Further, by using a combination of genetic approaches and 3D systems, I aim to describe the mechanism of action of a RhoGEF that is key for cell shape changes and YAP/TAZ activation required for TNBC invasion.

Chapter 2 Materials and Methods

Chapter 2 Materials and Methods

2.1. Cell culture

2.1.1 Cell lines

LM2s (subpopulation 4172 from MDA-MB-231) were obtained from Joan Massagué (Sloan Kettering Institute, New York) (Minn et al, 2005), and stably express a triple-fusion protein reporter construct encoding herpes simplex virus thymidine kinase 1, green fluorescent protein (GFP) and firefly luciferase (Minn et al, 2005). MDA-MB-231 were a gift from Janine Erler (Copenhagen). SUM159 and hs578t were a kind gift from Rachel Ratrajan (ICR).

LM2, MDA-MB-231, SUM159, hs578t cells were grown in Dulbecco's Modified Eagle Medium (DMEM) supplemented with 10% heat-inactivated fetal bovine serum (FBS) and 1% penicillin/streptomycin in T75 falcons.

MCF10A were obtained from ATCC and were grown in DMEM/F12 supplemented with 5% horse serum, 10µg/ml insulin, 20ng/ml epidermal growth factor, 100ng/ml cholera toxin, 500ng/ml hydrocortisone, and 100mg/ml penicillin/streptomyocin in T75 falcons.

T47D were obtained from from Rachel Ratrajan (ICR), and were grown in Roswell Park Memorial Institute (RPM1)-1640 culture medium (Gibco) supplemented with 10% heat-inactivated fetal bovine serum (FBS) and 1% penicillin/streptomycin in T75 falcons.

All cell lines were grown at 37°C and supplemented with 5% CO_2 in humidified incubators. Cells were routinely checked for mycoplasma infection in house by testing the media via PCR. Frozen stocks were kept in medium with 10% DMSO in liquid nitrogen.

2.1.2 Transfections

2.1.2.1 siRNA

All siRNAs were made up to a stock of 20μM. Briefly, for 384 well plates, siRNA reverse transfections were performed by adding 40nL of siRNA to each well followed by 5μl of Opti-MEM® Reduced Serum Media. 5 minutes later 5μl of mix containing Opti-MEM and RNAimax reagent in a 125:1 ratio were added per well. Plates were spun at 1000 rpm for 1 minute, and incubated at room temperature for 20 minutes to allow siRNA-RNAimax complexes to form. Cells were plated on top in 30μL of DMEM (10% FBS, 1% penicillin/streptomyocin), resulting in a total volume of 40μL per well: 40nL siRNA (final concentration of 20nM), 5μL Opti-MEM, 5μL of Opti-MEM and RNAimax mix (125:1) plus 30μL of cells. For transfections performed on 96 well plates and 6 well plates, 4 and 64 times the amounts used for 384 well plates were used, respectively. When siRNAs were transfected in combination, the same amount of each siRNA was used. siRNAs and sequences used can be found in Table 2.1.

Table 2.1: siRNA target sequences

siRNA	Sequences	Catalogue number
DOCK5 OTP pool	GAGGAGAGAUUGUUAAGUU, GAACAUUAAACACAACCUA, GCAAAUUCAUUCAAAGCAU, GGGUUGCGAUCUAUAACUA	# L-018931-00-0005
DOCK5 OTP pool deconvoluted (5-8)	GAGGAGAGAUUGUUAAGUU, GAACAUUAAACACAACCUA, GCAAAUUCAUUCAAAGCAU, GGGUUGCGAUCUAUAACUA	# LU-018931-00-0002
DOCK5 siGENOME pool deconvoluted (1-4)	AGAACUAUCUAAUUCGUUG, GUAACGGGAUGCCCAAGGA, GAGUGGCAGUGAUGGAUAU, UAUCAUACAUGGGAAGGUG	# MU-018931-01-0002
YAP OTP pool	GCACCUAUCACUCUCGAGA, UGAGAACAAUGACGACCAA, GGUCAGAGAUACUUCUUAA, CCACCAAGCUAGAUAAAGA	# L-012200-00-0005
WWTR1 (TAZ) OTP pool	CCGCAGGGCUCAUGAGUAU, GGACAAACACCCAUGAACA, AGGAACAAACGUUGACUUA, CCAAAUCUCGUGAUGAAUC	# L-016083-00-0005
LATS1 OTP pool	GGUGAAGUCUGUCUAGCAA, UAGCAUGGAUUUCAGUAAU, GGUAGUUCGUCUAUAUUAU, GAAUGGUACUGGACAAACU	#L-004632-00-0005
LATS2 OTP pool	GCACGCAUUUUACGAAUUC, ACACUCACCUCGCCCAAUA, AAUCAGAUAUUCCUUGUUG, GAAGUGAACCGGCAAAUGC	#L-003865-00-0005
RHOA OTP pool	CGACAGCCCUGAUAGUUUA, GACCAAAGAUGGAGUGAGA, GCAGAGAUAUGGCAAACAG, GGAAUGAUGAGCACACAAG	# L-003860-00
RAC1 OTP pool	GUGAUUUCAUAGCGAGUUU, GUAGUUCUCAGAUGCGUAA, AUGAAAGUGUCACGGGUAA, GAACUGCUAUUUCCUCUAA	# L-003560-00
RAC2 OTP pool	UGACAACUAUUCAGCCAAU, CCAAGGAGAUUGACUCGGU, CCAAGUGGUUCCCAGAAGU, UGAAAACCGUGUUCGACGA	# L-007741-00

RAC3 OTP pool	AAACUGACGUCUUUCUGAU, ACAAGAAGCUGGCACCCAU, GAAGACAUGCUUGCUGAUC, CGUGAUGGUGGACGGGAAA	# L-008836-00
CDC42 OTP pool	CGGAAUAUGUACCGACUGU, GCAGUCACAGUUAUGAUUG, GAUGACCCCUCUACUAUUG, CUGCAGGGCAAGAGGAUUA	# L-005057-00

2.1.2.2 Plasmid

For transfections with Talin mApple, Effectene Transfection Reagent (Qiagen) was used according to manufacturer's protocol. Briefly, cells were plated at a density of 1.0 x 10^6 cells /ml in 1ml in a 6 well plate. Then, 2.56ng of plasmid were combined with 150µl of EC buffer and vortexed. Then 8µl of Enhancer were added and mix was vortexed. After 10 minutes 5µl of Effectene were added, mix was vortexed again and following another 10 minute wait to allow complexes to form, 1ml of DMEM was added and mixture was dispensed dropwise per well. If siRNA was used as well, cells were reverse transfected as usual. Experiments were performed 48 hours later.

For all other plasmid transfections, either combined with siRNA or otherwise were performed in the same manner as with siRNA transfections but instead of using Lipofectamine RNAiMAX (Thermofisher Scientific), Lipofectamine 2000 (Thermofisher Scientific) was used instead. 2ng of plasmids were transfected.

2.1.3 Generation of CAAX-GFP tagged cell lines via lentiviral transduction

CAAX-GFP tag was a kind gift from Nicola Ferrari (previously Institute of Cancer Research, currently Astex Pharmaceuticals, UK), who generated it in HEK-293 cells using a second generation lentiviral vector (plasmid ECFP-CAAX pCSII-IRES2-hygro).

Cells were plated at a density of 6.4 x 10^4 cells /ml in a 6 well plate. 24 hours later, medium was removed and a solution containing lentivirus and DMEM in a 1:1 ratio was added per well according to the manufacturers protocol. Cells were incubated in a CAT2 incubator for 72 hours. Then, cells were selected with Hygromycin B (Invitrogen, cat # 10687-010) at a final concentration of 500 µg/ml (elucidated from carrying out a concentration curve). Cells were tested to ensure that the CAAX tag did not affect YAP/TAZ ratio or cell morphology by quantifying morphological features based on linear classifiers used for screens.

2.1.4 Drug treatments

Drugs were usually added on top of media already present. For example in 384 well plates drugs were added in 10 µl and made up to be 5 times more concentrated than the final concentration required. Appropriate amounts of DMSO or H_2O depending on what the drug was dissolved in were added to mock transfected cells. A list of drugs used can be found in Table 2.2. Drugs were added for a period of 4 hours, unless other stated, so as to eliminate any cell cycle effects as the doubling rate of these cells is 24 hours.

Table 2.2: Drugs used for drug treatments.

	Inhibitor type/target	Company and catalogue number	Final concentration.
PF-573288	FAK inhibitor	Tocris Biosciences, #3239; CAS 869288-64-2	2μM
C21	DOCK5 inhibitor	Alfa Aesar, #H60031.MD; CAS 54129-15-6	100μM
Blebbistatin	Myosin II light chain	Sigma, #B0560; CAS 856925-71-8	10μM
Uprosertib (GSK2141795)	AKT inhibitor		2μM
Wortmannin	PI3K inhibtor	Abcam, #ab120148	0.4μM
Y-27632	ROCK inhibitor	Sigma, #Y0503; CAS 129830-38-2	10μM
Palbociclib (PD-0332991) HCl	CDK4/6 inhibitor	Selleckchem, #S1116	500nM
Binimetinib (MEK162)	MEK inhibitor	Selleckchem, #S707	10μM
Adavosertib	Wee1 inhibitor		1mM
GSK2256098	FAK inhibitor clinic		40μM

2.2 High throughput RNA interference screening

2.2.1 Overview of RNAi screening methodology

Two human RhoGEF and RhoGAP libraries were used: siGENOME and ONTARGET*Plus* (Dharmacon). Both libraries were made up of SMARTpools, where each gene is targeted by a pool of 4 different siRNA strands per siRNA. Each siRNA library was arrayed across 2 black, optically clear bottom, 384 well Cell Carrier plates (PerkinElmer) from stock libraries of siGENOME and ONTARGET*Plus* stored at -80°C. Arrayed plates were also stored at 80°C prior to use. Individual siRNAs were arrayed in duplicate per plate, and each plate was screened in duplicate, resulting in 4 plates per screen per cell line: 1A, 1B, 2A and 2B. As positive controls *LATS1* (Dharmacon cat # M-004632-00) and *YAP* (Dharmacon cat # L-012200-00) siRNA were introduced on columns 23 and 24 with a minimum of 4 wells per control per screen. *LATS1* and *LATS2* siRNAs were used as controls for our ability to assess YAP/TAZ localisation, as in the absence of LATS1/2 YAP/TAZ nuclear localisation is expected to increase (Piccolo et al, 2013). *YAP* siRNA was used as a control to assess our ability to monitor both YAP levels and localisation. As a control to assess our ability to transfect cells *ECT2* siRNA (Dharmacon cat # L-006450-00, # M-006450-00) was used which results in multinucleate cells (Su et al, 2011; Miller and Bement, 2008). The screens performed on hs578t and SUM159 also included *TAZ* siRNA.

YAP/TAZ nuclear translocation can be sensitive to cell density, and thus some siRNAs might affect YAP/TAZ localisation simply because they reduce cell numbers (Sero et al, 2015). To account for density dependent effects cells were plated at increasing densities on columns 1, 2, 23 and 24. This is so that by

performing a linear regression, or similar analysis on these samples the relationship between YAP/TAZ localisation and cell density can be identified.

Mock transfected cells were used as negative controls, due to our previous observation that non-targeting siRNAs result in phenotypic changes (unpublished data).

All liquid dispensing steps were carried out using a Multidrop Dispenser (Thermo Scientific), except for siRNA plating on the assay plates which was carried out using the acoustic liquid handler Echo 550 (Labcyte Inc).

2.2.2.2 Screening reagents

- Dharmacon siGENOME siRNA library
- Dharmacon *ONTARGETPlus* siRNA library
- Opti-MEM Reduced Serum Media (Thermo Fisher, Gibco Life Technologies, cat # 31985062)
- Lipofectamine ® RNAimax reagent (Invitrogen, cat # 13778150)
- 8% methanol free formaldehyde in PBS (16% pre-made solution Thermo Scientific, cat # 28908), final concentration 4%
- PBS containing 0.05% of the preservative Sodium Azide (Sigma, cat # S2002-25G) (all PBS referred to in this study)
- Triton-X-100 (Sigma, cat # T9284), 10% in PBS
- Bovine Serum Albumin (BSA) (Sigma, cat # A2153-50G) 2% in PBS, filtered

- Triton-X-100, 0.01% and 0.5% BSA in PBS solution for antibody incubations
- Mouse YAP/TAZ antibody (Santa Cruz Biotechnology, cat # sc-101199) 1µg/ml (1:1000)
- Rat α-tubulin antibody (Bio-Rad, cat # MCA77G) 1µg/ml (1:1000)
- AlexaFluor 647 goat anti-mouse (Life Technologies, cat # A21235) 2µg/ml (1:1000)
- AlexaFluor 568 goat anti-rat 1:1000 (Life Technologies, cat # A11077) 2µg/ml (1:1000)
- Phalloidin 488 (Invitrogen, cat # A12379) 1:1000 from 300U in 1.5ml stock
- 2′-(4-Hydroxyphenyl)-5-(4-methyl-1-piperazinyl)-2,5′-bi(1H-benzimidazole) trihydrochloride (Hoechst) (Sigma Aldrich, cat # 33258) 10µg/ml (1:1000)

2.2.3 Plating siRNAs and reverse transfections

Day 0: Plating siRNAs. 40nl (0.08pmol) siRNA from the siGENOME and ONTARGET*Plus* libraries (stock concentration of 20µM) were arrayed using the acoustic liquid handler Echo 550 prior to transfection and kept at -80°C.

Day 1: Reverse transfection. Pre-stamped siRNA plates were thawed at room temperature for 30 to 60 minutes prior to use. Subsequently, 5µl of Opti-MEM® Reduced Serum Media were added per well. 5 minutes later, 5µl of mix containing Opti-MEM and RNAimax reagent in a 125:1 ratio were added, and plates were spun at 1000 rpm for 1 minute. Plates were incubated at room temperature for 20 minutes, so as to allow siRNA-RNAimax complexes to form. Cells were then

seeded in 30µl DMEM (10% FBS, 1% penicillin/streptomyocin), resulting in a total volume of 40µl per well: 40nl siRNA (final concentration of 20nM), 5µl Opti-MEM, 5µl of Opti-MEM and RNAimax mix (125:1) plus 30µl of cells. LM2 and MDA-MB-231 cells were seeded at 1000 cells/well (3.3 x 10^4 cells /ml), SUM159 were seeded at 2000 cells/well (6.67 x 10^4 cells /ml), and hs578t were seeded at 1500 cells/well (5.0 x 10^4 cells /ml).

2.2.4 Immunofluorescence staining and confocal imaging

Day 3: Immunofluorescence staining. Automated handling of plates on the Cell::Explorer robot station was carried out using the PlateWorks software (Perkin Elmer). Cells were fixed 48 hrs post transfection by addition of 40µl of warm 8% formaldehyde in PBS (final concentration 4%) for 15 minutes. Cells were washed with PBS three times and permeabilised with 0.1% Triton-X-100 in PBS for 10 minutes. Cells were then blocked with 2% BSA diluted in PBS for 2 hrs to prevent non specific binding of antibodies. All antibody incubations were performed in solution containing 0.5% BSA, 0.01% Triton-X-100 dissolved in PBS in a 1:1000 ratio. Plates were washed three times with PBS between steps using a Microplate Washer (BioTek). Antibodies were added sequentially to avoid any possible bleedthrough, with the mouse primary antibody for both YAP and TAZ (final concentration 1µg/ml), being added first and left overnight.

Day 4: Immunofluorescence staining and imaging. Staining procedures were continued in the following order with each antibody left on for 1.5 hrs: AlexaFluor 647 goat anti-mouse (final concentration 2µg/ml) to detect YAP/TAZ, rat primary

anti α-tubulin antibody (final concentration 1μg/ml), AlexaFluor 568 goat anti-rat to detect α-tubulin (final concentration 2μg/ml) and Phalloidin 488 combined in the same step. Finally the nuclear stain Hoechst (Sigma Aldrich, cat # 33258, final concentration 10μg/ml) was added for 15 minutes, upon which it was removed and 15μl of PBS were dispensed. All cells were imaged using an automated Opera Quadruple Enhanced High Sensitivity (QEHS) spinning-disk confocal microscope (PerkinElmer) with 20x air lens. Lasers and their corresponding filters used were: 405(450/50), 561 (600/40), 488 (540/751), 640 (690/50).

Of note, this same process was carried out for every RNAi transfection and any other combination of antibodies used throughout this thesis unless otherwise stated.

2.2.5 Data collection and analysis

Image processing and segmentation: Images were processed and analysed using the Columbus 2.6.0. Software Platform (PerkinElmer). To identify single cells, nuclei were segmented using the Hoechst signal. The cytoplasm was subsequently segmented based on the identified nuclei utilising α-tubulin intensity. Cells touching the image border were filtered out.

These features are broadly grouped into the following categories:

1. Nucleus area, roundness, width, length, width to length ratio.
2. Cell area, roundness, width, length, width to length ratio.
3. Cytoplasm area, roundness, width, length, width to length ratio.

4. Membrane region (protrusions) area.
5. YAP/TAZ stain intensity for nucleus, ring region, whole cell, cytoplasm, nucleus region.
6. Ratio of nuclear region YAP/TAZ intensity to ring region YAP/TAZ intensity.
7. Log10 of ratio of nuclear region YAP/TAZ intensity to ring region YAP/TAZ intensity (YAP/TAZ ratio)
8. Ratio of eroded nuclear region YAP/TAZ intensity to ring region YAP/TAZ intensity.
9. Log10 of ratio of eroded nuclear region YAP/TAZ intensity to ring region YAP/TAZ intensity.
10. Ratio of nuclear region intensity to nuclear area.
11. Ratio of nuclear region YAP/TAZ to nuclear area.
12. Ratio of cell area to whole cell YAP/TAZ.
13. Ratio of nuclear area to whole cell YAP/TAZ.
14. SER texture features (Spot, Hole, Edge, Ridge, Valley, Saddle, Bright, Dark) for α-tubulin and actin cytoplasm stains; and Hoechst, α-tubulin, and actin nucleus stains, at 0 and 1 pixel scale.
15. Haralick texture features (Correlation, Contrast, Variance, Homogeneity) for α-tubulin cytoplasm stain; and α-tubulin and actin nucleus stains, at 1 pixel scale.
16. Gabor texture features for cytoplasm actin stain.

Cell morphology features (types 1-4)

Five morphological properties for the nucleus, cytoplasm, and whole cell regions were calculated: area, roundness, width, length, and the ratio of width to length (15 features). Additionally, a membrane region mask was created to quantify protrusiveness, and its area was calculated. This membrane region mask was defined as a mask that extends slightly beyond the cytoplasm and encompasses a percentage of the cytoplasm. The inner border and outer borders were set at 10% and -5% relative to the distance from the cytoplasm edge to the centroid of the cell. Considering the inner border starts at the centroid of the cell and encompasses the whole cell when at 100%, the inner border was set at 10% of the distance from the cytoplasm edge to the centroid of the cell, and the outer border was set at -5%.

Cell region-specific features (types 5-13)

Feature calculations were made for YAP/TAZ, Hoechst and α-tubulin intensities for different cell regions. Specifically: Hoechst intensity was calculated for the nuclear region; α-tubulin intensity for the cytoplasm and whole cell regions (combined nuclear and cytoplasm regions); and YAP/TAZ intensity was calculated for the nuclear, cytoplasm, and whole cell regions. We identified two additional regions in which we calculated YAP/TAZ intensity: the “ring region” and “eroded nuclear region”. The ring region was defined by creating a mask around the nuclear segment and calculating a percentage of the distance from the cytoplasm edge to the centroid of the cell (inner border: 40%, considering 100% to encompass the whole cell). The outer border of the ring region was determined as 25% of the distance from the cytoplasm edge to the inner border. The eroded

nuclear region was established by eroding the nuclear region by 2%, such that the eroded nuclear region is a smaller version of the nuclear region and consequently is not in direct contact with the ring region. This was done to compensate for segmentation errors. However, for the purposes of our analyses there was no difference between using the eroded nuclear region or the nuclear region itself. The data for both is included so that users can choose their feature of preference.

To quantify the nuclear translocation of YAP/TAZ, ratios were taken for the nuclear to ring region, and eroded nuclear to ring region measurements. Using the ring region has been shown to improve nuclear translocation measurement accuracy (Sero et al, 2015). This is due to the ring region having a similar thickness to the nucleus and thus being more comparable than using the whole cytoplasm versus the nucleus. The logarithm of these features was also calculated as a derivative feature. The log10 of the ratio of nuclear region YAP/TAZ intensity to ring region YAP/TAZ intensity is hereafter referred to as 'YAP/TAZ ratio'. The ratio of YAP/TAZ intensity to nuclear and whole cell area were also calculated.

Texture features (types 14-16)

"Texture features" for both the nuclear and cytoplasmic regions were also measured. Three types of texture feature were calculated: Gaussian Derivative Textures, termed SER, (Saddle-Edge-Ridge) features in Columbus; Gabor features (Fogel and Sagi, 1989); and Haralick features (Boland and Murphy,

2001; Haralick et al, 1973; Sailem et al, 2016). SER features are calculated as the mean region intensity following convolution with a Gaussian kernel (which identify spot and hole textures), and derivatives of this kernel (which identify saddle, edge, ridge, valley, bright and dark textures). These textures were calculated for α-tubulin, Hoechst and actin channels. Two smoothing scales were used, 0 pixels to identify smaller objects, and 1 pixel to identify larger objects. The Gabor minimum and maximum features are the mean, minimum, and maximum values of a wavelet kernel projected at 8 different angles; these features identify actin structures, and are only calculated for this channel (Fogel and Sagi, 1989). SER and Gabor features were normalised to within the kernel used to calculate them, thus ensuring only local textures were detected. Haralick features are calculated from the co-occurrence matrix, which describes how similar neighbouring pixels are within an image. Such that the 1 pixel refers to the size of the image that is compared to another. Four features were defined from this matrix: correlation, contrast, variance, and homogeneity (Haralick et al, 1973; Haralick, 1979). These features were calculated for α-tubulin, and actin channels.

Microenvironment features (types 17-18)

To determine the fraction of a cell in contact with another cell, or the “neighbour fraction” (Sero et al, 2015), two membrane region masks were generated. Taking the edge of the cell as point 0, a membrane region 1 with an outer and inner border of 0 and 1 pixels respectively from the edge of the cell into the cytoplasm, and a membrane region 2 with an outer and inner border of -1 and 0 pixels respectively from the edge of the cell into the surrounding external area. The area of these membrane regions was obtained and the neighbour fraction was then

calculated as 1 minus the ratio of the area of membrane region 1 over twice the area of membrane region 2.

2.3 Nucleic acid manipulations

2.3.1 Quantitative Real-Time PCR (qRTPCR)

LM2 and MDA-MB-231 cells were were reverse transfected as stated previously and plated at a density of 5 x 10^4 cells/ml in 6 well plates. RNA was extracted using the phenol:chloroform (TRIzol®, ThermoFisher cat # 15596026), and RNAeasy kit (Qiagen cat # 74104) according to the manufacturer's protocol. RNA was converted to cDNA using a cDNA conversion kit (Applied Biosystems cat # 4387406) according to the manufacturers protocol. qRTPCR was performed on a QuantStudio® Flex Real-Time PCR system, using PCR mastermix SyBR green (Applied Biosystems cat # 4309155) and primers in Table 2.3.

Table 2.3: PCR primers used for qRT-PCR.

Gene	Forward (5'-3')	Reverse (5'-3')
DOCK5	GCTTTGAACTTCAGCTCTGG	CCACATGTCCCGGATTCTAA
ECT2	CCCGAGCTGGAGAAACTATG	ACCCTATGGAAAGGGAATGC
LATS1	TTCGAAACTCTCTGCTTCCA	TTGCGGTTAACTGATTGCTG
CTGF	GAAGCAGAGCCGCCTGTGCA	ACCGGCAGGGTGGTGGTTCT
WWTR1/TAZ	TATGGGACAGTCCGGGAGC	CGAGGCTTGGCTGACAAATC
YAP1	GACTTCCTGAACAGTGTGGA	CAGCCAAAACAGACTCCATG
GAPDH	AGATCCCTCCAAAATCAAG	GGCAGAGATGATGACCCTT

Fold changes were calculated on quadruplicate technical replicates using double delta Ct analysis and normalised to GAPDH.

2.4 Protein manipulations

2.4.1 Western blotting

Cells were reverse transfected in 6 well plates at a density of 3.3 x 10^4 cells /ml in a 6 well plate (same density as screens and all other experiments unless otherwise stated) for 48 hours. Cells were harvested by trypsinising, spinning down in 1.5ml eppendorfs and removing supernatant. Cells were then washed in PBS 3 times. Pellets were then resuspended in 500µl of solution containing a ratio of 3:1 of water to LDS Sample Buffer (4x) (Invitrogen) with a final concentration of 2mM DTT. Samples were then boiled at 100 C for 10 minutes and spun down for 2 minutes at 13 000 rpm. Samples were frozen at -20 C. Samples were boiled and spun down again prior to use. 16µl of sample were loaded into 1.0mm 15 well pre cast Novex 4-20% Tris-Glycine Gels (Invitrogen #XP04205BOX) and 30µl into 10 well pre cast gels. Ladder used was Color Protein Standard, Broad Range (11-245 kDa) (New England Biolabs, #P7712S). Lysates were run in 1x Tris-Glycine (Thermo) running buffer at 130V until the bands reached the bottom of the gel. Gels were transferred in transfer buffer at 4C at 0.2 A onto a methanol activated polyvinylidene fluoride (PVDF) membrane (Immobilon-FL). Membranes were then stained with Ponceau (Sigma) dissolved in acetic acid to ascertain where the proteins were before cutting the membrane at required places. Membranes were then blocked in either 5% milk (Marvel) or 5% BSA if staining for phospho-proteins in Tris-buffered saline (TBS, prepared in

house according to standard protocols) 0.1% Tween20 (TBST) solution for 1 hour at RT on a rolling shaker. Membranes were then washed once in TBST. Primary antibodies were diluted in either 5% milk TBST or 5% BSA TBST solution and incubated at 4C overnight on a rolling shaker. 10% glycerol was added to primary antibody solutions to be able to reuse them post storing at -20 C. Membranes were washed 3 x 15 minutes in TBST. Membranes were then incubated for one hour at RT in either appropriate (mouse or rabbit) Horse radish peroxidase (HRP) -linked secondary antibodies (Cell Signaling) in TBST for chemiluminescent detection or in either anti-rabbit or mouse conjugated antibodies (Cell signaling) Roti-®block (Roth) 1x diluted in water for LiCor fluorescence imaging. Membranes were washed 3 x 5 minutes with TBST. For fluorescence antibodies, last wash was done in water. For HRP-linked antibodies, membranes were treated with ECL substrate (Thermo, #32106) and exposed using Azure Biosystems c600 western blot imaging system. Descriptions of antibodies used and dilutions can be found in Tables 2.4 and 2.5. Western Blots were quantified using Image J and normalised to GAPDH unless otherwise stated.

2.4.2 Subcellular fractionation

Thermo's Subcellular Protein Fractionation Kit for Cultured Cells (#78840) was used according to the manufacturer's protocol to extract cytoplasmic, membrane, nuclear soluble, chromatin-bound and cytoskeletal proteins. Briefly, cells were harvested by trypsining them and centrifuging for 5 minutes. Cell pellets were washed with ice-cold PBS. Cells were counted so as to be able to use the corresponding ratios of Cytoplasmic Extraction Buffer (CEB), Membrane Extraction Buffer (MEB), Nuclear Extraction Buffer (NEB) and Pellet Extraction

Buffer (PEB): CEB:MEB:NEB:PEB 200:200:100:100µl respectively. Cells were then resuspended in ice-cold CEB containing protease inhibitors, incubated at 4°C for 10 minutes with gentle mixing, followed by centrifugation at 10000 rpm for 5 minutes. Supernatant containing the cytoplasmic extract was transferred to a pre-chilled tube on ice. Ice-cold MEB was then added to the pellet, vortexed for 5 seconds, and incubated at 4°C for 10 minutes with gentle mixing, followed by centrifugation at maximum rpm for 5 minutes. Supernatant containing membrane extract was transferred to pre-chilled tube on ice and ice-cold NEB was added to pellet, vortexed for 15 seconds, and incubated at 4°C for 30 minutes with gentle mixing. Mixture was centrifuged at maximum rpm for 5 minutes and supernatant containing soluble nuclear extract was transferred to pre-chilled tube on ice. Chromatin-bound extraction buffer was prepared by adding 5µL of 100mM CaCl2 and 3µL of Micrococcal Nuclease (300 units) per 100µL of room temperature NEB. This was then added to pellet and vortexed for 15 seconds, incubated at room temperature for 15 minutes, vortexed for 15 seconds and centrifuged at highest setting for 5 minutes. Supernatant containing chromatin-bound nuclear extract fraction was transferred to clean pre-chilled tube on ice and room temperature PEB was added to pellet, vortexed for 15 seconds and incubated at room temperature for 10 minutes. Tube was centrifuged at highest setting for 5 minutes and the last supernatant containing the cytoskeletal extract was transferred to a new tube. Fractions were stored at -80°C.

Protein concentrations of each subcellular fraction were measured using the Pierce BCA Protein Assay kit (Thermo). Samples were diluted in water (Sigma) to the lowest sample concentration to ensure the same amount of protein for each

fraction was loaded into the gels. 4µl of NuPage LDS Sample Buffer (4x) were added to 16µl of each sample, which were then boiled for 10 minutes and spun down before freezing. Samples were then run as described in Western Blotting subsection.

2.4.3 Mass spectrometry

2.4.3.1 siRNA transfections and sample collection

LM2, MDA-MB-231, and hs578t cells were reverse transfected with *DOCK5* siRNA. LM2 and MDA-MB-231 were both plated at a density of 3.3 x 10^4 cells /ml (low density, siRNA screening density) and 1.0 x 10^5 cells /ml (high density) in T75 falcons due to the requirement of 3 million cells per sample. hs578t cells were plated at 5.0 x 10^4 cells /ml (screening density). 48 hours later cells were collected by trypsinisation, and washed 3 x with cold PBS in clean mass spectrometry tubes. Cells were also counted prior to last wash to ensure there were at least 3 million cells per sample. Samples were then flash frozen with 70% ethanol and dry ice.

Samples were then given to Theo Roumeliotis in the Proteomics Core Facility at the ICR, run by Jyoti Choudhary. The following protocols (2.4.3.2 -2.4.3.4) were kindly provided and carried out by Theo Roumeliotis.

2.4.3.2 Sample preparation for TMT labelling

Cell pellets were dissolved in 150 µL lysis buffer containing 1% sodium deoxycholate (SDC), 100mM triethylammonium bicarbonate (TEAB), 10% isopropanol, 50mM NaCl and Halt protease and phosphatase inhibitor cocktail (100X) (Thermo, #78442) on ice, assisted with pulsed probe sonication for 15

sec. Samples were subsequently boiled at 90 °C for 5 min on a thermomixer and were re-sonicated for 5 sec. Protein concentration was measured with the Coomassie Plus Bradford Protein Assay (Pierce) according to manufacturer's instructions. Aliquots containing 100 µg of total protein were prepared for trypsin digestion. Samples were reduced with 5 mM tris-2-carboxyethyl phosphine (TCEP) for 1 h at 60 °C and alkylated with 10 mM Iodoacetamide (IAA) for 30 min in dark. Proteins were then digested by adding 75 ng/µL trypsin (Pierce) to each sample and incubating overnight. The resultant peptides were labelled with the Tandem Mass Tag - 10plex (TMT-10plex) multiplex reagents (Thermo) according to manufacturer's instructions and were combined in equal amounts to a single tube. The combined sample was then dried with a centrifugal vacuum concentrator.

2.4.3.3 Basic Reverse-Phase Peptide Fractionation and LC-MS/MS Analysis

Offline high pH Reversed-Phase (RP) peptide fractionation was performed with the XBridge C18 column (2.1 x 150 mm, 3.5 µm, Waters) on a Dionex Ultimate 3000 High Performance Liquid Chromatography (HPLC) system. Mobile phase A was 0.1% ammonium hydroxide and mobile phase B was 100% acetonitrile, 0.1% ammonium hydroxide. The TMT labelled peptide mixture was reconstituted in 100 mL mobile phase A and was fractionated using a multi-step gradient elution method at 0.2 mL/min as follows: for 5 minutes isocratic at 5% B, for 35 min gradient to 35% B, gradient to 80% B in 5 min, isocratic for 5 minutes and re-equilibration to 5% B. Fractions were collected every 30 sec and vacuum dried.

LC-MS/MS analysis was performed on the Dionex Ultimate 3000 system coupled with the Q Exactive HF Orbitrap Mass Spectrometer (Thermo Scientific). Each peptide fraction was reconstituted in 40 µL 0.1% formic acid and 7 µL were loaded to the Acclaim PepMap 100, 100 µm × 2 cm C18, 5 µm, 100 Å trapping column at 10 µL/min flow rate. The sample was then subjected to a gradient elution on the EASY-Spray C18 capillary column (75 µm × 50 cm, 2 µm) at 45 °C. Mobile phase A was 0.1% formic acid and mobile phase B was 80% acetonitrile, 0.1% formic acid. The gradient separation method at flow rate 250 nL/min was as follows: for 90 min gradient from 10%-38% B, for 10 min up to 95% B, for 5 min isocratic at 95% B, re-equilibration to 5% B in 5 min, for 10 min isocratic at 10% B. The top 15 precursor ions between 350-1,850 m/z were selected with mass resolution of 120 k, AGC 3×10^6 and IT 50 ms for HCD fragmentation with isolation width 1.0 Th. Collision energy was set at 35% with AGC 1×10^5 and IT 100 ms at 60k resolution. Targeted precursors were dynamically excluded for further isolation and activation for 30 seconds.

2.4.3.4 Database search and protein quantification

The SequestHT search engine was used to analyse the acquired mass spectra in Proteome Discoverer 2.2 (Thermo Scientific) for protein identification and quantification. The precursor mass tolerance was set at 20 ppm and the fragment ion mass tolerance was set at 0.02 Da. Spectra were searched for fully tryptic peptides with a maximum of 2 miss-cleavages. TMT6plex at N-terminus/K and Carbamidomethyl at C were defined as static modifications. Dynamic modifications included oxidation of M and Deamidation of N/Q. Peptide confidence was estimated with the Percolator node. Peptide False Discovery

Rate (FDR) was set at 0.01 and validation was based on q-value and decoy database search. All spectra were searched against reviewed UniProt human protein entries. The reporter ion quantifier node included a TMT 10plex quantification method with an integration window tolerance of 15 ppm and integration method based on the most confident centroid peak at the MS2 level. Only unique peptides were used for quantification, considering protein groups for peptide uniqueness. Peptides with average reported signal-to-noise >3 were used for protein quantification.

Abundance values were scaled within each cell line and the log2 ratio of abundance in si*DOCK5* containing samples to mock transfected samples was calculated. Log2 ratios above 0.5 and below -0.5 and permutation FDR <0.05 (t-test) were considered to be proteins which were significantly up (40% minimum increase) and down regulated (40% minimum decrease) respectively.

2.5 Microscopy

2.5.1 Immunofluorescence and confocal microscopy

Cells from all experiments carried out in this thesis were fixed and stained in the same manner as described for the RNAi screens unless stated otherwise. Briefly, cells were fixed 48 hours after transfection with paraformaldehyde in PBS (4% final concentration), permeabilised with 0.1% Triton-X-100 in PBS for 10 minutes, and blocked with 2% BSA dissolved in PBS for 2 hours. Antibody incubations were performed in PBS containing Triton-X-100, 0.01% and 0.5% BSA. Primary antibodies were left overnight at 4°C. Secondary antibodies were added for 1.5 hours at room temperature. Hoechst was used as a DNA stain and left for 15

minutes at the end at room temperature. Cells were washed 3 x with PBS between each step and were left in 30µl of PBS. Where antibodies used were close in species such as mouse and rat, they were added sequentially to avoid any possible bleedthrough. Antibodies and their dilutions can be found in Tables 2.4 and 2.5.

Unless otherwise stated cells were imaged using an automated Opera Quadruple Enhanced High Sensitivity (QEHS) spinning-disk confocal microscope (PerkinElmer) with 20x air lens. Lasers and their corresponding filters used were: 405(450/50), 561 (600/40), 488 (540/751), 640 (690/50).

Table 2.4: Primary antibodies used for Immunofluorescence (I.F) and Western Blot (W.B).

Target	Antibody and species	Company and cat number	W.B dilution	I.F Dilution
YAP/TAZ	Anti-YAP/TAZ (mouse)	Santa Cruz Biotechnologies, cat # A21235	1:1000	1:1000
α -tubulin	Anti- α-tubulin (rat)	Bio-Rad, cat # MCA77G		1:1000
GSK3β	Anti-GSK3β (rabbit)	CST, cat # 12456T	1:300	1:300
Golgi	Anti-GM180 (mouse)	Abcam, cat #52649		1:500
Beta-catenin	Anti- Beta-catenin (mouse)	BD Transduction Laboratories, cat # 610153	1:1000	1:1000
DOCK5	Anti-DOCK5 (rabbit)	Frank et al., 2017.	1:500	

PHH3	Anti- P-Histone H3 (S10) (mouse)	CST, cat # 9706S	1:1000	
KIF5B	Anti-KIF5B (rabbit)	Protein Tech, cat #231632-1-AP	1:1000	
PCNA	Anti- PCNA (mouse)	Santa Cruz Biotechnology, cat #sc-56	1:1000	
GAPDH	Anti-GAPDH (1D4) (mouse)	Novus, cat # NB300-221	1:2000	
FOXO3A	Anti-FOXO3A (75D8) (rabbit)	CST, cat # 2497S		1:200
Phospho-paxillin	Anti-Phospho-Paxillin (Tyr31) (rabbit)	Invitrogen, cat #44-720G		1:300
Paxillin	Anti-Paxillin (mouse)	BD transudction labs # 610052		1:300
SKP2	Anti- SKP2 (rabbit)	Protein tech, 15010-1-AP		1:100
pGSK3β	Anti-phospho GSK3β (Ser9) (D85E12 (rabbit)	CST, cat # 5558T	1:300	1:400

Table 2.5: Secondary antibodies used for Immunofluorescence (I.F) and Western Blot (W.B).

Secondary antibody/dyes	Company	Dilution
Phalloidin	Invitrogen, cat # A12379	1:1000
Hoechst	Sigma Aldrich, cat # 33258	1:1000

AlexaFluor 647 goat anti-mouse	Life Technologies, cat # A21235	1:1000
AlexaFluor 568 goat anti-rat	Life Technologies, cat # A11077	1:1000
AlexaFluor 647 goat anti-rabbit	Life Technologies, cat # A21245	1:1000
AlexaFluor 568 goat anti-rabbit	Life Technologies, cat # A11036	1:1000
Anti-mouse IgG (H+L) (DyLight TM 4X PEG Conjugate 680	CST, cat # 5470S	1:2000
Anti-rabbit IgG (H+L) (DyLight TM 4X PEG Conjugate 800	CST, cat # #5151S	1:2000
Anti-mouse IgG, HRP-linked antibody	CST, cat #7076S	1:2000
Anti-rabbit IgG, HRP-linked antibody	CST, cat #7074S	1:2000

2.5.2 Focal adhesion dynamics and Total Internal Reflection Fluorescence Imaging (TIRF)

LM2 CAAX-GFP cells were transfected with either just Talin mApple plasmid or both Talin mApple and si*DOCK5,* si*RAC1,* si*RHOA*, or si*CDC42* as stated in the transfections section.

35mm glass Mat-tek dishes were coated with 10µg/ml Fibronectin (human plasma, Sigma #F0895) for 1 hour. Fibronectin was then aspirated and Mat-tek dishes were washed 3 x PBS and left to dry. 48 hours after transfection, LM2 CAAX-GFP cells were plated at 1.5 x 10^5 cells /ml in 1ml of Liebnevitz medium (10% FBS, 1% penicillin/streptomyocin). Cells were live imaged using the TIRF (3i) approximately 1 hour after seeding. Lasers used were 647 And 488. Images were taken either every 3 minutes or every 1.5 minutes. Images were acquired

using Slidebook software (3i). Videos were processed to be the same length and analysed using the 'Focal Adhesion Analysis Server (FAAS)' (Berginski and Gomez, 2013) – a publicly available server to analyse focal adhesion dynamics with URL https://faas.bme.unc.edu/. Videos containing the same number of time frames were compared.

We displayed the data using estimation statistics using a website generated by Ho et al., 2019, as we think that by showing the effect size we can visualise and understand this type of data better. Estimation statistics, contrary to significance testing focuses on the magnitude of the effect, ie: the effect size, and its precision. (Ho et al., 2019).

2.5.3 Spreading assay and Super-Resolution via Optical-Reassignment (SoRa) microscopy

Cells pertaining to experiments imaged using the SoRa were fixed and stained with a slight variation to those from RNAi screens. Briefly, cells were reverse transfected as described in the transfection section in 6 well plates, and plated on 35mm glass Mat-tek dishes coated with 10µg/ml Fibronectin as described in section 2.5.2, at a density of 1.5 x 10^5 cells /ml 48 hours after transfection. They were fixed 3 hours after plating with paraformaldehyde in PBS (4% final concentration), permeabilised with 0.1% Triton-X-100 in PBS for 10 minutes, and blocked with 0.5% BSA dissolved in PBS with 0.3ml of glycine for 1 hour. Antibody incubations were performed in 0.5% BSA. Primary antibodies were added at room temperature for 1.5 hours. Secondary antibodies were added for

1.5 hours at room temperature. Hoechst was used as a DNA stain and left for 15 minutes at the end at room temperature. Cells were washed 3 x with PBS between each step and were left in 200µl of PBS. Where antibodies used were close in species such as mouse and rat, they were added sequentially to avoid any possible bleedthrough. Antibodies and their dilutions can be found in Tables 2.4 and 2.5. When drugs were used, they were added in 500µl on top of the 2ml solution of cells immediately after plating, with final concentrations as shown in Table 2.2. Cells were imaged using the SoRa (3i) microscope.

2.5.3 Scanning Electron Microscopy (SEM)

LM2 cells were reverse transfected in 6 well plates. 48 hours after transfection, cells were trypsinised and plated at a density of 1.5 x 10^5 cells /ml on collagen coated 5mm dishes. 16 hours later cells were fixed in 0.25% glutaraldehyde, and processed for SEM by David Robertson (ICR) and Innes Clatworthy (Natural History Museum). Images were taken by David Roberston at the Natural History Museum.

2.6 *In vitro* functional assays

2.6.1 3D collagen invasion assay

Cells were reverse transfected in 6 well plates as previously described. 48 hours later cells were trypsinised and resuspended in a solution containing rat-tail collagen I (Corning cat # 354249), ultrafiltered H_2O (prepared in house according to standard protocols), DMEM 5x and HEPES (1M pH 7.5, prepared in house according to standard protocols). Collagen solutions were prepared on ice and

96 well plates were prechilled prior to use. Collagen solutions were made up as in Table 2.6 starting with HEPES, followed by DMEM 5X with rat-tail collagen being added last. Neutralisation of collagen was tested with pH strips prior to use to ensure a pH of 7.4. DMEM 5X was made up using 12.5g DMEM powder, 25 ml of 1M HEPES ph 7.5, 5g $NaHCO_3$, H_2O up to 250 ml and was filtered under sterile conditions before aliquoting into 10ml batches and freezing them at -20 degrees. Cells were spun down in 1.5ml eppendorfs at 1000 rpm for 4 minutes, and supernatant was removed (Figure 2.1). Cell pellets were resuspended carefully so as to not introduce bubbles in 500 µL of collagen solution, and 100 µL of cell-collagen mix was dispensed per well of a 96 well plate. Once all conditions were dispensed, plates were spun down for 1 minute at 4 °C to ensure all cells were at the bottom of the plate. Collagen was allowed to polymerise at 37°C for one hour. Then 50 µL of DMEM were added on top of the collagen gels. 150 µL of PBS were added to all outside wells to prevent gel dehydration and edge effects due to dehydration. Cells were fixed 48 hours later with 50 µL/well of 16% PFA containing Hoechst (1:500) for 2 hours. Gels were then washed with PBS and left in PBS prior to sealing. The Opera QEHS spinning-disk confocal microscope (PerkinElmer) with 20x air lens was used to image these plates. A minimum of three Z stacks were taken per well, spaced 30 µm apart with the bottom of the plate being 0 µm and subsequent stacks being into the gel. 20 fields were imaged per well per stack, and all in the centre of the well to prevent edge effects. Columbus software was used to quantify cell number at every stack.

Table 2.6: Reagents used for collagen invasion assays.

	Stock	Final concentration
Rat-tail collagen I	10.31 mg/ml	2.0 mg/ml
UF H_2O (cold)	-	remaining
DMEM 5x	5x	1x
HEPES 1M pH 7.5	100%	2%

2.6.2. Spheroid invasion assay

Cells were reverse transfected in 96 well ultra-low attachment (ULA) plates as described in the siRNA transfections section. Quantities used per well: 20 µl OPTIMEM + 0.16 µl RNAimax, 20 µl OPTIMEM + 0.16 µl siRNA. Cells were plates at a density of 4.0 x 10^4 cells/ml in 120 µl, resulting in a final volume of 160 µl per well. 5 hours later a solution of 2.5% Matrigel in 40 µl of DMEM was added per well to promote spheroid formation, resulting in a total volume of 200 µl per well. 48 hours later 180 µl of medium was carefully removed from each well so as not to disturb the spheroid, and replaced with 180 µl of 100% Matrigel. Spheroids were imaged prior to adding 100% Matrigel and immediately after using the Celigo Imaging Cytometer (Nexcelom Bioscience). Spheroids were imaged every day for 8 days, following the protocol outlined in (Vinci et al., 2015). Images were processed using ImageJ. Invasion area was determined by drawing a circle to the edge of where cells invaded and subtracting the initial area of the spheroid at day 0. Proliferation was quantified by drawing a circle around the edge of the area of the spheroid where the spheroid is grey, rather than the edge, so as to exclude any invading cells.

2.6.3 Wound heal assay

Cells were reverse transfected as previously described and were plated in a 96 well Perkin Elmer Cell Carrier Ultra plate at a density of 2.7 x 10^6 cells/ml. 48 hours later a 10 µM pipette tip was used to scratch the monolayers from top to bottom of the well, resulting in a vertical cell-free gap or wound. Medium was removed and wells were carefully washed with warm PBS so as to remove debris. 100 µL of fresh medium was them added to all wells. Imaging began as soon as the wound was created, using a Basic Confocal Spinning Disk Microscope (3i). Images were taken every 10 minutes for 20 hours. Images were processed using ImageJ. We quantified Golgi orientation in cells that had their Golgi within 180 degrees of the wound and quantified the angle of orientation by drawing a line from the position of the Golgi towards the wound and another parallel to the wound (Figure 5.3E, insert), as described in (Zhang et al., 2008). A 90 degree angle is indicative of Golgi facing toward the wound and indicative of front-rear polarity.

2.6.4 Growth curve assay

Cells were reverse transfected in 6-well plates and plated at a density of 3.3 x 10^4 cells/ml per well, with three replicates per condition. When drugs were used one plate containing mock transfected cells and *DOCK5* siRNA would be treated with DMSO, and another with the drug. Binimetinib and FAKi (PF-573288) were added to a final concentration of 10µM and 2µM respectively. Drugs and DMSO were added in 500 µl DMEM 48 hours after transfection. Plates were incubated in the IncuCyte S3 Live-Cell Analysis System (Sartorius) at 37 degrees and 5%

CO_2 and imaged at 6 hour time points for a minimum of 156 hours (6.5 days). A minimum of 9 fields of view were imaged per well. Analysis of confluence over time was carried out using IncuCyte software (Sartorius).

2.6.5 Viability assay

Cells were reverse transfected as described in the siRNA section in white-opaque-384 well plates. Drugs were added 2 hours later in 10µl of medium containing 10% FBS. 72 hours later viability assay was performed by adding 25µl of CellTiter-Glo ® (#G7571 Promega) according to the manufacturer's protocol. Plate was shaken for 10 minutes added according to the manufacturer's protocol and luminescence signal was measured on an Envision multiassay station (Perkin Elmer)

2.7 Statistical analyses

Statistical analyses performed for each assay are indicated in text and figure legends. Most analyses were carried out using Prism 8 (GraphPad). Other software used included RStudio, Jupyter Notebooks, and MATLAB (Mathworks). PLSR analysis was obtained using RStudio, and PCA analysis was performed either in Jupyter Notebooks or using ClustVis (Metsalu et al, 2015).

Chapter 3 RNAi screens for regulators of cell shape and YAP/TAZ localisation in MDA-MB-231 and LM2

Chapter 3 RNAi screens for regulators of cell shape and YAP/TAZ localisation in MDA-MB-231 and LM2

3.1 Introduction

The process of metastasis depend on cancer cells' physical and mechanical interactions with the microenvironment (Kass et al., 2007; Wirtz et al., 2011). Therefore, cancer cells need to be able to remodel their cytoskeleton in order to metastasise. This morphological change is displayed when cancer cells undergo epithelial to mesenchymal transition (EMT) where epithelial cells lose their cobblestone epithelial appearance to become more spindly-shaped, a mesenchymal morphology (Dongre and Weinberg, 2019). Changes in phenotypic states are accompanied by expression of stem cell traits, drug resistance, and drive metastasis (Dongre and Weinberg, 2019; Kröger et al., 2019; Mani et al., 2008).

Rho GTPases are the master regulators of cell shape and cycle between an inactive GDP-bound state and an active GTP-bound state (Ridley, 2012). The rate of GDP-GTP exchange is regulated by RhoGEFs and RhoGAPs where RhoGEFs activate Rho GTPases by catalysing the exchange of GDP for GTP in response to fluctuations in the microenvironment such as changes in extracellular matrix stiffness, while RhoGAPs inhibit Rho GTPase activity by accelerating GTP hydrolysis (Burridge and Wennerberg, 2004). Gene expression data by the Pietenpol lab has shown that regulation of the actin cytoskeleton by Rho GTPases, focal adhesion components, as well as expression of TAZ, are upregulated in the M and MSL subtypes of TNBC (Lehmann et al, 2011). When

referring to TNBC in this Chapter I will be referring to M and MSL subtypes unless otherwise stated.

We hypothesise that by activating Rho GTPase signalling which regulates adhesions, cytoskeletal reorganisation, and TAZ localisation, which are upregulated in the TNBC M and MSL subtypes, RhoGEFs are the drivers of cell shape changes required for metastasis. For this reason, RhoGEFs are attractive therapeutic targets for intervention in TNBC. However, both RhoGEFs and RhoGAPs are large families of signalling enzymes (82 and 67 members respectively) (Hall, 2009) and which are dysregulated in TNBC remains unclear.

Towards the ultimate goal of identifying which RhoGEFs and RhoGAPs are essential for the cell shape changes driving TNBC metastasis, I performed high-throughput RNAi screens of 142 siRNAs targeting human RhoGEFs and RhoGAPs to identify genes that are key for morphogenesis and/or regulation of YAP/TAZ nuclear translocation. These screens were performed in the highly metastatic TNBC cell line LM2 (Minn et al., 2005), and its less metastatic parental cell line MDA-MB-231 (Pascual-Vargas et al., 2017), the latter of which is classed as belonging to the MSL subtype (Lehmann et al., 2011). In this chapter I describe how we performed and analysed these screens, and how we can infer function from RNAi screens. Further I discuss how we identify RhoGEF/GAPs which are regulating cell shape specifically in LM2 and thus may be driving metastasis. Lastly, I describe how cell shape is regulated differently in LM2 and MDA-MB-231s.

3.2 Results

3.2.1 Overview of RNAi screens and automated single-cell analysis workflow in 2D

We reasoned that if a gene is essential for LM2 and not MDA-MB-231 morphogenesis or YAP/TAZ localisation this gene might be important for LM2 metastasis. We used two RNAi libraries: siGENOME and ONTARGET*Plus* (Dharmacon). A detailed description of how the screens were performed can be found in the Materials and Methods section. Briefly, siRNAs were arrayed on day 0 in 384-well plates, cells were reverse transfected on day 1, fixed and stained on days 3 and 4, and imaged from day 4 onwards. Each screen was performed in duplicate resulting in 8 plates per cell line (Figure 3.1A). Cells were stained for α-tubulin, polymerised F-actin, and YAP/TAZ, which provide information on how each RNAi is disrupting the cytoskeleton and facilitate overall quantification of cell shape. Because YAP/TAZ are active transcriptional coactivators in the nucleus, and are sequestered in the cytoplasm in an inactive state (Piccolo et al., 2013), simultaneously quantifying cell shape and YAP/TAZ localisation, can be used to determine if gene depletion has affected cell shape in a manner that has resulted in the activation of YAP/TAZ "directly" – i.e., by altering the dynamics of a signalling cascade that regulate YAP/TAZ, or "indirectly" – i.e., by affecting cell shape which in turn affects YAP/TAZ localisation (Sero and Bakal., 2017).

Images were processed and analysed using Columbus 2.6.0 Software Platform (Perkin Elmer). To identify single cells, nuclei were segmented using the Hoechst

channel. The cytoplasm was then segmented based on the identified nuclei using the α-tubulin stain (Figure 3.1). Cells at the edges of the field were filtered out. A total of 126 features describing intensity, morphological, and texture features were extracted for each single cell. Detailed explanations of how features were obtained can be found in the Materials and Methods section.

3.2.2 Quantification of YAP/TAZ ratio.

To quantify the nuclear translocation of YAP/TAZ, the log10 ratio of nuclear region to ring region (perinuclear region) YAP/TAZ is calculated for every cell (Sero et al, 2015); and hereafter referred to as the 'YAP/TAZ ratio'. It is important to note that the antibody used in these screens and throughout this thesis recognises both YAP and TAZ. Indeed, by Western blotting we see that the YAP/TAZ antibody binds to both YAP and TAZ proteins (Appendix 2A, B). To estimate the contribution of YAP and TAZ individually, we used siRNA to target *YAP* and *TAZ*, alone and in combination and probed for YAP/TAZ via Western blotting and immunofluorescence (Appendix 2 and Figure 3.2). We found that contrary to depleting *YAP* alone, depleting *TAZ* alone did not significantly reduce total YAP/TAZ levels via immunofluorescence. However, depleting *YAP* and *TAZ* in combination significantly reduced total YAP/TAZ levels compared to both mock transfected cells and to depleting *YAP* on its own (Figure 3.2B). This suggests that what the YAP/TAZ antibody is binding to when *YAP* is depleted, is *TAZ*, which is lost when both *YAP* and *TAZ* in combination are knocked down. Further, the reason for si*TAZ* not significantly reducing YAP/TAZ levels via immunofluorescence could either be due to YAP/TAZ antibody being more specific to YAP, or because contrary to YAP, TAZ is a very unstable protein with

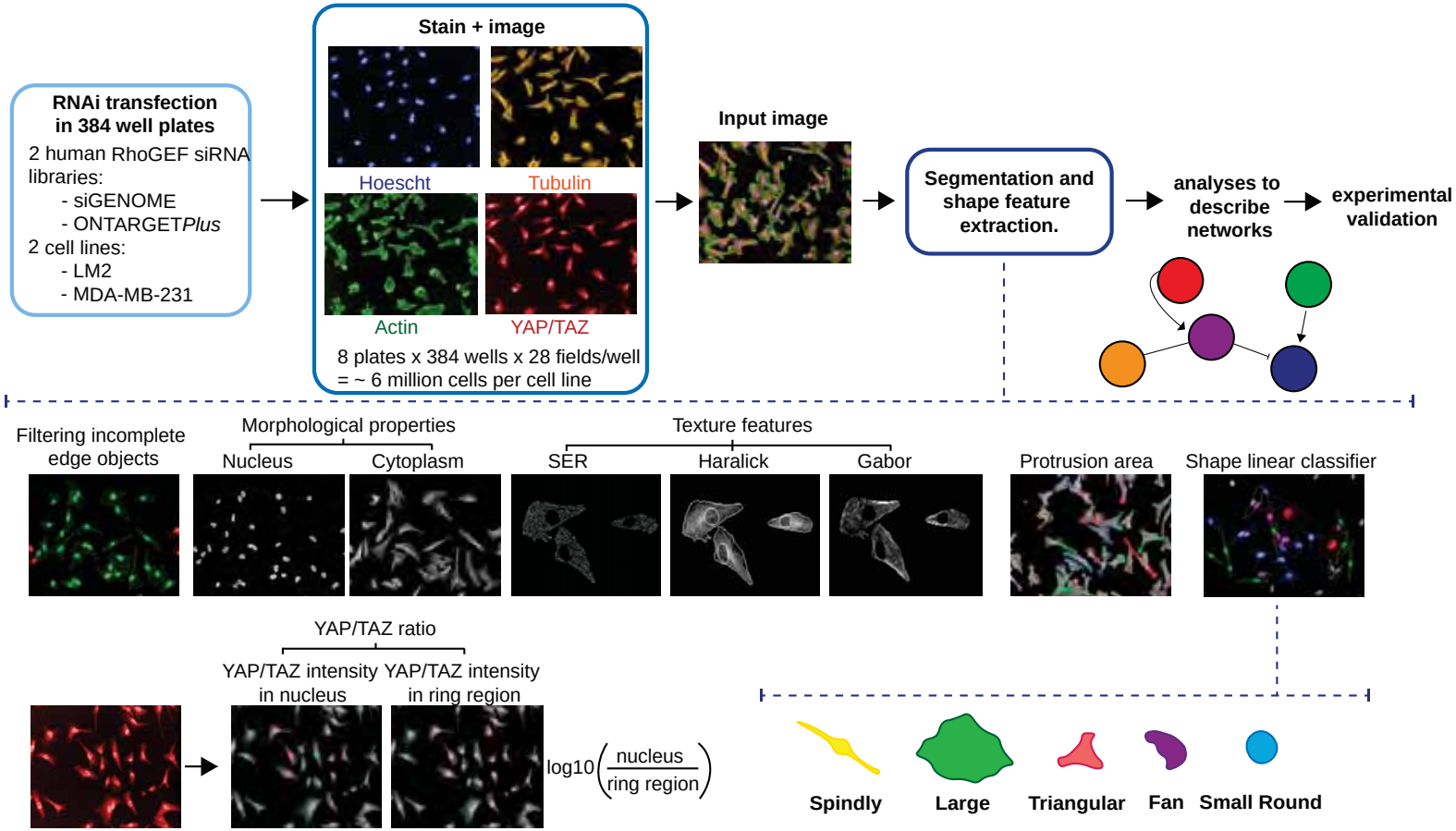

Figure 3.1 Experimental workflow for RNAi screens
RNAi screens were performed on the highly metastatic TNBC cell line LM2, and its less metastatic parental cell line MDA-MB-231, to identify RhoGEFs and RhoGAPs are essential for the cell shape changes driving TNBC metastasis. The screening approach is displayed in a sequential manner beginning with RNAi reverse transfection, followed by staining and imaging, and ending with image analysis and further processing.

a half-life of under 2 hours (Piccolo et al., 2014), suggesting there is less TAZ present at any given time in a cell. In fact, when we knock down *YAP*, there is less TAZ protein present than for mock, while *TAZ* mRNA levels are significantly higher (Appendix 2B,C).

YAP/TAZ nuclear translocation can be sensitive to cell density, and thus some siRNAs might affect YAP/TAZ localisation simply because they reduce cell numbers (Sero et al, 2015). However, one of the features of metastatic cancer cells is loss of cell-cell contact inhibition (Hanahan and Weinberg, 2011) and we wanted to account for any indirect effects on YAP/TAZ activity that might be induced by changes in cell density following RhoGEF depletion. We found an inverse linear relationship between cell number and YAP/TAZ ratio in LM2 (R^2 = 0.9307) (Figure 3.3A). This can be observed in images shown in Figure 3.3B, where at a low density (5.0 x 10^4 cells/ml) YAP/TAZ is more nuclear (indicated by white arrows), but at a high density (2.5 x 10^5 cells/ml) YAP/TAZ is mostly cytoplasmic (white arrows). Due to the inverse relationship between cell density and YAP/TAZ ratio observed in LM2, we plated our cells at a low density in our screens, and also generated a cell density curve. A cell density curve allows us to ensure that any effects seen in on YAP/TAZ translocation are due to gene knockdowns, should siRNAs result in a reduction in cell number. However, we found no significant difference in cell number between siRNA and mock transfected cells (P value between slopes = 1) or within siRNA and mock transfected cells (R values < 0.14) (Appendix 3). Therefore, we did not need to account for cell number when quantifying YAP/TAZ ratio Z-scores in these screens.

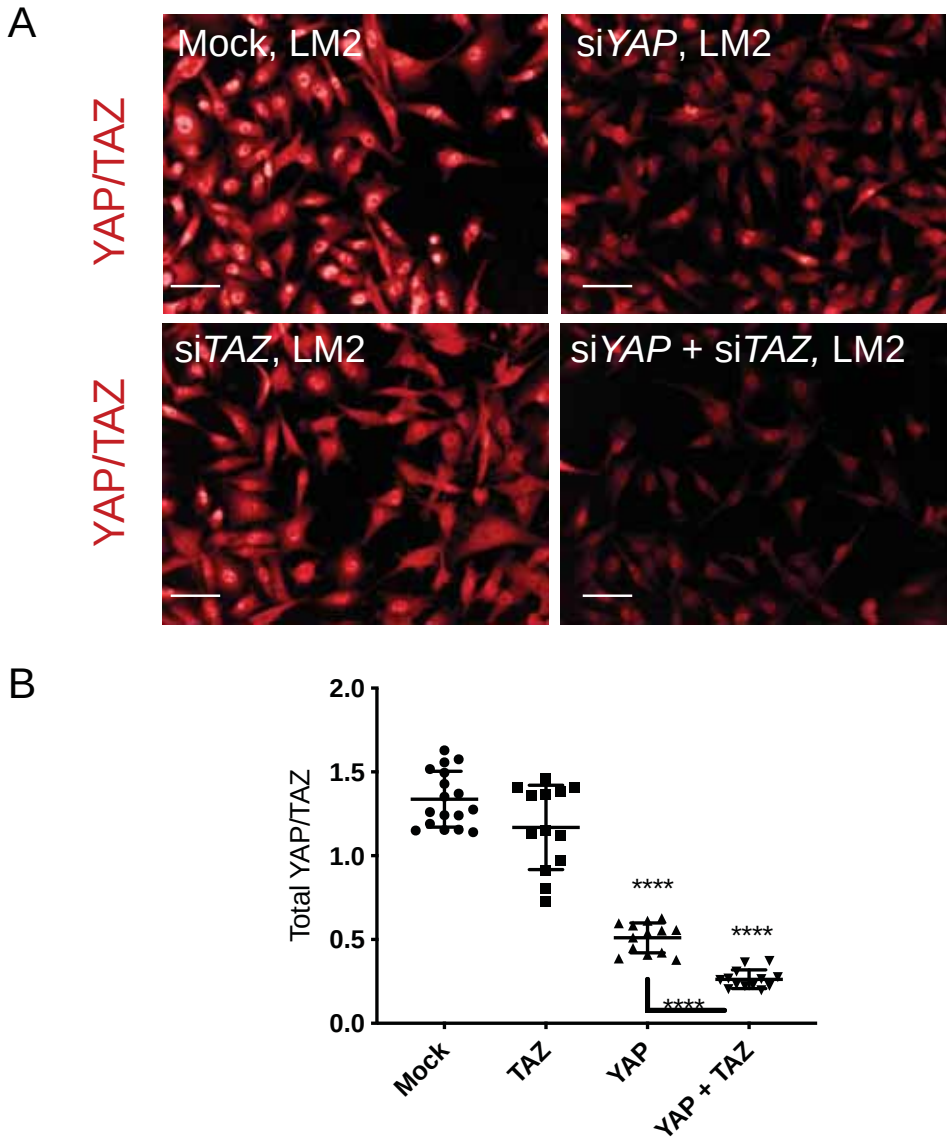

Figure 3.2 Validation that YAP/TAZ antibody binds both to YAP and TAZ via immunofluorescence

(A) Representative images of mock, siYAP, siTAZ, and siYAP + siTAZ transfected cells stained with YAP/TAZ antibody. All images taken at same intensity settings. Scale bar, 50µm. (B) Graph shows quantification of total cell YAP/TAZ intensity. Mean ± SD are shown (n = 3 biological repeats, 4 wells per condition, ANOVA, **** $P < 0.0001$).

A

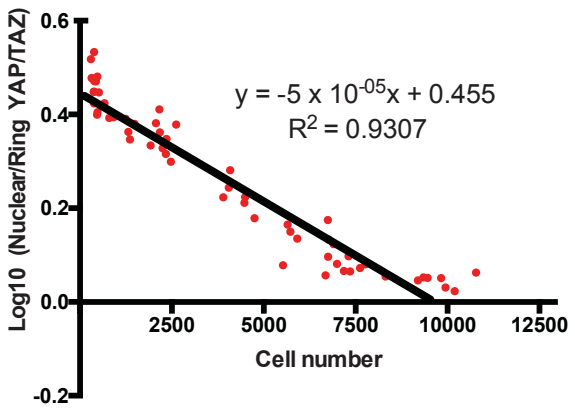

B

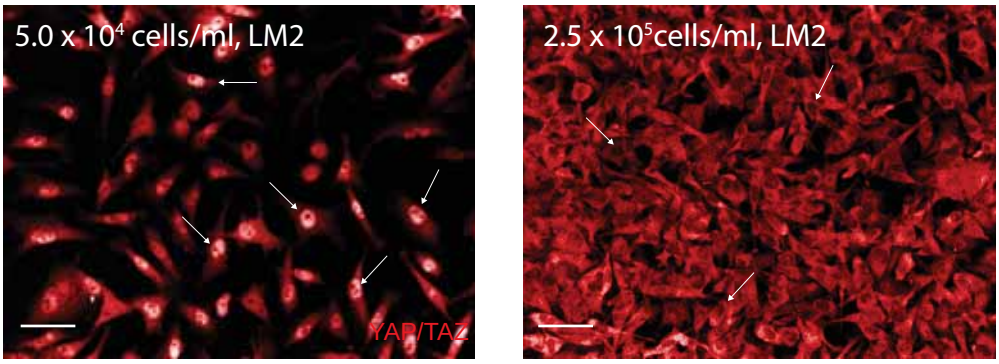

Figure 3.3 YAP/TAZ nuclear translocation is dependent on cell density

(A) Graph depicting the relationship between cell number and YAP/TAZ ratio in LM2 cells. Inverse linear relationship is indicated by $R^2 = 0.9307$ for LM2. (B) Representative images of the effect of cell density on YAP/TAZ nuclear translocation in LM2. LM2 cells plated at a low density (5.0×10^4 cells/ml) (left) and at a high density (2.5×10^5 cells/ml) (right) stained for YAP/TAZ. White arrows indicate YAP/TAZ nuclear translocation in left panel, and lack of YAP/TAZ in nucleus in right panel. Scale bar, 50µm.

3.2.3 Technical validation of screens.

To assess replicate plate reproducibility for each set of duplicate plates per screen, we first calculated the Z-scores of normalised well-averaged feature vectors for each well per plate and calculated the correlation (Person Correlation Coefficient; PCC) between well-averaged feature vectors between the duplicate plates. In the resulting correlation matrix, where each row is a well in plate A, and each column a well in plate B, the diagonal represents the correlation between replicate wells, whilst the off-diagonal is used to determine the null-value correlation. The positive and negative distribution of these values for each plate is presented in Figure 3.4A. Pairwise t-tests showed all correlation increases from null-value correlation were highly significant ($P<0.001$). Furthermore, in no cases did the interquartile ranges of positive to null distributions overlap, indicating a high level of reproducibility between replicate plates.

To determine siRNA knockdown efficiency, we ran analyses were to determine multinucleate cell percentage. The cytokinesis regulators *ECT2* and *RACGAP1* (Kim et al., 2014, Su et al, 2011) were top hits for both cell lines for multinucleate cell percentage Z-scores. The high number of multinucleate cells for these siRNAs was also observed by looking at the images (Figure 3.4E).

To test the reproducibility of siRNA effect, we compared the distribution of Pearson correlations between technical replicates and randomly drawn siRNAs. For the positive distribution, we compared correlations of well-averaged feature vectors for technical siRNA replicates across the screen. For the null distribution

we randomised feature vectors and performed the same calculation. The positive distribution showed a highly significant increase compared to the null distribution (pairwise t-test, $P<0.001$). For the positive distribution, a median correlation of 0.594 was observed, and a strong negative skew (-1.02) was also present; suggesting high levels of correlation were observed between the majority of replicates (Figure 3.4B). Meanwhile, the null distribution showed a median near zero (0.169) and no skew (0.02), indicating siRNA treatments induced reproducible changes in cell morphology.

Our ability to detect YAP/TAZ by immunolabelling was assessed first by calculating Z-scores of total YAP/TAZ. Z-score values were obtained by first normalising the data per plate, grouping normalised values per screen, and using the mean and standard deviations of the mock transfected cells per screen. Cells containing si*YAP* were hits for low total YAP/TAZ for both cell lines (siRNAs were considered hits when they were above 1.5, or below -1.5). Further, Z-scores of the YAP/TAZ ratio were also calculated. In this case, cells containing si*LATS1* were top hits for a high value of YAP/TAZ ratio. This was as expected, as when present LATS1 sequesters YAP/TAZ in the cytoplasm (Halder et al., 2012). Finally, the change in YAP/TAZ localisation can clearly be observed by looking at the images (Figure 3.4C).

Validating our ability to detect changes in YAP/TAZ localisation is that depletion of *ARHGEF7* is a hit for high nuclear region to ring region YAP/TAZ ratio, for both the siGENOME and ONTARGET*Plus* screens in the LM2 cell line (Figure 3.4D).

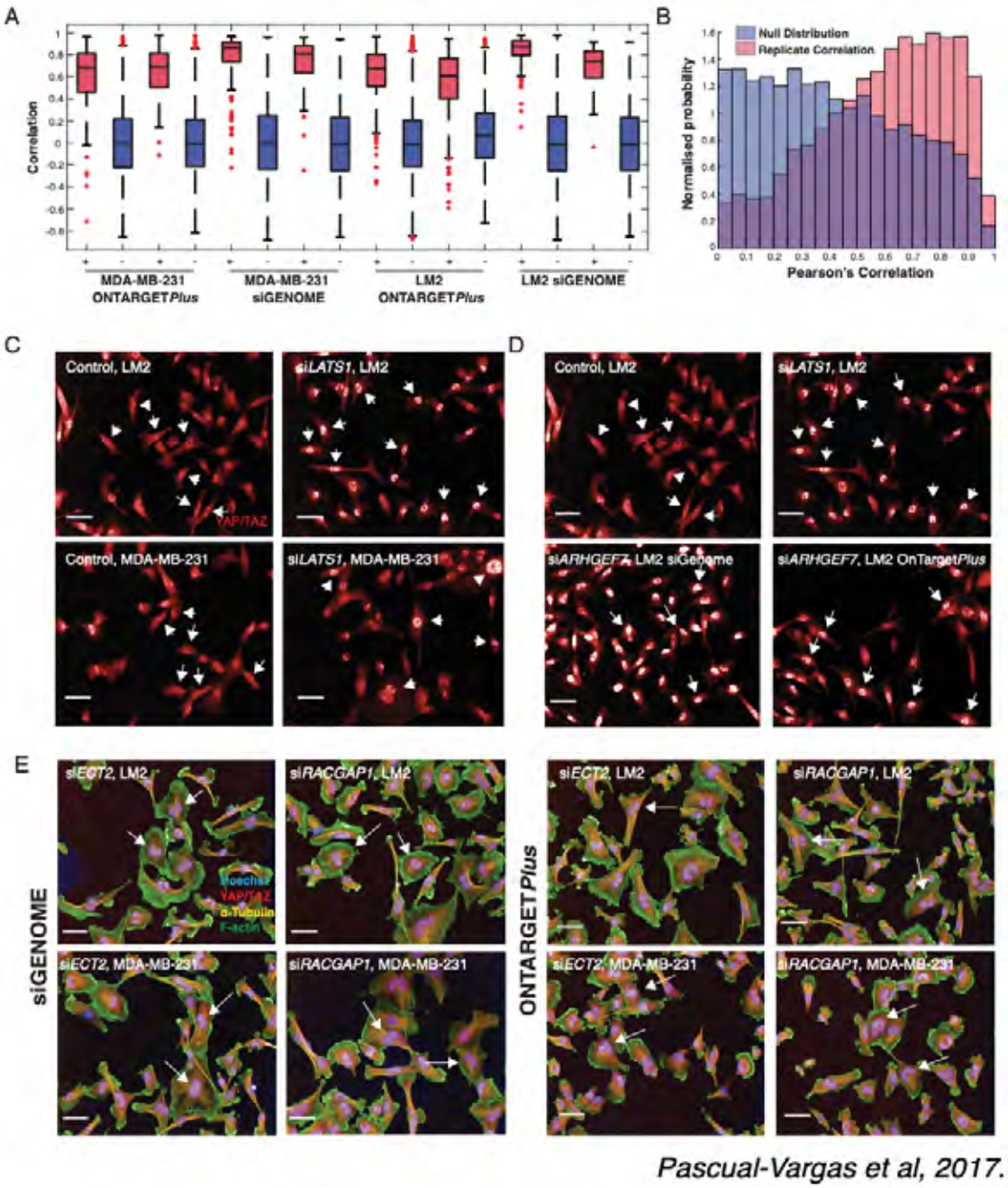

Figure 3.4 siRNA depletion is reproducible between replicate plates and over the screen (A) Pearson correlation coefficients between Z-scores of duplicate plates. The positive distribution (+) depicts the correlation between replicate wells, and the negative distribution (-) depicts the null correlation. Pairwise t-tests showed all correlation increases from null-value correlation were highly significant (P<0.001). (B) Pearson correlations between technical siRNA replicates (positive distribution) and randomly drawn siRNAs (negative distribution). Median of positive distribution is 0.594, with a skew of -1.02. Median of negative distribution is 0.1692, with no skew (0.02). The positive distribution showed a highly significant increase compared to the null distribution (pairwise t-test, P<0.001). (C) Representative images of si*LATS1* and mock transfected LM2 and MDA-MB-231 cells. The nuclear intensity of *LATS1* depleted cells is higher than that of control cells (white arrows). Stained for YAP/TAZ. (D) Representative images of si*ARHGEF7* from OnTARGETPlus and siGENOME screens showing increase nuclear YAP/TAZ compared to mock transfected LM2 cells (white arrows). si*LATS1* included as a comparison. (E) Representative images of multinuclear cells (white arrows) as a result of *ECT2* and *RACGAP1* knockdown for LM2 and MDA-MB-231 in both OnTARGETPlus and siGENOME screens. Stained for DNA (blue), YAP/TAZ (red), α-tubulin (yellow), and polymerised F-actin (green). Scale bar, 50µm. (A) and (B) were performed by Sam Cooper, Bakal lab.

Knockdown of *ARHGEF7* has previously been reported to increase nuclear YAP/TAZ (Heidary Arash et al., 2014).

We also assessed the performance of negative and positive controls by calculating the Z' factor, a widely used test to determine the dynamic range of RNAi screens (Birmingham et al., 2009, Zhang et al., 1999). The Z' factor is a statistical measure which requires the ratio of the sum of the standard deviations between controls and the difference between the means to be at least three standard deviations from each other (Birmingham et al., 2009). Values above 0.3 are deemed acceptable, whereas values between 0.5 and 1.0 are desirable (Zhang et al., 1999). The average of the values for each control are shown in Tables 3.1 and 3.2 for the LM2 and MDA-MB-231 cell lines respectively. All plates performed well (above 0.3) for at least one positive versus negative control for each cell line, with ONTARGET*Plus* plates performing better than siGENOME overall. si*YAP* performance was assessed using the total YAP/TAZ; while si*LATS1* performance was assessed using the YAP/TAZ ratio as in the absence of LATS1 YAP/TAZ nuclear localisation is expected to increase (Piccolo et al, 2013). si*YAP* and si*LATS1* were not included in the LM2 siGENOME screen, so si*ECT2* was used to calculate the Z' factor instead. si*ECT2* performance was assessed based on multinuclearity. LM2 screens performed very well (above 0.5) for si*ECT2* versus mock, with an average of 0.71 Z' factor for siGENOME, and 0.64 for ONTARGET*Plus*.

As an additional form of validating the reliability of the screens, we measured mRNA levels following quantitative knockdown of our controls using ONTARGET*Plus* siRNAs. We found that *LATS1* siRNA had an mRNA knockdown efficiency of 71% and 70% in LM2s and MD-MB-231s respectively (Figure 3.5A). Further, *YAP* mRNA was depleted by 99% in both cell lines by *YAP* siRNA (Figure 3.5B). We also quantified mRNA levels of *ECT2* following siRNA knockdown. Knockdown efficiency of *ECT2* mRNA by siRNA ranged between 88% and 99% for both cell lines, indicating that siRNA gene knockdown was efficient and the screens reliable (Figure 3.5C).

Table 3.1: Summary of average Z' factor to mock for LM2 siGENOME and ONTARGET*Plus* screens.

Average Z' factors for LM2 screens			
siGENOME	ONTARGET*Plus*		
ECT2/mock	*ECT2*/mock	*YAP*/mock	*LATS1*/mock
0.71	0.64	0.67	0.40

Table 3.2: Summary of average Z' factor to mock for MDA-MB-231 siGENOME and ONTARGETPlus screens.

Average Z' factors for MDA-MB-231 screens			
siGENOME		ONTARGET*Plus*	
YAP/mock	*LATS1*/mock	*YAP*/mock	*LATS1*/mock
0.53	0.29	0.76	0.57

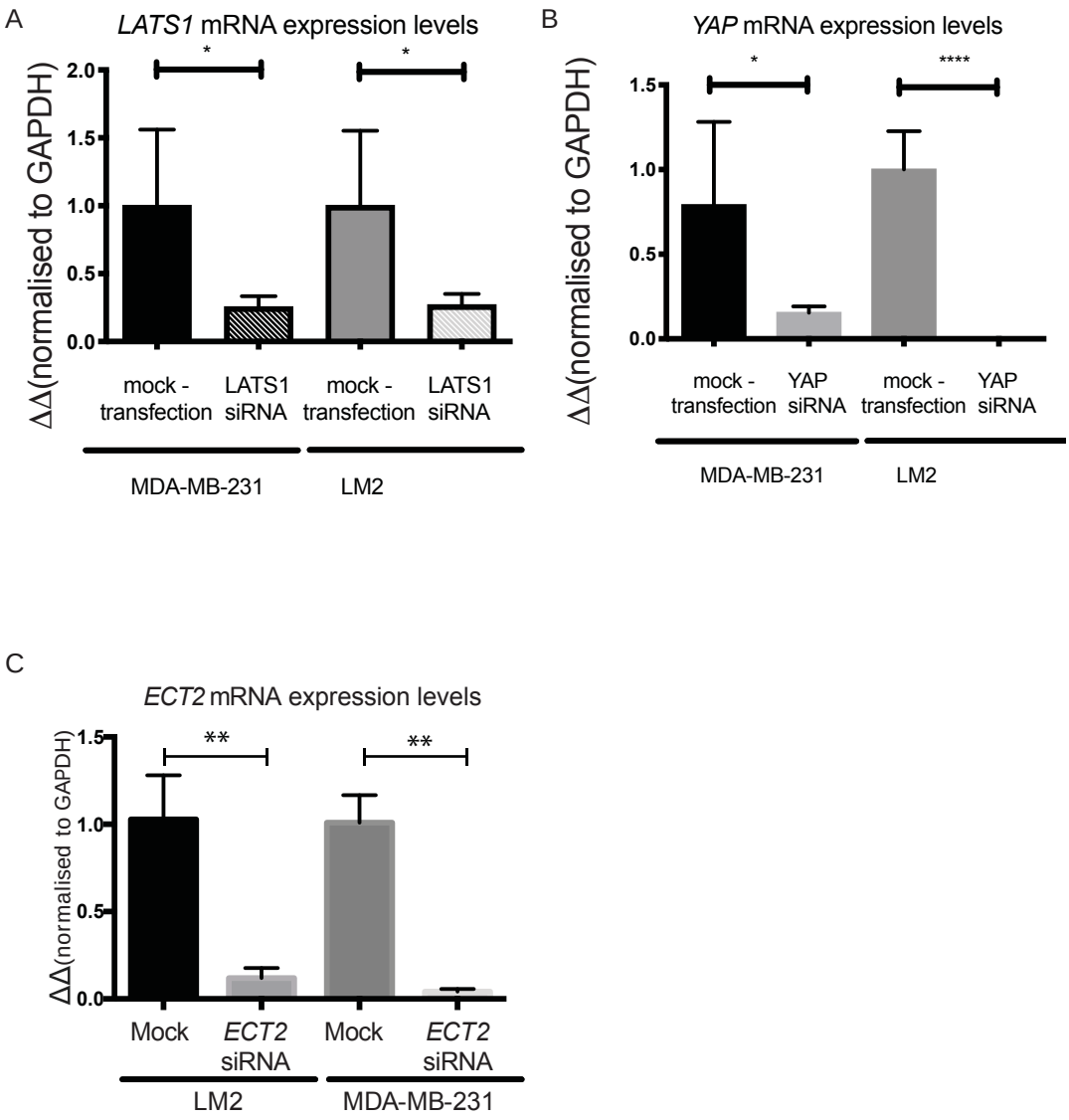

Figure 3.5 siRNA knockdown efficiency
(A) *LATS1* mRNA expression levels normalised to GAPDH for mock and si*LATS1* transfected LM2 and MDA-MB-231 cells. (B) *YAP* mRNA expression levels normalised to GAPDH for mock and si*YAP* transfected LM2 and MDA-MB-231 cells. (C) *ECT2* mRNA expression levels normalized to GAPDH for mock and si*ECT2* transfected LM2 and MDA-MB-231 cells. Data are shown as means ± standard deviation from at least 3 technical replicates. Significance obtained via student's T-test, *P < 0.05, **P < 0.01, ***P < 0.001, ****P < 0.0001.

3.2.4 Linear classification of shapes

To reduce the complexity of a high-dimensional single cell shape data (where each cell is described by > 100s features), we have previously classified cells on the basis of their similarity to a small number of “exemplar” or “reference” shapes (Bakal et al, 2007; Sailem et al, 2016). Here, we classified the population of single cells on the basis of their similarity to five visually distinctive reference shapes. Each cell classified in a binary fashion as being similar to only one of five shapes. The five shapes identified were: 1) “spindly” shape, elongated cells with typically two protrusions; 2) “large spread” shape, cells with a large area which are often circular; 3) “triangular” shape, cells with three distinct protrusions; 4) “fan” shape, asymmetrically-shaped cells with nucleus to one side; 5) “small round” shape, cells with low cell area and high roundness. To classify single cells into these reference shapes we manually trained these linear classifiers on approximately 1500 manually selected cells using Columbus software. For each siRNA-treated population we generated a feature vector or “morphological signature” comprised of the total number of cells classified into each shape, thus accounting for the heterogeneity in the population. Figure 3.6A shows specifically which features Columbus used to separate cells into each class and their contribution. For example cells classified as large and spread tended to score high for cell area and width, while those classified as spindly had low values for cytoplasm ratio width to length, and those classified as small and round had high values for cell roundness (Figure 3.6A). LM2 wild-type cells are very heterogenous compared to MDA-MB-231. Such that the 5 reference shapes are observed for LM2, whereas in MDA-MB-231 the predominant shape in wild-type populations is small round (70%) (Figure 3.6B).

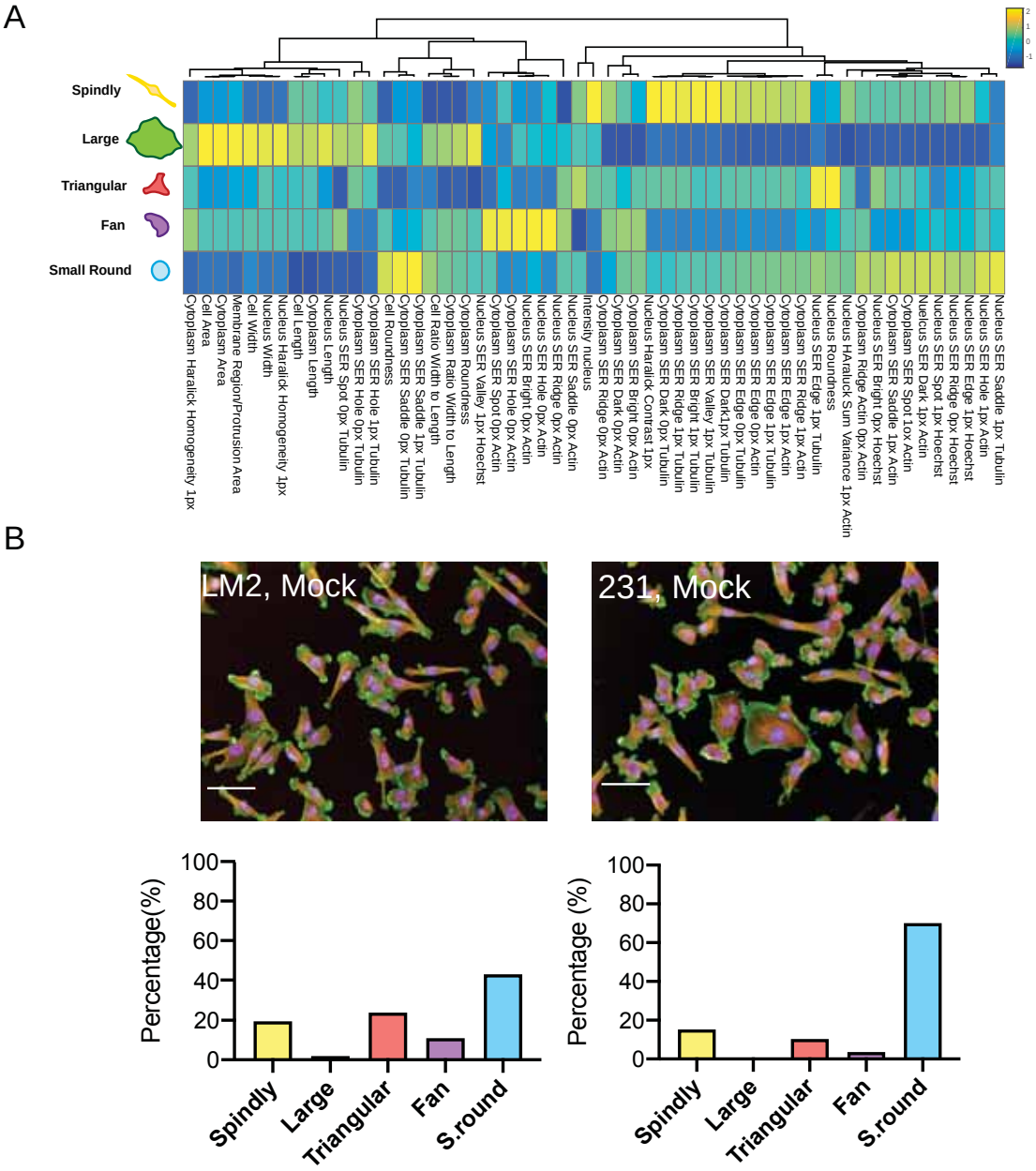

Figure 3.6 Linear classification of shapes
(A) Heat map and dendrogram of the features Columbus software used to classify cells into the 5 chosen shapes and their contribution, using single cell data. Yellow and dark blue represent a high and low score respectively in arbitrary units. (B) Percentage of cells classified into each shape from a mock transfected single cell population in LM2 and MDA-MB-231 with representative images. Scale bar 50µm.

Principal Component Analysis (PCA) of shape morphological signatures for LM2 and MDA-MB-231 siRNA and mock transfected populations shows that the proportion of cells within a given shape varies greatly between the two cell lines (Figure 3.7). Within individual cell lines, siRNA knockdowns result in the enrichment of a particular shape with each different distribution of shapes occupying different PC space. For example, depletion of *DOCK11* results in a high degree of fan shaped cells, while *FARP1* depletion enriches primarily for spindly shapes (Figure 3.7).

3.2.5 Filtering and shape hit identification

We have previously observed that following efficient gene depletion, many cells in a population can still appear wild-type (Yin et al., 2013b). For example, even a highly penetrant siRNA such as *ECT2* siRNA will lead to a clear phenotype (binucleate cells) only in a subpopulation of cells. The presence of cells with wild-type morphologies can potentially obscure the presence of phenotypes resulting from gene depletion. To identify and filter normal cells from our data set, we first performed PCA on single cell dataset comprised of texture and morphological features of populations which were either mock transfected or transfected with siRNAs which scored the highest for enriching for a particular shape. The data were projected into 2D principal component (PC) space and each data point (cell) colour coded by the shape of each cell (Figure 3.8A, B). We then reasoned that the region of shape space where different classified cells overlapped in PC space were normal cells, defined as those whose PC coordinates lay within 1 standard

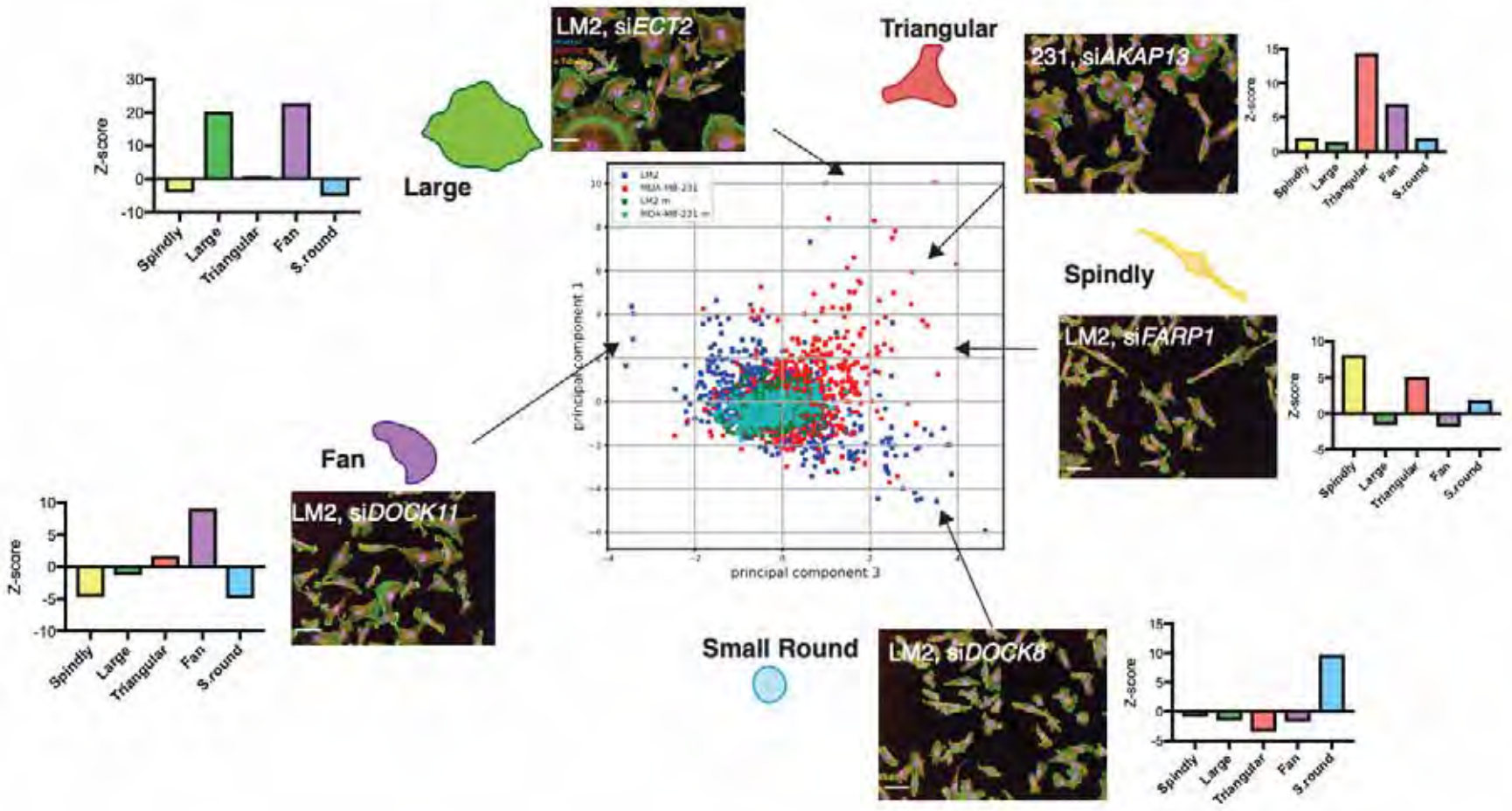

Figure 3.7 Linear classification of shapes
PCA of shape morphological signatures for LM2 and MDA-MB-231 siRNA and mock transfected populations. siRNA treated populations enrichment for each shape (as judged by Z-scores) are depicted: spindly in yellow, large round in green, triangular in pink, fan in purple, and small round in blue. Scale bar, 50µm.

deviation of the mean of PC1 and PC2 for the siRNA transfected population (black box, Figure 3.8B). We then trained new linear classifiers on the cells that fell in this space (black box, Figure 3.8A) and defined this population as 'normal'.

When we ran the classifiers again on the same data, performing the same PCA analysis on this new dataset and removing cells classified as 'normal' resulted in cells classified into the different shapes, separating better in PC shape space (Figure 3.8C). For example, cells classified into the most visually different shapes 'spindly' and 'large round' occupied separate PC space denoted by the 95% confidence intervals. We performed this same process for the MDA-MB-231 screens (Figure 3.9A-C).

In order to identify the effects of gene depletion on cell shape we calculated the percentage of cells classified into each shape from total number of cells classified. We normalised these percentages to each plate to remove any possible plate effects and calculated the Z-scores for each category. We determined genes as "hits" when at least 3 out of 4 replicates were either above 1.5, or below -1.5 for a particular shape. Those above 1.5 are considered 'positive' hits, thus enriching for a particular shape. On the other hand, those below -1.5 are considered 'negative' hits, which means that the particular shape they scored negatively for is significantly lacking in that population (Appendix 5).

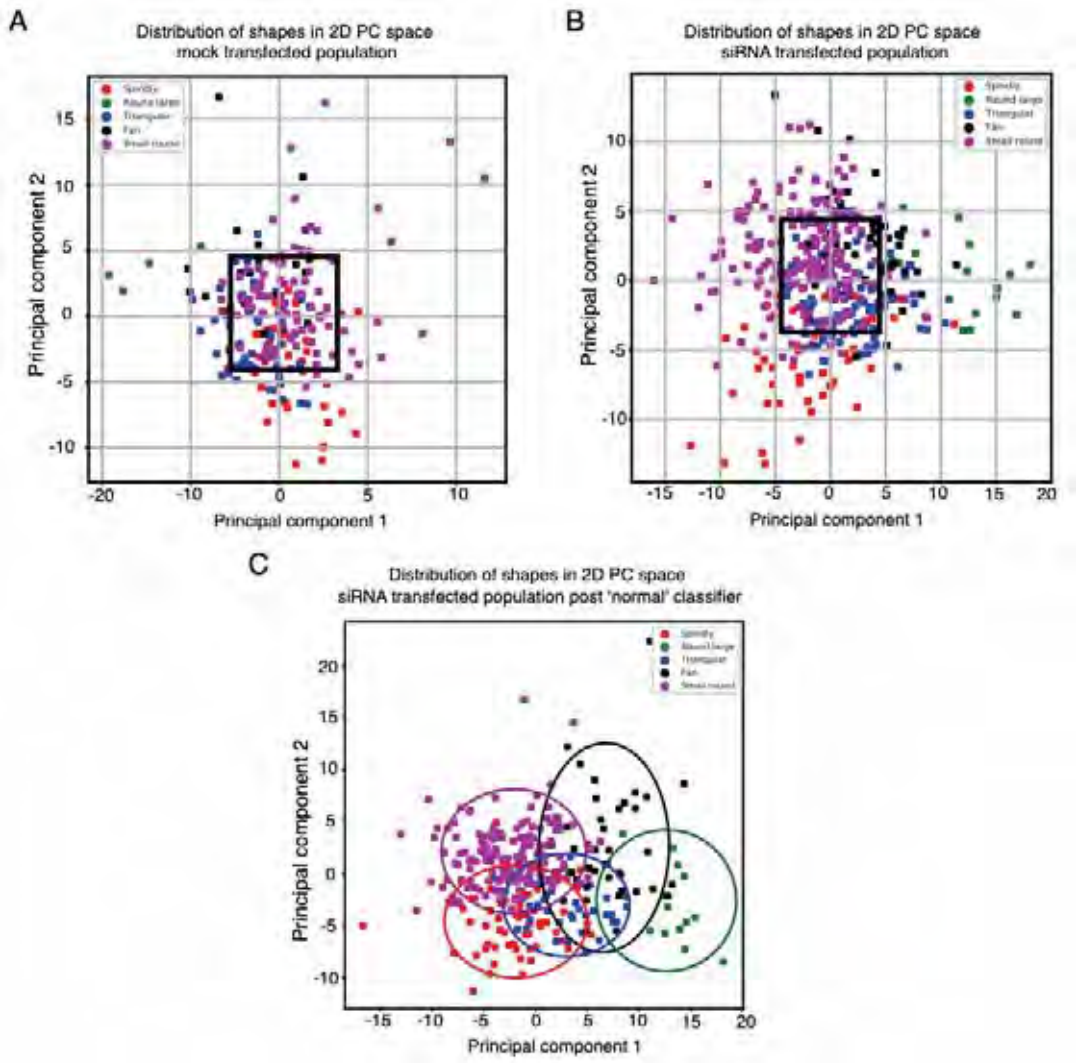

Figure 3.8 Shape filtering in LM2
(A) (B) PCA of single cell dataset comprised of texture and morphological features of populations which were either mock transfected (A) or transfected with siRNAs which scored the highest for enriching for a particular shape (B). Each data point represents a cell and is colour coded by the shape into which it has been classified. Spindly in red, round large in green, triangular in blue, fan in black, and small round in purple. Black box represents 1 standard deviation of the mean for PC1 and PC2 of (B), projected on (A). Single cells within black box shown in (A) were defined as 'normal' in the new classifiers. (C) PCA of single cell dataset comprised of texture and morphological features of siRNA transfected population, after running new classifiers on same data, removing cells classified as 'normal'. Ellipses represent 95% confidence intervals for each shape.

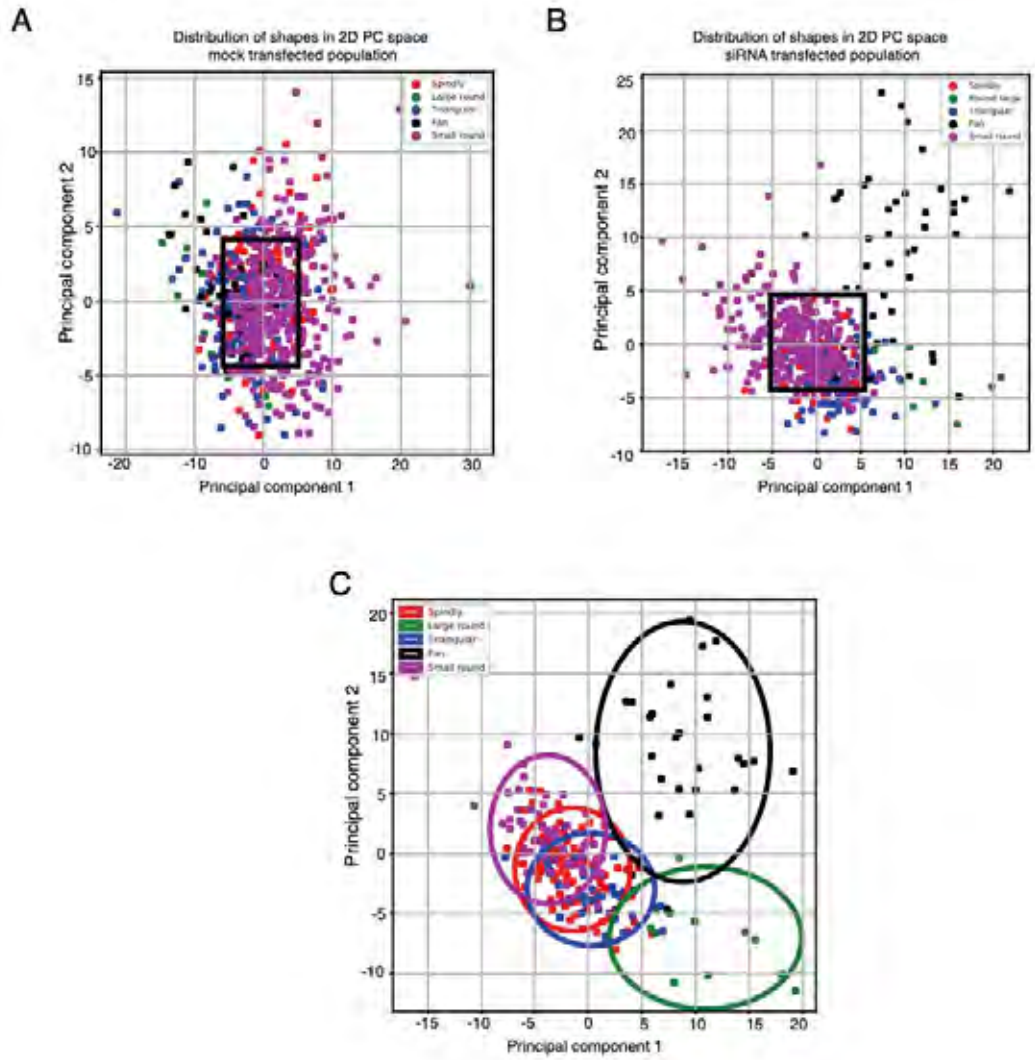

Figure 3.9 Shape filtering in MDA-MB-231
(A) (B) PCA of single cell dataset comprised of texture and morphological features of populations which were either mock transfected (A) or transfected with siRNAs which scored the highest for enriching for a particular shape (B). Each data point represents a cell and is colour coded by the shape into which it has been classified. Spindly in red, round large in green, triangular in blue, fan in black, and small round in purple. Black box represents 1 standard deviation of the mean for PC1 and PC2 of (B), projected on (A). Single cells within black box shown in (A) were defined as 'normal' in the new classifiers. (C) PCA of single cell dataset comprised of texture and morphological features of siRNA transfected population, after running new classifiers on same data, removing cells classified as 'normal'. Ellipses represent 95% confidence intervals for each shape.

3.2.6 Analysis of hits across screens

To understand how shape is regulated differently between LM2 and MDA-MB-231, and how each siRNA library is performing, we calculated the percentage of RhoGEF/GAPs which were hits for each shape, both positive and negative, for each screen (Table 3.3). We found the screen which resulted in the most categories with highest hits was LM2 siGENOME: highest negative hits for spindly (29.6%), highest negative hits for triangular (23.2%), highest positive and negative hits for small round (30.3% and 33.1% respectively), and highest positive and negative hits for normal (10.6%, 26.1% respectively). The proportion of positive and negative in LM2 siGENOME and OTP screens was relatively even (15.3 v 18.8% for siGENOME, 13.9% v 10.5% for OTP, positive and negative respectively, Table 3.4), with siGENOME having more negative than positive hits. On the other hand, MDA-MB-231 siGENOME had approximately double the number of positive hits than negative hits, and OTP had approximately triple the number of positive than negative hits (15.4% v 5.67% for OTP, 12.9 v 6.57% for siGENOME, Table 3.4). This is also reflected in every shape category individually, where for MDA-MB-231, there were at least double the number of positive than negative hits for every category, except for normal category, (Table 3.3, Figure 3.10), contrary to LM2. In LM2 OTP, small round had an equal number of positive and negative hits, and triangular had a relatively similar number of positive and negative hits; while in LM2 siGENOME spindly, triangular, and small round had higher numbers of negative than positive hits (Table 3.3, Figure 3.10). Further, of the RhoGEF/GAPs that were hits, LM2 OTP screen had the highest number of RhoGEF/GAPs which were hits for only 1 shape (42.9%). Further of the genes that were hits for two shapes, approximately 90% of them were a

Table 3.3: Percentage of RhoGEF/GAPs which score as hits (at least 3 out of 4 replicates are above 1.5 or below -1.5) for each shape for each screen. ** highlight figures mentioned in text and highest values per shape per screen.

		Spindly	Large round	Triangular	Fan	Small round	Normal
LM2 OTP	Above 1.5	19.4 **	2.78 **	14.6 **	26.4 **	18.1 **	2.08
	Below -1.5	9.72	0	11.8	7.64	18.1 **	16.0 **
LM2 siG	Above 1.5	27.5	4.23 **	12.7	6.34 **	30.3	10.6
	Below -1.5	29.6 **	0.70	23.2 **	0	33.1 **	26.1 **
231 OTP	Above 1.5	29.9 **	4.86 **	21.5 **	17.4 **	18.1 **	0.69
	Below -1.5	4.17	0	3.47	0	3.47	22.9 **
231 siG	Above 1.5	23.9 **	7.75 **	18.3 **	9.86 **	16.2 **	1.41
	Below -1.5	9.15	0	7.04	0	7.04	16.2 **

Table 3.4: Percentage of RhoGEF/GAPs which score as hits (at least 3 out of 4 replicates are above 1.5 or below -1.5) overall.

	LM2 OTP	LM2 siG	231 OTP	231 siG
Overall above 1.5 (%)	13.9	15.3	15.4	12.9
Overall below -1.5 (%)	10.5	18.8	5.67	6.57
Overall (%)	12.2	17.0	10.5	9.74

Table 3.5: Of RhoGEF/GAPs which score as hits (at least 3 out of 4 replicates are above 1.5 or below -1.5) for shapes for each screen, percentage of genes which are hits for 1 shape, 2, or more.

		Hits for 1 shape	Hits for 2 shapes	Hits for more than 2 shapes	Hits for 2 shapes or more
LM2 OTP	All	42.9**	30.0	26.7	57.1
	Positive	37.1	1.90		
	Negative	5.71	0.95		
	Both	-	27.6 **		
LM2 siG	All	20.5	38.5	41.2	79.5
	Positive	10.7	0		
	Negative	9.84	4.10		
	Both	-	33.6 **		
231 OTP	All	37.4	28.9	37.3	66.3
	Positive	33.7	12.0		
	Negative	3.61	3.61		
	Both	-	13.3		
231 siG	All	28.4	35.1	36.5	71.6
	Positive	25.7	10.8		
	Negative	2.70	4.05		
	Both	-	20.3		

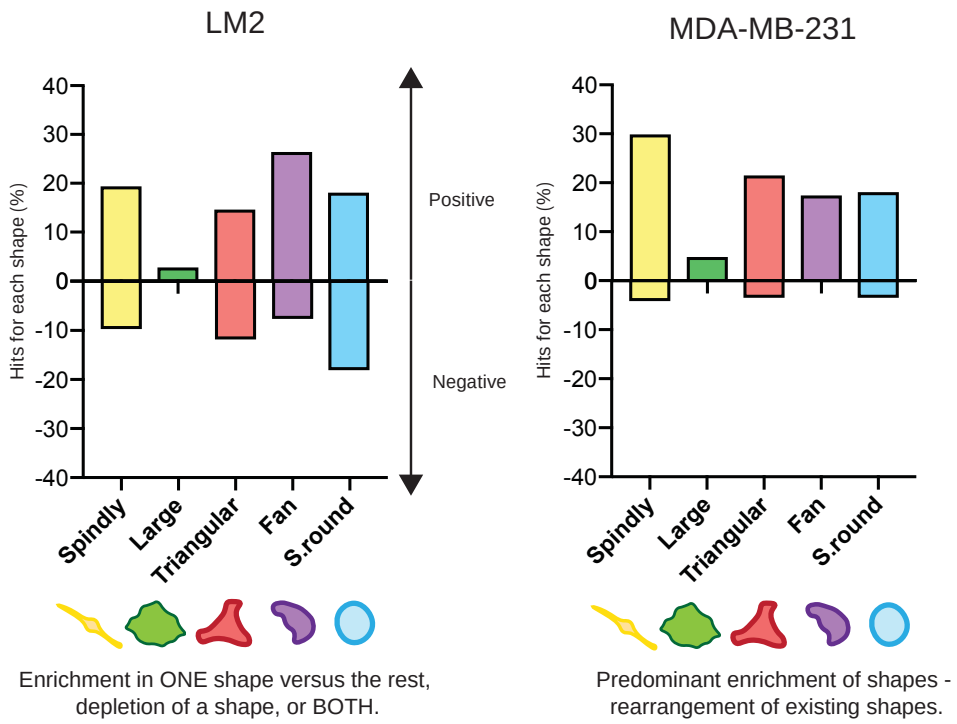

Figure 3.10 RNAi depletion affects LM2 and MDA-MB-231 shape populations differently.
Graphs depicting percentage of positive and negative hits for each shape for LM2 and MDA-MB-231. In LM2 there is a predominant enrichment in one shape versus the rest, depletion of a shape, or both. In MDA-MB-231 there is a predominant rearrangement of existing shapes.

positive hit for one shape, and a negative one for another, in the LM2 OTP and siGENOME screens, compared to approximately 50% in the MDA-MB-231 siGENOME screes (Table 3.5). This is highlighted in Figure 3.10 and is interesting because it suggests that RhoGEF/GAP depletion results in an enrichment of shapes in MDA-MB-231 which is not necessarily accompanied by a depletion of a particular shape, contrary to LM2 where RhoGEF/GAP depletion results both in enrichments of distinct shapes and depletion of shapes, commonly in combination. That is to say, the depletion of a RhoGEF/GAP results in a drastic change in the shapes present in the LM2 population, resulting in a distinct enrichment in one shape versus the rest (and depletion of another), while in MDA-MB-231 gene depletion results in rearrangement of existing shapes, but less depletion of any particular shape. Based on these observations, we hypothesise the morphology of LM2s is more *dynamic* than MDA-MB-231. Gene depletion prevents transitions between the shapes, resulting in depletion of certain forms. However, MDA-MB-231s are less dynamic, undergoing fewer transitions, and thus the effects of gene depletion are more subtle (Figure 3.17).

As a way of visualising what each siRNA was a hit for in every screen, we graphically represented each siRNA as a circle, and assigned each quarter of a circle to each screen: top right represents LM2 OTP, bottom right represents LM2 siGENOME, bottom left and top left represent MDA-MB-231 siGENOME and OTP screens respectively. Each quadrant is split into the 6 shapes, which are coloured if that gene was a hit for that particular shape. Block and faded colours represent positive and negative hits respectively for each shape (Figures 3.11

and 3.12). As a starting point, we focused on the LM2 OTP screen as OTP screens resulted in the least percentage of hits for normal shape out of the two (Table 3.3, Figure 3.11) suggesting that it was the screen where gene depletion had the strongest effect in LM2. siRNAs that were positive hits are found inside the shaded areas corresponding to the shape they were a hit for, and those that were negative hits only, outside the shaded areas for which they were a negative hit. Following this, we sorted the remaining ones first for hits in MDA-MB-231 OTP, then LM2 siGENOME and finally MDA-MB-231 siGENOME.

19 genes were shape hits for both LM2 OTP and siGENOME screens only: *SH3BP1, ARHGAP12, PLEKHG5/KIAA0720, ARHGEF26/SGEF, ARFGEF3/KIAA1244, TIAM1, ARHGEF17, FARP2, FGD3, FLJ10665/PLEKHG6, OBSCN, PLEKHG3, FGD2*, *MYO9A*, *PLEKHG3*, *FGD5, DNMBP, GRFL1/ARHGAP35,* and *ARHGAP44/KIAA0672* (Figure 3.11, Appendix 5 underlined). Out of these 19 genes, 5 of these genes were hits for at least one of the same shape: *FLJ10665/PLEKHG6*, *ARFGEF3*, *ARHGEF17*, *FGD3* were all negative hits for small round shape, and *OBSCN* was a hit for triangular shape. Within the group of siRNAs which were not a hit for the same shape in both libraries, some resulted in a phenotype that was not contradictory such as *PLEKHG5/KIAA0720*, which was a hit for fan shape in the OTP screen and a hit for not triangular and not spindly shape in siGENOME. However, there were others where the phenotype was opposing such as for *SH3BP1* which was a hit for triangular shape in LM2 OTP, while it was a negative hit for triangular

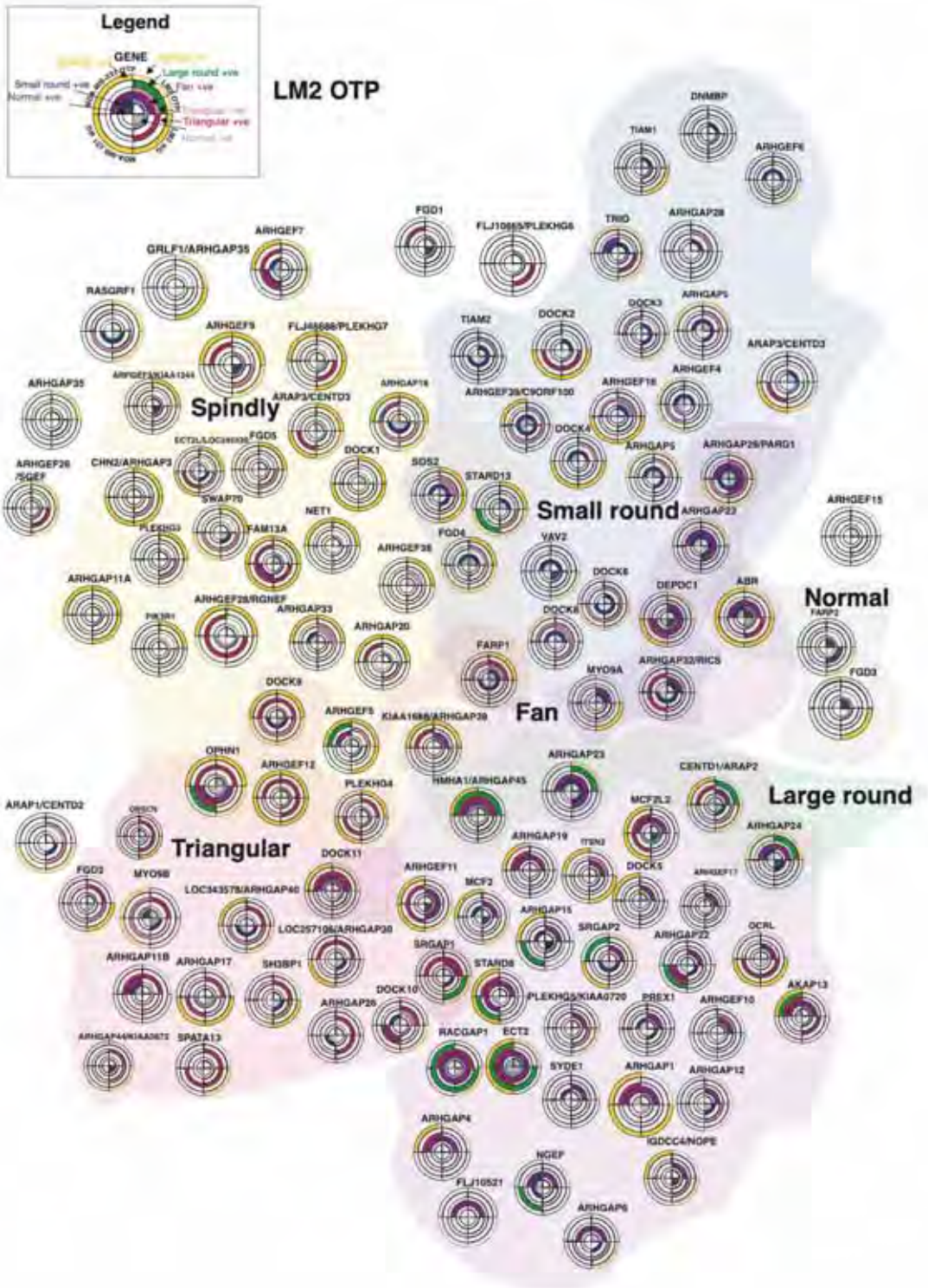

Figure 3.11 RhoGEF/GAP hits for shape in LM2 OTP screen
Graphical representation of each RhoGEF/GAP that was a hit for shape in the LM2 OTP screen, what shape they were a hit for, as well as whether they were hits for any shape in LM2 siGENOME, MDA-MB-231 OTP and siGENOME screens. Each quadrant represents the screen: top right LM2 OTP, bottom right LM2 siGENOME, bottom left MDA-MB-231 siGENOME, top left MDA-MB-231 OTP. Each quadrant is split into 6 shapes, which are coloured only if the gene is a hit for that shape. Solid and faded colours represent positive and negative hits respectively. Spindly in yellow, large round in green, triangular in pink, fan in purple, small round in blue, and normal in grey. Genes are grouped by positive hits in LM2 OTP screen corresponding to each shaded area. Those that are hits for more than one gene in LM2 OTP screen are found between the two shaded areas for that shape. Those genes that were negative hits only for LM2 OTP are found outside the shaded area of the shape for which they are a negative hit.

shape in siGENOME, as well as a hit for spindly and small round. Taken together with the fact that only 5 out of 19 genes that were hits for both LM2 OTP and siGENOME screens, were hits for the same shape category, and that they were mostly negative hits for that shape, would suggest that the siGENOME and OTP siRNA libraries are targeting the genes in subtly different ways resulting in the different phenotypes. Five genes were hits for shape only in the LM2 OTP screen: *ARHGEF38* which was a positive hit for spindly shape, and negative hit for fan shape; *ARHGEF10*, a positive hit for fan shape, and negative for small round and triangular; *ARHGAP28*, a hit for small round shape and a negative hit for triangular shape, *PIK3R1*, a hit for spindly shape; and *ARHGEF15*, a negative hit for normal (Figure 3.11, Appendix 5, bold). We propose these 24 genes are candidates for regulators of shape changes that drive metastasis.

Considering the OTP screens to be more effective as they result in the least number of hits for normal shape (Table 3.3) 12 genes were hits for LM2 OTP and MDA-MB-231 OTP screens and neither siGENOME screen: *DOCK11, HMHA1/ARHGAP45, DOCK5, KIAA1688/ARHGAP39, NET1,* ARHGAP33, *ARHGAP4*, *SYDE1*, *FLJ10521*, *ARHGAP19* and *ARHGAP11B*. Further, considering genes that were hits in LM2 OTP and MDA-MB-231 OTP that were also hits in siGENOME for the same or non-opposite phenotypes revealed 11 genes: *ARHGAP5*, *ARHGEF5, SOS2, ARHGEF6, DOCK8, ARHGAP20, IGDCC4/NOPE*, *ARHGEF18*, *ARHGAP23*, *PLEKHG7/FLJ46688,* and *ARHGAP11A*. Of these genes *DOCK11, HMHA1/ARHGAP45, ARHGEF18, NET1, ARHGEF5, ARHGAP5, ARHGAP33, SOS2, DOCK8, ARHGEF6, ARHGAP20, ARHGAP23, ARHGAP11A, PLEKHG7/FLJ46688, ARHGAP4,*

FLJ10521, ARHGAP19, ARHGAP11B, and KIAA1688/ARHGAP39 were hits for at least one of the same shapes in LM2 and MDA-MB-231. For example, *ARHGAP33* enriched for spindly shape in both cell lines, but also enriched for small round shape in MDA-MB-231, suggesting that it does not have the same exact function in both cell lines. Further, *ARHGEF5* enriched for spindly shape in both cell lines, while enriching for large round and fan shape in MDA-MB-231. *DOCK5, SYDE1,* and *IGDCC2/NOPE* on the other hand resulted in different phenotypes for both cell lines. For example, *DOCK5* was a hit for fan shape in LM2, and for spindly shape in MDA-MB-231 suggesting that it is regulating shape differently in both cell lines.

Only one gene was a hit just for both MDA-MB-231 siGENOME and OTP screens: *ARHGAP9,* a hit for spindly and fan in both screens. Two genes were hits for shape only in MDA-MB-231 OTP screen: *ARHGEF16*, a positive hit for triangular shape; and *TAGAP*, a positive hit for spindly shape and negative hit for normal shape (Figure 3.12). For the MDA-MB-231 siGENOME screen only two genes were also hits for shape: *FAM7A2* for spindly, and small round; and *DEF6* for negative spindly (Figure 3.12).

Out of all of the hits, six genes were hits for at least one of the same shape across all screens (Figure 3.11). *ECT2* was a positive hit for fan shape, and a negative hit for normal for all screens, while *RACGAP1* was a positive hit for fan shape and a negative hit for small round shape across all screens, and both were large

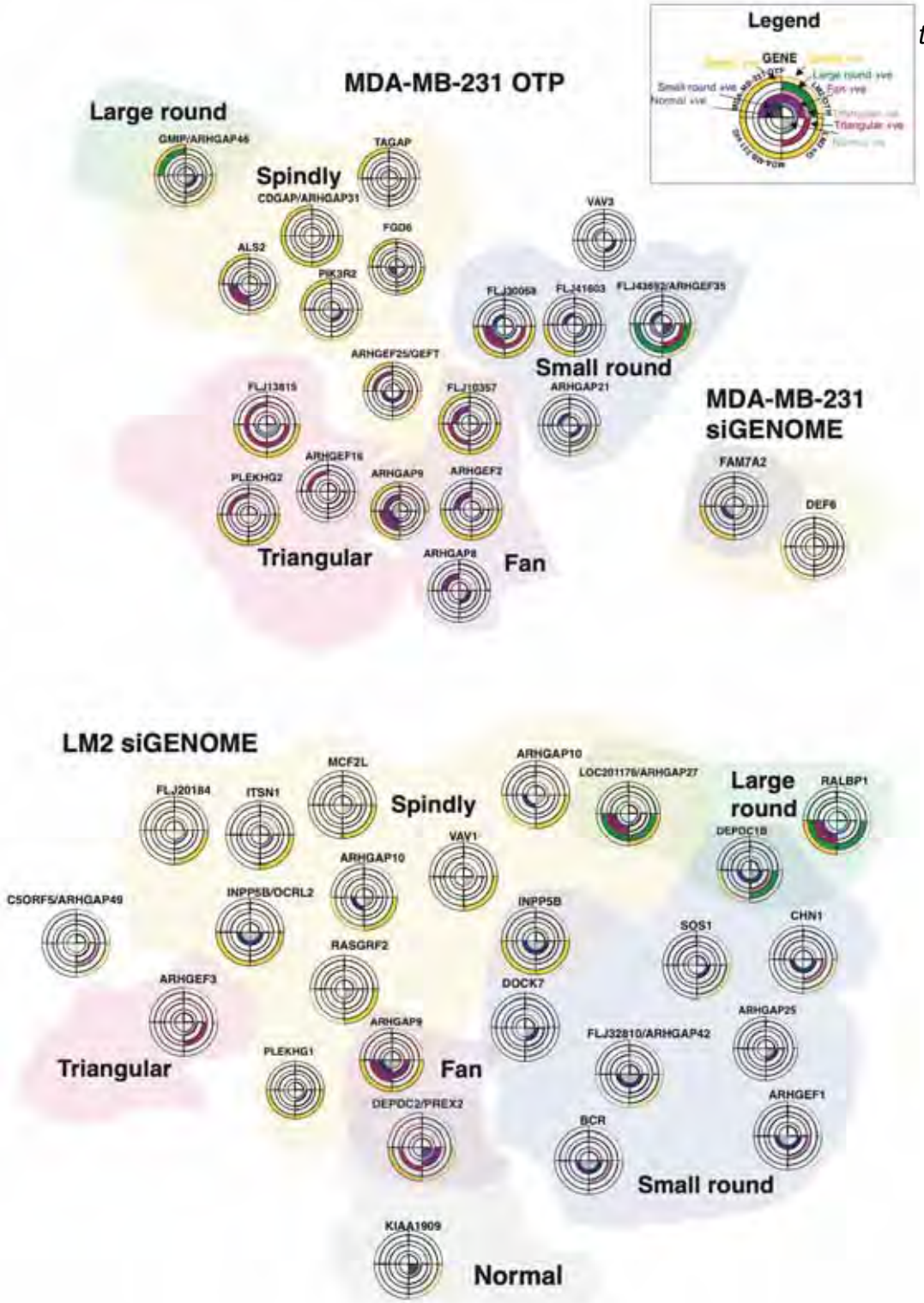

Figure 3.12 RhoGEF/GAP hits for shape in LM2 siGENOME, and MDA-MB-231 OTP and siGENOME screens only.
Graphical representation of each RhoGEF/GAP that was a hit for shape in the MDA-MB-231 OTP screen first, what shape they were a hit for, as well as whether they were hits for any shape in LM2 siGENOME and MDA-MB-231 siGENOME screens. Legend as in Figure 3.9. Genes are grouped by positive hits in MDA-MB-231 OTP screen corresponding to each shaded area. Those that are hits for more than one gene in MDA-MB-231 OTP screen are found between the two shaded areas for that shape. Those genes that were negative hits only for MDA-MB-231 OTP are found outside the shaded area of the shape for which they are a negative hit. Process is repeated with remaining hits for LM2 siGENOME, and finally for MDA-MB-231 siGENOME. None of the genes in this representation were hits in the LM2 OTP screen.

round for all but LM2 OTP. Further, *ARHGAP29/PARG1* and *ARHGEF39/C9ORF100* were hits for small round for all screens. Lastly, *ARHGEF12* and *FAM13A* were hits for spindly shape across all screens. This suggests that these six genes are the only ones regulating the cytoskeleton in the same way across cell lines. In fact, *FAM13A* is a RhoGAP which has been shown to regulate RHOA activity and actin cytoskeleton dynamics, as when depleted in primary bronchial epithelial cells results in the upregulation of epithelial to mesenchymal (EMT) markers (Corvol et al., 2018). Further it also suggests that the phenotype is likely to be due to the knockdown of that gene rather than due to off-target effects. In fact *ECT2* and *RACGAP1* are well known regulators of cytokinesis (Kim et al., 2014, Su et al, 2011), which results in larger cells, explaining the phenotype seen across all cell lines and screens.

3.2.7 Clustering of high-dimensional quantitative morphological signatures based on the effect of RhoGEF/GAPs and Rho GTPase siRNAs on the TNBC cell line LM2.

Having identified genes that were hits in LM2 and MDA-MB-231 siGENOME and OTP screens, and seen that each gene results in a complex signature of phenotypes, we performed a different analysis to identify local and conserved networks in these cell lines. We focused on those genes which were positive hits for the 5 reference shapes only as they give information on what shape RhoGEF/GAP depletion is enriching for, while negative hits only give information

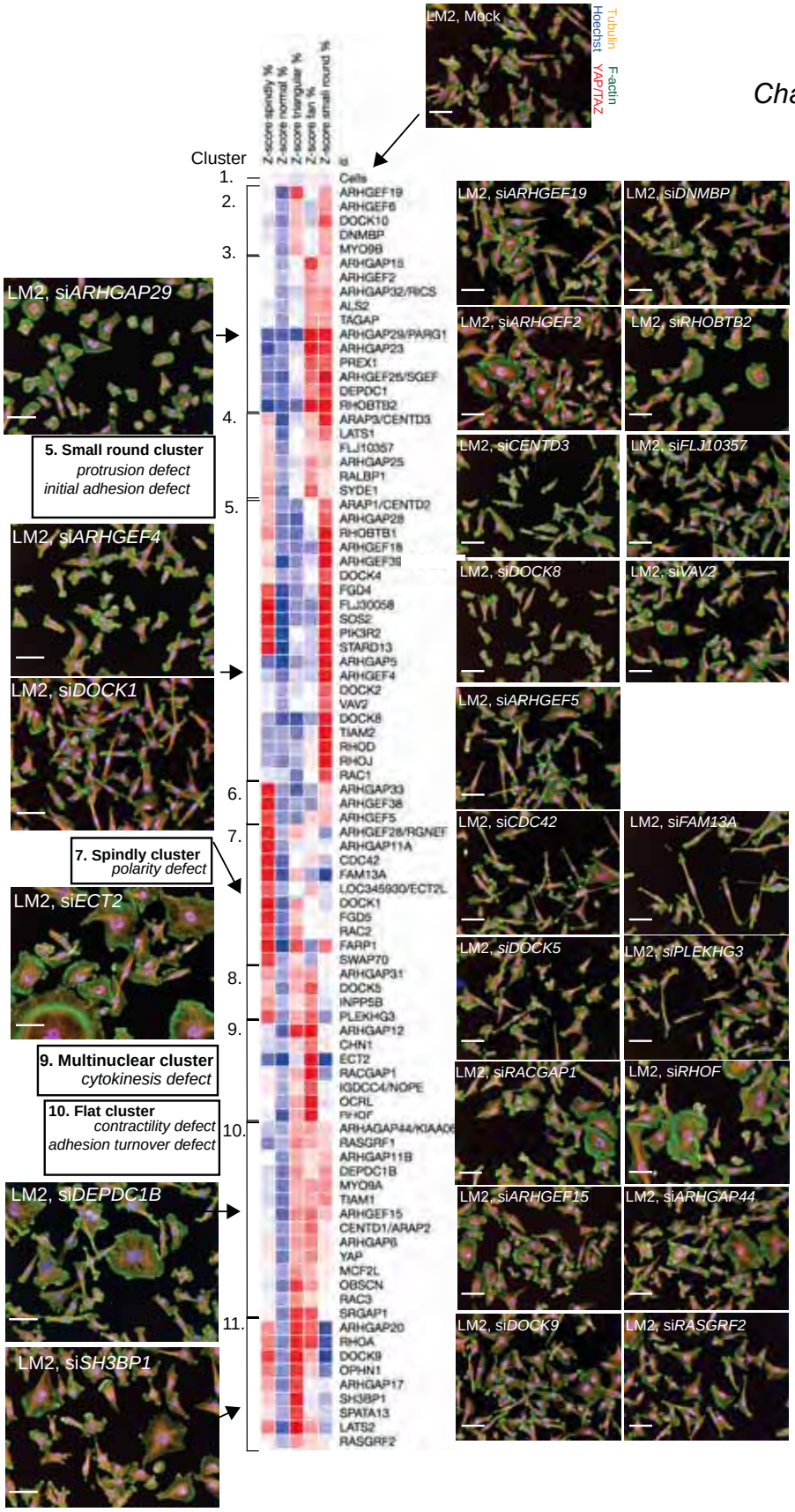

Figure 3.13 Hierarchical clustering of QMS based on the effect of RhoGEF/GAPs and RhoGTPase OTP siRNAs on the TNBC cell line LM2

Hierarchical clustering of QMS for siRNAs with a Z-score below -1 for normal shape. QMS is composed of Z-score of average percentage of cells classified into each shape. Phenoclusters: groups of genes grouped at the highest node of clustering with a PCC > 0.73, which results in 10 multigene clusters (2 to 11) and 1 singleton (1). On the left, representative images of siRNAs which enrich for a particular shape representative of each cluster referred to in text. Most distinctive clusters are labelled, below, what phenotypes suggest. On the right, representative images of siRNAs belonging to each cluster. Red and blue indicate high and low values respectively, in arbitrary units. DNA (blue), YAP/TAZ (red), α-tubulin (yellow), and F-actin (green). Scale bar, 50μm.

on what shape they are not enriching for, which although informative, makes it more difficult to infer function from. Further, we focused on those genes which were negative hits for normal shape, as this suggests they have a significant phenotype, i.e., not a normal phenotype. By ranking the siRNA transfected cells based on their normal Z-score, we identified those siRNAs which had a Z-score below a certain threshold, -1 for LM2 OTP screen. Then, we averaged the data per siRNA for siRNAs which had at least two replicates with a 'normal' Z-score below -1. The rest were discarded. This was done so as to ensure we were looking at genes which had enriched for a particular shape and did not enrich for normal cells. The result was each hit siRNA having a score for each shape class, resulting in a high-dimensional quantitative morphological signature (QMS) (Bakal et al., 2007). We then performed hierarchical clustering of these QMS. We also included mock transfected cells which were representative of the average of all mock transfected cells classified into each shape. We feature reduced based on shapes which gave similar information, i.e., by removing those which correlated highly with other shapes, resulting in the final clustering shown in Figure 3.13.

Genes clustered together based on their QMS. We defined "phenoclusters" as genes grouped at the highest node of clustering with a PCC of > 0.73 (Bakal et al., 2007). This resulted in 11 total clusters, comprising 10 multigene clusters and 1 singleton (Figure 3.13). The singleton is formed by mock transfected LM2s, thus not clustering with any siRNAs. Cluster 2 is characterised by siRNAs that enrich in the number of triangular cells which have smooth actin structures, small

lamella, and are lacking stress fibres, while clusters 3 and 4 are characterised by siRNAs that lead to fan shaped cells, with large lamellopodia. siRNAs in cluster 5 primarily enrich for small round phenotype suggesting that these cells have protrusion and initial adhesion defects. Indeed, *ARHGAP29* (cluster 3), and *ARHGEF4* (cluster 5), whose depletion resulted in small round cells, have already been shown to regulate protrusions in gastric and colorectal cell lines respectively (Kawasaki et al., 2003; Qiao et al., 2017) (Figure 3.13). Further, clusters 6 and 7 are characterised by siRNAs which result in very elongated spindly cells resembling polarity defects. *DOCK1* a member of this cluster has already been shown to promote the establishment of polarity and protrusion formation (Côté and Vuori, 2007). Further, the Rho GTPase *CDC42* whose depletion results in spindly phenotype is also found in cluster 7, and it is central to establishing polarity in eukaryotic cells (Cau, 2005; Etienne-Manneville and Hall, 2003; Hall, 1994; Johnson and Pringle, 1990; Stowers et al., 1995). On the other hand siRNAs in clusters 9 to 11 result in spread large cells, suggesting these cells have a defect in the upregulation of contractility and/or defects in adhesion turnover (Bakal et al., 2007). For example, SH3BP1 from cluster 11 has been shown to have RacGAP activity (Müller et al., 2018) with its depletion leading to RAC1 overactivation and RHOA inactivation resulting in contractility defects (Yamazaki et al., 2013). In addition, cells in cluster 9 were not only flat and spread, but also displayed cytokinesis defects. This would suggest that siRNAs present in this cluster regulate cytokinesis. In fact, ECT2 is a well-known regulator of cytokinesis. (Kim et al., 2014, Su et al, 2011). We propose that if a QMS belongs to a particular phenocluster this predicts function of the gene in determining

shape (Bakal et al., 2007; Yin et al., 2013b). Detailed tables of siRNAs included in the OTP clustering and their corresponding QMS' can be found in Appendix 5.

Hierarchical clustering was also performed on QMSs generated in the si*GENOME* dataset for LM2s and identified genes with Z-scores below -0.9 for 'normal' shape, as hits. In this case, phenoclusters were defined as groups of QMSs with a PCC of > 0.86, which lead to 8 shape clusters and one singleton formed by mock transfected cells (Figure 3.14). QMSs in the siGENOME screen broadly clustered in a similar manner as they did in the OTP screen, as we identified spindly (3), multinuclear (4), small round (6), and flat cluster (8 clusters). Although clusters could be grouped by the similar phenotypes as in the OTP screen, they were not necessarily comprised of similar QMSs. The reason for clusters not being formed by the same siRNAs, could be due to the siRNAs themselves targeting the genes differently in the siGENOME and OTP pools, firstly resulting in different genes being hits for different shapes as we saw in our previous analyses (Figures 3.11, 3.12). In cases where siRNAs co-clustered in both screens, they were hits for the same shape in both screens. Such as for example, the well-known regulators of cytokinesis *ECT2* and *RACGAP1* (Kim et al., 2014, Su et al, 2011) clustered together in both screens, due to their multinuclear phenotype and spread shape (Figures 3.11, 3.13, 3.14). Another example of genes which clustered together by phenotype from both screens were *ARHGEF39/C9ORF100* and *TIAM2* which enriched for small round cells in both screens (Figures 3.11, 3.13, 3.14).

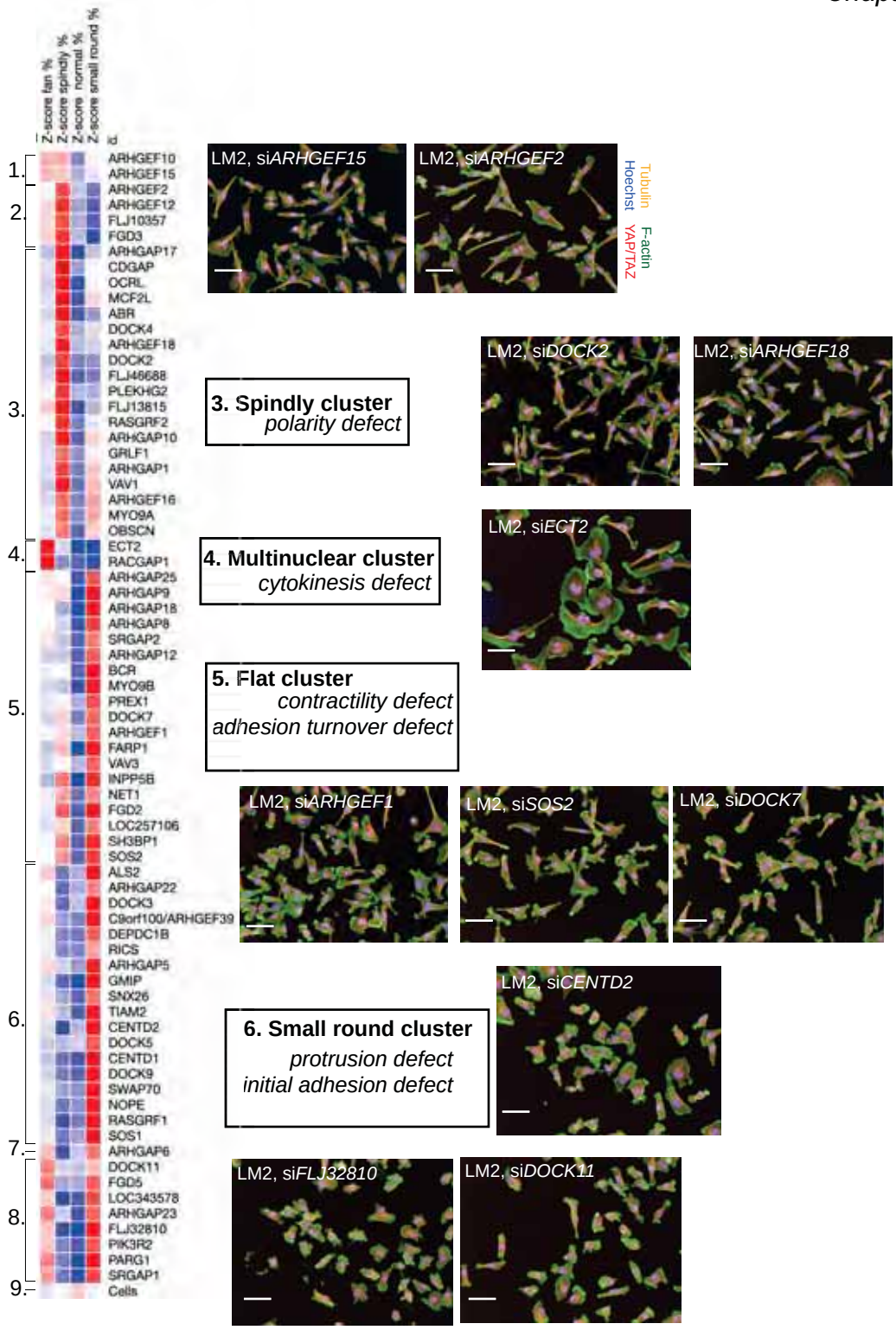

Figure 3.14 Hierarchical clustering of QMS based on the effect of RhoGEF/GAPs siGENOME siRNAs on the TNBC cell line LM2

Hierarchical clustering of QMS for siRNAs with a Z-score below -0.9 for normal shape in LM2 siGENOME screen. QMS is composed of Z-score of average percentage of cells classified into each shape. Phenoclusters: groups of genes grouped at the highest node of clustering with a PCC > 0.86, which results in 8 multigene clusters (1 to 8) and 1 singleton (9). Clusters are labelled on the left. Most distinctive clusters are labelled, below, what phenotypes suggest. On the right, representative images of siRNAs belonging to each cluster. Red and blue indicate high and low values respectively, in arbitrary units. DNA (blue), YAP/TAZ (red), α-tubulin (yellow), and polymerised F-actin (green). Scale bar, 50μm.

We reasoned that combining the siGENOME and OTP QMS of siRNAs used for clustering in both screens would be less informative than looking at how genes are clustering per screen. This is because the OTP screen contained Rho GTPases which were not present in the siGENOME screen, and because the QMS is a complex score that allows us to compare genes within screens rather than across screens. Further, the OTP screens resulted in the lowest percentage of hits for normal shape, suggesting the OTP library is more effective (Tables 3.3, 3.4). Therefore, for the purposes of understanding how interactions between hits in LM2 and MDA-MB-231 change within these two cell lines, we decided to focus on the OTP screens for clustering.

3.2.8 Conserved versus non conserved interactions in MDA-MB-231 and LM2.

In order to identify conserved versus non conserved interactions in MDA-MB-231 versus LM2, we filtered hits in MDA-MB-231 screens in the same manner as described for LM2. Then we performed hierarchical clustering on the QMS for siRNA hits in the MDA-MB-231 OTP screen. The list of genes identified in this way for OTP with each siRNAs corresponding QMS' can be found in Appendix 5.

We identified phenoclusters as groups of QMSs with a PCC of > 0.78 for this data, which revealed identified 8 shape clusters and a singleton formed by mock transfected cells (Figure 3.15). Although siRNAs largely grouped by the same phenotypes we observed for the LM2 screen, those phenotypes were less distinctive than those in LM2. This is unsurprising as we had already seen that

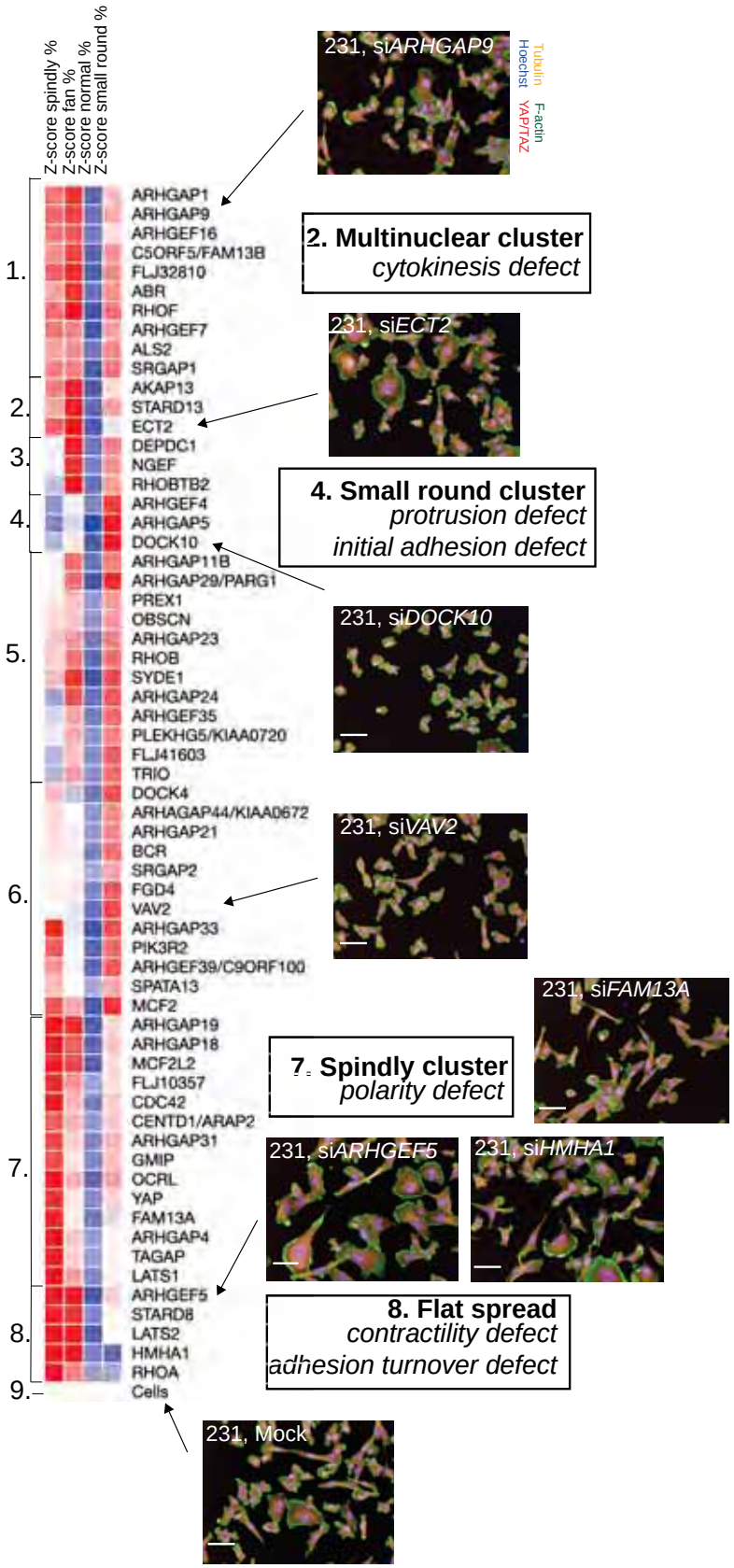

Figure 3.15 Hierarchical clustering of QMS based on the effect of RhoGEF/GAPs and Rho GTPases on the TNBC cell line MDA-MB-231
Hierarchical clustering of QMS for siRNAs with a Z-score below -1.5 for normal shape in MDA-MB-231 OTP screen. QMS is composed of Z-score of average percentage of cells classified into each shape. Phenoclusters: genes grouped at the highest node of clustering with a PCC > 0.78, which results in 8 multigene clusters (1 to 8) and 1 singleton (9). Clusters are labelled on the left. Most distinctive clusters are labelled, below, what phenotypes suggest. On the right, representative images of siRNAs belonging to each cluster. Red and blue indicate high and low values respectively, in arbitrary units. DNA (blue), YAP/TAZ (red), α-tubulin (yellow), and F-actin (green). Scale bar, 50μm.

the proportion of cells within a given shape varies greatly between the two cell lines (Figure 3.6, 3.7). Further, this supports the hypothesis that some genes will be regulating cell shape differently in LM2 and MDA-MB-231, conferring LM2 with more morphogenic capabilities.

We used hierarchical clustering to identify conserved versus non conserved interactions between RhoGEF/GAPs in LM2 versus MDA-MB-231, and how networks have rewired. For example, we found that *ARHGEF4* and *ARHGAP5* clustered together both in MDA-MB-231 and in LM2 (Figure 3.16). Further their depletion resulted in the same phenotype, small round cells indicative of protrusion and initial adhesion defects in both screens, which was also revealed in our first analysis (Figure 3.11). This suggests that they are performing the same function in both cell lines, and that this pathway has not been rewired. Therefore, it is likely that ARHGEF4 and ARHGAP5 are interacting in a conserved manner across both cell lines. ARHGEF4 is a RAC-specific GEF which has been shown to regulate membrane ruffling and lamellipodia formation in gastric and colorectal cell lines respectively (Kawasaki et al., 2003; Qiao et al., 2017). Further, ARHGAP5, a RHOA GAP and a RacGAP has been shown oncogenic, with its depletion preventing migration and invasion in lung cancer, breast cancer, hepatocellular carcinoma, nasopharyngeal carcinoma, and colorectal cancer (Héraud et al., 2019). In breast cancer it has also been shown to result in loss of adhesion as a result of overexpression (Chakravarty et al., 2003). *ARHGAP5* has also been shown to promote cancer in colorectal cancer where its loss results in YAP nuclear translocation (Frank et al., 2018), and has been

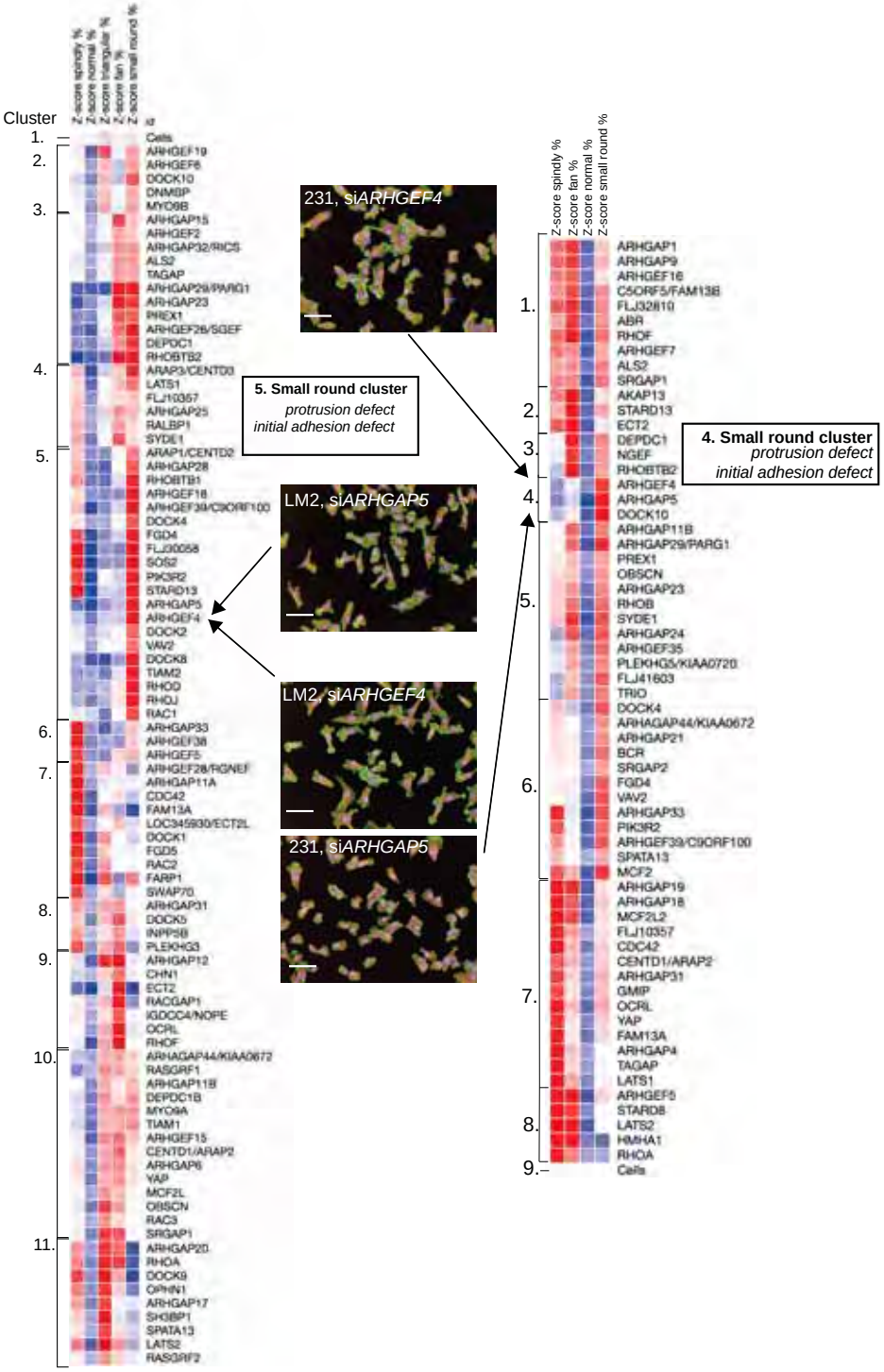

Figure 3.16 Hierarchical clustering
Shapes depicted are examples to illustrate the model but do not represent a result. Wild-type LM2 cells are highly heterogenous and are dynamically changing shape in transitions mediated by specific RhoGEFs, such that when a RhoGEF is depleted, the transition from Shape A to Shape B no longer occurs resulting in a complete depletion of Shape B and an enrichment in Shape A. Wild-type MDA-MB-231 have predominantly more of one particular shape, and we hypothesise that transitions between shapes are either slower than in LM2 or not taking place. In this case, depletion of said RhoGEF results in a rearrangement of existing shapes.

Identified as a risk factor for hereditary colorectal cancer (Héraud et al., 2019; Horpaopan et al., 2015). While neither the role of ARHGEF4 or ARHGAP5 have been described in MDA-MB-231 or LM2, the fact that their depletion results in the same phenotype in two different cell lines, suggest they participate in a conserved pathway/complex.

On the other hand, depletion of *ARHGEF5* resulted in different phenotypes between MDA-MB-231 and LM2. Although it enriched for spindly shape in both cell lines, it also enriched for large spread and fan in MDA-MB-231, suggesting that the pathway has been rewired between these two cell lines. Studies have shown that ARHGEF5 is phosphorylated by SRC resulting in increased activity towards RHOA (Kuroiwa et al., 2011; Yohe et al., 2007) and is upregulated during EMT in colorectal cancer cells, where it mediates invasion and migration through the activation of RHOA-ROCK signalling pathway (Komiya et al., 2016). Given the role of RHOA in mediating contractility (Hall, 1994; Narumiya et al., 2009) could suggest that the phenotype of *ARHGEF5* depletion in MDA-MB-231 is due to decreased RHOA activity, and in fact it clusters with RHOA in this screen. Whereas in LM2, the spindly phenotype is more akin to a polarity defect phenotype, as seen with CDC42 depletion. Altogether suggesting a rewiring of this pathway. In LM2, ARHGEF5 clusters closely with ARHGEF38, which was a hit for spindly shape only in the LM2 OTP screen (Figure 3.11, Table 3.3) and whose role is not well described (Liu et al., 2019). Further ARHGEF5 and ARHGEF38 cluster with ARHGAP33, a RHOGAP for CDC42 which has been shown to regulate protrusions in mature neurons (Kim et al., 2013) and be actin associated in epithelial cell lines (Müller et al., 2018), and although a hit for

spindly shape in both cell lines (Figure 3.11, Table 3.3), also enriched for small round shape in MDA-MB-231, suggesting that it does not have the same exact function in both cell lines. In fact, in MDA-MB-231 ARHGEF5 does not cluster with ARHGAP33, but rather clusters with STARD8, a RHOGAP which has been described as required for epithelial junction integrity, and whose loss is associated with carcinogenesis (Holeiter et al., 2012). This clustering suggests that ARHGEF5 and STARD8 could be part of the same pathway in MDA-MB-231, which is not conserved in LM2, where it becomes rewired to interact with other RhoGEF/GAPs that are specifically dysregulated in LM2s such as for example ARHGEF38 and ARHGAP33.

3.3 Discussion

We performed high-throughput RNAi screens of all human RhoGEFs and RhoGAPs in the highly metastatic TNBC cell line LM2 and its less metastatic parental cell line MDA-MB-231 and optimised an automated single-cell morphological analysis to identify RhoGEF/GAPs which regulate cell shape in each cell line and in both. Further, by classifying cells into 5 visually distinctive reference shapes and identifying a ‘normal’ population, we were able to identify regulators of cell shape in LM2 and MDA-MB-231 cells and begun to understand how these two cell lines regulate cell shape differently. Lastly, we have described how we can infer signalling networks by performing hierarchical clustering on QMS’ for each siRNA and identify conserved and non-conserved interactions between LM2 and MDA-MB-231.

Overall, we found that the OTP screens resulted in the least positive hits for normal shape (Table 3.3, 3.4) which suggests that gene depletion using the OTP library has the strongest effect. Interestingly, both OTP and siGENOME screens in MDA-MB-231 resulted in more positive than negative hits for every shape; contrary to LM2 screens where spindly, triangular, and small round in siGENOME had more negative than positive hits, and small round in OTP had an equivalent number (Tables 3.3, 3.4, Figures 3.11, 3.12). This suggests that depletion of RhoGEF/GAPs in LM2 cells results in a drastic change in the shapes present in the LM2 population where there is more enrichment in one shape versus the rest, which can be accompanied by a depletion of another shape or simply result in a depletion without enriching for any other shape. In contrast, in MDA-MB-231 cells, RhoGEF/GAP depletion results predominantly in a rearrangement of existing shapes, rather than depletion of a particular shape. In addition, LM2 OTP screen had more genes that were hits for one shape only compared to MDA-MB-231, which had more genes as hits for 2 shapes or more (Figure 3.11, 3.12). This is highlighted in Figures 3.5 and 3.6 where the shape space of MDA-MB-231 cells versus LM2 following RhoGEF/GAP depletion is very different.

Taken together, these data suggest that in wild-type conditions, LM2 cells are dynamically changing shape in fast transitions mediated by a particular set of RhoGEFs. Therefore, depleting a gene that is mediating a transition from one particular shape to another, results in a lack of said shape and an enrichment of another (Figure 3.17). MDA-MB-231 cells on the other hand, are not as dynamic. Therefore, depleting RhoGEF/GAPs results in an enrichment of various shapes, and thus a subtle rearrangement of the shapes already present in the wild-type

population (Figure 3.17). In fact, we saw an upregulation in cytoskeletal keratins and serpins in LM2 versus MDA-MB-231 wild-type cells via proteomics (data not shown), the latter of which has been shown to provide metastatic advantages (Valiente et al., 2014). Further, Minn et al., 2005, who generated LM2 from MDA-MB-231 and selected them to be highly metastatic to the lung, found no RhoGEF/GAPs were significantly up or downregulated when comparing gene expression levels between these two cell lines, suggesting that there are no big changes in signalling states. Taken together, we hypothesise that it is the ability of LM2 cells to dynamically change shape making them more plastic, that allows them to adapt to their extracellular environment much better than their parental counterpart MDA-MB-231, and thus conferring them with more invasive abilities.

We identified 6 genes as hits for shape across all screens and cell lines: *ECT2*, *RACGAP1*, *FAM13A, ARHGAP29/PARG1*, *ARHGEF39/C9ORF100*, and *ARHGEF12.* Thus, suggesting their function is conserved across cell lines and that the phenotypes observed are due to depletion of those genes rather than to off-target effects. We identified 19 shape hits for both LM2 siGENOME and OTP screens, and 5 genes as hits only in the LM2 OTP library. We hypothesise that these 24 genes are candidates for regulators of cell shape changes that drive metastasis. On the other hand, 23 genes were hits for LM2 and MDA-MB-231 OTP screens, suggesting that they are not regulating the cell shape changes that drive metastasis.

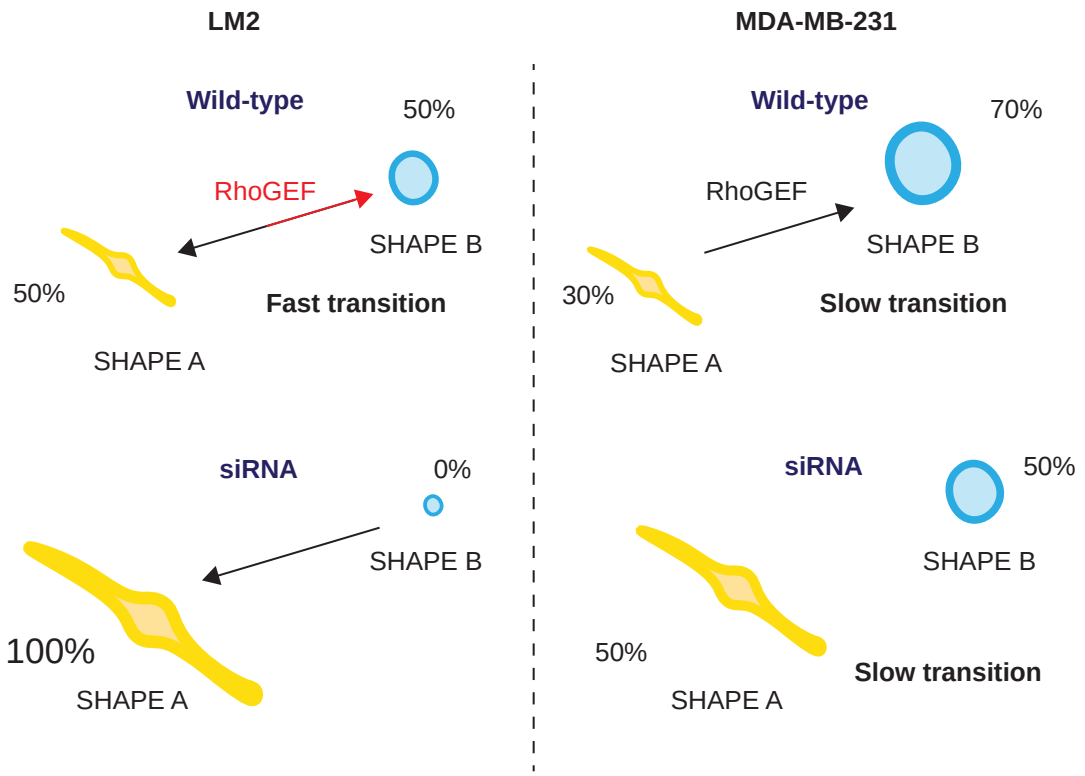

Figure 3.17 Graphical representation of proposed model
Shapes depicted are examples to illustrate the model but do not represent a result. Wild-type LM2 cells are highly heterogenous and are dynamically changing shape in transitions mediated by specific RhoGEFs, such that when a RhoGEF is depleted, the transition from Shape A to Shape B no longer occurs resulting in a complete depletion of Shape B and an enrichment in Shape A. Wild-type MDA-MB-231 have predominantly more of one particular shape, and we hypothesise that transitions between shapes are either slower than in LM2 or not taking place. In this case, depletion of said RhoGEF results in a rearrangement of existing shapes.

By assigning each siRNA with a high-dimensional QMS made up of Z-scores calculated on the percentage of cells classified into our five reference shapes, normal shape, and penetrance (inverse of normal), we were able to perform hierarchical clustering from which we can infer local networks in a similar manner as previously described by Bakal et al., 2007, and Yin et al., 2013. We observed QMS' clustering into three to four major clusters for each screen: (1) siRNAs resulting in small round cells indicative of protrusion and initial adhesion defects, (2) spindly cells indicative of polarity defects, (3) flat cells suggestive of contractility and adhesion turnover defects, and (4) multinuclear cells, indicative of cytokinesis defects. By clustering phenotypes in this way, combined with what is already known about the function of some RhoGEF/GAPs, we can begin to infer function of unknown RhoGEFs in said clusters.

Based on our hit identification and our clustering, we identified ARHGEF38 as a regulator of shape specifically in LM2s, ARHGEF5 and ARHGAP33 as regulating cell shape differently in LM2 and MDA-MB-231, and FAM13A as regulating cell shape in the same way in both cell lines. Given that ARHGEF38, ARHGEF5, and ARHGAP33 QMS' clustered together in LM2, but did not do so in MDA-MB-231, suggests their interactions are cell line specific and not conserved between both cell lines, perhaps allowing LM2 cells to change shape more effectively and as such being regulators of shape changes that drive metastasis. Therefore, their interactions warrant further studies.

Overall, by performing high-throughput RNAi screens of RhoGEF/GAPs in MDA-MB-231 and LM2, and carrying out single-cell morphological analysis, we have begun to understand how these two cell lines regulate cell shape differently, and how this could be linked to metastasis. We hypothesise that LM2 cells are able to dynamically change shape due to dysregulation of RhoGEF/GAPs, which makes them more plastic, allowing them to adapt to their extracellular environment much better than their parental counterpart MDA-MB-231. We hypothesise that is this dynamic ability to change shape that confers LM2 cells with more metastatic abilities.

Chapter 4

RhoGEF regulation of YAP/TAZ in TNBC cell lines.

Chapter 4 RhoGEF regulation of YAP/TAZ in TNBC cell lines*.*

4.1 Introduction

The metastatic process involves a series of steps which depend on cancer cells' physical and mechanical interactions with the microenvironment (Kass et al., 2007; Mouw et al., 2014; Wirtz et al., 2011). The normal mammary gland is a mechanically active tissue, where normal mammary epithelial cell growth and morphogenesis are supported by a soft matrix, and have an elasticity in the range of 1 kPa. However, malignant transformation of breast tissue results in increased chronic mammary gland tension, elevated compression force, increased tensile strength and extracellular matrix (ECM) stiffness, which leads to breast tumours being up to 10 times stiffer than normal breast tissue (Barnes et al., 2017; Butcher et al., 2009; Cox and Erler, 2011; Paszek et al., 2005). Therefore, during the first steps of metastasis, breast cancer cells are subjected to high tensile forces due to increased ECM stiffness (Butcher et al., 2009).

Further, breast cancer cells are then subjected to shear stresses when travelling through the blood and lymphatic systems, as well as during extravasation (Wirtz et al., 2011). Following extravasation, breast cancer cells that metastasise to the lung must adapt to a much softer matrix (200 Pa) compared to that of the transformed breast (Barnes et al., 2017; Butcher et al., 2009; Cox and Erler, 2011; Paszek et al., 2005). Therefore, breast cancer cells are subjected to different forces during the metastatic process, which they must adapt to in order to survive (Dongre and Weinberg, 2019; Kass et al., 2007; Shibue and Weinberg, 2009; Wirtz et al., 2011).

Cancer cells can adapt to their environment by remodelling their cytoskeleton (Fife et al., 2014; Kass et al., 2007; Wirtz et al., 2011). YAP and TAZ are “mechanotransducers” which integrate both geometrical cues (cell/tissue shape, volume) and mechanical cues (contractility, traction), to mediate a response to regulate proliferation, organ growth, and tissue homeostasis (Dupont et al., 2011; Halder et al., 2012; Pan, 2010; Totaro et al., 2018). Although YAP/TAZ transcription regulates a diverse number of targets, the effects of increased YAP/TAZ activity often result in increased cellular contractility(Calvo et al., 2013; Lin et al., 2017).

YAP/TAZ have been shown to be nuclear and active when intracellular contractile forces are high, when cells are on stiff matrices, and when cells are allowed to spread in conditions such as those observed at low densities (Dupont et al., 2011). Conversely, YAP/TAZ are inactive when cytoplasmic when, for example, contractile forces are low, when cells are on soft matrices and in confined spaces such as those observed at high densities (Dupont et al., 2011; Halder et al., 2012; Totaro et al., 2018). The latter of which explains contact inhibition of proliferation (CIP) where cells stop growing when they reach a critical density (Aragona et al., 2013; Zhao et al., 2010).

RhoGEFs activate Rho GTPases in response to fluctuations in the microenvironment resulting in cytoskeletal reorganisation and have been shown to be dysregulated in cancer (Cook et al., 2014; Rossman et al., 2005). RhoGEF-Rho GTPase regulation of cell shape, by controlling the structure and dynamics of the actin cytoskeleton, can regulate YAP/TAZ nuclear translocation, and thus

YAP/TAZ transcriptional activity (Bos et al., 2007; Jaffe and Hall, 2002; Vega and Ridley, 2008). Indeed, Rho GTPases have been shown to control YAP/TAZ localisation in LATS1-dependent and independent ways. For instance, CDC42 has been shown to be required for nuclear YAP in mouse kidney development via actin cytoskeletal rearrangement (Reginensi et al., 2013) and to promote nuclear YAP/TAZ downstream of integrin α3 and focal adhesion kinase (FAK) in stem cells (Hu et al., 2017). Further, although very little is known on specific RhoGEF-dependent regulation of YAP/TAZ, a few RhoGEFs have been described to regulate YAP/TAZ. For example, ARHGEF7 or β-Pix, has been shown to regulate YAP/TAZ in a LATS-independent manner (Heidary Arash et al., 2014; Sero and Bakal, 2017). Mechanistically, ARHGEF7 gets recruited to focal contacts via association with GIT1/2 and paxillin, and is phosphorylated by SRC, activating CDC42 and promoting a negative feedback cycle of adhesion disassembly, and FAK nuclear translocation of YAP in mammary epithelial cells (Sero and Bakal, 2017). In addition, the RhoGEF TRIO promotes YAP nuclear translocation, by activating RHO and RAC, downstream of Gαq G proteins, both by inhibiting LATS and by promoting F-actin rearrangement (Feng et al., 2012, 2019). Furthermore, TIAM1 has been shown to antagonise YAP/TAZ downstream of Wnt signalling, both by promoting TAZ degradation in the cytoplasm, as well as by directly suppressing YAP/TAZ -TEAD interaction in the nucleus (Diamantopoulou et al., 2017). Lastly, ARHGEF17 has been suggested to promote contractility via activation of RHOA-ROCK signalling, downstream of YAP, in a feedback control of the actomyosin cytoskeleton (Lin et al., 2017) .

YAP/TAZ signalling frequently appears to be rewired in cancer, where for example, mutations in Gαq G proteins upstream of Rho GTPases result in Hippo-independent activation of YAP, driving proliferation (Feng et al., 2012, 2019). In addition, loss of the Hippo pathway component *NF2* results in RAS-dependent activation of YAP/TEAD-driven transcription of oncogenic and wild-type RAS in thyroid cancer (Garcia-Rendueles et al., 2015). In fact, mutant RAS and YAP have been shown to converge in regulating the epithelial-to-mesenchymal transition (EMT) driving survival, and YAP activation has been shown to drive drug resistance by bypassing RAS oncogenic addictions in various cancers (Calses et al., 2019; Fisher et al., 2017; Garcia-Rendueles et al., 2015; Kapoor et al., 2014; Lin et al., 2015; Shao et al., 2014). In addition, YAP/TAZ have also been shown to be activated as a result of loss of polarity, which is frequently associated with EMT, driving tumourigenesis (Cordenonsi et al., 2011; Diepenbruck et al., 2014; Zanconato et al., 2016).

Therefore, because YAP/TAZ have been shown to be oncogenic, promoting breast cancer metastasis, stemness, drug resistance, and EMT (Cordenonsi et al., 2011; Fisher et al., 2017; Kim et al., 2016; Lamar et al., 2012; Lei et al., 2008; Nallet-Staub et al., 2014; Noto et al., 2017; Vincent-Mistiaen et al., 2018; Zanconato et al., 2016), we hypothesised that YAP/TAZ may be differentially regulated in metastatic versus weakly metastatic TNBC cell lines. Furthermore, we hypothesise that it is RhoGEFs which are differentially regulating YAP/TAZ in response to different signals and driving invasion in TNBC.

To understand how YAP/TAZ are differentially regulated in different TNBC cell lines, first we compared YAP/TAZ ratios in four TNBC cell lines, which vary in their metastatic ability and their morphology: LM2, MDA-MB-231, SUM159, and hs578t (Chu et al., 2014; Johnstone et al., 2018; Koedoot et al., 2019; Lamar et al., 2012; Minn et al., 2005; Sero et al., 2015). As well as in a non-transformed mammary epithelial cell line MCF10A, and nonmetastatic mammary carcinoma cell line T47D (Neve et al., 2006; Sero et al., 2015).

Then we performed high-throughput RNAi screens of 142 human RhoGEFs and RhoGAPs hs578t and SUM159 as we did for LM2 and MDA-MB-231 (Chapter 3). In this chapter I describe which RhoGEFs regulate YAP/TAZ in LM2, MDA-MB-231, hs578t, and SUM159. We found that in the TNBC cell lines SUM159 and hs578t which have a more spread-like phenotype, YAP/TAZ ratios were predominantly low under basal conditions, and they do not couple YAP/TAZ ratio to shape. On the other hand, we found that the cell lines which display more spindly-like phenotypes MDA-MB-231 and LM2 had high basal YAP/TAZ ratios. However, while MDA-MB-231 sustain nuclear and active YAP/TAZ regardless of shape, LM2 are able to downregulate YAP/TAZ by changing their shape and suggests YAP/TAZ is thus more mechanoresponsive in metastatic vs non-metastatic cells. We propose that LM2 cells' ability to re-couple YAP/TAZ to shape results in increased metastatic potential as they are able to regulate YAP/TAZ dynamics in response to environments of varying stiffness and geometry (such as across the body), whereas as non-metastatic MDA-MB-231 cells are far less adaptable. Further, we identify the RhoGEF DOCK5, as a regulator of YAP/TAZ activity in LM2 cell. We propose DOCK5 activates

YAP/TAZ downstream of focal adhesions and its mechanism of action warrants further study.

4.2 Results

4.2.1 Comparison of basal YAP/TAZ localisation in panel of breast cancer cell lines

To understand how YAP/TAZ is differentially regulated in breast cancer cell lines displaying more epithelial, spread-like phenotypes versus those with more mesenchymal spindly-like phenotypes, first we compared basal YAP/TAZ ratios (log10 ratio of nuclear to ring region YAP/TAZ), at various densities. We used four TNBC cell lines, which vary in their metastatic ability and their morphology: LM2 and MDA-MB-231, which display more spindly mesenchymal-like phenotypes with few cell to cell contacts, and SUM159 and hs578t, which display more spread cuboid shapes with more cell to cell contacts (Chu et al., 2014; Johnstone et al., 2018; Koedoot et al., 2019; Lamar et al., 2012; Minn et al., 2005; Sero et al., 2015). LM2 are more metastatic than MDA-MB-231 (Minn et al., 2005), which are more metastatic than SUM159 (Lamar et al., 2012). Further we used the non-transformed mammary epithelial cell line MCF10A, which is also triple-negative for estrogen, progesterone, and HER2 expression (Neve et al., 2006; Sero et al., 2015), as a model for a normal, cuboidal-like non-transformed epithelial cell line. Basal and luminal breast cancers arise from two distinct types of epithelial cells in the mammary gland (Perou et al., 2000), with Basal lines being characterised as being more invasive and having a worse outcome compared to their Luminal counterparts (Charafe-Jauffret et al., 2006; Neve et

al., 2006; Sørlie et al., 2003). All of the aforementioned cell lines are classified as Basal B (Lehmann et al., 2011; Neve et al., 2006; Sero et al., 2015). Therefore we also included T74D in this panel, which is a an estrogen and progesterone receptor positive nonmetastatic mammary carcinoma cell line, as a control for a non-invasive epithelial-like and luminal cell line (Neve et al., 2006; Sero et al., 2015).

YAP/TAZ ratio displayed an inverse relationship with cell density in all cell lines (Figure 4.1A). The highest levels of basal YAP/TAZ activity were exhibited by the more spindly-like TNBC cell lines (LM2 and MDA-MB-231), and the lowest by the more spread-like cell lines (SUM159 and hs578t). Further, intermediate levels of YAP/TAZ activation were displayed by the non-transformed epithelial (MCF10A) and luminal cell lines (T47D) (Figure 4.1A). Taken together these data suggest that YAP/TAZ is dysregulated in the more spindly-like versus spread-like TNBC cell lines, and that the spread-like TNBC cells may even downregulate YAP/TAZ signalling compared to cuboidal epithelial cells.

Between the more spindly-like cell lines, at low densities YAP/TAZ ratio was higher in LM2 cells v MDA-MB-231. However, while still dependent on cell density, a higher ratio was maintained in MDA-MB-231 cells compared to LM2 (Figure 4.1A). Thus, while basal levels of YAP/TAZ are higher in spindly-like vs spread-like cell lines, YAP/TAZ activity exhibits higher sensitivity to changes in cell density in more metastatic cells such as LM2 versus their less metastatic counterparts.

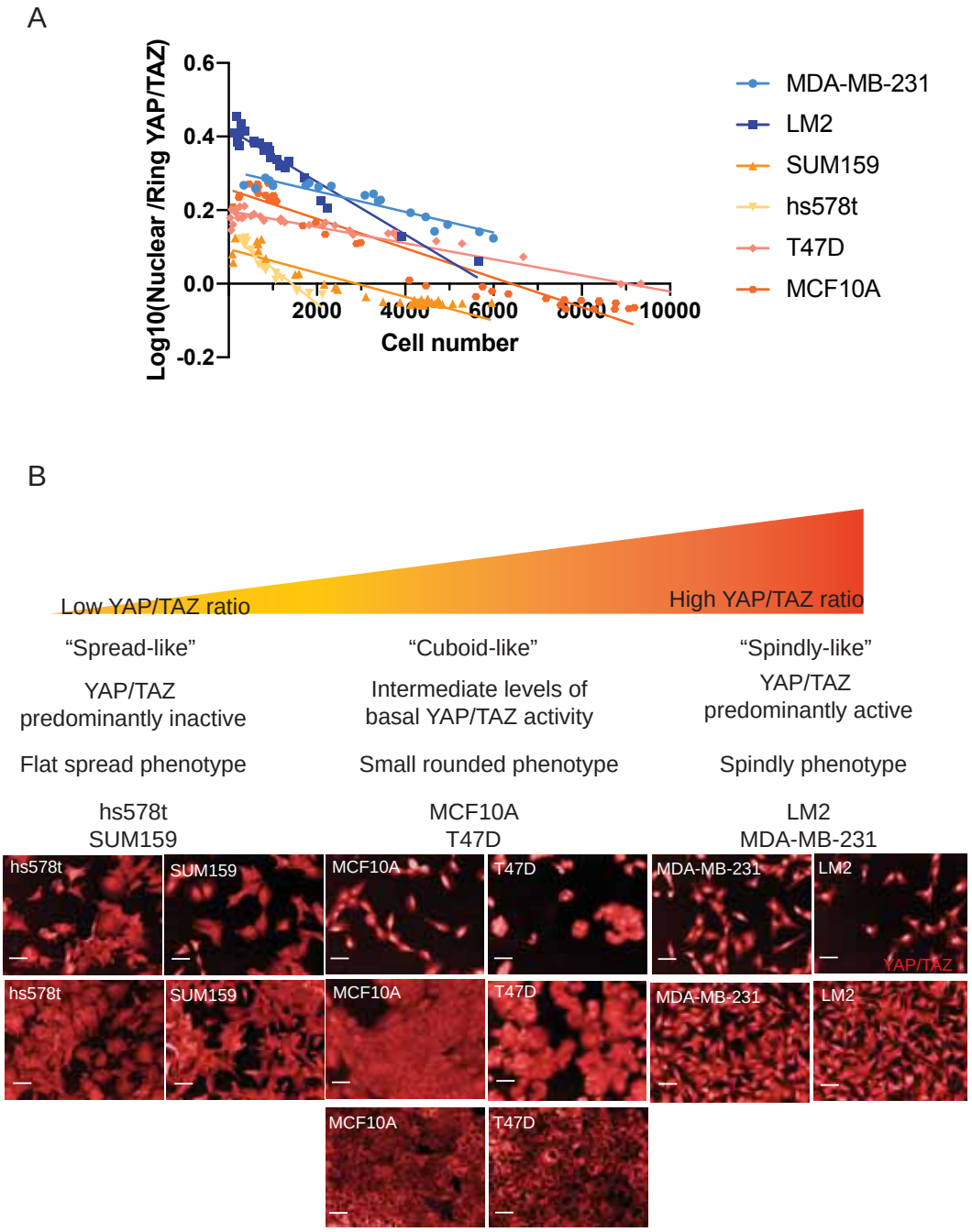

Figure 4.1 Comparison of basal YAP/TAZ localisation in panel of breast cancer cell lines

(A) Graph depicts log10 ratio of nuclear to ring region YAP/TAZ versus cell number for MDA-MB-231 (light blue), LM2 (dark blue), SUM159 (orange), hs578t (yellow), T47D (pink), and MCF10A (orange). (B) Representative images from left (low YAP/TAZ ratio) to right (high YAP/TAZ ratio) of hs578t, SUM159, MCF10A, T47D, MDA-MB-231, and LM2 at low (3.3 x 10^4 cells/ml) and high (1.3 x 10^5 cells/ml) densities, stained for YAP/TAZ. As well as 2.7 x 10^5 cells/ml for MCF10A and T47D. Descriptions for observed YAP/TAZ and morphology. n = 4 wells per condition, 500 to 10 000 cells/well Scale bar is 50µm.

Interestingly, when SUM159 and hs578t cells are at high densities, and/or cells are in contact with each other, YAP/TAZ are almost entirely cytoplasmic (Figure 4.1D). On the other hand, even though nuclear YAP/TAZ levels drop in LM2 and MDA-MB-231 cells when plated at higher densities, this cannot be due to cell-cell contacts. MCF10A grow more as epithelial sheets and T47D grow as colonies, and only result in more cytoplasmic than nuclear YAP/TAZ at very high densities 6000 cells/well (2.0 x 10^5/ml) and 9000 cells/well (3.0 x 10^5/ml) for MCF10A and T47D respectively (Figure 4.1D).

We hypothesise that constitute activation of YAP/TAZ is a characteristic of more spindly-like vs spread-like TNBC cell lines, which is likely due to mutations in signalling pathways. However, we propose that metastatic cells may further rewire the pathways regulating YAP/TAZ to “re-acquire” their ability to downregulate YAP/TAZ activation under certain conditions.

4.2.2 RhoGEFs which regulate YAP/TAZ localisation

We proposed that changes in RhoGEF activity may underpin both the increased basal YAP/TAZ activity in spindly-like vs spread-like lines, and the changes in YAP/TAZ regulation in more metastatic vs weakly metastatic cell lines. To first identify RhoGEFs which regulate YAP/TAZ localisation in the more spindly-like TNBC cell lines LM2 and MDA-MB-231 we quantified the effect of gene depletion on YAP/TAZ nuclear localisation using Z-scores, and genes which led to depletion above/below a Z-score threshold were considered “hits” (Figure 4.2). Z-score values were obtained by first normalising the data per plate, grouping

normalised values per screen, and using the mean and standard deviations of the mock transfected cells per screen. We considered siRNAs that led to Z-scores above 1.5 and below -1.5 as “hits”. Positive hits are siRNAs which result in increased YAP/TAZ ratio and are thus considered to be YAP/TAZ inhibitors, while negative hits are siRNAs which result in decreased YAP/TAZ ratio and are thus considered to be YAP/TAZ activators. We further identified hits which had the same effect for both the siGENOME and OTP screens for LM2s, for at least 6 out of 8 replicates overall. Z-score values for siRNAs for each screen can be found in Appendix 7.

We identified *ARHGEF15* and *ARHGEF7* as hits for increased YAP/TAZ ratio; and *FGD6*, *SWAP70*, *ARHGEF3*, *ARHGEF12*, and *DOCK7* as hits for decreased YAP/TAZ ratio only in LM2s (Table 4.1, Figure 4.2E). Further, the following RhoGEFs were hits for YAP/TAZ ratio specifically in MDA-MB-231: *ARHGEF40/FLJ10357*, *DOCK8, VAV2,* and *PLEKHG2* resulted in increased YAP/TAZ ratio; while depletion of *DOCK1* resulted in decreased YAP/TAZ ratio (Table 4.1, Figure 4.2E). In both LM2 and MDA-MB-231, *ARHGEF16* was a hit for increased YAP/TAZ ratio, and *DOCK5* and *ARHGEF2* were hits for decreased YAP/TAZ ratio (Table 4.1, Figure 4.2E). These data suggest that ARHGEF15 and ARHGEF7 are YAP/TAZ activators, and FGD6, SWAP70, ARHGEF3, ARHGEF12, and DOCK7 are YAP/TAZ inhibitors only in LM2 (highly metastatic) cells. In contrast, ARHGEF16 is a YAP/TAZ activator in both cell lines, and DOCK5 and ARHGEF2 are YAP/TAZ inhibitors in both cell lines, suggesting these RhoGEFs are regulators of YAP/TAZ in both highly metastatic and weakly metastatic TNBC cells.

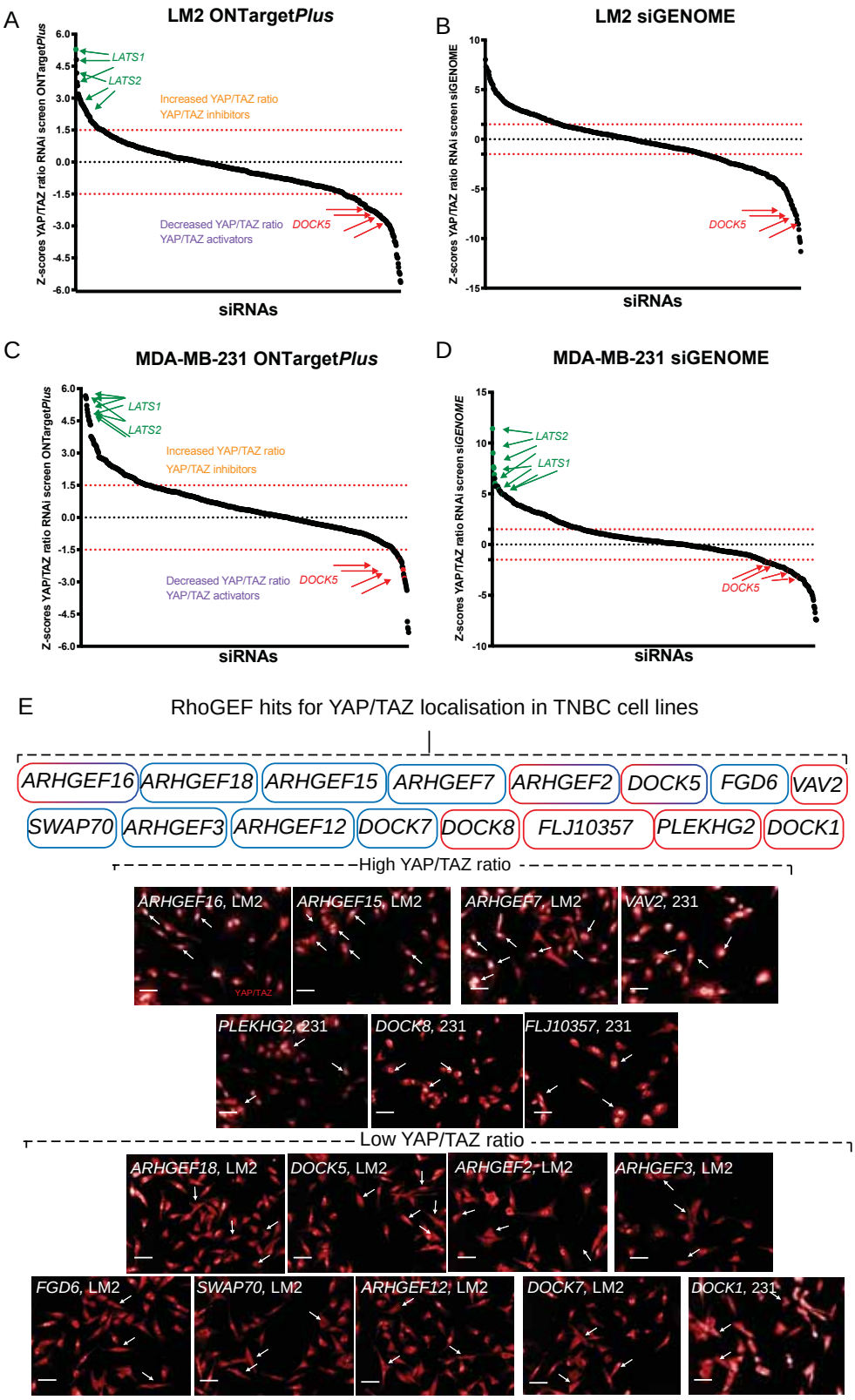

Figure 4.2 RhoGEFs which regulate YAP/TAZ localisation in LM2 and MDA-MB-231 cell lines

Z-scores for YAP/TAZ ratio following RhoGEF/GAP depletion via RNAi for (A) LM2 OTP, (B) LM2 siGENOME, (C) MDA-MB-231 OTP, (D) MDA-MB-231 siGENOME screens. Red dotted lines depict 1.5 and -1.5, thresholds for hit identification. Above 1.5 are positive hits, which result in increased YAP/TAZ ratio and are considered YAP/TAZ inhibitors. Below -1.5 are hits for decreased YAP/TAZ ratio, which are considered YAP/TAZ activators. *LATS1* and *LATS2* YAP/TAZ translocation controls are depicted in green.

Table 4.1: RhoGEF hits for YAP/TAZ translocation in LM2, MDA-MB-231, SUM159, hs578t. In bold, hits common to more than one cell line.

	High YAP/TAZ ratio	Low YAP/TAZ ratio
LM2	ARHGEF15 **ARHGEF16** **ARHGEF7**	**ARHGEF2** ARHGEF3 ARHGEF12 ARHGEF18 **DOCK5** DOCK7 FGD6 SWAP70
MDA-MB-231	FLJ10357 DOCK8 VAV2 **ARHGEF16** PLEKHG2	**ARHGEF2** DOCK1 **DOCK5**
SUM159	ARHGEF39	ARHGEF5 **ARHGEF7** **ARHGEF35** PLEKHG1 TRIO VAV1
Hs578t	ITSN2	**ARHGEF35**

We performed the screens in the same way as described in Chapters 2 and 3, in two additional TNBC cell lines SUM159 and hs578t – which are more epithelial-like than LM2 and MDA-MB-231- However, because the range of densities for mock-transfected cells for SUM159 OTP and siGENOME, and hs578t siGENOME screens did not cover the density range for siRNA transfected cells (Appendix 6), and we have observed that YAP/TAZ nuclear translocation is dependent on cell density in these cell lines, we had to correct for cell number. This was done to avoid identifying genes as hits for YAP/TAZ ratio when the change in YAP/TAZ ratio was a result of density rather than of gene depletion. Therefore, following a similar method to that described by Sero and Bakal, 2017,

we corrected for cell number using the linear regression of each cell density curve per screen which gave us the predicted ratio based on the cell density. Then we obtained the difference between the observed and predicted YAP/TAZ ratios and termed it YAP/TAZ diff. By plotting these values against cell density (Figure 4.3) we considered scores above +2 standard deviations (SD) from the mean of mock transfected wells and those below -2 SD from mock mean as hits. Only wells with total intensities greater than -2 SD and less than +2 SD from mock transfected wells were considered hits. This is because Sero and Bakal., 2017, saw that cells with high YAP ratios but low total YAP, had low levels of the YAP/TAZ target gene *CTGF*. Therefore those with a higher than expected ratio were considered activators of YAP/TAZ, and those with a lower than expected ratio were considered inhibitors. The list of genes obtained in this way for each screen can be found in Appendix 8.

Overall we considered RhoGEFs as hits in SUM159 and hs578t screens when at least 5 out of 8 replicates were hits and at least 2 replicates were hits per screen. No genes were hits across all cell lines. Further, no hits were shared between MDA-MB-231 and SUM159 or hs578t or between LM2 and hs578t (Table 4.1, Figure 4.4). Only one gene, *ARHGEF7*, was a hit for high YAP/TAZ ratio in LM2, and also a hit in SUM159, but for low YAP/TAZ ratio instead. This is particularly interesting as SUM159 are more phenotypically epithelial than LM2 and are less metastatic. Further, Sero and Bakal., 2017 showed that depletion of *ARHGEF7* results in lower YAP/TAZ ratio, while Heidary-Arash et al., 2014, showed that overexpression of ARHGEF7 inhibits YAP/TAZ nuclear translocation in breast

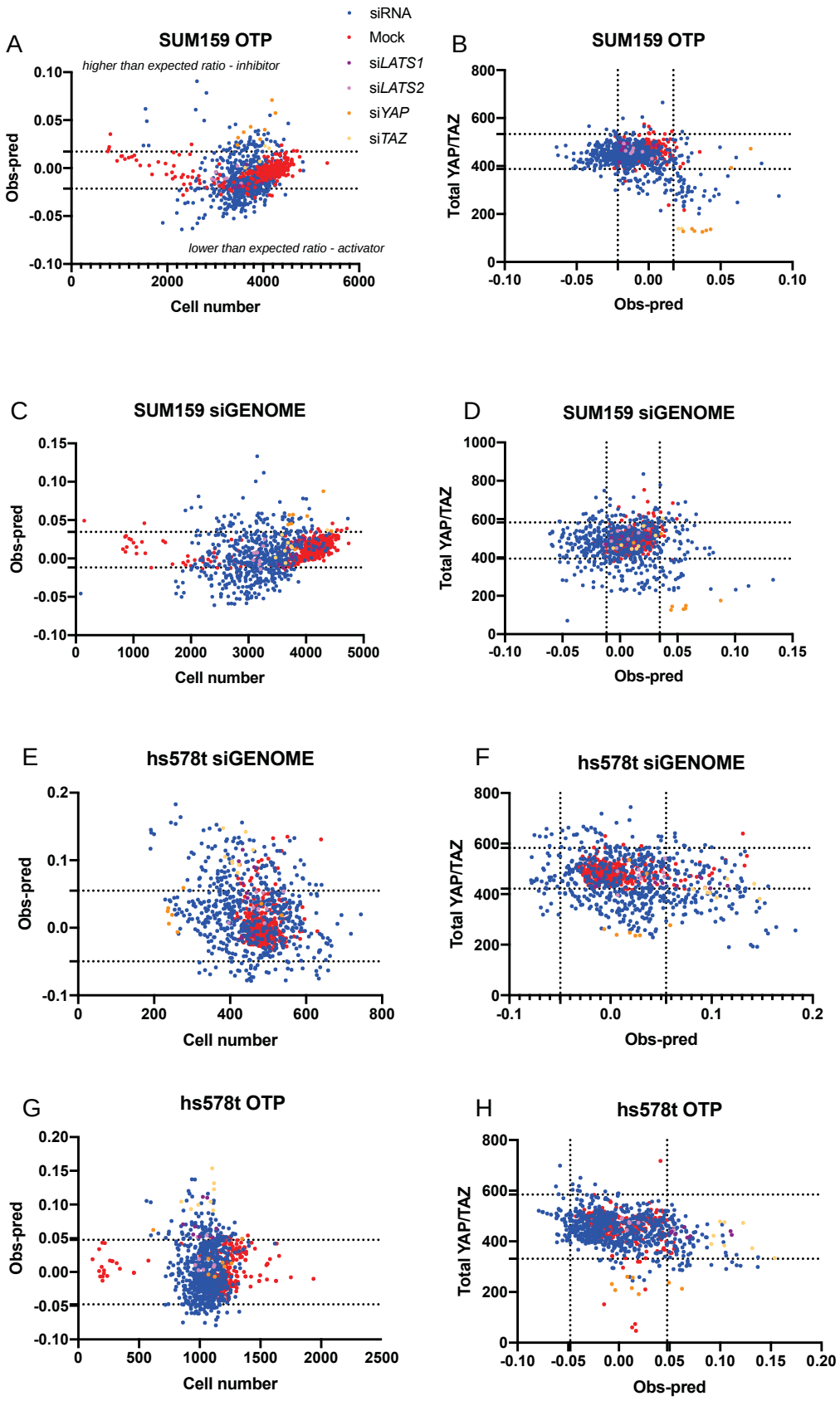

Figure 4.3 Correcting for cell number to identify regulators of YAP/TAZ in RNAi screens in the TNBC cell lines SUM159 and hs578t

(A) (C) (D) (E) Difference between observed YAP/TAZ ratios and those predicted from cell density curves (Obs-pred) for (A) SUM159 OTP, (C) SUM159 siGENOME, (D) hs578t siGENOME, and (E) hs578t OTP screens. Dotted lines represent 2 SD of mock transfected cells Obs-pred. siRNAs in blue (n = 668 wells OTP, 575 siGENOME), mock in red (n = 300 wells), si*LATS1* and si*LATS2* (n = 8 wells) in purple and pink respectively, and si*YAP* and si*TAZ* (n = 8 wells) for in orange and yellow respectively. (B) (D) (F) (G) Total YAP/TAZ intensities as a function of YAP/TAZ Obs-pred ratios.Dashed lines: 2 SD of mock transfected cells.

cancer cells by forming a scaffold with LATS1/2 and promoting YAP/TAZ phosphorylation and consequent sequestration in the cytoplasm. Overall, this suggests that the role of ARHGEF7 changes from an activator of YAP/TAZ to an inhibitor as breast cancer cells change in metastatic ability.

4.2.3 Clustering of YAP/TAZ ratios as a result of RhoGEF/GAPs and RhoGTPase siRNAs on the TNBC cell lines LM2, MDA-MB-231, SUM159, and hs587t.

We reasoned that if different genes regulate YAP/TAZ localisation similarly (i.e., as part of the same complex or pathway), or have “functional interactions”, depletion of these genes would result in similar YAP/TAZ levels across cell lines (Bakal et al., 2007; Sero et al., 2015). To establish functional relationships between genes, we performed hierarchical clustering of YAP/TAZ ratio Z-scores for LM2, MDA-MB-231, and Z-scores of YAP/TAZ diff (observed-predicted values) for SUM159, and hs578t screens, which groups siRNAs based on how they regulate YAP/TAZ across various TNBC cell lines.

We did not include si*YAP* and si*TAZ* in our clustering as they were controls for our ability to detect YAP/TAZ levels and not ratio, while we included *LATS1/2* as they are controls for YAP/TAZ ratio. We performed feature reduction based on screens which clustered together and thus provided little differing information, resulting in the final clustering, which at a Pearson Correlation Coefficient (PCC) of > 0.80 clustered genes into 30 groups (Figure 4.5).

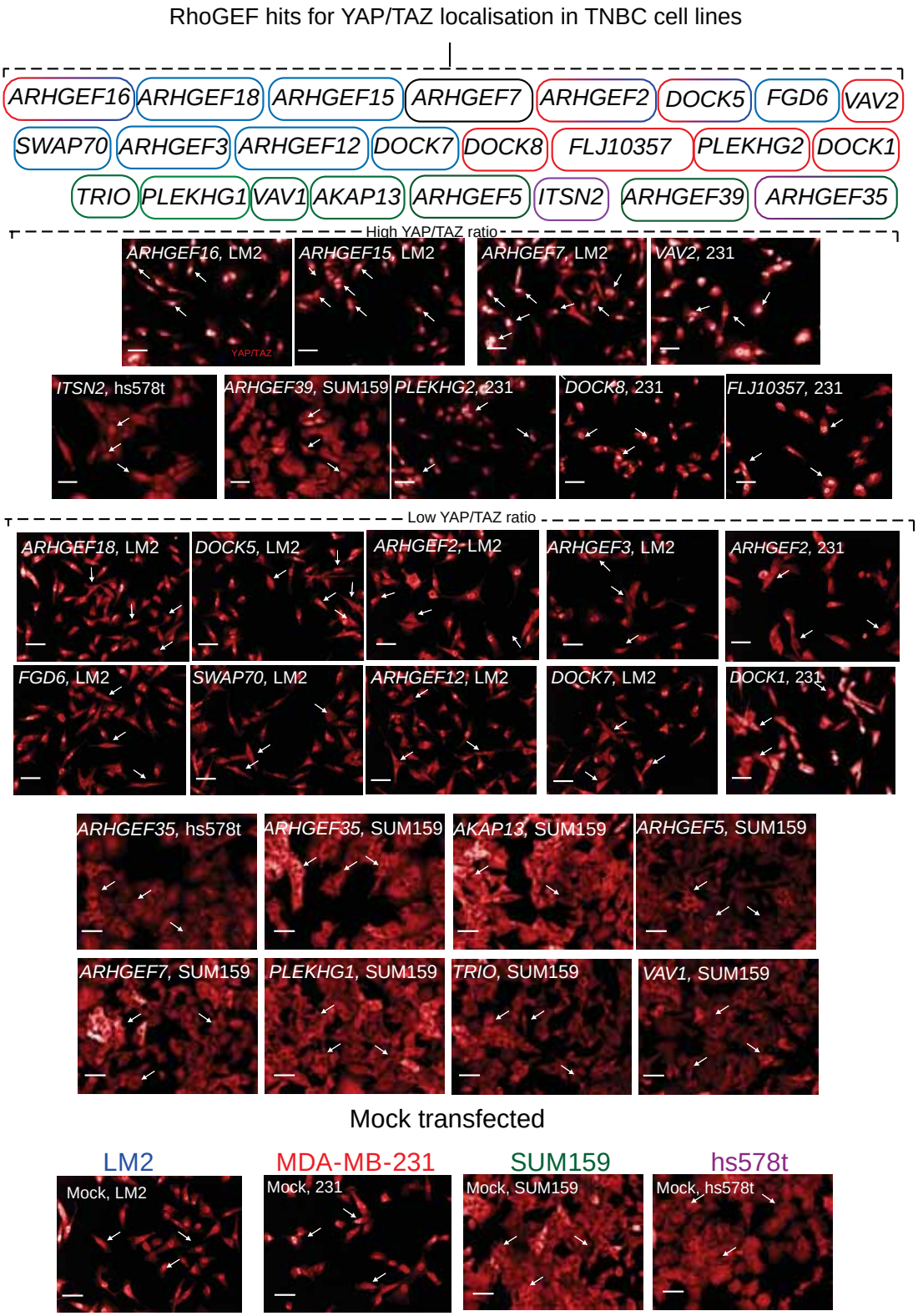

Figure 4.4 RhoGEF hits for YAP/TAZ localisation in TNBC cell lines
Representative images for RhoGEF hits for YAP/TAZ localisation in LM2 only (blue), MDA-MB-231 only (red), in LM2 and MDA-MB-231 (blue and red), in SUM159 only (green), in hs578t only (purple), and in SUM159 and hs589t (purple and green). ARHGEF7 is in black as it is a hit for high YAP/TAZ ratio in LM2, and low for SUM159. Cells were stained for YAP/TAZ. Hits for high and low YAP/TAZ ratio display high and low nuclear YAP/TAZ (white arrows) respectively. Cells stained for YAP/TAZ (red). Scale bar is 50µm.

By focusing on genes which were hits for each cell line we found that *DOCK5*, the strongest hit for low YAP/TAZ ratio in LM2 and MDA-MB-231, clustered with *ARHGEF5*, a hit for low YAP/TAZ ratio in SUM159, in cluster 22 (Figure 4.5). This could be indicative of DOCK5 and ARHGEF5 activating YAP/TAZ in a similar manner in the different cell lines. *DOCK5* is a RAC1-GEF, while *ARHGEF5* is a RHOA-GEF. ARHGEF5 has been shown to mediate migration and invasion in colorectal by activating the RHOA-ROCK signalling pathway in colorectal cancer cells (Komiya et al., 2016, Kuroiwa et al., 2011; Yohe et al., 2007), and DOCK5 has been identified as a key regulator of epilthelial invasion and metastasis downstream of RHOA-ROCK (Frank et al., 2017), but neither of them have been described to regulate YAP/TAZ.

Further, *DOCK8*, a hit for high YAP/TAZ ratio only in MDA-MB-231 cells (Table 4.1) clustered with our control for YAP/TAZ translocation to the nucleus LATS2 in cluster 12, supporting the idea that it is a YAP/TAZ inhibitor. Further, *DOCK8* also clustered with *ARHGAP5*, a RHOA and RAC-type GAP which has been shown to induce contact inhibition of proliferation by repressing YAP-TEAD regulated gene transcription by activating LATS kinases and inhibiting Rho-ROCK signalling (Frank et al., 2018). Interestingly, studies have shown that DOCK8 is activated by MOB1 when phosphorylated by the MST1 and MST2 kinases (Mou et al., 2012). As MST1 and MST2 are part of the Hippo signalling pathway and phosphorylate and activate LATS1/2 (Qin et al., 2013), this could suggest that DOCK8 may be regulating YAP/TAZ in a mechanistically similar way to LATS1/2 and warrants further study.

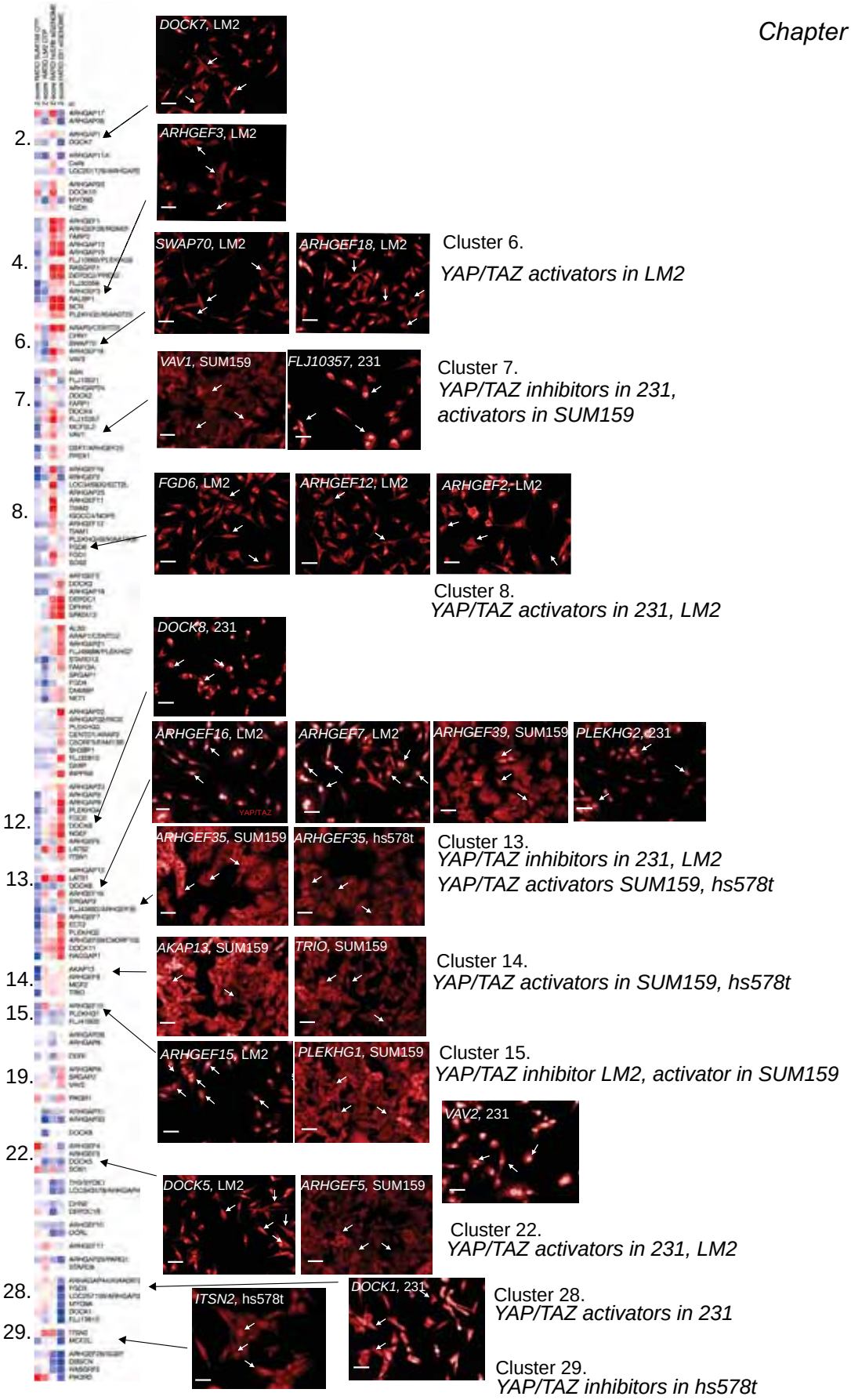

Figure 4.5 Hierarchical clustering of RhoGEF/GAPs for YAP/TAZ localisation in TNBC
Hierarchical clustering of average YAP/TAZ ratio Z-score for each RhoGEF/GAP siRNA grouped at a PCC > 0.80 results in 30 multigene clusters (labelled on the left). Description of clusters on the right. Representative images for RhoGEF hits for YAP/TAZ localisation in LM2, MDA-MB-231, SUM159, and hs578t. Cells were stained for YAP/TAZ (red). Hits for high and low YAP/TAZ ratio display high and low nuclear YAP/TAZ (white arrows) respectively. Scale bar is 50µm.

Cluster 13 is of particular interest as genes that were hits for high YAP/TAZ ratio in LM2 and MDA-MB-231, clustered with genes that were hits for low YAP/TAZ ratio in hs578t and SUM159. *LATS1*, a control for high YAP/TAZ ratio clustered with these genes, suggesting perhaps it has more of a role as an inhibitor in LM2 and MDA-MB-231 than in SUM159 and hs578t. *ARHGEF7* and *ARHGEF35* are members of this cluster, the former being a hit for high YAP/TAZ ratio in LM2, and low in SUM159, and the latter for low YAP/TAZ ratio in SUM159 and hs578t. This suggests ARHGEF7 and ARHGEF35 could activate YAP/TAZ in a similar manner in SUM159 and hs578t spread-type cells, while ARHGEF7 is an inhibitor of YAP/TAZ in more spindly-like cells – possibly due to dysregulated activity.

Finally, *ARHGEF39*, which was the only hit for high YAP/TAZ ratio in SUM159 clustered closely with *PLEKHG2*, a hit for high YAP/TAZ ratio in MDA-MB-231 in cluster 13, perhaps suggesting similar roles in inhibiting YAP/TAZ in these two cell lines. The regulators of cytokinesis *ECT2* and *RACGAP1* also clustered with *ARHGEF7*, *PLEKHG2*, and *ARHGEF39*.

Overall these data suggest that some of the differences in YAP/TAZ regulation observed between the more spread-like and more spindly-like TNBC cell lines can, at least in part, be explained by the differential activity of RhoGEFs.

4.2.4 Identifying how cell shape varies across cell lines and predicting YAP/TAZ ratio from cell shape.

There is a complex interplay of YAP/TAZ translocation with cell shape, mechanical forces, and cytoskeletal organisation – all of which themselves influence, and are influenced by RhoGEF activity. We therefore sought to understand how depletion of different RhoGEFs may be affecting YAP/TAZ dynamics, by integrating information as to how their depletion affects cell shape.

We performed the same filtering and shape hit identification steps for SUM159 and hs578t as described in Chapter 3 for LM2 and MDA-MB-231 (Appendices 9 and 10 respectively). Using single cell data from our filtering analysis we sought to identify whether YAP/TAZ localisation varied depending on shape. We observed that spindly shaped LM2 cells have low YAP/TAZ ratios (denoted by red 95% confidence interval for spindly shape, Figure 4.6A), and those classified as large round (denoted by green 95% confidence interval for large round shape, Figure 4.6A) have higher YAP/TAZ ratios. For MDA-MB-231, cells classified as fan (black 95% confidence interval, Figure 4.6D), large round (green 95% confidence interval, Figure 4.6D), and triangular (blue 95% confidence interval) displayed the highest YAP/TAZ ratios. In hs578t large round-shaped cells displayed the highest ratios (green 95% confidence interval, Figure 4.7B), while in SUM159, small round cells displayed the highest YAP/TAZ ratios (purple 95% confidence interval Figure 4.7D). However, because the range of YAP/TAZ ratios was narrow and below 1 (~ 0.3 to -0.4), compared to LM2 and MDA-MB-231 (~4.0 to 0.5), YAP/TAZ appeared to vary less with shape in SUM159 and hs578t.

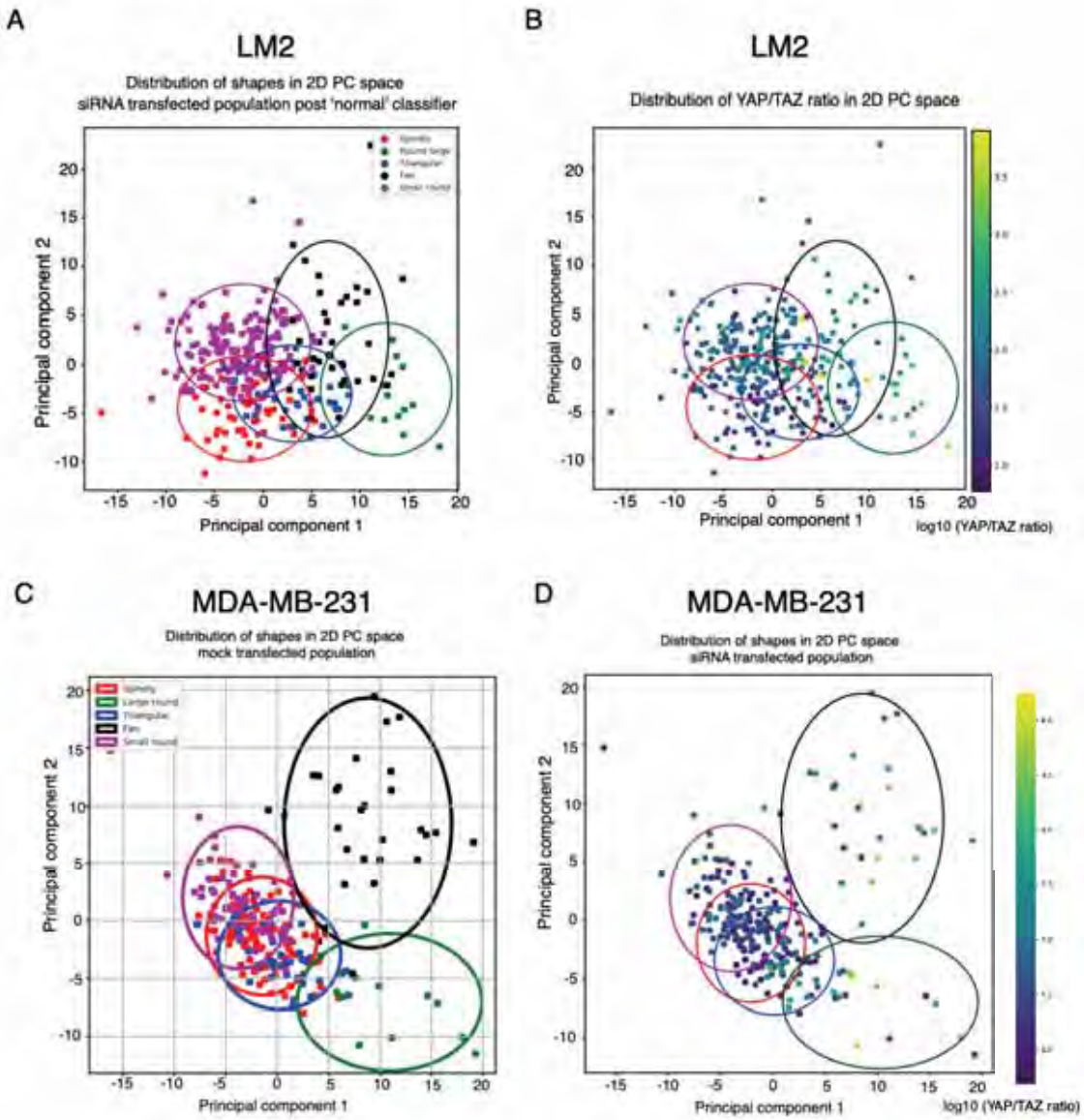

Figure 4.6 YAP/TAZ localisation and shape of single cells for LM2 and MDA-MB-231 cell lines

PCA of single cell dataset comprised of texture and morphological features of siRNA transfected population, removing cells classified as 'normal' for LM2 (A) (B) and MDA-MB-231 (C) (D). Ellipses represent 95% confidence intervals for each shape. Each dot represents one cell, colour coded by shape (A) and (C) and YAP/TAZ ratio (B) and (D). Shape colour coding: spindly in red, round large in green, triangular in blue, fan in black, and small round in purple. YAP/TAZ colour coding: purple to yellow indicative of high to low YAP/TAZ ratios in arbitrary units.

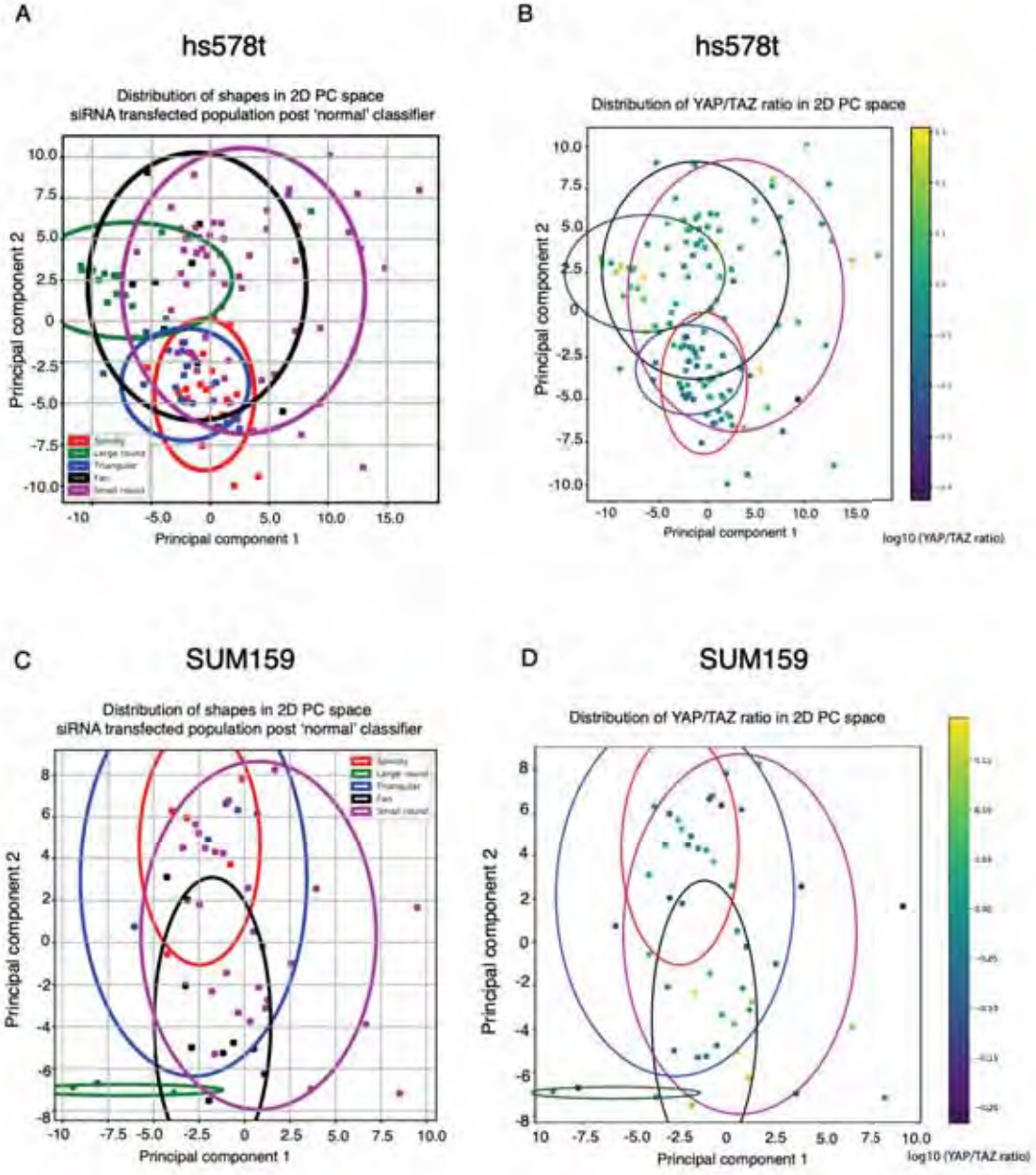

Figure 4.7 YAP/TAZ localisation and shape of single cells for hs578t and SUM159 cell lines

PCA of single cell dataset comprised of texture and morphological features of siRNA transfected population, removing cells classified as 'normal' for hs578t (A) (B) and SUM159 (C) (D). Ellipses represent 95% confidence intervals for each shape. Each dot represents one cell, colour coded by shape (A) and (C) and YAP/TAZ ratio (B) and (D). Shape colour coding: spindly in red, round large in green, triangular in blue, fan in black, and small round in purple. YAP/TAZ colour coding: purple to yellow indicative of high to low YAP/TAZ ratios in arbitrary units.

In order to assess the relationship between YAP/TAZ and cell shape/cytoskeletal organisation/mechanical force in LM2 cells, we first sought to determine if YAP/TAZ translocation is a good predictor of shape across cell lines. We carried out principal component analysis (PCA) on Z-scores of the percentage of cells classified into each shape as well as on YAP/TAZ ratios, for LM2, MDA-MB-231, SUM159, and hs578t siGENOME and OTP screens (Figure 4.8A, C, E, G). Then we performed Partial Least Squares Regression (PLSR) on the same data using shapes features as predictors of the YAP/TAZ ratio response (Figure 4.8B, D, F, H). Where PCA explores the variance in the data, PLSR maximises the correlation and the covariance in the data at the same time. In other words, PLSR maintains maximal variance while optimising correlation between the response and the predictor set. Both result in a score defined as the sum of the variance (covariance in PLSR) times the loading weight: . In the case of scores obtained by performing PCA analysis the sign represents directionality, and in PLSR the sign is indicative of whether the relationship of the predictor is positive or negative relative to the response.

In LM2, variance is manifested across all shapes parameters and YAP/TAZ ratio, with small round varying in an antagonistic way to the rest of the features (score of -0.22) (Figure 4.8A). The greatest variance in the data is explained by triangular shape (score of 0.32). On the other hand, in MDA-MB-231, the greatest variance in the data is explained by YAP/TAZ ratio (score of 0.34). These data suggest that LM2 cells explore a larger shape space that MDA-MB-231 cells, but MDA-MB-231 cells exhibit a broader range of YAP/TAZ activities.

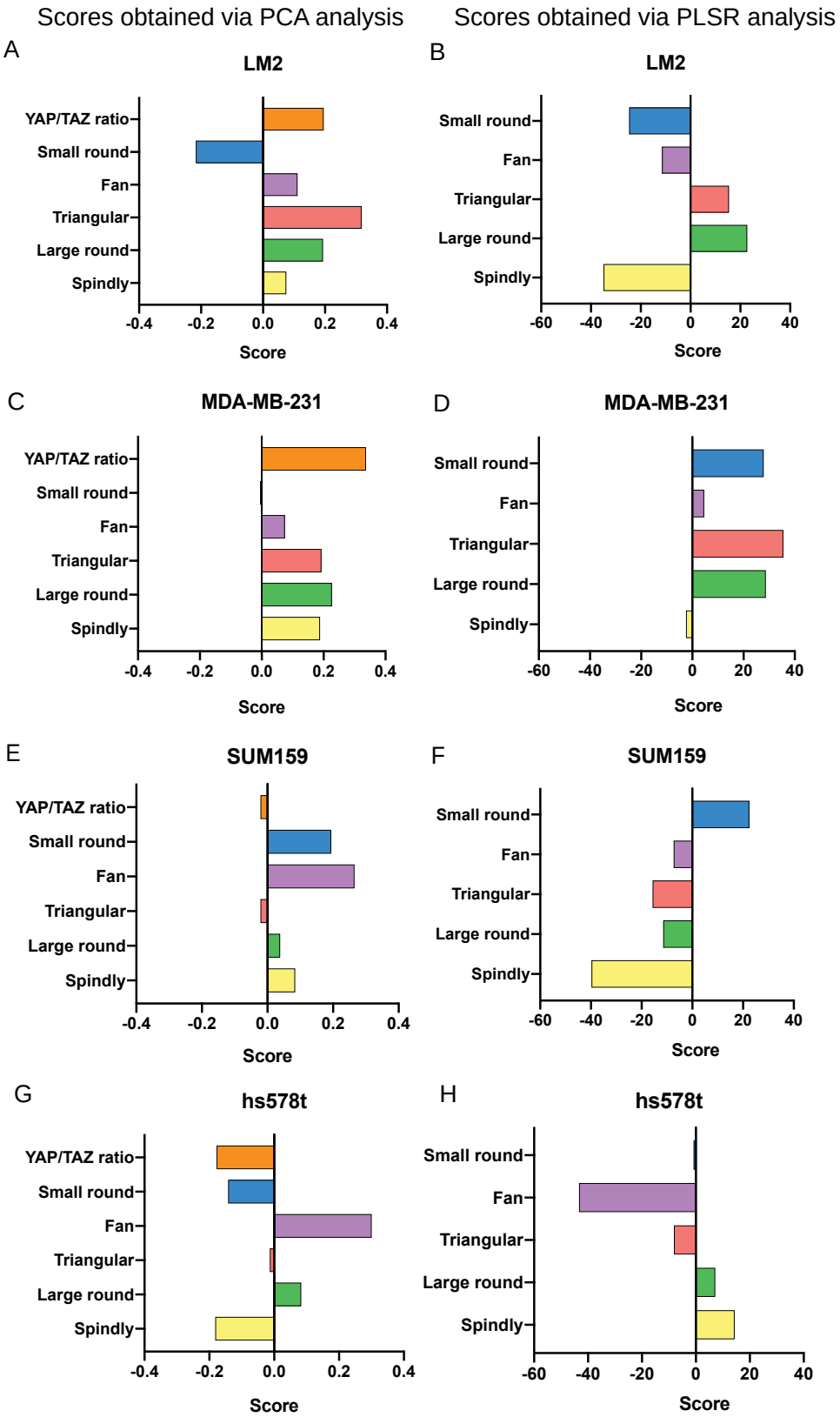

Figure 4.8 How shape varies across TNBC cell lines and predicting YAP/TAZ ratio from cell shape using PLSR analysis

(A) (C) (E) (F) Graphs show the result of the sum of the variance (covariance for PLSR (B) (D) (F) (H)) multiplied by the loading weight for each PC, obtained by PCA analysis (and PLSR) on Z-scores of percentage of cells classified into each shape as well as YAP/TAZ ratio for LM2, MDA-MB-231, SUM159, and hs578t, siGENOME and OTP screens. (B) (D) (F) (H) For PLSR analysis shapes were the predictors of YAP/TAZ ratio (response).

PLSR analysis reveals that in LM2, all shapes are predictive of YAP/TAZ ratio to varying degrees. Spindly shape is the strongest negative predictor of YAP/TAZ ratio (score of -34.9) and large round shape is a strong positive predictor of YAP/TAZ ratio (score of 22.7), with the rest of the shapes being weaker predictors of YAP/TAZ ratio (Figure 4.8B). In MDA-MB-231 cells, most shapes are predictors of positive YAP/TAZ ratio (scores of 35.5, 27.8, 27.8 for triangular, small round, and large round shapes respectively), and none are predictors of low YAP/TAZ ratio (Figure 4.8D). Notably, while both MDA-MB-231 and LM2 cells have high basal YAP/TAZ activity, LM2 cells are more capable of suppressing YAP/TAZ localisation at higher densities compared to MDA-MB-231 (Figure 4.1). The fact that certain shapes (such as the spindle shape) are predictors of low YAP/TAZ activity in LM2 cells suggest that the ability of LM2 cells to suppress YAP/TAZ at high densities is due to changes in cell shape and not contact inhibition. Thus, we propose that while dysregulation of signalling pathways result in the increased YAP/TAZ activity in MDA-MB-231 cells, these cells have uncoupled YAP/TAZ activity from shape – contrary to what is found in “normal” cell lines (Aragona et al., 2013; Dupont et al., 2011; Sero and Bakal, 2017). However, as these cells became metastatic, they re-acquired the ability to couple YAP/TAZ nuclear translocation to cell shape.

In SUM159 the variance is manifested mostly across small round and fan shape (scores of 0.19 and 0.26), while the variance in YAP/TAZ ratio is negligible (score of -0.02) (Figure 4.8E). In hs578t the variance is manifested across most shape parameters as well as YAP/TAZ ratio, with fan shape displaying the largest positive variance with a score of 0.30 (Figure 4.8G). Extending this analysis to

PLSR shows that all but one shape are negative predictors of YAP/TAZ ratio to a degree in SUM159 (Figure 4.8F), with spindly shape as a strong predictor of low YAP/TAZ ratio (score of -39.7) and small round as a weaker predictor of high YAP/TAZ ratio (score of 22.4), while in hs578t fan shape is the biggest negative predictor of YAP/TAZ ratio (score of -43.2) (Figure 4.8H). These data suggest that there is little variance in YAP/TAZ ratio in SUM159, supporting our single cell data (Figure 4.7D) with YAP/TAZ ratio being predominantly cytoplasmic and inactive. However, within that narrow range of ratios, those cells which are spindly tend to have lower YAP/TAZ ratios, while those that are small round tend to have higher YAP/TAZ ratios, suggestive of some regulation of YAP/TAZ ratio via shape. Similarly, in hs578t YAP/TAZ ratio is predominantly negative, and although it accounts for more variance than in SUM159, it seems to be explained predominantly by fan shape, suggesting that fan shape is probably the only regulator of YAP/TAZ ratio in hs578t. Overall, these data suggest that in the more spread-like TNBC cell lines SUM159 and hs578t YAP/TAZ activity is predominantly low, and any activity that is present is not dependent on shape.

Interestingly, because in normal basal epithelial cell lines, such as MCF10A, YAP/TAZ is highly coupled to shape (Figure 4.1) (Sero and Bakal., 2017), we propose that: (1) spread-like TNBC have uncoupled YAP/TAZ activation from shape, (2) EMT into a more spindly-type state is linked to increased YAP/TAZ activation in ways that are not due to shape/mechanical signals and could be due to activation in pathways such as RAS (Fisher et al., 2017; Shao et al., 2014); (3) the evolution of less metastatic to more metastatic spindly-like cells is driven by a re-coupling of YAP/TAZ to mechanical cues.

4.2.4 Understanding the phenotype of RhoGEFs that were hits for YAP/TAZ ratio hits in LM2

We wondered whether any RhoGEFs which were hits for YAP/TAZ rtaio, were also hits for shape in LM2 cells. Overlapping hits would suggest these genes regulate YAP/TAZ “indirectly” (i.e., by changing cell shape, which then affects YAP/TAZ), whereas those which affected YAP/TAZ but not cell shape would suggest they affect YAP/TAZ “directly” (i.e., by regulating YAP/TAZ downstream of different cues).

Given that our PLSR analysis showed that spindly shape was the strongest negative predictor of YAP/TAZ ratio in LM2 (Figure 4.9A), we would predict that genes that hits for low YAP/TAZ ratio would have a spindly phenotype. An example of this would be *SWAP70*, which was a hit for low YAP/TAZ ratio, and a hit for spindly shape (Figure 4.9Bi). This suggests that YAP/TAZ regulation by SWAP70 may be via regulation of shape. Indeed, SWAP70 has been shown to regulate the cytoskeleton by stabilising actin (Chacón-Martínez et al., 2013; Gomez-Cambronero, 2012; Hilpela et al., 2003) by activation of RAC1 and RHOA (Dwyer et al., 2015; Ocaña-Morgner et al., 2011). Further, depletion of *SWAP70* has been shown to result in actin polymerisation and impair migration, polarisation and adhesion (Chopin et al., 2010; Garbe et al., 2012). However, its function has not been linked to YAP/TAZ. We hypothesise that lack of SWAP70 resulting in unstable actin, could result in a lack of tension which is then sensed by YAP/TAZ, resulting in the low YAP/TAZ ratio observed following SWAP70 depletion in LM2.

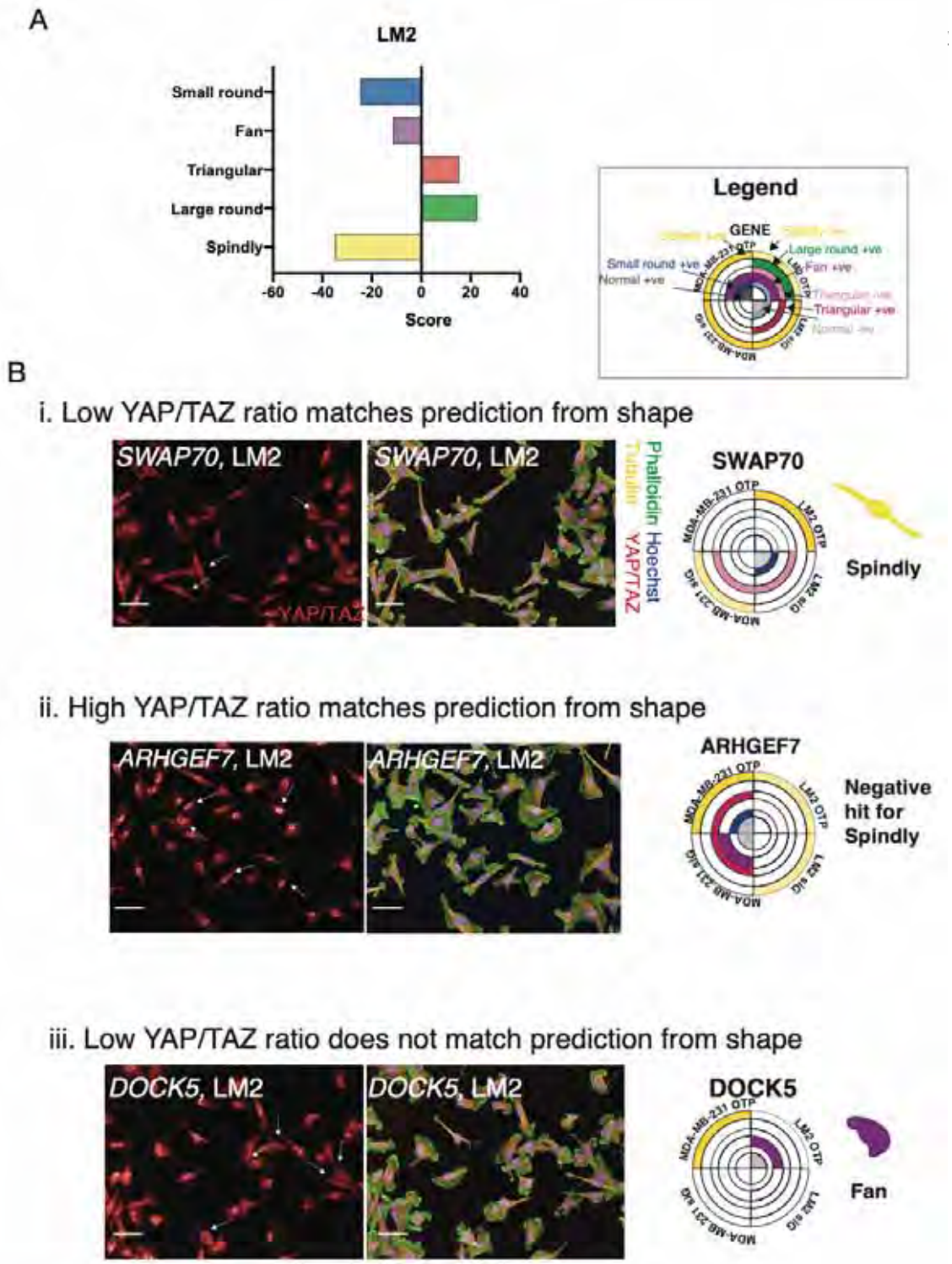

Figure 4.9 RhoGEFs which may be regulating YAP/TAZ via shape in LM2 cells
(A) Graph shows PLSR analysis on Z-scores of the percentage of cells classified into each shape for LM2 siGENOME and OTP screens, where shapes were the predictors of YAP/TAZ ratio (response). (B) Examples of hits for YAP/TAZ ratio in LM2 which were also hits for shape in LM2. Gene signature shows whether these genes were hits for any other shapes in any other screens. Each quadrant represents the screen: top right LM2 OTP, bottom right LM2 siGENOME, bottom left MDA-MB-231 siGENOME, top left MDA-MB-231 OTP. Each quadrant is split into 6 shapes, which are coloured only if the gene is a hit for that shape. Solid and faded colours represent positive and negative hits respectively. Spindly in yellow, large round in green, triangular in pink, fan in purple, small round in blue, and normal in grey. Representative images stained for DNA (blue), YAP/TAZ (red), α-tubulin (yellow), and polymerised F-actin (green). White arrows indicate high or low nuclear YAP/TAZ. Scale bar, 50μm.

Further, another example of possible YAP/TAZ regulation via shape is *ARHGEF7*, a hit for high YAP/TAZ ratio, which is also a negative hit for spindly shape, matching our prediction (Figure 4.9Bii). From our shape screens, we hypothesised that LM2 cells are dynamically changing shape in wild-type conditions, and that certain RhoGEFs are essential for specific transitions. Such that depletion of a RhoGEF can result in a significant reduction in that particular shape as it is required to mediate that particular transition. This suggests that ARHGEF7 is required for a transition to spindly shape in LM2, and that this could be how it mediates its inhibitory action on YAP/TAZ ratio. Studies have shown that ARHGEF7 couples YAP to cell-matrix adhesion via RAC1/CDC42 signalling (Sero and Bakal., 2017), and can also regulate YAP/TAZ in a GEF-independent manner by activating LATS1 phosphorylation of YAP/TAZ (Heidary Arash et al., 2014). Therefore, given that ARHGEF7 has been shown to regulate YAP/TAZ, together with our data, we hypothesise that ARHGEF7 is regulating YAP/TAZ via spindly shape in LM2 cells.

On the other hand, *DOCK5*, a hit for low YAP/TAZ ratio, was not a hit for spindly shape, but was a hit for fan shape (Figure 4.9Biii). Fan shape is a weak predictor for low YAP/TAZ ratio, which suggests that DOCK5 is less likely to be regulating YAP/TAZ via shape, but rather it could be regulating YAP/TAZ directly downstream of shape. In our clustering of the quantitative morphological signatures (QMS) for shape hits in the LM2 OTP screen discussed in Chapter 3, *DOCK5* was between a cluster composed of polarity regulators and another formed of contractility and adhesion turnover regulators, suggesting it may play

a role in regulating adhesion and polarity (Figure 3.11). In fact, DOCK5 has been shown to promote RAC1 mediated lamellipodial protrusion and focal adhesion turnover, downstream of GIT2, promoting invasion in MDA-MB-231 cells (Frank et al., 2017). However, this mechanism has not been linked to YAP/TAZ. Further, DOCK5 has been shown to regulate microtubule dynamics downstream of AKT in mast cells and osteoclasts (Guimbal et al., 2019; Ogawa et al., 2014). A role which, again, has not been linked to YAP/TAZ. Therefore, given our data and the literature we hypothesise that DOCK5 could be regulating YAP/TAZ via regulation of adhesions, front rear polarity, and microtubule dynamics, as well as perhaps via a direct signalling mechanism.

Conversely, in MDA-MB-231 cells, because no particular shape regulates YAP/TAZ as shown by our PLSR analysis (Figure 4.8D), we cannot identify RhoGEFs that regulate YAP/TAZ by changing shape specifically.

4.2.5 Identifying RhoGEFs which may be regulating YAP/TAZ via shape

To understand which of the RhoGEFs might be regulating YAP/TAZ via shape, we generated a signature for each cell line comprised of the best shape predictor for YAP/TAZ, and YAP/TAZ ratio, for RhoGEFs which were hits for YAP/TAZ ratio. Because the strongest shape predictors of YAP/TAZ ratio for all cell lines except for MDA-MB-231, were negative predictors of YAP/TAZ ratio, and MDA-MB-231 did not have one shape that was significantly stronger than the others at predicting YAP/TAZ ratio, we excluded MDA-MB-231 from this analysis. Therefore, we used the strongest negative predictors of YAP/TAZ ratio for LM2,

SUM159, and hs578t: averaged spindly Z-scores for LM2 and SUM159, and fan Z-score for hs578t, and their corresponding YAP/TAZ ratio Z-scores. Because there are differences between the OTP and siGENOME screens, for simplicity we used the OTP screens' scores.

We grouped the RhoGEFs by cell line and by whether or not they matched the shape prediction. Such that group 1 encompasses hits which matched shape prediction in LM2; group 2, hits for low YAP/TAZ ratio which did not match shape prediction in LM2; and group 3, hits for high YAP/TAZ ratio which did not match shape prediction. *ARHGEF7* is of particular interest, as it was a hit for high YAP/TAZ ratio in LM2, but a hit for low YAP/TAZ ratio in SUM159. Given that spindly shape was a negative predictor of YAP/TAZ ratio in SUM159 (Figure 4.10Bi), and *ARHGEF7* was a hit for low YAP/TAZ ratio we would expect *ARHGEF7* to have a spindly phenotype. However, it had no effect on spindly shape, suggesting that it is regulating YAP/TAZ ratio independently of shape, contrary to what we saw in LM2 cells (Figure 4.9Bii).

Further, only one out of the seven hits for SUM159 matched the shape prediction, *ARHGEF5*, while none did for hs587t (Figure 4.10). For example, *ARHGEF35* a hit for low YAP/TAZ ratio in both SUM159 and hs578t, did not match the shape predictor in either cell line (Figure 4.10Bi, ii), suggesting that *ARHGEF35* is regulating YAP/TAZ independently of shape in both SUM159 and hs578t. In addition, *ITSN2*, a hit for high YAP/TAZ ratio in hs578t had no effect on the predictor shape, and by looking at the images we observed that it did not enrich for spindly shape, a weak predictor of high YAP/TAZ ratio (Figure 4.10A). Lastly,

ARHGEF5 was the only hit in SUM159 whose phenotype matched YAP/TAZ ratio, (Figure 4.10Bi) suggesting shape-dependent regulation of YAP/TAZ. ARHGEF5 has been shown to mediate migration and invasion in colorectal by activating the RHOA-ROCK signalling pathway in colorectal cancer cells (Komiya et al., 2016, Kuroiwa et al., 2011; Yohe et al., 2007), but its role has not been linked to YAP/TAZ. Thus suggests that ARHGEF5 could be important to activate YAP/TAZ in SUM159.

Overall these data suggest that in LM2 cells, there is a combination of RhoGEFs which are regulating YAP/TAZ via shape, and independently of shape, whereas this does not seem to be the case in SUM159 and hs578t. This supports our hypothesis that YAP/TAZ are less dependent on shape in more spread-like cells such as SUM159 and hs578t, compared to more spindly-like cells such as LM2.

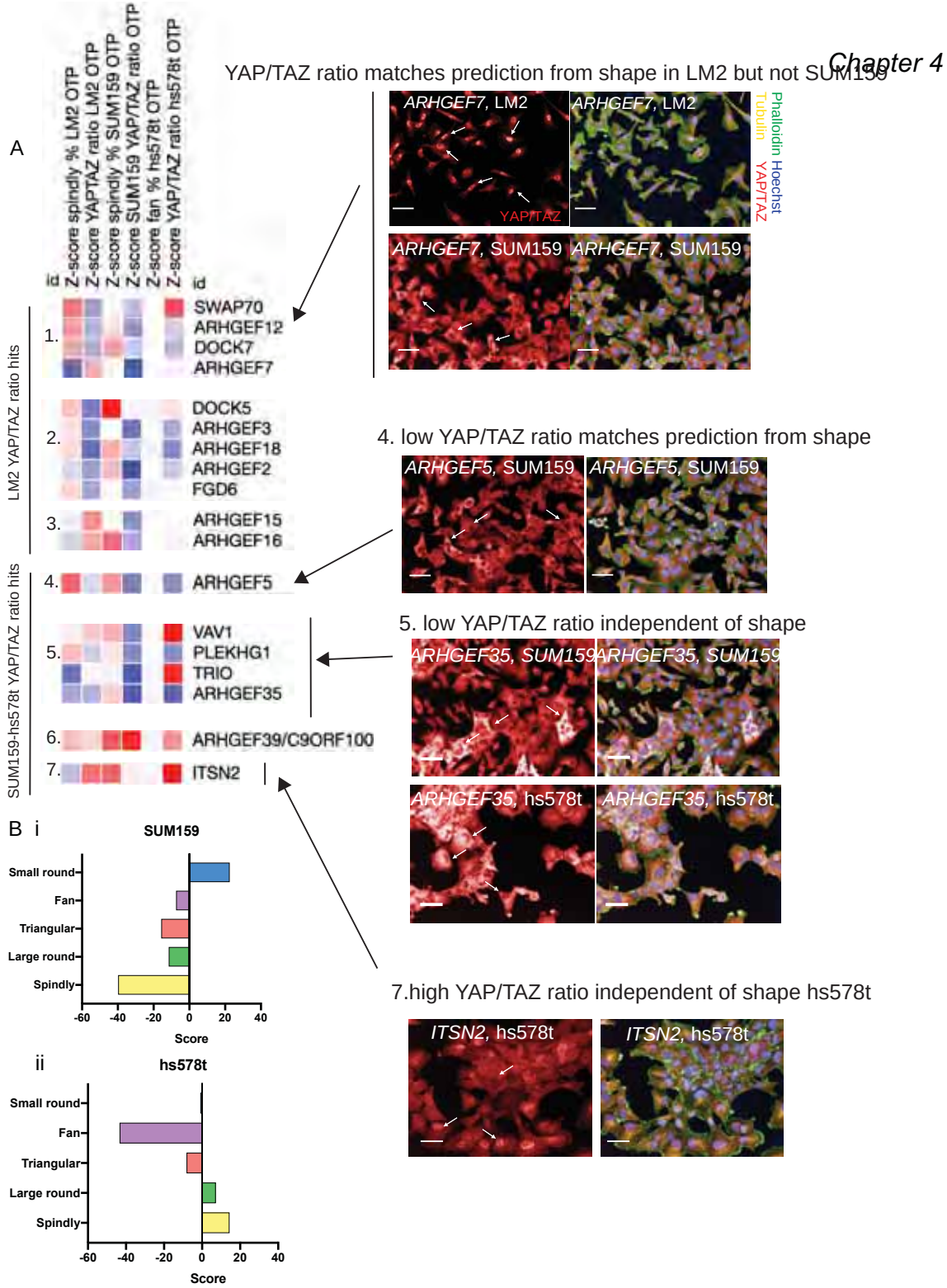

Figure 4.10 Identifying RhoGEFs which may be regulating YAP/TAZ via shape in LM2, hs587t and SUM159 TNBC cell lines

(A) Heatmap of Z-scores of percentage of cells classified as spindly in LM2 OTP, SUM159 OTP screens, and as fan in hs578t OTP screen, and corresponding Z-scores of YAP/TAZ ratios. Group 1: hits which matched shape prediction in LM2. Group 2 and 3: hits for low and high YAP/TAZ ratio respectively, which did not match shape prediction in LM2. Group 4: hit for low YAP/TAZ ratio which matches prediction from shape in SUM159. Group 5: hits for low YAP/TAZ ratio which do not match prediction from shape in SUM159, and in hs578t (ARHGEF35). Group 6: hit for high YAP/TAZ ratio in SUM159 which does not match prediction from shape. Group 7: hit for high YAP/TAZ ratio independent of shape in hs578t. Representative images for DNA (blue), YAP/TAZ (red), α-tubulin (yellow), and polymerised F-actin (green). White arrows indicate high or low nuclear YAP/TAZ. Scale bar, 50µm. (B) Graph shows PLSR analysis on Z-scores of the percentage of cells classified into each shape for (i) SUM159 (ii) hs578t siGENOME and OTP screens, where shapes were the predictors of YAP/TAZ ratio (response).

4.3 Discussion

Our data suggest that the RhoGEF-Rho pathways regulating YAP/TAZ are under a great deal of selection pressure during the evolution of breast cancer cells. For example, in comparison to normal epithelial cells which exhibit a wide dynamic range of YAP/TAZ activation that is in part controlled by cell shape, spread-like TNBC cells (less aggressive, weakly metastatic) have low basal YAP/TAZ activity, that is poorly coupled to cell shape. Spindly-like MDA-MB-231 and LM2 cells have very high basal levels of YAP/TAZ activity, but in MDA-MB-231 cells this is not connected to cell shape and could be due to the activation of YAP/TAZ by oncogenic pathways such as the RAS-AKT pathway. However, a derivative of MDA-MB-231 cells, the highly metastatic cell line LM2, appears to have "re-coupled" shape to YAP/TAZ activity.

We hypothesise that LM2 cells have gained the ability to suppress YAP/TAZ activity depending on their environment and depending on shape, compared to MDA-MB-231 where YAP/TAZ is constantly on. Our data suggest mutant oncogenic signalling is responsible for keeping YAP/TAZ nuclear and active in both these cell types. However, LM2 cells can downregulate YAP/TAZ by switching to a spindly shape (Figure 4.10A). An ability that LM2 cells have acquired, differing them from MDA-MB-231 cells. This ability may be important to the metastatic ability of LM2 cells. Notably, LM2 cells preferentially metastasise to the lungs, a tissue that is softer than breast cancer tissue which can be up to 10 times stiffer than normal breast (Barnes et al., 2017; Butcher et al., 2009; Cox and Erler, 2011). We propose high YAP/TAZ signalling, which promotes high

levels of contractility and traction, may not be beneficial for migration in such soft environments, which typically involves the adoption of poorly adherent amoeboid shapes (Sanz-Moreno and Marshall, 2010; Wolf et al., 2003).

Of the RhoGEFs that were hits for YAP/TAZ ratio in LM2, we found that *SWAP70* was a hit for low YAP/TAZ ratio and for spindly shape, while *ARHGEF7*, a hit for high YAP/TAZ ratio was a negative hit for spindly shape, as predicted from our PLSR analysis. This suggests that SWAP70 and ARHGEF7 are regulating YAP/TAZ via shape in LM2. SWAP70 has been shown to regulate the cytoskeleton by stabilising actin (Chacón-Martínez et al., 2013; Gomez-Cambronero, 2012; Hilpela et al., 2003) by activation of RAC1 and RHOA (Dwyer et al., 2015; Ocaña-Morgner et al., 2011), therefore we propose that lack of SWAP70 resulting in unstable actin, could resulting in the low YAP/TAZ ratio observed following SWAP70 depletion in LM2, due to decreased tension. On the other hand, ARHGEF7 has been shown to regulate YAP/TAZ via GEF-dependent and independent manners (Sero and Bakal., 2017; Heidary-Arash et al., 2014), where it behaves as a YAP activator coupling YAP to cell-matrix adhesion via RAC1/CDC42 signalling in MCF10A cells (Sero and Bakal., 2017), and inhibits YAP/TAZ translocation to the nucleus in MDA-MB-231 cells by mediated LATS1 phosphorylation in a GEF-independent manner (Heidary-Arash et al., 2014). This is interesting because contrary to LM2, *ARHGEF7* was a hit for low YAP/TAZ ratio in SUM159 and it appears to be regulating YAP/TAZ ratio independently of shape (Figure 4.9Bii), suggesting a switch from activator to inhibitor is occurring in these cell lines too. Further to this, ARHGEF7 was a shape hit for spindly in MDA-MB-231, but was not a hit for YAP/TAZ. Therefore, we propose that

ARHGEF7 is a YAP/TAZ activator in SUM159 independently of shape, via a mechanism that gets rewired in LM2, where ARHGEF7 downregulates YAP/TAZ ratio via spindly shape. In addition, we propose that ARHGEF7 is important for downregulating YAP/TAZ in LM2 and thus conferring LM2s with more metastatic abilities and warrants further studies to identify whether it could be a potential target for preventing metastasis in TNBC.

DOCK5 on the other hand was a hit for low YAP/TAZ ratio in both LM2 and MDA-MB-231, and a hit for fan shape in LM2, and spindly shape in MDA-MB-231 (Figure 4.8B). Because fan was a weak negative predictor of shape in LM2, this suggests that DOCK5 is less likely to be regulating YAP/TAZ via shape. In MDA-MB-231, spindly shape was not a predictor of YAP/TAZ, and thus suggests that DOCK5 is not regulating YAP/TAZ via shape in MDA-MB-231. Further, *DOCK5* was not a hit for YAP/TAZ ratio in either SUM159 or hs578t. These data suggest that DOCK5 regulates shape differently in LM2 and MDA-MB-231, while regulating YAP/TAZ in the same way. Perhaps DOCK5 activates YAP/TAZ independently of shape in MDA-MB-231, a pathway that is rewired in LM2, where DOCK5 could be activating YAP/TAZ both through a direct signalling pathway and via some aspect of shape regulation. In fact, DOCK5 has been shown to promote RAC1 mediated lamellipodial protrusion and focal adhesion turnover, downstream of GIT2, promoting invasion in MDA-MB-231 cells (Frank et al., 2017); and to be a key regulator of microtubule dynamics downstream of AKT in mast cells and osteoclasts via phosphorylation of GSK3ß (Guimbal et al., 2019; Ogawa et al., 2014). Further, from our clustering in Chapter 3, we found that DOCK5's QMS clusters close with other genes, between two clusters composed

of front rear polarity regulators, and adhesion turnover regulators. Therefore, we hypothesise that DOCK5 is unique in connecting focal adhesions, YAP/TAZ and polarity. For this reason, we propose that DOCK5 could be important for TNBC metastasis and its regulation of YAP/TAZ warrants further study, a mechanism we further explore in Chapter 5 of this thesis.

In the more spread-like cell lines SUM159 and hs578t, we found that YAP/TAZ ratios were predominantly lower in basal conditions and also decreased YAP/TAZ ratio at much lower densities compared to LM2 and MDA-MB-231. As YAP/TAZ translocate to the cytoplasm when they are in confined spaces, such as in cases where cells are at a high density due to contact inhibition of proliferation (CIP) (Aragona et al., 2013; Zhao et al., 2007), this suggests that YAP/TAZ are regulated by cell-cell contacts in SUM159 and hs578t cells, but by other factors such as secretion of paracrine factors (and not cell-cell contacts) in LM2 cells. Potentially, the mild decrease in YAP/TAZ ratio levels observed in MCF10A and T47D cells at medium densities could be a combination of E-cadherin-Hippo dependent YAP/TAZ inhibition as well as differences in shear stress in the epithelial sheet (Aragona et al., 2013), while that observed at very high densities is more mechanical and Hippo-independent, making them only sensitive to CIP at very high densities. In addition, our PLSR analysis revealed that spindly shape was the strongest predictor of YAP/TAZ ratio in SUM159 (Figure 4.5H), predicting low ratios, and fan was the strongest predictor of YAP/TAZ ratio in hs578t, predicting low ratios too (Figure 4.5H). Only one RhoGEF that was a hit for YAP/TAZ ratio in SUM159 matched the predicted shape, and none did so for

hs578t, suggesting that these two cell lines do not depend on YAP/TAZ and that YAP/TAZ regulation is predominantly not coupled to shape.

Overall, our data suggest that in more spread-like cells such as SUM159 and hs578t, YAP/TAZ activity is low, and shape is not coupled to YAP/TAZ (Figure 4.11B). While in more spindly-like cells such as MDA-MB-231 and LM2, YAP/TAZ are more nuclear and active. In fact, previous studies have shown that MDA-MB-231 display TEAD transcriptional activity, compared to SUM159 (Lamar et al., 2012), which is indicative of nuclear and active YAP/TAZ. Further, MDA-MB-231 has more sustained nuclear and active YAP/TAZ compared to LM2 and is uncoupled to shape. Whereas in LM2, which are more spindly than MDA-MB-231 and more metastatic, YAP/TAZ is coupled to shape and LM2 cells have the ability to switch YAP/TAZ off depending on their environment (Figure 4.10B). Such that, taken together with our phenotypic screens discussed in Chapter 3, LM2 cells are dynamically changing shape, mediated by a specific set of RhoGEF/GAPs, and display predominantly high levels of nuclear and active YAP/TAZ. The latter of which they can downregulate in response to their environment, making them more plastic, and consequently more metastatic than their parental counterpart, MDA-MB-231.

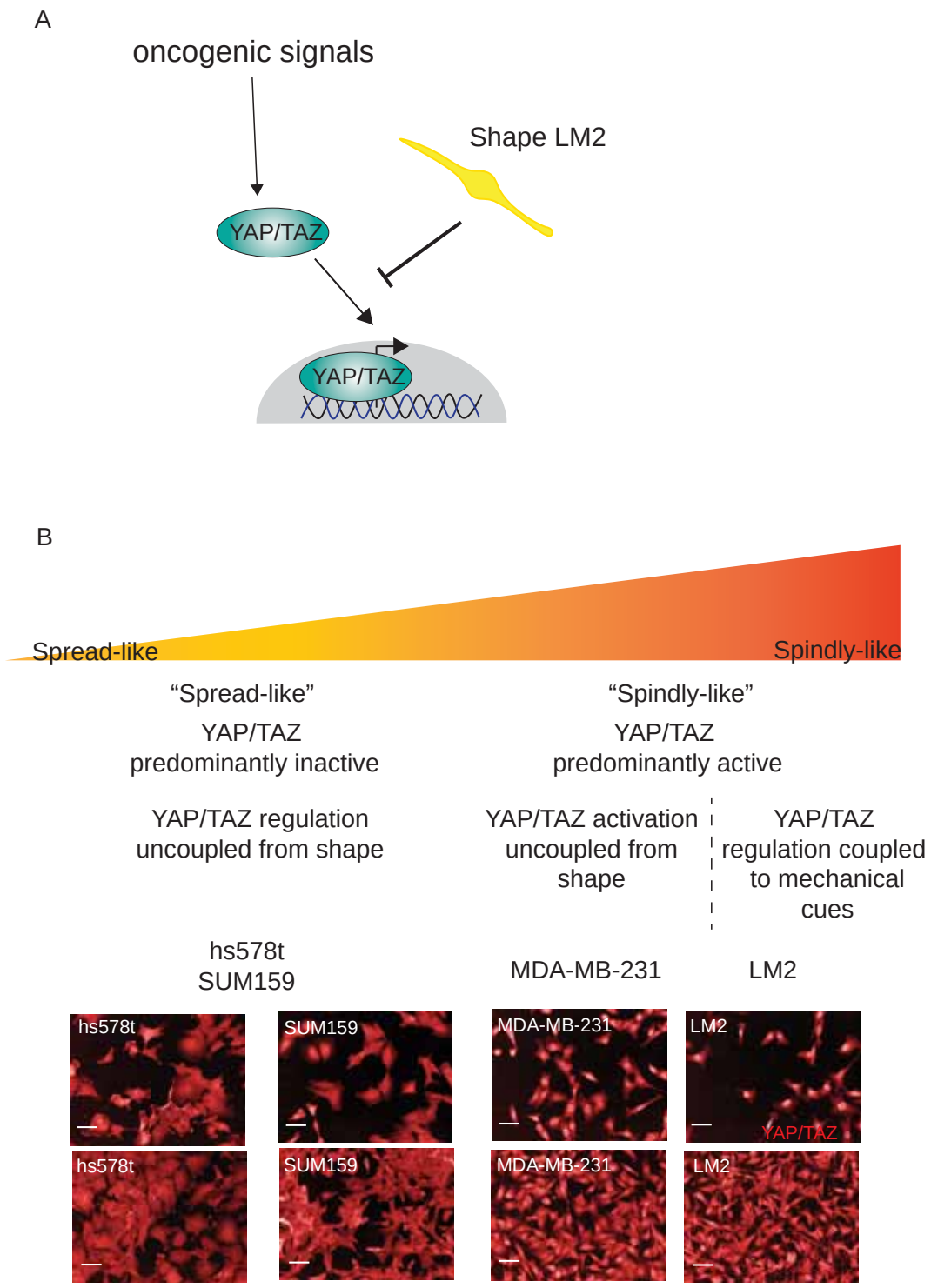

Figure 4.11 Working model of YAP/TAZ regulation in different TNBC cell lines
(A) Schematic representation of our hypothesis that mutant oncogenic signalling is responsible for keeping YAP/TAZ nuclear and active in MDA-MB-231 and LM2 cell lines, which LM2 cells are able to counter and can downregulate by regulating cell shape, such as switching to a spindly shape via RhoGEF signalling. (B) Summary of phenotypes observed for hs578, SUM159, MDA-MB-231, and LM2, as well as YAP/TAZ ratio. Left: spread-like, low YAP/TAZ ratio, YAP/TAZ ratio uncoupled from shape. Right: spindly-like, high YAP/TAZ ratio. Re-coupling of shape to YAP/TAZ ratio from MDA-MB-231 to LM2 cell lines. Representative images at low (3.3 x 10^4 cells/ml) and high (1.3 x 10^5 cells/ml) densities, stained for YAP/TAZ. Scale bar is 50µm.

Chapter 5

DOCK5 coordinates leading edge with microtubule dynamics and adhesions, driving invasion through YAP/TAZ

Chapter 5 DOCK5 coordinates leading edge with microtubule dynamics and adhesions, driving invasion through YAP/TAZ

5.1 Introduction

Cells need to dynamically remodel their cytoskeleton to metastasise (Fife et al., 2014; Kass et al., 2007; Wirtz et al., 2011). A classic example of cytoskeletal rearrangement displayed during the metastatic process are changes made during the epithelial to mesenchymal transition (EMT), where cells dismantle cell-cell adhesions, increase the number of cell-ECM adhesions in the form of focal adhesions, undergo changes in microtubule, actin, and intermediate filament organisation to become more elongated and mesenchymal-like (Dongre and Weinberg, 2019; Polyak and Weinberg, 2009). This cytoskeletal change allows cells to be more motile, and detach from the primary tumour to invade the surrounding tissue (Thiery and Sleeman, 2006).

Cell shape is regulated by Rho GTPases, which cycle between an inactive GDP-bound state, and an active GTP-bound state, the latter of which allows them to activate and recruit downstream effectors (Hall, 2009). RhoGEFs activate Rho GTPases by catalysing the exchange of GDP for GTP, while RhoGAPs induce GTP hydrolysis (Bos et al., 2007; Jaffe and Hall, 2005). Significant upregulation of RhoGEF mRNA and/or protein levels have been observed in breast cancer tissue (Adamowicz et al., 2006; Cook et al., 2014; Gatza et al., 2014; Lane et al., 2008; Laurin et al., 2013; Sosa et al., 2010). Further, RhoGEF such as BCR, LARG (ARHGEF12), and TIAM1 have also been found to be mutated in some cancers (Cook et al., 2014; Rossman et al., 2005).

RhoGEF-Rho GTPase signalling can lead to cell shape changes by regulating the cytoskeleton and by regulating transcription (Bos et al., 2007; Jaffe and Hall, 2002; Vega and Ridley, 2008). For example Rho GTPases have been shown to regulate transcription of NF-kB (Gastonguay et al., 2012; Sero et al., 2015) and serum response factor (SRF) (Jaffe and Hall, 2002; Medjkane et al., 2009; Miralles et al., 2003). The transcriptional coactivators YAP and TAZ, are also regulated by RhoGEF-Rho GTPase signaling both directly, and indirectly (Cordenonsi et al., 2011; Dupont et al., 2011; Pascual-Vargas et al., 2017; Piccolo et al., 2014; Sero and Bakal, 2017; Totaro et al., 2018). For example, RhoGEF-Rho GTPase signalling can affect cytoskeletal organisation, cell-cell and cell-ECM adhesions, and thus cell shape – all of which, in turn, affect YAP/TAZ activations. Conversely, RhoGEF-Rho GTPase signalling can also act downstream of particular signals to regulate YAP/TAZ localisation in the absence of cell shape changes (Feng et al., 2014, 2019; Sero and Bakal, 2017).

We previously identified DOCK5 as an activator of YAP/TAZ in TNBC (Chapter 4), a RhoGEF which belongs to the DOCK5 family of RhoGEFs (Gadea and Blangy, 2014). Its best described role is in osteoclasts, where DOCK5-deficient mice display increased bone mass as a result of DOCK5's requirement for the establishment of the sealing zone and osteoclast resorbing activity (Vives et al., 2011). DOCK5 also promotes myoblast fusion (Laurin et al., 2008) and neutrophil chemotaxis (Watanabe et al., 2014). DOCK5 has been shown to localise to focal adhesions (Müller et al., 2018), where in a mechanism restricted by GIT2, promotes RAC1 mediated lamellipodial protrusion and focal adhesion turnover, promoting invasion in MDA-MB-231 cells (Frank et al., 2017). Mechanistically,

DOCK5's effect on cell fates has been shown to be due, in part, due to DOCK5's ability to regulate microtubule dynamics (Guimbal et al., 2019) via NCK2 and AKT-dependent phosphorylation of GSK3β (Ogawa et al., 2014a).

Here, we show that *DOCK5* depletion affects cell shape, results in decreased invasion in 3D matrices, and decreased migration in 2D. Further we describe that *DOCK5* depletion results in unstable adhesions, decreased GSK3β stability and AKT signalling resulting in unstable microtubules and uncoupled nucleus from the cytoskeleton, leading to decreased YAP/TAZ activity. We propose that DOCK5-mediated activation of YAP/TAZ and DOCK5-mediated shape shapes, are drivers of TNBC metastasis.

5.2 Results

5.2.1 DOCK5 regulates TNBC cell shape and YAP/TAZ localisation

To understand the role of DOCK5 in regulating cell shape determination, we performed hierarchical clustering on the quantitative morphological signatures (QMS) for shape hits in the LM2 OTP screen, and defined "phenoclusters" as genes grouped at the highest node of clustering with a Pearson Correlation Coefficient (PCC) of > 0.73 (Figure 5.1Ai). This resulted in 10 multigene clusters and 1 singleton formed by mock transfected LM2 cells. We found that cluster 7 was characterised by genes whose depletion resulted in a spindly phenotype suggestive of polarity defects (Figure 5.1Ai), while those in cluster 9 displayed a flat spread phenotype indicative of contractility and adhesion turnover defects. In fact, we found that *DOCK1*, a gene found in cluster 7 has already been shown to promote the establishment of polarity and protrusion formation (Côté and Vuori,

2007). Further, the Rho GTPase *CDC42* whose depletion results in a spindly phenotype is also found in cluster 7, and it is central to establishing polarity in eukaryotic cells (Cau, 2005; Etienne-Manneville and Hall, 2003a; Hall, 1994; Johnson and Pringle, 1990; Stowers et al., 1995). In addition, *DEPDC1B*, a member of cluster 10 has been shown to control RHOA-ROCK-dependent adhesion dynamics during mitosis (Marchesi et al., 2014). *DOCK5* belonged to cluster 9, between the clusters composed of polarity regulators, and contractility and adhesion turnover regulators. Further, it clustered with *PLEKHG3*'s QMS. PLEKHG3 has been shown to selectively bind to new polymerised actin, which exerts a positive regulator effect on PLEKHG3 activity sustaining the leading edge and stable front rear polarity (Nguyen et al., 2016). Overall, we hypothesise that DOCK5 may play a role in regulating adhesion turnover and front rear polarity.

DOCK5 was also a hit for low YAP/TAZ ratio (Figure 5.1B), suggesting it is a YAP/TAZ activator. 4 out of 4 replicates of *DOCK5* siRNA were considered hits in our initial screen. We performed the same screens using another siRNA library which uses pooled small interfering RNA (siRNA) (Dharmacon siGENOME; siG), and *DOCK5* was also a hit for 4 out of 4 replicates (Appendix 11A). si*DOCK5* consistently reduced YAP/TAZ ratio in independent immunofluorescence experiments, without changing YAP/TAZ levels (Figure 5.1C), suggesting that DOCK5 is regulating YAP/TAZ localisation without altering total levels.

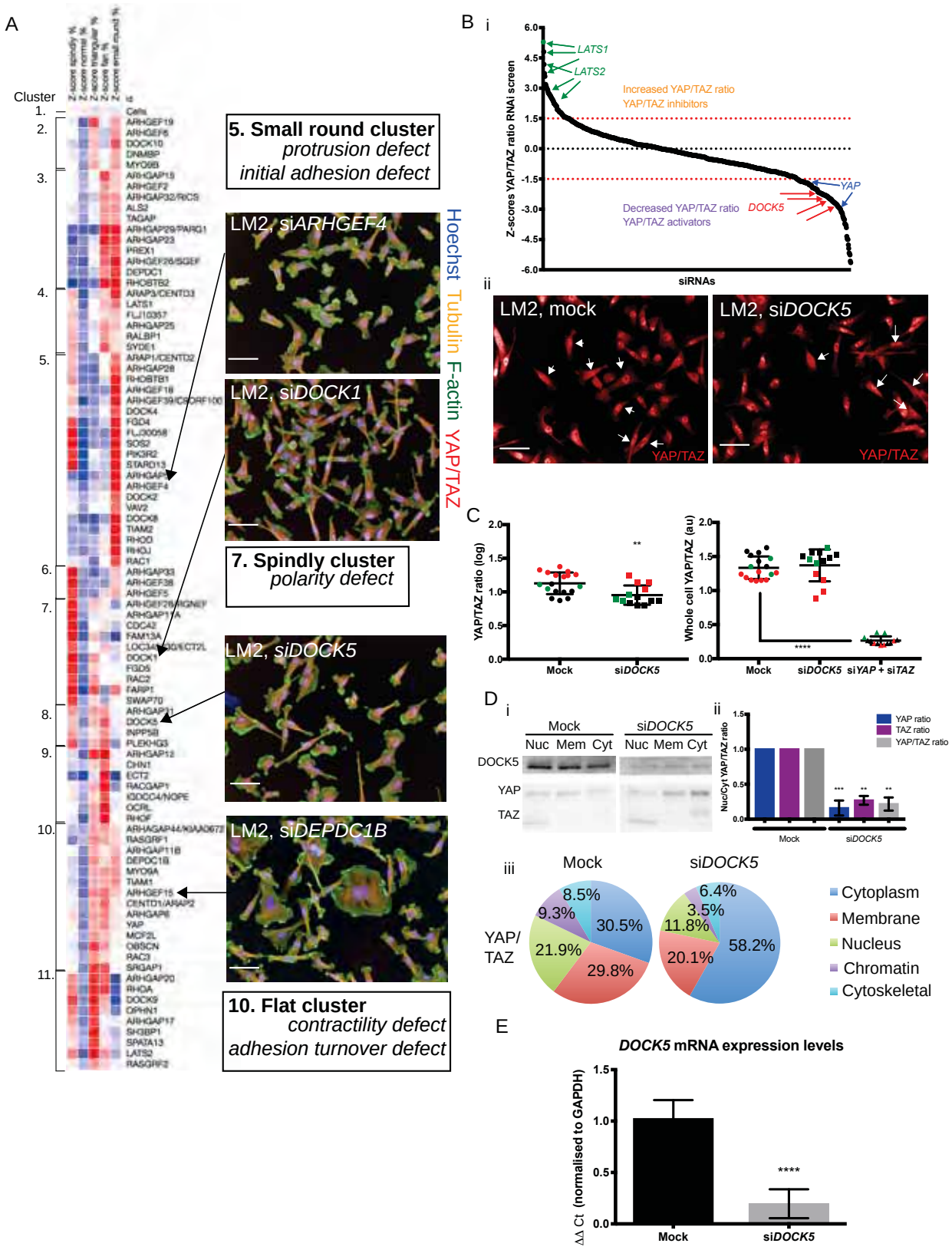

Figure 5.1: DOCK5 regulates shape and YAP/TAZ localisation.
(A) Clustering of high-dimensional quantitative signatures based on the effect of RhoGEF/GAPs and Rho GTPase siRNAs on the TNBC cell line LM2. Columns are Z-score values of the percentage of cells classified into that shape when said siRNA is depleted. -*Legend continued overleaf* -

Continuation of Figure 5.1 legend - Red and blue indicate high and low values respectively. Clustering performed using Pearson correlation. We identified 11 clusters and defined them as genes grouped at the highest node of clustering with a value of uncentered Pearson correlation coefficient above 0.73. - Numbering indicates clusters and images show siRNAs which enrich for a particular shape in example clusters. (B) (i) Z-scores per well for YAP/TAZ ratio for OTP siRNA screen in LM2. Red dotted lines indicate values from which above and below were considered hits Above 1.5 are siRNAs which are hits for high YAP/TAZ ratio and thus can be considered inhibitors of YAP/TAZ. Below -1.5 are siRNAs which are hits for low YAP/TAZ ratio and thus can be considered YAP/TAZ activators. *LATS1/2* and *YAP* siRNAs included as controls for high and low YAP/TAZ ratios are shown. Four individual replicates for si*DOCK5* are shown. (ii) Representative images showing YAP/TAZ staining for mock transfected LM2 and cells transfected with si*DOCK5*. Arrows point to cells with high YAP/TAZ ratio (mock) and low YAP/TAZ ratio (si*DOCK5*). (C) Graphs showing quantification of YAP/TAZ ratio, and whole cell YAP/TAZ levels in mock versus si*DOCK5* from 3 independent biological repeats separate from screen data. Dots represent individual wells. si*YAP* + si*TAZ* show YAP/TAZ antibody is working appropriately. Statistical significance obtained by performing student t-test on row means (** $P < 0.01$), left and ANOVA right (****$P < 0.0001$). (D) Validation of si*DOCK5* resulting in a decrease in YAP/TAZ ratio via subcellular fractionation. (i) Representative western blot of subcellular fractions for mock and si*DOCK5*. Nuc: nuclear fraction. Mem: membrane fraction. Cyt: cytoplasm fraction. Blotted for DOCK5, YAP and TAZ. Same amounts of protein loaded (6.5ng). (ii) Quantification of ratio of YAP/TAZ in the nucleus to the cytoplasm fraction from western blots of subcellular fractionations. N = 2. (iii) Representative distribution of YAP/TAZ in all fractions with and without *DOCK5*. (E) qRTPCR showing *DOCK5* mRNA levels in mock versus si*DOCK5* transfected cells. N = 3 biological repeats and at least 3 technical replicates each. Statistical significance obtained by performing student t-test on row means (**** $P < 0.0001$).

To validate our immunofluorescence imaging-based observations that DOCK5 depletion affects YAP/TAZ translocation, we performed subcellular fractionation on mock transfected and si*DOCK5* transfected LM2 cells. si*DOCK5* cytoplasmic fraction had significantly more YAP and TAZ than mock transfected cells, and the ratio of nuclear to cytoplasmic YAP/TAZ was significantly lower (Figure 1Di, ii), supporting our immunofluorescence results. The total amount of DOCK5 protein present in all fractions for mock and si*DOCK5* transfected cells showed that

DOCK5 protein was significantly reduced with si*DOCK5* (Appendix 11B), indicating that *DOCK5* siRNA is indeed depleting *DOCK5* as expected.

To validate that decreases in YAP/TAZ ratio and cell shape were due to *DOCK5* depletion, and not due to an off-target effect, we quantified mRNA expression levels with si*DOCK5* via quantitative RT-PCR and saw that there was a significant reduction in *DOCK5* mRNA expression levels (Figure 5.1E). Even though *DOCK5* was a hit across 8 out of 8 replicates from 2 different siRNA libraries, and the sequences of the pools are different for each library, we also tested the effect of each individual sequence. Each individual sequence knocked down *DOCK5* mRNA and protein levels (Appendix 11 F; G, i, ii). Further, all except for OTP6 significantly reduced YAP/TAZ ratio and none but siG3 reduced total YAP/TAZ levels (Appendix 11H). These data suggest that the decrease in YAP/TAZ ratio observed as a result of *DOCK5* siRNA is due to the depletion of *DOCK5*.

5.2.2 *DOCK5* depletion reduces single cell invasion in 3D collagen assays

To determine if DOCK5 contributes to the ability of LM2 cells to invade 3D tissues, we quantified the extent to which *DOCK5* depleted cells invade rat tail collagen I gels. We chose rat tail collagen I as our matrix because it is the most abundant type of collagen in mammalian tissues (Brown et al., 2003; Magzoub et al., 2008; Oldberg et al., 2007; Sabeh et al., 2004, 2009), and has been shown to form networks with physiological mechanical properties in vitro (Stamov and Pompe, 2012; Wolf et al., 2003), facilitating cell attachment, proliferation, and differentiation primarily through integrin mediated interactions (Sapudom et al., 2019) . We mixed the cells with collagen I solution after 48 hours of transfection

and spun the plates down to ensure cells were at the bottom of the plate, allowing us to quantify invasion into the gel (Figure 5.2A). Cells typically invaded from the bottom of the plate into depths of 30μM in the collagen gel within 24 hours. We quantified this single-cell invasion by calculating the invasion index, defined as the number of cells at various planes within the gel divided by the total number of cells in said planes, plus the bottom plane (Figure 5.2B). In a 2.0 mg/ml rat-tail collagen gel, *DOCK5* depletion significantly reduced invasion (Figure 5.2C). Images in Figure 5.2D shows representative wells for each condition at a bottom plane and middle plane (0μM and 30μM respectively). It is important to note, that only cells whose nucleus and cytoplasm were in a particular plane, and not spanning any other planes, were quantified as being present in said plane (Appendix 16). Further, depleting *TAZ* but not *YAP* significantly reduced invasion, by the same amount as depleting *DOCK5*. This could suggest that it is TAZ that drives LM2 invasion rather than YAP. Taken together these data suggest that DOCK5 promotes TAZ activation to promote shape changes that are required for 3D invasion.

Most solid tumours have stiffer extracellular matrices (Paszek et al, 2005) compared to healthy tissue. Because collagen pore size has been shown to be inversely proportional to collagen concentration (Sapudom et al, 2015), we used collagen gels of different concentrations as a way of varying pore size. LM2 cells invaded regardless of pore size in the rat tail collagen density range of 1.8 to 4.8 mg/ml, and depleting *DOCK5* consistently reduced invasion across these concentrations (Figure 5.2E). Overall these data suggest that DOCK5 is required for LM2 single cell invasion in rat tail collagen matrices independently of pore

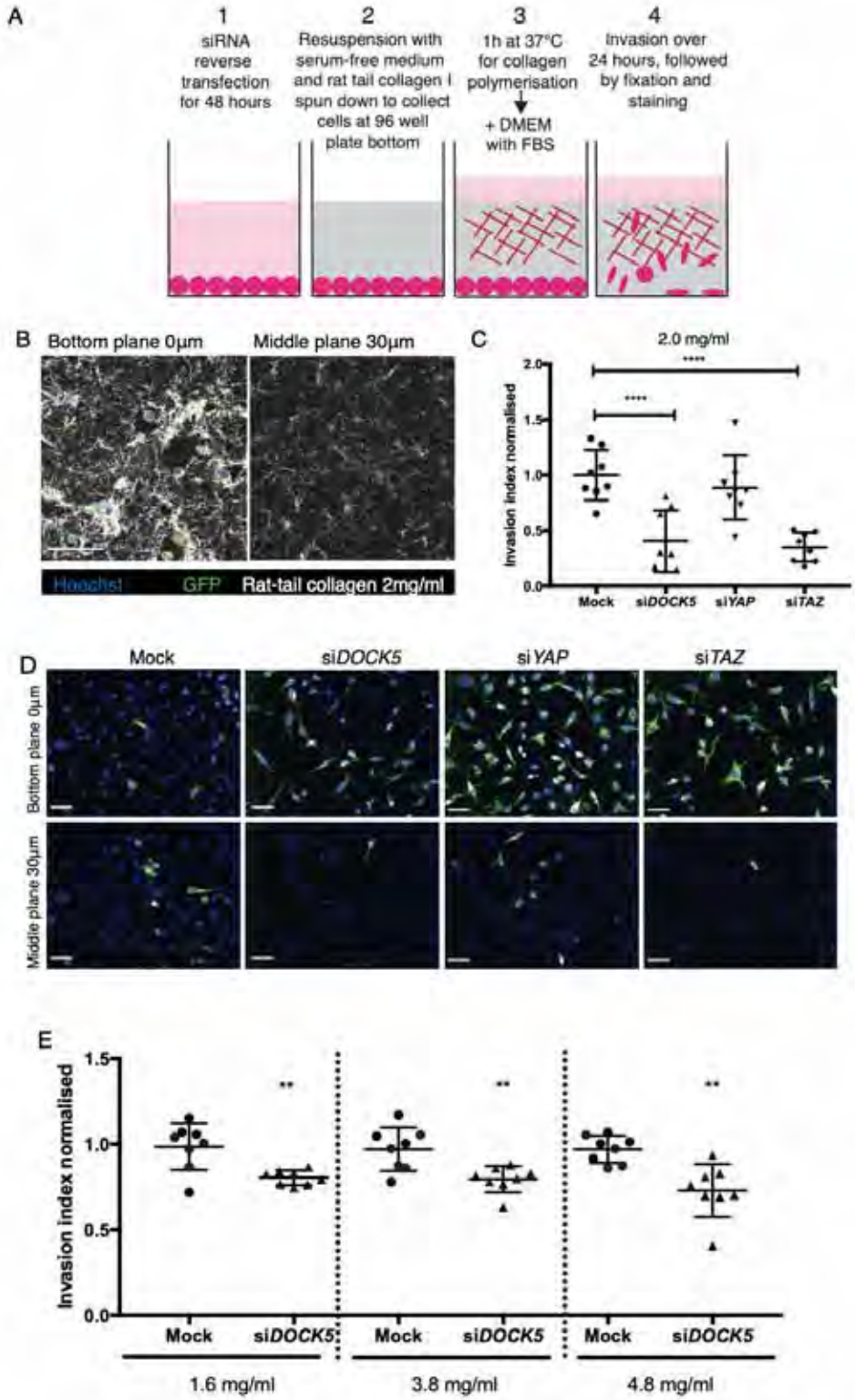

Figure 5.2: *DOCK5* depletion reduces single cell invasion in 3D collagen assays (A) Schematic of 3D invasion assay. (B) Representative 2-photon images of LM2 cells (GFP) stained for DNA (blue) mixed with rat-tail collagen I at 2 mg/ml (white) at the bottom (0 µm plane) and the middle (30 µm plane) of the plate. (C) Invasion index for knockdowns in rat-tail collagen I (2 mg/ml). (D) Representative confocal spinning disk images (1 field per well shown) for knockdowns shown in (C) at 0 µm and 30 µm. (E) Invasion index of mock versus si*DOCK5* transfected cells at 1.6mg/ml, 3.8mg/ml, and 4.8mg/ml.Mean ± SD are shown (n > 3 wells per condition 1000 cells/well. ANOVA, ** P < 0.01, **** P < 0.0001). Scale bars, 100 µm. Images in (B) taken by Aaron Farrugia on 2 photon microscope.

size, and we hypothesise that this decrease in invasion could be due to a lack of front rear polarity and consequent decreased YAP/TAZ ratio.

5.2.3 *DOCK5* depletion reduces invasion in Matrigel spheroid assays

In order to confirm that DOCK5 is required for invasion, we generated spheroids and quantified invasion into 100% Matrigel. We chose this assay as Matrigel is made up of more extracellular matrix components than just collagen type I recapitulating the basement membrane and spheroids have also been shown to recapitulate the hypoxic environment inside tumours (Klimkiewicz et al., 2017; Vinci et al., 2015), resembling the tumour microenvironment more closely than 3D collagen gels. Further, studies have shown that collagen downregulates E-cadherin expression while inducing significant upregulation of mesenchymal markers vimentin, fibronectin and snail compared to Matrigel (Carey et al., 2017). Due to their mesenchymal nature, LM2 cells required 2% Matrigel in ultra-low attachment plates to form spheroids. We imaged them immediately after adding 2% Matrigel (Figure 5.3A), and then added 100% Matrigel for the cells to invade into and counted that as day 0. Mock transfected LM2 cells invaded into the gel progressively after adding 100% Matrigel (Figure 5.3B) forming radial branches, while cells lacking *DOCK5* simply proliferated (Figure 5.3B). Overall this suggests that LM2 cells require DOCK5 to invade into Matrigel, and that without it, cells simply proliferate, supporting our hypothesis that DOCK5 plays a role in front rear polarity and is required for invasion.

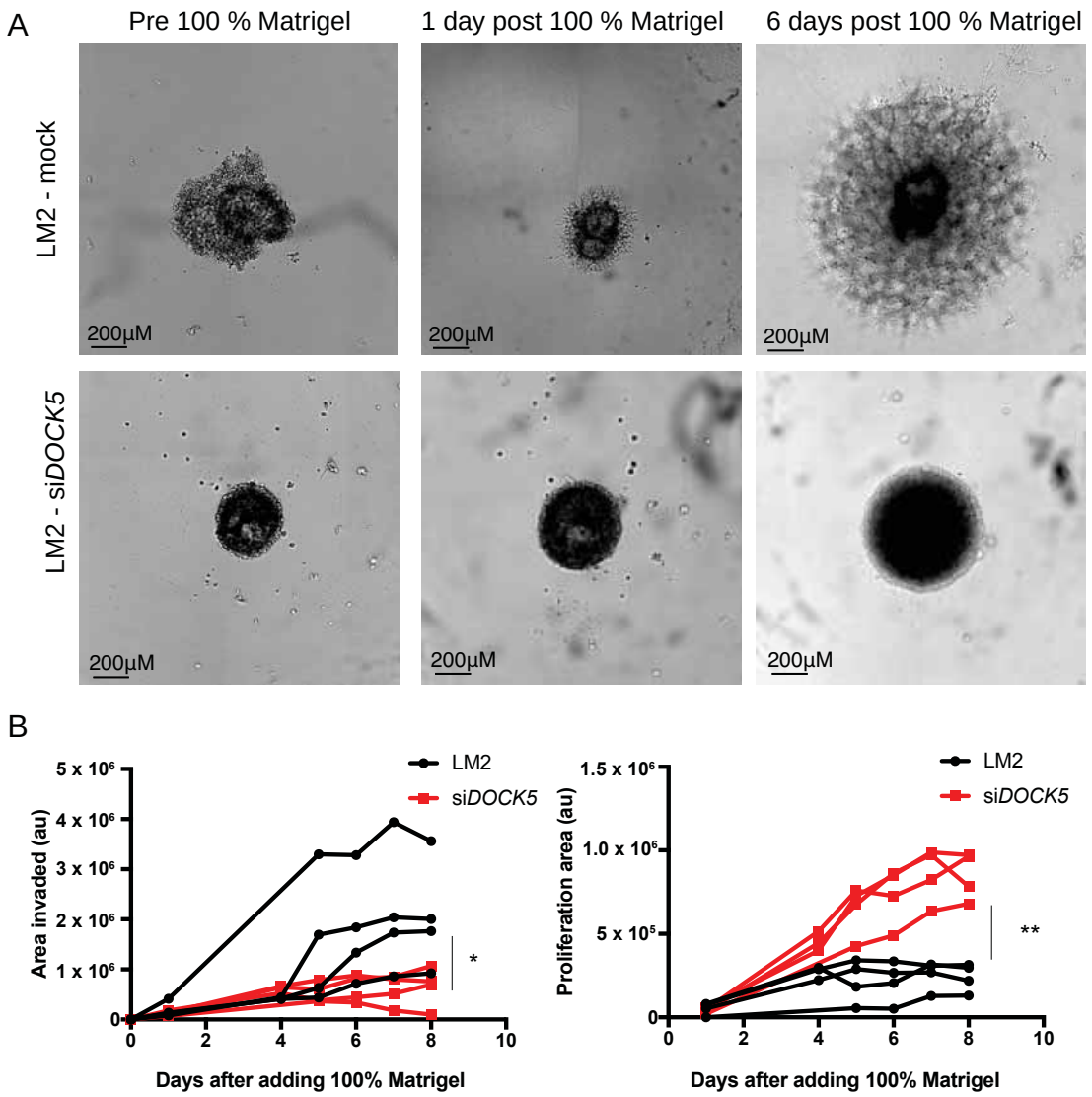

Figure 5.3 *DOCK5* depletion reduces invasion in Matrigel 3D spheroid assays (A) Representative images of mock transfected cells and si*DOCK5* transfected cell spheroids 48 hours post transfection and pre 100% Matrigel (left), and one (middle) and six (right) days post 100% Matrigel addition. Scale bar is 200µm. (B) Graphs show quantification of area of Matrigel invaded (left) and proliferation area (right) in arbitrary units over 8 days post adding 100% Matrigel to the spheroids. Proliferation area refers to how much the spheroid increased in size without invading into the matrix. Mock transfected cells in black, si*DOCK5* transfected cells in red. Each line represents one well. n is at least 3 wells. Statistical significance obtained by performing student t-test on row means (* P = 0.0294, ** P < 0.01).

5.2.4 *DOCK5* depletion reduces wound closure migration rates and affects Golgi orientation

To test our hypothesis that DOCK5 contributes to the establishment of front-rear polarity in migrating cells, we performed wound heal scratch assays in 2D, where we knocked down *DOCK5*, *YAP*, *TAZ*, and *YAP* and *TAZ* in combination. Even though LM2 cells are not an epithelial cell line, they were able to close the wound without any stimulants (data not shown). Three timepoints are shown in Figure 5.4A for all conditions. Cells transfected with si*DOCK5*, si*TAZ* and si*YAP* + si*TAZ* migrated less distance than mock transfected cells in the same amount of time (Figure 5.4A). Depleting *DOCK5*, *TAZ,* and *YAP* + *TAZ* significantly reduced migration rates (Figure 5.4B), but depleting *YAP* did not. Thus, DOCK5 promotes migration in both 2D and 3D, likely through activation of TAZ.

Cell polarity during cell migration is characterised by cellular protrusions, Golgi, microtubule organising centre (MTOC), and microtubule cytoskeleton to be oriented in the direction of migration (Etienne-Manneville and Hall, 2001). Therefore to determine if DOCK5 contributes to the establishment of leading edge polarity, we quantified the orientation of the Golgi following wounding in cells at the edge of the wound (Etienne-Manneville, 2004; Zhang et al., 2008). We quantified the angle of the Golgi oriented to the wound such that a 90 degree angle is indicative of Golgi facing toward the wound and indicative of front-rear polarity (Figure 5.4E, insert), in cells that had their Golgi within 180 degrees of the wound. *DOCK5* depleted populations had a higher frequency of Golgis oriented parallel to the wound (180 degrees) and other angles that were not 90 degrees compared to mock (35.4% to 17.7% respectively) (Figure 5.4C, Di),

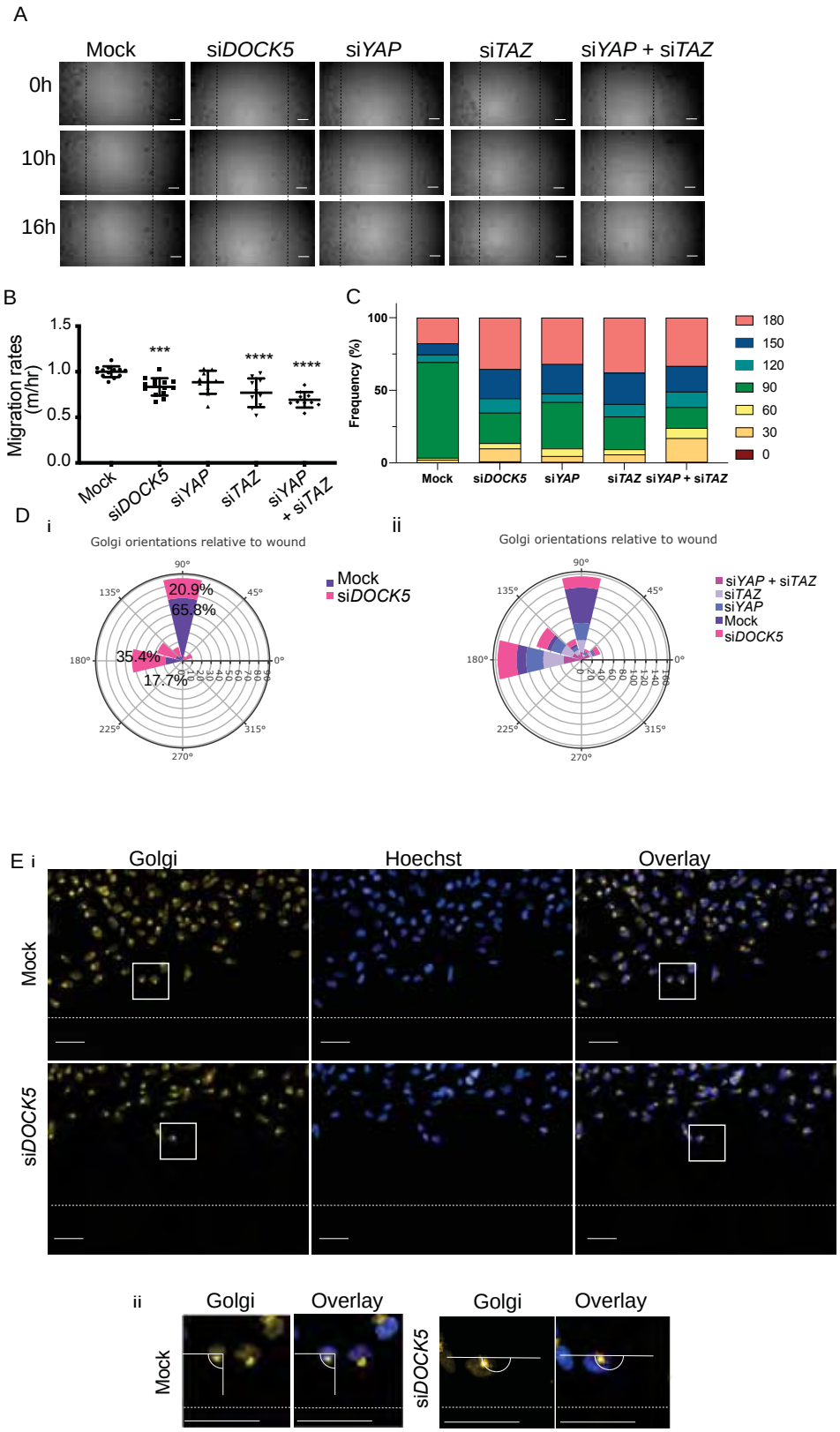

Figure 5.4 *DOCK5* depletion reduces wound closure migration rates and affects Golgi orientation (A) Brightfield images at 0, 10 and 16 hours post creating scratch wound for mock, si*DOCK5*, si*YAP*, si*TAZ*, and si*YAP* + si*TAZ* transfected cells. Dotted black line indicates the starting line from where cells migrated over time. Scale bar, 100 µm. (B) Graph shows migration rates (µm/hour). (n = 5 wells per condition, with at least 2 biological repeats). *Legend continued overleaf.*

Figure 5.4 Legend continued. Values were normalised to average of mock for each repeat. (C), (D) Percentage frequency of cells with Golgis orientated 0, 30, 60, 90, 120, 150, and 180 degrees relative to the wound depicted as a bar chart (C) and as a windrose plot (Di,ii). Percentages indicated on windrose plots. (E) Images depicting Golgi immunofluorescence stain and Hoechst, wound is shown with white dotted line. Angle measuring relative to wound is depicted in the inserts example of 90 degree angle and orientation towards the wound for mock (i) and 180 degree angle and orientation parallel to the wound for si*DOCK5*. Scale bar is 50 µm.

while mock transfected populations had a higher frequency of Golgis oriented directly facing the wound (65.8% to 20.9% respectively) (Figure 5.4C, Di). Cells lacking *YAP* and *TAZ* in combination had the slowest wound closure rates and had the least percentage of cells with Golgis oriented 90 degrees to the wound, and the highest oriented 30 degrees, suggesting these cells are unable to integrate cues from the microenvironment for directional motility. Taken together, these data support the idea that DOCK5 promotes the establishment of polarity in migrating cells.

5.2.5 *DOCK5* depletion alters focal adhesion dynamics

To determine if DOCK5 has a role in focal adhesion dynamics, we used Total Internal Reflection Fluorescence (TIRF) Microscopy to study focal adhesion dynamics in cells with and without *DOCK5* migrating on fibronectin (FN). For this purpose, we used LM2-CAAX GFP tagged cells which allows us to see the edge of the cells clearly, and transfected them with Talin mApple to follow adhesions over time (Figure 5.5A, white dotted line indicates edge of cell in first frame shown). While adhesions form at the edge of the cell in mock transfected cells (Figure 5.5Bi, adhesions coloured by FAAS software; Chapter 2 Materials and

Methods), those in si*DOCK5* transfected cells are not localised to the edge but rather are also found in the middle of the cell (Figure 5.5Bi). Further, in control cells adhesions start forming as focal contacts, maturing into adhesions and consequently turning over in a canonical manner (Figure 5.5A, Bii). In contrast, in cells lacking *DOCK5,* focal contacts begin to mature into adhesions which begin to turnover rapidly*,* as shown in Figure 5.5A, but instead of turning over the adhesion starts maturing again. Figure 5.5Bii shows a mock transfected cell which has moved from left to right and has clear front-rear polarity, and an si*DOCK5* transfected cell which has moved around in the same spot and does not have clear front-rear polarity.

Figure 5.5C shows the raw individual assembly and disassembly rates for adhesions (top), while the Cumming estimation plot below shows the mean difference in the assembly (orange, unpaired Hedges' g of 1.65) and disassembly (red, unpaired Hedges' g of 1.28) rates of si*DOCK5* transfected cells compared to mock as a bootstrap sampling distribution. Effect sizes based on Cohen's initial suggestions (Cohen, 1988) and expanded by Sawilowsky (Sawilowsky, 2009) indicate that values of 0.2 to 0.5 being small, 0.5 to 0.8 being medium, 0.8 to 1.2 being large, and 1.2 to 2.0 being very large effect sizes. Thus, *DOCK5* depletion causes a significant increase in focal adhesion assembly and disassembly rates in LM2s, suggesting focal adhesions are unstable in these cells.

Assembly and disassembly rates are calculated as the intensity of an adhesion over time and are based on the slope of a log-linear model. Because intensity

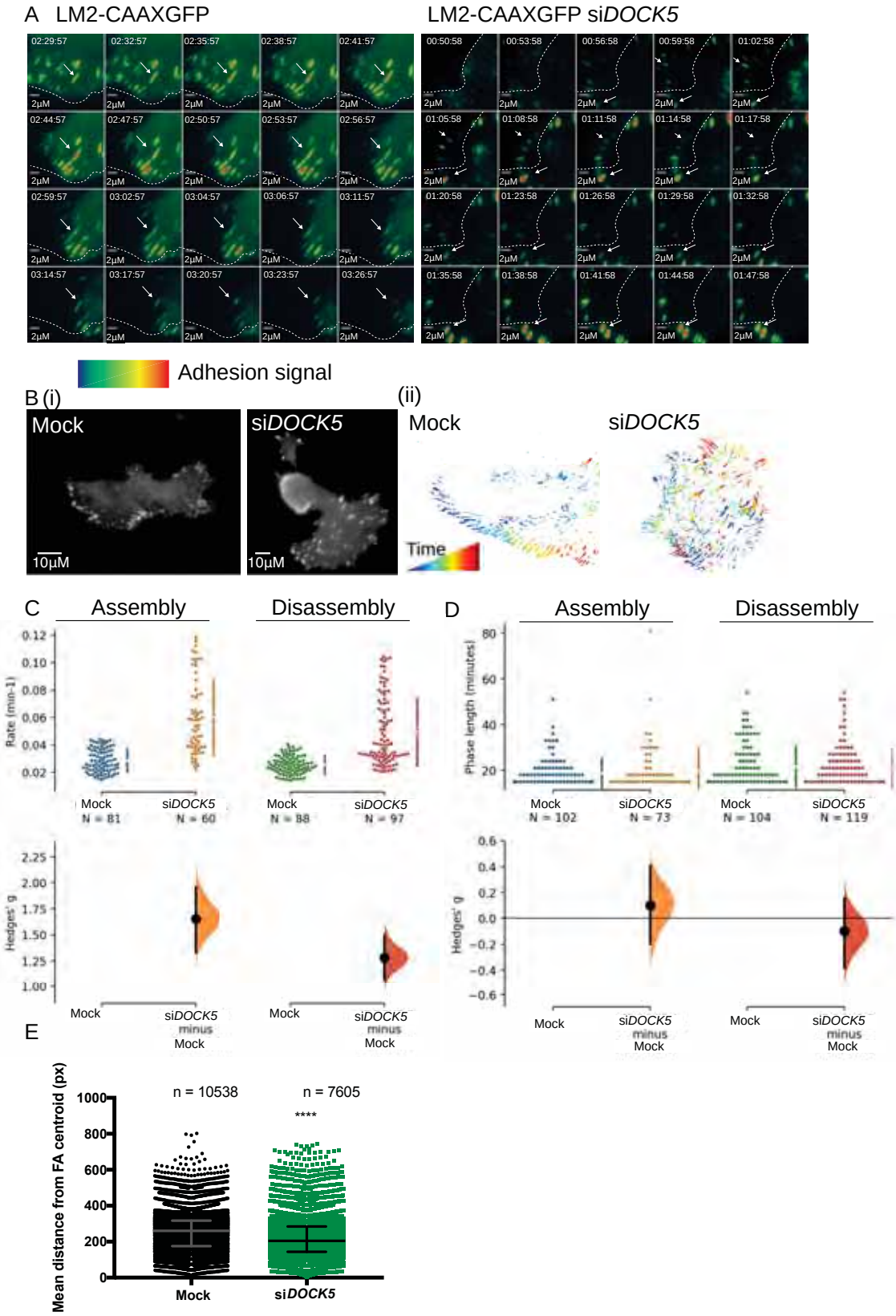

Figure 5.5 DOCK5 depletion alters focal adhesion dynamics
(A)Sequences of zoomed in sections of mock, and si*DOCK5* transfected LM2-CAAXGFP cells over time. Frames are every 3 minutes. Arrows indicate an example of an adhesion to follow. Dotted line represents the edge of the cell at the beginning of each sequence of frames shown. Adhesion signal represents Talin mApple intensity: red more intense, blue less intense. Scale bar is 2 μm. (B) (i) Representative images of how FAAS picks up adhesions on mock and si*DOCK5* transfected cells *Legend continued overleaf.*

Figure 5.5 legend continued - Scale bar is 10 µm. (ii) Focal adhesions tracked over time in same cells as in (i). Blue to red indicates adhesions which have been present for less, and longer amounts of time respectively. (C) Cumming estimation plots of Hedge's g for comparison between assembly and disassembly rates of adhesions in mock versus si*DOCK5* transfected cells. n shows adhesion number. Data is taken from 4 cells. Raw data is plotted in the top axes, while mean difference is plotted in lower axes as a bootstrap sampling distribution. Mean differences are shown as dots, 95% confidence intervals are shown by the ends of the vertical error bars. Generated using (Ho et al., 2019) website. Unpaired Hedge's g between mock and si*DOCK5* for assembly and disassembly rates are 1.65 (95% CI 1.33, 1.96), and 1.28 (95% CI 1.07, 1.50) respectively. Two-sided P values of Mann-Whitney tests are 3.64 x 10^{-15}, and 1.04 x 10^{-15} for assembly and disassembly rates respectively. (D) Cumming estimation plots of Hedge's g for comparison between assembly phase length and disassembly phase length of adhesions in mock versus si*DOCK5* transfected cells. n shows adhesion number. Data is taken from 4 cells. Raw data is plotted in the top axes, while mean difference is plotted in lower axes as a bootstrap sampling distribution. Mean differences are shown as dots, 95% confidence intervals are shown by the ends of the vertical error bars. Generated using (Ho et al., 2019) website. Unpaired Hedge's g between mock and si*DOCK5* for assembly phase length and disassembly phase length are 0.101 (95% CI -0.199, 0.405), and -0.00986 (95% CI -0.38, 0.155) respectively. Two-sided P values of Mann-Whitney tests are 0.602, and 0.437 for assembly and disassembly phase lengths respectively. (E) Mean distance from focal adhesion centroid in pixels. N number is individual adhesions from 4 cells, filtered by them being present for a minimum of 5 frames (phase length 5) and mean axial ratio less than 3. Unpaired Mann-Whitney test, $P < 0.001$.

scales with size, this means that a small adhesion that has assembled for a short amount of time could have the same assembly rate as a large adhesion which has been assembling for a longer amount of time (phase length). Assembly and disassembly phase length of adhesions in cells lacking *DOCK5* were very small compared to mock (Figure 5.5E, Hedge's g of 0.101 for assembly phase length, and -0.0986 for disassembly phase length). Therefore, most of the adhesions in cells lacking *DOCK5* are assembling and disassembling much faster than in mock transfected cells but spend similar amounts of time as those in mock assembling, and more adhesions spend less time disassembling. Taken together these data suggest that DOCK5 is required for correct localisation of adhesions

at the edge of the cell and for proper focal adhesion maturation, supporting our hypothesis that DOCK5 couples the polarisation of the leading edge with the formation of leading edge adhesions.

5.2.6 DOCK5 depletion alters protein levels of regulators of front rear polarity and of the cell cycle

In order to investigate how depletion of DOCK5 may affect YAP/TAZ localisation we carried out mass spectrometry analysis on mock and si*DOCK5* transfected TNBC cell lines. We used LM2 and its less metastatic parental cell line MDA-MB-231 plated at high and low densities, as well as hs578t, a cell line belonging to the same mesenchymal-stem like TNBC subtype as LM2 and MDA-MB-231 (Minn et al., 2005). Protein samples were processed 48 hours after transfection and labelled with TMT-10plex (Tandem Mass Tag) multiplex reagents before being submitted to LC-MS/MS (liquid chromatography mass spectrometry). Details of sample preparation, LC-MS/MS, mass spectra analysis and protein quantification are further described in the Material and Methods section of this thesis.

Protein abundance values obtained after analysis of mass spectra, were scaled within cell line, and due to there not being significant differences between cell lines we treated them as replicates. We calculated the log2 ratio of values in si*DOCK5* transfected lines versus mock transfected lines. DOCK5 protein was depleted by approximately 78% by siRNA (Figure 5.6A). Further, connective

tissue growth factor (CTGF), a target gene of the YAP/TAZ-TEAD transcription complex (Zanconato et al., 2015; Zhao et al., 2008) was significantly downregulated (log2 ratio: -0.77695) which supports that depleting *DOCK5* makes YAP/TAZ cytoplasmic and inactive.

We performed hierarchical clustering on the abundance values of those proteins which were significantly upregulated (40% increase) or downregulated (40% decrease) upon *DOCK5* depletion (log2 ratios above 0.5 and below -0.5 and permutation FDR <0.05 (false discovery rate) (t-test)). Among the RhoGEF/GAPs and Rho GTPases, ARHGEF10, ARHGAP12 and RHOBTB3 were significantly downregulated (log2 ratios: -0.64382, -0.50555, -0.59239 respectively), while RHOB and ARHGEF39 were significantly upregulated (log2 ratios: 1.631299, 0.749299) (Figure 5.6B). Further there were no changes in protein levels of DOCK5's closest homolog, DOCK1 (Gadea and Blangy, 2014b), suggesting that the *DOCK5* siRNA is not targeting *DOCK1*. YAP and TAZ (encoded by the WWTR1 gene) protein levels also remained unchanged, matching our immunofluorescence data and confirming that DOCK5 regulates YAP/TAZ localisation rather than YAP/TAZ levels.

Cell cycle regulators were significantly up and downregulated upon *DOCK5* depletion. For example, the oncogene MDM2 was downregulated (log2 ratio: -0.88837), while the cyclin dependent kinase (CDK) inhibitors p19 (log2 ratio: 0.56439), p21 (log2 ratio: 1.469904), p27 (log2 ratio: 0.698161), and p57 (log2 ratio: 0.686211) were upregulated. Further, CYCLIN E1 and CYCLIN D3 were also upregulated (log2 ratios: 0.745857, 0.721177 respectively), and so was

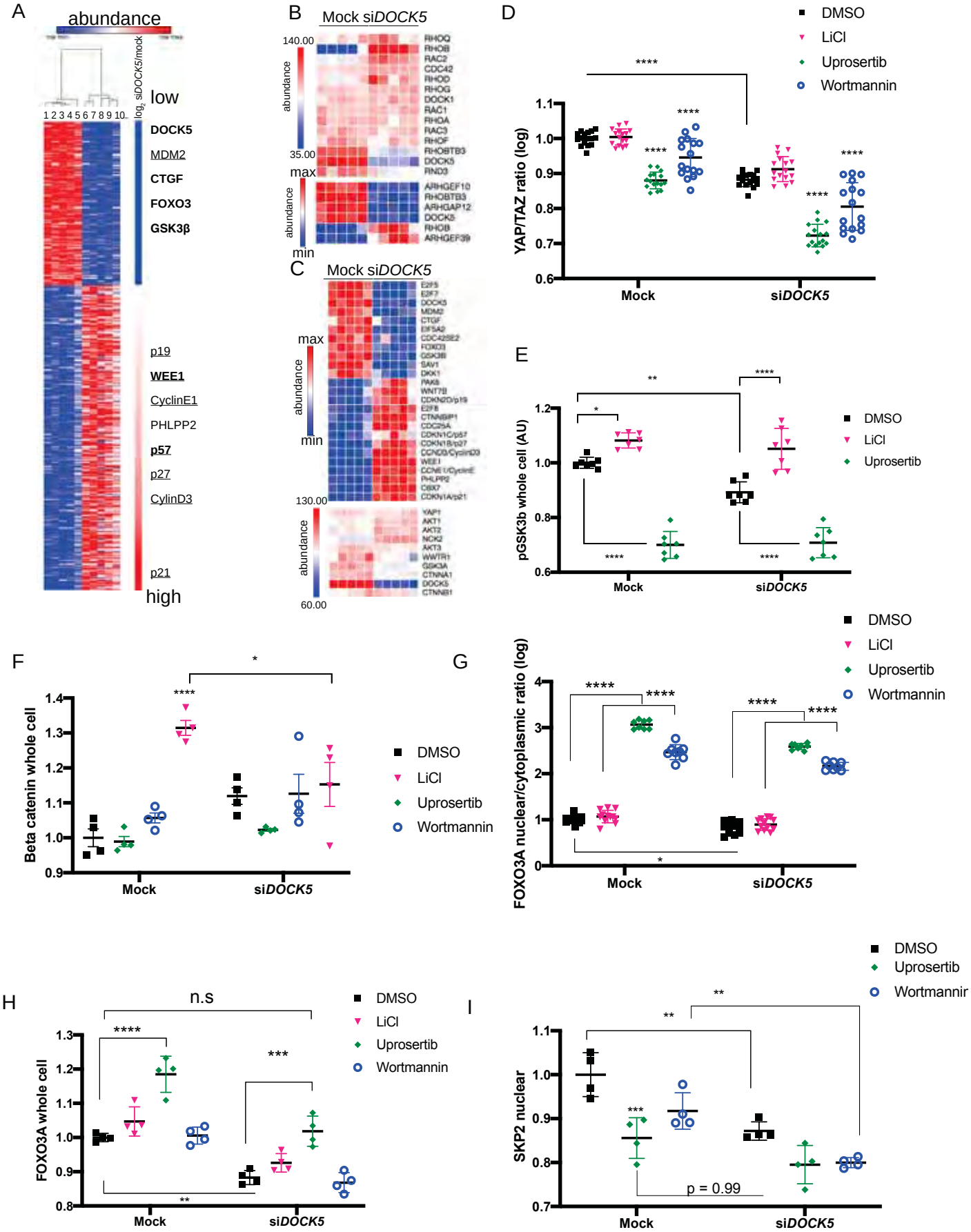

Figure 5.6: Proteomic data indicative of polarity and cell cycle defects with si*DOCK5*. (A-H) *Legend overleaf.*

Figure 5.6: Proteomic data indicative of polarity and cell cycle defects with si*DOCK5*. (A) Heat map of proteins significantly up or downregulated following *DOCK5* knockdown via siRNA in TNBC cell lines. Significance based on Log2 ratios for protein levels of si*DOCK5* v mock being above 0.5 and below -0.5 and permutation FDR <0.05 (t-test). 1 to 5 are mock transfected, while 7 to 10 are transfected with si*DOCK5*. 1 and 6: LM2 plated at low (screen) density; 2 and 8: LM2 plated at high density; 3 and 7: MDA-MB-231 plated at low (screen) density; 4 and 9: MDA-MB-231 plated at high density; 2 and 4: LM2 plated at high density; 5 and 10: hs578t. Red and blue indicate high and low protein abundance levels (row max to min respectively). Proteins up and downregulated based on log2 value. In bold: YAP/TAZ targets. Underlined: proteins involved in cell cycle. Not underlined: proteins involved in regulating polarity and AKT signaling pathways. (B) Top protein abundance levels of Rho GTPases. Bottom protein levels of Rho GTPases and RhoGEF/GAPs which were significantly upregulated or downregulated upon *DOCK5* knockdown. Row max (red) to min (blue). (C) Top: Heat map of protein levels of proteins regulating polarity and cell cycle that were significantly up and down regulated. Values normalized to cell line. Row max (red) to min (blue). Bottom: abundance levels of proteins of interest that were not significantly up or downregulated, with si*DOCK5* abundance levels for comparison. (D) (E) (F) (G) (H) Immunofluorescence quantifications of (D) YAP/TAZ ratio, (E) pGSK3β whole cell levels (F) beta catenin whole cell levels, (G) FOXO3A nuclear to cytoplasmic ratio (log) (H) FOXO3A whole cell levels (I) SKP2 nuclear levels of mock and si*DOCK5* transfected cells treated with DMSO (black), 5mM LiCl (pink), 2μM final Uprosertib (green), or 0.4μM final Wortmannin (blue). Mean per well ± SD are shown (n is at least 4 wells per condition, 1000 cells/well, 2 ways ANOVA, Tukey's multiple comparison's test * P < 0.05, ** P < 0.01, *** P < 0.001, **** P < 0.0001). (J) (K) Representative immunofluorescence images. (J) Stained for FOXO3A (yellow), YAP/TAZ (red), and merge including F-actin (green). (K) Stained for SKP2 (yellow), YAP/TAZ (red), and merge including F-actin (green). Scale bar is 50 μm. Experiments shown in D-K were performed by Mar Arias-García in the Bakal lab.

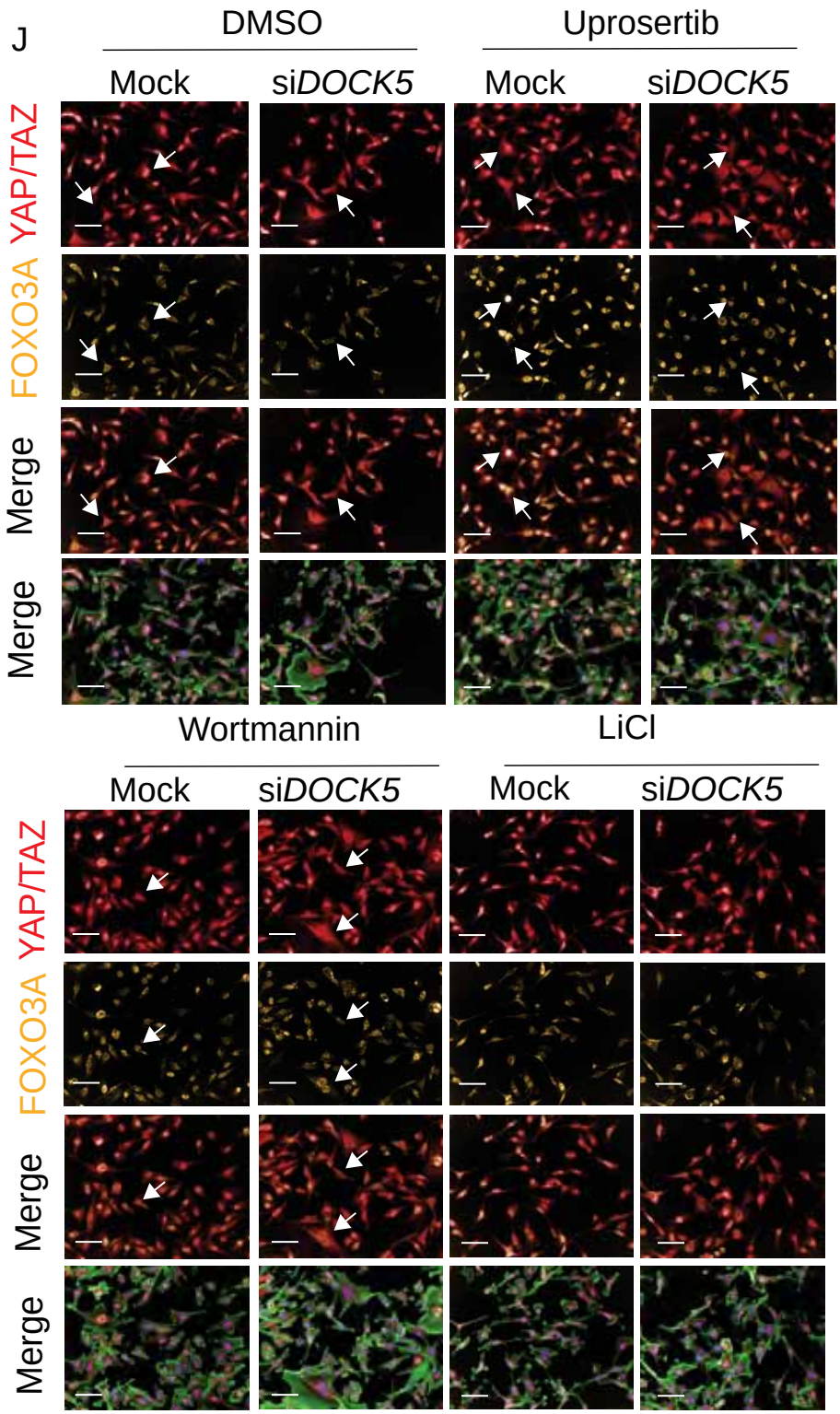

Figure 5.6: Proteomic data indicative of polarity and cell cycle defects with si*DOCK5*. *Continuation*. (J) Representative immunofluorescence images. Stained for FOXO3A (yellow), YAP/TAZ (red), and merge including F-actin (green). White arrows indicate examples of opposing localisation for FOXO3A and YAP/TAZ. Scale bar is 50 µm. performed by Mar Arias-García in the Bakal lab.

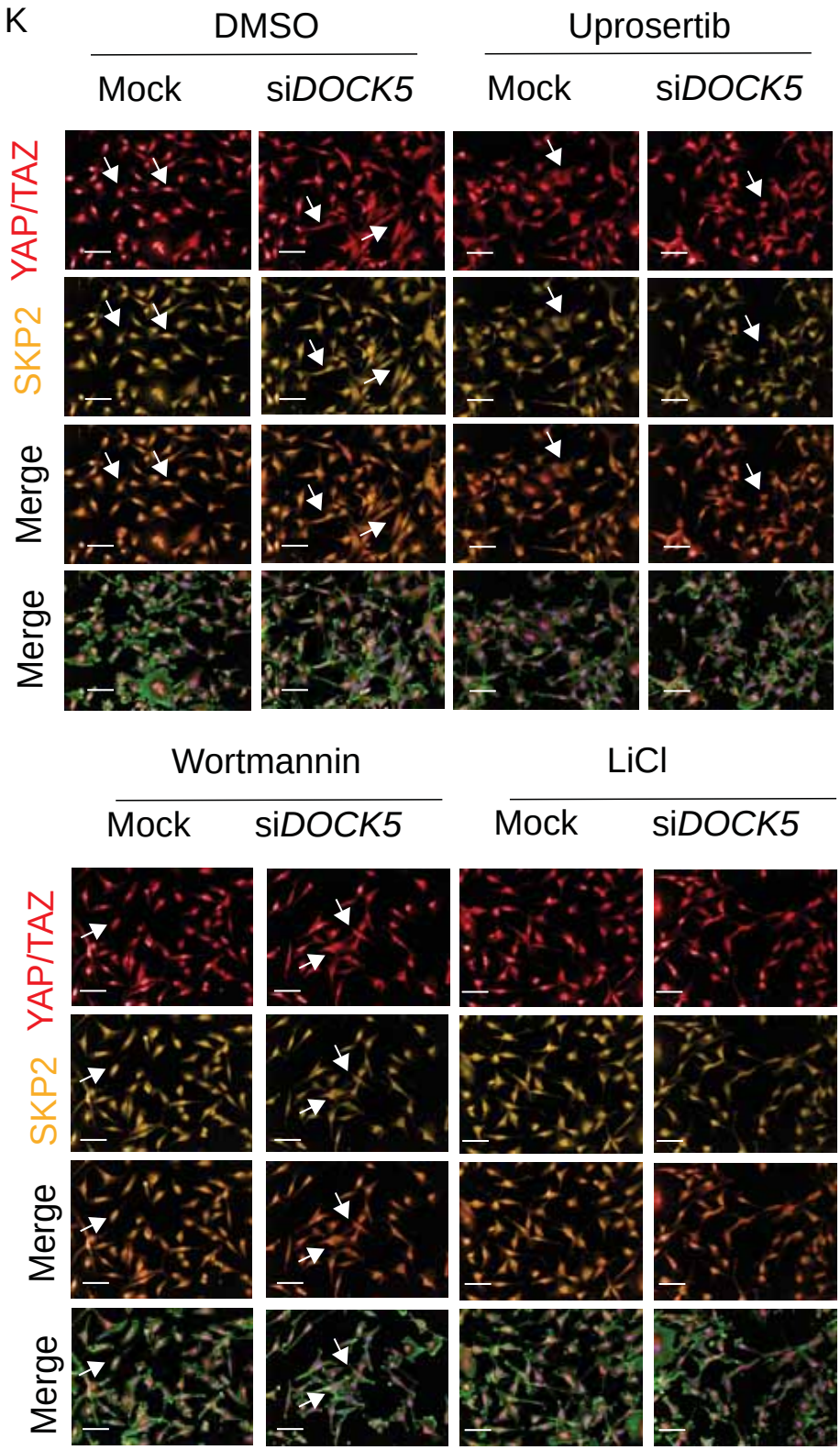

Figure 5.6: Proteomic data indicative of polarity and cell cycle defects with si*DOCK5*. *Continuation*. (K) Representative immunofluorescence Stained for SKP2 (yellow), YAP/TAZ (red), and merge including F-actin (green). White arrows indicate colocalization of SKP2 and YAP/TAZ. Scale bar is 50 µm. performed by Mar Arias-García in the Bakal lab.

WEE1 (log2 ratio: 0.724354) (Figure 5.6A, C). Upregulation of the CDK inhibitors p21, p27, p57, p19 would suggest that DOCK5 depleted cells are stalled in the cell cycle (Besson et al., 2008), although at what stage of the cell cycle is unclear.

Further there were also changes in proteins involved in the AKT signalling pathways and in establishment of front rear polarity. For example GSK3β was downregulated (log2 ratio: -0.58753); FOXO3A, a downstream target of AKT, was also downregulated (log2 ratio: -0.59131); while the AKT inhibitor PHLPP2 was upregulated (Ogawa et al., 2014b) (log2 ratio: 0.855787) (Figure 5.6A). GSK3β plays a role in the establishment of polarity where it has been described to be phosphorylated at the leading edge of migrating cells in a mechanism dependent on CDC42-PAR6-PKCζ, which leads to the the association of adenomatous polyposis coli protein (APC) with microtubule plus-ends, a mechanism required for centrosome reorientation and establishing cell polarity (Etienne-Manneville, 2004; Etienne-Manneville and Hall, 2003b, 2003a). Further, studies have shown that DOCK5 associates with NCK2 and AKT1 to phosphorylate and inactivate GSK3β in mast cells (Ogawa et al., 2014), releasing GSK3β's inhibition on microtubule polymerisation, and allowing APC to associate with microtubule plus-ends. Notably, NCK2 and AKT1 protein abundance levels were unchanged upon DOCK5 depletion, as were beta catenin's, whose stability is regulated by GSK3β (Clevers and Nusse, 2012; Gao et al., 2014; McCubrey et al., 2014) (Figure 5.6C). Alpha catenin, and GSK3β's closely related isoform GSK3α protein abundance levels were also unchanged (Figure 5.6C). Taken together, we hypothesise that DOCK5 regulates GSK3β levels and activity possibly through its association with NCK2 and AKT1, resulting in phosphorylated and stable GSK3β

at the leading edge, where APC then associates with microtubule plus-ends establishing cell polarity. Further, we reasoned that in the absence of DOCK5, YAP/TAZ translocation to the nucleus could be due to lack of polarity and cytoskeletal tension, or decreased GSK3β or AKT signalling; and that the upregulation of the CDK inhibitors could be due to a decrease in AKT signalling via a different signalling axis.

In order to test our hypothesis that YAP/TAZ translocation to the cytoplasm could be due to lack of stable GSK3β at the membrane, and decreased AKT signalling, we inhibited GSK3β and AKT, and quantified YAP/TAZ ratio via immunofluorescence. Inhibition of GSK3β by Lithium Chloride (LiCl, final concentration 5mM), had no effect on YAP/TAZ ratio compared to DMSO conditions for mock or si*DOCK5* transfected cells (Figure 5.6D). On the other hand, inhibiting AKT either directly with the AKT inhibitor Uprosertib (final concentration 2μM), or indirectly by inhibiting the upstream regulator of AKT phosphatidylinositol 4,5-bisphosphate 3-kinase (PI3K) with Wortmannin (final concentration 2μM) (Wymann et al., 1996) resulted in the same decrease in YAP/TAZ ratio in mock transfected cells as just depleting *DOCK5* by RNAi (Figure 5.6D). Furthermore, treating cells *DOCK5* depleted cells individually with Wortmannin, and Uprosertib decreased the ratio significantly compared to mock transfected cells (Figure 5.6D). This could be due to the significant decrease in GSK3β levels observed by depleting *DOCK5* via proteomics (Figure 5.6A), such that inhibiting AKT decreases the only present phosphorylated GSK3β (pGSK3β), resulting in an even bigger decrease in YAP/TAZ ratio than that observed only with si*DOCK5*.

Treatment with LiCl resulted in an increase in whole cell beta catenin levels via immunofluorescence (Figure 5.6F, Appendix 12) and is indicative of phosphorylated and inactive GSK3β. Both LiCl and AKT phosphorylate and inactivate GSK3β at serine 9 (Erdal et al., 2005; Huang et al., 2011; Ogawa et al., 2014; Schleicher et al., 2017). LiCl phosphorylation and inactivation of GSK3β has been shown to be largely independent of PI3K and AKT (Zhang et al, 2003). LiCl increased pGSK3β (Ser9) whole cell levels compared to DMSO in mock and si*DOCK5* transfected conditions via immunofluorescence, while Uprosertib resulted in a significant decrease (Figure 5.6E). These data suggest that increased pGSK3β (Ser9) levels are not sufficient to increase YAP/TAZ ratio. However, as Uprosertib treatment resulted in a significant decrease in pGSK3β (Ser9) whole cell levels (Figure 5.6E) and YAP/TAZ ratio (Figure 5.6D), this suggests that GSK3β is required to be phosphorylated at Ser9 by AKT, and may need to be associated with AKT at the leading edge for YAP/TAZ to be nuclear. Therefore, we propose that AKT is required to phosphorylate GSK3β at the leading edge establishing front rear polarity, for YAP/TAZ nuclear translocation. Such that, when DOCK5 is depleted, GSK3β is not phosphorylated by AKT, resulting in its degradation and unstable microtubules and polarity.

FOXO3A activity is inhibited by AKT where AKT phosphorylation results in FOXO3A extrusion from the nucleus and sequestration in the cytoplasm (Brunet et al., 2001; Manning and Toker, 2017). When FOXO3A is nuclear, it drives transcription of p21 and p27 (Manning and Toker, 2017). Therefore, because FOXO3A was significantly downregulated upon *DOCK5* depletion in our

proteomic data, we performed the same assays as before and quantified FOXO3A nuclear to cytoplasmic ratio. FOXO3A ratio increased significantly with Uprosertib and Wortmannin treatments for both mock and si*DOCK5* treated cells, while there was no difference with LiCl (Figure 5.6G), which suggests that the drugs are behaving as expected and AKT signalling is inhibited. The ratio of FOXO3A for si*DOCK5* treated cells was significantly lower to that of mock transfected cells, suggesting that there is some AKT signalling upon *DOCK5* depletion resulting in the extrusion of FOXO3A from the nucleus. However, FOXO3A nuclear extrusion has also been reported to occur in an AKT-independent manner (Hu et al., 2004). *DOCK5* depletion reduced FOXO3A whole cell levels as observed via proteomics, as well as ratio, however, Uprosertib treatment of *DOCK5* depleted cells increased nuclear to cytoplasmic ratio and increased whole cell total levels (Figure 5.6H). Suggesting the latter could be due to the increase in nuclear FOXO3A, as FOXO3A gets targeted for degradation when cytoplasmic (Hu et al., 2004; Nho and Hergert, 2014). The images in Figure 5.6J show that there is little colocalisation of FOXO3A with YAP/TAZ with treatments and DMSO, as when one is nuclear the other is cytoplasmic. These data suggest that YAP/TAZ translocate to the cytoplasm when there is decreased AKT signalling as observed by Uprosertib treatment and FOXO3A quantification of mock transfected cells. DOCK5 depletion resulted in a decrease in nuclear to cytoplasmic FOXO3A ratio, suggesting that there is AKT signalling. However, because DOCK5 depletion results in a decrease in whole cell FOXO3A via proteomics and immunofluorescence, this would suggest that although DOCK5 depletion results in decreased AKT signalling (Figure 5.6E), it does not result in

nuclear FOXO3A translocation, but rather it is affecting FOXO3A stability, by another mechanism not explored here.

We hypothesized that if DOCK5 regulates AKT activation, depletion of DOCK5 may result in decreased signalling via an AKT-SKP2 signalling axis that results in concomitant increases in p21, p27, and p57 (Chan et al., 2012; Chu et al., 2008; Manning and Toker, 2017; Zhao et al., 2013). In mock transfected cells SKP2 is predominantly localised to the nucleus, and the levels of nuclear SKP2 decreased upon *DOCK5* depletion. Treatment with Uprosertib significantly reduced nuclear SKP2 levels in mock transfected cells, to the level that of si*DOCK5* transfected cells treated with DMSO. Therefore, treatment with Uprosertib, as well as DOCK5 depletion result in decreased YAP/TAZ ratio, as well as decreased nuclear SKP2 levels, a colocalisation which can be observed from the images in Figure 5.6K. Therefore, this suggests that *DOCK5* depletion results in decreased AKT signalling via the AKT-SKP2 signalling axis, and this decreased signalling could be in part responsible for the decrease in YAP/TAZ ratio observed. Further this could explain increased p27 observed via proteomics, and via immunofluorescence (data not shown).

Overall these data support our hypothesis that DOCK5 plays a role in establishing polarity in migrating cells. We hypothesise that it is required to be at focal adhesions, where it recruits AKT and NCK2. AKT in this complex then phosphorylates and inactivates GSK3β, which is required for microtubule stabilisation and capture at the leading edge, Golgi reorientation, and establishment of front-rear polarity. In migrating cells, microtubule capture at the

leading edge is required to generate force on the nucleus which upregulates YAP/TAZ activity. We propose that in the absence of DOCK5, microtubules are not captured at the leading edge, and the nucleus is uncoupled from the cytoskeleton, leading to decreased YAP/TAZ activity.

5.2.7 DOCK5 regulation of focal adhesion dynamics is not RAC1 dependent

DOCK5 has been shown to be recruited to focal adhesions by GIT2, downstream of RHOA dependent activation of ROCK, and to activate RAC1 leading to protrusion formation and focal adhesion turnover (Frank et al., 2017). Therefore, we wondered whether the DOCK5 regulation of focal adhesion dynamics we observed (Figure 5.7) was via RacGEF activity or whether it was acting as a scaffold, or via interaction with other Rho GTPases. To test this, we knocked down *RAC1*, *RHOA*, and *CDC42* and performed the same experiments as with just si*DOCK5* with LM2-CAAXGFP cells migrating on fibronectin. Given our data showing the involvement of DOCK5 in AKT signalling we also treated mock transfected cells with Uprosertib.

Live imaging of focal adhesion dynamics revealed that cells lacking *DOCK5*, *RAC1*, and cells treated with Uprosertib had more dynamic adhesions compared to mock while cells lacking *CDC42* had more stable adhesions. This is represented by the tracked adhesions over time in representative cells in Figure 5.7A. Hedges' g between each condition and mock transfected cells shows that depleting *CDC42* had the biggest effect on assembly rates (Hedges' g: 0.851), followed by si*DOCK5* (Hedges' g: 0.375) (Figure 5.7B). On the other hand, every

condition except *RAC1*, had substantial effects on disassembly rates, with *DOCK5* having the largest effect (Hedges' g: 0.574) (Figure 5.7C).

RAC1 depletion had the biggest positive effect on assembly phase length (Hedges' g: 0.336), followed by si*DOCK5* (Hedges' g: 0.307) (Figure 5.7D), which can also be observed by the distribution of assembly phase lengths in Figure 5.7Fi. The effect sizes on the disassembly phase lengths were small, with si*RHOA* and si*RAC1* having the largest effects (Hedges' g: -0.255, and -0.251 respectively), with shorter disassembly phase lengths compared to mock (Figure 5.7E). This is also represented in Figure 5.7Fii, where the highest number of adhesions with shorter phase lengths are found in mock and si*RHOA* transfected cells. Stability phase lengths are indicative of how stable adhesions are for each condition. Depleting *DOCK5* resulted in the biggest decrease in stable adhesions compared to mock (Hedges' g of -0.507, Figure 5.7F).

These data suggest that in cells lacking *DOCK5*, adhesions assemble faster than in mock, but assemble for longer periods of time and are very unstable. Further, adhesions disassemble faster and for a shorter amount of time (graphical representation Figure 5.7I), suggesting that *DOCK5* depleted cells have problems assembling and disassembling adhesions, as well as in stabilising adhesions. In cells lacking *CDC42*, adhesions display faster assembly rates than in mock and si*DOCK5* transfected cells, but assemble for a similar time as in si*DOCK5* cells (Figure 5.7I). These adhesions are slightly more stable than in mock, and have faster and slightly longer disassembly rates, suggesting problems in assembly and disassembly. In cells lacking *RAC1* adhesions

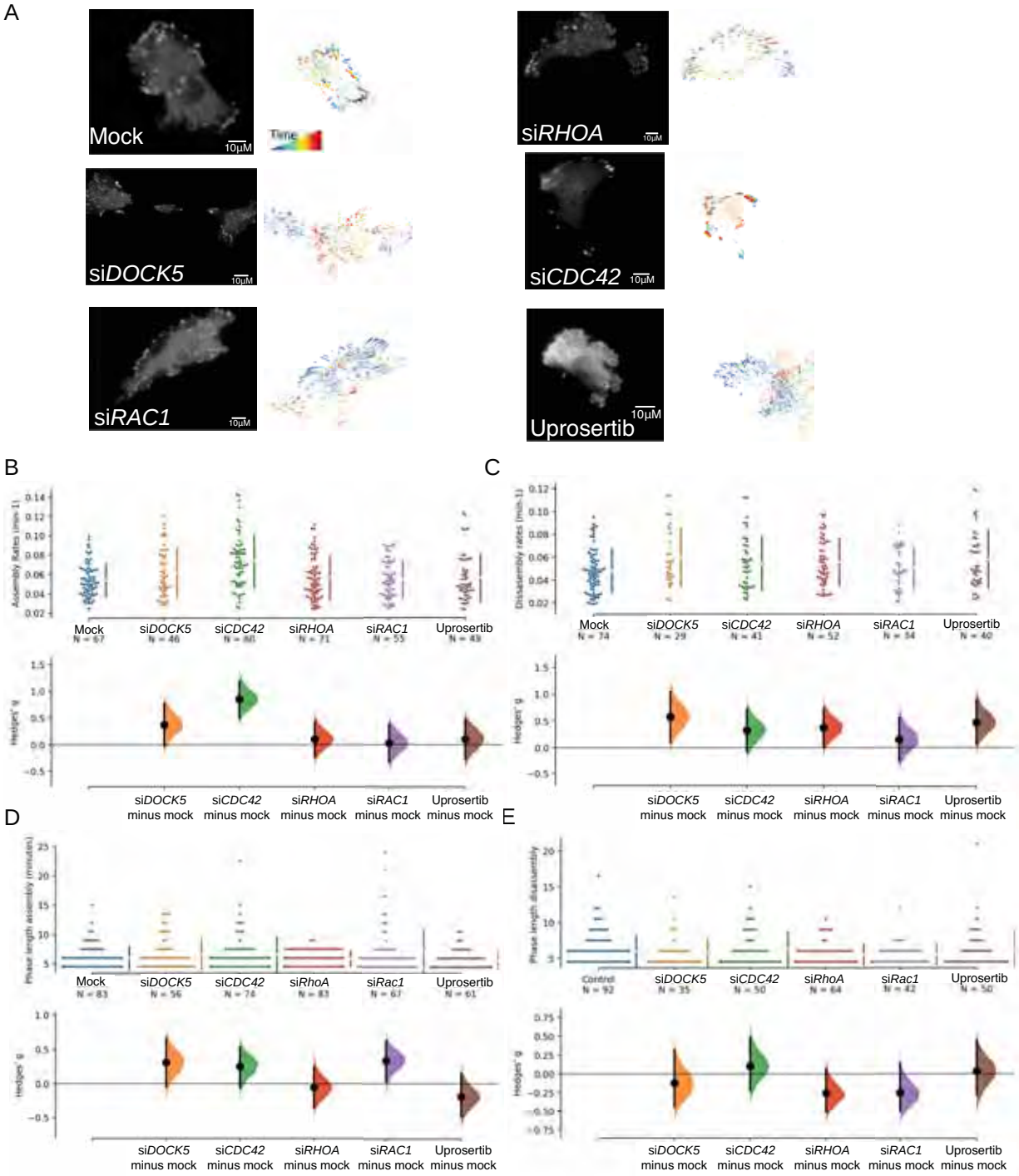

Figure 5.7 DOCK5 regulation of focal adhesion dynamics is not RAC1 dependent (A) Representative images of LM2-CAAXGFP cells transfected with Talin mApple and si*DOCK5*, si*CDC42*, si*RHOA*, si*RAC1*, mock, and treated with the AKT inhibitor Uprosertib. Left and right panels per condition show FAAS picking up the adhesions and adhesions tracked over time for the same cell. (B) (C) (D) (E) Cumming estimation plots of Hedge's g for comparison between (B) assembly and (C) disassembly rates, as well as (D) assembly and (E) disassembly phase lengths of adhesions in mock versus si*DOCK5,* si*CDC42*, si*RHOA*, si*RAC1* transfected cells, and Uprosertib treated cells. n shows adhesion number. Data is taken from 3 cells per condition. Raw data is plotted in the upper axes, while mean difference is plotted in lower axes as a bootstrap sampling distribution. Mean differences are shown as dots, 95% confidence intervals are shown by the ends of the vertical error bars. Generated using (Ho et al., 2019) website.

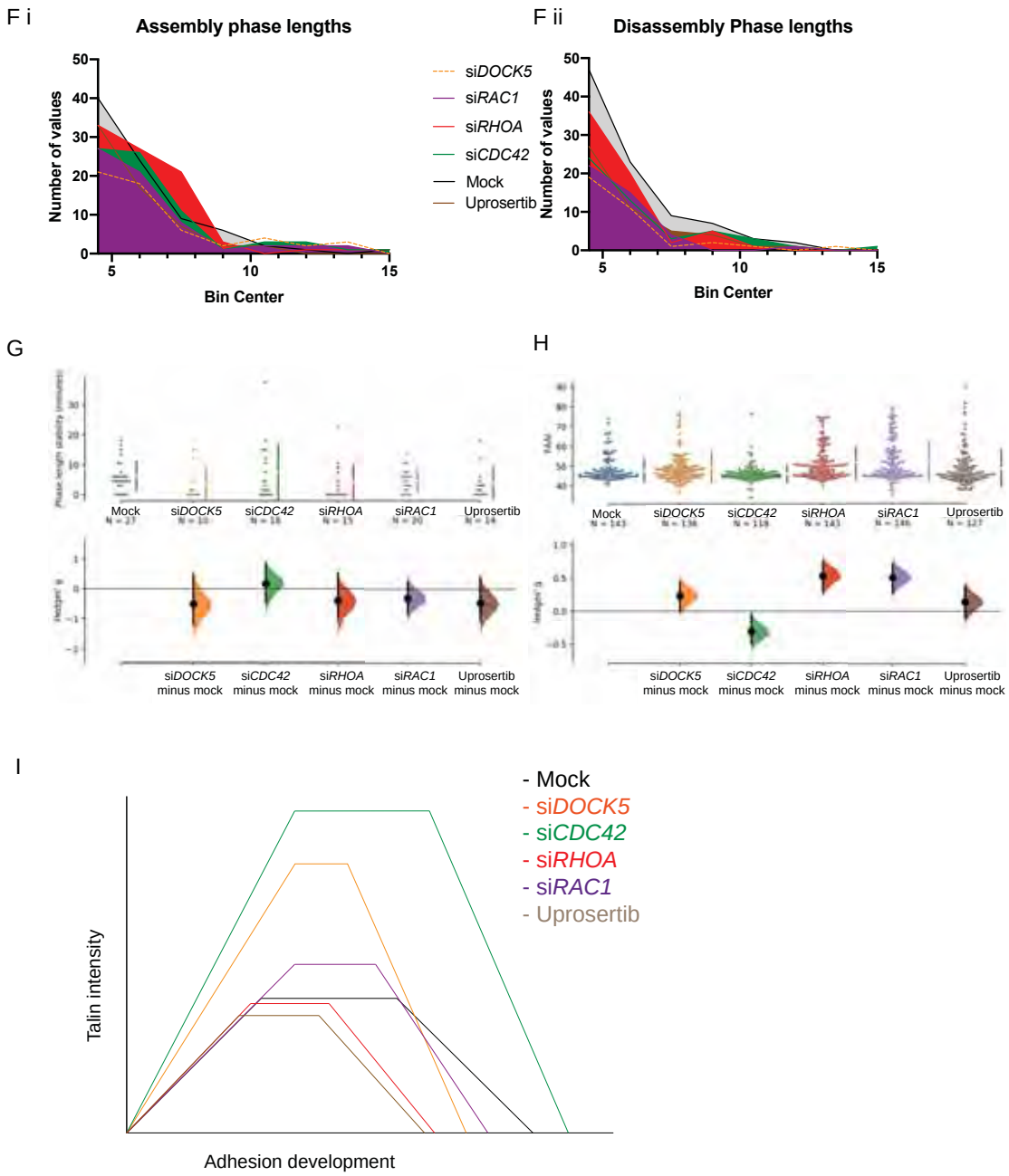

Figure 5.7 DOCK5 regulation of focal adhesion dynamics is not RAC1 dependent (F) Histograms of (i) assembly and (ii) disassembly phase lengths for all conditions. (G) (H) Cumming estimation plots of Hedge's g for comparison between (G) stability phase length, and (H) Focal Adhesion Alignment Index (FAAI) of adhesions in mock versus si*DOCK5,* si*CDC42*, si*RHOA*, si*RAC1* transfected cells, and Uprosertib treated cells. n shows adhesion number. Data taken as for B-E. (I) Summary of results and how each siRNA and treatment is affecting adhesion life cycle. Not to scale. Unpaired Hedge's g values and Mann Whitney significance can be found in Appendix 13.

assemble at the same rate as in mock but for longer, they are more stable and disassemble at similar rates to mock but for a shorter amount of time. This suggests that they are having more problems assembling than disassembling. In cells lacking *RHOA* adhesions assemble at the same rate as in mock for the same amount of time, but are less stable, and disassemble faster and for longer times, indicative of problems in the disassembly phase. Adding Uprosertib resulted in similar assembly rates as for mock and less stable adhesions that disassemble faster but for the same time as those in mock.

Focal Adhesion Alignment Index (FAAI) is directly related to the standard deviation of the distribution of focal adhesion deviation from the dominant focal adhesion angle (Wu et al., 2012), where a cell with a high number of aligned adhesions will have a FAAI of around 74.3, and a cell with a low number of aligned adhesions will have a low FAAI of around 45 (Wu et al., 2012). Each dot in Figure 5.7G shows the FAAI for each image, i.e., for each timepoint. Overall LM2 cells have a low FAAI. Depleting *RAC1*, and *RHOA* had the biggest positive effect on FAAI (Hedges' g of 0.505, and 0.528 respectively), while depleting *CDC42* had a negative effect of -0.315 Hedges' g. Depleting *DOCK5*, and treating with Uprosertib, had a small positive effect on FAAI (Hedges' g of 0.231 and 0.138 respectively).

Taken together, these data show that none of the conditions presented in this experiment recapitulates *DOCK5* depletion. However, some aspects of si*DOCK5* transfected cells' adhesion dynamics are similar to other conditions. Such that si*DOCK5* transfected cells have similar adhesion assembly and disassembly

rates to those in si*CDC42* cells, and disassembly rates as in si*RHOA*, and Uprosertib treated cells; but have similar adhesion assembly phase lengths to those in si*RAC* cells. Further, these data suggest that *CDC42* is required for adhesion alignment. We hypothesise that DOCK5 is not regulating focal adhesions dynamics via RAC1, but rather that there is an interplay with RHOA and CDC42, and that DOCK5's regulation of focal adhesion dynamics is upstream of AKT.

5.2.8 Reduction of YAP/TAZ ratio using DOCK5 inhibitor C21

Having seen that DOCK5 regulation of focal adhesion dynamics does not appear to be RAC1-dependent, we wondered whether its effect on YAP/TAZ was also RAC1-independent. C21 is a DOCK5 inhibitor which blocks DOCK5's DHR2 catalytic domain, specifically hindering the interaction between DOCK5 and RAC1 in a non-competitive manner (Ferrandez et al., 2017). Treatment with C21 decreased YAP/TAZ by the same amount as *DOCK5* siRNA (Figure 5.8A). In order to test whether the decrease in YAP/TAZ ratio with C21 could be due to it hindering DOCK5's interaction with NCK2 and AKT, we treated cells with C21 and measured SKP2 nuclear to ring region ratio, as well as GSK3β at the membrane. C21 treatment significantly reduced SKP2 nuclear to ring region ratio (Figure 5.8B), which can be observed from the images in Figure 5.8Di by the colosalisation of YAP/TAZ and SKP2 (white arrows). Further, C21 treatment significantly reduced GSK3β at the membrane in mock transfected cells to the same levels as just depleting *DOCK5* (Figure 5.8C), which can also be observed from the images in Figure 5.8D ii, white arrows).

These data suggest that DOCK5 can be inhibited, and that its inhibition results in the same phenotype observed by just depleting *DOCK5*: decreased YAP/TAZ ratio and decreased AKT signalling via the SKP2 signalling axis. We hypothesise that C21 blocking of DOCK5's DHR2 domain is also hindering DOCK5's interaction with AKT and NCK2, and that DOCK5's interaction with AKT-NCK2 is required for GSK3β stability at the membrane.

5.2.9 Inhibiting focal adhesion turnover, and contractility, further reduces YAP/TAZ ratio in si*DOCK5* background

Having shown that YAP/TAZ translocation to the cytoplasm as a result of *DOCK5* depletion is in part due to a decrease in AKT signalling, we reasoned that YAP/TAZ translocation to the cytoplasm could also be a result of lack of tension due to alterations in focal adhesions. We treated mock and si*DOCK5* transfected cells with the FAK inhibitor PF-573288 (FAKi), as FAK plays a role in focal adhesion turnover by transiently inactivating the RHOA effector ROCK (Webb et al., 2004). FAKi did not reduce YAP/TAZ ratio in mock transfected cells, but it further decreased YAP/TAZ ratio in *DOCK5* depleted cells (Figure 5.9Ai). In addition, whole cell YAP/TAZ levels were reduced by the same amounts when treating mock and si*DOCK5* transfected cells with FAKi compared to DMSO (Figure 5.9Aii), but not to the levels of depleting si*YAP* plus si*TAZ*.

Treating with FAKi increased cell size significantly (Figure 5.9B, C). This increase in cell area could be due to more focal contacts maturing into adhesions, and these adhesions being unable to turn over. Therefore, this increase in adhesions

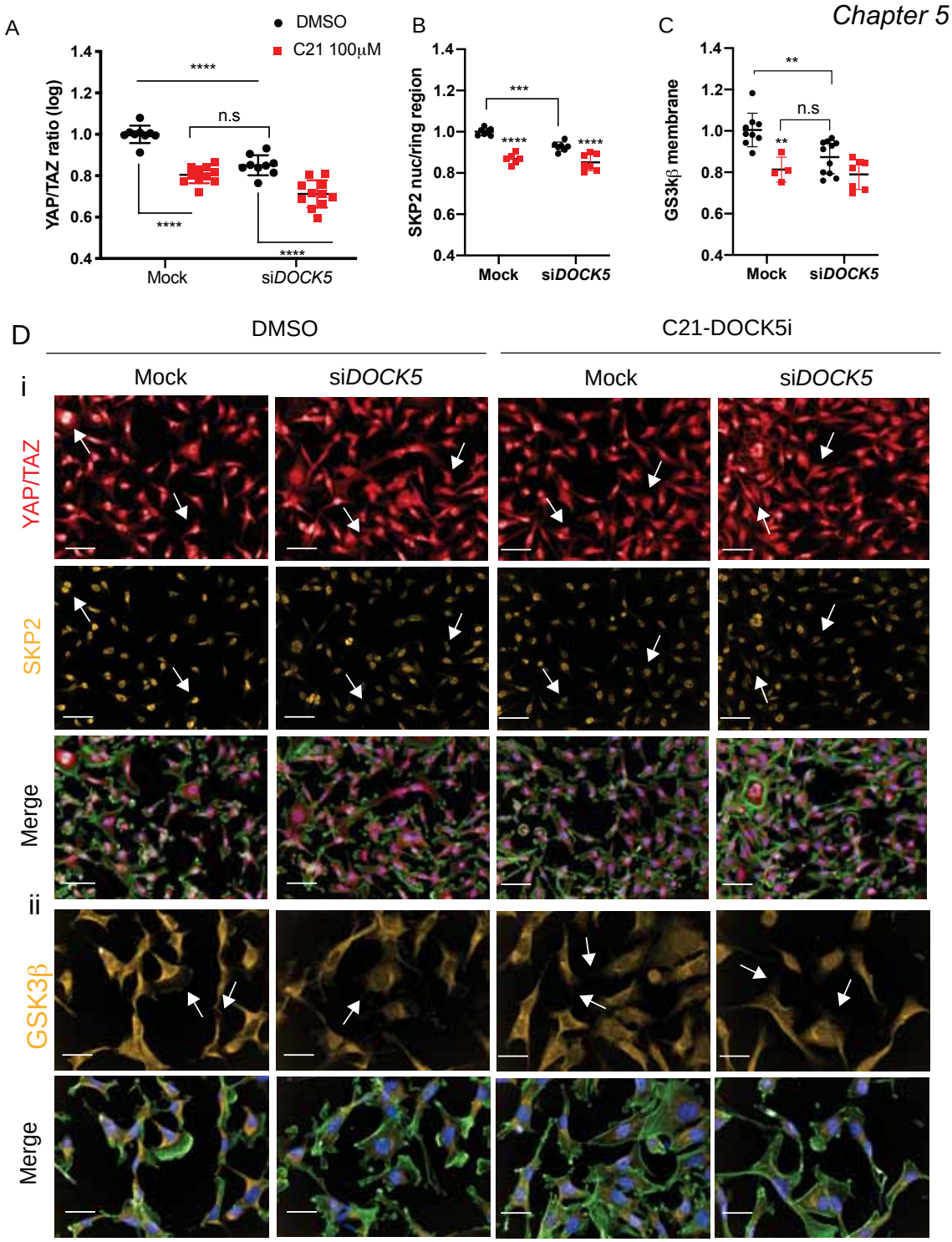

Figure 5.8: Inhibition of DOCK5 using C21 reduces YAP/TAZ ratio
Immunofluorescence quantifications for mock and si*DOCK5* transfected cells, treated with DMSO or DOCK5 inhibitor C21 (100μM) of (A) YAP/TAZ ratio (log) (n = 3 biological repeats), (B) GSK3β at the membrane and (C) SKP2 nuclear to ring region ratio (log) (n = 2 biological repeats for B and C). (D) Representative images of quantifications shown in A-C. (i) Cells stained for YAP/TAZ (red), SKP2 (yellow) and merge including F-actin (green). Imaged at 20x. Scale bar, 50 μm. White arrows indicate YAP/TAZ colocalisation with SKP2. (ii) Cells stained for GSK3β (yellow) and merge including F-actin (green), and DNA (blue). White arrows indicate GSK3β at the membrane (mock) and lack thereof (si*DOCK5* and C21). Imaged at 40x. Scale bar, 20 μm. Part of A and B-D performed by Mar Arias-García in the Bakal lab.

would suggest an increase in tension and if YAP/TAZ translocation to the nucleus were dependent on tension we would expect increased YAP/TAZ ratio with FAKi. Further, spread cells have been shown to display high YAP/TAZ ratios (Dupont et al., 2011; Sero and Bakal, 2017). However, there was no relationship between cell area and YAP/TAZ ratio for mock transfected cells plated at low density (1000 cells per well) (Figure 5.9D). There was an inverse relationship between cell area and cell number, with FAKi increasing cell area up to densities above 2000 cells per well (Figure 5.9E i), and a positive relationship between YAP/TAZ ratio and cell area (Figure 5.9E ii). Therefore, even though FAKi increased cell area, there was no change in YAP/TAZ ratio in mock transfected cells, and a decrease in si*DOCK5* transfected cells (Figure 5.9A), suggesting YAP/TAZ become dependent on tension when FAK signalling is inhibited in mock transfected cells, which is lost when *DOCK5* is depleted. In fact, Kim and Gumbiner, 2015 showed that integrins signal via FAK-SRC-PI3K-PDK1 pathway which inhibits LATS1/2, thus allowing YAP to translocate to the nucleus. Therefore, DOCK5 could be coordinating tension from focal adhesions via a signalling pathway where FAK signalling through SRC results in YAP/TAZ translocation to the nucleus(Kim and Gumbiner, 2015).

We then asked whether inhibiting contractility would have the opposite effect to inhibiting focal adhesion turnover. ROCK inhibits RAC1 activity via different mechanisms (Guilluy et al., 2011), so we treated cells with the ROCK inhibitor Y-27632 (Y27), and the myosin light-chain II inhibitor Blebbistatin (bleb) to distinguish the roles of ROCK as a RAC1 inhibitor and a myosin-II activator. Bleb

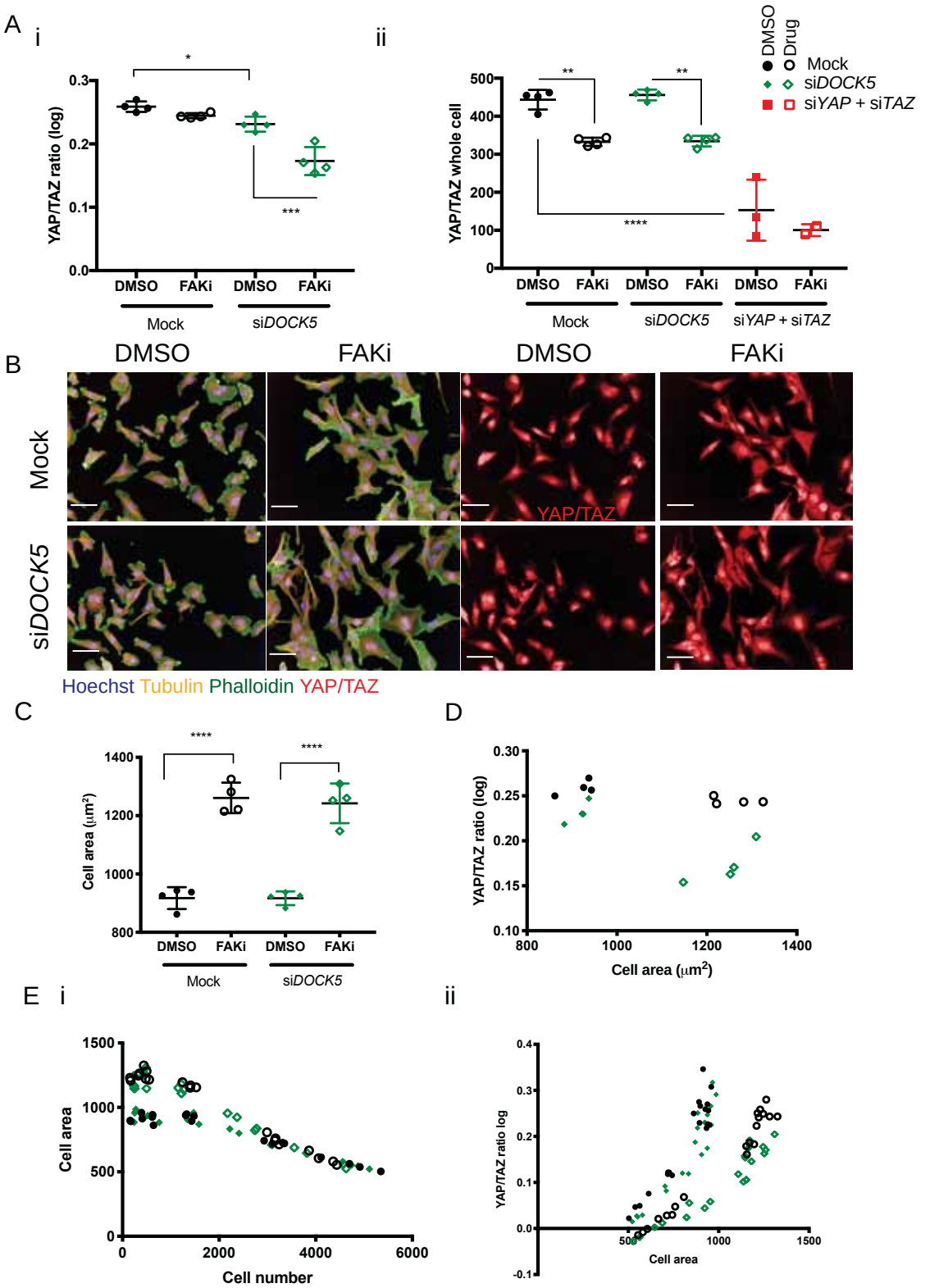

Figure 5.9 Inhibiting focal adhesion turnover, and contractility, further reduces YAP/TAZ ratio in si*DOCK5* background (A) (i) YAP/TAZ ratio (log) of mock (black) and si*DOCK5* (green) transfected cells treated with DMSO (filled) or 2μM final PF-573288 (open). (ii) Whole cell levels of YAP/TAZ intensity of mock, si*DOCK5,* and si*YAP* + si*TAZ* transfected cells treated with DMSO or 2μM final PF-573288. (B) Representative images of experiment quantified in A. Stained for YAP/TAZ (red), DNA (blue), α-tubulin (yellow), and F-actin (green). (C) (D) For mock and si*DOCK5* transfected cells treated with DMSO or FAKi quantification of (C) cell area (μm^2) and (D) YAP/TAZ ratio in relation to cell area (μm^2). (E) For mock and si*DOCK5* transfected cells treated with DMSO or FAKi and plated at various densities (i) quantification of cell area (μm^2) in relation to cell number and (ii) YAP/TAZ ratio in relation to cell area. *Continued overleaf.*

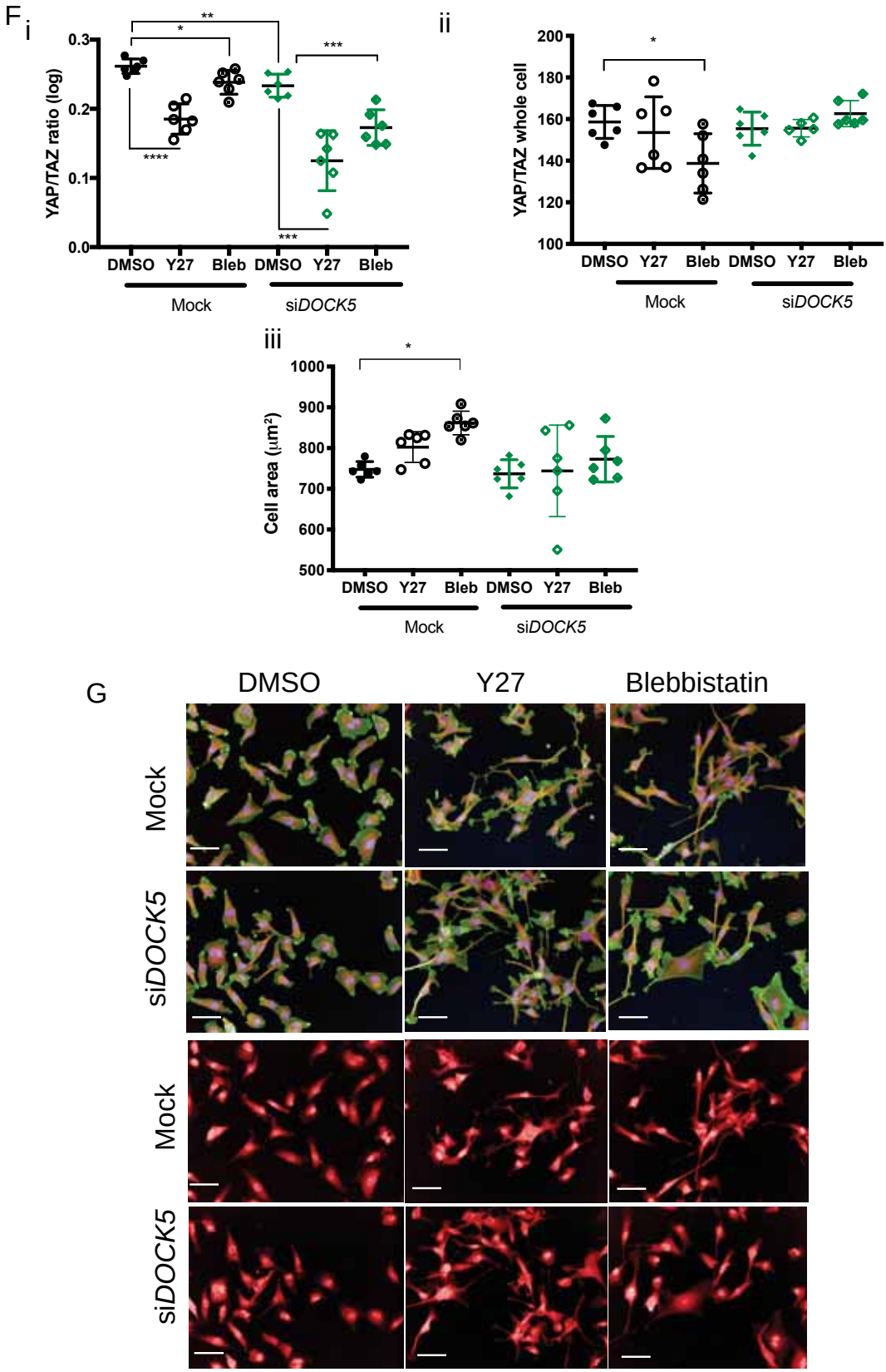

Figure 5.9 *Continuation.* F) (i) YAP/TAZ ratio, (ii) whole cell levels and (iii) cell area for mock or si*DOCK5* transfected cells treated with DMSO, 10μM final Y27 or 10μM final blebbistatin. (G) Representative images of experiment quantified in (F). Stained for YAP/TAZ (red), DNA (blue), α-tubulin (yellow), and F-actin (green). Scale bar 50μm. Mean ± SD are shown (n = 1 biological repeat, 4 wells, ANOVA, * P < 0.05, ** P < 0.01, *** P < 0.001, **** P < 0.0001).

and Y27 decreased YAP/TAZ ratio in mock and si*DOCK5* transfected cells, with bleb reducing YAP/TAZ ratio by the same amount as just depleting cells of *DOCK5* (Figure 5.9F i). Treatment with bleb decreased whole cell YAP/TAZ levels only in mock transfected cells (Figure 5.9F ii), and increased cell area (Figure 5.9F iii). This suggests that in cells treated with Y27, hyper RAC activation as a result of ROCK inhibition accelerates the process of focal adhesion turnover which results in less stable adhesions and consequently lower YAP/TAZ ratio in a tension dependent manner. Conversely, treating with bleb reduced YAP/TAZ ratio by less than Y27, due to there being slower turnover of adhesions and increased tension than in Y27 treated cells. Both of these effects were enhanced in si*DOCK5* transfected cells, suggesting that tension is decreased in this background.

Taken together these data support our hypothesis where lack of *DOCK5* alters focal adhesion dynamics and stabilisation of front rear polarity, resulting in decreased tension and signalling via FAK, ROCK, and myosin II contractility, resulting in YAP/TAZ translocation to the cytoplasm.

5.2.10 *DOCK5* depletion effect on growth

Given that the CDK inhibitors p21, p27, p57, and p19 are present to regulate the cell cycle at all stages (Besson et al., 2008), we reasoned that the increase in abundance seen as a result of *DOCK5* depletion via proteomics would result in defects in the cell cycle, such as cell cycle arrest, or slower cycling. Further, we performed a viability screen 48 hours post-transfection using the RhoGEF/GAP and Rho GTPase siRNA library used for our phenotypic screens, and found that

DOCK5 did not decrease viability (data not shown). Given that our assays are all performed over 48 hours for optimal siRNA knockdown, this suggests that either the upregulation of CDK inhibitors has not performed a full effect at 48 hours, or these cells have evolved mechanisms to keep proliferating despite CDK inhibitors, by upregulating CYCLIN D, or CYCLIN E for example (Asghar et al., 2017) as shown by our proteomic data.

Therefore, we performed growth curve assays over 160 hours to elucidate whether *DOCK5* knockdown cells grow slower. We also knocked down *YAP*, *TAZ*, *YAP* + *TAZ*, and the Rho GTPases *RAC1*, *RHOA*, and *CDC42*, alone and in combination with *DOCK5*. In order to quantify significance, we normalized values to mock transfected cells per well, pooled the mocks, and compared values at 50% confluency. Cells lacking *DOCK5* grew at a slower rate from 60 hours post-transfection and reached confluence at 160 hours compared to mock transfected cells which reached confluence at 136 hours (Figure 5.10A). Cells lacking *RHOA*, *RAC1*, *YAP*, or *TAZ* grew at the same rate as mock transfected cells (Figure 5.11), while cells lacking *CDC42* grew at a slower rate than mock (Figure 5.10B), reaching confluency at 204 hours compared to 138 hours for mock transfected cells. Double knockdown of *DOCK5* and *RHOA*, and *DOCK5* and *RAC1* resulted in slower growth rates compared to mock, reaching confluency with an approximate 6-hour delay (Figure 5.11E, F). However, cells with the double *DOCK5* and *CDC42* knockdown, and *YAP* and *TAZ* double knockdown displayed significantly slower growth rates (Figure 5.10C, D, E), such that at time point 156, where mock transfected cells were confluent, cells with the double knockdown were at 32% confluency. This suggests that the effect of

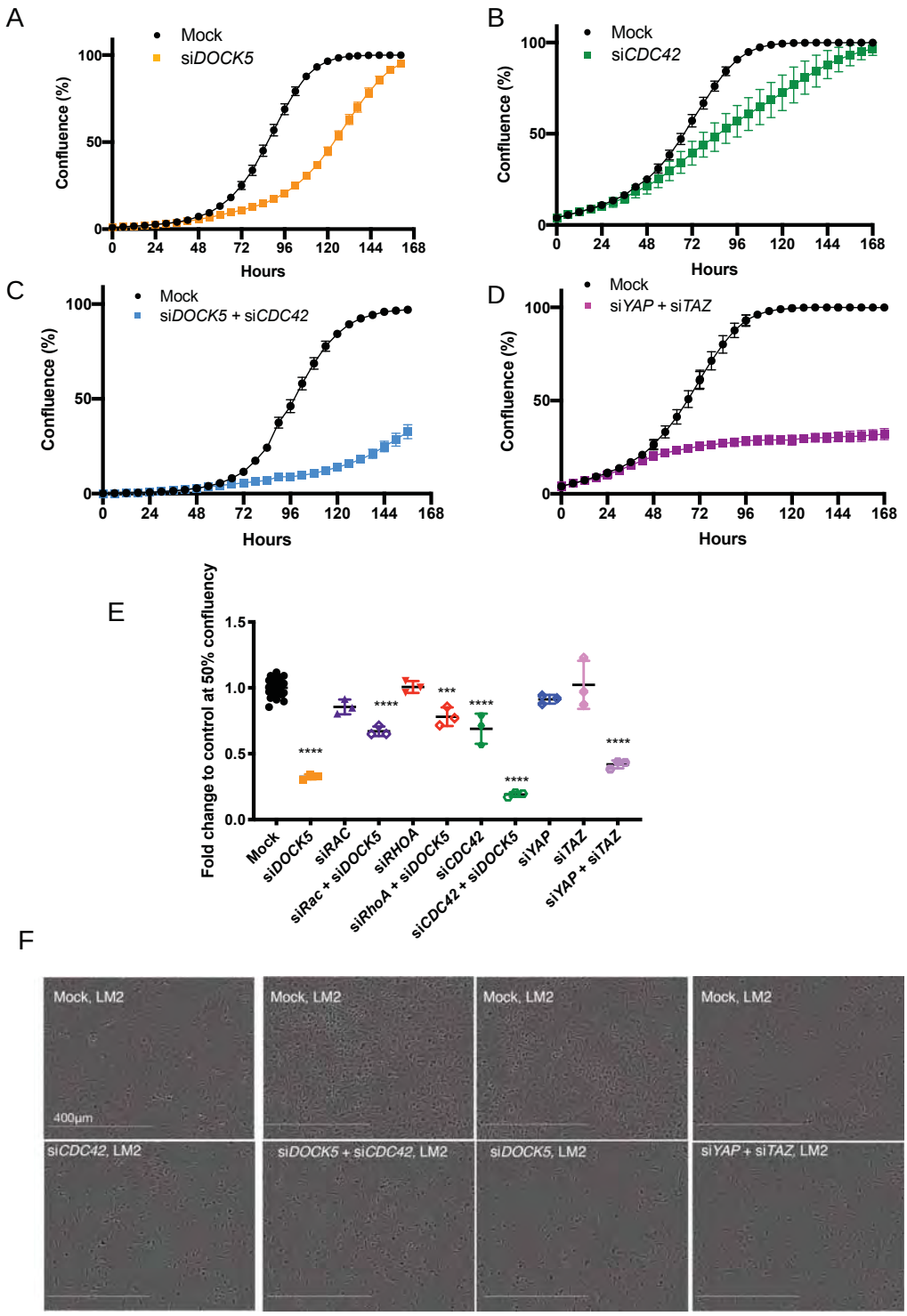

Figure 5.10 *DOCK5* depletion results in slow growth rates. Growth curves for mock and (A) si*DOCK5*, (B) si*CDC42*, (C) si*DOCK5* + si*CDC42* and (D) si*YAP* +si*TAZ* transfected cells. Mock and siRNA transfected wells represented as circles and squares respectively. Averages per well are shown. (E) Fold change to control mock transfected wells per 6 well plate at 50% confluency. (F) Representative images for cells at 50% confluency for si*CDC42* (72 hours), si*DOCK5* + si*CDC42* (120 hours), si*DOCK5* (84 hours), si*YAP* + si*TAZ* (72 hours), and their corresponding mock transfected cells. Scale bar is 400 µm. Experiments performed in triplicate, representative experiment shown with n = 3 wells per condition. One-way ANOVA, * P < 0.05, ** P < 0.01, *** P < 0.001, **** P < 0.0001.

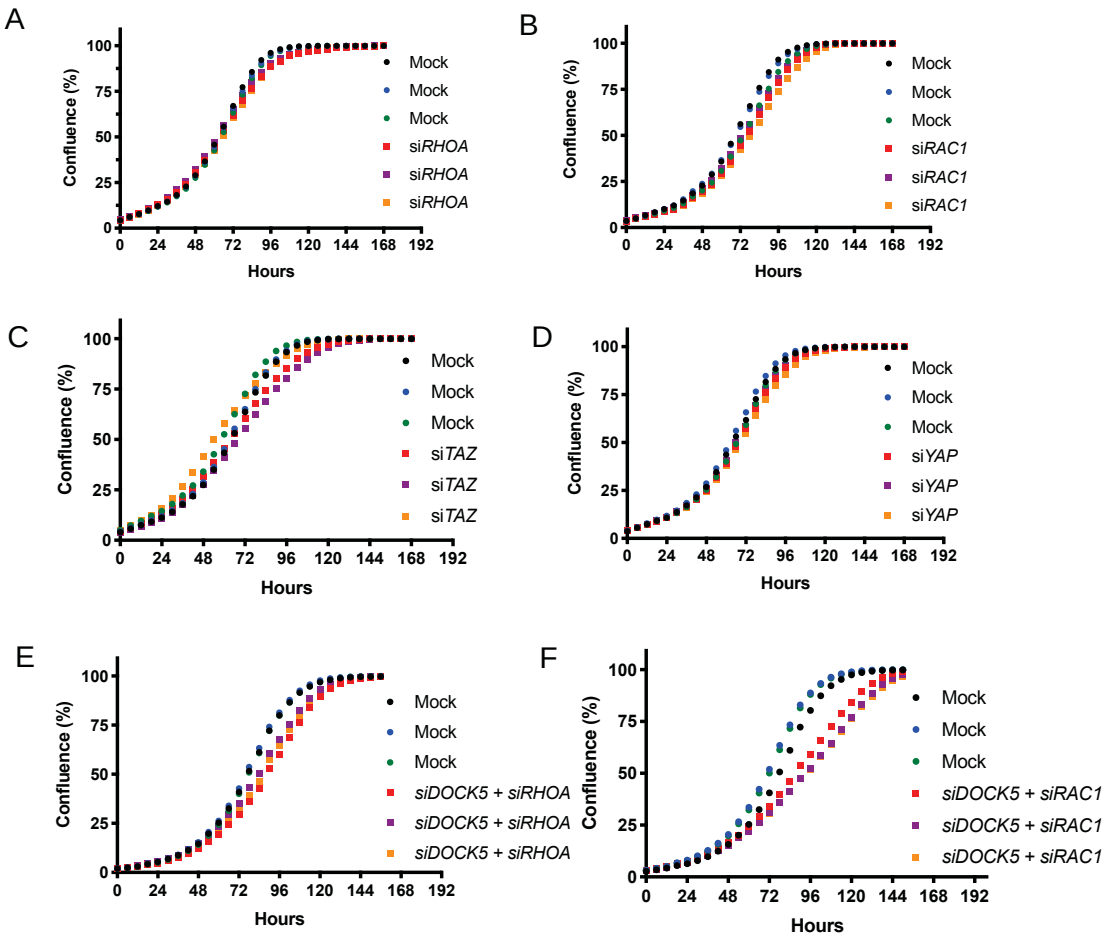

Figure 5.11 *RHOA*, *RAC1, YAP, TAZ* depletion do not affect growth rates. Growth curves for mock and (A) si*RHOA*, (B) si*RAC1*, (C) si*DOCK5* + si*RHOA*, (D) si*TAZ,* (E) si*YAP,* (F) si*DOCK5* + si*RAC1* transfected cells. Data per well is shown, wells indicated by differing colours. Representative experiments shown with n = 3. Mock and siRNA transfected wells represented as circles and squares respectively.

DOCK5 on proliferation is not via RAC1. Instead these data suggest that it could be due to a lack of front rear polarity and decreased YAP/TAZ activity.

5.2.11 Inhibition of mutant KRAS (G13D) signalling and knockdown of *DOCK5* in TNBC cells is synthetic lethal.

Studies have shown that sensitivity to the CDK4/6 inhibitor Palbociclib is dependent on CDK2 activity levels after mitosis (Asghar et al., 2017), such that cells with low CDK2 activity are sensitive, while those with high CDK2 activity as a result of increased CYCLIN E1 expressed, are insensitive. Given that LM2 cells had high levels of CYCLIN E1 upon *DOCK5* depletion we reasoned they would be more resistant to Palbociclib than mock transfected cells. There were no significant differences in viability between the knockdown and mock for Palbociclib (Figure 5.12A). Further due to the upregulation of WEE1, we also used a WEE1 inhibitor which also resulted in no effect. On the other hand, cells lacking *DOCK5* were more dependent on FAK and mitogen activated protein kinase kinase (MAP2K) for survival, as inhibiting them over 72 hours reduced their viability significantly (Figure 5.12A). Therefore, we proceeded to do growth curve assays with FAK inhibition and the MAP2K inhibitor, Binimetinib.

FAK inhibition (PF563288) did not affect growth rate of mock or si*DOCK5* transfected cells (Figure 5.12D). However, we found that treatment with Binimetinib significantly slowed growth rates of mock and si*DOCK5* transfected cells (Figure 5.12D), with si*DOCK5* transfected cells' confluency only increasing from 7 to 10% from the point of drug-addition (48 hours from start of imaging) to 160 hours later when the experiment was terminated (point at which mock DMSO

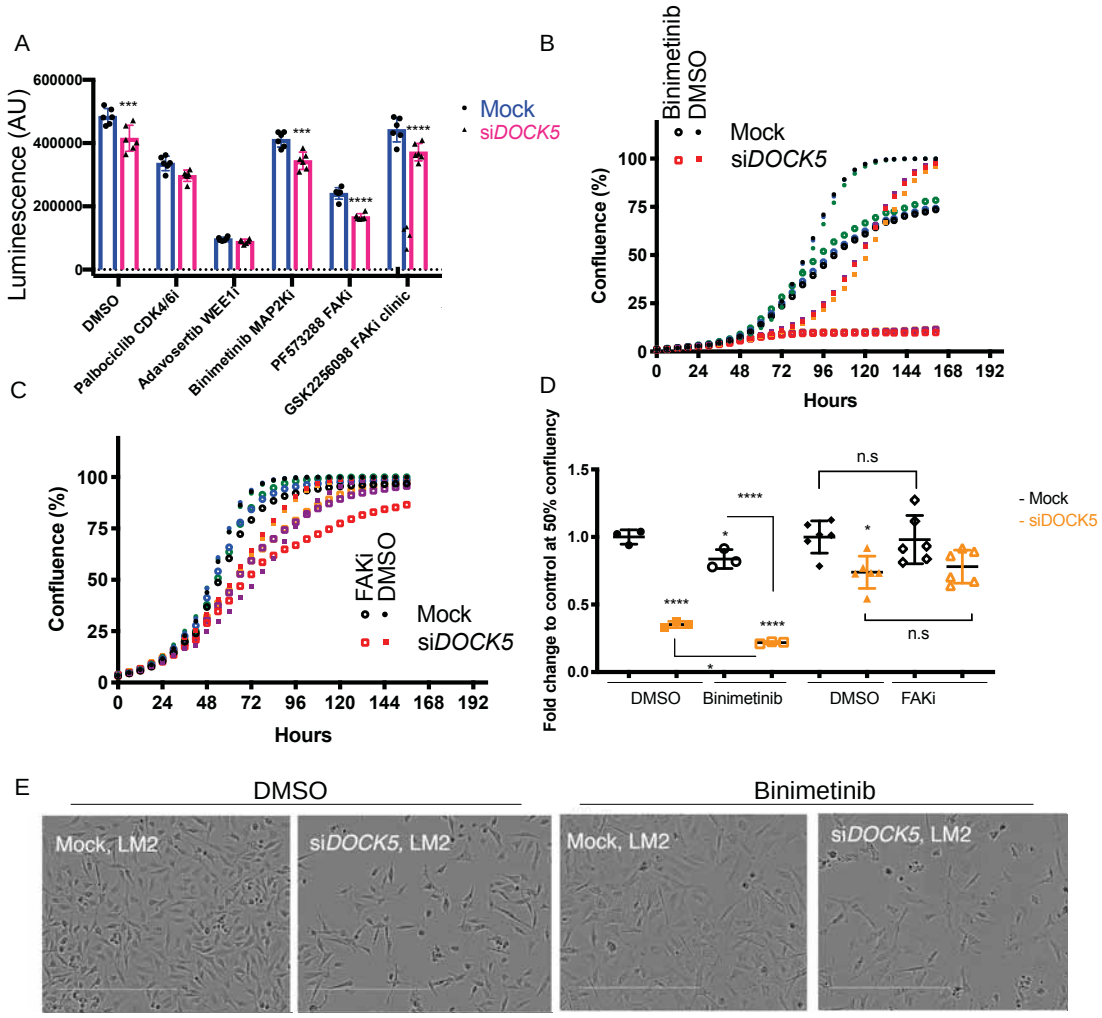

Figure 5.12 Inhibition of mutant KRAS (G13D) signalling and knockdown of *DOCK5* in TNBC cells is synthetic lethal. (A) Viability assay for mock and si*DOCK5* transfected cells treated with DMSO, CDK4/6 inhibitor Palbociclib (500nM), WEE1 inhibitor Adavosertib (1mM), MAP2K inhibitor Binimetinib (10μM), FAKi P573288 (2μM), and FAKi used in the clinic GSK2256098 (40μM). Significance is between mock and si*DOCK5* transfected cells, student's t-test. (N = 4 wells, 1000 cells per well. ANOVA, * P < 0.05, ** P < 0.01, *** P < 0.001, **** P < 0.0001). (B) Growth curves for mock and si*DOCK5* transfected cells treated with DMSO (closed circle, square) and 10 μM final Binimetinib (open circle, square). Representative experiment, n = 3 wells. (C) Growth curves for mock and si*DOCK5* transfected cells treated with DMSO (closed circle, square) and 2 μM final FAKi (open circle, square). Representative experiment, n = 3 wells. (D) Fold change to control mock transfected DMSO treated wells condition at 50% confluency. (n is at least 3 wells per condition). (E) Representative images for cells at 50% confluency (96 hours) for si*DOCK5* and mock transfected cells treated with DMSO and Binimetinib. Scale bar is 400 μm. Experiment shown in A was performed by Mar Arias-García in the Bakal lab.

treated cells had reached confluency). Because proteomics was performed on samples transfected for 48 hours, this would suggest that the upregulation of expression of the CDK inhibitors p21, p27, and p57 is having an effect that can only be observed 72 hours after transfection and explains why there were no significant differences in si*DOCK5* transfected cells and mock transfected cells when we performed cell cycle analysis via flow cytometry at the 48 hour time point. LM2 cells have mutant KRAS (G13D) which is upstream of MAP2K, therefore these data suggest that inhibition of mutant KRAS (G13D) signalling and knockdown of *DOCK5* in TNBC cells is synthetic lethal.

5.2.12 *DOCK5* depletion results in nucleus uncoupling from cytoskeleton

Given the polarity and growth defects observed with si*DOCK5* by itself and combined with si*CDC42*, and our hypothesis that in the absence of DOCK5, microtubules are not captured at the leading edge, reducing YAP/TAZ ratio due to decreased tension on the nucleus, we performed a spreading assay in order to understand whether the defect in growth had to do with defects in cytoskeletal architecture. We plated cells on fibronectin and fixed them after 3 hours. We found that the nucleus of cells lacking *DOCK5*, *CDC42*, alone in combination was detached from the cytoskeleton compared to mock transfected cells, and cells treated with FAK inhibitor (Figure 5.13A, B). Nuclei height for these conditions was above imaging depth of the SoRa microscope, > 23μm. Further, tubulin in cells lacking *DOCK5*, *CDC42,* alone and in combination looked irregular and unstable, while paxillin was irregular and did not localise to focal adhesions as observed for mock transfected cells and cells treated with FAK inhibitor. Nuclei

in *DOCK5*, and *CDC42* depleted cells were not round, but rather displayed blebs, possibly as a result of unstable tubulin dynamics. Interestingly, we observed the same phenotype upon depletion of *DOCK5* via scanning electron microscopy (SEM) (Figure 5.14A, B). On the other hand depletion of *RHOA, RAC1* and *RAC2*, triple knockdown of *RAC1-3*, as well as when combined with *DOCK5* resulted in spread cells, that did not display the "uncoupled" nucleus phenomenon (Figure 5.13A, B), with nuclear depths of ~10μm. In fact, depleting *DOCK5* in combination with *RAC1* and *RAC2* rescued the phenotype observed with *DOCK5* alone, and there appear to be fewer but more stable adhesions in these cells. The latter suggests that adhesions are unstable as a result of *DOCK5* depletion, but that those that are present are slow to turnover, as a result of *RAC1* and *RAC2* depletion.

These data suggest that DOCK5 is not acting via RAC1, recapitulating our focal adhesion dynamics data. Further, CDC42 and DOCK5 are acting synergistically to regulate microtubule stability and nuclear tension during cell spreading, and that RAC1 and RAC2 are mediating an inhibitory effect. Because DOCK5 localises to (Frank et al., 2017; Müller et al., 2018) and regulates focal adhesion dynamics, these data suggest that the lack of tension on the nucleus is downstream of focal adhesions. Such that lack of DOCK5 at focal adhesions results in decreased microtubule stability and consequent lack of tension on the nucleus. This lack of tension on the nucleus could be part of the reason for YAP/TAZ being cytoplasmic as they are not able to enter the nucleus when cells are depleted of *DOCK5*.

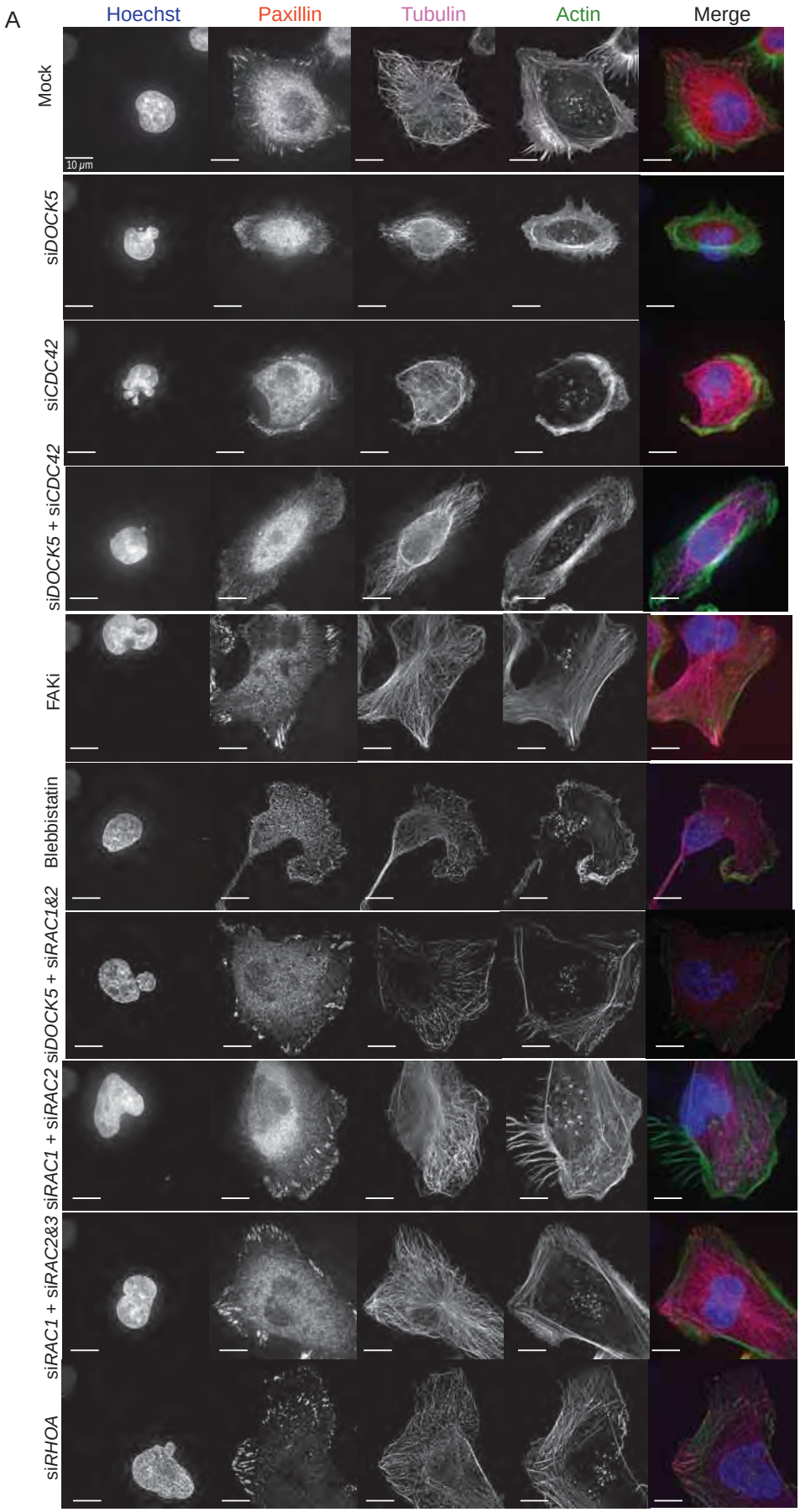
A
Hoechst
Paxillin
Tubulin
Actin
Merge
Mock
10 µm
siDOCK5
siCDC42
siDOCK5 + siCDC42
FAKi
Blebbistatin
siDOCK5 + siRAC1&2
siRAC1 + siRAC2
siRAC1 + siRAC2&3
siRHOA

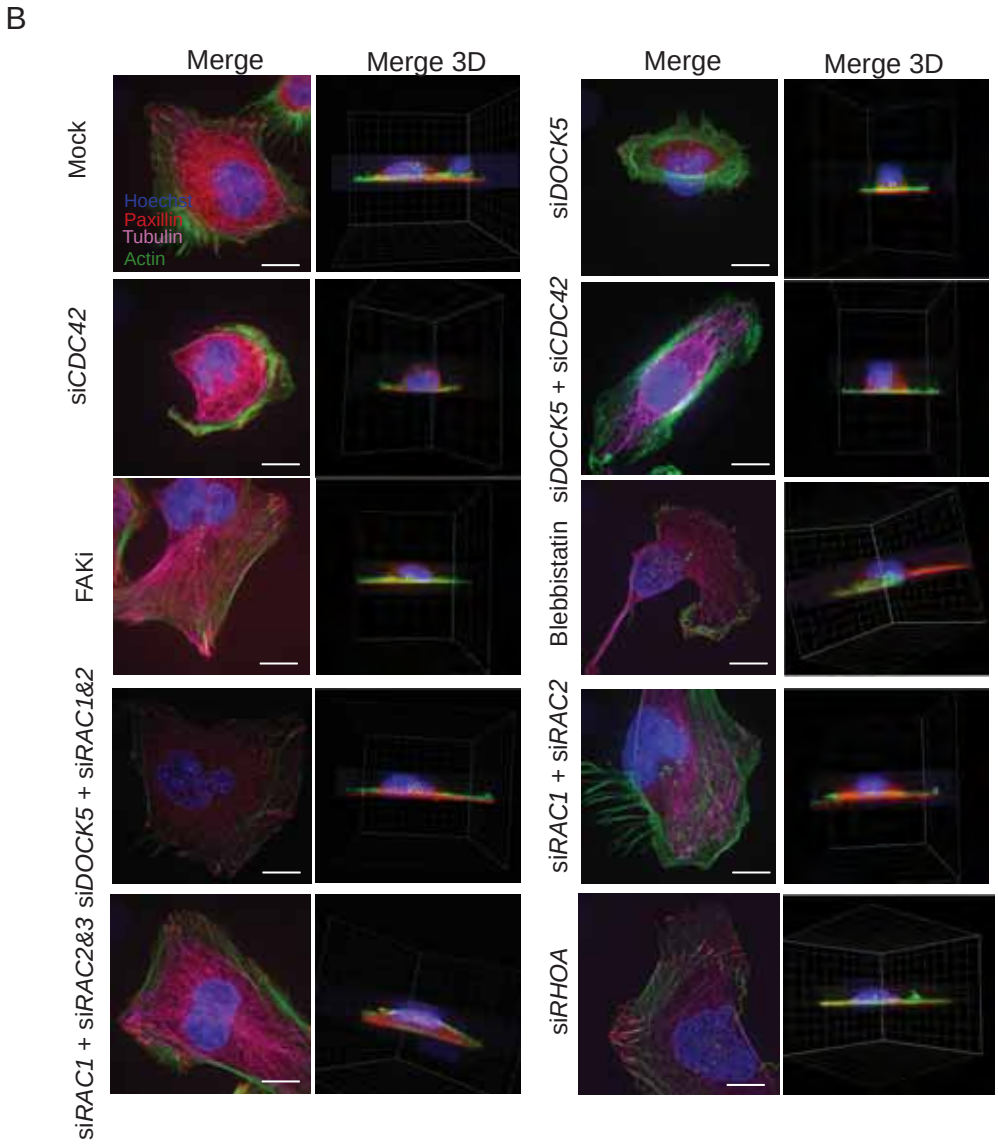

Figure 5.12 *DOCK5* depletion results in nucleus uncoupling from cytoskeleton Images taken on SoRA for mock, si*DOCK5*, si*CDC42,* si*DOCK5* + si*CDC42,* si*DOCK5* + si*RAC1*+ si*RAC2,* si*RAC1*+ si*RAC2,* si*RAC1* + si*RAC2*+ si*RAC3,* si*RHOA,* and treated with FAKi, and Blebbistatin. Stained for DNA (blue), Paxillin (orange), α-tubulin (pink), F-actin (green). (A) 2D images. (B) 3D projections. Scale bar = 10μm.

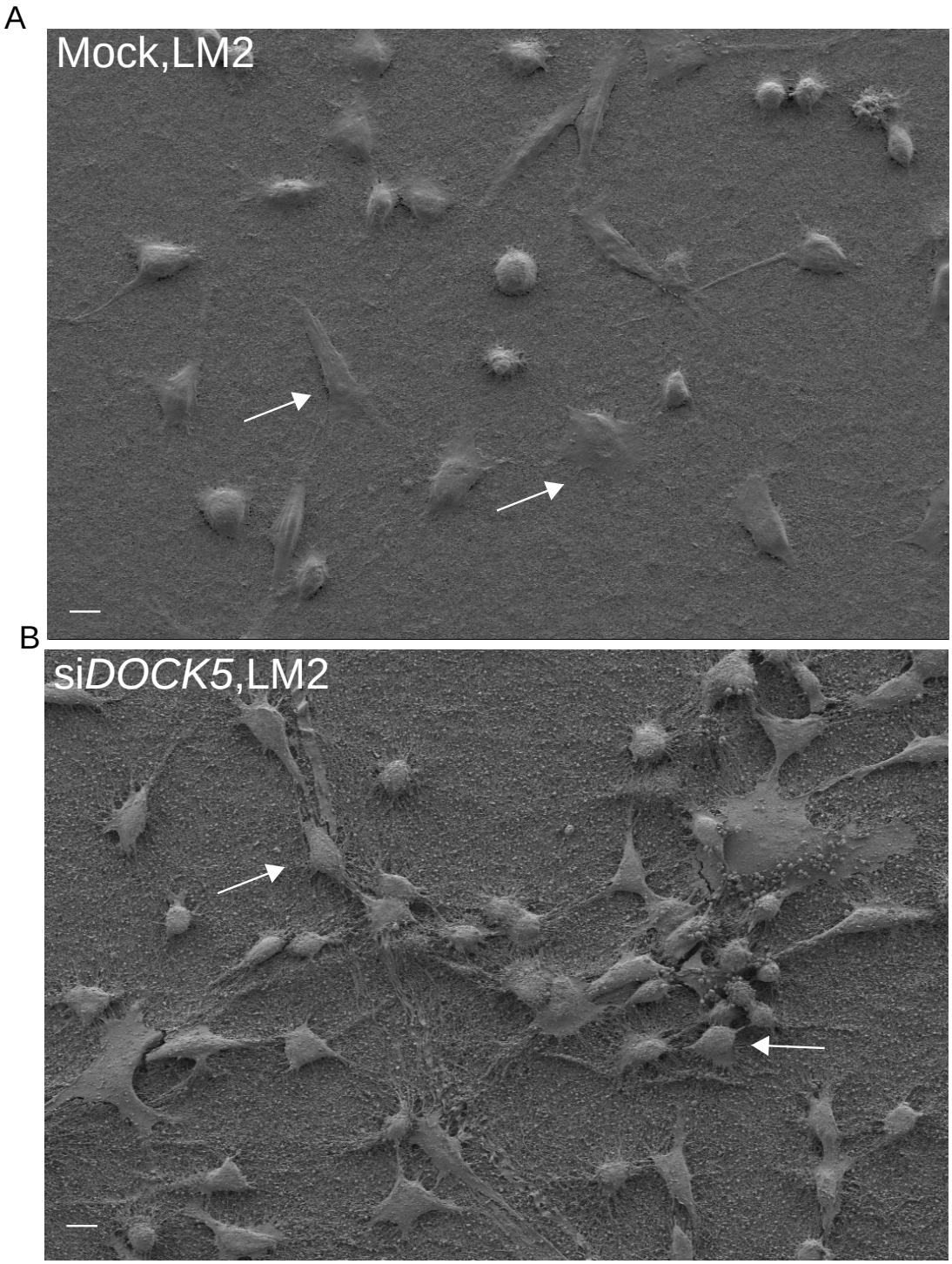

Figure 5.13 Phenotype of *DOCK5* depletion observed via SEM
SEM images of (A) mock (B) si*DOCK5* transfected LM2 cells on a thin layer of collagen type I (2µg/ml). Arrows pointing to differing phenotypes. Samples prepared by myself up until fixation, then prepared for SEM by David Robertson (ICR) and Innes Clatworthy (Natural History Museum). Images were taken by David Robertson.

5.3 Discussion

Cancer cells need to dynamically remodel their cytoskeleton in order to metastasise (Fife et al., 2014; Kass et al., 2007; Wirtz et al., 2011). Because RhoGEFs activate the signalling pathways which lead to cytoskeleton and transcriptional changes, they present attractive therapeutic targets. Although RhoGEF-Rho GTPase signalling, and YAP/TAZ signalling have been shown to be dysregulated in YAP/TAZ, only a few studies link RhoGEF-Rho GTPase signalling to YAP/TAZ (Diamantopoulou et al., 2017; Feng et al., 2014, 2019; Heidary Arash et al., 2014; Lin et al., 2017; Sabra et al., 2017; Sero and Bakal, 2017; Sorrentino et al., 2014), and none do so in highly metastatic TNBC. By performing high-throughput RNAi screens on 142 RhoGEF/GAPs, we identified DOCK5 as a key regulator of cell shape and activator of YAP/TAZ in the highly metastatic TNBC cell line LM2.

More generally, these data suggest that DOCK5 plays an important role in coordinating leading edge with microtubule dynamics and adhesions driving invasion through YAP/TAZ in TNBC. We show that DOCK5 is required for single cell invasion in 3D collagen assays as well as for 2D migration, and that this is likely due to the effect of DOCK5 in stabilising front rear polarity, as observed by the low frequency of Golgis oriented towards the wound in *DOCK5* depleted cells (Figure 5.3). The most dramatic effects were observed in wound healing assays and 3D collagen rather than in 2D migration, suggesting a bigger role for DOCK5 in collective rather than single cell migration. Further, our data show that DOCK5 regulates focal adhesion dynamics, confirming that DOCK5 localises to focal adhesions (Frank et al., 2017; Müller et al., 2018). FAK inhibition, blebbistatin and

Y27 treatments all decreased YAP/TAZ ratio further in *DOCK5* depleted cells, suggesting that there is decreased tension in cells depleted of *DOCK5* mediated by FAK which is in part responsible for the decrease in nuclear YAP/TAZ. DOCK5 is a RAC1-GEF, and its closest homologue DOCK1, has been shown to activate RAC1 at the front of migrating cells (Goicoechea et al., 2014; Kiyokawa et al., 1998). However, our data suggest that DOCK5 is not mediating its regulation of focal adhesions via RAC1, as the phenotype we observed by depletion of each Rho GTPase was that DOCK5 regulates focal adhesion dynamics in a more similar way to CDC42. Our spreading and growth assays also suggest that DOCK5 is not mediating its effect on microtubule dynamics via RAC1, but rather that there is synergistic interplay with CDC42. In fact, treatment with C21, reduced YAP/TAZ ratio to the same level as just depleting *DOCK5*, and also decreased nuclear to ring region SKP2, and GSK3β at the membrane. Suggesting that although C21 inhibits the interaction of DOCK5 with RAC1 (Ferrandez et al., 2017), this also somehow results in blocking the interaction of DOCK5 with AKT- NCK2, preventing GSK3β phosphorylation and stabilisation at the membrane.

Proteomic analysis of TNBC cell lines depleted of *DOCK5* demonstrate the interplay between DOCK5 and AKT signalling, as displayed by the significant downregulation of GSK3β levels, FOXO3A and the upregulation of the AKT inhibitor PHLPP2. Our data suggest that there is a decrease in AKT signalling via the AKT-SKP2 signalling axis. Further, our data suggest that increasing pGSK3β at the leading edge is not sufficient to drive YAP/TAZ into the nucleus and that it must be phosphorylated by AKT to have an effect on YAP/TAZ. Given that studies

have shown that DOCK5 associates with NCK2 and AKT1 to phosphorylate and inactivate GSK3β in mast cells and regulates microtubule dynamics (Guimbal et al., 2019; Ogawa et al., 2014) and that microtubule capture at the leading edge is required to generate force on the nucleus, suggests that the interaction between DOCK5, NCK2, and AKT1 is required for pGSK3β to be stable at the leading edge for microtubule stability to exert force on the nucleus and allow YAP/TAZ translocation to the nucleus. Indeed, we found that depletion of *DOCK5* resulted in a nucleus that is uncoupled from the cytoskeleton (Figure 5.13), a phenotype recapitulated both by *CDC42* depletion alone, and by combined depletion of *DOCK5* and *CDC42*. Further, the fact that this phenotype was rescued by a combined depletion of *DOCK5, RAC1*, and *RAC2*, suggests that RAC1 and RAC2 may be inhibiting CDC42 in the absence of *DOCK5*, and that DOCK5 and CDC42 are working synergistically to regulate microtubule dynamics in TNBC cells. *DOCK5* depletion resulted in slower growth rates at a 72 hour time point, which was recapitulated by *CDC42* depletion, and also enhanced when both were depleted in combination. This effect on growth is likely a combination of the uncoupled nucleus from cytoskeleton and the concomitant increase in p21, p27, and p57 observed via proteomics. In fact, cross-inhibition between the RAS and AKT signalling pathways has been observed (Castellano and Downward, 2011; Gire et al., 2000; Mendoza et al., 2011), which could explain the increase in protein abundance levels of CYLIN D and E, and of p21 and p27, and the decrease in GSK3β as a result of DOCK5 depletion. Such that AKT signalling is dampened in the absence of DOCK5, resulting in signalling via RAS. We also found that *DOCK5* depletion is synthetic lethal with MEK (MAP2K) inhibition, which could mean that in LM2 cells mutant KRAS (G13D) signalling via MEK, and

DOCK5 signalling via YAP/TAZ converge to drive viability and invasion (Figure 5.14), suggesting a potential new combination therapy for TNBC, which requires further studies. In fact, a study showed that depleting *DOCK5* in cells expressing KRAS (G13D) impaired their viability (Luo et al., 2009), suggesting that cells can be dependent on DOCK5 for survival. Because of the way Minn et al, 2005, selected LM2 cells to be highly metastatic to the lung through a series of selection rounds after tail-vein injections, these data suggest that LM2 have become more dependent on DOCK5-YAP/TAZ signalling for survival. Interestingly, our spheroid assays suggest that without *DOCK5*, cells only proliferate, contrary to 2D, where DOCK5 is required for proliferation and microtubule stability. This could suggest that in a 3D environment cells require DOCK5 to invade, and without it they primarily proliferate, such as for example in a primary tumour. Such that, in cells with non dysregulated DOCK5 simply proliferate as do MDA-MB-231 in a primary tumour context, whereas those with dysregulated DOCK5 as are LM2 invade local tissue and metastasise. An interesting avenue to pursue.

Further, CDC42 has been shown to regulate microtubule stability and establishment of polarity via PAR6 and PKCζ mediated phosphorylation of GSK3β at the leading edge of migrating cells (Etienne-Manneville, 2004; Etienne-Manneville and Hall, 2003b, 2003a). Therefore, the synergistic effect observed with *DOCK5* and *CDC42* depletion suggests that GSK3β phosphorylation at the leading edge is mediated both by DOCK5-AKT, and CDC42-PAR6-PKCζ signalling. In addition, the significant decrease in protein abundance levels of GSK3β upon DOCK5 depletion, suggests that DOCK5 is required for GSK3β stability. Overall, we propose that DOCK5 gets recruited to focal adhesions,

where it forms a complex with NCK2 and AKT resulting in the phosphorylation and stabilisation of GSK3β at the leading edge, which is then enhanced and maintained by CDC42-PAR6-PKCζ, establishing polarity by promoting microtubule capture and stability which generates force on the nucleus leading to increased YAP/TAZ activity, driving invasion in TNBC (Figure 5.14A). Furthermore, when DOCK5 is not present, focal adhesions do not mature into focal contacts, AKT and NCK2 no longer associate, GSK3β does not get phosphorylated and stabilised at the leading edge, and consequently CDC42 cannot establish polarity, resulting in microtubule dynamic instability, decreased tension on the nucleus, and cytoplasmic YAP/TAZ (Figure 5.14B). In addition, cells lacking DOCK5, become dependent on KRAS signalling via MEK, which when inhibited is synthetic lethal with *DOCK5* depletion. Therefore, this mechanism warrants further studies, and we propose DOCK5 is an attractive therapeutic target for TNBC.

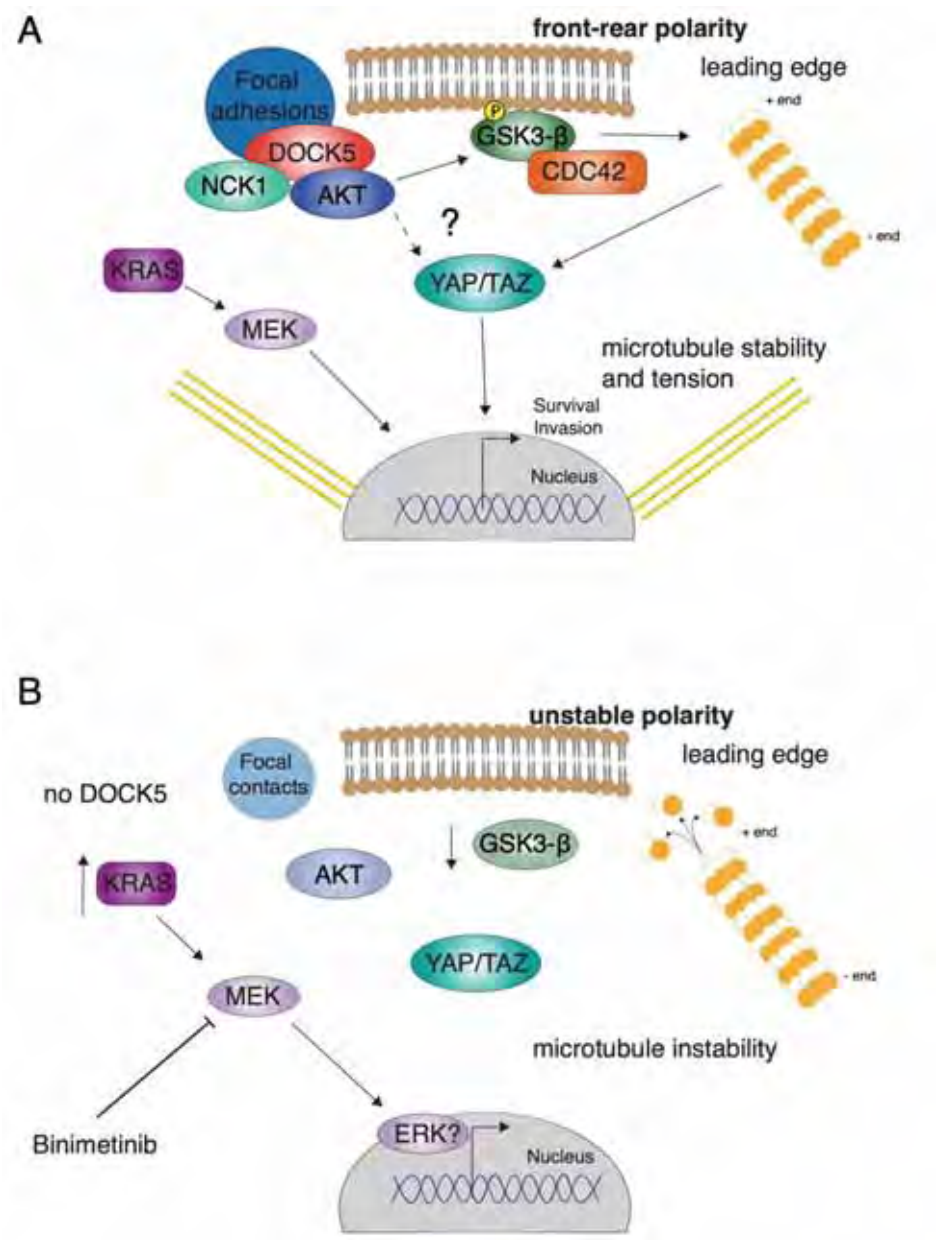

Figure 5.14 Proposed model: DOCK5 coordinates leading edge with microtubule dynamics and adhesions driving invasion through YAP/TAZ. Schematic representation of our proposed model where (A) DOCK5 gets recruited to focal adhesions where it forms a complex with NCK2 and AKT (Ogawa et al., 2014), resulting in the phosphorylation and stabilisation of GSK3β at the leading edge which is then enhanced and maintained by CDC42 establishing polarity by promoting microtubule capture and stability (Etienne-Manneville and Hall, 2003b; Guimbal et al., 2019; Ogawa et al., 2014). Microtubule stability results in microtubule tension which drives YAP/TAZ into the nucleus driving invasion. Dashed line indicates a possible AKT signalling axis we have not yet described. Further KRAS signalling through MEK also drives viability in these cells, which may be antagonised by AKT signalling. (B) When DOCK5 is depleted, focal adhesions do not mature into focal contacts and the association between AKT, NCK2 does not occur. As a result there is decreased AKT signalling, GSK3β does not get phosphorylated and stabilised at the leading edge, resulting in unstable microtubule dynamics, lack of microtubule tension, and consequent cytoplasmic YAP/TAZ and decreased invasion. KRAS signalling via MEK is no longer antagonised via AKT signalling, driving survival, possibly via ERK. Inhibition of MEK with Binimetinib in *DOCK5* knockdown background, is synthetic lethal.

Chapter 6 Discussion

Chapter 6 Discussion

6.1 Key contributions of this thesis

This thesis explores which RhoGEFs regulate TNBC cell shape, and which do so by regulating YAP/TAZ by using a combination of genetic approaches and 3D systems.

By performing high-throughput phenotypic and RNAi screens on RhoGEF/GAPs and Rho GTPases, we identified RhoGEF/GAPs which are regulating cell shape specifically in LM2, MDA-MB-231 and in both cell lines (Pascual-Vargas et al., 2017). Further, we found that the shape space that LM2 cells explore is very distinct to that of their parental and less invasive counterpart MDA-MB-231.

Further, we identified RhoGEFs which are regulating YAP/TAZ in LM2 specifically, MDA-MB-231, and both cell lines, and which ones are doing so via shape. We also found that within TNBC, more spread-like cell lines such as SUM159 and hs578t have low basal levels of YAP/TAZ activity, where shape is not coupled to YAP/TAZ, in contrast to more spindly-like cell lines such as LM2 and MDA-MB-231. Both LM2 and MDA-MB-231 have high basal levels of YAP/TAZ activity, however, we found that MDA-MB-231 sustain higher nuclear and active YAP/TAZ regardless of shape, indicating YAP/TAZ regulation uncoupled from shape. On the other hand, LM2 cells which are more metastatic than MDA-MB-231, have re-acquired the ability to downregulate YAP/TAZ by changing their shape, and thus have restored mechanotransduction making them more plastic and able to adapt to their

environment. The latter of which is particularly relevant as LM2 metastasise to the lung a tissue that is softer than breast cancer tissue which can be up to 10 times stiffer than normal breast (Barnes et al., 2017; Butcher et al., 2009; Cox and Erler, 2011). We propose high YAP/TAZ signalling, which promotes high levels of contractility and traction, may not be beneficial for migration in such soft environments, which typically involves the adoption of poorly adherent amoeboid shapes (Sanz-Moreno and Marshall, 2010; Wolf et al., 2003). Overall, we propose that mutant oncogenic signalling such as RAS-AKT pathway, is responsible for keeping YAP/TAZ nuclear and active in MDA-MB-231 and LM2 cell lines, which LM2 are able to counter and can downregulate by dynamically changing shape mediated by a specific set of RhoGEF/GAPs (Figure 6.1A).

Finally, we identified DOCK5 as a regulator of invasion via YAP/TAZ in LM2 cells and explored its mechanism of action. We found that DOCK5 regulates focal adhesion dynamics in LM2 cells in a RAC-independent manner. Further, depletion of DOCK5 resulted in a downregulation of GSK3β and upregulation of CDK inhibitor p21, p27, and p57. Because GSK3β has been shown to play a role in establishing front rear polarity (Etienne-Manneville, 2004; Etienne-Manneville and Hall, 2003a, 2003b) we hypothesised that DOCK5 contributes to the establishment of front-rear polarity in migrating cells. This role in establishing front-rear polarity, in part, explains how *DOCK5* depletion reduced invasion in 3D collagen gels, and spheroids; and also reduced wound-closure migration rates; reducing growth rates, as well as resulting in an “uncoupled” nucleus phenotype. The latter of which was

recapitulated by *CDC42* depletion. We also found that inhibiting AKT signalling reduces YAP/TAZ ratio, as well as inhibition of DOCK5 interaction with RAC1 using the inhibitor C21 (Vives et al., 2015). Collectively, our data suggests that DOCK5 coordinates leading edge microtubule dynamics and adhesions, driving invasion through YAP/TAZ. More specifically, we propose that DOCK5 gets recruited to focal adhesions, where it forms a complex with NCK2 and AKT (Ogawa et al., 2014) resulting in the phosphorylation and stabilisation of GSK3β at the leading edge, which is enhanced by CDC42, resulting in microtubule stability, polarity and tension (Etienne-Manneville and Hall, 2003b; Guimbal et al., 2019; Ogawa et al., 2014), which drives YAP/TAZ into the nucleus. Interestingly, we also found that inhibition of mutant KRAS (G13D) by treatment with Binimetinib, a drug used in the clinic to treat metastatic melanoma, is synthetic lethal in combination with *DOCK5* knockdown. This work is in preparation for publication.

6.2 Limitations of this thesis

I have identified several limitations within this thesis, detailed below for each chapter.

6.2.1 RNAi screens for regulators of cell shape and YAP/TAZ localisation in MDA-MB-231 and LM2

siRNA screens are useful tools to identify specific genes which are important for the aspect being studied. In this case, we performed RNAi screens using two siRNA libraries, OTP and siGENOME, so that hits

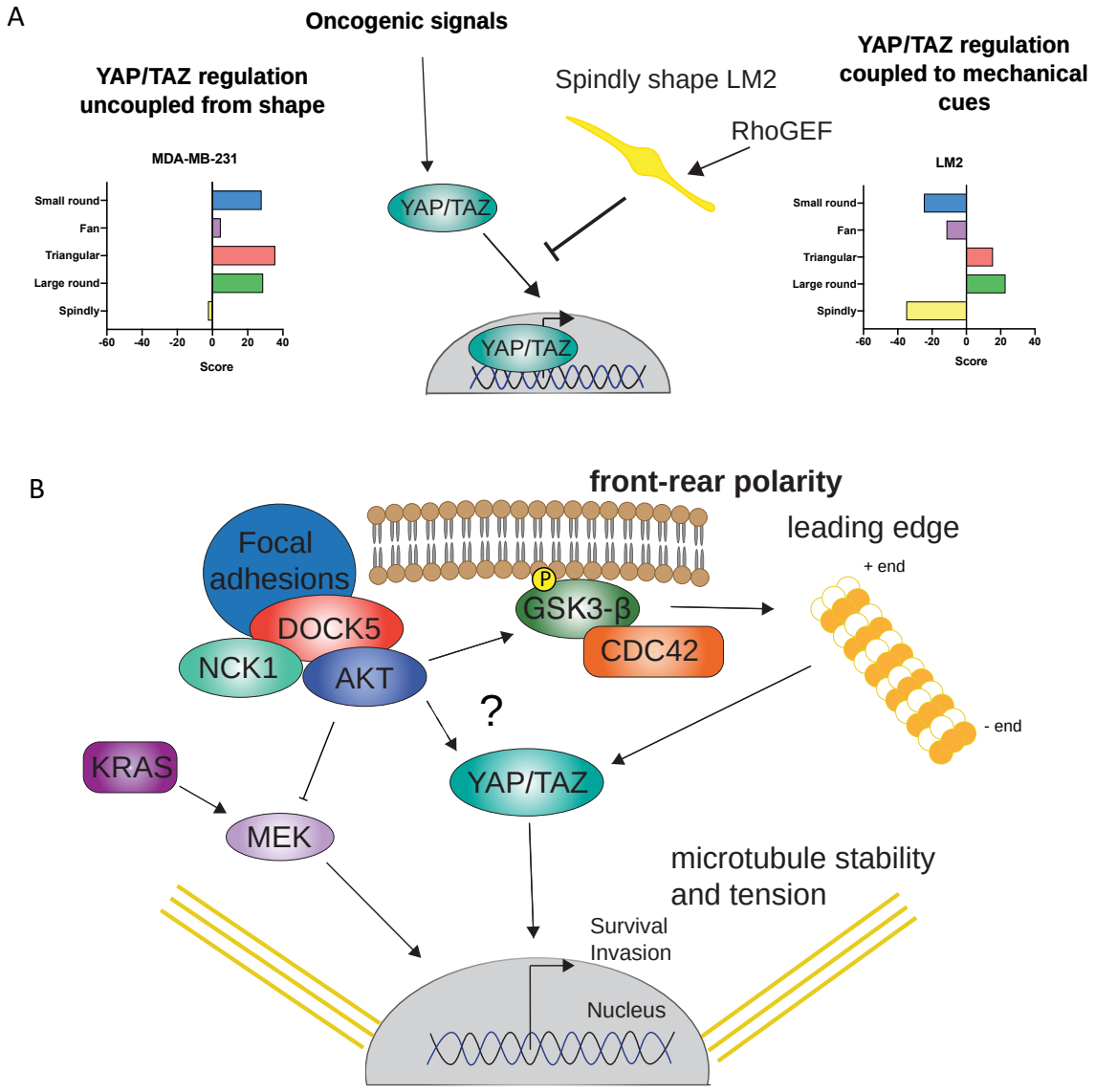

Figure 6.1 Schematic representation of overall conclusions from this thesis
(A) Schematic representation of our hypothesis that mutant oncogenic signals keep YAP/TAZ nuclear and active in LM2 and MDA-MB-231, which LM2 are able to counter and downregulate via changes in shape, mediated by a specific set of RhoGEFs. PLSR analysis shows that there are no negative predictors of YAP/TAZ ratio for MDA-MB-231 and as such YAP/TAZ regulation appears uncoupled from shape in this cell line, whereas in LM2 spindly shape is a strong negative predictor of YAP/TAZ suggesting restored mechanotransduction.
(B) We propose that DOCK5 gets recruited to focal adhesions where it forms a complex with NCK2 and AKT (Ogawa et al., 2014), resulting in the phosphorylation and stabilisation of GSK3β at the leading edge which is then enhanced and maintained by CDC42 establishing polarity by promoting microtubule capture and stability (Etienne-Manneville and Hall, 2003b; Guimbal et al., 2019; Ogawa et al., 2014). Microtubule stability results in microtubule tension which drives YAP/TAZ into the nucleus driving invasion. Dashed line indicates a possible AKT signalling axis we have not yet described. Further KRAS signalling through MEK also drives viability in these cells, which may be antagonised by AKT signalling.

identified for both screens are likely to be due to depletion of the gene rather than to off-target effects. This is because the sequences targeted between both libraries are different and the OTP library contains a patented dual strand modification that reduces off-target effects. In addition, before performing our screens, we could have explored the expression levels of all RhoGEF/GAPs in patient/cell line databases. However, in an effort to not bias our screens we did not do so, as well as because mRNA expression does not necessarily correlate with protein expression or essentiality. Further, technically it is as easy to screen all RhoGEF/GAPs than to just test a few.

However, it is impractical, time consuming, and expensive to validate all the genes targeted in these screens. Therefore, any genes to be studied should be validated via mRNA and protein levels to ensure that the gene being targeted has been depleted significantly. We were able to do so for *DOCK5* using the individual siRNAs that form the pools for both OTP and siGENOME. The same process should be carried out for any other genes that require further study. Even so, validating siRNA gene knockdown in this manner only shows whether the gene was depleted, but not if the phenotype is due to depletion of that particular gene. Therefore, provided the gene of interest is not required for cell growth, generation of CRISPR knockout cell lines is an could be an additional form of validation. Further, overexpression to rescue the phenotype would be another form of validation.

In addition, even though the screens were performed in duplicate plates, they were not performed on duplicate days. Doing so would provide more robust results.

6.2.2 Regulation of YAP/TAZ in TNBC cell lines

Aside from the siRNA screening limitations, we only performed these screens in 2D which do not recapitulate *in vivo* environments. Validation of hits that regulate YAP/TAZ in LM2, MDA-MB-231, SUM159, and hst578 in a 3D environment would provide more information on how RhoGEFs are regulating YAP/TAZ differentially in these different cell lines. Further, it would be interesting to see how these cells' regulation of YAP/TAZ differs from 2D to 3D.

In addition, LM2, MDA-MB-231, SUM159, and hs578t were all classified as MSL by Lehmann et al., 2012. Therefore, using cell lines classified into other subtypes varying in metastatic ability would reinforce our findings on the differences between highly and weakly metastatic cell lines.

6.2.3 DOCK5 coordinates leading edge with microtubule dynamics and adhesions, driving invasion through YAP/TAZ

Although proteomics of total protein abundance provided information which led us to a mechanistic insight of how DOCK5 is regulating YAP/TAZ,

phospho-proteomics would have been more informative given that we are looking at YAP/TAZ activity.

Although studies have shown that DOCK5 forms a complex with NCK2 and AKT in osteoclasts (Ogawa et al., 2014), we did not perform a co-immunoprecipitation assay to confirm this. We have also not shown how GSK3β gets degraded upon DOCK5 depletion, or how DOCK5 regulates microtubule instability. Further, our data is primarily immunofluorescence based, western blot validation of this data would be useful.

A further limitation of this study is that Y27632 is not the best ROCK inhibitor, and that the concentration we used of blebbistatin may not completely inhibit contractility, resulting in active RHOA. A solution to this would have been to knock down RHOA. In addition, we did not show that DOCK5 affects contractility, which could be explored by measuring phosphor-myosin levels.

It is important to note that there are limitations of measuring viability with the Incucyte. For example, because it measures area covered by cells, if cells are bigger this may give confounding results. However, we checked the images and the data represents them correctly.

In addition, we did not rescue the phenotype of *DOCK5* depletion by establishing front rear polarity in an si*DOCK5* background. We were also

not able to generate a *DOCK5* CRISPR knockout cell line due to the defect in cell growth as a result of *DOCK5* depletion.

A limitation of this study is that the concentration of C21 used was 100μM, which was obtained by performing a dose-response curve. It is also the concentration used in assays and the concentration used by Vives et al., 2015, who identified C21 as a DOCK5 inhibitor. For this reason, and because C21 is specific for the inhibition of DOCK5's GEF activity on RAC1, we do not have reason to believe it is having off-target effects. However, it is a very large amount and could therefore be having off-target effects. To solve this limitation, lower concentrations could be tested to find the lowest concentration required for the desired effect.

Further, a limitation is that we used microtubule staining to measure cell size, due to the microtubule phenotype arising after this quantification. Such that was has been quantified as cell size change could be due to microtubule change rather than cell size. A solution to this would be to use microtubule staining to estimate microtubule reorganisation or stabilisation and adjust cell size to this. Further, quantifying cell size with the F-actin stain as well would allow us to understand better cell size changes versus microtubule specific changes.

Lastly, our studies are performed in 2D and morphological changes were not assessed in a 3D context. Linear classifiers were run in 3D, where 4 instead of 5 shapes were identified: Spindly, large spread, small round, and

star. A preliminary experiment showed that LM2 cells in bovine collagen versus rat tail had higher proportion of spindly cells. Further, the ratio of spindly to round cells in mock versus si*DOCK5* transfected cells was significantly higher in *DOCK5* KD cells compared to mock, in a 2mg/ml rat tail collagen gel. Given the effect on microtubules *DOCK5* depletion has, and the loss of polarity observed in 2D, although *DOCK5* was a hit for fan shape and not spindly shape in LM2, these data suggest that 2D data relates to 3D. Such that the loss of polarity is recapitulated in 3D, and perhaps could explain the decrease in invasion observed with si*DOCK5*. More repeats would confirm if this is the case.

6.3 Future directions

The work presented in this thesis would be additive to stratification based on DNA/RNA as it is completely different and is based on deregulated activity rather than expression. Changes in activity or rewiring of Rho GTPase signalling pathways are very difficult to stratify so perhaps a combination of both would be a more useful approach.

siRNA screens generated a lot of data which would be interesting to pursue. Hits outlined in Chapters 3 and 4, as well as genetic interactions could be validated and further explored. To confirm that LM2 are dynamically changing shape compared to MDA-MB-231, live imaging of these cells could be performed. In addition, given that LM2 cells were obtained for their lung colonisation advantage, could suggest that they may not necessarily

be more invasive than MDA-MB-231, but rather just better at adapting. Because Minn et al., 2005, show that LM2 cells injected into the mammary fat pad also metastasise to the lung, this is unlikely to be the case. However, testing invasive capabilities of LM2 versus MDA-MB-231 in collagen invasion assays would be interesting.

This thesis was focused on identifying RhoGEFs rather than Rho GTPases as Rho GTPases are more difficult to target due to their ubiquitous and conserved nature. However, interestingly ARHGEF2, ARHGEF3, ARHGEF18 and ARHGEF12 all of which are GEFs for RHOA, were hits for low YAP/TAZ ratio in LM2, which could make RHOA an interesting avenue to pursue regarding YAP/TAZ activation and invasiveness in LM2. Further, the paralogs ARHGEF5 and ARHGEF35 were hits for low YAP/TAZ ratio in SUM159, suggesting that perhaps paralogs could be differentially expressed.

Further processing of proteomic data to identify more relevant pathways involved in DOCK5-YAP/TAZ signalling would be interesting to pursue. We observed that there were nuclear abnormalities following *DOCK5* depletion, and experiments performed by Mar Arias-Garcia (Bakal lab) show that *DOCK5* depleted cells have less DNA damage to wild-type LM2 cells (data not shown), which suggest that DOCK5 either allows cells to keep dividing despite DNA damage, or prevents cells from sensing DNA damage. It is important to note that the BRCA1 mutation status in LM2 and MDA-MB-231 is wild-type, with a BRCA1 allelic loss (Elstrodt et al, 2006). Studies have

shown that BRCA1 regulates microtubule stability indirectly (Sung and Giannakakou et al., 2014), where *BRCA1* knockdown results in increased microtubule dynamics conferring taxane resistance and suggesting BRCA1 is not acting as it should. This could also suggest a synergistic effect between BRCA1 and DOCK5. However, our DNA damage data seems to suggest the opposite phenotype such that there is less DNA damage with DOCK5 depletion. Future studies to reconcile this data would involve recapitulating the DOCK5 phenotype by depleting BRCA1 in LM2 cells. In addition, we did not use gene ontology programmes to gain a further understanding of the signalling pathways affected by DOCK5 depletion. Preliminary post hoc analysis using Ingenuity Pathway Analysis (QIAGEN) revealed that DOCK5 depletion affects the following pathways the most in order: liver x receptor/retinoid x receptor, acute phase response signalling, G1/S checkpoint regulation, hepatic fibrosis and cyclins and cell cycle regulation. Cell cycle regulation is of most interest to us as we observed a growth defect in 2D, which is not observed in 3D spheroids, and which is an interesting avenue to pursue. Further, it links GSK3β and cyclin dependent kinases. Of course, PI3K/AKT as well as Wnt signalling pathways were also altered. Of particular interest, is that proteins involved in the inhibition of matrix metalloproteases (A2M, TIMP2, TIMP3) were upregulated and MMP14 was downregulated. This could suggest that DOCK5 depletion reduces invasion in 3D collagen as a result of decreased matrix metalloprotease secretion. Although to confirm this, 3D collagen invasion assays with matrix metalloprotease inhibitors as well as knocking down

A2M, TIMP2, and TIMP3 would have to be performed. Nevertheless, it is an interesting avenue to pursue.

Further, we measured focal adhesion dynamics on fibronectin, while quantifying invasion in collagen. The reason for this is because fibronectin is a better model to study adhesion dynamics as LM2 cells adhere much better to fibronectin than to collagen, and we do not extrapolate our findings from fibronectin to 3D. However, arguably, less stable adhesions would make it harder for cells to invade if they cannot form proper attachments to the matrix to exert force to move through the matrix. Combining this with the proteomic data showing enrichment in metalloprotease inhibition, could explain how DOCK5 depletion reduces invasion in 3D collagen. Preliminary data from a collaboration with John-Robert Davis at the Francis Crick Institute, using traction force microscopy suggest that DOCK5 is required to exert force on a fibronectin as predicted from focal adhesion analysis. Nevertheless, studying focal adhesion dynamics on collagen would be an interesting avenue to explore further.

In addition, in Chapter 4 of this thesis we discuss that larger cells have higher YAP/TAZ ratios, while those that are spindly have lower YAP/TAZ ratios. A relationship which varies depending on cell lines. Although we saw no effect of nuclear size on YAP/TAZ ratio, studying this further could give insights on whether cells are stressed and whether nuclear size can give an indication of the relationship between DNA damage and YAP/TAZ.

Studying YAP/TAZ dynamics live would also be interesting to understand how shuttling to and from the nucleus is regulated. I generated constructs to endogenously tag YAP and TAZ using the CRISPR Cas-9 system. However, cells did not survive the transfection. Further studies to explore and correct this would be interesting.

The upregulation of p21, p27, p57, CYCLIN E, and CYCLIN D as a result of DOCK5 depletion is also an avenue that would be interesting to explore further, aside from the effect on cell growth we observed after 72 hours of transfection. Cell cycle analysis at 72 hours via FACS would provide more information. Further, the fact that inhibition of KRAS (G13D) is synthetic lethal with *DOCK5* knockdown suggests that KRAS is signalling via MEK, which could explain increased levels of CYCLIN D and CYCLIN E, therefore testing whether there is more nuclear ERK would be a first step to understand this mechanism better for potential combination therapies to treat TNBC. In addition, testing a combination of C21 and Binimetinib on growth in LM2 cells would suggest a new avenue of treatment for TNBC. Further, although the mitotic index was quantified, it was not followed up on. Given that invasiveness without proliferation is not as dangerous, and that DOCK5 was a hit for increased multinuclearity in both LM2 and MDA-MB-231, would be important to keep in mind for future assays.

Lastly, although Frank et al., 2017 showed that DOCK5 is required for metastasis *in vivo* using MDA-MB-231 cells, testing this in LM2 cells *in vivo* would confirm our results. Also, although DOCK5 does not appear to

depend on RAC1 to regulate YAP/TAZ, using the DOCK5 inhibitor C21, reduced YAP/TAZ ratio to the same levels as just depleting *DOCK5* suggesting that using it would be able to reduce metastasis. C21 blocks the DHR2 catalytic domain of DOCK5, specifically hindering the interaction between DOCK5 and RAC1 (Ferrandez et al., 2017), however our data shows that treatment with C21 also reduced SKP2 nuclear to ring region ratio and GSK3β at the membrane, which suggests that C21 may be disrupting the interaction DOCK5 and AKT-NCK2. This avenue would be interesting to explore further, as well as understanding what role RAC1 may be playing. Nevertheless, testing this inhibitor *in vivo*, alone and in combination with Binimetinib would present DOCK5 as a target to prevent TNBC metastasis as current available treatments are for when metastasis has already taken place. Therefore, the idea behind our approach would be preventing metastasis, such that intervention would occur after primary tumour resection, in such a way that this would prevent the cells' ability to change shape and metastasise.

Bibliography

Abercrombie, M. (1979). Contact inhibition and malignancy. Nature *281*, 259–262.

Adamowicz, M., Radlwimmer, B., Rieker, R.J., Mertens, D., Schwarzbach, M., Schraml, P., Benner, A., Lichter, P., Mechtersheimer, G., and Joos, S. (2006). Frequent amplifications and abundant expression of TRIO, NKD2, and IRX2 in soft tissue sarcomas. Genes. Chromosomes Cancer *45*, 829–838.

Alfano, D., Ragno, P., Stoppelli, M.P., and Ridley, A.J. (2012). RhoB regulates uPAR signalling. Journal of Cell Science *125*: 2369-2380.

Amin, E., Dubey, B.N., Zhang, S.-C., Gremer, L., Dvorsky, R., Moll, J.M., Taha, M.S., Nagel-Steger, L., Piekorz, R.P., Somlyo, A.V., et al. (2013). Rho-kinase: regulation, (dys)function, and inhibition. Biol. Chem. *394*, 1399–1410.

Anders, C.K., and Carey, L.A. (2009). Biology, Metastatic Patterns, and Treatment of Patients with Triple-Negative Breast Cancer. Clin. Breast Cancer *9*, S73–S81.

Aragona, M., Panciera, T., Manfrin, A., Giulitti, S., Michielin, F., Elvassore, N., Dupont, S., and Piccolo, S. (2013). A Mechanical Checkpoint Controls Multicellular Growth through YAP/TAZ Regulation by Actin-Processing Factors. Cell *154*, 1047–1059.

Aronheim, A., Broder, Y.C., Cohen, A., Fritsch, A., Belisle, B., and Abo, A. (1998). Chp, a homologue of the GTPase Cdc42Hs, activates the JNK pathway and is implicated in reorganizing the actin cytoskeleton. Curr. Biol. CB *8*, 1125–1128.

Asghar, U.S., Barr, A.R., Cutts, R., Beaney, M., Babina, I., Sampath, D., Giltnane, J., Lacap, J.A., Crocker, L., Young, A., et al. (2017). Single-Cell Dynamics Determines Response to CDK4/6 Inhibition in Triple-Negative Breast Cancer. Clin. Cancer Res. *23*, 5561–5572.

Bakal, C., Aach, J., Church, G., and Perrimon, N. (2007). Quantitative Morphological Signatures Define Local Signaling Networks Regulating Cell Morphology. Science *316*, 1753–1756.

Bao, Y., Hata, Y., Ikeda, M., and Withanage, K. (2011). Mammalian Hippo pathway: from development to cancer and beyond. J. Biochem. (Tokyo) *149*, 361–379.

Barnes, J.M., Przybyla, L., and Weaver, V.M. (2017). Tissue mechanics regulate brain development, homeostasis and disease. J. Cell Sci. *130*, 71–82.

Bauer, K.R., Brown, M., Cress, R.D., Parise, C.A., and Caggiano, V. (2007). Descriptive analysis of estrogen receptor (ER)-negative, progesterone receptor (PR)-negative, and HER2-negative invasive breast cancer, the so-called triple-negative phenotype. Cancer *109*, 1721–1728.

Bellovin, D.I., Simpson, K.J., Danilov, T., Maynard, E., Rimm, D.L., Oettgen, P., and Mercurio, A.M. (2006). Reciprocal regulation of RhoA and RhoC characterizes the EMT and identifies RhoC as a prognostic marker of colon carcinoma. Oncogene *25*, 6959–6967.

Bernards, R., and Weinberg, R.A. (2002). Metastasis genes: A progression puzzle. Nature *418*, 823–823.

Besson, A., Dowdy, S.F., and Roberts, J.M. (2008). CDK Inhibitors: Cell Cycle Regulators and Beyond. Dev. Cell *14*, 159–169.

Birmingham, A., Selfors, L.M., Forster, T., Wrobel, D., Kennedy, C.J., Shanks, E., Santoyo-Lopez, J., Dunican, D.J., Long, A., Kelleher, D., et al. (2009). Statistical methods for analysis of high-throughput RNA interference screens. Nat. Methods *6*, 569–575.

Bishop, A.L., and Hall, A. (2000). Rho GTPases and their effector proteins. 15.

Bos, J.L., Rehmann, H., and Wittinghofer, A. (2007). GEFs and GAPs: Critical Elements in the Control of Small G Proteins. Cell *129*, 865–877.

Bouquier, N., Vignal, E., Charrasse, S., Weill, M., Schmidt, S., Léonetti, J.-P., Blangy, A., and Fort, P. (2009). A Cell Active Chemical GEF Inhibitor Selectively Targets the Trio/RhoG/Rac1 Signaling Pathway. Chem. Biol. *16*, 657–666.

Brown, E., McKee, T., diTomaso, E., Pluen, A., Seed, B., Boucher, Y., and Jain, R.K. (2003). Dynamic imaging of collagen and its modulation in tumors in vivo using second-harmonic generation. Nat. Med. *9*, 796–800.

Brugnera, E., Haney, L., Grimsley, C., Lu, M., Walk, S.F., Tosello-Trampont, A.-C., Macara, I.G., Madhani, H., Fink, G.R., and Ravichandran, K.S. (2002). Unconventional Rac-GEF activity is mediated through the Dock180–ELMO complex. Nat. Cell Biol. *4*, 574–582.

Brunet, A., Park, J., Tran, H., Hu, L.S., Hemmings, B.A., and Greenberg, M.E. (2001). Protein Kinase SGK Mediates Survival Signals by Phosphorylating the Forkhead Transcription Factor FKHRL1 (FOXO3a). Mol. Cell. Biol. *21*, 952–965.

Burridge, K., and Wennerberg, K. (2004). Rho and Rac Take Center Stage. Cell *116*, 167–179.

Butcher, D.T., Alliston, T., and Weaver, V.M. (2009). A tense situation: forcing tumour progression. Nat. Rev. Cancer *9*, 108–122.

Calses, P.C., Crawford, J.J., Lill, J.R., and Dey, A. (2019). Hippo Pathway in Cancer: Aberrant Regulation and Therapeutic Opportunities. Trends Cancer *5*, 297–307.

Calvo, F., Sanz-Moreno, V., Agudo-Ibáñez, L., Wallberg, F., Sahai, E., Marshall, C.J., and Crespo, P. (2011). RasGRF suppresses Cdc42-mediated tumour cell movement, cytoskeletal dynamics and transformation. Nature Cell Biology, *13*(7): 819-826.

Calvo, F., Ege, N., Grande-Garcia, A., Hooper, S., Jenkins, R.P., Chaudhry, S.I., Harrington, K., Williamson, P., Moeendarbary, E., Charras, G., et al. (2013). Mechanotransduction and YAP-dependent matrix remodelling is required for the generation and maintenance of cancer-associated fibroblasts. Nat. Cell Biol. *15*, 637–646.

Cancello, G., Maisonneuve, P., Rotmensz, N., Viale, G., Mastropasqua, M.G., Pruneri, G., Veronesi, P., Torrisi, R., Montagna, E., Luini, A., et al. (2010). Prognosis and adjuvant treatment effects in selected breast cancer subtypes of very young women (<35 years) with operable breast cancer. Ann. Oncol. *21*, 1974–1981.

Carey, L.A., Perou, C.M., Livasy, C.A., Dressler, L.G., Cowan, D., Conway, K., Karaca, G., Troester, M.A., Tse, C.K., Edmiston, S., et al. (2006). Race, Breast Cancer Subtypes, and Survival in the Carolina Breast Cancer Study. JAMA *295*, 2492–2502.

Carey, S.P., Martin, K.E., and Reinhart-King, C.A. (2017). Three-dimensional collagen matrix induces a mechanosensitive invasive epithelial phenotype. Sci. Rep. *7*.

Carr, H.S., Zuo, Y., Oh, W., and Frost, J.A. (2013). Regulation of Focal Adhesion Kinase Activation, Breast Cancer Cell Motility, and Amoeboid Invasion by the RhoA Guanine Nucleotide Exchange Factor Net1. Mol. Cell. Biol. *33*, 2773–2786.

Castellano, E., and Downward, J. (2011). RAS Interaction with PI3K: More Than Just Another Effector Pathway. Genes Cancer *2*, 261–274.

Cau, J. (2005). Cdc42 controls the polarity of the actin and microtubule cytoskeletons through two distinct signal transduction pathways. J. Cell Sci. *118*, 2579–2587.

Chacón-Martínez, C.A., Kiessling, N., Winterhoff, M., Faix, J., Müller-Reichert, T., and Jessberger, R. (2013). The Switch-associated Protein 70 (SWAP-70) Bundles Actin Filaments and Contributes to the Regulation of F-actin Dynamics. J. Biol. Chem. *288*, 28687–28703.

Chaffer, C.L., and Weinberg, R.A. (2011). A Perspective on Cancer Cell Metastasis. Science *331*, 1559–1564.

Chakravarty, G., Hadsell, D., Buitrago, W., Settleman, J., and Rosen, J.M. (2003). p190-B RhoGAP Regulates Mammary Ductal Morphogenesis. Mol. Endocrinol. *17*, 1054–1065.

Chan, C.-H., Li, C.-F., Yang, W.-L., Gao, Y., Lee, S.-W., Feng, Z., Huang, H.-Y., Tsai, K.K.C., Flores, L.G., Shao, Y., et al. (2012). The Skp2-SCF E3 Ligase Regulates Akt Ubiquitination, Glycolysis, Herceptin Sensitivity, and Tumorigenesis. Cell *149*, 1098–1111.

Chang, C., Goel, H.L., Gao, H., Pursell, B., Shultz, L.D., Greiner, D.L., Ingerpuu, S., Patarroyo, M., Cao, S., Lim, E., et al. (2015). A laminin 511 matrix is regulated by TAZ and functions as the ligand for the α6Bβ1 integrin to sustain breast cancer stem cells. Genes Dev. *29*, 1–6.

Charafe-Jauffret, E., Ginestier, C., Monville, F., Finetti, P., Adélaïde, J., Cervera, N., Fekairi, S., Xerri, L., Jacquemier, J., Birnbaum, D., et al. (2006). Gene expression profiling of breast cell lines identifies potential new basal markers. Oncogene *25*, 2273–2284.

Chen, Y.-A., Lu, C.-Y., Cheng, T.-Y., Pan, S.-H., Chen, H.-F., and Chang, N.-S. (2019). WW Domain-Containing Proteins YAP and TAZ in the Hippo Pathway as Key Regulators in Stemness Maintenance, Tissue Homeostasis, and Tumorigenesis. Front. Oncol. *9*.

Chopin, M., Quemeneur, L., Ripich, T., and Jessberger, R. (2010). SWAP-70 controls formation of the splenic marginal zone through regulating T1B-cell differentiation. Eur. J. Immunol. *40*, 3544–3556.

Chu, I.M., Hengst, L., and Slingerland, J.M. (2008). The Cdk inhibitor p27 in human cancer: prognostic potential and relevance to anticancer therapy. Nat. Rev. Cancer *8*, 253–267.

Chu, J.E., Xia, Y., Chin-Yee, B., Goodale, D., Croker, A.K., and Allan, A.L. (2014). Lung-Derived Factors Mediate Breast Cancer Cell Migration through CD44 Receptor-Ligand Interactions in a Novel Ex Vivo System for Analysis of Organ-Specific Soluble Proteins. Neoplasia N. Y. N *16*, 180–191.

Clevers, H., and Nusse, R. (2012). Wnt/β-Catenin Signaling and Disease. Cell *149*, 1192–1205.

Cohen, J. (1988). Statistical power analysis for the behavioral sciences (New York, NY: Psychology Press).

Cook, D.R., Rossman, K.L., and Der, C.J. (2014). Rho guanine nucleotide exchange factors: regulators of Rho GTPase activity in development and disease. Oncogene *33*, 4021–4035.

Cooper, S., Sadok, A., Bousgouni, V., and Bakal, C. (2015). Apolar and polar transitions drive the conversion between amoeboid and mesenchymal shapes in melanoma cells. Mol. Biol. Cell *26*, 4163–4170.

Cordenonsi, M., Zanconato, F., Azzolin, L., Forcato, M., Rosato, A., Frasson, C., Inui, M., Montagner, M., Parenti, A.R., Poletti, A., et al. (2011). The Hippo transducer TAZ confers cancer stem cell-related traits on breast cancer cells. Cell *147*, 759–772.

Cortes, J.R., Ambesi-Impiombato, A., Couronnée, L., Quinn, S.A., Kim, C.S., da Silva Almeida, A.C., West, Z., Belver, L., Sanchez Martin, M., Scourzic, L., Bhagay, G., Bernarnd, O.A., Ferrando, A.A., and Palomero, T. (2018). RHOA

G17V induces T folicular helper cell specification and promotes lymphomagenesis. Cancer Cell. *33*:259-273.

Corvol, H., Rousselet, N., Thompson, K.E., Berdah, L., Cottin, G., Foussigniere, T., Longchampt, E., Fiette, L., Sage, E., Prunier, C., et al. (2018). FAM13A is a modifier gene of cystic fibrosis lung phenotype regulating rhoa activity, actin cytoskeleton dynamics and epithelial-mesenchymal transition. J. Cyst. Fibros. *17*, 190–203.

Coso, O.A., Chiariello, M., Yu, J.-C., Teramoto, H., Crespo, P., Xu, N., and Miki, T. (1995). The Small GTP-Binding Proteins Racl, and Cdc42 Regulate the Activity of the JNK/SAPK Signaling Pathway. 10.

Côté, J.-F., and Vuori, K. (2002). Identification of an evolutionarily conserved superfamily of DOCK180-related proteins with guanine nucleotide exchange activity. J. Cell Sci. *115*, 4901–4913.

Côté, J.-F., and Vuori, K. (2007). GEF what? Dock180 and related proteins help Rac to polarize cells in new ways. Trends Cell Biol. *17*, 383–393.

Cox, T.R., and Erler, J.T. (2011). Remodeling and homeostasis of the extracellular matrix: implications for fibrotic diseases and cancer. Dis. Model. Mech. *4*, 165–178.

D'Andrea, A.D., and Grompe, M. (2003). The Fanconi anaemia/BRCA pathway. Nat. Rev. Cancer *3*, 23–34.

Debily, M.-A., Camarca, A., Ciullo, M., Mayer, C., El Marhomy, S., Ba, I., Jalil, A., Anzisi, A., Guardiola, J., and Piatier-Tonneau, D. (2004). Expression and molecular characterization of alternative transcripts of the ARHGEF5/TIM oncogene specific for human breast cancer. Hum. Mol. Genet. *13*, 323–334.

Dent, R., Trudeau, M., Pritchard, K.I., Hanna, W.M., Kahn, H.K., Sawka, C.A., Lickley, L.A., Rawlinson, E., Sun, P., and Narod, S.A. (2007). Triple-Negative Breast Cancer: Clinical Features and Patterns of Recurrence. Clin. Cancer Res. *13*, 4429–4434.

Diamantopoulou, Z., White, G., Fadlullah, M.Z.H., Dreger, M., Pickering, K., Maltas, J., Ashton, G., MacLeod, R., Baillie, G.S., Kouskoff, V., et al. (2017). TIAM1 Antagonizes TAZ/YAP Both in the Destruction Complex in the Cytoplasm and in the Nucleus to Inhibit Invasion of Intestinal Epithelial Cells. Cancer Cell *31*, 621-634.e6.

Diepenbruck, M., Waldmeier, L., Ivanek, R., Berninger, P., Arnold, P., Nimwegen, E. van, and Christofori, G. (2014). Tead2 expression levels control the subcellular distribution of Yap and Taz, zyxin expression and epithelial–mesenchymal transition. J. Cell Sci. *127*, 1523–1536.

Dobrokhotov, O., Samsonov, M., Sokabe, M., and Hirata, H. (2018). Mechanoregulation and pathology of YAP/TAZ via Hippo and non-Hippo mechanisms. Clin. Transl. Med. *7*, 23.

Dongre, A., and Weinberg, R.A. (2019). New insights into the mechanisms of epithelial–mesenchymal transition and implications for cancer. Nat. Rev. Mol. Cell Biol. *20*, 69–84.

Dupont, S., Morsut, L., Aragona, M., Enzo, E., Giulitti, S., Cordenonsi, M., Zanconato, F., Le Digabel, J., Forcato, M., Bicciato, S., et al. (2011). Role of YAP/TAZ in mechanotransduction. Nature *474*, 179–183.

Dwyer, J., Azzi, S., Leclair, H.M., Georges, S., Carlotti, A., Treps, L., Galan-Moya, E.M., Alexia, C., Dupin, N., Bidère, N., et al. (2015). The guanine exchange factor SWAP70 mediates vGPCR-induced endothelial plasticity. Cell Commun. Signal. *13*, 11.

Elosegui-Artola, A., Andreu, I., Beedle, A.E.M., Lezamiz, A., Uroz, M., Kosmalska, A.J., Oria, R., Kechagia, J.Z., Rico-Lastres, P., Le Roux, A.-L., et al. (2017). Force Triggers YAP Nuclear Entry by Regulating Transport across Nuclear Pores. Cell *171*, 1397-1410.e14.

Elstrodt, F., Hollestelle, A., Nagel, J.H., Gorin, M., Wasielewski, M., van den Ouweland, A., Merajver, S.D, Ethier, S.P., Schutte, M. (2006). BRCA1 mutation analysis of 41 human breast cancer cell lines reveals three new deleterious mutants. Cancer Res. *66*(1):41-5.

Erdal, E., Ozturk, N., Cagatay, T., Eksioglu-Demiralp, E., and Ozturk, M. Lithium-mediated downregulation of PKB/Akt and cyclin E with growth inhibition in hepatocellular carcinoma cells. 8.

Etienne-Manneville, S. (2004). Cdc42 - the centre of polarity. J. Cell Sci. *117*, 1291–1300.

Etienne-Manneville, S., and Hall, A. (2001). Integrin-Mediated Activation of Cdc42 Controls Cell Polarity in Migrating Astrocytes through PKCζ. Cell *106*, 489–498.

Etienne-Manneville, S., and Hall, A. (2003a). Cell polarity: Par6, aPKC and cytoskeletal crosstalk. Curr. Opin. Cell Biol. *15*, 67–72.

Etienne-Manneville, S., and Hall, A. (2003b). Cdc42 regulates GSK-3b and adenomatous polyposis coli to control cell polarity. *421*, 4.

Feng, H., Hu, B., Jarzynka, M.J., Li, Y., Keezer, S., Johns, T.G., Tang, C.K., Hamilton, R.L., Vuori, K., Nishikawa, R., et al. (2012). Phosphorylation of dedicator of cytokinesis 1 (Dock180) at tyrosine residue Y722 by Src family kinases mediates EGFRvIII-driven glioblastoma tumorigenesis. Proc. Natl. Acad. Sci. *109*, 3018–3023.

Feng, X., Degese, M.S., Iglesias-Bartolome, R., Vaque, J.P., Molinolo, A.A., Rodrigues, M., Zaidi, M.R., Ksander, B.R., Merlino, G., Sodhi, A., et al. (2014). Hippo-Independent Activation of YAP by the GNAQ Uveal Melanoma Oncogene through a Trio-Regulated Rho GTPase Signaling Circuitry. Cancer Cell *25*, 831–845.

Feng, X., Arang, N., Rigiracciolo, D.C., Lee, J.S., Yeerna, H., Wang, Z., Lubrano, S., Kishore, A., Pachter, J.A., König, G.M., et al. (2019). A Platform of Synthetic Lethal Gene Interaction Networks Reveals that the GNAQ Uveal Melanoma Oncogene Controls the Hippo Pathway through FAK. Cancer Cell *35*, 457-472.e5.

Ferrandez, Y., Zhang, W., Peurois, F., Akendengué, L., Blangy, A., Zeghouf, M., and Cherfils, J. (2017). Allosteric inhibition of the guanine nucleotide exchange factor DOCK5 by a small molecule. Sci. Rep. *7*, 1–13.

Fife, C.M., McCarroll, J.A., and Kavallaris, M. (2014). Movers and shakers: cell cytoskeleton in cancer metastasis: Cytoskeleton and cancer metastasis. Br. J. Pharmacol. *171*, 5507–5523.

Fisher, M.L., Grun, D., Adhikary, G., Xu, W., and Eckert, R.L. (2017). Inhibition of YAP function overcomes BRAF inhibitor resistance in melanoma cancer stem cells. Oncotarget *8*, 110257–110272.

Fort, P., and Blangy, A. (2017). The Evolutionary Landscape of Dbl-Like RhoGEF Families: Adapting Eukaryotic Cells to Environmental Signals. Genome Biol. Evol. *9*, 1471–1486.

Foulkes, W.D., Smith, I.E., and Reis-Filho, J.S. (2010). Triple-Negative Breast Cancer. N. Engl. J. Med. *363*, 1938–1948.

Frank, S.R., Köllmann, C.P., van Lidth de Jeude, J.F., Thiagarajah, J.R., Engelholm, L.H., Frödin, M., and Hansen, S.H. (2017). The focal adhesion-associated proteins DOCK5 and GIT2 comprise a rheostat in control of epithelial invasion. Oncogene *36*, 1816–1828.

Frank, S.R., Köllmann, C.P., Luong, P., Galli, G.G., Zou, L., Bernards, A,m Getz, G., Calogero, R.A., Frödin, M., and Hansen, S.H. (2018). p190 RhoGAP promotes contact inhibition in epithelial cells by repressing YAP activity. JCB *217*(9) 3183-3201.

Gadea, G., and Blangy, A. (2014a). Dock-family exchange factors in cell migration and disease. Eur. J. Cell Biol. *93*, 466–477.

Gadea, G., Sanz-Moreno, V., Self, A., Godi, A., and Marshall, C.J. (2008). DOCK10-Mediated Cdc42 Activation Is Necessary for Amoeboid Invasion of Melanoma Cells. Curr. Biol. *18*, 1456–1465.

Galli, G.G., Carrara, M., Yuan, W.-C., Valdes-Quezada, C., Gurung, B., Pepe-Mooney, B., Zhang, T., Geeven, G., Gray, N.S., de Laat, W., et al. (2015). YAP Drives Growth by Controlling Transcriptional Pause Release from Dynamic Enhancers. Mol. Cell *60*, 328–337.

Gao, C., Xiao, G., and Hu, J. (2014). Regulation of Wnt/β-catenin signaling by posttranslational modifications. Cell Biosci. *4*, 13.

Gao, Y., Dickerson, J.B., Guo, F., Zheng, J., and Zheng, Y. (2004). Rational design and characterization of a Rac GTPase-specific small molecule inhibitor. Proc. Natl. Acad. Sci. *101*, 7618–7623.

Garbe, A.I., Roscher, A., Schüler, C., Lutter, A.-H., Glösmann, M., Bernhardt, R., Chopin, M., Hempel, U., Hofbauer, L.C., Rammelt, S., et al. (2012). Regulation of bone mass and osteoclast function depend on the F-actin modulator SWAP-70. J. Bone Miner. Res. *27*, 2085–2096.

Garcia-Rendueles, M.E.R., Ricarte-Filho, J.C., Untch, B.R., Landa, I., Knauf, J.A., Voza, F., Smith, V.E., Ganly, I., Taylor, B.S., Persaud, Y., et al. (2015). NF2 Loss Promotes Oncogenic RAS-Induced Thyroid Cancers via YAP-Dependent Transactivation of RAS Proteins and Sensitizes Them to MEK Inhibition. Cancer Discov. *5*, 1178–1193.

Gastonguay, A., Berg, T., Hauser, A.D., Schuld, N., Lorimer, E., and Williams, C.L. (2012). The role of Rac1 in the regulation of NF-kB activity, cell proliferation, and cell migration in non-small cell lung carcinoma. Cancer Biol. Ther. *13*, 647–656.

Gatza, M.L., Silva, G.O., Parker, J.S., Fan, C., and Perou, C.M. (2014). An integrated genomics approach identifies drivers of proliferation in luminal-subtype human breast cancer. Nat Genet *46*, 1051–1059.

Gire, V., Marshall, C., and Wynford-Thomas, D. (2000). PI-3-kinase is an essential anti-apoptotic effector in the proliferative response of primary human epithelial cells to mutant RAS. Oncogene *19*, 2269–2276.

Gligorijevic, B., Wyckoff, J., Yamaguchi, H., Wang, Y., Roussos, E.T., and Condeelis, J. (2012). N-WASP-mediated invadopodium formation is involved in intravasation and lung metastasis of mammary tumors. J. Cell Sci. *125*, 724–734.

Goicoechea, S.M., Awadia, S., and Garcia-Mata, R. (2014). I'm coming to GEF you: Regulation of RhoGEFs during cell migration. Cell Adhes. Migr. *8*, 535–549.

van Golen, K.L., Wu, Z.F., Qiao, X.T., Bao, L.W., and Merajver, S.D. (2000). RhoC GTPase, a novel transforming oncogene for human mammary epithelial cells that partially recapitulates the inflammatory breast cancer phenotype. Cancer Res. *60*, 5832–5838.

van Golen, K.L., Bao, L., DiVito, M.M., Wu, Z., Prendergast, G.C., and Merajver, S.D. (2002). Reversion of RhoC GTPase-induced inflammatory breast cancer phenotype by treatment with a farnesyl transferase inhibitor. Mol. Cancer Ther. *1*, 575–583.

Gomez-Cambronero, J. (2012). Structure analysis between the SWAP-70 RHO-GEF and the newly described PLD2-GEF. Small GTPases *3*, 202–208.

Gou, W., Zhao, Y., Lu, H., Yang, X., Xiu, Y., Zhao, S., Liu, J., Zhu, Z., Sun, H., Liu, Y., et al. (2014). The role of RhoC in epithelial-to-mesenchymal transition of ovarian carcinoma cells. BMC Cancer *14*, 477.

Gouw, L.G., Reading, N.S., Jenson, S.D., Lim, M.S., and Elenitoba-Johnson, K.S.J. (2005). Expression of the Rho-family GTPase gene RHOF in lymphocyte subsets and malignant lymphomas. Br. J. Haematol. *129*, 531–533.

Guilluy, C., Garcia-Mata, R., and Burridge, K. (2011). Rho protein crosstalk: another social network? Trends Cell Biol. *21*, 718–726.

Guimbal, S., Morel, A., Guérit, D., Chardon, M., Blangy, A., and Vives, V. (2019). Dock5 is a new regulator of microtubule dynamic instability in osteoclasts. Biol. Cell boc.201900014.

Haffty, B.G., Yang, Q., Reiss, M., Kearney, T., Higgins, S.A., Weidhaas, J., Harris, L., Hait, W., and Toppmeyer, D. (2006). Locoregional relapse and distant metastasis in conservatively managed triple negative early-stage breast cancer. J. Clin. Oncol. Off. J. Am. Soc. Clin. Oncol. *24*, 5652–5657.

Hakem, A., Sanchez-Sweatman, O., You-Ten, A., Duncan, G., Wakeham, A., Khokha, R., and Mak, T.W. (2005). RhoC is dispensable for embryogenesis and tumor initiation but essential for metastasis. Genes Dev. *19*, 1974–1979.

Halder, G., Dupont, S., and Piccolo, S. (2012). Transduction of mechanical and cytoskeletal cues by YAP and TAZ. Nat. Rev. Mol. Cell Biol. *13*, 591–600.

Hall, A. (1994). Small GTP-Binding Proteins and the Regulation of the Actin Cytoskeleton. Annu. Rev. Cell Biol. *10*, 31–54.

Hall, A. (1998). Rho GTPases and the Actin Cytoskeleton. Science *279*, 509–514.

Hall, A. (2009). The cytoskeleton and cancer. Cancer Metastasis Rev. *28*, 5–14.

Hanahan, D., and Weinberg, R.A. (2011). Hallmarks of Cancer: The Next Generation. Cell *144*, 646–674.

Harvey, K.F., Zhang, X., and Thomas, D.M. (2013). The Hippo pathway and human cancer. Nat. Rev. Cancer *13*, 246–257.

Heidary Arash, E., Song, K.M., Song, S., Shiban, A., and Attisano, L. (2014). Arhgef7 promotes activation of the Hippo pathway core kinase Lats. EMBO J. *33*, 2997–3011.

Héraud, C., Pinault, M., Lagrée, V., and Moreau, V. (2019). p190RhoGAPs, the ARHGAP35- and ARHGAP5-Encoded Proteins, in Health and Disease. Cells *8*, 351.

Hilpela, P., Oberbanscheidt, P., Hahne, P., Hund, M., Kalhammer, G., Small, J.V., and Bahler, M. (2003). SWAP-70 Identifies a Transitional Subset of Actin Filaments in Motile Cells□V. Mol. Biol. Cell *14*, 12.

Hiramoto-Yamaki, N., Takeuchi, S., Ueda, S., Harada, K., Fujimoto, S., Negishi, M., and Katoh, H. (2010). Ephexin4 and EphA2 mediate cell migration through a RhoG-dependent mechanism. J. Cell Biol. *190*, 461–477.

Ho, J., Tumkaya, T., Aryal, S., Choi, H., and Claridge-Chang, A. (2019). Moving beyond P values: data analysis with estimation graphics. Nat. Methods *16*, 565–566.

Hocker, H.J., Cho, K.-J., Chen, C.-Y.K., Rambahal, N., Sagineedu, S.R., Shaari, K., Stanslas, J., Hancock, J.F., and Gorfe, A.A. (2013). Andrographolide derivatives inhibit guanine nucleotide exchange and abrogate oncogenic Ras function. Proc. Natl. Acad. Sci. *110*, 10201–10206.

Holeiter, G., Bischoff, A., Braun, A.C., Huck, B., Erlmann, P., Schmid, S., Herr, R., Brummer, T., and Olayioye, M.A. (2012). The RhoGAP protein Deleted in Liver Cancer 3 (DLC3) is essential for adherens junctions integrity. Oncogenesis *1*, e13.

Hong, W., and Guan, K.-L. (2012). The YAP and TAZ transcription co-activators: Key downstream effectors of the mammalian Hippo pathway. Semin. Cell Dev. Biol. *23*, 785–793.

Horpaopan, S., Spier, I., Zink, A.M., Altmüller, J., Holzapfel, S., Laner, A., Vogt, S., Uhlhaas, S., Heilmann, S., Stienen, D., et al. (2015). Genome-wide CNV analysis in 221 unrelated patients and targeted high-throughput sequencing reveal novel causative candidate genes for colorectal adenomatous polyposis. Int. J. Cancer *136*, E578–E589.

Hossain, Z., Ali, S.M., Ko, H.L., Xu, J., Ng, C.P., Guo, K., Qi, Z., Ponniah, S., Hong, W., and Hunziker, W. (2007). Glomerulocystic kidney disease in mice with a targeted inactivation of Wwtr1. Proc. Natl. Acad. Sci. *104*, 1631–1636.

Hu, J.K.-H., Du, W., Shelton, S.J., Oldham, M.C., DiPersio, C.M., and Klein, O.D. (2017). An FAK-YAP-mTOR Signaling Axis Regulates Stem Cell-Based Tissue Renewal in Mice. Cell Stem Cell *21*, 91-106.e6.

Hu, M.C.-T., Lee, D.-F., Xia, W., Golfman, L.S., Ou-Yang, F., Yang, J.-Y., Zou, Y., Bao, S., Hanada, N., Saso, H., et al. (2004). IκB Kinase Promotes Tumorigenesis through Inhibition of Forkhead FOXO3a. Cell *117*, 225–237.

Huang, H.-S., Liu, Z.-M., and Cheng, Y.-L. Involvement of Glycogen Synthase Kinase-3b in Arsenic Trioxide–Induced p21 Expression. 9.

Hudis, C.A., and Gianni, L. (2011). Triple-Negative Breast Cancer: An Unmet Medical Need. The Oncologist *16*, 1–11.

Jaffe, A.B., and Hall, A. (2002). Rho GTPases in transformation and metastasis. In Advances in Cancer Research, (Academic Press), pp. 57–80.

Jaffe, A.B., and Hall, A. (2005). RHO GTPASES: Biochemistry and Biology. Annu. Rev. Cell Dev. Biol. *21*, 247–269.

Jamieson, C., Lui, C., Brocardo, M.G., Martino-Echarri, E., and Henderson, B.R. (2015). Rac1 augments Wnt signaling by stimulating β-catenin–lymphoid enhancer factor-1 complex assembly independent of β-catenin nuclear import. J. Cell Sci. *128*, 3933–3946.

Johnson, D.I., and Pringle, J.R. (1990). Molecular characterization of CDC42, a Saccharomyces cerevisiae gene involved in the development of cell polarity. J. Cell Biol. *111*, 143–152.

Johnstone, C.N., Pattison, A.D., Gorringe, K.L., Harrison, P.F., Powell, D.R., Lock, P., Baloyan, D., Ernst, M., Stewart, A.G., Beilharz, T.H., et al. (2018). Functional and genomic characterisation of a xenograft model system for the study of metastasis in triple-negative breast cancer. Dis. Model. Mech. *11*.

Jordan, P., Brazåo, R., Boavida, M.G., Gespach, C., and Chastre, E. (1999). Cloning of a novel human Rac1b splice variant with increased expression in colorectal tumors. Oncogene *18*, 6835–6839.

Justice, R.W., Zilian, O., Woods, D.F., Noll, M., and Bryant, P.J. (1995). The Drosophila tumor suppressor gene warts encodes a homolog of human myotonic dystrophy kinase and is required for the control of cell shape and proliferation. Genes Dev. *9*, 534–546.

Kang, H.S., Beak, J.Y., Kim, Y.-S., Herbert, R., and Jetten, A.M. (2009). Glis3 Is Associated with Primary Cilia and Wwtr1/TAZ and Implicated in Polycystic Kidney Disease. Mol. Cell. Biol. *29*, 2556–2569.

Kapoor, A., Yao, W., Ying, H., Hua, S., Liewen, A., Wang, Q., Zhong, Y., Wu, C.-J., Sadanandam, A., Hu, B., et al. (2014). Yap1 Activation Enables Bypass of Oncogenic Kras Addiction in Pancreatic Cancer. Cell *158*, 185–197.

Kass, L., Erler, J.T., Dembo, M., and Weaver, V.M. (2007). Mammary epithelial cell: Influence of extracellular matrix composition and organization during development and tumorigenesis. Int. J. Biochem. Cell Biol. *39*, 1987–1994.

Kawasaki, Y., Sato, R., and Akiyama, T. (2003). Mutated APC and Asef are involved in the migration of colorectal tumour cells. Nat. Cell Biol. *5*, 211–215.

Kawazu, M., Ueno, T., Kontani, K., Ogita, Y., Ando, M., Fukumura, K., Yamato, A., Soda, M., Takeuchi, K., Miki, Y., et al. (2013). Transforming mutations of RAC guanosine triphosphatases in human cancers. Proc. Natl. Acad. Sci. *110*, 3029–3034.

Kim, N.-G., and Gumbiner, B.M. (2015). Adhesion to fibronectin regulates Hippo signaling via the FAK–Src–PI3K pathway. J. Cell Biol. *210*, 503–515.

Kim, H., Guo, F., Brahma, S., Xing, Y., and Burkard, M.E. (2014). Centralspindlin assembly and 2 phosphorylations on MgcRacGAP by Polo-like kinase 1 initiate Ect2 binding in early cytokinesis. Cell Cycle *13*, 2952–2961.

Kim, M.H., Kim, J., Hong, H., Lee, S.-H., Lee, J.-K., Jung, E., and Kim, J. (2016). Actin remodeling confers BRAF inhibitor resistance to melanoma cells through YAP/TAZ activation. EMBO J. *35*, 462–478.

Kim, Y., Ha, C.M., and Chang, S. (2013). SNX26, a GTPase-activating Protein for Cdc42, Interacts with PSD-95 Protein and Is Involved in Activity-dependent Dendritic Spine Formation in Mature Neurons. J. Biol. Chem. *288*, 29453–29466.

Kiyokawa, E., Hashimoto, Y., Kobayashi, S., Sugimura, H., Kurata, T., and Matsuda, M. (1998). Activation of Rac1 by a Crk SH3-binding protein, DOCK180. Genes Dev. *12*, 3331–3336.

Kleer, C.G., Griffith, K.A., Sabel, M.S., Gallagher, G., van Golen, K.L., Wu, Z.-F., and Merajver, S.D. (2005). RhoC-GTPase is a Novel Tissue Biomarker Associated with Biologically Aggressive Carcinomas of the Breast. Breast Cancer Res. Treat. *93*, 101–110.

Klimkiewicz, K., Weglarczyk, K., Collet, G., Paprocka, M., Guichard, A., Sarna, M., Jozkowicz, A., Dulak, J., Sarna, T., Grillon, C., et al. (2017). A 3D model of tumour angiogenic microenvironment to monitor hypoxia effects on cell interactions and cancer stem cell selection. Cancer Lett. *396*, 10–20.

Koedoot, E., Fokkelman, M., Rogkoti, V.-M., Smid, M., van de Sandt, I., de Bont, H., Pont, C., Klip, J.E., Wink, S., Timmermans, M.A., et al. (2019). Uncovering the signaling landscape controlling breast cancer cell migration identifies novel metastasis driver genes. Nat. Commun. *10*, 2983.

Komiya, Y., Onodera, Y., Kuroiwa, M., Nomimura, S., Kubo, Y., Nam, J.-M., Kajiwara, K., Nada, S., Oneyama, C., Sabe, H., et al. (2016). The Rho guanine nucleotide exchange factor ARHGEF5 promotes tumor malignancy via epithelial–mesenchymal transition. Oncogenesis *5*, e258–e258.

Kröger, C., Afeyan, A., Mraz, J., Eaton, E.N., Reinhardt, F., Khodor, Y.L., Thiru, P., Bierie, B., Ye, X., Burge, C.B., et al. (2019). Acquisition of a hybrid E/M state is essential for tumorigenicity of basal breast cancer cells. Proc. Natl. Acad. Sci. *116*, 7353–7362.

Kuroiwa, M., Oneyama, C., Nada, S., and Okada, M. (2011). The guanine nucleotide exchange factor Arhgef5 plays crucial roles in Src-induced podosome formation. J. Cell Sci. *124*, 1726–1738.

Kutys, M.L., and Yamada, K.M. (2014). An extracellular-matrix-specific GEF–GAP interaction regulates Rho GTPase crosstalk for 3D collagen migration. Nat. Cell Biol. *16*, 909–917.

Lallemand, D., Curto, M., Saotome, I., Giovannini, M., and McClatchey, A.I. (2003). NF2 deficiency promotes tumorigenesis and metastasis by destabilizing adherens junctions. Genes Dev. *17*, 1090–1100.

Lamar, J.M., Stern, P., Liu, H., Schindler, J.W., Jiang, Z.-G., and Hynes, R.O. (2012). The Hippo pathway target, YAP, promotes metastasis through its TEAD-interaction domain. Proc. Natl. Acad. Sci. *109*, E2441–E2450.

Lambert, A.W., Pattabiraman, D.R., and Weinberg, R.A. (2017). Emerging Biological Principles of Metastasis. Cell *168*, 670–691.

Lane, J., Martin, T.A., Mansel, R.E., and Jiang, W.G. (2008). The expression and prognostic value of the guanine nucleotide exchange factors (GEFs) Trio, Vav1 and TIAM-1 in human breast cancer. Int. Semin. Surg. Oncol. *5*, 23.

Lang, S., Busch, H., Boerries, M., Brummer, T., Timme, S., Lassmann, S., Aktories, K., and Schmidt, G. (2017). Specific role of RhoC in tumor invasion and metastasis. Oncotarget *8*, 87364–87378.

Laurin, M., Fradet, N., Blangy, A., Hall, A., Vuori, K., and Côté, J.-F. (2008). The atypical Rac activator Dock180 (Dock1) regulates myoblast fusion in vivo. Proc. Natl. Acad. Sci. *105*, 15446–15451.

Laurin, M., Huber, J., Pelletier, A., Houalla, T., Park, M., Fukui, Y., Haibe-Kains, B., Muller, W.J., and Cote, J.-F. (2013). Rac-specific guanine nucleotide exchange factor DOCK1 is a critical regulator of HER2-mediated breast cancer metastasis. Proc. Natl. Acad. Sci. *110*, 7434–7439.

Lehmann, B.D., Bauer, J.A., Chen, X., Sanders, M.E., Chakravarthy, A.B., Shyr, Y., and Pietenpol, J.A. (2011). Identification of human triple-negative breast cancer subtypes and preclinical models for selection of targeted therapies. J. Clin. Invest. *121*, 2750–2767.

Lei, Q.-Y., Zhang, H., Zhao, B., Zha, Z.-Y., Bai, F., Pei, X.-H., Zhao, S., Xiong, Y., and Guan, K.-L. (2008). TAZ Promotes Cell Proliferation and Epithelial-Mesenchymal Transition and Is Inhibited by the Hippo Pathway. Mol. Cell. Biol. *28*, 2426–2436.

Leong, H.S., Robertson, A.E., Stoletov, K., Leith, S.J., Chin, C.A., Chien, A.E., Hague, M.N., Ablack, A., Carmine-Simmen, K., McPherson, V.A., et al. (2014). Invadopodia Are Required for Cancer Cell Extravasation and Are a Therapeutic Target for Metastasis. Cell Rep. *8*, 1558–1570.

Li, Q., Li, S., Mana-Capelli, S., Roth Flach, R.J., Danai, L.V., Amcheslavsky, A., Nie, Y., Kaneko, S., Yao, X., Chen, X., et al. (2014). The Conserved Misshapen-Warts-Yorkie Pathway Acts in Enteroblasts to Regulate Intestinal Stem Cells in Drosophila. Dev. Cell *31*, 291–304.

Liao, Y.C., Ruan, J.W., Lua, I., Li, M.H., Chen, W.L., Wang, J.R.Y., Kao, R.H., and Chen, J.H. (2012). Overexpressed hPTTG1 promotes breast cancer cell invasion and metastasis by regulating GEF-H1/RhoA signalling. Oncogene *31*, 3086–3097.

Lionarons, D.A., Hancock, D.C., Rana, S., East, P., Moore, C., Murillo, M.M., Carvalho, J., Spencer-Dene, B., Herbert, E., Stamp, G., Damry, D., Calado, D.P., Rosewell, I., Fritsch, R., Neubig, R.R., Molina-Arcas, M., and Downward, J. (2019). RAC1P29S induces a mesenchymal phenotypic switch via serum response factor to promote melanoma development and therapy resistance. Cancer Cell. *36*: 68-83.

Lin, C., Yao, E., Zhang, K., Jiang, X., Croll, S., Thompson-Peer, K., and Chuang, P.-T. (2017). YAP is essential for mechanical force production and epithelial cell proliferation during lung branching morphogenesis. ELife *6*, e21130.

Lin, L., Sabnis, A.J., Chan, E., Olivas, V., Cade, L., Pazarentzos, E., Asthana, S., Neel, D., Yan, J.J., Lu, X., et al. (2015). The Hippo effector YAP promotes

resistance to RAF- and MEK-targeted cancer therapies. Nat. Genet. *47*, 250–256.

Liu, K., Wang, A., Ran, L., Zhang, W., Jing, S., Wang, Y., Zhang, X., Liu, G., Sen, W., and Song, F. (2019). ARHGEF38 as a novel biomarker to predict aggressive prostate cancer. Genes Dis.

Liu, X., Li, H., Rajurkar, M., Li, Q., Cotton, J.L., Ou, J., Zhu, L.J., Goel, H.L., Mercurio, A.M., Park, J.-S., et al. (2016). Tead and AP1 Coordinate Transcription and Motility. Cell Rep. *14*, 1169–1180.

Luo, J., Emanuele, M.J., Li, D., Creighton, C.J., Schlabach, M.R., Westbrook, T.F., Wong, K.-K., and Elledge, S.J. (2009). A genome-wide RNAi screen identifies multiple synthetic lethal interactions with the Ras oncogene. Cell *137*, 835–848.

Magzoub, M., Jin, S., and Verkman, A.S. (2008). Enhanced macromolecule diffusion deep in tumors after enzymatic digestion of extracellular matrix collagen and its associated proteoglycan decorin. FASEB J. *22*, 276–284.

Makita, R., Uchijima, Y., Nishiyama, K., Amano, T., Chen, Q., Takeuchi, T., Mitani, A., Nagase, T., Yatomi, Y., Aburatani, H., et al. (2008). Multiple renal cysts, urinary concentration defects, and pulmonary emphysematous changes in mice lacking TAZ. Am. J. Physiol.-Ren. Physiol. *294*, F542–F553.

Mani, S.A., Guo, W., Liao, M.-J., Eaton, E.N., Ayyanan, A., Zhou, A.Y., Brooks, M., Reinhard, F., Zhang, C.C., Shipitsin, M., et al. (2008). The Epithelial-Mesenchymal Transition Generates Cells with Properties of Stem Cells. Cell *133*, 704–715.

Manning, B.D., and Toker, A. (2017). AKT/PKB Signaling: Navigating the Network. Cell *169*, 381–405.

Marchesi, S., Montani, F., Deflorian, G., D'Antuono, R., Cuomo, A., Bologna, S., Mazzoccoli, C., Bonaldi, T., Di Fiore, P.P., and Nicassio, F. (2014). DEPDC1B Coordinates De-adhesion Events and Cell-Cycle Progression at Mitosis. Dev. Cell *31*, 420–433.

Marinissen, M.J., Chiariello, M., and Gutkind, J.S. (2001). Regulation of gene expression by the small GTPase Rho through the ERK6 (p38γ) MAP kinase pathway. Genes Dev. *15*, 535–553.

Marra, A., Viale, G., and Curigliano, G. (2019). Recent advances in triple negative breast cancer: the immunotherapy era. BMC Med. *17*, 90.

Maurer, T., Garrenton, L.S., Oh, A., Pitts, K., Anderson, D.J., Skelton, N.J., Fauber, B.P., Pan, B., Malek, S., Stokoe, D., et al. (2012). Small-molecule ligands bind to a distinct pocket in Ras and inhibit SOS-mediated nucleotide exchange activity. Proc. Natl. Acad. Sci. U. S. A. *109*, 5299–5304.

McClatchey, A.I., and Yap, A.S. (2012). Contact inhibition (of proliferation) redux. Curr. Opin. Cell Biol. *24*, 685–694.

McCubrey, J.A., Steelman, L.S., Bertrand, F.E., Davis, N.M., Abrams, S.L., Montalto, G., D'Assoro, A.B., Libra, M., Nicoletti, F., Maestro, R., et al. (2014). Multifaceted roles of GSK-3 and Wnt/β-catenin in hematopoiesis and leukemogenesis: opportunities for therapeutic intervention. Leukemia *28*, 15–33.

Medjkane, S., Perez-Sanchez, C., Gaggioli, C., Sahai, E., and Treisman, R. (2009). Myocardin-related transcription factors and SRF are required for cytoskeletal dynamics and experimental metastasis. Nat. Cell Biol. *11*, 257–268.

Meller, N., Irani-Tehrani, M., Kiosses, W.B., Pozo, M.A.D., and Schwartz, M.A. (2002). Zizimin1, a novel Cdc42 activator, reveals a new GEF domain for Rho proteins. Nat. Cell Biol. *4*, 639–647.

Mendoza, M.C., Er, E.E., and Blenis, J. (2011). The Ras-ERK and PI3K-mTOR Pathways: Cross-talk and Compensation. Trends Biochem. Sci. *36*, 320–328.

Meng, Z., Moroishi, T., Mottier-Pavie, V., Plouffe, S.W., Hansen, C.G., Hong, A.W., Park, H.W., Mo, J.-S., Lu, W., Lu, S., et al. (2015). MAP4K family kinases act in parallel to MST1/2 to activate LATS1/2 in the Hippo pathway. Nat. Commun. *6*, 8357.

Minden, A., Lin, A., Claret, F.-X., Abo, A., and Karin, M. (1995). Selective activation of the JNK signaling cascadeand c-Jun transcriptional activity by the small GTPases Rac and Cdc42Hs. Cell *81*, 1147–1157.

Minn, A.J., Gupta, G.P., Siegel, P.M., Bos, P.D., Shu, W., Giri, D.D., Viale, A., Olshen, A.B., Gerald, W.L., and Massagué, J. (2005). Genes that mediate breast cancer metastasis to lung. Nature *436*, 518–524.

Miralles, F., Posern, G., Zaromytidou, A.-I., and Treisman, R. (2003). Actin dynamics control SRF activity by regulation of its coactivator MAL. Cell *113*, 329–342.

Miyamoto, Y., Yamauchi, J., Sanbe, A., and Tanoue, A. (2007). Dock6, a Dock-C subfamily guanine nucleotide exchanger, has the dual specificity for Rac1 and Cdc42 and regulates neurite outgrowth. Exp. Cell Res. *313*, 791–804.

Morin-Kensicki, E.M., Boone, B.N., Howell, M., Stonebraker, J.R., Teed, J., Alb, J.G., Magnuson, T.R., O'Neal, W., and Milgram, S.L. (2006). Defects in Yolk Sac Vasculogenesis, Chorioallantoic Fusion, and Embryonic Axis Elongation in Mice with Targeted Disruption of Yap65. Mol. Cell. Biol. *26*, 77–87.

Moroishi, T., Hansen, C.G., and Guan, K.-L. (2015). The emerging roles of YAP and TAZ in cancer. Nat. Rev. Cancer *15*, 73–79.

Mou, F., Praskova, M., Xia, F., Buren, D.V., Hock, H., Avruch, J., and Zhou, D. (2012). The Mst1 and Mst2 kinases control activation of rho family GTPases and thymic egress of mature thymocytes. J. Exp. Med. *209*, 741–759.

Mouw, J.K., Ou, G., and Weaver, V.M. (2014). Extracellular matrix assembly: a multiscale deconstruction. Nat. Rev. Mol. Cell Biol. *15*, 771–785.

Müller, P.M., Rademacher, J., Bagshaw, R.D., Alp, K.M., Giudice, G., Heinrich, L.E., Barth, C., Eccles, R.L., Sanchez-Castro, M., Brandenburg, L., et al. (2018). Spatial Organization of Rho GTPase signaling by RhoGEF/RhoGAP proteins (Cell Biology).

Nallet-Staub, F., Marsaud, V., Li, L., Gilbert, C., Dodier, S., Bataille, V., Sudol, M., Herlyn, M., and Mauviel, A. (2014). Pro-Invasive Activity of the Hippo Pathway Effectors YAP and TAZ in Cutaneous Melanoma. J. Invest. Dermatol. *134*, 123–132.

Narumiya, S., Tanji, M., and Ishizaki, T. (2009). Rho signaling, ROCK and mDia1, in transformation, metastasis and invasion. Cancer Metastasis Rev. *28*, 65–76.

Neve, R.M., Chin, K., Fridlyand, J., Yeh, J., Baehner, F.L., Fevr, T., Clark, L., Bayani, N., Coppe, J.-P., Tong, F., et al. (2006). A collection of breast cancer cell lines for the study of functionally distinct cancer subtypes. Cancer Cell *10*, 515–527.

Nguyen, T.T.T., Park, W.S., Park, B.O., Kim, C.Y., Oh, Y., Kim, J.M., Choi, H., Kyung, T., Kim, C.-H., Lee, G., et al. (2016). PLEKHG3 enhances polarized cell migration by activating actin filaments at the cell front. Proc. Natl. Acad. Sci. *113*, 10091–10096.

Nho, R.S., and Hergert, P. (2014). FoxO3a and disease progression. World J. Biol. Chem. *5*, 346–354.

Nobes, C.D., and Hall, A. (1995). Rho, Rac, and Cdc42 GTPases regulate the assembly of multimolecular focal complexes associated with actin stress fibers, lamellipodia, and filopodia. Cell *81*, 53–62.

Noto, A., De Vitis, C., Pisanu, M.E., Roscilli, G., Ricci, G., Catizone, A., Sorrentino, G., Chianese, G., Taglialatela-Scafati, O., Trisciuoglio, D., et al. (2017). Stearoyl-CoA-desaturase 1 regulates lung cancer stemness via stabilization and nuclear localization of YAP/TAZ. Oncogene *36*, 4573–4584.

Ocaña-Morgner, C., Reichardt, P., Chopin, M., Braungart, S., Wahren, C., Gunzer, M., and Jessberger, R. (2011). Sphingosine 1-phosphate-induced motility and endocytosis of dendritic cells is regulated by SWAP-70 through RhoA. J. Immunol. Baltim. Md 1950 *186*, 5345–5355.

Ogawa, K., Tanaka, Y., Uruno, T., Duan, X., Harada, Y., Sanematsu, F., Yamamura, K., Terasawa, M., Nishikimi, A., Côté, J.-F., et al. (2014a). DOCK5 functions as a key signaling adaptor that links FcεRI signals to microtubule dynamics during mast cell degranulation. J. Exp. Med. *211*, 1407–1419.

Ogawa, K., Tanaka, Y., Uruno, T., Duan, X., Harada, Y., Sanematsu, F., Yamamura, K., Terasawa, M., Nishikimi, A., Côté, J.-F., et al. (2014b). DOCK5 functions as a key signaling adaptor that links FcεRI signals to microtubule dynamics during mast cell degranulation. J. Exp. Med. *211*, 1407–1419.

Oldberg, A., Kalamajski, S., Salnikov, A.V., Stuhr, L., Morgelin, M., Reed, R.K., Heldin, N.-E., and Rubin, K. (2007). Collagen-binding proteoglycan fibromodulin

can determine stroma matrix structure and fluid balance in experimental carcinoma. Proc. Natl. Acad. Sci. *104*, 13966–13971.

Olson, M.F. (2018). Rho GTPases, their post-translational modifications, disease-associated mutations and pharmacological inhibitors. Small GTPases *9*, 203–215.

Overholtzer, M., Zhang, J., Smolen, G.A., Muir, B., Li, W., Sgroi, D.C., Deng, C.-X., Brugge, J.S., and Haber, D.A. (2006). Transforming properties of YAP, a candidate oncogene on the chromosome 11q22 amplicon. Proc. Natl. Acad. Sci. *103*, 12405–12410.

Palomero, T., Couronné, L., Khiabanian, H., Kim, M.-Y., Ambesi-Impiombato, A., Perez-Garcia, A., Carpenter, Z., Abate, F., Allegretta, M., Haydu, J.E., et al. (2014). Recurrent mutations in epigenetic regulators, RHOA and FYN kinase in peripheral T cell lymphomas. Nat. Genet. *46*, 166–170.

Pan, D. (2010). The Hippo Signaling Pathway in Development and Cancer. Dev. Cell *19*, 491–505.

Pascual-Vargas, P., Cooper, S., Sero, J., Bousgouni, V., Arias-Garcia, M., and Bakal, C. (2017). RNAi screens for Rho GTPase regulators of cell shape and YAP/TAZ localisation in triple negative breast cancer. Sci. Data *4*, 170018.

Paszek, M.J., Zahir, N., Johnson, K.R., Lakins, J.N., Rozenberg, G.I., Gefen, A., Reinhart-King, C.A., Margulies, S.S., Dembo, M., Boettiger, D., et al. (2005). Tensional homeostasis and the malignant phenotype. Cancer Cell *8*, 241–254.

Perou, C.M., Sørlie, T., Eisen, M.B., Rijn, M. van de, Jeffrey, S.S., Rees, C.A., Pollack, J.R., Ross, D.T., Johnsen, H., Akslen, L.A., et al. (2000). Molecular portraits of human breast tumours. Nature *406*, 747–752.

Pertz, O., Hodgson, L., Klemke, R.L., and Hahn, K.M. (2006). Spatiotemporal dynamics of RhoA activity in migrating cells. Nature *440*, 1069–1072.

Peyroche, A., Antonny, B., Robineau, S., Acker, J., Cherfils, J., and Jackson, C.L. (1999). Brefeldin A acts to stabilize an abortive ARF-GDP-Sec7 domain protein complex: involvement of specific residues of the Sec7 domain. Mol. Cell *3*, 275–285.

Piccolo, S., Dupont, S., and Cordenonsi, M. (2014). The Biology of YAP/TAZ: Hippo Signaling and Beyond. Physiol. Rev. *94*, 1287–1312.

Polyak, K., and Weinberg, R.A. (2009). Transitions between epithelial and mesenchymal states: acquisition of malignant and stem cell traits. Nat. Rev. Cancer *9*, 265–273.

Pulgar, T.G. del, Benitah, S.A., Valerón, P.F., Espina, C., and Lacal, J.C. (2005). Rho GTPase expression in tumourigenesis: Evidence for a significant link. BioEssays *27*, 602–613.

Qiao, Y., Chen, J., Lim, Y.B., Finch-Edmondson, M.L., Seshachalam, V.P., Qin, L., Jiang, T., Low, B.C., Singh, H., Lim, C.T., et al. (2017). YAP Regulates Actin Dynamics through ARHGAP29 and Promotes Metastasis. Cell Rep. *19*, 1495–1502.

Qin, F., Tian, J., Zhou, D., and Chen, L. (2013). Mst1 and Mst2 kinases: regulations and diseases. Cell Biosci. *3*, 31.

Reddy, S.M., Barcenas, C.H., Sinha, A.K., Hsu, L., Moulder, S.L., Tripathy, D., Hortobagyi, G.N., and Valero, V. (2018). Long-term survival outcomes of triple-receptor negative breast cancer survivors who are disease free at 5 years and relationship with low hormone receptor positivity. Br. J. Cancer *118*, 17–23.

Reginensi, A., Scott, R.P., Gregorieff, A., Bagherie-Lachidan, M., Chung, C., Lim, D.-S., Pawson, T., Wrana, J., and McNeill, H. (2013). Yap- and Cdc42-Dependent Nephrogenesis and Morphogenesis during Mouse Kidney Development. PLOS Genet. *9*, e1003380.

Ren, F., Zhang, L., and Jiang, J. (2010). Hippo signaling regulates Yorkie nuclear localization and activity through 14-3-3 dependent and independent mechanisms. Dev. Biol. *337*, 303–312.

Ridley, A.J. (1996). Rho: theme and variations. Curr. Biol. CB *6*, 1256–1264.

Ridley, A.J. (2004). Rho Proteins and Cancer. Breast Cancer Res. Treat. *84*, 13–19.

Ridley, A.J. (2012). Historical Overview of Rho GTPases. In Rho GTPases, F. Rivero, ed. (New York, NY: Springer New York), pp. 3–12.

Ridley, A.J., Paterson, H.F., Johnston, C.L., Diekmann, D., and Hall, A. (1992). The small GTP-binding protein rac regulates growth factor-induced membrane ruffling. Cell *70*, 401–410.

Robineau, S., Chabre, M., and Antonny, B. (2000). Binding site of brefeldin A at the interface between the small G protein ADP-ribosylation factor 1 (ARF1) and the nucleotide-exchange factor Sec7 domain. Proc. Natl. Acad. Sci. U. S. A. *97*, 9913–9918.

Rossman, K.L., Der, C.J., and Sondek, J. (2005). GEF means go: turning on RHO GTPases with guanine nucleotide-exchange factors. Nat. Rev. Mol. Cell Biol. *6*, 167–180.

Sabeh, F., Ota, I., Holmbeck, K., Birkedal-Hansen, H., Soloway, P., Balbin, M., Lopez-Otin, C., Shapiro, S., Inada, M., Krane, S., et al. (2004). Tumor cell traffic through the extracellular matrix is controlled by the membrane-anchored collagenase MT1-MMP. J. Cell Biol. *167*, 769–781.

Sabeh, F., Shimizu-Hirota, R., and Weiss, S.J. (2009). Protease-dependent versus -independent cancer cell invasion programs: three-dimensional amoeboid movement revisited. J. Cell Biol. *185*, 11–19.

Sabra, H., Brunner, M., Mandati, V., Wehrle-Haller, B., Lallemand, D., Ribba, A.-S., Chevalier, G., Guardiola, P., Block, M.R., and Bouvard, D. (2017). β1 integrin–dependent Rac/group I PAK signaling mediates YAP activation of Yes-associated protein 1 (YAP1) via NF2/merlin. J. Biol. Chem. *292*, 19179–19197.

Sadok, A., and Marshall, C.J. (2014). Rho GTPases. Small GTPases *5*, e983878.

Sahai, E., and Marshall, C.J. (2002). RHO–GTPases and cancer. Nat. Rev. Cancer *2*, 133–142.

Sahai, E., and Marshall, C.J. (2003). Differing modes of tumour cell invasion have distinct requirements for Rho/ROCK signalling and extracellular proteolysis. Nat. Cell Biol. *5*, 711–719.

Sanchez-Vega, F., Mina, M., Armenia, J., Chatila, W.K., Luna, A., La, K.C., Dimitriadoy, S., Liu, D.L., Kantheti, H.S., Saghafinia, S., et al. (2018). Oncogenic Signaling Pathways in The Cancer Genome Atlas. Cell *173*, 321-337.e10.

Sanz-Moreno, V., and Marshall, C.J. (2010). The plasticity of cytoskeletal dynamics underlying neoplastic cell migration. Curr. Opin. Cell Biol. *22*, 690–696.

Sanz-Moreno, V., Gadea, G., Ahn, J., Paterson, H., Marra, P., Pinner, S., Sahai, E., and Marshall, C.J. (2008). Rac Activation and Inactivation Control Plasticity of Tumor Cell Movement. Cell *135*, 510–523.

Sapudom, J., Kalbitzer, L., Wu, X., Martin, S., Kroy, K., and Pompe, T. (2019). Fibril bending stiffness of 3D collagen matrices instructs spreading and clustering of invasive and non-invasive breast cancer cells. Biomaterials *193*, 47–57.

Sawilowsky, S.S. (2009). New Effect Size Rules of Thumb. J. Mod. Appl. Stat. Methods *8*, 597–599.

Schleicher, S.B., Zaborski, J.J., Riester, R., Zenkner, N., Handgretinger, R., Kluba, T., Traub, F., and Boehme, K.A. Combined application of arsenic trioxide and lithium chloride augments viability reduction and apoptosis induction in human rhabdomyosarcoma cell lines. 18.

Schlessinger, K., Hall, A., and Tolwinski, N. (2009). Wnt signaling pathways meet Rho GTPases. Genes Dev. *23*, 265–277.

Schnelzer, A., Prechtel, D., Knaus, U., Dehne, K., Gerhard, M., Graeff, H., Harbeck, N., Schmitt, M., and Lengyel, E. (2000). Rac1 in human breast cancer: overexpression, mutation analysis, and characterization of a new isoform, Rac1b. Oncogene *19*, 3013–3020.

Sero, J.E., and Bakal, C. (2017). Multiparametric Analysis of Cell Shape Demonstrates that β-PIX Directly Couples YAP Activation to Extracellular Matrix Adhesion. Cell Syst. *4*, 84-96.e6.

Sero, J.E., Sailem, H.Z., Ardy, R.C., Almuttaqi, H., Zhang, T., and Bakal, C. (2015). Cell shape and the microenvironment regulate nuclear translocation of NF-κB in breast epithelial and tumor cells. Mol. Syst. Biol. *11*, 790.

Shang, X., Marchioni, F., Sipes, N., Evelyn, C.R., Jerabek-Willemsen, M., Duhr, S., Seibel, W., Wortman, M., and Zheng, Y. (2012). Rational Design of Small Molecule Inhibitors Targeting RhoA Subfamily Rho GTPases. Chem. Biol. *19*, 699–710.

Shang, X., Marchioni, F., Evelyn, C.R., Sipes, N., Zhou, X., Seibel, W., Wortman, M., and Zheng, Y. (2013). Small-molecule inhibitors targeting G-protein–coupled Rho guanine nucleotide exchange factors. Proc. Natl. Acad. Sci. *110*, 3155–3160.

Shao, D.D., Xue, W., Krall, E.B., Bhutkar, A., Piccioni, F., Wang, X., Schinzel, A.C., Sood, S., Rosenbluh, J., Kim, J.W., et al. (2014). KRAS and YAP1 Converge to Regulate EMT and Tumor Survival. Cell *158*, 171–184.

Shibue, T., and Weinberg, R.A. (2009). Integrin β1-focal adhesion kinase signaling directs the proliferation of metastatic cancer cells disseminated in the lungs. Proc. Natl. Acad. Sci. *106*, 10290–10295.

Shibue, T., Brooks, M.W., Inan, M.F., Reinhardt, F., and Weinberg, R.A. (2012). The Outgrowth of Micrometastases Is Enabled by the Formation of Filopodium-like Protrusions. Cancer Discov. *2*, 706–721.

Shiu, J.-Y., Aires, L., Lin, Z., and Vogel, V. (2018). Nanopillar force measurements reveal actin-cap-mediated YAP mechanotransduction. Nat. Cell Biol. *20*, 262–271.

Shriver, M., Stroka, K.M., Vitolo, M.I., Martin, S., Huso, D.L., Konstantopoulos, K., and Kontrogianni-Konstantopoulos, A. (2015). Loss of giant obscurins from breast epithelium promotes epithelial-to-mesenchymal transition, tumorigenicity and metastasis. Oncogene *34*, 4248–4259.

Simpson, K.J., Dugan, A.S, and Mercurio A.M. (2004). Functional analysis of the contribution of RhoA and RhoC GTPases to invasive breast carcinoma. Cancer Res. 1; *64*(23):8694-701.

Sjöblom, T., Jones, S., Wood, L.D., Parsons, D.W., Lin, J., Barber, T.D., Mandelker, D., Leary, R.J., Ptak, J., Silliman, N., et al. (2006). The consensus coding sequences of human breast and colorectal cancers. Science *314*, 268–274.

Sørlie, T., Tibshirani, R., Parker, J., Hastie, T., Marron, J.S., Nobel, A., Deng, S., Johnsen, H., Pesich, R., Geisler, S., et al. (2003). Repeated observation of breast tumor subtypes in independent gene expression data sets. Proc. Natl. Acad. Sci. *100*, 8418–8423.

Sorrentino, G., Ruggeri, N., Specchia, V., Cordenonsi, M., Mano, M., Dupont, S., Manfrin, A., Ingallina, E., Sommaggio, R., Piazza, S., et al. (2014). Metabolic control of YAP and TAZ by the mevalonate pathway. Nat. Cell Biol. *16*, 357–366.

Sosa, M.S., Lopez-Haber, C., Yang, C., Wang, H., Lemmon, M.A., Busillo, J.M., Luo, J., Benovic, J.L., Klein-Szanto, A., Yagi, H., et al. (2010). Identification of the

Rac-GEF P-Rex1 as an essential mediator of ErbB signaling in breast cancer. Mol. Cell *40*, 877–892.

Stamov, D.R., and Pompe, T. (2012). Structure and function of ECM-inspired composite collagen type I scaffolds. Soft Matter *8*, 10200.

Stein, C., Bardet, A.F., Roma, G., Bergling, S., Clay, I., Ruchti, A., Agarinis, C., Schmelzle, T., Bouwmeester, T., Schübeler, D., et al. (2015). YAP1 Exerts Its Transcriptional Control via TEAD-Mediated Activation of Enhancers. PLOS Genet. *11*, e1005465.

Stowers, L., Yelon, D., Berg, L.J., and Chant, J. (1995). Regulation of the polarization of T cells toward antigen-presenting cells by Ras-related GTPase CDC42. Proc. Natl. Acad. Sci. *92*, 5027–5031.

Sun, Q., Burke, J.P., Phan, J., Burns, M.C., Olejniczak, E.T., Waterson, A.G., Lee, T., Rossanese, O.W., and Fesik, S.W. (2012). Discovery of Small Molecules that Bind to K-Ras and Inhibit Sos-Mediated Activation. Angew. Chem. Int. Ed. *51*, 6140–6143.

Sung, M., and Giannakakou,P. (2014). BRCA1 regulates microtubule dynamics and taxane-induced apoptotic cell signalling. Oncogene, *33*(11):1418-28.

Talmadge, J.E., and Fidler, I.J. (2010). AACR Centennial Series: The Biology of Cancer Metastasis: Historical Perspective. Cancer Res. *70*, 5649–5669.

Tapon, N., Harvey, K.F., Bell, D.W., Wahrer, D.C.R., Schiripo, T.A., Haber, D.A., and Hariharan, I.K. (2002). salvador Promotes both cell cycle exit and apoptosis in Drosophila and is mutated in human cancer cell lines. Cell *110*, 467–478.

Terry, S.J., Elbediwy, A., Zihni, C., Harris, A.R., Bailly, M., Charras, G.T., Balda, M.S., and Matter, K. (2012). Stimulation of Cortical Myosin Phosphorylation by p114RhoGEF Drives Cell Migration and Tumor Cell Invasion. PLoS ONE *7*, e50188.

Thiery, J.P., and Sleeman, J.P. (2006). Complex networks orchestrate epithelial–mesenchymal transitions. Nat. Rev. Mol. Cell Biol. *7*, 131–142.

Tian, Y., Kolb, R., Hong, J.-H., Carroll, J., Li, D., You, J., Bronson, R., Yaffe, M.B., Zhou, J., and Benjamin, T. (2007). TAZ Promotes PC2 Degradation through a SCFβ-Trcp E3 Ligase Complex. Mol. Cell. Biol. *27*, 6383–6395.

Totaro, A., Panciera, T., and Piccolo, S. (2018). YAP/TAZ upstream signals and downstream responses. Nat. Cell Biol. *20*, 888–899.

Tozluoğlu, M., Tournier, A.L., Jenkins, R.P., Hooper, S., Bates, P.A., and Sahai, E. (2013). Matrix geometry determines optimal cancer cell migration strategy and modulates response to interventions. Nat. Cell Biol. *15*, 751–762.

Valiente, M., Obenauf, A.C., Jin, X., Chen, Q., Zhang, X.H.-F., Lee, D.J., Chaft, J.E., Kris, M.G., Huse, J.T., Brogi, E., et al. (2014). Serpins Promote Cancer Cell Survival and Vascular Co-Option in Brain Metastasis. Cell *156*, 1002–1016.

Vanharanta, S., and Massagué, J. (2013). Origins of Metastatic Traits. Cancer Cell *24*, 410–421.

Varelas, X., Samavarchi-Tehrani, P., Narimatsu, M., Weiss, A., Cockburn, K., Larsen, B.G., Rossant, J., and Wrana, J.L. (2010). The Crumbs Complex Couples Cell Density Sensing to Hippo-Dependent Control of the TGF-β-SMAD Pathway. Dev. Cell *19*, 831–844.

Vega, F.M., and Ridley, A.J. (2008). Rho GTPases in cancer cell biology. FEBS Lett. *582*, 2093–2101.

Vega, F.M., Colomba, A., Reymond, N., Thomas, M., and Ridley, A.J. (2012). RhoB regulates cell migration through altered focal adhesion dynamics. Open Biology. *2*(5):120076.

Vial, E., Sahai, E., and Marshall, C.J. (2003). ERK-MAPK signaling coordinately regulates activity of Rac1 and RhoA for tumor cell motility. Cancer Cell *4*, 67–79.

Vincent-Mistiaen, Z., Elbediwy, A., Vanyai, H., Cotton, J., Stamp, G., Nye, E., Spencer-Dene, B., Thomas, G.J., Mao, J., and Thompson, B. YAP drives cutaneous squamous cell carcinoma formation and progression. ELife *7*.

Vinci, M., Box, C., and Eccles, S.A. (2015). Three-Dimensional (3D) Tumor Spheroid Invasion Assay. J. Vis. Exp.

Vives, V., Laurin, M., Cres, G., Larrousse, P., Morichaud, Z., Noel, D., Côté, J.-F., and Blangy, A. (2011). The Rac1 Exchange Factor Dock5 Is Essential for Bone Resorption by Osteoclasts. J. Bone Miner. Res. Off. J. Am. Soc. Bone Miner. Res. *26*, 1099–1110.

Vives, V., Cres, G., Richard, C., Busson, M., Ferrandez, Y., Planson, A.-G., Zeghouf, M., Cherfils, J., Malaval, L., and Blangy, A. (2015). Pharmacological inhibition of Dock5 prevents osteolysis by affecting osteoclast podosome organization while preserving bone formation. Nat. Commun. *6*, 6218.

Wang, Y., Xu, X., Maglic, D., Dill, M.T., Mojumdar, K., Ng, P.K.-S., Jeong, K.J., Tsang, Y.H., Moreno, D., Bhavana, V.H., et al. (2018). Comprehensive Molecular Characterization of the Hippo Signaling Pathway in Cancer. Cell Rep. *25*, 1304-1317.e5.

Watanabe, M., Terasawa, M., Miyano, K., Yanagihara, T., Uruno, T., Sanematsu, F., Nishikimi, A., Côté, J.-F., Sumimoto, H., and Fukui, Y. (2014). DOCK2 and DOCK5 Act Additively in Neutrophils To Regulate Chemotaxis, Superoxide Production, and Extracellular Trap Formation. J. Immunol. *193*, 5660–5667.

Webb, D.J., Donais, K., Whitmore, L.A., Thomas, S.M., Turner, C.E., Parsons, J.T., and Horwitz, A.F. (2004). FAK–Src signalling through paxillin, ERK and MLCK regulates adhesion disassembly. Nat. Cell Biol. *6*, 154–161.

Weigelt, B., Peterse, J.L., and Veer, L.J. van't (2005). Breast cancer metastasis: markers and models. Nat. Rev. Cancer *5*, 591–602.

Williams, K.C., Cepeda, M.A., Javed, S., Searle, K., Parkins, K.M., Makela, A.V., Hamilton, A.M., Soukhtehzari, S., Kim, Y., Tuck, A.B., et al. (2019). Invadopodia are chemosensing protrusions that guide cancer cell extravasation to promote brain tropism in metastasis. Oncogene *38*, 3598–3615.

Wirtz, D., Konstantopoulos, K., and Searson, P.C. (2011). The physics of cancer: the role of physical interactions and mechanical forces in metastasis. Nat. Rev. Cancer *11*, 512–522.

Wolf, K., Mazo, I., Leung, H., Engelke, K., Strongin, A.Y., Bröcker, E.-B., and Friedl, P. (2003). Compensation mechanism in tumor cell migration: mesenchymal–amoeboid transition after blocking of pericellular proteolysis. J. Cell Biol. 11.

Wolf, K., te Lindert, M., Krause, M., Alexander, S., te Riet, J., Willis, A.L., Hoffman, R.M., Figdor, C.G., Weiss, S.J., and Friedl, P. (2013). Physical limits of cell migration: Control by ECM space and nuclear deformation and tuning by proteolysis and traction force. J. Cell Biol. *201*, 1069–1084.

Wu, C., Asokan, S.B., Berginski, M.E., Haynes, E.M., Sharpless, N.E., Griffith, J.D., Gomez, S.M., and Bear, J.E. (2012). Arp2/3 Is Critical for Lamellipodia and Response to Extracellular Matrix Cues but Is Dispensable for Chemotaxis. Cell *148*, 973–987.

Wu, S., Huang, J., Dong, J., and Pan, D. (2003). hippo encodes a Ste-20 family protein kinase that restricts cell proliferation and promotes apoptosis in conjunction with salvador and warts. Cell *114*, 445–456.

Wu, X., Tu, X., Joeng, K.S., Hilton, M.J., Williams, D.A., and Long, F. (2008). Rac1 Activation Controls Nuclear Localization of β-catenin during Canonical Wnt Signaling. Cell *133*, 340–353.

Wymann, M.P., Bulgarelli-Leva, G., Zvelebil, M.J., Pirola, L., Vanhaesebroeck, B., Waterfield, M.D., and Panayotou, G. (1996). Wortmannin inactivates phosphoinositide 3-kinase by covalent modification of Lys-802, a residue involved in the phosphate transfer reaction. Mol. Cell. Biol. *16*, 1722–1733.

Xiao, Y., Peng, Y., Wan, J., Tang, G., Chen, Y., Tang, J., Ye, W.-C., Ip, N.Y., and Shi, L. (2013). The Atypical Guanine Nucleotide Exchange Factor Dock4 Regulates Neurite Differentiation through Modulation of Rac1 GTPase and Actin Dynamics. J. Biol. Chem. *288*, 20034–20045.

Xu, T., Wang, W., Zhang, S., Stewart, R.A., and Yu, W. (1995). Identifying tumor suppressors in genetic mosaics: the Drosophila lats gene encodes a putative protein kinase. Dev. Camb. Engl. *121*, 1053–1063.

Yang, J., Zhang, Z., Roe, S.M., Marshall, C.J., and Barford, D. (2009). Activation of Rho GTPases by DOCK Exchange Factors Is Mediated by a Nucleotide Sensor. Science *325*, 1398–1402.

Yin, F., Yu, J., Zheng, Y., Chen, Q., Zhang, N., and Pan, D. (2013a). Spatial Organization of Hippo Signaling at the Plasma Membrane Mediated by the Tumor Suppressor Merlin/NF2. Cell *154*, 1342–1355.

Yin, Z., Sadok, A., Sailem, H., McCarthy, A., Xia, X., Li, F., Garcia, M.A., Evans, L., Barr, A.R., Perrimon, N., et al. (2013b). A screen for morphological complexity identifies regulators of switch-like transitions between discrete cell shapes. Nat. Cell Biol. *15*, 860–871.

Yohe, M.E., Rossman, K.L., Gardner, O.S., Karnoub, A.E., Snyder, J.T., Gershburg, S., Graves, L.M., Der, C.J., and Sondek, J. (2007). Auto-inhibition of the Dbl Family Protein Tim by an N-terminal Helical Motif. J. Biol. Chem. *282*, 13813–13823.

Yu, F.-X., Luo, J., Mo, J.-S., Liu, G., Kim, Y.C., Meng, Z., Zhao, L., Peyman, G., Ouyang, H., Jiang, W., et al. (2014). Mutant Gq/11 Promote Uveal Melanoma Tumorigenesis by Activating YAP. Cancer Cell *25*, 822–830.

Zanconato, F., Forcato, M., Battilana, G., Azzolin, L., Quaranta, E., Bodega, B., Rosato, A., Bicciato, S., Cordenonsi, M., and Piccolo, S. (2015). Genome-wide association between YAP/TAZ/TEAD and AP-1 at enhancers drives oncogenic growth. Nat. Cell Biol. *17*, 1218–1227.

Zanconato, F., Cordenonsi, M., and Piccolo, S. (2016). YAP/TAZ at the roots of cancer. Cancer Cell *29*, 783–803.

Zender, L., Spector, M.S., Xue, W., Flemming, P., Cordon-Cardo, C., Silke, J., Fan, S.-T., Luk, J.M., Wigler, M., Hannon, G.J., et al. (2006). Identification and Validation of Oncogenes in Liver Cancer Using an Integrative Oncogenomic Approach. Cell *125*, 1253–1267.

Zhang, S., Schafer-Hales, K., Khuri, F.R., Zhou, W., Vertino, P.M., and Marcus, A.I. (2008). The Tumor Suppressor LKB1 Regulates Lung Cancer Cell Polarity by Mediating cdc42 Recruitment and Activity. Cancer Res. *68*, 740–748.

Zhang H., Schaefer, A., Wang, Y., Hodge R.G, Blake, D.R., Diehl, J.N., Papageorge, A.G., Stachler, M., Liao, J., Zhou, J., Wu, Z., Akarca, F., de Klerk, L.K., Derks, S., Pierobon, M., Hoadley, K.A., Want, T.C,, Church, G., Wong, K-K., Petricoin, E.F., Cox, A.D., Lowy, RD.r., Der, C.J., and Bass, A.J. (2019). Gain of function RhoA mutations promote focal adhesion kinase activation and dependency in diffuse gastric cancer. Cancer Discovery.

Zhao, B., Wei, X., Li, W., Udan, R.S., Yang, Q., Kim, J., Xie, J., Ikenoue, T., Yu, J., Li, L., et al. (2007). Inactivation of YAP oncoprotein by the Hippo pathway is involved in cell contact inhibition and tissue growth control. Genes Dev. *21*, 2747–2761.

Zhao, B., Ye, X., Yu, J., Li, L., Li, W., Li, S., Yu, J., Lin, J.D., Wang, C.-Y., Chinnaiyan, A.M., et al. (2008). TEAD mediates YAP-dependent gene induction and growth control. Genes Dev. *22*, 1962–1971.

Zhao, B., Li, L., Lei, Q., and Guan, K.-L. (2010). The Hippo–YAP pathway in organ size control and tumorigenesis: an updated version. Genes Dev. *24*, 862–874.

Zhao, R., Yang, H.-Y., Shin, J., Phan, L., Fang, L., Che, T.-F., Su, C.-H., Yeung, S.-C.J., and Lee, M.-H. (2013). CDK inhibitor p57Kip2 is downregulated by Akt during HER2-mediated tumorigenicity. Cell Cycle *12*, 935–943.

Cancer Research UK https://www.cancerresearchuk.org/health-professional/cancer-statistics/statistics-by-cancer-type/breast-cancer Accessed: September, 2019

Appendices

Appendix 1: Software and equipment

Software	Source
Columbus	Perkin Elmer
Morpheus	Broad Institute
Focal Adhesion Analysis Server	Berginski and Gomez, 2013.
Jupyter Notebooks	
RStudio	RStudio Inc.
Fiji, Image J	Schneider et al, 2012.
Estimation Stats	Ho et al., 2019.
SlideBook	3i – Intelligent Imaging Innovations
IncuCyte software	Sartorius
GraphPad Prism	GraphPad software
ClustVis	Metsalu et al, 2015.
MATLAB	Mathworks
Adobe Creative Cloud	Adobe
Word	Microsoft
Excel	Microsoft

Equipment	Source
Opera Quadruple Enhanced High Sensitivity (QEHS) spinning-disk confocal microscope	Perkin Elmer
Total Internal Reflection Fluorescence Microscope	3i – Intelligent Imaging Innovations
Advanced Spinning Disk Microscope	3i – Intelligent Imaging Innovations
Basic Spinning Disk Microsope	3i – Intelligent Imaging Innovations
Celigo Imaging Cytometer	Nexcelom Bioscience
IncuCyte S3 Live-Cell Analysis System	Sartorius
Super-resolution via Optical Reassignment	3i – Intelligent Imaging Innovations
Scanning Electron Microscope	Hitachi

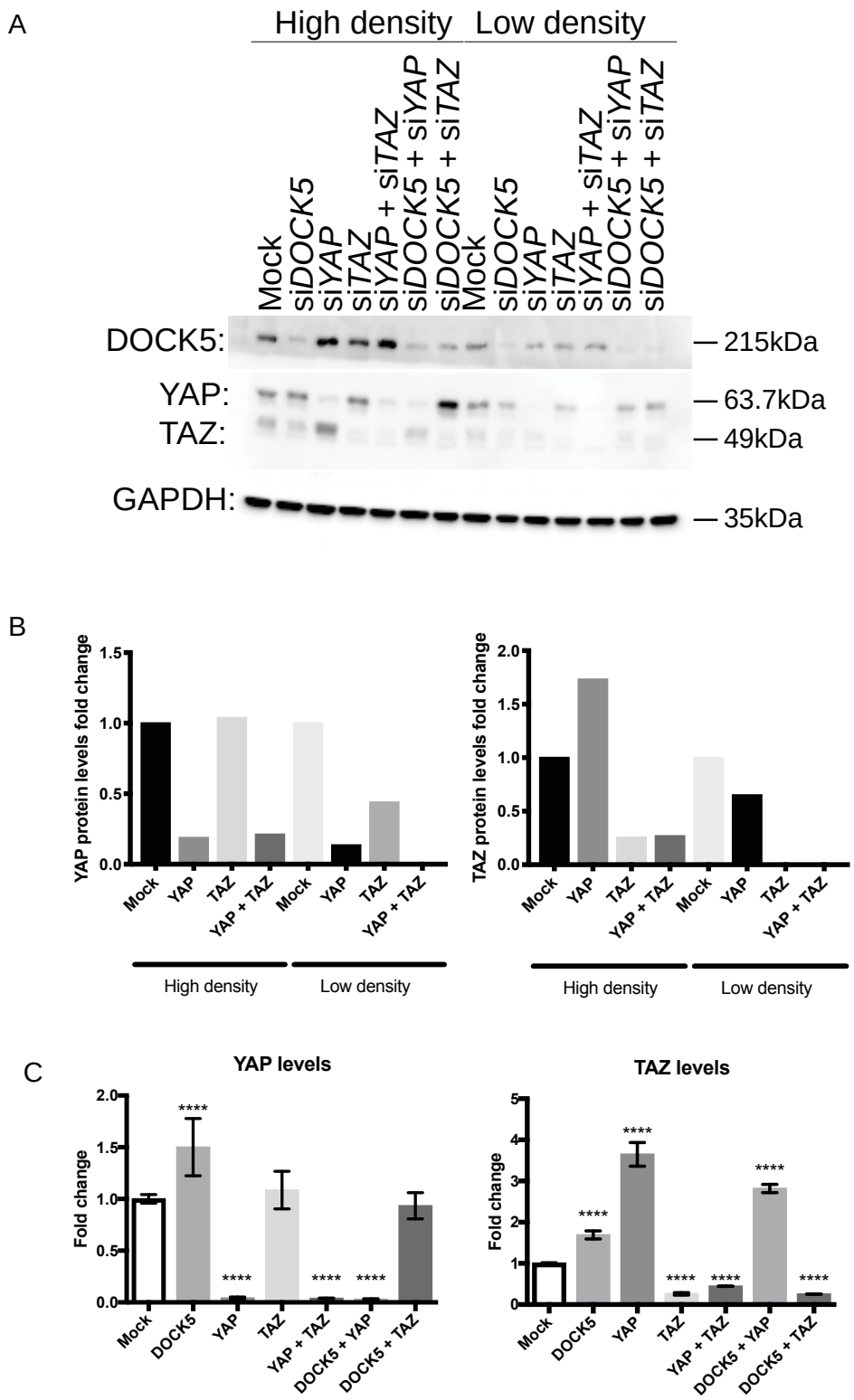

Appendix 2 Validation that YAP/TAZ antibody binds both to YAP and TAZ via western blotting (A) Western blot showing DOCK5, YAP, TAZ, and GAPDH levels in LM2 cells after mock si*DOCK5*, si*YAP*, si*TAZ*, si*YAP* + si*TAZ*, si*DOCK5* + si*YAP*, si*DOCK5* +si*TAZ* transfections, aboth at high and low densities. (B) Graphs show densitometry of 1 western blot for YAP, and TAZ protein levels. Mean is shown. (C) *YAP* and (D) *TAZ* mRNA levels following mock, si*DOCK5*, si*YAP*, si*TAZ*, si*YAP* + si*TAZ*, si*DOCK5* + si*YAP*, si*DOCK5* +si*TAZ* transfections in LM2 cells. Mean ± SD are shown (n = 1, 4 wells per condition, ANOVA, **** P < 0.0001

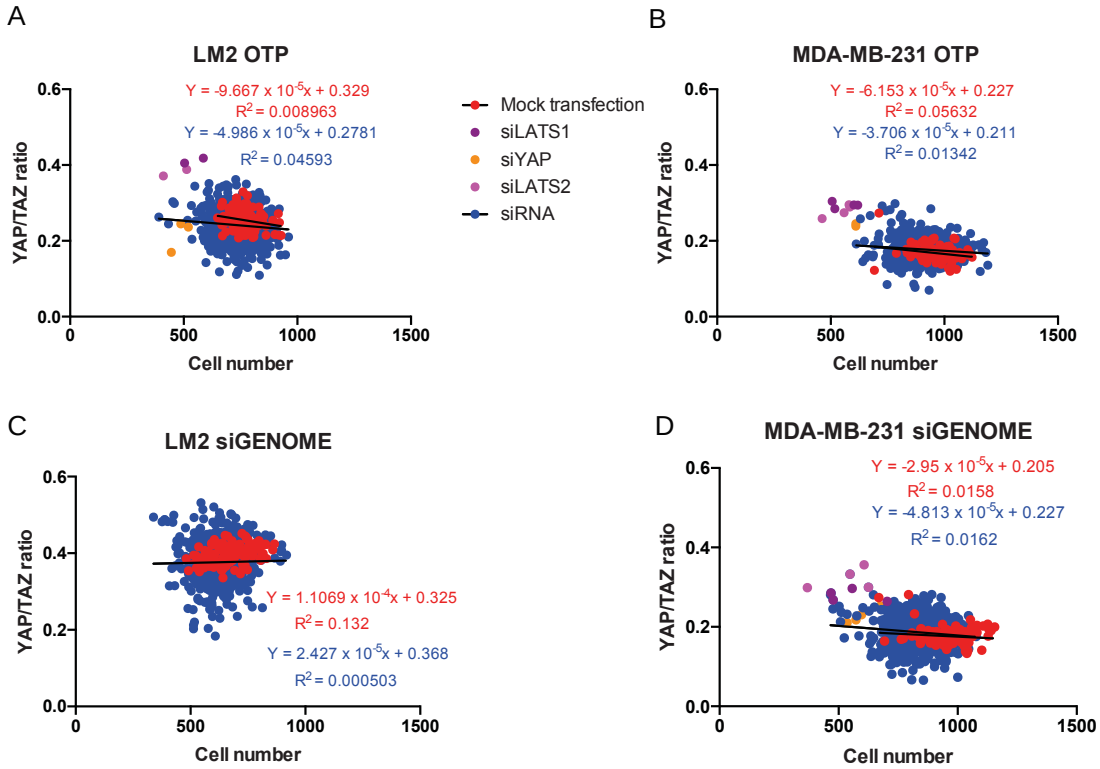

Appendix 3 siRNAs do not decrease viability in LM2, MDA-MB-231, siGENOME or OTP screens.
siRNA transfections do not decrease cell viability in LM2s or MDA-MB-231s. Plots depicting cell number against YAP/TAZ ratio for OTP and siGENOME screens in LM2s and MDA-MB-231s. Transfected cells are shown in blue and mock-transfected in red. Cells transfected with the control siRNA *LATS1*, *LATS2* and *YAP*, are shown in purple, pink and yellow respectively. (A) Analysis of LM2 OTP screen revealed no correlation between cell number and YAP/TAZ ratio for mock transfected, or siRNA transfected cells: linear regression slope of -9.667 $x10^{-5}$ and an R^2 value of 0.008963, and -4.986 $x10^{-5}$ and an R^2 value of 0.04594 respectively. Slopes were not significantly different to each other, P = 1. (B) Analysis of MDA-MB-231 OTP screen revealed no correlation between cell number and YAP/TAZ ratio for mock transfected, or siRNA transfected cells: linear regression slope of -9.390 $x10^{-5}$ and an R^2 value of 0.1207, and -3.706 $x10^{-5}$ and an R^2 value of 0.01342 respectively. Slopes were not significantly different to each other, P = 1. (C) Analysis of LM2 siGENOME screen revealed no correlation between cell number and YAP/TAZ ratio for mock transfected, or siRNA transfected cells: linear regression slope of 1.069 $x10^{-4}$ and an R^2 value of 0.132, and 1.417 $x10^{-5}$ and an R^2 value of 0.00005027 respectively. Slopes were not significantly different to each other, P = 1. (D) Analysis of MDA-MB-231 siGENOME screen revealed no correlation between cell number and YAP/TAZ ratio for mock transfected, or siRNA transfected cells: linear regression slope of -2.950 $x10^{-5}$ and an R^2 value of 0.01577, and -4.813 $x10^{-5}$ and an R^2 value of 0.01617 respectively. Slopes were not significantly different to each other, P = 1.

Appendix 4 RhoGEF/GAP hits for LM2 and MDA-MB-231.

Table 4.1: RhoGEF/GAP hits (at least 3/4 replicates) above 1.5 for LM2 OTP screen. Underlined hits in LM2 OTP and siGENOME only. In bold, hits in LM2 OTP only.

Spindly	Large round	Triangular	Fan	Small round	Normal
ARFGEF3	ARHGAP23	ARHGAP44 /KIAA0672	ABR	ARAP3 /CENTD3	ABR
ARHGAP11A	ARHGAP24	ARHGAP11B	AKAP13	ARHGAP23	FARP2
ARHGAP18	CENTD1 /ARAP2	ARHGAP17	ARHGAP1	**ARHGAP28**	FGD3
ARHGAP20	HMHA1	ARHGAP26	ARHGAP12	ARHGAP29 /PARG1	
ARHGAP33		ARHGEF12	ARHGAP15	ARHGAP32 /RICS	
ARHGEF12		DOCK10	ARHGAP19	ARHGAP5	
ARHGEF28 /RGNEF		DOCK11	ARHGAP22	ARHGEF18	
ARHGEF38		DOCK9	ARHGAP23	ARHGEF39 /C9ORF100	
ARHGEF5		FARP1	ARHGAP24	ARHGEF4	
ARHGEF9		FGD2	ARHGAP29 /PARG1	ARHGEF6	
CHN2		HMHA1	ARHGAP32 /RICS	DEPDC1	
DOCK1		LOC257106 /ARHGAP30	ARHGAP4	DNMBP	
DOCK9		LOC343578 /ARHGAP40	ARHGAP6	DOCK2	
FAM13A		MYO9B	**ARHGEF10**	DOCK3	
FARP1		OBSCN	ARHGEF11	DOCK4	
FGD4		OPHN1	ARHGEF17	DOCK6	
FGD5		PLEKHG4	CENTD1 /ARAP2	DOCK8	
FLJ46688 /PLEKHG7		RACGAP1	DEPDC1	FARP1	
KIAA1688 /ARHGAP39		SH3BP1	DOCK11	FGD4	
LOC345930/ECT2L		SPATA13	DOCK5	MYO9A	
NET1		SRGAP1	ECT2	SOS2	
OPHN1			FLJ10521	STARD13	
PIK3R1			HMHA1	TIAM1	
PLEKHG3			IGDCC4/NOPE	TIAM2	
PLEKHG4			ITSN2	TRIO	
SOS2			KIAA1688 /ARHGAP39	VAV2	
STARD13			MCF2		
SWAP70			MCF2L2		
			MYO9A		
			NGEF		
			OCRL		
			PLEKHG5 /KIAA0720		
			PREX1		
			RACGAP1		
			SRGAP1		
			SRGAP2		
			STARD8		
			SYDE1		

Table 4.2: RhoGEF/GAP hits (at least 3/4 replicates) below 1.5 for LM2 OTP screen.

Spindly	Large round	Triangular	Fan	Small round	Normal
ABR		ARAP1 /CENTD2	ARHGAP33	ABR	ARAP3 /CENTD3
ARHGAP23		**ARHGAP28**	ARHGEF18	AKAP13	ARHGAP29 /PARG1
ARHGAP24		ARHGAP29 /PARG1	**ARHGEF38**	ARFGEF3	ARHGAP5
ARHGAP29 /PARG1		ARHGAP33	DOCK10	ARHGAP1	ARHGAP6
ARHGAP35		ARHGAP5	DOCK8	ARHGAP20	**ARHGEF15**
ARHGAP5		**ARHGEF10**	FARP1	**ARHGEF10**	ARHGEF26 /SGEF
ARHGEF26 /SGEF		ARHGEF18	SOS2	ARHGEF11	**ARHGEF38**
ARHGEF7		ARHGEF39 /C9ORF100		ARHGEF12	ARHGEF39 /C9ORF100
DEPDC1		ARHGEF5		ARHGEF17	CENTD1 /ARAP2
DOCK11		DOCK4		ARHGEF9	DEPDC1
ECT2		DOCK6		DOCK11	DOCK1
RASGRF1		DOCK8		DOCK9	DOCK5
SRGAP2		FGD4		ECT2	DOCK8
TRIO		ITSN2		FAM13A	ECT2
		MCF2		FARP2	FAM13A
		SOS2		FGD1	FARP1
		TIAM2		FGD2	FGD4
				FGD3	MYO9A
				FLJ10665 /PLEKHG6	MYO9B
				HMHA1	OPHN1
				KIAA1688 /ARHGAP39	PREX1
				MCF2L2	SOS2
				NET1	STARD13
				OPHN1	
				PLEKHG4	
				RACGAP1	

Table 4.3: RhoGEF/GAP hits (at least 3/4 replicates) above 1.5 for LM2 siGENOME screen

Spindly	Large round	Triangular	Fan	Small round	Normal
ABR	DEPDC1B	ABR	ARHGAP23	ARHGAP12	ARHGAP15
ARHGAP1	ECT2	AKAP13	ARHGEF11	ARHGAP18	ARHGAP24
ARHGAP10	FLJ43692 /ARHGEF355	ARHGAP26	DEPDC1	ARHGAP21	ARHGEF11
ARHGAP11 A	LOC201176	ARHGEF12	DEPDC2 /PREX2	ARHGAP22	ARHGEF9
ARHGAP17	RACGAP1	ARHGEF3	ECT2	ARHGAP23	DEPDC1
ARHGEF12	RALBP1	DOCK2	FARP2	ARHGAP25	DEPDC2/PREX
ARHGEF18		FAM13A1	OPHN1	ARHGAP5	FGD1
ARHGEF2		FLJ10665	PARG1	ARHGAP6	FLJ43692 /ARHGEF35
ARHGEF5		FLJ13815	RACGAP1	ARHGAP8	KIAA0672
CDGAP		FLJ30058		ARHGEF1	KIAA1244
CHN2		FLJ43692 /ARHGEF35		BCR	KIAA1909
DOCK1		FLJ46688		C9orf100 /ARHGEF39	MCF2
DOCK2		OBSCN		CENTD1	MCF2L2
DOCK4		OCRL		CENTD2	OPHN1
FAM13A		RGNEF		CHN1	OPHN1
FGD2		SGEF		DEPDC1B	VAV2
FGD3		SPATA13		DOCK3	
FGD6		TRIO		DOCK6	
FLJ10357				DOCK7	
FLJ13815				DOCK9	
FLJ20184				FARP1	
FLJ30058				FLJ32810	
FLJ46688				GEFT	
GRLF1				GMIP	
INPP5B				INPP5B	
ITSN1				LOC257106	
ITSN2				LOC343578	
LOC201176				LOC345930	
MCF2L				MYO9B	
MYO9A				NOPE	
OBSCN				PARG1	
OCRL				PIK3R2	
PLEKHG1				PREX1	
PLEKHG2				RASGRF1	
RASGRF2				RICS	
SH3BP1				SH3BP1	
SOS2				SOS1	
TIAM1				SOS2	
VAV1				SRGAP1	
				SRGAP2	
				SWAP70	
				TIAM2	

				VAV3	

Table 4.4: RhoGEF/GAP hits (at least 3/4 replicates) below 1.5 for LM2 siGENOME screen.

Spindly	Large round	Triangular	Fan	Small round	Normal
ALS2	SRGAP1	ARHGAP12		ABR	ABR
ARHGAP18		ARHGAP18		AKAP13	ARHGAP1
ARHGAP21		ARHGAP20		ARHGAP11A	ARHGAP10
ARHGAP6		ARHGAP21		ARHGAP15	ARHGAP12
ARHGEF11		ARHGAP6		ARHGAP17	ARHGAP17
ARHGEF6		ARHGEF1		ARHGAP24	ARHGAP18
ARHGEF7		ARHGEF9		ARHGEF11	ARHGAP23
ARHGEF9		BCR		ARHGEF12	ARHGAP25
C5ORF5		C5ORF5		ARHGEF17	ARHGAP8
CENTD1		C9orf100/ ARHGEF39		ARHGEF2	BCR
CENTD2		CENTD1		ARHGEF3	CENTD1
CENTD3		CENTD2		ARHGEF5	DEPDC1B
CHN1		CHN1		ARHGEF9	DOCK7
DEPDC2/PREX2		CHN2		CENTD3	DOCK9
DOCK10		DEPDC1B		DEPDC1	ECT2
DOCK3		DOCK6		DEPDC2 /PREX2	FARP1
DOCK6		DOCK8		DNMBP	FGD2
DOCK9		DOCK9		DOCK10	FLJ13815
FARP2		PLEKHG3		DOCK2	FLJ32810
FGD4		KIAA0720 /PLEKHG5		ECT2	FLJ46688
FLJ32810				FAM13A1	GMIP
FLJ43692/ARHGEF 35				FGD1	INPP5B
GEFT				FGD3	LOC257106
GMIP				FGD6	MCF2L
KIAA0672				FLJ10357	MYO9B
KIAA0720 /PLEKHG5				FLJ10665	OBSCN
KIAA1909				FLJ13815	OCRL
LOC343578				FLJ20184	PARG1
MCF2				FLJ30058	PIK3R2
NOPE				FLJ41603	RACGAP1
OPHN1				FLJ43692 /ARHGEF35	RASGRF1
PARG1				FLJ46688	RASGRF2
PIK3R2				ITSN1	SH3BP1
RACGAP1				KIAA1244	SRGAP2
RASGRF1				KIAA1909	SWAP70
SGEF				LOC201176	TIAM2
					VAV1

SOS1 SPATA13 SRGAP1 STARD13 TRIO VAV2				MCF2L2 OPHN1 PLEKHG1 PLEKHG4 RACGAP1 RALBP1 RGNEF SGEF TIAM1 TRIO VAV2	

Table 4.5: RhoGEF/GAP hits (at least 3/4 replicates) above 1.5 for MDA-MB-231 OTP screen.

Spindly	Large round	Triangular	Fan	Small round	Normal
ABR AKAP13 ALS2 ARHGAP1 ARHGAP11A ARHGAP15 ARHGAP18 ARHGAP19 ARHGAP20 ARHGAP31 ARHGAP33 ARHGAP4 ARHGAP9 ARHGEF11 ARHGEF12 ARHGEF28 /RGNEF ARHGEF39 /C9ORF100 ARHGEF5 ARHGEF7 ARHGEF9 CENTD1/ ARAP2 DOCK11 DOCK5 DOCK9 ECT2 FAM13A FGD6 FLJ10357	AKAP13 ARHGEF5 ECT2 GMIP HMHA1 RACGAP1 SRGAP2	AKAP13 ARHGAP1 ARHGAP11B ARHGAP18 ARHGAP19 ARHGAP20 ARHGAP32 /RICS ARHGAP4 ARHGEF11 ARHGEF12 ARHGEF16 ARHGEF28 /RGNEF ARHGEF7 ARHGEF9 CENTD1 /ARAP2 DOCK11 DOCK9 ECT2 FAM13A FGD1 FLJ13815 GEFT/ARHGEF25 HMHA1 KIAA1688 /ARHGAP39 LOC257106/ ARHGAP30 MCF2L2 OPHN1	ABR AKAP13 ARHGAP1 ARHGAP11B ARHGAP19 ARHGAP23 ARHGAP24 ARHGAP29 /PARG1 ARHGAP4 ARHGAP6 ARHGAP8 ARHGAP9 ARHGEF2 ARHGEF5 ARHGEF9 DOCK11 ECT2 FLJ10357 FLJ10521 HMHA1 MCF2L2 NGEF RACGAP1 STARD8 TRIO	ABR ARHGAP11B ARHGAP21 ARHGAP23 ARHGAP24 ARHGAP29 /PARG1 ARHGAP33 ARHGAP5 ARHGEF35 ARHGEF39 /C9ORF100 ARHGEF4 ARHGEF6 ARHGEF7 DOCK10 DOCK4 DOCK8 FGD4 FLJ30058 FLJ41603 MCF2 NGEF PREX1 SOS2 SYDE1 TRIO VAV2	MYO9B

FLJ46688 /PLEKHG7 GEFT/ARHGEF25 GMIP HMHA1 IGDCC4/NOPE ITSN2 KIAA1688 /ARHGAP39 LOC343578 /ARHGAP40 MCF2 MCF2L2 NET1 OPHN1 PIK3R2 STARD8 TAGAP		PLEKHG2 RACGAP1 SRGAP1 STARD8			

Table 4.6: RhoGEF/GAP hits (at least 3/4 replicates) below 1.5 for MDA-MB-231 OTP screen.

Spindly	Large round	Triangular	Fan	Small round	Normal
ARHGAP24 ARHGAP5 ARHGEF4 DOCK8 MYO9B TRIO		ARHGEF18 DOCK3 DOCK8 FARP1 MYO9B		DOCK11 HMHA1 MYO9B RACGAP1 VAV3	ABR AKAP13 ALS2 ARHGAP1 ARHGAP11B ARHGAP18 ARHGAP21 ARHGAP23 ARHGAP24 ARHGAP29/PARG1 ARHGAP33 ARHGAP5 ARHGAP9 ARHGEF35 ARHGEF39 /C9ORF100 ARHGEF4 ARHGEF5 ARHGEF7 CENTD1 /ARAP2 DOCK10 DOCK4 ECT2 FGD4

					GMIP HMHA1 MCF2 NGEF PIK3R2 PREX1 STARD13 SYDE1 TAGAP VAV2

Table 4.7: RhoGEF/GAP hits (at least 3/4 replicates) above 1.5 for MDA-MB-231 siGENOME screen.

Spindly	Large round	Triangular	Fan	Small round	Normal
ABR ARHGAP1 ARHGAP17 ARHGAP9 ARHGEF11 ARHGEF12 ARHGEF18 ARHGEF2 CDGAP CENTD3 CHN2 DEPDC1 DEPDC2 /PREX2 DOCK1 DOCK2 DOCK4 ECT2 FAM13A1 FAM7A2 FLJ10357 FLJ13815 FLJ30058 FLJ41603 INPP5B LOC257106 LOC345930 MCF2L2 OCRL PLEKHG1 PLEKHG2	ARHGAP15 ARHGAP22 ECT2 FLJ43692 /ARHGEF35 LOC201176 NGEF OPHN1 RACGAP1 RALBP1 STARD13 STARD8	ALS2 ARHGAP17 ARHGAP22 ARHGAP9 ARHGEF11 ARHGEF7 CENTD3 DEPDC1 DEPDC2 /PREX2 DOCK10 DOCK2 ECT2 FAM13A1 FLJ10357 FLJ13815 FLJ30058 LOC201176 LOC345930 MCF2L2 OCRL OPHN1 PLEKHG4 RALBP1 RGNEF RICS SPATA13	ALS2 ARHGAP22 ARHGAP9 ARHGEF7 DEPDC1 DOCK10 ECT2 FAM13A FLJ30058 LOC20116 OPHN1 RACGAP1 RALBP1 STARD8	ARHGAP10 ARHGAP18 ARHGAP26 ARHGAP9 ARHGEF1 BCR C9orf100 /ARHGEF39 CHN1 DEPDC1B DOCK6 DOCK9 FAM7A2 FARP1 FLJ32810 GEFT INPP5B LOC343578 NGEF PARG1 RASGRF1 RICS SRGAP2 TIAM2	ARHGEF4 FGD6

PLEKHG4 RALBP1 SRGAP2 STARD8					

Table 4.8: RhoGEF/GAP hits (at least 3/4 replicates) below 1.5 for MDA-MB-231 siGENOME screen.

Spindly	Large round	Triangular	Fan	Small round	Normal
ARHGAP10 ARHGEF4 CENTD2 DEF6 DEPDC1B DOCK6 DOCK9 FGD4 MYO9B PARG1 PIK3R2 STARD13 SWAP70		ARHGAP18 ARHGEF4 C9orf100 /ARHGEF39 DOCK6 DOCK9 LOC343578 MYO9B PARG1 RASGRF1 SWAP70		ARHGAP17 ARHGEF4 ECT2 FGD6 FLJ13815 FLJ30058 FLJ43692 /ARHGEF35 LOC345930 MCF2L2 RACGAP1 RGNEF	ARHGAP18 ARHGAP22 ARHGAP26 ARHGAP9 ARHGEF1 ARHGEF7 BCR C9orf100 /ARHGEF39 DEPDC1 ECT2 FAM7A2 FLJ32810 GEFT INPP5B LOC343578 NGEF OPHN1 RALBP1 RICS SPATA13 SRGAP2 STARD8

Appendix 5.1: LM2 OTP screen averaged percentage Z-scores: average QMS for each "hit" gene. Signature for mock-transfected cells named "cells" is also shown.

Genes (siRNAs OTP)	Z-score normal % normalised	Z-score spindly % normalised	Z-score large round % normalised	Z-score triangular % normalised	Z-score fan % normalised	Z-score small round % normalised
ALS2	-1.544161432	-0.535040944	-0.864724619	-0.365763496	1.900916655	1.985439442
ARAP1/CENTD2	-1.943239359	1.204047292	0.185519295	-2.126740293	0.155681098	2.498076191
ARAP3/CENTD3	-3.71859924	1.363946566	-0.877878256	-0.897701649	1.092747086	3.974568357
ARHAGAP44/KIAA0672	-1.584904589	-1.171316766	-1.231486941	1.568764041	1.791724243	0.903754664
ARHGAP11A	-1.834080668	5.097366203	-1.204239592	-0.459474661	-0.280095201	-0.290297291
ARHGAP11B	-2.081183311	0.142879559	-0.924591017	1.509595186	0.577788214	1.355820062
ARHGAP12	-2.837927395	-0.632368497	1.174922176	3.916753826	5.572456226	-0.319449571
ARHGAP15	-1.541692498	-0.07943109	0.170507214	-0.21167279	3.423891932	1.112858492
ARHGAP17	-2.266952353	1.721519669	-1.179895721	3.500105394	-0.294231255	-0.434434862
ARHGAP20	-1.700668384	2.061154057	-1.289609567	3.8031994	2.846770117	-3.900567168
ARHGAP23	-2.069524399	-3.626421426	1.958136669	-0.776303209	4.223841823	3.646439121
ARHGAP25	-1.727051974	1.115473624	1.536001822	-0.785212626	1.966489868	1.304072844
ARHGAP28	-2.413388695	1.363518302	-0.661163225	-2.922239183	0.09409905	3.067560746
ARHGAP29/PARG1	-2.936319626	-2.854517356	-0.135102935	-3.516534671	5.849975572	4.725102576
ARHGAP31	-1.592149186	1.858720701	-0.871133013	1.731051991	1.909515437	-0.213581911
ARHGAP32/RICS	-1.864757092	-0.041203878	-0.155916179	-0.958681651	2.080487202	1.911522348

ARHGAP33	-1.904453795	6.075055363	-0.801679776	-2.909159044	-1.518825409	1.158901002
ARHGAP5	-5.015488294	-2.495842222	-0.533332885	-1.901879776	-1.233887927	10.38453658
ARHGAP6	-2.108591999	0.714240361	-0.038143477	1.877604872	2.209307918	0.599508505
ARHGEF15	-2.758461823	-0.328002637	-1.0412531	2.144381113	2.597600156	1.154518552
ARHGEF18	-2.021325327	0.732022588	-0.813993941	-2.139383875	-1.989291608	4.773831967
ARHGEF19	-2.782188511	-0.313766776	-1.150312368	3.324511962	-0.305645694	1.773773729
ARHGEF2	-1.241148497	-0.102520646	-0.288084241	-0.199614551	1.805943418	0.958109531
ARHGEF26/SGEF	-3.201383213	-2.390132005	-0.020757316	-0.380119562	2.709786232	4.809307467
ARHGEF28/RGNEF	-1.414765146	4.070567485	-0.900972388	1.322463647	0.290947961	-1.891634705
ARHGEF38	-2.144281255	6.216178806	-1.25623654	-1.649776277	-1.968794785	1.058897056
ARHGEF39/C9ORF100	-4.349828247	1.320094482	-0.869624895	-2.061483124	-0.802432437	6.853539946
ARHGEF4	-2.429210818	-1.062292843	-1.02318671	-0.911525956	-1.010169394	5.238247558
ARHGEF5	-2.008200428	3.418029628	-0.190706789	-2.144606704	0.867783758	1.45168579
ARHGEF6	-1.723484815	0.080995403	-0.064469167	-1.217967131	-1.099367003	1.850811948
CDC42	-2.832435758	6.857417393	-0.743713361	0.005251705	0.739894697	-1.156841623
Cells	0.376658268	0.165324891	-0.108540241	-0.677518303	0.367251255	-0.484222721
CENTD1/ARAP2	-1.885674034	-0.230375236	1.991374922	1.606217593	2.748683351	0.487276786
CHN1	-1.318958025	-0.867395299	-0.194276726	0.957998356	2.614660211	0.441578407
DEPDC1	-2.278581507	-2.015291221	0.207411263	-1.084628233	2.144500054	3.663762251

DEPDC1B	-2.460352928	-0.770242686	0.296167087	1.971398242	0.764202435	1.937013952
DNMBP	-1.50785012	-0.405549842	-0.715062355	1.131166639	-0.187085431	1.565142564
DOCK1	-2.824741975	4.794434589	-1.081396717	1.895726863	-0.032814368	-0.839263807
DOCK10	-2.151142089	-0.77614946	-0.818834358	1.343459285	-1.150748472	3.202660605
DOCK2	-1.57865762	-0.429396427	-0.300210881	-0.718484718	0.145197233	2.941069683
DOCK4	-1.666166395	0.619387609	-0.850574814	-1.606469059	-0.07052453	3.122453059
DOCK5	-2.221565666	1.184452057	-0.786190561	1.41155992	3.10155197	-0.359979403
DOCK8	-3.232251628	-1.573994185	-0.958236348	-3.832141654	-1.783354011	9.147951537
DOCK9	-2.018900595	3.43307527	-0.086206507	5.207366954	1.564460514	-4.298823446
ECT2	-5.423698103	-2.562274844	8.371793108	-0.684372471	22.11429754	-4.669123754
FAM13A	-3.493955799	15.50756143	-0.487295225	1.358162477	-1.654498319	-4.074466875
FARP1	-6.682138351	7.350213397	-1.143150623	3.188096697	-2.095044119	2.515019852
FGD4	-3.847105536	3.196475209	-1.079966445	-2.068135738	-0.879726817	5.061395767
FGD5	-2.329359098	4.098399556	-1.201679675	1.076082558	-0.095317377	-0.224246925
FLJ10357	-2.000431864	1.116632795	-0.194548296	0.259433191	0.792631825	1.180526414
FLJ30058	-7.229179696	5.039924147	0.036015568	-1.896873432	-2.173396135	7.390929815
IGDCC4/NOPE	-1.581366004	0.478207326	-1.45337457	0.771232646	3.078158417	-0.290385046
INPP5B	-1.249969689	1.885996915	0.703234052	0.582931423	2.01987249	-0.620460308
LATS1	-2.67355912	0.708542306	-1.001327305	0.016937021	1.351725928	2.485329851

LATS2	-3.05838048	2.265351722	-0.233729932	4.534607949	1.902334212	-1.554381466
LOC345930/ECT2L	-1.611121782	3.017745612	0.46470543	-0.052621727	1.272116564	-0.712027926
MCF2L	-1.67461141	-0.170495345	-0.879531758	1.935522415	1.301041008	0.340176557
MYO9A	-2.385258381	-0.609914694	-0.072480149	1.516449902	1.901077022	1.967516086
MYO9B	-1.934818977	0.011088284	0.384303578	1.550247265	-0.353695793	1.777107148
OBSCN	-2.351798986	-0.398256807	-1.454754172	3.574649318	1.864759696	-0.203594431
OCRL	-1.836435916	0.030296901	1.250997801	1.639601724	5.071302481	-0.51814169
OPHN1	-2.052992546	2.349233049	-0.837567275	3.722798142	1.031957916	-2.313899458
PIK3R2	-5.787971342	3.51004604	-0.938565499	-0.07092601	-0.956514194	4.531425524
PLEKHG3	-1.940091061	3.093344171	0.026220345	1.488474858	2.874815395	-1.960197171
PREX1	-2.167601316	-2.134301063	-0.526248946	-0.233092737	3.146923114	2.998824906
RAC1	-0.848270077	-0.49921813	-0.802995602	-2.406826652	0.004290765	3.350387693
RAC2	-2.604923749	3.422861719	-0.847544178	1.912171876	-0.0608528	0.148953849
RAC3	-1.551134092	-0.186533702	-1.365967361	1.950861595	0.798902504	0.131651455
RACGAP1	-1.287707447	0.396648769	-0.843761061	1.434835623	4.877841457	-1.975892506
RALBP1	-1.701448557	1.407079159	-1.008909084	-0.340262551	1.807086965	0.707388544
RASGRF1	-1.382992257	-2.201780179	-1.434346199	2.142595993	1.570017051	0.902387958
RASGRF2	-1.374789165	0.393844435	0.460418402	1.909550653	0.937429843	-0.347524204
RHOA	-2.26371022	2.277136066	0.35161157	3.948155953	3.554828534	-3.379623832

RHOBTB1	-2.392852688	2.066719034	-1.085619596	-2.586883304	-0.680349441	4.211816431
RHOBTB2	-3.125474371	-5.856517335	0.001955597	-2.536164057	4.834415617	7.544561017
RHOD	-1.745689931	-1.716174454	-0.868028854	-1.296718668	0.459006356	4.474866385
RHOF	-3.42698725	-0.340332374	-1.225277626	1.604499869	7.143671642	0.070098201
RHOJ	-2.261334385	-1.51136762	-0.477853208	-1.481954638	0.556468034	4.877258359
SH3BP1	-1.691443787	1.040656755	-0.960421861	-4.524732132	-0.427141916	-1.445499096
SOS2	-5.226868441	5.253408869	-1.342496493	-1.996601585	-1.873324657	5.83662201
SPATA13	-1.56381166	0.596966129	-0.15576732	3.547580612	0.646687578	-0.8995163
SRGAP1	-2.223359427	0.23696478	-0.412889929	3.582831528	3.138292912	-0.133404895
STARD13	-6.767380072	4.417893088	-0.181019473	-0.863975884	-1.085086598	6.323952486
SWAP70	-1.703991612	3.492325518	-1.26679374	0.783721473	-1.511266432	0.259303709
SYDE1	-2.341781219	1.61250981	1.049521044	0.139876929	2.976345348	0.705631645
TAGAP	-1.810685632	-0.201460967	1.519550812	-0.268014554	1.820666713	1.715050963
TIAM1	-2.4877162	-0.819052346	0.114465382	1.416933442	1.572673158	2.060725655
TIAM2	-1.678041452	-1.875827544	-1.333474097	-2.431777357	-0.607942224	5.903871743
VAV2	-1.755121304	-0.134976651	-1.005023162	-0.007466875	-0.13479026	2.67534246
YAP	-2.345546979	0.37322755	-1.420118141	1.472861091	2.169654239	0.562874888

Appendix 5.2: LM2 siGENOME screen averaged percentage Z-scores: average QMS for each "hit" gene. Signature for mock-transfected cells named "cells" is also shown.

Genes (siRNAs siGENOME)	Z-score spindly %	Z-score large round %	Z-score triangular %	Z-score fan %	Z-score small round %	Z-score normal %
ABR	7.552233257	-0.761526562	1.394353349	-0.758181468	-1.863374665	-3.191809222
ALS2	-2.421468634	0.213473818	-1.33671729	1.010498556	4.461050713	-1.531658107
ARHGAP1	3.547066142	-0.755722649	-0.042349336	-0.657211737	1.094393006	-2.356698417
ARHGAP10	4.150938384	-1.20261221	1.711163778	-0.836351253	0.843756175	-3.056282217
ARHGAP12	-1.050489306	-0.065884726	-2.105515314	-0.968799728	3.029965912	-2.879765823
ARHGAP17	8.172793912	-1.182457587	2.135389154	-1.223969634	-1.077697663	-4.035470042
ARHGAP18	-1.58377096	0.584520433	-2.856295693	0.073657196	7.05002567	-6.973218406
ARHGAP22	-2.713281274	-0.422217516	-0.806356696	0.019169613	2.298458501	-1.548969393
ARHGAP23	-0.968177329	-0.365035937	-1.248051976	2.350978795	2.813401072	-3.627090654
ARHGAP25	0.068997709	-0.320710975	-1.503485602	0.477340619	3.076801711	-3.486711931
ARHGAP5	-0.839875857	0.040297371	-1.818434221	0.729438692	4.036331471	-1.788050171
ARHGAP6	-3.539722606	1.765686186	-2.547765245	1.340426533	2.47860107	-1.024097247
ARHGAP8	-0.794523016	-0.138230723	-1.137385569	-0.076460297	3.512933648	-3.634564491
ARHGAP9	0.784588304	-0.692902027	-0.167766132	0.36974171	4.62286753	-7.776181323
ARHGEF1	0.751036391	-1.010993917	-2.383191572	-0.177147667	2.967333864	-1.279626289
ARHGEF10	1.549054077	-0.482779771	1.145618353	1.400620279	0.221894557	-2.056702916
ARHGEF12	3.878136172	0.312668566	2.987635386	0.779124647	-3.313673732	-1.744346007

ARHGEF15	1.093461741	-0.844317824	1.79381577	1.404392796	-0.512134277	-1.575080701
ARHGEF16	2.71219435	0.259470979	-0.436916557	-0.792342041	1.746071609	-2.260414788
ARHGEF18	4.112550724	0.881728425	-1.180459951	-0.433339252	-0.854761773	-1.382186379
ARHGEF2	3.316655292	0.033281295	1.92497646	-0.092850595	-2.521850119	-1.148662784
BCR	0.105249122	-0.66421826	-2.507888575	-0.250434555	6.267243862	-2.898152782
C9orf100/ARHGEF39	-1.720771809	-0.189631276	-2.962805445	0.756451299	6.383900785	-2.283936882
CDGAP	4.404276859	-0.564992758	1.242770553	-0.59704252	-0.163169989	-1.724954702
CENTD1	-2.526073676	-0.885151086	-3.540999219	-1.095090774	10.87710826	-3.534922469
CENTD2	-4.133527459	-1.048681608	-3.821204539	-0.69165534	8.550869622	-1.314346704
DEPDC1B	-2.168763902	2.074481761	-2.042420874	-0.290460626	2.927048057	-2.480797034
DOCK11	-0.856826214	0.051918716	-0.565922944	2.291745546	1.234833403	-1.166113902
DOCK2	3.625567911	-0.178536812	4.765254588	-1.109385644	-2.000305282	-2.268274919
DOCK3	-2.633488671	0.124210633	-0.974815489	0.427779649	4.32222853	-1.236423695
DOCK4	3.382009685	-0.039017711	0.09044556	-0.311842326	-0.653376594	-1.512704429
DOCK5	-1.289900366	-0.053466254	-0.227306664	-0.936272603	3.090654488	-0.937060304
DOCK7	0.937151865	-0.869110472	0.822698959	-0.83597694	2.864331312	-2.29550389
DOCK9	-2.328411319	-1.238267881	-3.432410111	-0.793415794	9.704364587	-3.035901115
ECT2	-0.750221909	14.58683035	2.296826032	14.14274469	-5.442267829	-4.985213017
FARP1	1.294612674	-0.788201546	-0.129088276	-1.12434213	8.233281078	-5.245338573

FGD2	2.862549751	-1.110812344	-2.437556222	-0.434435517	4.493602936	-3.167577286
FGD3	3.76993446	-1.086374114	3.84551143	0.937370025	-4.241875954	-1.284490471
FGD5	-1.628880592	-0.00495189	-1.316798278	2.540183251	2.978530596	-1.613257726
FLJ10357	3.266265499	0.900176799	2.71571549	0.79875807	-3.10369026	-1.538755367
FLJ13815	8.405373303	-0.76202	3.69358791	1.052656761	-1.383394594	-3.934212132
FLJ32810	-3.939841604	0.156861073	-0.838849612	1.057378046	5.986027538	-5.510810925
FLJ46688	6.437695907	0.438664849	2.95335948	-0.807120845	-2.398756594	-3.031460257
GMIP	-2.814754923	-1.430947443	-2.351307641	-0.659464032	6.908808642	-6.123589131
GRLF1	2.639840387	-1.203279723	1.653335138	-0.679188018	0.312036952	-1.977929509
INPP5B	2.615770153	-1.239575153	-0.56794458	-1.322029934	3.950346092	-5.244385692
LOC257106	0.870838868	-0.960205948	-1.15693461	-0.628662385	2.400560523	-2.838612883
LOC343578	-4.184043096	-0.189724288	-2.474012495	0.957278274	3.289722825	-3.216694925
MCF2L	7.456136896	-1.286151213	-1.516366311	-0.584325948	0.816438963	-3.64237077
MYO9A	2.71181943	-1.392029273	-0.551908921	-0.330934387	1.591057791	-2.05449179
MYO9B	-1.124088492	0.121661852	-1.372160067	-0.765003771	8.123316304	-3.719867166
NET1	1.744332156	0.823273228	0.309646308	-0.316422782	2.143061975	-2.540476792
NOPE	-2.485253397	-1.213701937	-2.98975261	-0.69961641	7.705276089	-1.961814183
OBSCN	2.405408196	-0.023436897	2.700194353	-0.590506298	0.907598267	-2.816781949
OCRL	8.269507431	-0.486229825	2.408959239	-0.960222367	-0.215729746	-4.105833305

PARG1	-2.33336309	-0.201270973	-2.520050978	2.294939003	4.327263461	-4.824676094
PIK3R2	-2.213011122	-0.727487182	0.591424611	1.171629732	3.104914182	-3.282697174
PLEKHG2	3.722629266	-0.782620606	0.770113054	-0.207134851	-1.510891297	-1.364299199
PREX1	-0.126365775	-0.075590137	-1.244874968	-0.511675214	3.275878586	-1.437623723
RACGAP1	-2.069035141	17.85018613	0.742743583	9.424081634	-4.407244689	-3.011933154
RASGRF1	-3.75832273	-0.936011061	-2.315348589	-0.67246996	9.038523169	-2.39695096
RASGRF2	3.802810017	-0.159021028	0.829753481	0.129738103	-0.473579281	-2.268788824
RICS	-2.134548164	-0.479031051	2.280105513	-0.31555434	1.849874884	-2.199916917
SH3BP1	2.144792942	-1.076198009	-1.74647557	0.01856294	4.065448189	-2.981407208
SNX26	-1.621803178	-0.158283702	-1.455556995	-0.513885316	2.541289889	-2.817523609
SOS1	-2.419878668	-1.203892982	-0.352948963	-0.445990265	5.323964422	-1.661065396
SOS2	1.961048612	-0.995300135	-1.087598512	-0.059563264	3.580494142	-2.81312379
SRGAP1	-2.393266916	-1.676621946	-0.247703737	1.79112306	3.39940503	-4.182259875
SRGAP2	-1.079414878	-0.457819491	0.336066426	0.459295686	2.449523446	-3.067586653
SWAP70	-1.666650163	1.115128255	-3.025451818	-0.467606301	6.400591526	-2.018603416
TIAM2	-1.246450809	-0.086977231	-2.420631414	0.566920397	6.999752069	-3.04051571
VAV1	4.224368257	-1.170247771	0.097067283	-0.972568813	1.188920585	-2.641397983
VAV3	0.186909471	-0.561159799	-0.656557958	-0.66252392	2.81546253	-1.417762188
Cells	-0.861225628	-0.094347402	0.065672611	0.05238158	0.890028032	-0.166874884

Appendix 5.3: MDA-MB-231 OTP screen averaged percentage Z-scores: average QMS for each "hit" gene. Signature for mock-transfected cells named "cells" is also shown.

Genes (siRNAs OTP)	Z-score spindly %	Z-score large round %	Z-score triangular %	Z-score fan %	Z-score small round %	Z-score normal %
ABR	1.63808018	0.69027826	0.702583483	3.84998999	2.018804012	-2.583340062
AKAP13	2.349334973	5.920865369	9.073055612	6.8041128	0.654515324	-3.27302168
ALS2	1.701037644	0.102292158	0.491042586	2.081106248	2.219724118	-2.487268811
ARHAGAP44/KIAA0672	0.662770116	-0.19551292	0.36163352	-0.009777502	2.018759274	-1.921157697
ARHGAP1	2.573259646	2.5813898	6.538458275	3.771295583	1.103838084	-2.857976608
ARHGAP11B	0.170412936	-0.188267387	2.015685462	2.75884551	2.377948677	-2.553200411
ARHGAP18	5.765508514	1.377744505	1.352067952	3.143454624	1.02567785	-2.879700813
ARHGAP19	5.581796613	3.576085965	4.105419033	3.928738925	0.726663137	-3.179098597
ARHGAP21	0.654378084	-1.043219788	0.98591276	0.379734124	2.15213423	-1.841846361
ARHGAP23	1.052802871	0.62261243	0.314020736	1.981903687	2.247414248	-2.474193661
ARHGAP24	-1.699748464	0.411014497	-0.823359247	3.211858037	3.126592196	-2.599964318
ARHGAP29/PARG1	0.152026522	-0.016692069	-0.733671552	2.674013684	3.989592557	-3.707818489
ARHGAP31	3.421713274	0.827918637	0.599269971	0.919945179	1.384888964	-2.193839882
ARHGAP33	4.045828974	-0.096210748	0.401159919	-0.452765458	3.259196493	-3.762983429
ARHGAP4	6.131553558	0.736969538	1.934383226	1.152747185	0.055983192	-1.797376884
ARHGAP5	-2.185782686	-1.043219788	-1.543095203	-0.775017085	7.362896408	-4.538711219
ARHGAP9	2.753666021	0.208223464	2.856198694	3.615562994	1.411945371	-2.649679267

ARHGEF16	2.506458982	2.709883464	4.483290659	2.992828171	0.639013019	-2.427256897
ARHGEF35	-0.797624171	1.995577954	0.972668389	1.619082659	2.716827111	-2.317660872
ARHGEF39/C9ORF100	1.969818136	-0.30291046	-0.610667334	0.234293324	3.049664973	-2.711689158
ARHGEF4	-1.944994074	-0.116586587	-0.483267781	-0.320859019	3.69084405	-2.174145619
ARHGEF5	6.552778465	4.15628125	2.101642108	6.623656522	0.929721415	-3.490662836
ARHGEF7	2.481273933	-0.368453576	9.105477654	2.194470385	1.667836122	-3.379552984
BCR	0.596072948	0.771800763	0.33089261	0.291989742	2.709429802	-2.235594559
C5ORF5/FAM13B	2.117183266	0.281311542	2.407349189	3.463372501	1.957072083	-2.812277419
CDC42	4.278598339	-0.544037902	3.029347208	1.333949512	0.94566092	-2.290327349
CENTD1/ARAP2	3.098629526	0.591343345	1.313151518	1.408220117	1.008166103	-1.903196956
DEPDC1	-0.263180182	-1.043219788	0.686130267	4.986953794	2.284742139	-2.512732391
DOCK10	-1.345486038	-0.625557822	-1.282317777	0.424567587	4.822006279	-3.317503029
DOCK4	1.241160382	-0.169314393	0.584296633	-1.099071371	3.153072989	-2.401482894
ECT2	2.942773447	3.281724558	5.255373609	17.26752429	-0.402172043	-3.304782735
FAM13A	10.49645299	-0.377359737	4.211681692	0.381792675	-0.581432277	-2.452957464
FGD4	0.279756391	-0.615750094	-1.267691054	0.416382007	3.037227283	-2.25014059
FLJ10357	4.029187601	-0.08980207	0.927122558	1.902287569	0.607936473	-1.670234627
FLJ32810	3.05458979	1.576515555	1.037606232	3.96712749	2.135982964	-3.22747717
FLJ41603	-1.418016095	-1.043219788	-0.462283174	1.213401001	3.135520806	-2.025882451

GMIP	3.314273086	2.115547141	2.006159394	0.563251052	1.173617041	-2.139719265
HMHA1	9.621715227	7.010921171	10.52777202	7.6528031	-2.752805653	-2.356442167
LATS1	6.208694341	0.984626731	3.811570313	1.665151783	0.214681507	-2.186117636
LATS2	6.246039793	1.755386496	7.888344243	8.284782881	-0.041649663	-3.30875145
MCF2	3.142607398	1.126429806	1.167046264	1.534433074	3.775371493	-3.548359103
MCF2L2	5.812649342	-0.489763477	2.896602626	3.429847856	0.639248709	-3.021780565
NGEF	-0.278717659	-0.199296369	1.505599458	3.679290274	2.066691279	-2.278881917
OBSCN	0.729262917	3.101444121	0.768441333	1.115578836	1.949057082	-1.99829329
OCRL	5.104568925	0.387779182	-0.05388096	1.314351948	1.671930133	-2.759988036
PIK3R2	3.066895937	-0.070404019	-0.138844754	-0.097930744	2.77730597	-3.014367231
PLEKHG5/KIAA0720	-0.369864225	1.399873035	0.714394359	1.577701645	2.213082343	-1.965356361
PREX1	0.382332779	0.628261603	1.031100425	1.24892208	1.815097136	-1.858869031
RHOA	4.966373613	3.315676158	9.132984123	2.251713735	-1.630291352	-1.79361147
RHOB	0.948099924	2.242561229	-0.021994004	2.506256768	2.698685498	-2.766600941
RHOBTB1	-1.647805033	-0.112134441	-0.943247058	-0.835177294	2.839821353	-1.672931811
RHOBTB2	-1.18768113	2.736939784	0.249740108	10.24286723	1.752577222	-2.651615376
RHOC	6.937503586	-0.228765132	4.394241284	2.337192695	-1.51713045	-1.537162566
RHOF	2.790008119	0.981885197	5.484736002	6.370860748	2.621667181	-3.676282128
RHOH	2.229301605	-1.043219788	1.927646081	2.703707814	1.27436218	-2.278490647

RHOJ	-0.919610593	0.599523148	-1.656543889	-0.692288249	2.706171059	-1.703375324
SPATA13	1.267081597	-1.043219788	0.61182321	0.096204076	1.627470226	-1.546068521
SRGAP1	2.307178355	0.425124351	3.255164329	2.234725795	2.505743845	-3.485661988
SRGAP2	0.192001874	1.393341253	0.192872337	-0.074192759	1.668184629	-1.5543946
STARD13	1.652887819	-0.750280702	-0.254026887	8.137184255	1.727257103	-2.799199275
STARD8	4.592912499	0.711230966	3.87067179	3.69169724	0.114792421	-2.112483033
SYDE1	1.213291193	1.916587414	1.885289412	3.765750777	3.322098013	-3.853098798
TAGAP	5.190427418	0.172500139	2.151919901	0.896990021	0.233295113	-1.810274794
TRIO	-1.330861022	1.126608755	0.44680432	1.767232156	2.668281058	-1.999896622
VAV2	0.216167116	-0.103083794	-0.184227005	-0.494515858	3.321125844	-2.625076655
YAP	3.849331244	-0.113790133	3.521684208	0.589584206	0.943216858	-2.136454656
Cells	-0.161724132	-0.080515929	-0.303842462	0.160074894	-0.017281176	0.122756911

Appendix 5.4: MDA-MB-231 siGENOME screen averaged percentage Z-scores: average QMS for each "hit" gene. Signature for mock-transfected cells named "cells" is also shown.

Genes (siRNAs SiGENOME)	Z-score spindly %	Z-score large round %	Z-score triangular %	Z-score fan %	Z-score small round %	Z-score normal %
ALS2	0.336173564	1.029159843	4.219245805	2.958636942	0.048336129	-1.50069501
ARHGAP1	3.22520698	-0.642360155	-0.506952523	3.162418705	3.713626817	-3.883969922
ARHGAP12	0.694145884	-0.822173747	-0.642878827	-0.16804157	2.061369443	-1.688710326
ARHGAP18	-0.154478292	-0.117091974	-1.62345835	0.139167652	4.054652415	-2.834017164
ARHGAP21	0.432148435	0.060347716	-0.844401973	2.953701817	3.03918946	-2.542297819
ARHGAP22	0.801858235	2.673343352	2.631969432	2.858280864	1.035693145	-1.590076724
ARHGAP26	0.333203589	0.178858403	1.29795746	0.042521428	3.177623846	-2.400463962
ARHGAP6	0.678755591	0.984726388	1.861097411	0.634802004	1.546728877	-1.540313051
ARHGAP8	2.669555434	0.326171111	1.081712638	1.545171092	2.986020363	-3.221661975
ARHGAP9	3.011439401	1.064285939	1.620650197	2.107585603	1.998697923	-2.548627735
ARHGEF1	-0.332957747	-0.580006795	-1.106550343	-0.622083456	3.458952384	-1.763529915
ARHGEF11	3.953781482	1.472714618	3.069560052	1.293112728	-0.670699669	-1.58176055
ARHGEF19	0.431053725	-0.329791985	0.992438468	-0.521001554	1.558780684	-1.19081593
ARHGEF6	-0.052893011	1.002425251	2.348907754	0.84855828	1.487385907	-1.579714154
ARHGEF7	1.506177602	-0.510777735	4.253402478	3.004955192	1.064656383	-2.385622243
BCR	0.385933657	-0.15805532	-1.093978425	-0.614742457	3.006439467	-1.77026004

C5ORF5	1.371849735	1.066022772	1.464205552	2.991223745	1.288316714	-1.891385126
C9orf100/ARHGEF39	0.391613472	-0.109567321	-1.455310892	0.214858761	3.308228666	-2.052187336
CENTD3	3.692070127	0.438268635	4.308731559	0.704971153	-0.708199741	-1.488252119
CHN1	-0.024965437	-0.822173747	-1.061590254	-0.666154798	3.146604708	-1.679037484
CHN2	4.113849536	-0.420112648	0.239750247	-0.463193337	2.861698647	-2.931899509
DEPDC1	12.05041438	0.51383367	10.88609877	2.879493359	-1.195453048	-2.795389058
DEPDC2/PREX2	4.693641317	1.575164381	3.78351006	1.137827731	-1.353132759	-1.414981776
DOCK10	1.057628981	1.548017445	4.594321698	3.29625549	0.48304784	-2.213179967
DOCK2	4.184006022	0.318063258	3.477975802	0.294784571	-0.237939141	-1.74541494
DOCK4	5.736749908	0.188933196	1.131592035	4.701269334	-0.142021994	-2.661642938
DOCK9	-2.386373968	-0.38946458	-1.939881777	0.593854955	5.206108141	-2.448310686
ECT2	4.23592991	8.486647402	7.289090047	9.50427094	-2.033917351	-3.654491449
FAM13A1	6.847721317	0.096126743	2.654160985	2.813538071	0.803232164	-2.774325759
FAM7A2	2.364250578	0.467018479	0.927616066	0.468282912	3.086628095	-3.015900988
FARP1	-0.574139136	-0.554590356	-1.095256618	-0.331760654	3.195184062	-1.591904976
FLJ10357	5.542674778	-0.085916864	3.341524841	0.086417723	-1.126160795	-1.427259623
FLJ20184	2.414792984	-0.17734656	-0.449617384	2.722770208	0.875886665	-1.690821193
FLJ32810	-0.122508165	0.751900852	-0.80309541	1.60176696	3.274652895	-2.692382658
FLJ41603	2.367823824	0.083868335	0.819939964	0.095749727	1.154798683	-1.572990455

GEFT	0.173483013	-0.579617092	-0.433822343	-0.470462447	4.431044333	-2.769567971
GMIP	-0.804244317	-0.822173747	-1.034721125	2.002002888	3.560806512	-2.815988687
INPP5B	3.544155745	0.456823404	-0.632460138	-0.169893306	2.198684522	-2.209247513
ITSN1	-0.177746758	0.857850307	1.054536241	0.456104813	1.52638801	-1.24831188
KIAA0720	-0.145655541	-0.822173747	1.994255582	0.586688495	4.67559864	-3.274210693
LATS1	5.984939784	0.10422992	2.879467364	0.46114365	1.853124174	-3.206901628
LATS2	7.871039865	1.18202454	9.998545997	2.385803829	0.622833492	-4.027617918
LOC343578	-1.105688929	1.260862217	-1.772923518	0.149080912	4.001251037	-2.698975648
LOC345930	5.506650808	-0.115918656	2.824177911	3.707630853	-2.11094	-1.332630509
NGEF	0.533935623	2.044747681	0.61855462	1.183239594	2.168049286	-2.053851506
OPHN1	0.212504769	4.39487106	3.944789059	3.056180342	0.530673709	-2.013093384
PARG1	-2.578541832	-0.457113499	-1.631052127	0.239628442	3.133776417	-1.814977228
PIK3R1	0.300037066	0.53088774	-0.563775893	0.339556089	1.475482787	-1.208722195
PLEKHG2	3.670002472	1.391998255	2.201828074	1.121463964	0.009910828	-1.738629133
PLEKHG4	4.705204636	1.599045579	2.17684005	1.195778635	-0.699234656	-1.556696863
RALBP1	4.594825136	5.954820687	8.732688294	6.17890091	0.609359978	-4.90743491
RASGRF1	-1.292767705	-0.382363227	-1.614408389	0.391296423	4.278608491	-2.201352305
RICS	0.259917026	-0.237511364	2.980803241	1.081400533	4.715688063	-4.165783246
SNX26	1.3108349	1.033558233	0.744565254	-0.020574368	1.526498154	-1.595129555

SOS2	0.916867583	-0.822173747	-0.958706387	-0.493000279	2.260311979	-1.404633782
SPATA13	0.255814491	2.126749507	3.492864769	0.639425009	1.31290202	-1.789690659
SRGAP2	0.764115808	-0.648870421	0.261256505	0.944021216	2.566287227	-2.253971598
STARD8	2.431526802	6.00234449	1.52339158	4.067793798	0.807886009	-1.929760794
YAP	2.338475611	1.025336846	2.711199105	1.704877233	2.623669596	-3.238296193
Cells	0.264231506	0.332450701	0.746107017	-0.046543967	-0.019968256	-0.06407675

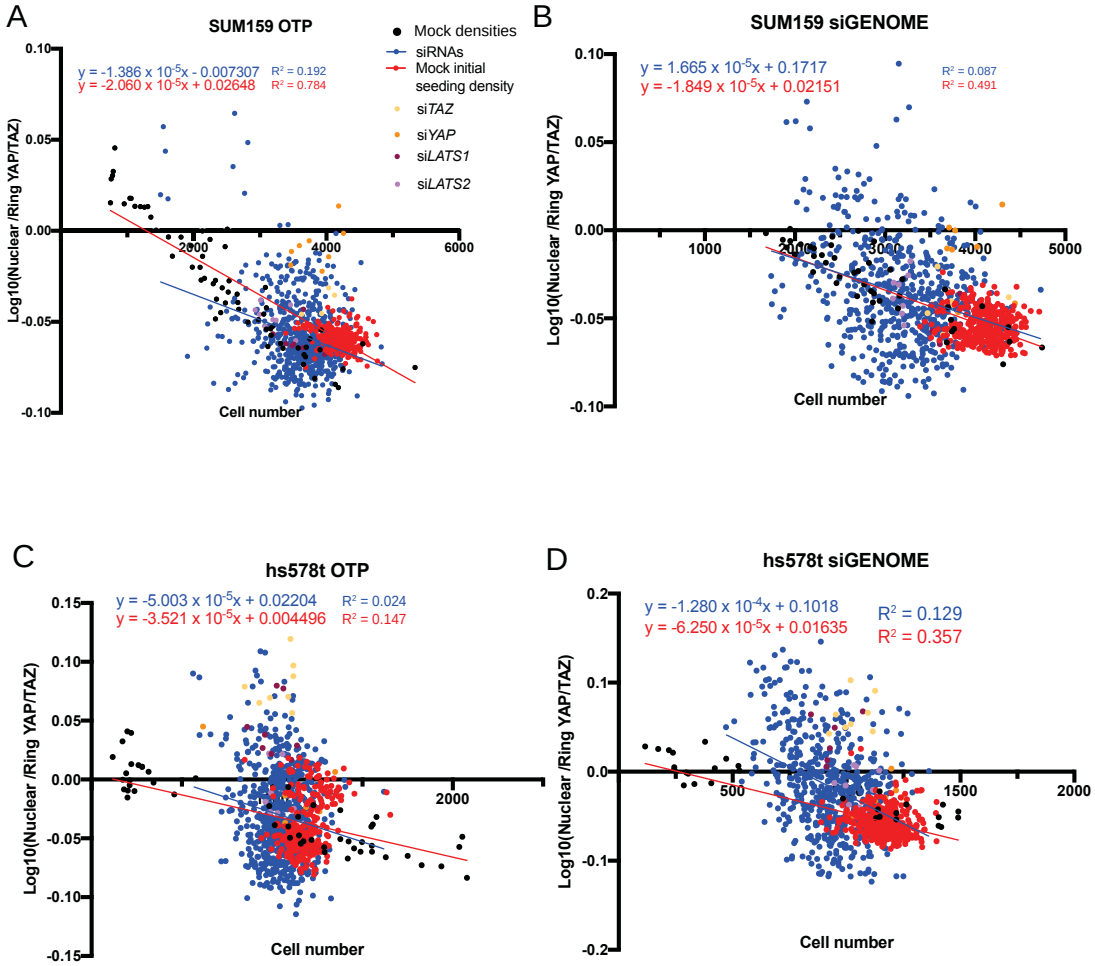

Appendix 6 YAP/TAZ ratio versus density in SUM159 and hs578t screens

Mock transfected cells at initial seeding density do not cover the range of densities for siRNA transfected populations in SUM159 and hs578t screens. Plots depicting cell number against YAP/TAZ ratio for OTP and siGENOME screens in SUM159 and hs578t. Transfected cells are shown in blue, mock-transfected at initial seeded density in red, and mock transfected at various densities in black. Cells transfected with the control siRNA *LATS1*, *LATS2* and *YAP* and *TAZ* are shown in purple, pink, yellow and orange respectively. (A) SUM159 OTP, (B) SUM159 siGENOME, (C) hs578t OTP, (D) hs578t siGENOME.

Appendix 7: YAP/TAZ ratio Z-scores for LM2 and MDA-MB-231.

Table 7.1: YAP/TAZ ratio Z-scores for LM2 OTP screen.

Genes LM2 OTP	Well Name	Z-score YAP/TAZ RATIO
LATS1	I23	5.285713712
LATS1	J23	4.802706264
LATS2	K23	4.179569653
ARHGEF15	M22	3.733272143
LATS2	L23	3.585020412
RHOBTB2	K20	3.183818788
HMHA1	M17	3.183407385
Cells	B22	3.106353616
DOCK11	N18	3.037810649
RHOBTB2	K20	2.975473409
ITSN2	C17	2.949810623
PIK3R2	G21	2.916927354
LATS1	J23	2.835257272
ITSN2	E15	2.747914489
HMHA1	M15	2.738363491
ITSN2	C17	2.708638836
ARHGEF15	M22	2.693409254
ARHGEF17	G12	2.632448388
ARHGEF7	F22	2.618993985
VAV1	J22	2.596504052
HMHA1	M15	2.541081484
ITSN2	E15	2.504996362
ARHGEF17	I10	2.468879282
HMHA1	M17	2.443630751
RHOBTB2	I08	2.419191709
AKAP13	I22	2.347155094
ARHGAP29/PARG1	I05	2.346402406
LATS2	L23	2.236631339
PIK3R2	C21	2.230650548
DOCK4	N22	2.22420702
Cells	O21	2.187859184
ABR	D08	2.144633839
FLJ10357	L22	2.136533612
ARHGAP19	C03	2.124191606
MYO9A	I03	2.094658385
STARD8	I21	1.951566468
ABR	D08	1.938696864
ARHGEF16	I07	1.917636504
Cells	B22	1.914871356
RHOBTB2	I08	1.894556872
VAV1	J22	1.848592899
ARHGEF16	C13	1.831519738
OBSCN	F21	1.812435958
Cells	O22	1.801704247
RHOF	G17	1.801457771
DOCK11	N18	1.771849423
ECT2	D09	1.738107198
PLEKHG2	H22	1.737593942
RHOF	M17	1.696254546
KIAA1688/ARHGAP39	C05	1.663713541
ARHGEF39/C9ORF100	L19	1.657806008
MCF2	C03	1.631070052
Cells	O03	1.620574587
Cells	B20	1.576058371
KIAA1688/ARHGAP39	C05	1.571649997
Cells	B21	1.571485729
ARHGEF15	K08	1.562081084
RHOF	G17	1.55333514
MCF2L2	C22	1.551982012
STARD8	E07	1.545895594
ARHGAP23	E06	1.517915502
Cells	M20	1.513823549
LOC343578/ARHGAP40	I13	1.511166171
ARHAGAP44/KIAA0672	D21	1.50429589
ARHGEF7	D18	1.502102888
DEPDC1	K21	1.495187375
Cells	B20	1.494654027
MYO9A	I03	1.456652684
ARHGEF17	G12	1.450777317
DOCK4	N22	1.437649449
ARHGEF16	C13	1.4266314
ARHGEF9	F12	1.405844112
Cells	B21	1.387068521
Cells	B19	1.359137842
DOCK8	N20	1.349479302
VAV2	L18	1.343646851
DOCK11	D04	1.341827126
SRGAP3	K03	1.32252478

KIAA1688/ARHGAP39	K19	1.309423345
ABR	L12	1.297267198
ARHGEF16	I07	1.291528066
Cells	O22	1.283779629
NGEF	G21	1.265305365
DOCK8	N20	1.247832712
Cells	O21	1.222903844
ECT2	D09	1.221032052
AKAP13	I22	1.208610159
ARHGEF7	F22	1.207333937
C5ORF5/FAM13B	E05	1.182368288
FLJ10357	D12	1.175812232
Cells	B03	1.174225805
PIK3R1	M05	1.158312955
TAGAP	E10	1.157957133
Cells	B04	1.151035979
ARHGAP12	I11	1.13714155
ARHAGAP44/KIAA0672	D21	1.13118603
FLJ10357	L22	1.130633001
Cells	M14	1.118138367
MCF2L2	C22	1.103236771
ARHGEF39/C9ORF100	L19	1.092006018
ARHGAP29/PARG1	G09	1.088304989
RND2	C04	1.057576779
ARHAGAP44/KIAA0672	D19	1.035226825
MCF2	G09	1.033044567
SRGAP2	G13	1.025813761
ARHGEF15	K08	1.017542833
ARHGAP1	M21	1.015589016
ARHGAP19	I07	1.015237819
ECT2	L13	1.008070932
Cells	B17	1.005504654
VAV2	L18	0.972806893
FLJ10357	D12	0.959874511
Cells	B13	0.955065615
ECT2	L13	0.950558091
NGEF	G21	0.945410663
ARHGAP29/PARG1	G09	0.945076581
TRIO	M21	0.931584926
Cells	B18	0.926352416

ABR	L12	0.923459646
PLEKHG5/KIAA0720	H09	0.901500382
ARHGEF9	L14	0.898047571
RND2	I04	0.882748168
Cells	B18	0.878310555
ARHGAP23	E06	0.854975191
KIAA1688/ARHGAP39	K19	0.853818332
Cells	O17	0.848168447
ARHGAP26	F16	0.847235255
Cells	B14	0.842149357
STARD8	E07	0.832735882
LOC257106/ARHGAP30	I17	0.831288945
SRGAP2	C15	0.831045728
RASGRF2	E21	0.82866473
PLEKHG2	H22	0.813704563
ARHGAP10	D22	0.807667905
Cells	O15	0.807667905
RND2	I04	0.799129196
MYO9A	E17	0.792618318
Cells	B07	0.792604361
RASGRF1	I03	0.791711006
NGEF	E11	0.781884097
FGD2	I17	0.780278714
Cells	B07	0.764134488
Cells	O07	0.753849756
PLEKHG5/KIAA0720	L21	0.734832253
Cells	B04	0.728793266
TIAM1	H19	0.720181135
ARHGAP28	C19	0.718867072
OCRL	E22	0.70886537
Cells	O17	0.707140035
ARHGEF17	I10	0.698811034
ARHGAP24	M07	0.684625
ARHGAP19	I07	0.681155736
ARHGAP9	C20	0.671182404
Cells	B17	0.667449534
ARHGAP23	G16	0.661718963
RASGRF1	I03	0.660456834
ARHGAP19	C03	0.65569074
FGD3	K03	0.654602233
ARHGEF11	M13	0.653879041
RHOV	E19	0.647753176

ARHGAP1	I09	0.641955058
PREX1	C18	0.638433498
ARHGAP28	C07	0.636855905
DOCK11	D04	0.631119751
DEF6	J06	0.60950906
FGD3	K13	0.604063846
ARHGAP29/PARG1	I05	0.598055507
ARHGAP12	G17	0.593216801
TAGAP	E08	0.588730988
ARHGAP32/RICS	G20	0.586818445
ARHGAP24	M07	0.582173625
VAV2	D06	0.565564486
FLJ46688/PLEKHG7	F20	0.563731461
RACGAP1	H18	0.557479073
LOC345930/ECT2L	J17	0.548987024
ARHGEF7	D18	0.548505653
PREX1	C18	0.545953209
RHOV	E19	0.544974298
Cells	O18	0.543201233
ARHGEF26/SGEF	G22	0.530043222
Cells	M22	0.527543072
Cells	O05	0.527022585
DEF6	J06	0.525983836
Cells	B19	0.51396258
RACGAP1	J12	0.506858279
ARHGAP4	G18	0.500774102
Cells	M06	0.49354862
FLJ10521	K17	0.490475873
ARHGAP12	G17	0.475357223
FLJ32810	G22	0.462458678
AKAP13	K04	0.460106016
Cells	O15	0.45504367
Cells	O11	0.452831552
VAV2	D06	0.450441927
Cells	B08	0.443769603
ARHGAP9	C20	0.442488172
ARHGEF9	L14	0.431433564
FGD2	I17	0.426073433
ARHGEF39/C9ORF100	H11	0.425012439
ARHGAP10	D22	0.423265744
ARHGAP21	J04	0.422726118

RHOD	M14	0.421559628
ARHGAP12	I11	0.412623803
Cells	O08	0.409950496
Cells	B14	0.409737792
LOC345930/ECT2L	D03	0.400049548
RACGAP1	J12	0.398743079
RACGAP1	H18	0.396465085
BCR	D07	0.395523565
BCR	H13	0.392490691
ARHGAP24	C09	0.39169459
ARHAGAP44/KIAA0672	D19	0.38685088
Cells	O04	0.383149836
RND1	E09	0.376896349
PLEKHG2	N04	0.36124136
PREX2	E17	0.360948794
ARHGEF39/C9ORF100	H11	0.360560708
FGD1	I19	0.360528858
ARHGAP9	G04	0.352153877
LOC343578/ARHGAP40	K17	0.343282023
ARHGAP26	H04	0.343171482
Cells	B10	0.342751546
FLJ32810	G22	0.340940714
FGD5	K19	0.327587173
Cells	O11	0.310136478
PREX2	E17	0.309724536
Cells	B10	0.305895871
Cells	O16	0.303090877
TIAM1	D13	0.284540424
PLEKHG5/KIAA0720	H09	0.275947197
ARHGEF28/RGNEF	E22	0.27518843
ARHGAP23	G16	0.265784682
ARHGAP28	C07	0.243425177
ARHGAP22	E12	0.238557723
Cells	O08	0.235294463
TAGAP	E10	0.233123416
RASGRF2	E21	0.232725815
RHOU	E16	0.222983988
FGD2	M15	0.213327242
DOCK1	L15	0.212197956
ITSN1	M08	0.211358083
Cells	B08	0.211030043

RHOQ	M20	0.207858612
OBSCN	F21	0.197161765
BCR	H13	0.19397121
SYDE1	C22	0.192306589
Cells	O03	0.189661364
Cells	O18	0.187590101
Cells	O06	0.185928595
RND2	C04	0.183378568
SRGAP3	K03	0.183058417
C5ORF5/FAM 13B	E05	0.182560246
Cells	O12	0.179256271
INPP5B	K07	0.177634383
DEF6	L08	0.176550013
TRIO	M21	0.169271114
Cells	M20	0.16858132
FGD3	K13	0.168384581
Cells	B09	0.167298173
RHOJ	C07	0.165596543
TRIO	G03	0.164791791
ARHGAP5	N03	0.163065386
DEF6	L08	0.160236411
DOCK8	N10	0.157088397
TIAM1	D13	0.154433358
SRGAP3	G07	0.151333674
SRGAP2	C15	0.143724419
FLJ41603	J16	0.141835263
BCR	D07	0.136030736
ARHGEF9	F12	0.132882722
Cells	M04	0.127630234
DOCK4	N12	0.126904188
ARHGAP28	C19	0.124872614
PREX1	E12	0.123864087
RHOQ	G08	0.121631652
FLJ10521	E03	0.113441609
Cells	I22	0.112624026
Cells	K06	0.106458829
Cells	O05	0.100494848
FLJ41603	J14	0.095268972
Cells	O07	0.092516055
RHOQ	M20	0.090895022
ARHGAP8	C11	0.085287423
Cells	O16	0.085194564
LOC343578/A RHGAP40	I13	0.079460839

TIAM2	D11	0.069667197
ARHGAP6	G05	0.068529366
FARP2	I06	0.056479571
VAV3	N19	0.047862808
ARHGAP22	C12	0.045390889
FLJ10521	K17	0.041377612
PIK3R1	M13	0.040587293
INPP5B	K07	0.035650263
Cells	O19	0.031210378
TAGAP	E08	0.0281808
ARHGAP1	I09	0.025553816
ARHGAP24	C09	0.019791108
DOCK2	F06	0.01879387
RHOBTB1	M16	0.006942329
VAV1	F14	-0.002056473
LOC257106/A RHGAP30	K05	-0.006977862
LOC257106/A RHGAP30	K05	-0.007982402
DOCK3	H21	-0.013867857
TIAM2	H07	-0.014801049
Cells	O04	-0.016480795
ARHGAP10	L04	-0.018113882
LOC345930/E CT2L	D03	-0.019625795
ARHGEF28/R GNEF	E22	-0.027325667
ITSN1	I12	-0.030941629
Cells	B16	-0.033511553
DOCK10	F18	-0.036357789
CHN2	F19	-0.037710918
FLJ46688/PL EKHG7	F20	-0.043320981
ARHGAP25	G12	-0.049257747
DOCK4	N12	-0.050935772
PIK3R1	M05	-0.054584487
ARHGAP22	C12	-0.055755142
OBSCN	L05	-0.062020575
RHOU	E16	-0.070372645
ARHGAP8	M11	-0.070962885
ARHGEF11	K09	-0.071738189
Cells	B09	-0.072099051
DEPDC1B	C18	-0.072378438
Cells	K18	-0.073510071
RHOC	M03	-0.081710931
LOC257106/A RHGAP30	I17	-0.082660531

FLJ10665/PLEKHG6	N05	-0.085303721
FGD1	I19	-0.096837219
MCF2	G09	-0.099114966
Cells	B12	-0.099674881
Cells	B13	-0.108238135
TIAM2	H07	-0.109046409
TIAM1	H19	-0.112279504
MYO9A	E17	-0.115218239
ARHGAP9	G04	-0.122170285
Cells	K20	-0.127008991
TRIO	G03	-0.130274233
PLEKHG5/KIAA0720	L21	-0.138612216
Cells	I18	-0.141954349
CENTD1/ARAP2	C13	-0.144262204
FARP2	M18	-0.154173306
SRGAP2	G13	-0.155065682
OCRL	E22	-0.162713959
CENTD1/ARAP2	C17	-0.166990331
MCF2L2	E10	-0.173708318
ARHGAP21	J04	-0.17498454
MCF2	C03	-0.179536398
FGD3	K03	-0.185528564
ARHGAP5	N03	-0.189065522
DOCK2	F06	-0.190979855
MCF2L	K15	-0.192620825
ARHGAP8	M11	-0.193072938
Cells	K14	-0.19955056
Cells	B15	-0.204612345
TIAM2	D11	-0.206991985
FARP1	I21	-0.213104394
RHOH	G13	-0.219694847
PLEKHG2	N04	-0.223696126
ARHGEF5	G20	-0.230228471
CHN2	F19	-0.238923257
LOC343578/ARHGAP40	K17	-0.239266662
ARHGEF26/SGEF	G22	-0.239603909
VAV3	N19	-0.240029316
RHOV	M07	-0.241773486
DOCK10	F18	-0.250026388
ARHGAP17	N15	-0.256824449
ARHGAP26	F16	-0.263511799

ARHGEF6	J20	-0.271942163
AKAP13	K04	-0.273995186
IGDCC4/NOPE	J15	-0.277354678
Cells	O06	-0.279804899
RASGRF2	K07	-0.285053513
Cells	B11	-0.289579496
Cells	O13	-0.290482622
DOCK2	F10	-0.293032307
ARHGAP6	G05	-0.300112213
FLJ41603	J14	-0.305839825
Cells	M04	-0.312596782
Cells	M18	-0.317084292
VAV1	F14	-0.3177619
RASGRF1	G15	-0.319814923
ARHGAP20	N21	-0.320281519
ARHGAP4	C14	-0.323561914
Cells	B11	-0.330300745
ARHGAP10	L04	-0.331619508
RHOU	M12	-0.334299574
Cells	O12	-0.334299574
GEFT/GEFT/ARHGEF25	E18	-0.336192447
PREX2	C11	-0.336639314
RAC3	G04	-0.339132002
ARHGAP4	C14	-0.347392053
NGEF	E11	-0.348137307
RHOQ	G08	-0.351741273
Cells	O20	-0.361100233
ARHGAP15	C04	-0.365939615
FGD1	M09	-0.369927345
DEPDC1B	C18	-0.376791841
SYDE1	E18	-0.376943769
Cells	I20	-0.380104536
PREX1	E12	-0.382245482
Cells	I12	-0.383463502
ARHGAP6	I15	-0.383967697
RHOH	G13	-0.387518018
SYDE1	E18	-0.393337561
SRGAP1	E11	-0.394049205
ARHGEF1	C19	-0.394097023
MCF2L	K15	-0.402407282
ARHGAP15	C04	-0.403878786
MCF2L	K05	-0.4112211
RHOJ	C07	-0.416167019

ARHGEF19	M19	-0.418360056
SPATA13	N17	-0.421719513
SRGAP3	G07	-0.427185123
LOC201176/ARHGAP27	I06	-0.450847282
ARHGAP26	H04	-0.454902543
DOCK3	H21	-0.463665933
ARHGEF11	K09	-0.482470325
ARAP1/CENTD2	G06	-0.493101137
GEFT/ARHGEF25	E18	-0.495231155
OPHN1	H17	-0.501507447
ARAP1/CENTD2	C16	-0.504193934
PLEKHG4	D14	-0.504586981
LOC345930/ECT2L	J17	-0.515905949
C5ORF5/FAM13B	K13	-0.528905719
ARHGAP32/RICS	G20	-0.52893377
ARHGEF1	C19	-0.529221198
Cells	M06	-0.531118992
INPP5B	G11	-0.531707817
SOS2	C21	-0.532162811
FGD1	M09	-0.53577247
ARHGAP32/RICS	E20	-0.538259986
DOCK2	F10	-0.541175143
ITSN1	M08	-0.543004394
PLEKHG4B/KIAA1909	J10	-0.543387261
ARHGAP11B	J18	-0.54541414
ARHGEF6	J20	-0.549895993
RAC3	G16	-0.551853166
DOCK3	D05	-0.551993145
Cells	K06	-0.557458723
ARHGAP8	C11	-0.558590356
Cells	B06	-0.561605025
PREX2	C11	-0.561931642
OCRL	I08	-0.565224066
FLJ13815	K11	-0.572755278
SRGAP1	E11	-0.577437897
Cells	M18	-0.577697803
DNMBP	D17	-0.582275232
Cells	K04	-0.588283505
Cells	K08	-0.588906194

SOS2	G19	-0.596319775
GEFT/ARHGEF25	C16	-0.597201284
ARHGAP6	I15	-0.597757264
RAC3	G04	-0.598052099
Cells	K08	-0.600655881
GMIP	E15	-0.606074602
RASGRF1	G15	-0.608517118
Cells	K14	-0.608787744
DEPDC1B	G08	-0.6194644
RHOJ	G11	-0.623533996
ARAP1/CENTD2	G06	-0.637804657
RAC3	G16	-0.640550288
FLJ32810	E04	-0.640900674
GMIP	E15	-0.640926403
CENTD1/ARAP2	C17	-0.648301528
OPHN1	H17	-0.650504819
PLEKHG1	N08	-0.660336761
CHN1	F13	-0.660544431
Cells	O14	-0.666585215
Cells	K22	-0.670778098
PLEKHG3	L17	-0.671137073
ALS2	F17	-0.683386608
PLEKHG4	F08	-0.689638996
OBSCN	L05	-0.689812453
ARHGEF19	M19	-0.690572188
IGDCC4/NOPE	H03	-0.690705809
ARHGAP31	M19	-0.694347279
ARHGAP15	I04	-0.69715685
Cells	B16	-0.698873629
FLJ10665/PLEKHG6	N05	-0.70244705
FARP2	M18	-0.702957539
PLEKHG3	J11	-0.705254738
Cells	K16	-0.713467972
PLEKHG1	N06	-0.714648547
CHN1	F03	-0.715039106
ARHGAP11B	D20	-0.718427976
ARHGAP17	N15	-0.725589207
FLJ41603	J16	-0.728014029
RND1	M11	-0.728567058
Cells	M16	-0.72860844
ARHGAP5	F09	-0.733757027

IGDCC4/NOPE	H03	-0.741617802
ARHGEF1	I11	-0.743541395
Cells	B15	-0.743711558
ARHGEF4	J13	-0.751369661
ARHGEF10	E07	-0.755289068
RHOB	K14	-0.764088568
RHOU	M12	-0.766300736
ARHGEF10	E05	-0.773672955
OCRL	I08	-0.774600768
RHOD	E20	-0.77544602
Cells	O09	-0.785954503
RHOG	I18	-0.789117286
Cells	B12	-0.789485383
ARHGAP15	I04	-0.790790666
Cells	I12	-0.791199444
RHOH	K11	-0.79276102
PLEKHG1	N06	-0.795356004
PLEKHG4	D14	-0.797227796
CENTD1/ARAP2	C13	-0.797989242
ARHGAP25	E14	-0.799285914
ARHGEF6	H20	-0.806941257
FLJ13815	K15	-0.810944487
LOC201176/ARHGAP27	I06	-0.811451771
Cells	B05	-0.81851284
Cells	I16	-0.821012117
SRGAP1	E03	-0.821880608
ARHGAP25	G12	-0.822846143
RALBP1	N11	-0.829664487
ITSN1	I12	-0.834237129
FGD5	G05	-0.836290152
Cells	K18	-0.845142467
DOCK7	N16	-0.84730182
ARHGEF5	C08	-0.851297064
DOCK10	J08	-0.853083775
FLJ10665/PLEKHG6	J09	-0.871248666
Cells	I18	-0.871651201
FARP2	I06	-0.878843717
ARHGAP22	E12	-0.885124973
PLEKHG3	J11	-0.887662383
ARAP1/CENTD2	C16	-0.891443796
FARP1	I21	-0.899283007

ARHGAP5	F09	-0.902686778
ARHGAP21	F04	-0.907280664
ARHGEF11	M13	-0.908659208
SH3BP1	L16	-0.912485296
ARHGEF5	C08	-0.915798128
Cells	I14	-0.930156157
Cells	M14	-0.930762121
RHOA	M10	-0.934088695
RHOJ	G11	-0.934928568
PLEKHG4B/KIAA1909	H06	-0.939267912
DOCK10	J08	-0.956018712
Cells	M10	-0.959890786
IGDCC4/NOPE	J15	-0.966752605
FGD5	K19	-0.967773582
OPHN1	F15	-0.968056892
RHOG	G18	-0.970063255
Cells	M12	-0.971014477
ARHGEF4	H15	-0.975242472
PLEKHG3	L17	-0.975709068
Cells	M16	-0.979465248
Cells	I16	-0.984936011
RHOH	K11	-0.988307163
LOC201176/ARHGAP27	G14	-0.990139907
ARHGAP11B	J18	-0.998190204
ARHGEF5	G20	-1.000402322
ARHGEF2	K22	-1.005571219
ARFGEF3	J03	-1.012739134
RASGRF2	K07	-1.014185519
FARP1	I15	-1.015589363
Cells	O10	-1.016993207
SH3BP1	L20	-1.017248451
MCF2L	K05	-1.026862656
OPHN1	F15	-1.027798552
ARHGEF12	C06	-1.038859142
FARP1	I15	-1.044531994
FGD5	G05	-1.045070089
ARHGEF35	K18	-1.059649707
ARHGEF19	C15	-1.060342211
ALS2	F17	-1.0737
FLJ46688/PLEKHG7	D10	-1.084239322
RAC1	C14	-1.087866063
DOCK8	N10	-1.092078137

FGD6	E08	-1.093268736
RHOB	K14	-1.103836358
ARHGEF4	J13	-1.105009977
DOCK1	N13	-1.106309318
DEPDC1	K09	-1.108602955
ARHGAP20	N21	-1.115219752
RHOG	I18	-1.116581056
ARHGAP4	G18	-1.119258792
DEPDC1B	G08	-1.120504169
GEFT/GEFT/ ARHGEF25	C16	-1.123293416
RALBP1	F07	-1.126450505
SOS1	I14	-1.131853178
ARHGAP11B	D20	-1.132491288
RHOG	G18	-1.135596762
ARHGEF12	C06	-1.136171469
ARHGEF1	I11	-1.137104661
CHN2	L11	-1.138276828
ARHGEF38	H14	-1.14189279
Cells	K12	-1.142031396
Cells	O19	-1.142143899
ARHGEF10	E07	-1.145083345
DEPDC1	K09	-1.148614102
SOS1	K06	-1.163375858
PLEKHG4	F08	-1.169246479
ARHGAP17	L09	-1.173245308
DNMBP	J19	-1.190687007
DOCK6	F05	-1.194869259
ARAP3/CENT D3	C08	-1.196402057
YAP	N23	-1.200684079
FLJ46688/PL EKHG7	D10	-1.204682907
ARHGAP20	J21	-1.207047417
LOC201176/A RHGAP27	G14	-1.210293826
DOCK6	D15	-1.21381306
ARHGEF28/R GNEF	G14	-1.21866566
SOS2	G19	-1.224974835
FLJ10665/PL EKHG6	J09	-1.227530986
Cells	K16	-1.233611068
RALBP1	F07	-1.23424997
ARHGEF6	H20	-1.237779595
RHOC	M03	-1.24450103
SPATA13	F11	-1.250580834

DOCK6	D15	-1.256667679
SPATA13	F11	-1.257348331
ARHGAP20	J21	-1.263644359
CHN1	F13	-1.269944572
FLJ13815	K15	-1.272707003
ARHGEF28/R GNEF	G14	-1.276874526
ALS2	N07	-1.288795055
SOS2	C21	-1.306397792
DOCK1	N13	-1.320989263
RAC1	C14	-1.333821579
RHOB	E04	-1.33715474
DOCK3	D05	-1.339111614
RND1	E09	-1.340213945
ARHGEF26/S GEF	G10	-1.34472699
SPATA13	N17	-1.350342366
GMIP	E13	-1.351477085
ARHGEF19	C15	-1.352672061
RHOF	M17	-1.354351807
SH3BP1	L20	-1.356591469
ARFGEF3	J03	-1.356918086
ARHGAP32/R ICS	E20	-1.374827899
DNMBP	D17	-1.381269477
ARHGEF38	D16	-1.389346515
ARHGEF35	G06	-1.392117363
ARHGAP18	G03	-1.399690957
MCF2L2	E10	-1.401151397
RHOBTB1	I20	-1.413430269
DOCK7	N16	-1.419258349
PLEKHG4B/K IAA1909	J10	-1.424061265
ARHGEF38	H14	-1.45466997
ARAP3/CENT D3	C08	-1.469609968
CHN2	L11	-1.494890554
RHOBTB1	I20	-1.504409115
PLEKHG4B/K IAA1909	H06	-1.518803657
SOS1	I14	-1.538750588
RAC1	E14	-1.547263405
PLEKHG1	N08	-1.554410248
RHOD	E20	-1.557770965
DNMBP	J19	-1.59240914
ARHGEF35	K18	-1.598482444
GMIP	E13	-1.61296002

ARHGEF12	K10	-1.615796521
ARAP3/CENTD3	C10	-1.618565927
Cells	O20	-1.62241127
Cells	B06	-1.630175287
ARHGEF4	H15	-1.63204708
ARHGAP17	L09	-1.632723044
ARHGEF38	D16	-1.633706168
RAC2	C09	-1.644979461
YAP	M23	-1.648170016
Cells	B05	-1.659528391
RHOBTB1	M16	-1.660123961
ARHGEF10	E05	-1.680373349
DEPDC1	K21	-1.681677451
ALS2	N07	-1.6822026
FGD6	E08	-1.688527938
FGD6	C10	-1.692497457
RHOC	I09	-1.69271016
ARHGEF2	K22	-1.701813877
ARHGAP25	E14	-1.72062123
RAC2	K21	-1.728561884
ARHGAP35	H12	-1.74335298
SH3BP1	L16	-1.788894751
DOCK7	L06	-1.791505698
DOCK1	L15	-1.793021202
ARHGEF3	I13	-1.797198171
FLJ13815	K11	-1.797588839
DOCK6	F05	-1.808038079
RALBP1	N11	-1.81335567
ARHGEF35	G06	-1.882958535
SOS1	K06	-1.901669038
ARHGEF12	K10	-1.932511041
ARHGAP31	M19	-1.933913119
ARHGEF26/SGEF	G10	-1.943802667
CDC42	M04	-1.949681778
ARHGAP18	E19	-1.957834894
SWAP70	H16	-1.962928877
FAM13A	E21	-1.9648198
ARHGAP31	E09	-1.981560163
SWAP70	H16	-2.006233226
RAC2	K21	-2.010234168
ARFGEF3	J07	-2.013605444
ARHGAP31	E09	-2.017575753
VAV3	L07	-2.028536519

VAV3	L07	-2.135133751
RHOD	M14	-2.151426851
ARHGEF2	K12	-2.153298643
DOCK5	H05	-2.162309623
DOCK7	L06	-2.164699559
ARHGAP18	G03	-2.180259287
ARFGEF3	J07	-2.190649404
MYO9B	E16	-2.204843035
ARHGAP35	L10	-2.214131887
SWAP70	H10	-2.218641204
RND3	C20	-2.227213141
Cells	O13	-2.230292675
FGD2	M15	-2.239671257
FGD4	M06	-2.269051969
RND3	C20	-2.279729692
ARHGEF3/KIAA1244	G07	-2.284409172
ARHGAP18	E19	-2.28555415
ARHGEF3	I13	-2.28662129
RHOC	I09	-2.298229068
RND3	C12	-2.301255302
ARHGEF3KIAA1244	G07	-2.313673399
Cells	O09	-2.323985173
RAC2	C09	-2.348528128
SWAP70	H10	-2.351794301
ARAP3/CENTD3	C10	-2.356130644
ARHGEF2	K12	-2.361032904
ARHGAP21	F04	-2.404892938
DOCK9	L03	-2.424495796
MYO9B	G10	-2.426291882
DOCK5	J05	-2.428324462
DOCK5	J05	-2.451132612
FLJ32810	E04	-2.493058222
FAM13A	G15	-2.493309684
DOCK9	L03	-2.494992646
FGD6	C10	-2.498725414
DOCK9	N09	-2.511916996
ARHGAP35	H12	-2.573133106
NET1	M05	-2.583598126
ARHGAP11A	H08	-2.591340539
Cells	O14	-2.627039343
CDC42	E06	-2.641970419
ARHGEF18	C05	-2.655175089

RAC1	E14	-2.662360669
FAM13A	G15	-2.665027397
ARHGEF18	I05	-2.694275842
ARHGAP35	L10	-2.713872879
ARHGAP11A	N14	-2.721345009
ARHGAP11A	H08	-2.736269492
DOCK5	H05	-2.765970235
ARHGEF18	C05	-2.782390957
ARHGAP11A	N14	-2.79874671
ARHGEF18	I05	-2.865643165
NET1	M05	-2.867756274
FLJ10521	E03	-2.896638573
FGD4	M06	-2.90541058
FGD4	K16	-2.940259605
RHOV	M07	-2.956036257
YAP	N23	-2.966597339
MYO9B	E16	-3.016456888
CDC42	E06	-3.069753587
MYO9B	G10	-3.135701715
DOCK9	N09	-3.163811503
CDC42	M04	-3.168065214
NET1	E13	-3.233875723
RND3	C12	-3.354229373
NET1	E13	-3.402895347
Cells	O10	-3.463879458
FGD4	K16	-3.489588903
CHN1	F03	-3.515951583
SRGAP1	E03	-3.708392907
RHOA	I16	-3.739917713
RHOB	E04	-3.759981346
ARHGAP33	G19	-3.811215411
RHOA	I16	-3.912825772
ARHGAP33	M09	-4.345931455
RND1	M11	-4.453529797
STARD13	M03	-4.495653162
RHOA	M10	-4.498526541
STARD13	I19	-4.768069539
FLJ30058	C06	-4.942965351
STARD13	I19	-5.165176617
STARD13	M03	-5.197153507
ARHGAP33	G19	-5.259914208
FLJ30058	C06	-5.570190937
ARHGAP33	M09	-5.645580711

Table 7.2 YAP/TAZ ratio Z-scores for LM2 siGENOME screen.

Genes LM2 siGENOME	Well Name	Z-score YAP/TAZ RATIO
DEPDC2/PREX2	C20	7.324759821
DEPDC2/PREX2	C20	6.666789788
RACGAP1	N16	6.535543952
RACGAP1	N16	6.524137541
RACGAP1	F08	6.279856509
ECT2	F17	6.262900145
ECT2	F17	6.250405485
C9orf100/ARHGEF39	C04	6.208069816
ECT2	L09	5.902697783
DEPDC1	C21	5.569402836
RACGAP1	F08	5.534329421
ECT2	L09	5.370940719
C9orf100/ARHGEF39	C04	5.330518936
INPP5B	K13	5.313723159
OPHN1	L12	5.179279111
ARHGAP22	G17	5.134519594
DEPDC1	I17	5.036974433
DEPDC1	I17	5.035444997
DEPDC2/PREX2	E14	4.718831791
ARHGAP15	I07	4.691775277
C5ORF5	E09	4.602301516
DEPDC1	C21	4.585713684
SPATA13	H11	4.535921855
C5ORF5	E09	4.303278623
ARHGEF11	K05	4.27173077
DOCK8	J03	4.266448227
DOCK3	N05	4.248374747
DEPDC2/PREX2	E14	4.247495942
KIAA0720	G20	4.213860342
CENTD2	L08	4.086161277
OPHN1	H18	4.06267112
NGEF	I05	4.022800412
ARHGEF11	G13	4.00792257
FLJ32810	C22	3.936073861
RGNEF	E07	3.867702822
DOCK8	J03	3.820527403
C9orf100/ARHGEF39	I16	3.783770382
ARHGAP21	N04	3.780148602
C9orf100/ARHGEF39	I16	3.704606395
CENTD3	N22	3.62511357
FLJ32810	C20	3.617568055
ARHGAP5	J06	3.596711835
DOCK3	N05	3.544179304
ARHGAP5	J08	3.496451577
INPP5B	K13	3.492977681
RALBP1	D20	3.488230022
KIAA0720	G20	3.474563022
CENTD2	L08	3.394813279
FLJ32810	C20	3.356052667
NGEF	I05	3.339601396
FARP2	K22	3.337519314
ARHGEF7	M12	3.337435132
RALBP1	D20	3.300076434
INPP5B	G13	3.26615951
ARHGEF11	K05	3.250659122
ARHGAP21	D04	3.250232028
DOCK3	H03	3.200909056
SRGAP2	K09	3.193843776
OPHN1	H18	3.167269818
FARP2	M10	3.162018816
SRGAP1	M15	3.139551921
FARP2	M10	3.097652785
ARHGEF9	D03	3.094248059
KIAA1909	E08	3.071600066
ARHGAP22	G17	3.030679059
NGEF	K11	2.99440287
DOCK11	F21	2.972460928
SPATA13	H11	2.966855323
FARP2	K22	2.957940774
OPHN1	L12	2.953134936
NOPE	J07	2.913895697
ARHGAP5	J08	2.902312962
KIAA1909	G22	2.882348211
RALBP1	D18	2.846356962
FLJ43692/ARHGEF35	M03	2.8320261
RALBP1	D18	2.810805943
C5ORF5	G05	2.802882046
FLJ32810	C22	2.78930314

SRGAP2	C19	2.73486349
ARHGAP21	N04	2.731491272
ARHGAP8	I21	2.72082873
ARHGAP15	C03	2.705606826
SRGAP1	M15	2.672835051
SPATA13	J19	2.672160633
ARHGEF7	C18	2.665861
ARHGEF16	K19	2.662845349
ARHGEF16	G17	2.660255395
SRGAP2	M05	2.624629806
RASGRF1	E21	2.618133273
PLEKHG2	C22	2.606068879
DOCK3	H03	2.588663804
SRGAP2	E19	2.574313382
ARHGAP22	C13	2.572704865
CENTD3	N22	2.563896762
NOPE	J07	2.556020258
NGEF	K11	2.552683683
ARHGAP15	I07	2.529081054
ARHGEF16	K19	2.486748557
ARHGAP8	I21	2.456640307
ARHGAP5	J06	2.45389919
ALS2	J15	2.448101208
KIAA1244	L22	2.424606416
ALS2	J15	2.397058869
CENTD2	H06	2.394015826
ALS2	D17	2.386401923
KIAA0720	G16	2.385740885
C5ORF5	G05	2.385061298
ALS2	D17	2.380348826
FLJ41603	H21	2.352107252
MCF2	C08	2.348370181
Cells	M22	2.334895673
MCF2	C08	2.310152984
BCR	J16	2.302987553
KIAA0720	G16	2.296478498
BCR	H12	2.275036902
SRGAP2	M05	2.22797728
PIK3R1	M11	2.210532494
ARHGEF11	G13	2.207322469
RGNEF	C17	2.200008489
INPP5B	G13	2.183745336
FLJ43692/ARHGEF35	M03	2.182390871

ARHGEF7	M12	2.171606754
ARHGEF15	I07	2.166214696
KIAA1909	G22	2.155644125
Cells	N07	2.12985834
PLEKHG2	C22	2.088803953
RGNEF	E07	2.046454181
ARHGEF9	D03	2.02457973
KIAA1909	E08	2.018120644
PIK3R1	M13	1.999986973
RASGRF1	M11	1.998633784
BCR	G11	1.998101195
SH3BP1	N06	1.987262413
ARHGAP24	E15	1.980995834
ARHGAP24	E03	1.95847708
ITSN1	C07	1.945353838
ARHGAP24	E15	1.875814854
RASGRF1	M11	1.842485535
DOCK4	D07	1.840078826
ARHGEF15	I13	1.837459279
AKAP13	C03	1.828264069
CENTD2	H06	1.815792937
ARHGEF1	M15	1.802117271
BCR	J16	1.786688509
Cells	M18	1.783978584
CHN1	L10	1.779637594
DEPDC1B	I13	1.776297458
ARHGEF16	G17	1.745724866
Cells	E22	1.745370413
DOCK8	J11	1.698301746
SRGAP2	C19	1.696322053
LOC345930	L03	1.65893409
Cells	N21	1.617879703
ARHGAP22	C13	1.608131652
VAV2	I12	1.602984808
BCR	G11	1.585901058
Cells	N07	1.576872303
ARHGEF7	C18	1.566862579
VAV2	K10	1.562541441
ITSN1	C07	1.562049159
DOCK8	J11	1.558887378
RGNEF	C17	1.54470991
STARD13	K15	1.508875168
SH3BP1	N06	1.5076794

Cells	F07	1.498293452
SRGAP2	K09	1.48326371
ARHGAP23	C08	1.43734316
Cells	E22	1.425530613
Cells	N21	1.417974766
SRGAP1	K05	1.398794219
ARHGAP21	D04	1.393032502
FLJ10665	D15	1.379303318
FLJ30058	C16	1.367925596
Cells	G22	1.336795159
FLJ10665	H17	1.332208385
FLJ10665	D15	1.320569064
RASGRF1	E21	1.295670156
DOCK11	D19	1.288942309
BCR	H12	1.28565415
GEFT	M06	1.279370168
NET1	C19	1.268837333
GEFT	M06	1.263178341
ARHGAP15	C03	1.256787121
SPATA13	J19	1.2545373
ARHGAP23	C08	1.247155053
DEPDC1B	I13	1.240752217
VAV3	I04	1.236484981
Cells	K17	1.222555868
GEFT	I22	1.203652149
FLJ43692/ARHGEF35	M09	1.201837001
Cells	M20	1.199936097
ARHGEF1	K21	1.184688021
Cells	G03	1.172271587
Cells	M16	1.166358304
SOS2	C05	1.150501804
DOCK11	D19	1.147809641
Cells	D21	1.124052551
Cells	K17	1.12310861
DOCK9	L05	1.118180012
PLEKHG4	K04	1.111611564
Cells	L04	1.108165593
VAV2	I12	1.105157206
GMIP	K03	1.095515887
Cells	I22	1.08176036
PIK3R1	M11	1.071908193
STARD13	I09	1.064318003
KIAA1244	J10	1.061453546

VAV3	E20	1.053303552
Cells	K12	1.041346369
MCF2	K06	1.036925425
VAV3	E20	1.035857691
ARHGEF15	I07	1.030877393
DOCK11	F21	1.010201569
Cells	M08	0.997464013
Cells	G14	0.985821526
Cells	N17	0.97792978
BCR	C09	0.951933768
Cells	N15	0.939814983
ARHGEF6	I20	0.938984842
DEF6	J05	0.92032883
CHN1	L10	0.913388557
TRIO	E06	0.904087552
ARHGAP23	C10	0.896177706
Cells	I16	0.88748166
FLJ43692/ARHGEF35	M09	0.883630519
KIAA1244	L22	0.877941933
ARHGAP10	N20	0.874988244
VAV2	K10	0.871800303
STARD13	K15	0.848525388
ARHGAP23	C10	0.822826336
BCR	C09	0.819743317
AKAP13	C03	0.806401572
ARHGEF1	K21	0.801970474
Cells	M10	0.796700979
Cells	M14	0.782814472
ABR	G07	0.772501005
Cells	E18	0.746887217
FLJ41603	H21	0.746174578
Cells	I08	0.739347293
Cells	I14	0.724920906
LOC345930	L03	0.720849428
ARHGEF17	K07	0.715217055
DOCK4	H07	0.711960466
ARHGEF6	G08	0.709985157
SGEF	M21	0.686772607
Cells	N11	0.686335023
DEPDC1B	E07	0.673749958
FLJ10665	H17	0.673522028
Cells	N09	0.666154661
TRIO	E06	0.651473313

NET1	K15	0.645066906
Cells	E11	0.63606761
Cells	G20	0.635849275
Cells	I18	0.611168591
LOC345930	D09	0.604780384
Cells	L04	0.603318492
DEF6	J05	0.581752548
DEF6	F05	0.580255429
Cells	N19	0.578013187
PIK3R1	M13	0.575379087
ARHGAP4	G09	0.575178022
GMIP	I19	0.573167376
KIAA1244	J10	0.562744586
DOCK9	L05	0.558505921
Cells	G16	0.535518024
FLJ20184	F06	0.535423387
CHN1	N14	0.527163997
CENTD3	H20	0.522295879
Cells	I10	0.513120978
Cells	N17	0.512667843
GMIP	I19	0.512347802
NOPE	D05	0.493341851
ITSN1	E13	0.490024091
Cells	E05	0.489477111
STARD13	I09	0.473833966
ARHGEF5	K03	0.45485331
Cells	F07	0.45485331
MCF2	K06	0.432645944
VAV3	I04	0.427230847
DNMBP	D10	0.425647491
NOPE	D05	0.422745615
ARHGEF1	M15	0.420503
DEPDC1B	E07	0.411448319
Cells	G10	0.39793955
ARHGEF17	K07	0.387574835
Cells	G18	0.386127003
Cells	G14	0.375168981
ARHGEF17	G09	0.35732687
DOCK4	D07	0.354643154
CENTD1	L16	0.337506017
Cells	N09	0.321390319
DEF6	F05	0.30137087
Cells	I11	0.301177196

FLJ20184	F06	0.291112958
ITSN1	E13	0.290846025
ARHGEF15	I13	0.28939202
CENTD3	H20	0.28636154
FGD4	M20	0.281296724
CENTD1	L16	0.256682647
ARHGEF6	G08	0.250829967
Cells	C12	0.245146993
Cells	K18	0.244376438
NET1	C19	0.228513205
Cells	N11	0.223845692
DOCK4	H07	0.221675961
Cells	N10	0.21747776
DNMBP	D10	0.212267914
ARHGAP4	G07	0.202739091
Cells	K22	0.187877277
ARHGAP25	M07	0.187776745
Cells	M16	0.18759914
NET1	K15	0.185575316
DOCK2	F09	0.185407255
GEFT	I22	0.173815257
PREX1	C10	0.17376895
Cells	L17	0.13831629
CHN1	N14	0.136077926
SRGAP2	E19	0.135859357
PLEKHG4	K04	0.127482664
Cells	M14	0.111070588
Cells	M12	0.109612869
Cells	K08	0.105340246
Cells	G03	0.103351867
Cells	G12	0.099157508
Cells	I06	0.068597113
FLJ20184	H14	0.058347891
Cells	I15	0.046314342
FGD4	M20	0.038753937
SOS2	C05	0.022470988
Cells	E05	0.00762948
Cells	K14	-0.00587349
FLJ30058	C18	-0.019935631
FLJ41603	F11	-0.049899347
Cells	K16	-0.056265451
ARHGAP12	K19	-0.05685479
DOCK6	F13	-0.063855337
DOCK6	L21	-0.064120813

DOCK9	H05	-0.070368517
Cells	C12	-0.09032113
ABR	G07	-0.090375828
Cells	K04	-0.096286772
Cells	N19	-0.116247957
Cells	M06	-0.123823167
AKAP13	K09	-0.128062714
FLJ46688	J21	-0.128132947
DNMBP	H16	-0.140518666
Cells	D21	-0.158857658
Cells	I06	-0.158857658
CDGAP	M03	-0.174280913
Cells	K14	-0.181227119
PLEKHG3	I18	-0.183121268
FAM13A1	M21	-0.193610316
ARHGAP4	G07	-0.195251377
SWAP70	N03	-0.200537494
SOS2	K17	-0.216007487
Cells	L17	-0.222840987
Cells	G08	-0.242953961
Cells	N13	-0.244355835
Cells	M16	-0.245530343
Cells	I06	-0.245668334
FGD2	M22	-0.247025171
FLJ30058	C16	-0.25111529
LOC201176	E06	-0.266288871
DOCK6	L21	-0.282527339
PREX1	C14	-0.28723374
SRGAP1	K05	-0.292516393
DOCK2	F09	-0.293031723
DNMBP	H16	-0.298392122
CENTD1	F10	-0.312530675
Cells	L13	-0.319833717
FAM13A1	M21	-0.322877152
Cells	E04	-0.347346784
ARHGEF18	G05	-0.349151817
ARHGEF6	I20	-0.354172316
DOCK9	H05	-0.3602555
CDGAP	I15	-0.362162709
Cells	K08	-0.371730764
DOCK10	D11	-0.372398444
Cells	E11	-0.395867344
AKAP13	K09	-0.396561371

MYO9A	J18	-0.403630972
Cells	I11	-0.428124297
FLJ46688	J21	-0.433441353
Cells	G22	-0.437534258
ABR	E17	-0.446104246
FLJ10357	N08	-0.462540661
Cells	I10	-0.464024523
ABR	E17	-0.468393342
Cells	E18	-0.470648983
Cells	I15	-0.485717192
DOCK10	D11	-0.495967442
FLJ30058	C18	-0.496747792
ARHGEF5	K03	-0.5005587
ARHGAP10	N20	-0.507498973
ARHGAP26	D16	-0.511057741
TIAM2	C06	-0.515987462
TRIO	K12	-0.521614444
SOS1	I03	-0.524048856
Cells	F20	-0.554597307
FAM13A1	G21	-0.573578053
SGEF	M21	-0.575673814
CDGAP	I15	-0.586573415
ARHGAP4	G09	-0.590732899
ARHGEF17	G09	-0.59217031
PLEKHG1	M08	-0.607972779
ARHGEF10	C11	-0.610170421
ARHGEF9	H15	-0.625430236
MCF2L2	G10	-0.625978128
Cells	K10	-0.641859169
MCF2L2	I10	-0.651412673
PREX1	C14	-0.666751557
ARHGEF9	H15	-0.667657964
CENTD1	F10	-0.679800908
CDGAP	M03	-0.705402612
FAM7A2	N10	-0.713002562
Cells	C07	-0.715020959
Cells	D14	-0.718144169
Cells	K10	-0.722844969
SOS2	K17	-0.724543829
Cells	E04	-0.732897702
SGEF	I09	-0.736522679
ARHGAP10	D22	-0.742827632
Cells	N15	-0.748610926

ARHGAP8	I03	-0.754066353
FGD4	K14	-0.75505319
ARHGAP10	D22	-0.762449506
FLJ10521	M07	-0.777048519
LOC343578	E14	-0.791613718
PLEKHG4	E16	-0.793011148
ARHGAP9	E21	-0.793318122
DOCK5	J17	-0.794292429
MCF2L2	I10	-0.795306776
Cells	F20	-0.81233714
Cells	D14	-0.820879015
Cells	E20	-0.821617969
Cells	E20	-0.828484554
PLEKHG3	I18	-0.82896221
DOCK2	J13	-0.839136028
Cells	I08	-0.841628548
KIAA0672	L06	-0.856221023
Cells	K20	-0.864746332
FLJ41603	F11	-0.876721523
Cells	N13	-0.88759841
ARHGAP9	E21	-0.890531938
ARHGAP25	K21	-0.900385038
LOC345930	D09	-0.911743211
FAM7A2	N10	-0.926050852
Cells	L13	-0.934485953
ARHGAP6	C12	-0.938888915
ARHGAP12	K11	-0.93908998
FGD1	K08	-0.94782085
Cells	I12	-0.964273325
FARP1	C21	-0.965488287
ARHGAP26	J20	-0.967425559
LOC201176	E06	-1.001872411
ARHGAP12	K11	-1.01897582
Cells	G03	-1.022116848
LOC201176	E04	-1.034344349
FARP1	M05	-1.047772571
ARHGAP25	K21	-1.048888071
DOCK2	J13	-1.049961427
Cells	I04	-1.052802275
GMIP	K03	-1.068826933
MYO9A	J18	-1.070355154
PLEKHG3	C16	-1.116564017
ARHGAP12	K19	-1.127387007

FLJ10521	M07	-1.138005612
PLEKHG3	C16	-1.139651115
FGD4	K14	-1.141779771
LOC201176	E04	-1.163946342
Cells	K06	-1.16916528
RICS	M19	-1.195145787
Cells	G04	-1.218469284
ARHGAP24	E03	-1.219776205
FAM13A1	G21	-1.22480282
PLEKHG1	M08	-1.227272662
MCF2L2	G10	-1.240498628
Cells	M04	-1.242044112
SWAP70	N03	-1.244342471
TIAM2	C06	-1.251941437
FGD2	M22	-1.270702833
PIK3R2	C11	-1.289847228
ARHGEF18	G05	-1.291696491
ARHGEF10	C11	-1.315026487
MYO9A	H04	-1.330104803
Cells	G06	-1.345401111
ARHGAP26	D16	-1.349354148
Cells	C07	-1.36243156
7H3	I05	-1.393772942
Cells	G08	-1.406530348
RICS	M19	-1.411700963
Cells	I20	-1.416266615
PREX1	C10	-1.443220158
DOCK10	H09	-1.449182235
ITSN2	M19	-1.451151361
ARHGAP26	J20	-1.46181746
OCRL	C15	-1.474474826
FLJ20184	H14	-1.509300759
FARP1	C21	-1.519070528
PLEKHG1	I08	-1.52392872
FGD1	M18	-1.525923455
FLJ10357	N08	-1.528253044
SGEF	I09	-1.530868993
SWAP70	F03	-1.542186978
FAM7A2	F22	-1.543864381
SOS1	I03	-1.565524768
FGD2	G14	-1.606657625
ARHGEF3	G21	-1.609119032
PLEKHG1	I08	-1.623231103

Cells	K04	-1.636030257
DOCK6	F13	-1.643633437
Cells	F16	-1.652377166
SH3BP1	F12	-1.659605238
GRLF1	F04	-1.694018807
PIK3R2	E13	-1.70388957
ARHGEF5	E15	-1.7073121
DOCK5	J09	-1.731697132
Cells	F16	-1.772775291
SWAP70	F03	-1.777643408
PIK3R2	C11	-1.814090808
FGD1	M18	-1.816487941
7H3	G15	-1.827186479
ARHGAP20	D12	-1.828126245
ARHGAP6	C14	-1.861122111
LOC343578	E12	-1.865990255
ARHGEF19	E09	-1.89590037
PLEKHG2	G06	-1.898329781
TIAM1	G04	-1.908259711
TIAM2	M14	-1.931727526
FLJ10357	H22	-1.938316434
FGD2	G14	-1.964102219
ARHGEF2	I21	-2.011456239
TIAM1	K16	-2.02061169
ARHGEF19	C15	-2.066229778
SOS1	K13	-2.074215678
KIAA0672	L14	-2.078099232
FARP1	M05	-2.080013661
OCRL	E11	-2.089481266
FLJ10357	H22	-2.1056123
ARHGAP20	L20	-2.124428394
ARHGEF4	L11	-2.142861602
CHN2	L18	-2.143736769
MYO9A	H04	-2.14518997
FAM7A2	F22	-2.149460908
ARHGAP6	C14	-2.154723211
ARHGAP18	C04	-2.155931299
Cells	G03	-2.159401491
TIAM1	G04	-2.167913262
FGD1	K08	-2.187845959
RICS	G19	-2.189159057
Cells	K06	-2.191219969
OCRL	C15	-2.204786365

DOCK7	L19	-2.228737379
Cells	G06	-2.232337686
ARHGEF3	E19	-2.239951397
FLJ46688	D13	-2.249400846
Cells	I04	-2.260687799
PLEKHG4	E16	-2.2761605
FGD6	G12	-2.282231972
TRIO	K12	-2.295580358
VAV1	M04	-2.303126588
SNX26	M09	-2.316413666
DOCK5	J17	-2.32785006
KIAA0672	L06	-2.33851616
TIAM2	M14	-2.369948058
RICS	G19	-2.398177041
SH3BP1	F12	-2.418529973
ARHGAP8	I03	-2.439132659
SOS1	K13	-2.448693469
ARHGEF3	G21	-2.471970078
ARHGEF18	I19	-2.476901966
TIAM1	K16	-2.477842618
VAV1	M04	-2.491990098
ARHGAP9	E05	-2.495355614
ARHGEF19	E09	-2.51441252
ARHGEF2	I21	-2.517870729
CHN2	L18	-2.5209257
ARHGEF4	H13	-2.535446887
DOCK7	L19	-2.552370477
ARHGAP6	C12	-2.556533174
GRLF1	F04	-2.558948887
FGD5	E18	-2.571429536
OCRL	E11	-2.577022341
FGD6	G12	-2.580878985
7H3	G15	-2.581938813
SNX26	K07	-2.591891512
ARHGAP1	N12	-2.593736782
FGD6	E12	-2.659357463
ARHGEF5	E15	-2.664898811
SNX26	M09	-2.674227479
ARHGAP18	C06	-2.750330442
DOCK5	J09	-2.771256026
ARHGAP20	L20	-2.791009112
PLEKHG2	G06	-2.791469861
CHN2	H10	-2.798033615

Cells	G04	-2.826226668
ARHGEF3	E19	-2.836978553
ARHGEF19	C15	-2.843648417
ITSN2	M19	-2.852190292
LOC343578	E12	-2.870416293
CHN2	H10	-2.873171273
ARHGEF18	I19	-2.882247015
FGD3	E22	-2.922580841
ARHGAP18	C06	-2.939255351
SNX26	K07	-2.940270145
7H3	I05	-2.953807848
FLJ10521	C13	-2.966175105
GRLF1	J12	-2.973121744
ITSN2	M17	-2.976895902
GRLF1	J12	-2.989981414
ITSN2	M17	-2.995533633
FLJ13815	M17	-3.01845758
FLJ10521	C13	-3.030448548
OBSCN	F19	-3.044329095
MYO9B	D06	-3.06995472
FLJ46688	D13	-3.074641134
DOCK10	H09	-3.088479911
MYO9B	D08	-3.099036419
ARHGEF4	H13	-3.278226894
ARHGAP18	C04	-3.286067151
FGD3	E22	-3.302774202
OBSCN	L15	-3.337245979
ARHGAP20	D12	-3.344520806
ARHGEF4	L11	-3.345643737
MYO9B	D06	-3.358851668
ARHGEF10	G15	-3.365087234
STARD8	C09	-3.373925299
PIK3R2	E13	-3.386151146
FGD6	E12	-3.388935539
ABR	J04	-3.39246389
ARHGEF2	E03	-3.414779539
STARD8	C09	-3.418116347
ABR	J22	-3.447899926
KIAA0672	L14	-3.46667143
LOC257106	E10	-3.557102273
DOCK7	F15	-3.56610219
ARHGAP11A	N18	-3.566813264
FGD5	E18	-3.639999117
ARHGEF2	E03	-3.760279903

VAV1	K20	-3.763889968
MYO9B	D08	-3.773911999
ABR	J22	-3.774392479
LOC343578	E14	-3.906854199
VAV1	K20	-3.92472948
DOCK7	F15	-3.943254672
ARHGAP11A	N18	-3.959964715
FGD5	I14	-4.00204483
ARHGAP9	E05	-4.007989708
OBSCN	L15	-4.038710126
STARD8	C05	-4.038711789
ARHGEF10	G15	-4.067912661
FGD5	I14	-4.13122931
ARHGAP1	N12	-4.276547959
LOC257106	E10	-4.35494082
FLJ13815	M17	-4.361913725
OBSCN	F19	-4.37377208
ABR	J04	-4.385586837
LOC257106	E08	-4.485719272
DOCK1	L07	-4.660006438
LOC257106	E08	-4.666144207
ARHGEF12	M13	-4.853254286
DOCK1	H19	-4.90448255
DOCK1	L07	-5.061813212
STARD8	C05	-5.084992404
DOCK1	H19	-5.259824128
ARHGEF12	M13	-5.398149542
RASGRF2	G19	-5.404883084
FGD3	G18	-5.433651711
ARHGAP17	F18	-5.540371762
ARHGAP1	F14	-5.817797888
RASGRF2	G19	-5.876014066
ARHGAP11A	J14	-5.92008305
FGD3	G18	-6.149978522
RASGRF2	I17	-6.236510675
ARHGAP11A	J14	-6.254472518
ARHGAP17	F18	-6.294873385
PARG1	C17	-6.504322099
RASGRF2	I17	-6.598656696
ARHGAP1	F14	-6.741412783
FLJ13815	E17	-6.784038802
PARG1	G11	-6.804072815
PARG1	C17	-6.810780398

PARG1	G11	-7.169680764
FLJ13815	E17	-7.32219746
ARHGAP17	H08	-7.519779216
ARHGAP17	H08	-7.559831188
ARHGEF12	I11	-7.607185208
ARHGEF12	I11	-8.089895921
MCF2L	E10	-8.795573576
MCF2L	E10	-9.030044239
MCF2L	K18	-9.243114443
MCF2L	K18	-10.0809012

Table 7.3. YAP/TAZ ratio Z-scores for MDA-MB-231 OTP screen.

Genes 231 OTP	Well Name	Z-score YAP/TAZ ratio
HMHA1	M17	7.486248767
LATS1	J23	7.28551586
HMHA1	M17	6.618187834
HMHA1	M15	6.559336311
LATS2	K23	6.420068092
LATS1	J23	6.391673857
LATS1	I23	6.381694524
HMHA1	M15	6.200551477
LATS1	I23	6.195368347
LATS2	L23	6.1059672
PIK3R2	G21	5.668356102
LATS2	K23	5.600378792
ITSN2	C17	5.537145204
Cells	B04	5.215490893
ITSN2	E15	5.0294673
PIK3R2	C21	4.890740649
LATS2	L23	4.742345376
PIK3R2	G21	4.705894448
PIK3R2	C21	4.567015258
ITSN2	E15	4.497583189
ARHGEF15	M22	4.480523678
ITSN2	C17	4.329378997
MCF2	C03	4.320267667
ARHGEF15	M22	3.775048569
ARHGEF16	C13	3.751947239
RHOBTB2	K20	3.723507884
YAP	M23	3.671892036
ARHGEF39/C9 ORF100	L19	3.635819414
RHOBTB2	K20	3.621058084
AKAP13	I22	3.543736827
STARD8	I21	3.431195735
ARHGEF39/C9 ORF100	H11	3.422963244
ARHGEF39/C9 ORF100	H11	3.406033776
ARHGEF15	K08	3.38102528
ARHGEF16	C13	3.371332376
YAP	N23	3.325758035
RHOBTB2	I08	3.312528759
ARHGEF16	I07	3.218507591
ARHGEF15	K08	3.136150703
MCF2	G09	3.104519042
ARHGEF17	G12	3.063227271
TRIO	M21	3.01187768
VAV2	L18	2.824806532
ARHGEF17	G12	2.800492245
SOS2	C21	2.794041515
MCF2	G09	2.782353015
SOS2	C21	2.781680723
ARHGAP1	M21	2.775693851
ARHGEF16	I07	2.763717575
FLJ10357	D12	2.760740315
DOCK8	N20	2.743490681
STARD8	E07	2.720690765
STARD8	I21	2.712192114
VAV2	D06	2.710664047
STARD8	E07	2.706952645
TRIO	M21	2.702845104
ARHGEF39/C9 ORF100	L19	2.688514201
DOCK11	N18	2.682619245
RHOBTB2	I08	2.670209568
ARHGAP5	N03	2.669630754
DOCK8	N20	2.61705997
DOCK10	F18	2.566391421
RND2	C04	2.54090899
VAV2	D06	2.532483742
TRIO	G03	2.530892989
OBSCN	F21	2.516274217
ARHGAP29/PARG1	I05	2.505969419
FLJ10357	L22	2.460005552
MYO9A	I03	2.439120021
PLEKHG2	H22	2.435667669
SOS2	G19	2.433446995
ARHGAP24	M07	2.427941787
RASGRF1	I03	2.396097006
ARHGAP24	M07	2.377654856
AKAP13	K04	2.372381701
VAV2	L18	2.368569159
AKAP13	I22	2.359030801
ARHGEF17	I10	2.354068701
ARHGAP5	F09	2.347115531
DEF6	J06	2.321267788

ARHGAP23	E06	2.317260121
ABR	D08	2.309313206
ARHGAP26	F16	2.308020819
SOS2	G19	2.299706145
ARHGAP24	C09	2.284358511
OBSCN	F21	2.267181384
PLEKHG2	H22	2.262141074
ARHGAP29/PARG1	I05	2.247963922
ABR	L12	2.245727757
VAV1	J22	2.235000943
ARHGEF9	L14	2.224447638
ARHGEF17	I10	2.190865921
DOCK11	N18	2.18894106
ARHGAP5	F09	2.158561984
PLEKHG2	N04	2.15461446
ARHGAP29/PARG1	G09	2.130773956
ARHGAP19	I07	2.129785528
ARHGAP26	H04	2.124178742
DOCK10	J08	2.121658587
RND3	I04	2.070997009
ARHGAP1	M21	2.050441588
PIK3R1	M05	2.043385333
FGD5	K19	2.032138718
ARHGAP1	I09	1.982277254
DEF6	L08	1.977665894
ARHGEF11	M13	1.968704563
RHOF	G17	1.968575325
DOCK8	N10	1.967541415
DOCK10	F18	1.963858112
ARHGAP23	E06	1.962043561
ARHGAP1	I09	1.961934004
MCF2	C03	1.944033886
DOCK8	N10	1.94122203
ARHGAP19	C03	1.929370425
FLJ10357	L22	1.928210303
FLJ32810	G22	1.920936604
ARHGAP29/PARG1	G09	1.901257577
SYDE1	C22	1.899830769
FGD2	I17	1.899044894
DEF6	L08	1.886961074
ARHGEF9	F12	1.88233845
ARHGAP24	C09	1.868840659

VAV1	J22	1.867397018
MYO9A	E17	1.865061377
TRIO	G03	1.839774664
DOCK4	N22	1.826376996
ARHGEF9	L14	1.82479725
KIAA1688/ARHGAP39	C05	1.822158501
SYDE1	C22	1.798158354
FGD1	I19	1.770193892
TIAM1	H19	1.770000034
Cells	B03	1.709193217
ARHGAP44/KIAA0672	D21	1.693878428
ARHGEF11	K09	1.686511821
RHOF	M17	1.683280854
ARHGAP19	I07	1.679622418
YAP	N23	1.676354793
Cells	B20	1.675074195
KIAA1688/ARHGAP39	K19	1.654933312
TIAM2	D11	1.654688356
MYO9A	E17	1.647340531
PIK3R1	M13	1.628652768
ARHGAP44/KIAA0672	D21	1.618244493
ARHGAP44/KIAA0672	D19	1.615882862
KIAA1688/ARHGAP39	K19	1.611509326
FGD5	K19	1.600503454
Cells	O21	1.591614559
Cells	B21	1.584226545
FLJ10357	D12	1.583120847
DOCK2	F06	1.582926989
Cells	O21	1.563476561
DEF6	J06	1.541221683
GMIP	E15	1.539403576
FLJ10521	K17	1.531877695
ARHGEF11	M13	1.529588317
SYDE1	E18	1.516786028
PLEKHG5/KIAA0720	H09	1.510424067
FGD2	I17	1.507920483
LOC343578/ARHGAP40	I13	1.50643661
ARHGAP12	G17	1.505041183
RHOF	G17	1.5037854
MYO9A	I03	1.501785187

ARHGAP10	D22	1.497775746
OBSCN	L05	1.493946131
KIAA1688/ARHGAP39	C05	1.489517057
ARHGAP26	F16	1.487741278
PIK3R1	M05	1.48012824
NGEF	E11	1.461830309
Cells	B20	1.459953522
TIAM2	H07	1.450139592
ABR	L12	1.448595828
PREX1	C18	1.436176424
RASGRF1	G15	1.42924364
Cells	B22	1.427920413
RHOB	K14	1.407420809
ARHGAP44/KIAA0672	D19	1.39781701
DOCK10	J08	1.393902465
ARHGAP12	I11	1.393874192
RHOF	M17	1.387341467
ARHGAP12	I11	1.385790308
RASGRF2	E21	1.37905291
FGD2	M15	1.376700521
RHOBTB1	I20	1.373818742
DOCK3	H21	1.371686303
RHOV	E19	1.362145029
DOCK4	N12	1.359994786
ARHGEF6	H20	1.359990199
ARHGAP21	J04	1.358568573
DOCK3	H21	1.357348333
ARHGAP23	G16	1.350555774
ARHGAP19	C03	1.346020636
Cells	B19	1.332317298
FGD2	M15	1.327098945
ABR	D08	1.323936863
LOC343578/ARHGAP40	K17	1.320437806
TIAM1	H19	1.315776967
PREX1	C18	1.315501294
DOCK2	F06	1.308719759
DOCK4	N22	1.296533988
Cells	B18	1.292675637
FLJ46688/PLEKHG7	F20	1.286776465
RHOJ	C07	1.274563406
FGD1	I19	1.264667343
RHOV	E19	1.258667044

RHOV	M07	1.256948521
PLEKHG5/KIAA0720	L21	1.253971262
RHOJ	G11	1.252722063
NGEF	E11	1.242944374
ARHGAP10	D22	1.236631842
Cells	B21	1.233400874
PIK3R1	M13	1.231676017
ARHGAP6	G05	1.229647835
Cells	B10	1.226845118
ARHGAP6	I15	1.216536629
ARHGAP26	H04	1.210084249
PREX2	C11	1.209202098
ARHGAP23	G16	1.206436426
RHOJ	G11	1.205232419
PLEKHG5/KIAA0720	H09	1.203302713
DOCK11	D04	1.201802007
PREX2	E17	1.19747251
Cells	B18	1.196115504
FLJ10521	K17	1.19530822
RHOQ	M20	1.194536338
NGEF	G21	1.192992573
ARHGAP4	C14	1.192182817
RND3	C20	1.191448809
ARHGEF9	F12	1.1884258
FGD1	M09	1.181640767
RHOBTB1	M16	1.179249851
ITSN1	M08	1.17433878
FLJ46688/PLEKHG7	D10	1.173916058
LOC257106/ARHGAP30	I17	1.169615392
ARHGAP5	N03	1.164598338
TIAM1	D13	1.163676586
ECT2	D09	1.15070446
SRGAP3	G07	1.131008576
MCF2L	K15	1.124791274
MCF2L2	C22	1.116116737
DOCK2	F10	1.102805149
OBSCN	L05	1.102241289
NGEF	G21	1.098798749
DEPDC1	K09	1.088041049
RND2	I04	1.087961469
ARHGEF6	J20	1.08755498

LOC345930/ECT2L	D03	1.075923496
ARHGAP17	N15	1.074398398
RHOV	M07	1.063968914
DOCK4	N12	1.060544088
ITSN1	I12	1.044324629
ARHGAP28	C19	1.037166103
LOC345930/ECT2L	J17	1.03715188
RASGRF2	E21	1.027975201
TIAM2	H07	1.027458976
ARHGAP12	G17	1.023336714
Cells	B22	1.022871002
RHOQ	M20	1.019769272
PLEKHG2	N04	1.007906265
Cells	B07	1.006197098
TIAM1	D13	1.003440376
BCR	H13	1.002117149
ARHGAP10	L04	1.001158897
IGDCC4/NOPE	H03	0.998638742
MCF2L	K15	0.995278535
Cells	B14	0.987561658
Cells	B04	0.982871618
FAM13A	E21	0.975883595
ARHGAP4	C14	0.972104314
RHOBTB1	I20	0.969973772
RHOJ	C07	0.962751161
PREX1	E12	0.959802507
PREX2	E17	0.950842122
AKAP13	K04	0.940807655
PLEKHG5/KIAA0720	L21	0.934600957
Cells	B14	0.924391098
YAP	M23	0.920913552
Cells	O11	0.920384698
SRGAP3	K03	0.914601088
ARHGEF6	J20	0.912192881
OPHN1	F15	0.910483714
Cells	O07	0.905716103
ARHGEF4	J13	0.89389076
FLJ46688/PLEKHG7	F20	0.887658056
PREX1	E12	0.85937409
BCR	H13	0.851241983
INPP5B	K07	0.8417018

RND2	C04	0.838588407
ARHGEF19	M19	0.83444095
ARHGAP9	C20	0.831631318
ARHGEF7	F22	0.831365795
INPP5B	G11	0.829194682
ARHGAP4	G18	0.81378148
SOS1	I14	0.813061162
OPHN1	H17	0.81080065
SRGAP3	G07	0.806321302
RAC3	G04	0.795927812
CENTD1/ARAP2	C17	0.795233928
ARHGAP6	G05	0.783489083
RND1	M11	0.77749945
ARHGAP11B	J18	0.775120378
C5ORF5/FAM13B	E05	0.762884417
SRGAP3	K03	0.753363232
Cells	B08	0.749595731
RHOQ	G08	0.748109486
ARHGEF11	K09	0.748002525
DOCK2	F10	0.744859862
DOCK3	D05	0.730339162
RASGRF1	I03	0.723853641
ARHGAP6	I15	0.720630637
ARAP3/CENTD3	C08	0.718940486
RACGAP1	J12	0.718781273
FAM13A	E21	0.717475688
ARAP1/CENTD2	G06	0.711165791
ARHGAP17	N15	0.709854825
RACGAP1	J12	0.69428156
VAV1	F14	0.692978356
ARHGEF1	C19	0.692730695
SRGAP2	G13	0.689588467
ARHGEF6	H20	0.688291929
MCF2L	K05	0.684911753
FARP2	I06	0.682585456
FGD5	G05	0.677545146
Cells	O18	0.676107218
INPP5B	K07	0.67342477
ARHGAP17	L09	0.666430616
C5ORF5/FAM13B	K13	0.663075352
BCR	D07	0.659622021

RHOBTB1	M16	0.652178872
ARHGAP25	G12	0.638887949
DOCK11	D04	0.637788784
Cells	O12	0.632828549
RHOB	K14	0.629628887
ARHGAP9	C20	0.619953965
GMIP	E15	0.613531391
Cells	O22	0.607756238
TIAM2	D11	0.605559179
ARHGAP4	G18	0.605136973
ARHGAP25	G12	0.596404525
INPP5B	G11	0.592606283
Cells	O17	0.587401139
IGDCC4/NOPE	J15	0.586017547
Cells	O22	0.577526843
PLEKHG4	F08	0.572344829
FARP2	M18	0.571957113
RHOH	G13	0.56814457
ARHGAP8	C11	0.550510899
ARHGEF4	J13	0.550014759
FGD5	G05	0.540531635
SPATA13	N17	0.533767071
FGD1	M09	0.527575043
RACGAP1	H18	0.524597783
Cells	B19	0.51877538
PLEKHG4B/KIAA1909	J10	0.508565521
ARHGEF7	D18	0.508333124
LOC257106/ARHGAP30	K05	0.505915374
Cells	B17	0.503460592
LOC343578/ARHGAP40	I13	0.499333509
ARHGAP11A	H08	0.498937237
ARHGEF19	M19	0.49697543
PREX2	C11	0.495189314
SOS1	I14	0.491893726
ARHGAP10	L04	0.490304163
Cells	I16	0.487309679
SYDE1	E18	0.487051744
LOC345930/ECT2L	J17	0.479222141
RASGRF1	G15	0.472249441
ARAP1/CENTD2	G06	0.47068084

GEFT/ARHGEF25	E18	0.462427299
ARHGAP17	L09	0.45275761
ALS2	F17	0.434770213
Cells	O08	0.433405423
MCF2L	K05	0.426348215
Cells	O17	0.424363375
CENTD1/ARAP2	C17	0.422882337
ARHGAP28	C07	0.420445464
SPATA13	F11	0.41887385
ARHGAP32/RICS	G20	0.40538648
RND1	M11	0.402848249
ARHGEF4	H15	0.399497743
DEPDC1	K09	0.396854009
BCR	D07	0.390247474
RAC3	G16	0.388050416
DEPDC1B	G08	0.387943641
ITSN1	M08	0.385052521
ARHGEF7	F22	0.384237874
ARHGAP9	G04	0.375839796
VAV1	F14	0.374415731
Cells	B11	0.37357568
LOC201176/ARHGAP27	I06	0.372065125
FAM13A	G15	0.368523947
DOCK7	N16	0.368083034
ARHGAP21	J04	0.363494955
OPHN1	H17	0.359682517
GMIP	E13	0.358487577
LOC201176/ARHGAP27	G14	0.356662816
ECT2	D09	0.356193072
Cells	B17	0.35472858
ALS2	N07	0.354512969
Cells	B07	0.350635807
RHOG	G18	0.345918594
Cells	O08	0.34423849
FLJ10665/PLEKHG6	N05	0.341007522
CENTD1/ARAP2	C13	0.34074099
LOC343578/ARHGAP40	K17	0.331163467
CHN2	F19	0.329807814
ARHGAP28	C07	0.327219781
ARHGAP11A	N14	0.321621715

DOCK7	L06	0.308439365
Cells	B09	0.305879468
PLEKHG4	F08	0.30218546
Cells	B13	0.293447674
ARAP1/CENTD2	C16	0.292853373
ARHGEF4	H15	0.290669042
PLEKHG1	N06	0.28652728
ARHGAP28	C19	0.285754738
ALS2	F17	0.28068303
DOCK3	D05	0.280131685
ECT2	L13	0.275941468
Cells	O15	0.273351053
CENTD1/ARAP2	C13	0.264157628
ITSN1	I12	0.26055896
PLEKHG1	N06	0.253965245
FAM13A	G15	0.252740452
Cells	O18	0.252285142
ARHGEF7	D18	0.241622948
SRGAP2	C15	0.236481657
SH3BP1	L20	0.230249941
PLEKHG3	J11	0.224997247
Cells	O12	0.222019988
ARHGAP8	M11	0.217236391
ALS2	N07	0.210166084
ARHGAP11B	J18	0.205865597
Cells	B09	0.205371487
ARHGEF1	I11	0.198134119
ARHGAP22	C12	0.193455988
CHN2	F19	0.188893551
ARHGAP8	C11	0.188233015
RASGRF2	K07	0.187278067
VAV3	N19	0.182754712
ARHGAP8	M11	0.1735287
PLEKHG1	N08	0.172784935
DOCK6	F05	0.168344594
MCF2L2	C22	0.166334205
RAC3	G16	0.158835922
ARHGAP25	E14	0.158148324
SRGAP1	E11	0.155546884
RHOU	E16	0.155485342
RACGAP1	H18	0.155162245
Cells	K08	0.153860743
Cells	B10	0.150703509

SRGAP2	G13	0.140570752
RHOQ	G08	0.136285937
C5ORF5/FAM13B	E05	0.135371334
PLEKHG4B/KIAA1909	J10	0.134687038
RALBP1	N11	0.133584349
LOC257106/ARHGAP30	K05	0.131838304
Cells	O06	0.129766837
RASGRF2	K07	0.123935823
ARHGEF12	K10	0.121818656
OPHN1	F15	0.117747636
OCRL	E22	0.116649354
ECT2	L13	0.110510268
RAC1	C14	0.100999897
RALBP1	N11	0.095777054
ARHGAP22	C12	0.095105685
ARAP1/CENTD2	C16	0.094962091
ARAP3/CENTD3	C08	0.093508521
DEPDC1B	G08	0.088908464
RHOU	E16	0.081978515
PLEKHG4	D14	0.080600155
Cells	O16	0.067919234
RND1	E09	0.066310626
SRGAP1	E11	0.059105465
ARHGAP21	F04	0.057939901
ARHGAP11B	D20	0.05784549
PLEKHG4B/KIAA1909	H06	0.052261053
ARHGAP31	M19	0.05170385
FLJ10521	E03	0.050992961
ARHGEF10	E05	0.048411064
Cells	O15	0.043219006
ARAP3/CENTD3	C10	0.04057014
FLJ13815	K11	0.030191016
DEPDC1	K21	0.025132593
RHOU	M12	0.024824997
CHN1	F13	0.024804103
RHOH	G13	0.024693835
Cells	O05	0.01551981
RHOH	K11	0.014659367
SRGAP2	C15	0.011893908
FLJ46688/PLEKHG7	D10	0.011384171

GEFT/ARHGEF25	C16	0.010855091
ARHGEF35	G06	0.008153503
Cells	I20	0.008006561
FLJ41603	J14	0.005892991
Cells	K18	0.002166188
FARP2	M18	0.00115143
TAGAP	E08	-0.018881504
ARHGEF28/RGNEF	G14	-0.026470924
GMIP	E13	-0.040801338
ARHGEF12	C06	-0.041798298
CHN1	F13	-0.042637614
SOS1	K06	-0.042831472
ARHGEF35	K18	-0.045610104
ARHGEF35	K18	-0.047532279
VAV3	N19	-0.056519193
FLJ41603	J14	-0.057047731
Cells	B11	-0.058945108
RHOG	G18	-0.061095351
SPATA13	F11	-0.07438275
FLJ13815	K15	-0.079117441
LOC201176/ARHGAP27	I06	-0.083071151
Cells	M18	-0.083478151
Cells	K20	-0.086036434
RND1	E09	-0.091970636
ARHGAP25	E14	-0.09324614
ARHGAP11A	N14	-0.09549924
DEPDC1	K21	-0.099937762
FGD3	K13	-0.111198754
PLEKHG3	L17	-0.116064385
Cells	O13	-0.118931376
RHOH	K11	-0.128064407
LOC257106/ARHGAP30	I17	-0.128106948
LOC345930/ECT2L	D03	-0.130344205
ARHGEF1	C19	-0.132494448
FGD6	E08	-0.13581873
ARHGAP32/RICS	G20	-0.136163335
FGD6	C10	-0.136408993
GEFT/ARHGEF25	E18	-0.145120234
RAC3	G04	-0.146333192
Cells	O05	-0.157249811

PLEKHG4	D14	-0.168257648
DEPDC1B	C18	-0.172276232
ARHGAP15	C04	-0.177290347
C5ORF5/FAM13B	K13	-0.178304438
SWAP70	H10	-0.18134356
Cells	B12	-0.183249339
PLEKHG3	L17	-0.186415688
FLJ13815	K11	-0.189346759
ARHGEF18	I05	-0.189448322
ARHGEF19	C15	-0.199262252
PLEKHG4B/KIAA1909	H06	-0.201148902
ARHGAP11B	D20	-0.212935593
RALBP1	F07	-0.215912852
RHOG	I18	-0.217239122
SWAP70	H16	-0.225120304
ARHGEF1	I11	-0.22594732
FLJ32810	E04	-0.235431548
FGD6	E08	-0.238352569
SPATA13	N17	-0.239510392
Cells	M16	-0.245056981
FARP2	I06	-0.251584834
RALBP1	F07	-0.256010738
OCRL	I08	-0.256162255
ARHGAP15	I04	-0.262473967
MCF2L2	E10	-0.264734351
PLEKHG1	N08	-0.267706842
Cells	M12	-0.27517495
DOCK7	N16	-0.2765056
FLJ41603	J16	-0.282184447
ARHGAP15	I04	-0.282791656
RND3	C12	-0.284665497
Cells	B05	-0.29310225
DNMBP	D17	-0.308979784
ARHGEF5	G20	-0.311777245
DOCK6	D15	-0.312398119
Cells	K08	-0.313122164
ARHGAP15	C04	-0.314130623
RND3	C20	-0.321470149
ARHGEF12	K10	-0.322212049
GEFT/ARHGEF25	C16	-0.323150252
OCRL	I08	-0.323826455
IGDCC4/NOPE	J15	-0.325605788

ARHGEF28/RGNEF	E22	-0.329353711
ARHGEF28/RGNEF	E22	-0.331695172
ARHGAP22	E12	-0.3357016
MCF2L2	E10	-0.338531842
RND3	C09	-0.341308292
ARHGEF26/SGEF	G22	-0.350807338
ARHGAP31	E09	-0.351657611
Cells	K12	-0.360819288
Cells	M10	-0.361347811
Cells	I14	-0.36895928
FLJ41603	J16	-0.37077472
FLJ13815	K15	-0.37453099
Cells	O19	-0.37453463
CHN2	L11	-0.381646973
Cells	K18	-0.385911342
FGD3	K03	-0.389126618
DNMBP	D17	-0.38996667
FLJ10665/PLEKHG6	J09	-0.390137676
DNMBP	J19	-0.398738649
Cells	K16	-0.399135391
ARHGAP18	G03	-0.40640324
ARHGAP21	F04	-0.409740194
RHOC	I09	-0.409740194
ARHGAP11A	H08	-0.416491938
Cells	M04	-0.418249568
RHOU	M12	-0.421895112
PLEKHG3	J11	-0.423568737
Cells	O06	-0.426691809
SWAP70	H16	-0.426735085
CHN2	L11	-0.443923835
SH3BP1	L16	-0.446702467
Cells	M20	-0.450137087
Cells	I16	-0.451658223
FLJ10665/PLEKHG6	J09	-0.458398571
Cells	K14	-0.464672387
ARHGAP32/RICS	E20	-0.468447058
ARHGAP35	H12	-0.4711853
ARHGEF35	G06	-0.47261483
ARHGAP18	E19	-0.474306249
ARHGEF10	E07	-0.482630831
DOCK6	D15	-0.48372936

FARP1	I21	-0.489765605
ARHGEF38	D16	-0.49566499
ARHGEF5	G20	-0.501068165
ARHGEF5	C08	-0.501564303
ARHGAP31	M19	-0.502081066
Cells	M06	-0.506306444
DOCK6	F05	-0.507022685
RHOB	E04	-0.512425859
ARHGAP9	G04	-0.512746415
Cells	K10	-0.517067073
Cells	K20	-0.524222047
ARHGEF18	I05	-0.526378137
ARHGAP35	L10	-0.537732566
DEPDC1B	C18	-0.538503673
ARHGEF38	H14	-0.538724986
Cells	B12	-0.543356279
LOC201176/ARHGAP27	G14	-0.549010931
Cells	I22	-0.557743379
Cells	M10	-0.563853932
ARHGAP35	L10	-0.574196463
FGD4	K16	-0.588089625
FARP1	I21	-0.590028206
FGD4	M06	-0.592548361
ARHGAP32/RICS	E20	-0.59728604
FLJ10665/PLEKHG6	N05	-0.60461064
ARHGEF10	E07	-0.605437656
RAC2	K21	-0.606044135
Cells	B06	-0.610577162
DOCK7	L06	-0.617456964
STARD13	I19	-0.621357158
DNMBP	J19	-0.624728802
FARP1	I15	-0.626829818
ARHGEF26/SGEF	G22	-0.628538986
RAC2	C09	-0.634658908
ARHGEF12	C06	-0.638298868
FGD3	K13	-0.643039343
VAV3	L07	-0.643597655
ARHGEF5	C08	-0.654452171
Cells	I18	-0.665124317
ARHGAP18	G03	-0.665969393
SOS1	K06	-0.6708271
ARHGAP22	E12	-0.672786336

Cells	I12	-0.678025804
ARHGEF3	I13	-0.67842749
DOCK9	L03	-0.680495309
ARHGAP31	E09	-0.681534952
Cells	O20	-0.687698238
Cells	O04	-0.691392245
OCRL	E22	-0.691828706
ARHGAP20	N21	-0.697953243
Cells	B16	-0.698459491
Cells	B15	-0.700979646
CDC42	M04	-0.708023156
RAC1	E14	-0.714714112
RHOG	I18	-0.717029758
ARHGAP18	E19	-0.71892077
SH3BP1	L16	-0.721164841
Cells	I20	-0.726363048
TAGAP	E08	-0.731378243
Cells	O10	-0.733790628
ARHGEF28/RGNEF	G14	-0.750930411
Cells	M14	-0.759716445
IGDCC4/NOPE	H03	-0.760971905
FLJ10521	E03	-0.76114027
ARHGEF19	C15	-0.77516267
ARHGEF26/SGEF	G10	-0.789255872
ARHGEF3	I13	-0.791792056
RHOD	M14	-0.801440583
Cells	K10	-0.80479768
RHOC	M03	-0.805533769
Cells	B15	-0.806512951
SRGAP1	E03	-0.828674613
RAC2	K21	-0.842043707
Cells	K06	-0.853753914
Cells	O20	-0.857358496
Cells	I14	-0.858928319
Cells	M12	-0.870646701
ARAP3/CENTD3	C10	-0.875208606
FGD4	K16	-0.881716324
RAC1	C14	-0.892123711
ARHGAP20	J21	-0.894773105
ARHGAP35	H12	-0.90233357
Cells	O19	-0.905047583
ARHGEF18	C05	-0.917906835

SWAP70	H10	-0.947373263
TAGAP	E10	-0.948506332
VAV3	L07	-0.966457956
ARHGEF10	E05	-0.982998287
TAGAP	E10	-0.983179778
Cells	O09	-0.985975547
FGD4	M06	-0.989393882
Cells	B06	-0.991433856
Cells	O14	-0.997719182
Cells	K16	-1.019830712
Cells	K22	-1.021070156
Cells	M18	-1.021182833
ARHGEF38	H14	-1.060263284
SH3BP1	L20	-1.071764732
NET1	M05	-1.078033607
ARHGEF18	C05	-1.083122426
CHN1	F03	-1.095141734
Cells	K12	-1.103493195
RND3	C12	-1.123008682
ARHGAP20	N21	-1.129922953
ARHGEF3KIAA1244	G07	-1.139809715
FGD6	C10	-1.151247342
RHOD	E20	-1.184349254
ARHGAP33	M09	-1.194254314
ARFGEF3	J07	-1.198904746
FARP1	I15	-1.216448275
ARFGEF3	J07	-1.220777772
Cells	B05	-1.233859979
DOCK9	N09	-1.245217674
ARHGEF38	D16	-1.247013232
ARHGAP20	J21	-1.261758005
ARHGEF26/SGEF	G10	-1.272990214
ARFGEF3	J03	-1.27499027
CDC42	E06	-1.279290756
ARHGAP33	G19	-1.286311215
ARHGAP33	G19	-1.293720453
DOCK9	N09	-1.30568761
RHOC	I09	-1.31573462
RHOB	E04	-1.320743921
RHOD	M14	-1.327270476
CDC42	E06	-1.330049109
DOCK1	N13	-1.355186039
FGD3	K03	-1.358077868

RAC1	E14	-1.363909653
ARHGEF3KIA A1244	G07	-1.399428696
CDC42	M04	-1.42605863
ARHGAP33	M09	-1.431344451
DOCK1	L15	-1.448939422
ARHGEF2	K22	-1.48319699
ARFGEF3	J03	-1.532307703
NET1	E13	-1.557443995
RHOD	E20	-1.56287266
Cells	O14	-1.590529746
DOCK1	L15	-1.62238709
NET1	M05	-1.631985755
DOCK1	N13	-1.645989903
FLJ30058	C06	-1.669299473
NET1	E13	-1.680415275
ARHGEF2	K12	-1.744000724
Cells	O13	-1.779153656
ARHGEF2	K22	-1.815362896
RHOC	M03	-1.850483533
ARHGEF2	K12	-1.873254056
CHN1	F03	-1.875048785
DOCK9	L03	-1.901207216
DOCK5	J05	-1.985673174
FLJ32810	E04	-1.991899149
DOCK5	H05	-2.024125647
FLJ30058	I10	-2.052344069
Cells	O10	-2.116531331
STARD13	M03	-2.297754021
FLJ30058	C06	-2.325464371
DOCK5	J05	-2.433553907
STARD13	I19	-2.632009586
Cells	I10	-2.744557645
DOCK5	H05	-2.832262468
STARD13	M03	-2.907183046
MYO9B	G10	-2.998941408
MYO9B	E16	-3.087076857
SRGAP1	E03	-3.192722318
MYO9B	G10	-3.296797923
MYO9B	E16	-3.39252128
RHOA	I16	-4.847726708
RHOA	I16	-5.128225866
RHOA	M10	-5.187352037
RHOA	M10	-5.3534572

Table 7.4 YAP/TAZ ratio Z-scores for MDA-MB-231 siGENOME screen.

Genes 231 siGENOME	Well Name	Z-score YAP/TAZ ratio
LATS2	N23	11.42489929
LATS2	N23	9.010644891
LATS2	O23	7.654609345
LATS1	M23	7.533750744
LATS2	O23	6.91316105
ARHGAP9	E21	6.504977158
LATS1	M23	6.021887697
Cells	B03	5.755204014
SPATA13	H11	5.749646088
ARHGAP9	E21	5.747261396
OPHN1	H18	5.7414263
RALBP1	D20	5.735449667
BCR	J16	5.730596345
RALBP1	D18	5.577351979
RALBP1	D18	5.522314465
LATS1	L23	5.384657936
SPATA13	H11	5.295066137
Cells	B04	5.289592798
ARHGAP22	C13	5.248638995
OPHN1	L12	5.144201663
SPATA13	J19	5.088148789
OPHN1	H18	5.05710708
SPATA13	J19	5.018234357
BCR	H12	4.969871909
BCR	J16	4.947603531
CENTD3	N22	4.944646671
LATS1	L23	4.921369255
DOCK8	J03	4.910965322
NGEF	I05	4.888189983
ARHGAP22	G17	4.885747339
DEPDC1	C21	4.812216186
RASGRF1	M11	4.774453877
DEPDC1	I17	4.687743741
BCR	G11	4.67688545
RASGRF1	E21	4.657390785
ARHGAP15	I07	4.61008583
YAP	B23	4.606847921
ARHGAP9	E05	4.570304466
ARHGAP15	C03	4.558216206
ARHGAP22	C13	4.541729858
ARHGAP22	G17	4.500119297
PLEKHG4	K04	4.485474192
DEPDC2/PREX2	C20	4.463622032
INPP5B	K13	4.407515901
DEPDC2/PREX2	C20	4.355359524
RACGAP1	N16	4.343550089
NGEF	I05	4.314583663
ECT2	F17	4.28778318
BCR	C09	4.232133694
NGEF	K11	4.103424911
FLJ32810	C22	4.102232395
ECT2	F17	4.064271011
PLEKHG4	K04	4.036324184
DEPDC1	C21	4.021506703
OPHN1	L12	4.01405336
ALS2	D17	4.000795298
PLEKHG4	E16	3.972594396
ARHGEF1	M15	3.91890249
DOCK11	F21	3.892130034
FLJ46688	J21	3.890871795
ALS2	D17	3.868789707
DEPDC1	I17	3.866482432

RALBP1	D20	3.865338267
BCR	H12	3.843373286
BCR	G11	3.837082093
CENTD3	N22	3.833073203
FLJ32810	C22	3.821103077
BCR	C09	3.779140203
ARHGAP10	D22	3.776434989
ARHGAP21	N04	3.736980955
PLEKHG2	C22	3.720506281
RASGRF1	E21	3.71722827
DOCK11	F21	3.673927008
ARHGAP15	I07	3.662668797
ARHGEF7	C18	3.630203981
ALS2	J15	3.593650968
CENTD3	H20	3.582980796
ARHGAP9	E05	3.566991804
C9orf100/ARHGEF39	I16	3.546680611
ARHGEF16	G17	3.546051491
PLEKHG4	E16	3.536431444
DOCK3	H03	3.528488193
DEPDC2/PREX2	E14	3.508173153
FLJ32810	C20	3.501702301
RACGAP1	F08	3.490059871
C9orf100/ARHGEF39	I16	3.474221027
PIK3R1	M13	3.466536454
ARHGAP10	N20	3.451937748
C9orf100/ARHGEF39	C04	3.438849558
ECT2	L09	3.377847602
DOCK11	D19	3.365305508
INPP5B	K13	3.316946312
ARHGEF18	I19	3.296228206
NGEF	K11	3.276977155

ARHGAP15	C03	3.270189838
DOCK8	J03	3.251371998
DOCK11	D19	3.250966471
ARHGAP5	J06	3.232830553
ARHGAP5	J08	3.197261659
PIK3R1	M11	3.19025135
ITSN1	C07	3.182359277
CENTD2	L08	3.179617801
INPP5B	G13	3.15923338
PIK3R1	M11	3.148944902
ARHGAP10	N20	3.146183246
ARHGEF16	G17	3.143205376
ECT2	L09	3.139388757
RGNEF	C17	3.129990056
INPP5B	G13	3.125134693
ARHGEF16	K19	3.118672681
DOCK8	J11	3.104684124
C9orf100/ARHGEF39	C04	3.085564087
FLJ32810	C20	3.069523904
C5ORF5	G05	3.060590712
CENTD3	H20	3.035936342
RACGAP1	F08	3.032281041
DOCK3	N05	3.02813368
ARHGAP10	D22	3.007256286
PIK3R1	M13	3.005979691
RACGAP1	N16	2.972043016
PLEKHG2	C22	2.969297387
ARHGAP4	G07	2.951723112
ARHGEF1	K21	2.944342927
DEPDC2/PREX2	E14	2.930080757
RGNEF	C17	2.880631978
RGNEF	E07	2.842416256
ARHGAP23	C08	2.806590733

CENTD2	H06	2.781963196
ALS2	J15	2.776575641
STARD13	I09	2.752010408
FLJ46688	D13	2.751666371
KIAA0720	G16	2.749838721
FGD2	M22	2.749135778
SRGAP2	E19	2.739555837
ARHGAP21	D04	2.732827511
C5ORF5	E09	2.695232218
ARHGEF16	K19	2.671512713
YAP	B23	2.600170581
ARHGAP4	G09	2.596108488
FAM13A1	M21	2.587536813
FLJ46688	J21	2.574946612
ARHGEF18	I19	2.574735729
FLJ10357	H22	2.500643903
DOCK3	H03	2.493975238
ARHGAP21	D04	2.456228079
ARHGAP21	N04	2.421249044
ARHGEF7	M12	2.419298774
RASGRF1	M11	2.41917295
YAP	B24	2.347716735
DOCK8	J11	2.32379846
ARHGAP8	I21	2.31463519
FAM13A1	G21	2.308304896
FGD2	M22	2.293286172
FLJ10357	H22	2.236339182
CENTD2	L08	2.227480291
SRGAP2	C19	2.196430359
RICS	M19	2.195730671
FAM13A1	G21	2.188038143
ARHGAP4	G09	2.162330265
C5ORF5	E09	2.156297172

FLJ46688	D13	2.14217171
FAM13A1	M21	2.130263062
SRGAP2	K09	2.126058338
FGD2	G14	2.116698358
ARHGAP8	I21	2.112491667
ARHGEF6	I20	2.095742703
DOCK3	N05	2.055982362
ITSN1	C07	2.054849947
PLEKHG2	G06	2.037800813
ARHGEF1	K21	2.028301111
DNMBP	H16	1.98623222
ARHGEF7	C18	1.984828966
PLEKHG3	I18	1.953193919
NET1	K15	1.953121351
ARHGEF7	M12	1.951366269
DNMBP	H16	1.927138723
KIAA0720	G20	1.904742075
KIAA1244	L22	1.894357627
SRGAP2	C19	1.878945003
ARHGAP23	C10	1.861724827
KIAA0720	G20	1.798687145
C5ORF5	G05	1.793262332
Cells	B22	1.786596533
Cells	B21	1.775520965
PLEKHG3	C16	1.772889153
RICS	G19	1.760406795
SRGAP2	M05	1.750369876
ARHGEF6	G08	1.748215869
VAV2	I12	1.725229648
CENTD1	L16	1.720098167
NET1	C19	1.717704899
NET1	K15	1.716161689
ARHGAP12	K19	1.695276716

CENTD2	H06	1.68813629
VAV2	K10	1.681155149
FARP2	M10	1.675320726
DNMBP	D10	1.666533944
STARD13	K15	1.63804133
ARHGEF18	G05	1.637303449
DOCK4	D07	1.635534177
SRGAP2	E19	1.628991689
VAV2	K10	1.614969712
ARHGAP5	J06	1.612516147
FARP2	M10	1.606791161
ITSN1	E13	1.59560704
CHN1	N14	1.570090225
ITSN1	E13	1.560236331
STARD13	K15	1.554027232
SH3BP1	N06	1.498108907
Cells	G22	1.480984838
Cells	B03	1.463594427
ARHGAP18	C06	1.462962342
TRIO	E06	1.461527508
CENTD1	L16	1.418999042
ARHGAP5	J08	1.41277076
FGD1	M18	1.405410064
VAV2	I12	1.39094032
NET1	C19	1.390207224
ARHGEF15	I13	1.37410984
ARHGAP23	C10	1.360175503
FLJ20184	H14	1.353232446
YAP	B24	1.329852833
DOCK10	D11	1.32324708
RGNEF	E07	1.319849835
ARHGEF3	G21	1.319786923
ARHGAP8	I03	1.315925146
KIAA0720	G16	1.314942705

SRGAP2	M05	1.308647543
ARHGAP18	C04	1.285301554
ARHGEF6	I20	1.272253463
Cells	O03	1.256648138
AKAP13	K09	1.25369578
DNMBP	D10	1.248822263
ARHGAP18	C04	1.237365232
ARHGEF15	I13	1.232339337
DEF6	F05	1.230703627
SRGAP1	M15	1.202084751
RICS	M19	1.191789146
DEF6	J05	1.189938889
SWAP70	N03	1.188673593
PLEKHG3	C16	1.176536452
ARHGEF11	K05	1.168991201
ARHGEF6	G08	1.166218895
CENTD1	F10	1.163578544
PREX1	C14	1.150433518
Cells	E22	1.135917454
ARHGAP18	C06	1.111981812
FGD2	G14	1.111925897
ARHGAP23	C08	1.101882938
ARHGAP4	G07	1.101358321
FARP2	K22	1.077135598
Cells	O21	1.067069689
Cells	E22	1.064123031
Cells	B08	1.061722167
ABR	E17	1.057715394
Cells	B22	1.057507075
KIAA1244	J10	1.05666098
ARHGEF15	I07	1.0492027
GMIP	I19	1.045660962
FGD5	E18	1.041842004

ARHGAP12	K19	1.039846999
FLJ20184	F06	1.024541223
Cells	O15	0.995153507
GEFT	I22	0.982078775
MCF2	C08	0.981094655
Cells	K17	0.971299849
FARP2	K22	0.96647345
ARHGEF9	H15	0.964716094
GEFT	I22	0.954771889
Cells	E20	0.943899793
STARD13	I09	0.933021899
FLJ10357	N08	0.925140428
GMIP	I19	0.923185333
FGD1	K08	0.90700451
SRGAP1	M15	0.899649436
ARHGEF15	I07	0.886759764
Cells	M22	0.885363311
Cells	M16	0.876278801
Cells	O03	0.873804231
FLJ10665	H17	0.85455318
Cells	M18	0.851003348
Cells	B04	0.847676158
ARHGAP24	E15	0.835574324
RICS	G19	0.834066051
CENTD1	F10	0.833855154
TIAM2	M14	0.814708152
PLEKHG3	I18	0.8093195
Cells	O22	0.796783117
Cells	O15	0.795919259
AKAP13	C03	0.795541787
Cells	B17	0.792773662
Cells	B13	0.791862519
VAV1	K20	0.787363236

Cells	O07	0.7823025
ARHGEF9	H15	0.777800622
FAM7A2	F22	0.757417156
Cells	M22	0.75216025
Cells	M20	0.747703674
FLJ20184	H14	0.734643036
FLJ10665	H17	0.723606796
Cells	K18	0.718984899
ABR	E17	0.715077425
ARHGEF9	D03	0.712372212
VAV3	E20	0.706081018
CHN1	L10	0.703291756
ARHGEF3	G21	0.700690869
FGD1	M18	0.695278211
TIAM2	M14	0.69507143
CHN1	N14	0.67814812
MCF2	K06	0.677985824
DOCK4	H07	0.668988159
PREX1	C10	0.668214923
SOS2	K17	0.6538046
DEF6	F05	0.651344301
Cells	B10	0.634333091
ARHGAP6	C12	0.630264398
Cells	B19	0.62247106
TIAM1	K16	0.617060633
ARHGAP20	L20	0.615173275
Cells	K08	0.609384677
Cells	C07	0.605868092
LOC345930	L03	0.604729895
TRIO	E06	0.603825384
TIAM1	K16	0.595460368
Cells	G22	0.582118823
PLEKHG2	G06	0.561437948
FLJ10665	D15	0.558175064

SOS2	K17	0.555847323
Cells	B07	0.543372324
AKAP13	C03	0.539646729
Cells	B14	0.538100255
DOCK9	L05	0.5338826
Cells	O17	0.526278714
ARHGAP26	D16	0.523057284
Cells	O04	0.521862282
FGD4	M20	0.519421314
VAV1	M04	0.515465505
ARHGEF17	K07	0.515114033
SH3BP1	N06	0.506021072
Cells	O05	0.502601656
Cells	B09	0.499227532
SRGAP2	K09	0.498573594
Cells	B21	0.491424869
Cells	B19	0.490581338
TIAM2	C06	0.478906029
Cells	G14	0.475681198
TIAM1	G04	0.469352473
Cells	O17	0.464923935
Cells	B15	0.457332155
VAV3	I04	0.444538601
Cells	O21	0.443413892
GEFT	M06	0.437438881
Cells	B20	0.433572697
Cells	I22	0.433324377
VAV1	M04	0.42945725
Cells	G18	0.427694469
KIAA1244	L22	0.42197073
Cells	I22	0.416045783
ARHGAP12	K11	0.406175456
DEF6	J05	0.397812547

ARHGEF3	E19	0.391835914
FGD1	K08	0.385418897
Cells	E20	0.384731743
Cells	B11	0.376212584
FAM7A2	F22	0.370167278
DOCK10	H09	0.366511977
Cells	G20	0.365911115
Cells	G20	0.365348354
SWAP70	N03	0.36339972
Cells	O16	0.35962314
PREX1	C10	0.350251126
VAV1	K20	0.349430472
DOCK9	H05	0.344228698
FLJ10357	N08	0.338046211
TRIO	K12	0.337691332
Cells	O06	0.33502015
Cells	K16	0.332893208
Cells	O18	0.332447049
ARHGAP26	J20	0.329427276
Cells	B14	0.329049805
Cells	E16	0.324663117
Cells	B17	0.310487455
Cells	O18	0.306199505
NOPE	J07	0.303598618
Cells	O22	0.29602104
FGD5	I14	0.295203185
Cells	K20	0.294235342
FLJ30058	C16	0.287087438
GMIP	K03	0.286151937
Cells	O11	0.279206511
Cells	B20	0.268780173
Cells	I18	0.26710377
MCF2	K06	0.256575258

Cells	M18	0.241576928
ARHGEF3	E19	0.237311134
Cells	B18	0.224301437
Cells	B18	0.221776104
PREX1	C14	0.204735826
Cells	K18	0.188721784
Cells	K22	0.18314773
ARHGEF11	G13	0.176225426
FGD5	I14	0.171867182
Cells	I18	0.166359992
KIAA1909	G22	0.16157824
Cells	I20	0.160392475
Cells	M14	0.160326898
TIAM1	G04	0.152518921
FLJ30058	C18	0.150983214
DOCK4	D07	0.148366734
Cells	B08	0.14434037
Cells	M20	0.136784718
FGD6	G12	0.135946817
AKAP13	K09	0.133834077
FLJ41603	H21	0.133142046
Cells	K17	0.132653361
MCF2	C08	0.131820895
Cells	M08	0.131568736
Cells	K16	0.127210461
ARHGEF9	D03	0.125472973
ARHGAP8	I03	0.123997183
FAM7A2	N10	0.122239438
FLJ10665	D15	0.120482081
ARHGEF5	K03	0.11633472
Cells	I20	0.104388467
ARHGAP26	J20	0.096441446
ARHGAP6	C14	0.092257866

Cells	K22	0.090761701
Cells	K12	0.08702533
SRGAP1	K05	0.086292708
Cells	K20	0.072446156
Cells	O19	0.060290028
ARHGAP6	C12	0.055206803
STARD8	C05	0.05207927
Cells	M16	0.043534078
ARHGAP20	L20	0.0431584
Cells	B07	0.041101888
ARHGAP24	E15	0.039404913
Cells	O12	0.037534859
CHN1	L10	0.035125255
Cells	M10	0.034716133
Cells	G18	0.033435205
FLJ43692/ARHGEF35/ARHGEF353692	M03	0.031665098
Cells	O08	0.029099549
Cells	E18	0.025369221
STARD8	C05	0.013696497
ARHGAP25	K21	0.012664217
DOCK10	H09	0.010400865
ARHGAP20	D12	0.005410384
FLJ30058	C18	-0.001648545
Cells	I16	-0.006566828
GEFT	M06	-0.015078468
VAV3	E20	-0.019333194
FLJ20184	F06	-0.031915865
Cells	O11	-0.04640861
FGD4	K14	-0.058990997
Cells	O16	-0.061822034

ARHGAP12	K11	-0.062795829
Cells	K10	-0.071880339
Cells	I10	-0.084261648
Cells	B13	-0.085099449
SH3BP1	F12	-0.088924507
Cells	G08	-0.10382265
CHN2	L18	-0.106568365
Cells	G12	-0.12228472
ARHGAP25	M07	-0.127266548
TIAM2	C06	-0.138411663
Cells	B10	-0.146061112
DEPDC1B	I13	-0.149538251
Cells	E18	-0.156498158
DOCK10	D11	-0.157391112
ARHGAP26	D16	-0.166570402
Cells	M14	-0.172762362
ABR	J04	-0.178127918
ARHGEF11	G13	-0.178397846
DEPDC1B	I13	-0.181788846
Cells	G16	-0.183165966
NOPE	D05	-0.189796764
Cells	I11	-0.195400376

SRGAP1	K05	-0.205068718
LOC345930	L03	-0.206597091
KIAA1244	J10	-0.208029366
Cells	B09	-0.214131823
SOS2	C05	-0.225014186
FGD5	E18	-0.229583313
Cells	K14	-0.229980125
ARHGAP1	N12	-0.230215961
ABR	J22	-0.23256502
DOCK9	L05	-0.248670475
Cells	M06	-0.254522955
Cells	O06	-0.267166583
ARHGEF12	M13	-0.272603397
Cells	I12	-0.286025693
Cells	G12	-0.286449902
Cells	O07	-0.301705234
Cells	K10	-0.303893412
Cells	I11	-0.305008222
Cells	G03	-0.306612366
Cells	O04	-0.308248075
Cells	M12	-0.31818922
DOCK4	H07	-0.318691456

ARHGAP20	D12	-0.320264254
DOCK2	J13	-0.321648317
GMIP	K03	-0.326320781
ARHGEF18	G05	-0.353441792
Cells	O05	-0.359458388
LOC201176	E06	-0.360753117
CHN2	L18	-0.388523701
Cells	O12	-0.392550065
ARHGAP6	C14	-0.394746769
NOPE	D05	-0.405195363
VAV3	I04	-0.418595605
Cells	O20	-0.419602196
FLJ30058	C16	-0.419875697
Cells	K06	-0.426908866
MCF2L2	I10	-0.437406273
ABR	J22	-0.44426197
DOCK2	J13	-0.452416104
Cells	C07	-0.455638827
DOCK6	L21	-0.473785558
Cells	B16	-0.477932919
Cells	G03	-0.497017979
Cells	G04	-0.513578026
MCF2L2	G10	-0.527349781
DEPDC1B	E07	-0.527790889
ARHGAP25	M07	-0.534396927
FGD4	K14	-0.534519795
Cells	M08	-0.555512754
Cells	G10	-0.574202229
Cells	G16	-0.576656763
Cells	B12	-0.585764307
PLEKHG1	M08	-0.59745423
Cells	B16	-0.604185807
Cells	I08	-0.609038647
Cells	B06	-0.611632593
Cells	K08	-0.61197464
DOCK2	F09	-0.615990837
Cells	I04	-0.618204465
MCF2L2	G10	-0.637277484
FLJ43692/ARHGEF35/ARHGEF353692	M09	-0.639542313
Cells	I14	-0.656659064
FAM7A2	N10	-0.660177427
FLJ41603	F11	-0.67384301
Cells	I04	-0.679077292
TRIO	K12	-0.679365567

FLJ41603	H21	-0.684105971
Cells	K06	-0.701356231
CHN2	H10	-0.703928951
Cells	K12	-0.706733553
SOS2	C05	-0.710255326
ARHGEF17	K07	-0.711261917
ARHGAP1	F14	-0.712960539
SH3BP1	F12	-0.713904218
NOPE	J07	-0.718874261
Cells	I12	-0.719127626
Cells	I06	-0.728701883
FLJ43692/ARHGEF35	M09	-0.729726943
ARHGEF17	G09	-0.739568139
Cells	K14	-0.743194422
CDGAP	M03	-0.748456576
ARHGAP25	K21	-0.755129455
FGD6	G12	-0.769015071
ARHGEF11	K05	-0.78361064
CDGAP	I15	-0.791534739
FGD6	E12	-0.792481222
ARHGEF12	M13	-0.793739461
Cells	B05	-0.798334137

Cells	B11	-0.799464447
Cells	M12	-0.802304279
Cells	I10	-0.813230768
FGD4	M20	-0.81408005
Cells	K04	-0.824942293
ARHGEF12	I11	-0.831020966
Cells	G08	-0.859397048
SWAP70	F03	-0.873574704
ABR	G07	-0.874203823
CDGAP	M03	-0.87723402
Cells	G14	-0.87972595
MCF2L2	I10	-0.898573746
STARD8	C09	-0.898717309
SOS1	K13	-0.906414733
STARD8	C09	-0.915072008
Cells	G06	-0.918219709
ARHGEF5	E15	-0.930487338
DOCK6	F13	-0.942274534
FGD6	E12	-0.944054129
CDGAP	I15	-0.94897537
KIAA1909	E08	-0.949069023
KIAA1909	G22	-0.949607375
SOS1	I03	-0.954731097

Cells	M06	-0.970550237
ARHGEF10	C11	-0.979329663
ARHGEF19	C15	-0.980185377
ARHGAP24	E03	-0.982682001
Cells	G06	-1.012859786
ARHGAP1	N12	-1.013805402
Cells	K04	-1.033897718
FLJ43692/ARHGEF35	M03	-1.040919614
ARHGEF5	E15	-1.051238002
DOCK6	L21	-1.072376411
ARHGEF12	I11	-1.079862931
FARP1	C21	-1.080617875
ARHGEF10	G15	-1.085345583
Cells	M10	-1.091539992
PLEKHG1	M08	-1.150508359
DEPDC1B	E07	-1.157641711
LOC201176	E06	-1.172134251
Cells	B15	-1.185806626
Cells	B12	-1.189707166
SOS1	I03	-1.231417047
DOCK2	F09	-1.232361457
FARP1	M05	-1.233525875

Cells	M04	-1.237252314
LOC343578	E12	-1.250498888
Cells	B05	-1.270045704
PLEKHG1	I08	-1.292362167
ARHGEF10	C11	-1.32462723
PIK3R2	E13	-1.344274145
ARHGEF4	H13	-1.348937268
ARHGEF17	G09	-1.361456743
ARHGAP17	F18	-1.387439371
ARHGEF2	I21	-1.403733562
Cells	O10	-1.416127213
Cells	I08	-1.421983012
DOCK6	F13	-1.437660394
SWAP70	F03	-1.438363336
7H3	G15	-1.491363587
Cells	O09	-1.499611347
MYO9B	D06	-1.511942086
FARP1	C21	-1.513929661
ARHGEF10	G15	-1.535596973
Cells	G04	-1.554645491
7H3	I05	-1.581991142
LOC343578	E14	-1.639239953

KIAA1909	E08	-1.695007664
ABR	J04	-1.712190769
Cells	O14	-1.718607786
LOC345930	D09	-1.730309405
PIK3R2	C11	-1.732162708
FLJ10521	M07	-1.744635409
Cells	B06	-1.755600002
PIK3R2	C11	-1.776398231
DOCK5	J17	-1.782383424
7H3	G15	-1.791123929
ARHGAP17	F18	-1.80030846
SNX26	M09	-1.802333043
7H3	I05	-1.81163734
ARHGAP1	F14	-1.814648488
FLJ10521	C13	-1.837564415
OCRL	C15	-1.849545721
FLJ41603	F11	-1.857643157
Cells	O19	-1.867720651
DOCK5	J17	-1.883311226
PLEKHG1	I08	-1.897403499
FLJ10521	M07	-1.923008656
KIAA0672	L14	-1.949809139
CHN2	H10	-1.952766

SNX26	K07	-1.960579353
MYO9B	D06	-1.97077203
ARHGEF19	C15	-1.972457435
Cells	O20	-1.997062082
FARP1	M05	-2.011211185
OCRL	E11	-2.01559925
ARHGEF19	E07	-2.016603885
MYO9B	D08	-2.021528742
Cells	O14	-2.055687491
ARHGEF2	I21	-2.07136311
SOS1	K13	-2.095825511
OCRL	E11	-2.099197751
KIAA0672	L06	-2.100357394
ARHGEF19	E09	-2.120300477
FLJ10521	C13	-2.129674355
KIAA0672	L14	-2.130199402
LOC343578	E12	-2.137800568
KIAA0672	L06	-2.13891589
ARHGAP11A	N18	-2.140998503
ARHGEF4	L11	-2.166119767
ARHGEF4	H13	-2.219824578
Cells	O10	-2.220878992
LOC201176	E04	-2.278354396

LOC345930	D09	-2.306286513
OCRL	C15	-2.349601531
Cells	O13	-2.355492492
MYO9A	J18	-2.392709146
ARHGAP24	E03	-2.398467406
LOC257106	E08	-2.435757856
ARHGEF4	L11	-2.452790042
ITSN2	M17	-2.463886235
ARHGAP17	H08	-2.512682202
DOCK5	J09	-2.5181534
ITSN2	M19	-2.523284881
PARG1	C17	-2.52813758
DOCK7	F15	-2.537062555
Cells	O09	-2.550488758
ARHGAP17	H08	-2.592595017
GRLF1	J12	-2.627531262
ARHGAP11A	N18	-2.679056952
MYO9A	J18	-2.718562323
SNX26	M09	-2.745197789
GRLF1	J12	-2.752942874
PARG1	C17	-2.806317965
MYO9B	D08	-2.837289322

SGEF	M21	-2.861465958
GRLF1	F04	-2.920603175
LOC343578	E14	-2.9244166
ARHGAP11A	J14	-2.943293059
DOCK7	L19	-2.994115806
ITSN2	M19	-2.99597167
PARG1	G11	-2.998557926
SNX26	K07	-3.022654511
PARG1	G11	-3.101084726
MCF2L	K18	-3.160612199
DOCK5	J09	-3.202700282
LOC257106	E08	-3.209614831
LOC257106	E10	-3.226664877
DOCK7	L19	-3.234848279
MYO9A	H04	-3.252658079
LOC201176	E04	-3.257832783
ITSN2	M17	-3.270456433
DOCK7	F15	-3.314683522
ARHGEF2	E03	-3.335947755
FGD3	E22	-3.353374361
RASGRF2	I17	-3.356519958
ARHGAP11A	J14	-3.467307871

RASGRF2	G19	-3.565537812
RASGRF2	G19	-3.773122777
LOC257106	E10	-3.795137615
RASGRF2	I17	-3.827102738
PIK3R2	E13	-3.836823796
FGD3	E22	-3.938378545
MYO9A	H04	-3.956007766
OBSCN	L15	-3.999956313
OBSCN	F19	-4.019548818
MCF2L	K18	-4.083536183
MCF2L	E10	-4.105297782
FGD3	G18	-4.29540307
SGEF	M21	-4.424252441
OBSCN	F19	-4.469732825
MCF2L	E10	-4.510152022

ARHGEF2	E03	-4.569902139
FGD3	G18	-4.614129495
SGEF	I09	-4.65074424
OBSCN	L15	-4.874773633
GRLF1	F04	-4.922990186
SGEF	I09	-5.167881315
FLJ13815	E17	-5.379436561
FLJ13815	M17	-5.988057651
FLJ13815	M17	-6.006578512
FLJ13815	E17	-6.191550865
DOCK1	H19	-6.595477909
DOCK1	H19	-7.234187995
DOCK1	L07	-7.312552031
DOCK1	L07	-7.318732362

Appendix 8 Observed-predicted scores for YAP/TAZ ratio for SUM159 and hs578t screens.

Table 8.1: Lower than expected observed – predicted scores for YAP/TAZ ratio for SUM159 OTP screen.

	SUM159 OTP	Lower than expected
	Genes/siRNAs	Obs-pred YAP/TAZ ratio
L13	ECT2	-0.0639931
D09	ECT2	-0.0629144
H18	RACGAP1	-0.0575583
D09	ECT2	-0.057151
K04	AKAP13	-0.052529
J12	RACGAP1	-0.052073
H18	RACGAP1	-0.0520052
I22	AKAP13	-0.0509317
E19	RHOV	-0.0504288
J12	RACGAP1	-0.0488046
K22	ARHGEF2	-0.0475919
E20	RHOD	-0.0472299
C06	FLJ30058	-0.0467757
K04	AKAP13	-0.0456124
K22	ARHGEF2	-0.0443366
F22	ARHGEF7	-0.0432156
E20	RHOD	-0.0431837
D20	ARHGAP11B	-0.0428813
E19	RHOV	-0.0426123
D03	LOC345930/ECT2L	-0.0423701
C15	ARHGEF19	-0.0419441
D18	ARHGEF7	-0.0417282
M14	RHOD	-0.0416001
J18	ARHGAP11B	-0.0409994
L20	SH3BP1	-0.0404068
D20	ARHGAP11B	-0.0403765
D18	ARHGEF7	-0.0401008
E18	GEFT/GEFT/ARHGEF25	-0.0399874
C22	MCF2L2	-0.0390687
M21	TRIO	-0.0389214
C16	GEFT/GEFT/ARHGEF25	-0.0388685
F05	DOCK6	-0.0388289
F05	DOCK6	-0.038761
L16	SH3BP1	-0.0386068
L20	SH3BP1	-0.0384394
I16	RHOA	-0.0384209
K18	ARHGEF35	-0.0383761
F07	RALBP1	-0.0379832
M21	TRIO	-0.0375859
F22	ARHGEF7	-0.0374902
K12	ARHGEF2	-0.0373312
D15	DOCK6	-0.0372938
J18	ARHGAP11B	-0.0370376
N03	ARHGAP5	-0.0367847
C06	FLJ30058	-0.036717
M07	RHOV	-0.0366114
C22	MCF2L2	-0.0365266
M14	RHOD	-0.0363033
I10	FLJ30058	-0.0362173
M07	RHOV	-0.036159

E16	RHOU	-0.03605
C15	ARHGEF19	-0.0359868
E19	ARHGAP18	-0.0357858
E03	FLJ10521	-0.0355701
M19	ARHGEF19	-0.0350803
G03	TRIO	-0.0350196
L16	SH3BP1	-0.0347635
G06	ARHGEF35	-0.0346555
E03	FLJ10521	-0.0343548
G03	TRIO	-0.0341735
D14	PLEKHG4	-0.0336615
G06	ARHGEF35	-0.0336419
C04	RND2	-0.0335163
K18	ARHGEF35	-0.0334036
M19	ARHGEF19	-0.0333215
M10	RHOA	-0.0332756
C04	RND2	-0.0329986
E16	RHOU	-0.0328319
C09	ARHGAP24	-0.0323922
H03	IGDCC4/NOPE	-0.0320962
E10	MCF2L2	-0.0318741
M03	RHOC	-0.0317153
I16	RHOA	-0.0315554
J11	PLEKHG3	-0.0314776
C16	GEFT/GEFT/ARHGEF25	-0.0310788
C03	ARHGAP19	-0.0308815
I21	FARP1	-0.0308168
E10	MCF2L2	-0.0306652
G20	ARHGEF5	-0.0303614

H20	ARHGEF6	-0.030047
E18	GEFT/GEFT/ARHGEF25	-0.0300247
M12	RHOU	-0.0299356
C04	ARHGAP15	-0.0297533
N11	RALBP1	-0.0295917
D03	LOC345930/ECT2L	-0.0294941
C07	ARHGAP28	-0.0293108
J22	VAV1	-0.0289865
I21	FARP1	-0.0289529
I15	FARP1	-0.0288558
G18	RHOG	-0.0286492
M22	ARHGEF15	-0.0286325
D14	PLEKHG4	-0.0286085
I13	ARHGEF3	-0.0284561
G04	ARHGAP9	-0.0282088
J20	ARHGEF6	-0.0281361
M03	STARD13	-0.0280283
N06	PLEKHG1	-0.0278122
J03	ARFGEF3	-0.0277459
K03	SRGAP3	-0.0276764
F09	ARHGAP5	-0.0271567
I04	RND2	-0.0270876
E15	GMIP	-0.0270829
M12	RHOU	-0.0270761
K17	FLJ10521	-0.0270531
C13	CENTD1/ARAP2	-0.0269004
H22	PLEKHG2	-0.0268544
I11	ARHGAP12	-0.026553
G17	RHOF	-0.0264873

E18	SYDE1	-0.0264859
E09	RND1	-0.0264675
C04	ARHGAP15	-0.026319
M07	ARHGAP24	-0.0262829
I03	RASGRF1	-0.0262266
F07	RALBP1	-0.0260768
G07	SRGAP3	-0.0260665
F08	PLEKHG4	-0.0260319
C21	SOS2	-0.025876
N08	PLEKHG1	-0.0258
I18	RHOG	-0.0257131
D16	ARHGEF38	-0.0256111
C03	ARHGAP19	-0.0255964
C08	ARHGEF5	-0.0254539
M22	ARHGEF15	-0.0254436
K11	FLJ13815	-0.0251543
I04	ARHGAP15	-0.0251364
K17	FLJ10521	-0.0250874
G20	ARHGEF5	-0.0247744
L11	CHN2	-0.0246339
E22	ARHGEF28/RGNEF	-0.0244206
J22	VAV1	-0.0243997
D22	ARHGAP10	-0.0242699
N22	DOCK4	-0.0242586
N08	PLEKHG1	-0.0242075
D22	ARHGAP10	-0.0242052
I20	RHOBTB1	-0.0241679
M10	RHOA	-0.0240802
H20	ARHGEF6	-0.0238966

G07	ARHGEF3KIAA1244	-0.023803
J09	FLJ10665/PLEKHG6	-0.0237477
J07	ARFGEF3	-0.0237103
I15	FARP1	-0.0236562
L22	FLJ10357	-0.0235678
E09	RND1	-0.023533
G15	RASGRF1	-0.0234965
M17	RHOF	-0.0234411
C06	ARHGEF12	-0.0233944
F19	CHN2	-0.0233371
C10	FGD6	-0.023267
I10	FLJ30058	-0.0231668
G10	MYO9B	-0.0231492
I04	ARHGAP15	-0.0231133
E13	GMIP	-0.0230578
G17	ARHGAP12	-0.0230165
C06	ARHGEF12	-0.0229933
J20	ARHGEF6	-0.0229284
N20	DOCK8	-0.0228889
I03	RASGRF1	-0.022876
I13	ARHGEF3	-0.0228154
M03	RHOC	-0.0227889
M03	STARD13	-0.0227004
G17	RHOF	-0.022641
F11	SPATA13	-0.0225631
D16	ARHGEF38	-0.0225176
I04	RND2	-0.0223921
C18	PREX1	-0.0223541
F14	VAV1	-0.0222832

N22	DOCK4	-0.0222827
F08	PLEKHG4	-0.0219935
H14	ARHGEF38	-0.021968
H03	IGDCC4/NOPE	-0.0218855
C13	ARHGEF16	-0.0218788
K10	ARHGEF12	-0.0218587
C18	PREX1	-0.021721
D05	DOCK3	-0.0216609
G20	ARHGAP32/RICS	-0.0215823
J14	FLJ41603	-0.021492
I07	ARHGAP19	-0.0214899
D05	DOCK3	-0.0214815
D12	FLJ10357	-0.0214775
G04	ARHGAP9	-0.0214263
N05	FLJ10665/PLEKHG6	-0.0214063

Table 8.2: Higher than expected observed – predicted scores for YAP/TAZ ratio for SUM159 OTP screen.

	SUM159 OTP	Higher than expected
	Genes/siRNAs	Obs-pred YAP/TAZ ratio
F13	CHN1	0.0173201
M11	ARHGAP8	0.0173907
J15	IGDCC4/NOPE	0.0180296
I14	SOS1	0.0181692
N09	DOCK9	0.0183132
F18	DOCK10	0.0187285
C16	ARAP1/CENTD2	0.018918
I08	RHOBTB2	0.0190137
K06	SOS1	0.0214692
M04	CDC42	0.0226575
L21	PLEKHG5/KIAA0720	0.0230377
I14	SOS1	0.0261341
J08	DOCK10	0.0269781
K06	SOS1	0.0275254
C18	DEPDC1B	0.0275455
L09	ARHGAP17	0.0299836
H11	ARHGEF39/C9ORF100	0.0496222
H08	YAP	0.05741165
L19	ARHGEF39/C9ORF100	0.0608773
J22	YAP	0.0709372
H11	ARHGEF39/C9ORF100	0.0784798

Table 8.3: Lower than expected observed – predicted scores for YAP/TAZ ratio for SUM159 siGENOME screen.

	SUM159 siGENOME	Lower than expected
	Genes/siRNAs	Obs-pred YAP/TAZ ratio
E07	DEPDC1B	-0.0608628
M09	FLJ43692/ARHGEF35	-0.0593334
M03	FLJ43692/ARHGEF35	-0.0588847
I13	DEPDC1B	-0.0586988
I09	SGEF	-0.058373
F15	DOCK7	-0.0525668
C14	ARHGAP6	-0.0524725
E19	SRGAP2	-0.0512432
F15	DOCK7	-0.0507037
N16	RACGAP1	-0.0500776
E07	DEPDC1B	-0.0499538

I13	DEPDC1B	-0.0494097
M21	SGEF	-0.0493609
N10	FAM7A2	-0.048954
M17	FLJ13815	-0.0464686
E17	FLJ13815	-0.0462261
N18	ARHGAP11A	-0.0461103
F08	RACGAP1	-0.0456313
C12	ARHGAP6	-0.045057
F22	FAM7A2	-0.0449149
F08	RACGAP1	-0.0446723
F22	FAM7A2	-0.043384
C19	SRGAP2	-0.0432751
G15	7H3	-0.0423211
M09	SNX26	-0.0413112
I05	7H3	-0.0411691
F05	DEF6	-0.0393217
K07	SNX26	-0.0391353
J11	DOCK8	-0.0381909
M09	FLJ43692/ARHGEF35	-0.0378141
N16	RACGAP1	-0.0372809
M21	FAM13A1	-0.0372327
J14	ARHGAP11A	-0.0370781
C09	STARD8	-0.0365122
G19	RICS	-0.0359518
H22	FLJ10357	-0.035673
G21	FAM13A1	-0.0347797
N08	FLJ10357	-0.0347308
I09	SGEF	-0.0341269
C16	FLJ30058	-0.0336582

C18	FLJ30058	-0.0332192
E11	OCRL	-0.0324331
J05	DEF6	-0.0319543
G15	7H3	-0.0316654
D12	ARHGAP20	-0.0316408
C14	ARHGAP6	-0.0311284
C12	ARHGAP6	-0.0310377
N10	FAM7A2	-0.0307728
M21	FAM13A1	-0.0307089
K12	TRIO	-0.0304868
L20	ARHGAP20	-0.0298262
C16	PLEKHG3	-0.0297149
K14	FGD4	-0.0296013
E13	PIK3R2	-0.0295619
C19	SRGAP2	-0.029445
H22	FLJ10357	-0.0294009
G18	FGD3	-0.0293894
F11	FLJ41603	-0.0293876
L15	OBSCN	-0.0290371
C15	OCRL	-0.0285066
M19	RICS	-0.0285013
E19	SRGAP2	-0.0277755
C18	ARHGEF7	-0.0275151
M13	PIK3R1	-0.0273
H21	FLJ41603	-0.0267761
C16	FLJ30058	-0.0265799
M12	ARHGEF7	-0.0265631
M11	PIK3R1	-0.0262706
M08	PLEKHG1	-0.026104

K19	ARHGEF16	-0.0257979
L14	KIAA0672	-0.025625
N08	FLJ10357	-0.0255644
F19	OBSCN	-0.025487
C04	ARHGAP18	-0.0253047
K09	AKAP13	-0.0240745
M19	RICS	-0.0236918
E10	MCF2L	-0.0232904
K18	MCF2L	-0.0230681
I05	7H3	-0.0228755
C21	FARP1	-0.0225442
E08	LOC257106	-0.0224945
K20	VAV1	-0.022419
D16	ARHGAP26	-0.0223187
C06	ARHGAP18	-0.0223036
H21	FLJ41603	-0.0220622
K21	ARHGAP25	-0.0217298
E06	TRIO	-0.0216995
J14	ARHGAP11A	-0.0203459
J10	KIAA1244	-0.0199782
G19	RICS	-0.0195868
L22	KIAA1244	-0.0193897
M20	FGD4	-0.0192451
C03	AKAP13	-0.0191603
D09	LOC345930	-0.0191121
E10	LOC257106	-0.0190952
K09	SRGAP2	-0.0189584
L06	KIAA0672	-0.0188963
I08	PLEKHG1	-0.0188909

J03	DOCK8	-0.018735
M09	SNX26	-0.0186422
J20	ARHGAP26	-0.0185077
E14	DEPDC2/PREX2	-0.0183522
C15	OCRL	-0.0180223
M13	PIK3R1	-0.0178843
C18	FLJ30058	-0.017488
F11	FLJ41603	-0.0173669
G13	INPP5B	-0.016514
D12	ARHGAP20	-0.0163206
L18	CHN2	-0.0162362
K18	MCF2L	-0.0161963
M05	SRGAP2	-0.0159909
N18	ARHGAP11A	-0.0157055
I15	CDGAP	-0.015038
E06	TRIO	-0.0148124
L20	ARHGAP20	-0.0147597
K03	ARHGEF5	-0.0147465
J13	DOCK2	-0.0144899
K16	TIAM1	-0.0142386
K03	ARHGEF5	-0.0142183
N06	SH3BP1	-0.01408
E22	FGD3	-0.0140164
K07	SNX26	-0.0139015
L20	LATS2	-0.0137522
H10	CHN2	-0.0135916
E11	OCRL	-0.0135429
D07	DOCK4	-0.0133249
H07	DOCK4	-0.0132218

M04	VAV1	-0.0129238
G17	ARHGEF16	-0.0126718
E13	ITSN1	-0.0125327
F12	LATS1	-0.0123866
G13	INPP5B	-0.0121786
K20	VAV1	-0.012125

Table 8.4: Higher than expected observed – predicted scores for YAP/TAZ ratio for SUM159 siGENOME screen.

	SUM159 siGENOME	Higher than expected
	Genes/siRNAs	Obs-pred YAP/TAZ ratio
C03	ARHGAP15	0.0350046
G08	ARHGEF6	0.0356789
N19	YAP	0.0357897
G16	KIAA0720	0.0359184
K15	NET1	0.035955
I07	ARHGAP15	0.0375343
M07	FLJ10521	0.0382299
I10	MCF2L2	0.0400897
M10	FARP2	0.04029834
L05	DOCK9	0.04199853
M15	SRGAP1	0.04739741
E12	FGD6	0.04827308
D04	ARHGAP21	0.04936576
J19	SPATA13	0.050963724
K05	SRGAP1	0.05163816
H05	DOCK9	0.05199921
M15	SRGAP1	0.0522683
H11	SPATA13	0.05292661
N04	ARHGAP21	0.0542768
K13	SOS1	0.05457199
H15	ARHGEF9	0.0561688
L05	DOCK9	0.0585797
D22	ARHGAP10	0.0588504
K05	SRGAP1	0.0590495
C04	C9orf100/ARHGEF39	0.0626334
N04	ARHGAP21	0.064850328
I16	C9orf100/ARHGEF39	0.0668856
K21	ARHGEF1	0.0736698
N20	ARHGAP10	0.0776011
M15	ARHGEF1	0.0781488
I16	C9orf100/ARHGEF39	0.080974

Table 8.5: Lower than expected observed – predicted scores for YAP/TAZ ratio for hs578t siGENOME screen.

	hs578t siGENOME	Lower than expected
	Genes/siRNAs	Obs-pred YAP/TAZ ratio
E07	DEPDC1B	-0.078554
F19	OBSCN	-0.07793
I13	DEPDC1B	-0.077897
E07	DEPDC1B	-0.075524
I17	RASGRF2	-0.073156
I05	7H3	-0.07286
E12	LOC343578	-0.0680848
I13	DEPDC1B	-0.06666

L15	OBSCN	-0.06572
H10	CHN2	-0.063866
E14	LOC343578	-0.0631649
F05	DEF6	-0.061722
G15	7H3	-0.06065
F19	OBSCN	-0.059936
G15	7H3	-0.058756
F12	SH3BP1	-0.0560574
M09	FLJ43692/ARHGEF35	-0.0550642
M03	FLJ43692/ARHGEF35	-0.0526533

Table 8.6: Higher than expected observed – predicted scores for YAP/TAZ ratio for hs578t siGENOME screen.

	hs578t siGENOME	Higher than expected
	Genes/siRNAs	Obs-pred YAP/TAZ ratio
M13	ARHGEF12	0.0555501
N14	CHN1	0.05623497
I10	MCF2L2	0.05662924
M19	ITSN2	0.0568012
I05	NGEF	0.0568422
L12	OPHN1	0.0572665
C19	NET1	0.0582464
I22	GEFT	0.05835142
I17	DEPDC1	0.0585402
I03	SOS1	0.0624733
K11	NGEF	0.0637301
K22	FARP2	0.0637727
H18	OPHN1	0.0654778
E11	LATS1	0.0656039
I22	GEFT	0.06656702
D22	ARHGAP10	0.0670388
G16	KIAA0720	0.0714102
H11	SPATA13	0.0729661
H18	OPHN1	0.0737448
K13	SOS1	0.0751729
H07	DOCK4	0.0777096
H15	ARHGEF9	0.0797614
M19	ITSN2	0.0805106
M10	FARP2	0.0842164
J19	SPATA13	0.0862328
C21	DEPDC1	0.0883138
L12	OPHN1	0.0885613
M17	ITSN2	0.0885743
N17	LATS1	0.0899376
D22	ARHGAP10	0.0912308
C20	DEPDC2/PREX2	0.0921314
E09	ARHGEF19	0.0922658
C21	DEPDC1	0.0927897
J15	TAZ	0.0933282
C20	DEPDC2/PREX2	0.0959109
E07	RGNEF	0.0973263
D07	DOCK4	0.0974222
K22	FARP2	0.0981132
E11	LATS1	0.0986694
H20	CENTD3	0.1005921
E14	DEPDC2/PREX2	0.1079405
C15	ARHGEF19	0.1081868
L03	LOC345930	0.1103926
C15	ARHGEF19	0.1130798

D09	LOC345930	0.1137685
E21	RASGRF1	0.1139605
N07	TAZ	0.1154598
N17	LATS1	0.1156962
C17	RGNEF	0.1199214
L03	LOC345930	0.1229544
H15	ARHGEF9	0.125215
E07	RGNEF	0.127123
C17	RGNEF	0.129005
N22	CENTD3	0.1301396
D03	ARHGEF9	0.133514
N07	TAZ	0.1420194
N22	CENTD3	0.155978

Table 8.7: Lower than expected observed – predicted scores for YAP/TAZ ratio for hs578t OTP screen.

	hs578t OTP	Lower than expected
	Genes/siRNAs	Obs-pred YAP/TAZ ratio
G06	ARHGEF35	-0.07913428
G06	ARHGEF35	-0.07545297
I10	FLJ30058	-0.07488798
K18	ARHGEF35	-0.07077644
K18	ARHGEF35	-0.06694392
I19	STARD13	-0.06154994
J14	FLJ41603	-0.06152987
G20	ARHGEF5	-0.06111103
M14	RHOD	-0.06104858
K17	FLJ10521	-0.06099717
J11	PLEKHG3	-0.06001864
I18	RHOG	-0.05961735
H06	PLEKHG4B/KIAA1909	-0.05941613
J07	ARFGEF3	-0.05884654
J16	FLJ41603	-0.05746795
H06	PLEKHG4B/KIAA1909	-0.05603736
N08	PLEKHG1	-0.05552288
C06	FLJ30058	-0.05474472
M14	RHOD	-0.05387211
N08	PLEKHG1	-0.05324914
M12	RHOU	-0.05320644
J10	PLEKHG4B/KIAA1909	-0.05290204
J18	ARHGAP11B	-0.0527345
G14	ARHGEF28/RGNEF	-0.05238759
J13	ARHGEF4	-0.05234682
E13	NET1	-0.05199472
E03	FLJ10521	-0.05173594
N06	PLEKHG1	-0.05158845
F08	PLEKHG4	-0.05147223
E20	RHOD	-0.04992505
F08	PLEKHG4	-0.04989928
L16	SH3BP1	-0.04930955
J18	ARHGAP11B	-0.04881774
G20	ARHGEF5	-0.04871002
G10	ARHGEF26/SGEF	-0.04855772
C08	ARHGEF5	-0.04838744
J16	FLJ41603	-0.04827283
E20	RHOD	-0.04812424
K17	FLJ10521	-0.04810643
K11	FLJ13815	-0.04809698

Table 8.8: Higher than expected observed – predicted scores for YAP/TAZ ratio for hs578t OTP screen.

	hs578t OTP	Higher than expected
	Genes/siRNAs	Obs-pred YAP/TAZ ratio
K09	DEPDC1	0.0486268
E18	SYDE1	0.0486482
N19	VAV3	0.04886277
I15	FARP1	0.04914495
D07	BCR	0.04955249
N21	ARHGAP20	0.0495976
L19	ARHGEF39/C9ORF100	0.04968227
G09	MCF2	0.05045781
G17	ARHGAP12	0.05055672
K20	RHOBTB2	0.0505708
J14	LATS1	0.05125366
K17	LOC343578/ARHGAP40	0.05127047
C17	CENTD1/ARAP2	0.05187798
G07	SRGAP3	0.05197832
F14	LATS2	0.05220563
L13	ECT2	0.05221466
F15	LATS1	0.05231586
E20	ARHGAP32/RICS	0.05248487
E15	GMIP	0.05302346
K07	INPP5B	0.0535809
C21	PIK3R2	0.05428838
J06	LATS2	0.05429047
L09	ARHGAP17	0.05431783
G15	FAM13A	0.05452028
N07	ALS2	0.05475768
N17	SPATA13	0.05493559
N05	FLJ10665/PLEKHG6	0.05543699
E08	TAGAP	0.05547325
F15	LATS1	0.05558387
D19	ARHAGAP44/KIAA0672	0.05611104
K13	C5ORF5/FAM13B	0.05621286
I15	FARP1	0.05625698
H07	TIAM2	0.05640058
M15	HMHA1	0.05644694
E22	OCRL	0.05690178
G21	PIK3R2	0.05706389
L15	DOCK1	0.05720793
E10	TAGAP	0.05750319
K21	DEPDC1	0.05776804
H11	ARHGEF39/C9ORF100	0.05887644
N15	ARHGAP17	0.06001151
J09	FLJ10665/PLEKHG6	0.06079336
N04	PLEKHG2	0.06166081
K03	SRGAP3	0.06227382
F21	OBSCN	0.06279076
C14	ARHGAP4	0.06378225
G18	ARHGAP4	0.06384971
N06	LATS1	0.06437807
D21	ARHAGAP44/KIAA0672	0.06469839
G08	DEPDC1B	0.06471844
H13	BCR	0.06585564
N04	PLEKHG2	0.06637438
C03	ARHGAP19	0.06665219

D03	LATS1	0.067394
M21	ARHGAP1	0.06854267
M05	PIK3R1	0.06999075
F17	ALS2	0.0701259
I21	FARP1	0.07031796
D03	LATS1	0.07058592
E21	FAM13A	0.07077726
I21	FARP1	0.07281425
H22	PLEKHG2	0.07287456
J21	ARHGAP20	0.07340098
I09	ARHGAP1	0.07374728
C18	DEPDC1B	0.07388094
D03	LOC345930/ECT2L	0.07551967
E07	STARD8	0.07747423
M13	PIK3R1	0.07832391
H22	PLEKHG2	0.08225881
J17	LOC345930/ECT2L	0.08599518
I21	STARD8	0.0868172
L19	ARHGEF39/C9ORF100	0.08685086

I07	ARHGAP19	0.08731311
N08	TAZ	0.09125441
N07	TAZ	0.09339669
N07	TAZ	0.09971348
E10	TAGAP	0.10194593
E08	TAGAP	0.10235363
G21	PIK3R2	0.10330167
F20	TAZ	0.1041548
F17	TAZ	0.10426768
C21	PIK3R2	0.10536892
C14	ARHGAP4	0.10583986
N06	LATS1	0.11018942
J14	LATS1	0.11139645
E15	ITSN2	0.11605126
F17	TAZ	0.12256197
N08	TAZ	0.13159647
C17	ITSN2	0.13736135
F20	TAZ	0.15369242

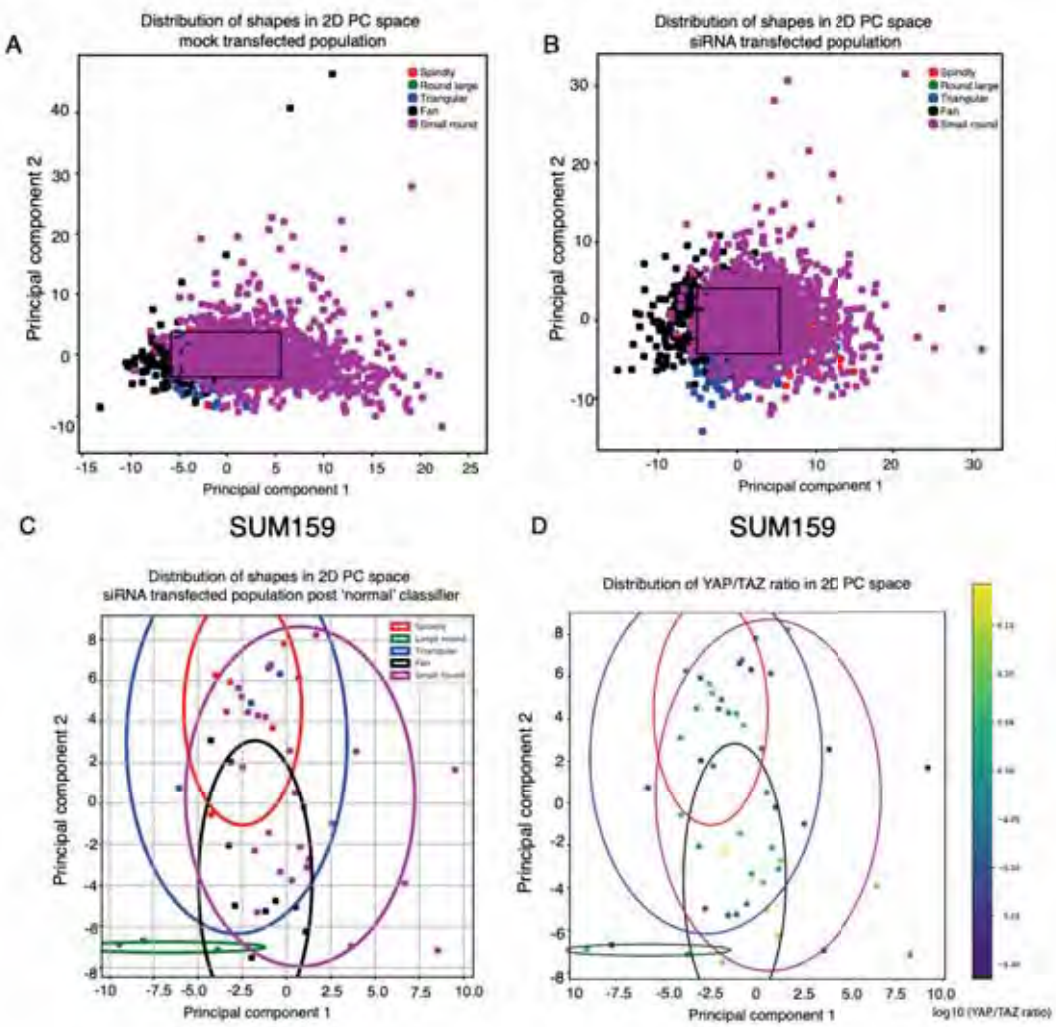

Appendix 9 Shape filtering in SUM159

(A) (B) PCA of single cell dataset comprised of texture and morphological features of populations which were either mock transfected (A) or transfected with siRNAs which scored the highest for enriching for a particular shape (B). Each data point represents a cell and is colour coded by the shape into which it has been classified. Spindly in red, round large in green, triangular in blue, fan in black, and small round in purple. Black box represents 1 standard deviation of the mean for PC1 and PC2 of (B), projected on (A). Single cells within black box shown in (A) were defined as 'normal' in the new classifiers. (C) PCA of single cell dataset comprised of texture and morphological features of siRNA transfected population, after running new classifiers on same data, removing cells classified as 'normal'. Ellipses represent 95% confidence intervals for each shape.

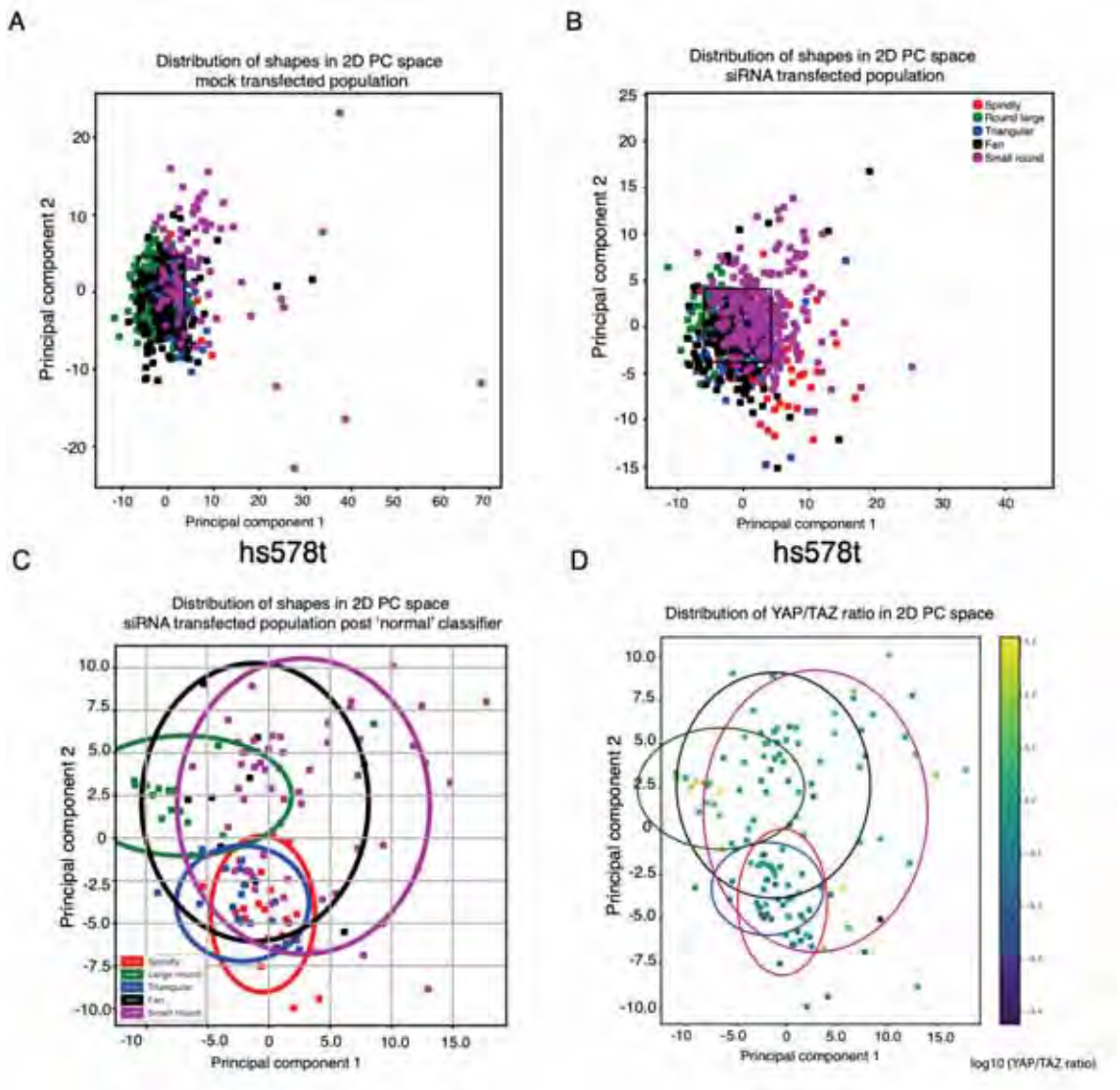

Appendix 10 Shape filtering in hs578t

(A) (B) PCA of single cell dataset comprised of texture and morphological features of populations which were either mock transfected (A) or transfected with siRNAs which scored the highest for enriching for a particular shape (B). Each data point represents a cell and is colour coded by the shape into which it has been classified. Spindly in red, round large in green, triangular in blue, fan in black, and small round in purple. Black box represents 1 standard deviation of the mean for PC1 and PC2 of (B), projected on (A). Single cells within black box shown in (A) were defined as 'normal' in the new classifiers. (C) PCA of single cell dataset comprised of texture and morphological features of siRNA transfected population, after running new classifiers on same data, removing cells classified as 'normal'. Ellipses represent 95% confidence intervals for each shape.

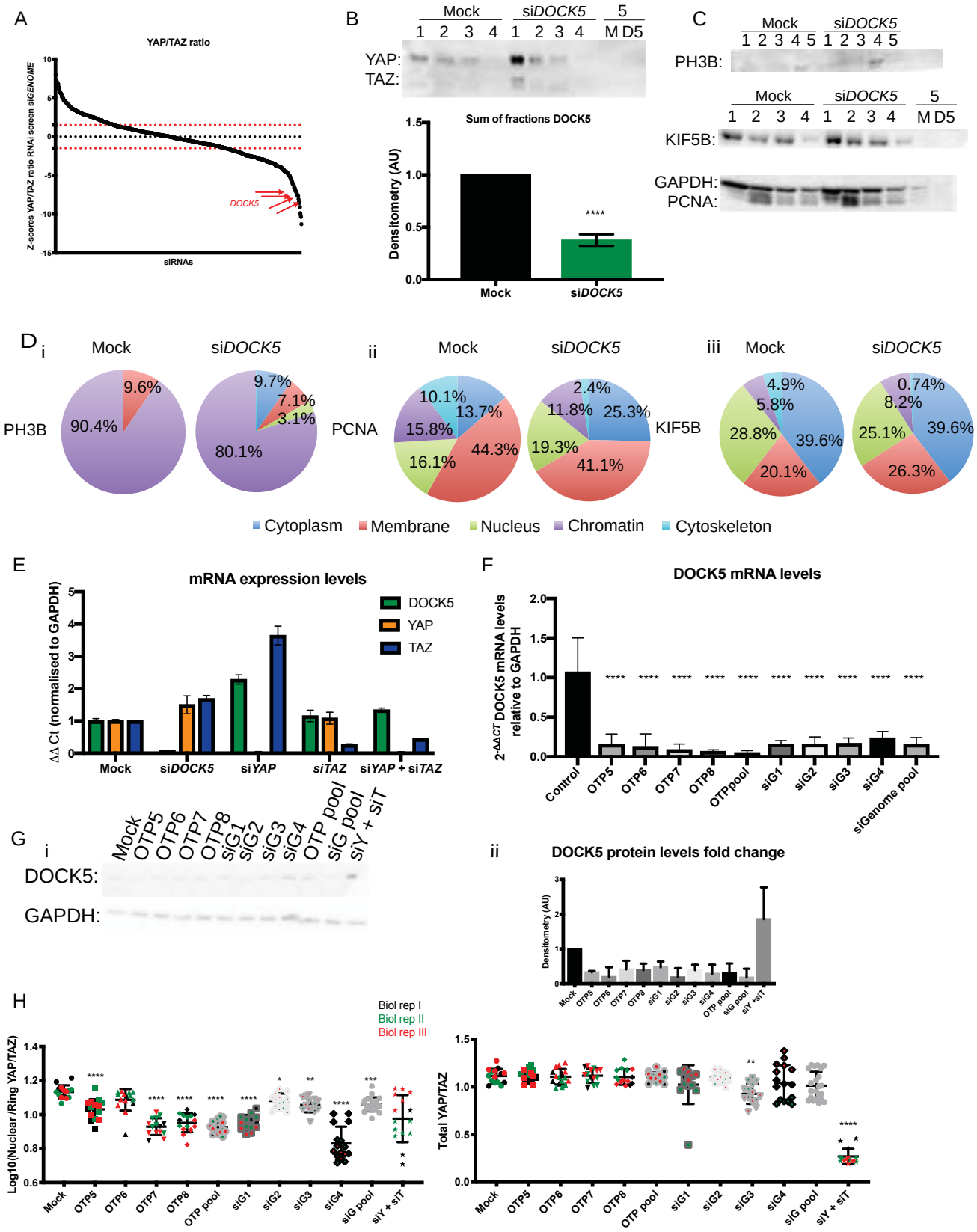

Appendix 11: Validation of *DOCK5* siRNA knockdown. *Legend overleaf.*

Appendix 11: Validation of *DOCK5* siRNA knockdown. (A) Z-scores per well for YAP/TAZ ratio for siGENOME siRNA screen in LM2. Red dotted lines indicate values from which above and below were considered hits. Above 1.5 are siRNAs which are hits for high YAP/TAZ ratio and thus can be considered inhibitors of YAP/TAZ. Below -1.5 are siRNAs which are hits for low YAP/TAZ ratio and thus can be considered YAP/TAZ activators. Four individual replicates for si*DOCK5* as hits for low YAP/TAZ ratio are shown. (B) Representative western blot of subcellular fractions for mock and si*DOCK5*. 1: nuclear fraction; 2: membrane fraction; 3: cytoplasm fraction; 4: chromatin bound fraction, 5: cytoskeletal fraction. M is mock, D5: si*DOCK5*. Blotted for YAP and TAZ. Loaded 5ng of protein for all except for cytoskeleton (2.5ng). Below, quantification of DOCK5 protein levels upon *DOCK5* knockdown adding all fractions from western blot. Mean ± SD are shown (n = 2, T-test, **** P < 0.0001). (C) Same subcellular fractions as in (B). blotted for PH3B, KIF5B, GAPDH, and PCNA as controls for each fraction: chromatin bound, cytoskeleton bound, whole cell, nuclear respectively. (D) Pie charts depicting the distribution of (i) PH3B, (ii) PCNA, (iii) KIF5B, in each fraction. (E) mRNA expression levels of DOCK5, YAP, and TAZ, for mock, si*DOCK5*, si*YAP*, si*TAZ*, and si*YAP* + si*TAZ* transfected cells. N = 1 biological repeat, each data point is 4 wells. (F) Validation of DOCK5 siRNA knockdown via qRTPCR. DOCK5 mRNA levels following *DOCK5* knockdown with deconvoluted siRNAs for DOCK5 OTP5 to 8 and in pooled combination (OTP pool), as well as siG1-4 and in pooled combination (siGENOME pool). Mean ± SD are shown (n = 1 biological repeat, each data point is 4 wells, ANOVA, **** P < 0.0001). (G) Validation of DOCK5 siRNA knockdown via western blots. GAPDH as loading control. (i) and (ii) quantifications of (i). Mean ± SD are shown (n = 2). (H) Graphs showing YAP/TAZ ratio and YAP/TAZ levels upon transfection with DOCK5 deconvoluted and pooled siRNAs for OTP and siGENOME. Mean ± SD are shown (n = 3, ANOVA, *P < 0.1** P < 0.01, *** P < 0.001**** P < 0.0001). Experiments depicted in E, F were performed by Mar Arias-Garcia, Bakal lab.

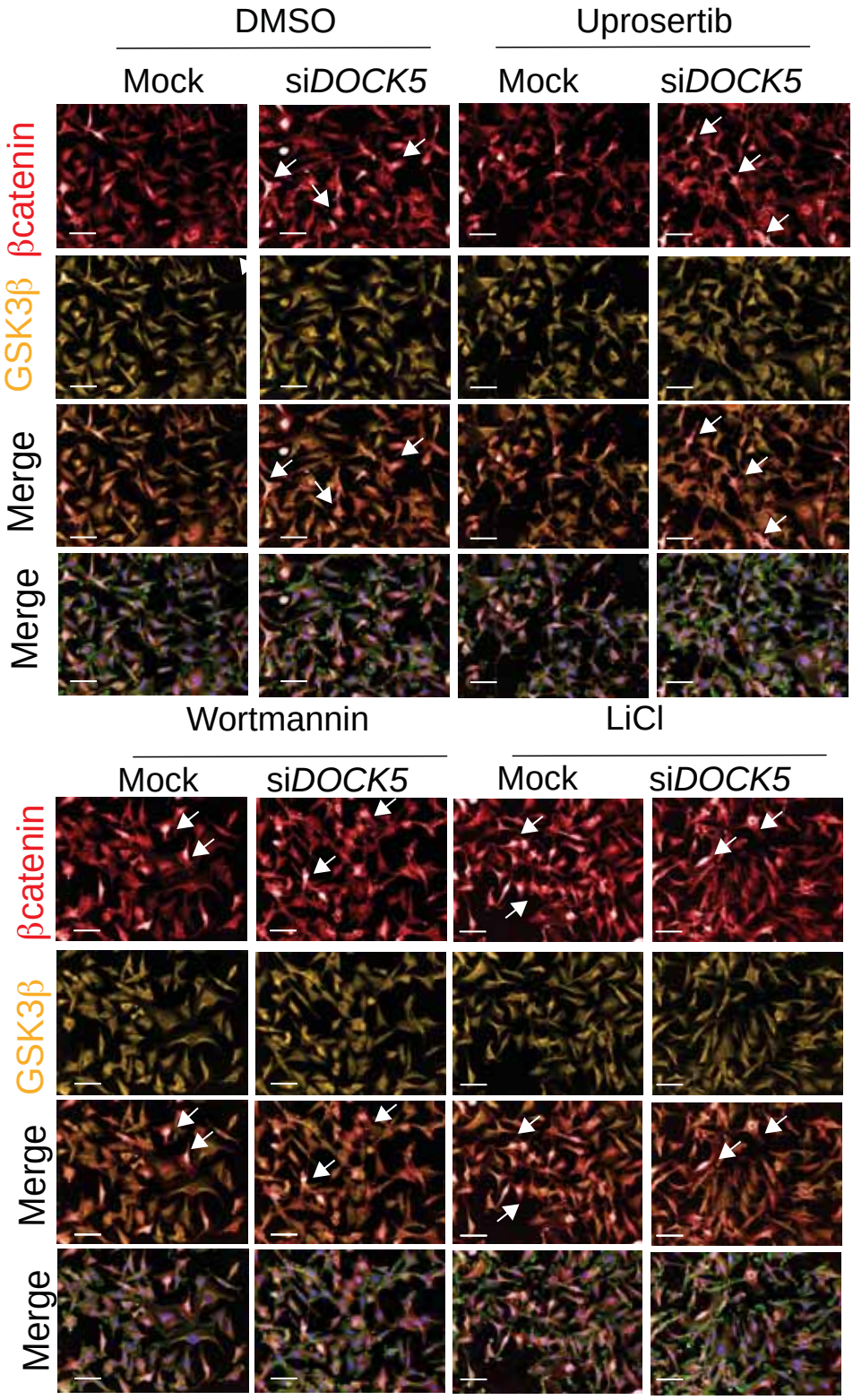

Appendix 12 Beta catenin increase in response to LiCl treatment
Representative images of mock and si*DOCK5* transfected cells treated with DMSO, 5mM LiCl, 2μM final Uprosertib, or 0.4μM final Wortmannin. Stained for GSK3β (yellow), βcatenin (red), and merge including F-actin (green) and DNA (blue). Scale bar is 50 μm. Experiment performed by Mar Arias-Garcia, Bakal lab.

Appendix 13: Hedge's g values for Figure 5.7 DOCK5 regulation of focal adhesion dynamics is not RAC1 dependent Chapter 5. (B) Unpaired Hedge's g for assembly rates between mock and conditions: si*DOCK5*: 0.375 (95% CI -0.0214, 0.776); si*CDC42*: 0.851 (95% CI -0.499, 1.19); si*RHOA*: 1.06 (95% CI -0.229, 0.436); si*RAC1*: 0.0311 (95% CI -0.332, 0.387); Uprosertib: 0.105 (95% CI -0.276, 0.479). Two-sided P values of Mann-Whitney tests are 0.242, 2.090 x 10^{-5}, 0.922, 0.963, 0.808 respectively. (C) Unpaired Hedge's g for disassembly rates between mock and conditions: si*DOCK5*: 0.574 (95% CI 0.0979, 1.04); si*CDC42*: 0.321 (95% CI -0.0767, 0.715); si*RHOA*: 0.376 (95% CI 0.0138, 0.732); si*RAC1*: 0.145 (95% CI -0.252, 0.558); Uprosertib: 0.467 (95% CI 0.0641, 0.887). Two-sided P values of Mann-Whitney tests are 0.0363, 0.1840, 0.0580, 0.4030, 0.0652 respectively. (D) Unpaired Hedge's g for assembly rate phase lengths between mock and conditions: si*DOCK5*: 0.307 (95% CI -0.0508, 0.662); si*CDC42*: 0.256 (95% CI -0.0605, 0.536); si*RHOA*: -0.0537 (95% CI -0.35, 0.247); si*RAC1*: 0.336 (95% CI 0.0297, 0.621); Uprosertib: -0.187 (95% CI -0.471, 0.148). Two-sided P values of Mann-Whitney tests are 0.140, 0.154, 0.471, 0.237, 0.390 respectively. (E) Unpaired Hedge's g for disassembly rate phase lengths between mock and conditions: si*DOCK5*: -0.12 (95% CI -0.439, 0.39); si*CDC42*: 0.106 (95% CI -0.224, 0.483); si*RHOA*: -0.255 (95% CI -0.505, 0.0726); si*RAC1*: -0.251 (95% CI -0.494, 0.14); Uprosertib: 0.037 (95% CI -0.285, 0.456). Two-sided P values of Mann-Whitney tests are 0.550, 0.633, 0.270, 0.435, 0.818 respectively. (F) Histograms of (i) assembly and (ii) disassembly phase lengths for all conditions. (G) Unpaired Hedge's g for stability phase lengths between mock and conditions: si*DOCK5*: -0.507 (95% CI -1.20, 0.494); si*CDC42*: 0.167 (95% CI -0.464, 0.856); si*RHOA*: -0.395 (95% CI -1.03, 0.517); si*RAC1*: -0.299 (95% CI -0.827, 0.259); Uprosertib: -0.456 (95% CI -1.04, 0.393). Two-sided P values of Mann-Whitney tests are 0.0602, 0.6390, 0.06080, 0.4590, 0.0476 respectively. (H) Unpaired Hedge's g for FAAI between mock and conditions: si*DOCK5*: 0.231 (95% CI -0.000746, 0.443); si*CDC42*: -0.315 (95% CI -0.509, -0.0483); si*RHOA*: 0.528 (95% CI 0.287, 0.741); si*RAC1*: 0.505 (95% CI 0.276, 0.716); Uprosertib: 0.138 (95% CI -0.0977, 0.377). Two-sided P values of Mann-Whitney tests are 0.0161, 0.0683, 1.2700 x 10^{-6}, 7.8800 x 10^{-4}, and 0.8540 respectively. N equals the FAAI per image taken. Difference in n numbers is due to the software failing to record a number in certain images.

Appendix 14: siGENOME RhoGEF/GAP siRNA catalogue numbers and sequences

STODJ Custom Plates siGENOME GEFGAP LIBRARY Order Numbers 254546, 254547								
Plate	**Well**	**Pool Catalog Number**	**Duplex Catalog Number**	**Gene Symbol**	**GENE ID**	**Gene Accession**	**GI Number**	**Sequence**
Plate 1	A02	M-009654-00	D-009654-01	ARHGEF18	23370	NM_015318	14670376	GCACAGAGCCUCCUAGAGA
Plate 1	A02	M-009654-00	D-009654-02	ARHGEF18	23370	NM_015318	14670376	UCAGGGCGCUUGAAAGAUA
Plate 1	A02	M-009654-00	D-009654-03	ARHGEF18	23370	NM_015318	14670376	CAAGAGCGGUUGAGCAUGA
Plate 1	A02	M-009654-00	D-009654-04	ARHGEF18	23370	NM_015318	14670376	GCACUGAGGACUAUGAAGA
Plate 1	A03	M-024506-02	D-024506-01	RGNEF	64283	NM_001080479	122937433	GCAAGGAUGCCAAAGAUAA
Plate 1	A03	M-024506-02	D-024506-02	RGNEF	64283	NM_001080479	122937433	GUGCGUGAAUUAACAGUAU
Plate 1	A03	M-024506-02	D-024506-03	RGNEF	64283	NM_001080479	122937433	GAUAUUAAACUCUUCCGGA
Plate 1	A03	M-024506-02	D-024506-04	RGNEF	64283	NM_001080479	122937433	GACUAGCCCUCGGAAUAAA
Plate 1	A04	M-009883-01	D-009883-01	ARHGEF2	9181	NM_004723	15011973	GGACAAGCCUUCAGUGGUA
Plate 1	A04	M-009883-01	D-009883-02	ARHGEF2	9181	NM_004723	15011973	CAACAUUGCUGGACAUUUC
Plate 1	A04	M-009883-01	D-009883-03	ARHGEF2	9181	NM_004723	15011973	GAAUUAAGAUGGAGUUGCA
Plate 1	A04	M-009883-01	D-009883-05	ARHGEF2	9181	NM_004723	15011973	GUGCGGAGCAGAUGUGUAA
Plate 1	A05	M-008868-01	D-008868-01	AKAP13	11214	NM_006738	31563329	GAAGACAUAUGGCAAGUUU
Plate 1	A05	M-008868-01	D-008868-02	AKAP13	11214	NM_006738	31563329	CGAAACAGCUGGAUUCAGA
Plate 1	A05	M-008868-01	D-008868-03	AKAP13	11214	NM_006738	31563329	UCAACAGACUCACUAAAUA
Plate 1	A05	M-008868-01	D-008868-05	AKAP13	11214	NM_006738	31563329	GGAAGAAGCUUGUACGUGA
Plate 1	A06	M-013243-00	D-013243-01	ARHGEF3	50650	NM_019555	9506400	CAAACUAGAUCUCUGGAAU
Plate 1	A06	M-013243-00	D-013243-02	ARHGEF3	50650	NM_019555	9506400	CGAGGGAUCGUUCCUAAAU
Plate 1	A06	M-013243-00	D-013243-03	ARHGEF3	50650	NM_019555	9506400	GUGAAGGCCACGCCAUUAA
Plate 1	A06	M-013243-00	D-013243-04	ARHGEF3	50650	NM_019555	9506400	UGGCUUAACUGUAUUCGUC
Plate 1	A07	M-008480-00	D-008480-01	ARHGEF12	23365	NM_015313	7662087	AGACAGAGAUUUGGGAUUA
Plate 1	A07	M-008480-00	D-008480-02	ARHGEF12	23365	NM_015313	7662087	GGAGGAAUGUGAAGUAGAA
Plate 1	A07	M-008480-00	D-008480-03	ARHGEF12	23365	NM_015313	7662087	GAGAAGACCUGAGCUCAUU
Plate 1	A07	M-008480-00	D-008480-04	ARHGEF12	23365	NM_015313	7662087	GACAGGAAGUGAUUAAUGA
Plate 1	A08	M-009421-00	D-009421-01	ARHGEF1	9138	NM_004706	39777602	AGAACGAGCUGGAGACAAA
Plate 1	A08	M-009421-00	D-009421-02	ARHGEF1	9138	NM_004706	39777602	CAACGUCGCCUUUGAACUU
Plate 1	A08	M-009421-00	D-009421-03	ARHGEF1	9138	NM_004706	39777602	GGUGUGCUCUCAUCACUGA
Plate 1	A08	M-009421-00	D-009421-04	ARHGEF1	9138	NM_004706	39777602	UGACGUGGCGGGUGACUAA
Plate 1	A09	M-003915-02	D-003915-01	NET1	10276	NM_005863	114145480	GAAGUCGCCUAGUCAAAUA

Plate 1	A09	M-003915-02	D-003915-02	NET1	10276	NM_005863	114145480	GGAGGAUGCUAUAUUGAUA
Plate 1	A09	M-003915-02	D-003915-03	NET1	10276	NM_005863	114145480	UCACGUCCUUGGCAAAUUU
Plate 1	A09	M-003915-02	D-003915-05	NET1	10276	NM_005863	114145480	GGCAAUAUAUGAAAUGUCC
Plate 1	A10	M-010360-00	D-010360-01	ARHGEF11	9826	NM_014784	38026914	GAACCUGCCUGAACUCAUA
Plate 1	A10	M-010360-00	D-010360-02	ARHGEF11	9826	NM_014784	38026914	GGAAAGACAUCUGGAAUAU
Plate 1	A10	M-010360-00	D-010360-03	ARHGEF11	9826	NM_014784	38026914	GCAAGUGGCUGCACAGUUC
Plate 1	A10	M-010360-00	D-010360-04	ARHGEF11	9826	NM_014784	38026914	GAAGAUCCCUGAGAUGCUA
Plate 1	A11	M-008365-01	D-008365-01	ITSN1	6453	NM_001001132	47717124	GGACAUAGUUGUACUGAAA
Plate 1	A11	M-008365-01	D-008365-03	ITSN1	6453	NM_001001132	47717124	GAUAUCAGAUGUCGAUUGA
Plate 1	A11	M-008365-01	D-008365-04	ITSN1	6453	NM_001001132	47717124	GGCCAUAACUGUAGAGGAA
Plate 1	A11	M-008365-01	D-008365-17	ITSN1	6453	NM_001001132	47717124	CAAGAAAACUCCACGAAGA
Plate 1	B02	M-009841-00	D-009841-01	ITSN2	50618	NM_006277	22325384	GAUCAAACGUGACAAGUUG
Plate 1	B02	M-009841-00	D-009841-02	ITSN2	50618	NM_006277	22325384	GACAGGAGCUUCUCAAUCA
Plate 1	B02	M-009841-00	D-009841-03	ITSN2	50618	NM_006277	22325384	CCAAACAUGUGGGCUAUUA
Plate 1	B02	M-009841-00	D-009841-04	ITSN2	50618	NM_006277	22325384	AAACUCAGCUGGCUACUAU
Plate 1	B03	M-009833-00	D-009833-01	SGEF	26084	NM_015595	21361486	GAGAUGAUGUACACAAUUA
Plate 1	B03	M-009833-00	D-009833-02	SGEF	26084	NM_015595	21361486	GAAGGAAGUUAGCAAGUUG
Plate 1	B03	M-009833-00	D-009833-03	SGEF	26084	NM_015595	21361486	CAAAUGGCCUUGCCGCUAA
Plate 1	B03	M-009833-00	D-009833-04	SGEF	26084	NM_015595	21361486	GAAAGGACAAGGAACAUUU
Plate 1	B04	M-032365-01	D-032365-01	FLJ43692	445328	NM_001003702	51172609	GGAAGUAACUGGAAAGCAA
Plate 1	B04	M-032365-01	D-032365-02	FLJ43692	445328	NM_001003702	51172609	CGAAAGAGCCAGAGAGUUG
Plate 1	B04	M-032365-01	D-032365-04	FLJ43692	445328	NM_001003702	51172609	GGACCCAUCCUAUAAGUGG
Plate 1	B04	M-032365-01	D-032365-17	FLJ43692	445328	NM_001003702	51172609	GGAGGAUGUUUGUGCCGAU
Plate 1	B05	M-005093-02	D-005093-01	ARHGEF5	7984	NM_005435	50959190	GCACGGAGACUCAAAGUGA
Plate 1	B05	M-005093-02	D-005093-03	ARHGEF5	7984	NM_005435	50959190	GCCAGAAGAUUGAGUUUGA
Plate 1	B05	M-005093-02	D-005093-04	ARHGEF5	7984	NM_005435	50959190	CAAUGGCUCUUCUCUCGUU
Plate 1	B05	M-005093-02	D-005093-18	ARHGEF5	7984	NM_005435	50959190	CUUCCAAGUAUGUGACGUA
Plate 1	B06	M-009354-00	D-009354-01	NGEF	25791	NM_019850	29789101	GGAGAAACCUCAUUGAACA
Plate 1	B06	M-009354-00	D-009354-02	NGEF	25791	NM_019850	29789101	GGACCAAGUUUGUUUCGUU
Plate 1	B06	M-009354-00	D-009354-03	NGEF	25791	NM_019850	29789101	GAAAUUCCAUCUUCAAUCG
Plate 1	B06	M-009354-00	D-009354-04	NGEF	25791	NM_019850	29789101	UAAAUCGACUCUCCAAGAA
Plate 1	B07	M-008370-02	D-008370-01	ARHGEF19	128272	NM_153213	141802042	GAGUCUACCUGCCCUAUGU
Plate 1	B07	M-008370-02	D-008370-03	ARHGEF19	128272	NM_153213	141802042	GGACAAGCAGUGGCUGUUU

Plate 1	B07	M-008370-02	D-008370-05	ARHGEF19	128272	NM_153213	141802042	GGAGUGCAAUGCUAGUGUA
Plate 1	B07	M-008370-02	D-008370-06	ARHGEF19	128272	NM_153213	141802042	AAUGGAGGCUCGAAGUGUA
Plate 1	B08	M-010234-01	D-010234-01	ARHGEF16	27237	NM_014448	163792207	GCGGAGAGCUGUUCUUAGU
Plate 1	B08	M-010234-01	D-010234-02	ARHGEF16	27237	NM_014448	163792207	GAUACGCUCUGCCUCAAGA
Plate 1	B08	M-010234-01	D-010234-03	ARHGEF16	27237	NM_014448	163792207	CCAACGAGGUCUACCAACA
Plate 1	B08	M-010234-01	D-010234-04	ARHGEF16	27237	NM_014448	163792207	GUUCAACGAUGUCCUGGUU
Plate 1	B09	M-009731-00	D-009731-01	ARHGEF15	22899	NM_173728	32307165	UGAUGAAGCUCCUCAGAAU
Plate 1	B09	M-009731-00	D-009731-02	ARHGEF15	22899	NM_173728	32307165	GCAUGAAGCAGACUGAAGA
Plate 1	B09	M-009731-00	D-009731-03	ARHGEF15	22899	NM_173728	32307165	GGUUACAGGUUCUGGACUA
Plate 1	B09	M-009731-00	D-009731-04	ARHGEF15	22899	NM_173728	32307165	GAACGGUGCUCCAGAUGCU
Plate 1	B10	M-009323-00	D-009323-01	RASGRF1	5923	NM_002891	24797098	UCAAGAAGAUUCCUUAUGA
Plate 1	B10	M-009323-00	D-009323-02	RASGRF1	5923	NM_002891	24797098	GAGAUCACCUCGUCCAUGA
Plate 1	B10	M-009323-00	D-009323-03	RASGRF1	5923	NM_002891	24797098	CCAACAAGAUUCCAGAUGA
Plate 1	B10	M-009323-00	D-009323-04	RASGRF1	5923	NM_002891	24797098	CCACUAAGCACUUCAAUGA
Plate 1	B11	M-024516-01	D-024516-01	RASGRF2	5924	NM_006909	38505169	CAACAGAGGUGAACAUUUG
Plate 1	B11	M-024516-01	D-024516-04	RASGRF2	5924	NM_006909	38505169	GAAGGAACACCAAACUUUA
Plate 1	B11	M-024516-01	D-024516-05	RASGRF2	5924	NM_006909	38505169	CUGCACACCUAUCGUAUUU
Plate 1	B11	M-024516-01	D-024516-06	RASGRF2	5924	NM_006909	38505169	GCACAGUACUUGCUUGACA
Plate 1	C02	M-013460-01	D-013460-02	ARHGEF10	9639	NM_014629	62548863	GAAUACGGAUGGAGUUCGA
Plate 1	C02	M-013460-01	D-013460-03	ARHGEF10	9639	NM_014629	62548863	GACGAUGGGAAUCACAUUA
Plate 1	C02	M-013460-01	D-013460-04	ARHGEF10	9639	NM_014629	62548863	GACCUAACCCGUUUAAAGG
Plate 1	C02	M-013460-01	D-013460-17	ARHGEF10	9639	NM_014629	62548863	CGUGGUUGCUAACGCGAAA
Plate 1	C03	M-017096-01	D-017096-01	FLJ10521	55160	NM_001011722	74136546	CCAAGUAUGUGGUGAAGUG
Plate 1	C03	M-017096-01	D-017096-02	FLJ10521	55160	NM_001011722	74136546	GACGAGAGCCCGACAGUUG
Plate 1	C03	M-017096-01	D-017096-03	FLJ10521	55160	NM_001011722	74136546	CCAUGGUGCUAGAUGUGUA
Plate 1	C03	M-017096-01	D-017096-17	FLJ10521	55160	NM_001011722	74136546	AGGUCAGCGUUUCGGACAU
Plate 1	C04	M-009751-01	D-009751-01	ARHGEF17	9828	NM_014786	21361457	GCACCACUCUGAAGCGAAA
Plate 1	C04	M-009751-01	D-009751-02	ARHGEF17	9828	NM_014786	21361457	GAGCAAAGCAUGCGUGAGA
Plate 1	C04	M-009751-01	D-009751-04	ARHGEF17	9828	NM_014786	21361457	GCUACGAGCUUCUGGUGAA
Plate 1	C04	M-009751-01	D-009751-05	ARHGEF17	9828	NM_014786	21361457	AGUGAUGGGUUAAAUCUAA
Plate 1	C05	M-008611-00	D-008611-01	ABR	29	NM_001092	38679953	GAAGAUCUCUGCCCUCAAG
Plate 1	C05	M-008611-00	D-008611-02	ABR	29	NM_001092	38679953	CAACCUGGCUACCGUGUUU
Plate 1	C05	M-008611-00	D-008611-03	ABR	29	NM_001092	38679953	GAAGAGAUCUACAUUAACC

Plate 1	C05	M-008611-00	D-008611-04	ABR	29	NM_001092	38679953	CAGAGGAAC UCAAAGUGA A
Plate 1	C06	M-003875-05	D-003875-02	BCR	613	NM_021574	82546844	GUAAAGCUC UCGGUCAAG U
Plate 1	C06	M-003875-05	D-003875-03	BCR	613	NM_021574	82546844	GCAUUCCGC UGACCAUCA A
Plate 1	C06	M-003875-05	D-003875-06	BCR	613	NM_021574	82546844	CAGGAGCGC UUCCGCAUG A
Plate 1	C06	M-003875-05	D-003875-13	BCR	613	NM_021574	82546844	CAGAAGAAG UGUUUCAGA A
Plate 1	C07	M-005194-01	D-005194-01	SOS1	6654	NM_005633	15529995	CAAAGAAGC UGUUCAAUA U
Plate 1	C07	M-005194-01	D-005194-03	SOS1	6654	NM_005633	15529995	GAAAUAGCA UGGAGAAGG A
Plate 1	C07	M-005194-01	D-005194-04	SOS1	6654	NM_005633	15529995	GAGCACCAC UUCUAUGAU U
Plate 1	C07	M-005194-01	D-005194-05	SOS1	6654	NM_005633	15529995	GGCAGAAAU UCGACAAUA U
Plate 1	C08	M-005195-02	D-005195-01	SOS2	6655	NM_006939	154689779	GGACGAAGC UGUGGAAUU A
Plate 1	C08	M-005195-02	D-005195-02	SOS2	6655	NM_006939	154689779	GCACCAACC UCUCCAAAU A
Plate 1	C08	M-005195-02	D-005195-04	SOS2	6655	NM_006939	154689779	GCAAACAGC CACCUCGAU U
Plate 1	C08	M-005195-02	D-005195-05	SOS2	6655	NM_006939	154689779	UACUCUAGA UCGAAUGUU A
Plate 1	C09	M-008519-02	D-008519-05	FARP1	10160	NM_00100171 5	159032536	CAGGAAAAC UCGUGUCCA U
Plate 1	C09	M-008519-02	D-008519-10	FARP1	10160	NM_00100171 5	159032536	CCGGAAAAU UCGGGGAUC A
Plate 1	C09	M-008519-02	D-008519-11	FARP1	10160	NM_00100171 5	159032536	GAUCAGUAC CUUGGAACG U
Plate 1	C09	M-008519-02	D-008519-12	FARP1	10160	NM_00100171 5	159032536	GAAAAUUCG GGGAUCAGU A
Plate 1	C10	M-009237-01	D-009237-01	FARP2	9855	NM_014808	7662309	GAACAUACC UCAAGGAUU U
Plate 1	C10	M-009237-01	D-009237-02	FARP2	9855	NM_014808	7662309	CGAAAUUGC UCGAAAGUU G
Plate 1	C10	M-009237-01	D-009237-03	FARP2	9855	NM_014808	7662309	GCACUCGGC UGGAGAAAG A
Plate 1	C10	M-009237-01	D-009237-05	FARP2	9855	NM_014808	7662309	GGAUUUGGC UUGAACCUA U
Plate 1	C11	M-009612-01	D-009612-01	FGD1	2245	NM_004463	24797152	CCAAAGAGC UCAUAAAAGA
Plate 1	C11	M-009612-01	D-009612-02	FGD1	2245	NM_004463	24797152	CAAGAUGUA UGGUGAGUA U
Plate 1	C11	M-009612-01	D-009612-03	FGD1	2245	NM_004463	24797152	CCAAUGAGC UCCUGCAAA C
Plate 1	C11	M-009612-01	D-009612-05	FGD1	2245	NM_004463	24797152	UCUCAAGGA CUAUCUGUU A
Plate 1	D02	M-008431-00	D-008431-01	FGD2	221472	NM_173558	34222232	GCUGAUGGA UGCUGAGUU U
Plate 1	D02	M-008431-00	D-008431-02	FGD2	221472	NM_173558	34222232	CGACAAGUC UCCACUCUU C
Plate 1	D02	M-008431-00	D-008431-03	FGD2	221472	NM_173558	34222232	GGGCCGAAC UGAAAUACG A
Plate 1	D02	M-008431-00	D-008431-04	FGD2	221472	NM_173558	34222232	AAGCAGCCA UUGACCAAA U
Plate 1	D03	M-010371-01	D-010371-01	FGD3	89846	NM_033086	134133264	GCACAUACA UUCAUCAUA A
Plate 1	D03	M-010371-01	D-010371-02	FGD3	89846	NM_033086	134133264	GGACGGCUC UCCAGACAU A
Plate 1	D03	M-010371-01	D-010371-03	FGD3	89846	NM_033086	134133264	CCAGAAGGC UGACAAGGA U

Plate 1	D03	M-010371-01	D-010371-17	FGD3	89846	NM_033086	134133264	GCAGGAGGUAUGCGGGAAC
Plate 1	D04	M-007123-00	D-007123-01	FGD4	121512	NM_139241	21245127	GAGAAUAUGUGAAAGGAUU
Plate 1	D04	M-007123-00	D-007123-02	FGD4	121512	NM_139241	21245127	GGAGAAAGCUGCCACUCUU
Plate 1	D04	M-007123-00	D-007123-03	FGD4	121512	NM_139241	21245127	GGUAUGAGAUGCUCCUUAA
Plate 1	D04	M-007123-00	D-007123-04	FGD4	121512	NM_139241	21245127	GCAGCAAGCCAUUCUAAUA
Plate 1	D05	M-028077-01	D-028077-01	FGD5	152273	NM_152536	50080161	GAACGUGUCUUCCUCUAGG
Plate 1	D05	M-028077-01	D-028077-02	FGD5	152273	NM_152536	50080161	GAAAGGCUGUCAAAUUGGG
Plate 1	D05	M-028077-01	D-028077-03	FGD5	152273	NM_152536	50080161	GCUCCUCACAGACUAUUUA
Plate 1	D05	M-028077-01	D-028077-04	FGD5	152273	NM_152536	50080161	AAAGUGCCCUACGCUCUAA
Plate 1	D06	M-026895-01	D-026895-01	FGD6	55785	NM_018351	154240685	GCUCAAAGAUGCCUUAAUA
Plate 1	D06	M-026895-01	D-026895-03	FGD6	55785	NM_018351	154240685	GAAUUCCGAGUCUAAAGUA
Plate 1	D06	M-026895-01	D-026895-04	FGD6	55785	NM_018351	154240685	GCUCGUCUGUUACGCCAAA
Plate 1	D06	M-026895-01	D-026895-17	FGD6	55785	NM_018351	154240685	GAUUGAAAGUGUAGAACGU
Plate 1	D07	M-005047-00	D-005047-01	TRIO	7204	NM_007118	6005921	GAUAAGAGGUACAGAGAUU
Plate 1	D07	M-005047-00	D-005047-02	TRIO	7204	NM_007118	6005921	GGAAGUCGCUCCUUGACAA
Plate 1	D07	M-005047-00	D-005047-03	TRIO	7204	NM_007118	6005921	CAACGGAGAGUCCAUGUUA
Plate 1	D07	M-005047-00	D-005047-04	TRIO	7204	NM_007118	6005921	GAACACCAACUUCAGAUAA
Plate 1	D08	M-004121-01	D-004121-01	GEFT	115557	NM_001111270	162287075	GAACACAGCCUGGAUAUGU
Plate 1	D08	M-004121-01	D-004121-02	GEFT	115557	NM_001111270	162287075	GGAUGAAGAUGAGCUGUAA
Plate 1	D08	M-004121-01	D-004121-03	GEFT	115557	NM_001111270	162287075	GCACCGAGACUAUUUCUUG
Plate 1	D08	M-004121-01	D-004121-04	GEFT	115557	NM_001111270	162287075	GCAUGUGGCUCAGAUCUUG
Plate 1	D09	M-003904-03	D-003904-01	MCF2	4168	NM_005369	153791324	GGUAUCAUCUGUUGAAGAA
Plate 1	D09	M-003904-03	D-003904-04	MCF2	4168	NM_005369	153791324	GCAACAGGAUCAAUUAACA
Plate 1	D09	M-003904-03	D-003904-05	MCF2	4168	NM_005369	153791324	GGUGAUAACCGCAAGUUUG
Plate 1	D09	M-003904-03	D-003904-19	MCF2	4168	NM_005369	153791324	CUAGAAUGUCAUCGGCAAA
Plate 1	D10	M-009313-00	D-009313-01	MCF2L2	23101	NM_015078	31742504	GCACAUUGCUUUCUCAAGA
Plate 1	D10	M-009313-00	D-009313-02	MCF2L2	23101	NM_015078	31742504	GGAAUAGUGUUCUGUAAGA
Plate 1	D10	M-009313-00	D-009313-03	MCF2L2	23101	NM_015078	31742504	GGACCAAGCCAGAGACUUA
Plate 1	D10	M-009313-00	D-009313-04	MCF2L2	23101	NM_015078	31742504	GAAUGUAACUACCAUGGAA
Plate 1	D11	M-010098-01	D-010098-01	MCF2L	23263	NM_001112732	163644324	AAACAGAGCUGCCCAAUGA
Plate 1	D11	M-010098-01	D-010098-02	MCF2L	23263	NM_001112732	163644324	CGACAUCGCUUUCAAAUUC
Plate 1	D11	M-010098-01	D-010098-03	MCF2L	23263	NM_001112732	163644324	UCAAGGAAAUGCUGAAAUA
Plate 1	D11	M-010098-01	D-010098-04	MCF2L	23263	NM_001112732	163644324	CAACAGGCCUUCACAACAA

Plate 1	E02	M-010063-01	D-010063-01	PREX1	57580	NM_020820	112789552	GAGAUGAGCUGCCCUGUGA
Plate 1	E02	M-010063-01	D-010063-03	PREX1	57580	NM_020820	112789552	GAAAGAAGAGUGUACAAUC
Plate 1	E02	M-010063-01	D-010063-17	PREX1	57580	NM_020820	112789552	CCACGGACAUCAUGCGGAA
Plate 1	E02	M-010063-01	D-010063-18	PREX1	57580	NM_020820	112789552	AAGAUGGGACAGCGGAUUA
Plate 1	E03	M-014602-01	D-014602-02	DEPDC2	80243	NM_025170	47578116	CUGAUAGACUGGUUAAUUG
Plate 1	E03	M-014602-01	D-014602-03	DEPDC2	80243	NM_025170	47578116	UAUGAAACAUCGACUUAUG
Plate 1	E03	M-014602-01	D-014602-04	DEPDC2	80243	NM_025170	47578116	GAACGGCGGAAAGGUUUAA
Plate 1	E03	M-014602-01	D-014602-17	DEPDC2	80243	NM_025170	47578116	GAAGCGGACUCCACGGAAA
Plate 1	E04	M-003935-01	D-003935-02	VAV1	7409	NM_005428	7108366	GCAGCGAGUUCUCAAAUAU
Plate 1	E04	M-003935-01	D-003935-03	VAV1	7409	NM_005428	7108366	GCAGAAAUACAUCUACUAA
Plate 1	E04	M-003935-01	D-003935-04	VAV1	7409	NM_005428	7108366	GAAGGACUGUACCGGAUCA
Plate 1	E04	M-003935-01	D-003935-05	VAV1	7409	NM_005428	7108366	CGACAAAGCUCUACUCAUC
Plate 1	E05	M-005199-02	D-005199-03	VAV2	7410	NM_003371	40549447	UCACAGAGGCCAAGAAAUU
Plate 1	E05	M-005199-02	D-005199-04	VAV2	7410	NM_003371	40549447	GAAAGUCUGCCACGAUAAA
Plate 1	E05	M-005199-02	D-005199-19	VAV2	7410	NM_003371	40549447	GGGACGACAUCUACGAGGA
Plate 1	E05	M-005199-02	D-005199-20	VAV2	7410	NM_003371	40549447	AUCCAAAUCUCCCGUUAUA
Plate 1	E06	M-010178-03	D-010178-02	VAV3	10451	NM_001079874	120432041	GCAGAGACCGAACUUAUUA
Plate 1	E06	M-010178-03	D-010178-04	VAV3	10451	NM_001079874	120432041	GCAAAGCACAUCAAGAUUU
Plate 1	E06	M-010178-03	D-010178-05	VAV3	10451	NM_001079874	120432041	AGACCGAACUUAUUAAUAG
Plate 1	E06	M-010178-03	D-010178-19	VAV3	10451	NM_001079874	120432041	GUAUGCAGCCCUCGUGUAA
Plate 1	E07	M-015006-01	D-015006-01	C9ORF100	84904	NM_032818	90652856	CAACAGCCCUGACCAUCAA
Plate 1	E07	M-015006-01	D-015006-02	C9ORF100	84904	NM_032818	90652856	GGAGCUCUAUAACCAAUUU
Plate 1	E07	M-015006-01	D-015006-03	C9ORF100	84904	NM_032818	90652856	CGUCGUAGCUUUGGCUGAA
Plate 1	E07	M-015006-01	D-015006-04	C9ORF100	84904	NM_032818	90652856	AAAUAAAGGUUUCCGGAGG
Plate 1	E08	M-003932-02	D-003932-01	TIAM1	7074	NM_003253	115583669	GAACCGAAGCUGUAAAGAA
Plate 1	E08	M-003932-02	D-003932-02	TIAM1	7074	NM_003253	115583669	GAAAGGAUGCACGCUAUUU
Plate 1	E08	M-003932-02	D-003932-04	TIAM1	7074	NM_003253	115583669	GAAGUGGUCUUACCUAACG
Plate 1	E08	M-003932-02	D-003932-17	TIAM1	7074	NM_003253	115583669	CAUUCAAUCCUGCGUGAUA
Plate 1	E09	M-008434-02	D-008434-05	TIAM2	26230	NM_001010927	73695942	GAACUUCAGGCGUCACAUA
Plate 1	E09	M-008434-02	D-008434-06	TIAM2	26230	NM_001010927	73695942	CGACCUAAAUUCUGUUCUA
Plate 1	E09	M-008434-02	D-008434-07	TIAM2	26230	NM_001010927	73695942	GUGUAAGGAUCGCCUGGUA
Plate 1	E09	M-008434-02	D-008434-08	TIAM2	26230	NM_001010927	73695942	UAAGAGAGCCGUCAUACUG

Plate 1	E10	M-010231-00	D-010231-01	ARHGEF6	9459	NM_004840	22027524	GAGGAUGUCUUAUAUCUUA
Plate 1	E10	M-010231-00	D-010231-02	ARHGEF6	9459	NM_004840	22027524	GGAAGAAUGUUCAAAGUUU
Plate 1	E10	M-010231-00	D-010231-03	ARHGEF6	9459	NM_004840	22027524	GGACGUUCCUCUUCUCUUA
Plate 1	E10	M-010231-00	D-010231-04	ARHGEF6	9459	NM_004840	22027524	GAACGGUGGUGACUAGAUU
Plate 1	E11	M-009616-00	D-009616-01	ARHGEF7	8874	NM_003899	22027526	GGAAGAAGAUGCUCAGAUU
Plate 1	E11	M-009616-00	D-009616-02	ARHGEF7	8874	NM_003899	22027526	GAAGAGCCCUCCCAAAGGA
Plate 1	E11	M-009616-00	D-009616-03	ARHGEF7	8874	NM_003899	22027526	UCAAAGAGCUCGAGAGACA
Plate 1	E11	M-009616-00	D-009616-04	ARHGEF7	8874	NM_003899	22027526	GGAGGGCGAUGACAUUAAA
Plate 1	F02	M-024745-01	D-024745-01	PLEKHG1	57480	NM_001029884	71274147	GUGAAGAGUUCCACAUUUA
Plate 1	F02	M-024745-01	D-024745-02	PLEKHG1	57480	NM_001029884	71274147	GAGAUGACACGUUUACAUA
Plate 1	F02	M-024745-01	D-024745-03	PLEKHG1	57480	NM_001029884	71274147	CCAGUUGUAUGACCAGAUU
Plate 1	F02	M-024745-01	D-024745-04	PLEKHG1	57480	NM_001029884	71274147	AGAAACAUCUGGACCGAUC
Plate 1	F03	M-023690-01	D-023690-01	PLEKHG2	64857	NM_022835	45237196	UGACAGCGGUUGCCUGGUA
Plate 1	F03	M-023690-01	D-023690-02	PLEKHG2	64857	NM_022835	45237196	GGAGAUUUGUUCUGAUUUC
Plate 1	F03	M-023690-01	D-023690-04	PLEKHG2	64857	NM_022835	45237196	AGCGAGAGCCCAACCAAUA
Plate 1	F03	M-023690-01	D-023690-17	PLEKHG2	64857	NM_022835	45237196	UCAGAAAUCCGGAGCGCCU
Plate 1	F04	M-022051-01	D-022051-01	PLEKHG3	26030	NM_015549	55749620	GCCAAGAGUUUGAUAUCUA
Plate 1	F04	M-022051-01	D-022051-02	PLEKHG3	26030	NM_015549	55749620	UAGACAAGAUUAAGAGCUA
Plate 1	F04	M-022051-01	D-022051-03	PLEKHG3	26030	NM_015549	55749620	GUAAGAAACUCCAUCUCCA
Plate 1	F04	M-022051-01	D-022051-05	PLEKHG3	26030	NM_015549	55749620	CCGCCCAUCUUCAGAAAUU
Plate 1	F05	M-022573-01	D-022573-01	PLEKHG4	25894	NM_015432	70912385	GGACAAGGCUGACGAGCUA
Plate 1	F05	M-022573-01	D-022573-02	PLEKHG4	25894	NM_015432	70912385	GAAUACAGGCCCUAGAGUU
Plate 1	F05	M-022573-01	D-022573-03	PLEKHG4	25894	NM_015432	70912385	GAAUAAGCCUCGCUCCGAU
Plate 1	F05	M-022573-01	D-022573-04	PLEKHG4	25894	NM_015432	70912385	GAAGUUCGCUCUCGGGCGU
Plate 1	F06	M-013873-01	D-013873-01	KIAA0720	57449	NM_020631	111154086	UCAAGUCGGUGCUGAGGAA
Plate 1	F06	M-013873-01	D-013873-02	KIAA0720	57449	NM_020631	111154086	UCAAAGGCUUCAAGAUGUU
Plate 1	F06	M-013873-01	D-013873-03	KIAA0720	57449	NM_020631	111154086	ACAGCAAGAUGGAUGUGUA
Plate 1	F06	M-013873-01	D-013873-04	KIAA0720	57449	NM_020631	111154086	GCCCAGCUCUACCGAAUCA
Plate 1	F07	M-031878-01	D-031878-01	KIAA1909	153478	NM_052909	148529024	GCUGUGACGUGAAUUUGAA
Plate 1	F07	M-031878-01	D-031878-02	KIAA1909	153478	NM_052909	148529024	GAGAUGCCGGGAUGAGUUU
Plate 1	F07	M-031878-01	D-031878-03	KIAA1909	153478	NM_052909	148529024	CGAGGGAAGCACCACGUUA
Plate 1	F07	M-031878-01	D-031878-04	KIAA1909	153478	NM_052909	148529024	GGACCGAUGUCAUAGGGAG

Plate 1	F08	M-020318-01	D-020318-01	FLJ10665	55200	NM_018173	141803343	GCUGAGACCCUGUUUGGAA
Plate 1	F08	M-020318-01	D-020318-02	FLJ10665	55200	NM_018173	141803343	GACCAUGGCUUACGCCCGA
Plate 1	F08	M-020318-01	D-020318-03	FLJ10665	55200	NM_018173	141803343	GAGGAUACCCUGUGCUGGA
Plate 1	F08	M-020318-01	D-020318-04	FLJ10665	55200	NM_018173	141803343	GCGAAGAGCAAGAGAGCUU
Plate 1	F09	M-032389-00	D-032389-01	FLJ46688	440107	NM_001004330	51972239	UGAAGUGGCUGGACAAUUU
Plate 1	F09	M-032389-00	D-032389-02	FLJ46688	440107	NM_001004330	51972239	UACAGAGGCUCACUCGAUA
Plate 1	F09	M-032389-00	D-032389-03	FLJ46688	440107	NM_001004330	51972239	GACAGUGUAUAGCAGCAUU
Plate 1	F09	M-032389-00	D-032389-04	FLJ46688	440107	NM_001004330	51972239	UGAGUUGCAAGCAGUAAUA
Plate 1	F10	M-015469-00	D-015469-01	SPATA13	221178	NM_153023	23308552	GAAGAAACUUGCCAUGUUA
Plate 1	F10	M-015469-00	D-015469-02	SPATA13	221178	NM_153023	23308552	GGAGAGCAUCGACAAGAUA
Plate 1	F10	M-015469-00	D-015469-03	SPATA13	221178	NM_153023	23308552	GGACCAACGUCAUCCGGGA
Plate 1	F10	M-015469-00	D-015469-04	SPATA13	221178	NM_153023	23308552	GCGCAGCUAGCCACUAUUU
Plate 1	F11	M-008235-01	D-008235-01	ARHGEF4	50649	NM_015320	15011978	GCACAAAGAUGGAGUCAAG
Plate 1	F11	M-008235-01	D-008235-02	ARHGEF4	50649	NM_015320	15011978	GAAAGGAGGCUGCACAUAG
Plate 1	F11	M-008235-01	D-008235-03	ARHGEF4	50649	NM_015320	15011978	UCACCAAGCUCAGCAAGUA
Plate 1	F11	M-008235-01	D-008235-17	ARHGEF4	50649	NM_015320	15011978	GACUUGAGAACAUCGACAA
Plate 1	G02	M-020314-01	D-020314-01	ARHGEF9	23229	NM_015185	7662107	UGGCUGAGCUCCUAAAGUA
Plate 1	G02	M-020314-01	D-020314-02	ARHGEF9	23229	NM_015185	7662107	GAUCUGCAAGUAUCCCUUA
Plate 1	G02	M-020314-01	D-020314-03	ARHGEF9	23229	NM_015185	7662107	CAAGCGACGUUUAGAGAAU
Plate 1	G02	M-020314-01	D-020314-04	ARHGEF9	23229	NM_015185	7662107	GAGAUUCCAUCGUUAGUGC
Plate 1	G03	M-017817-01	D-017817-01	DEF6	50619	NM_022047	145312240	GCAGAGGGCUGACGAGGAU
Plate 1	G03	M-017817-01	D-017817-02	DEF6	50619	NM_022047	145312240	GGAGAAGAGUGGCAAAGUC
Plate 1	G03	M-017817-01	D-017817-03	DEF6	50619	NM_022047	145312240	GAUAGCAACGGGAACAGUA
Plate 1	G03	M-017817-01	D-017817-04	DEF6	50619	NM_022047	145312240	GGAGAUAAGCGUCCGGUCA
Plate 1	G04	M-010323-01	D-010323-01	SWAP70	23075	NM_015055	93102363	GGACAAGUAUCCAUUAAUU
Plate 1	G04	M-010323-01	D-010323-02	SWAP70	23075	NM_015055	93102363	CAAGAGGGCUGAACUAGAA
Plate 1	G04	M-010323-01	D-010323-03	SWAP70	23075	NM_015055	93102363	GAGAGAAGCUUAUCAGACA
Plate 1	G04	M-010323-01	D-010323-04	SWAP70	23075	NM_015055	93102363	GAGAUUGAAUACCUGCUUA
Plate 1	G05	M-011253-01	D-011253-01	DOCK1	1793	NM_001380	100913207	GUACCGAGGUUACACGUUA
Plate 1	G05	M-011253-01	D-011253-02	DOCK1	1793	NM_001380	100913207	UAAAUGAGCAGCUGUACAA
Plate 1	G05	M-011253-01	D-011253-03	DOCK1	1793	NM_001380	100913207	GAAAUGGUGGGCCCAAUAU
Plate 1	G05	M-011253-01	D-011253-04	DOCK1	1793	NM_001380	100913207	GGCCCAAGCCUGACUAUUU

Plate 1	G06	M-019915-00	D-019915-01	DOCK2	1794	NM_004946	31377467	GACAUGAGACGGCUAAUUG
Plate 1	G06	M-019915-00	D-019915-02	DOCK2	1794	NM_004946	31377467	GACCGGAAAUUUCAGCAUU
Plate 1	G06	M-019915-00	D-019915-03	DOCK2	1794	NM_004946	31377467	CAACGACACUUUGGGAAUG
Plate 1	G06	M-019915-00	D-019915-04	DOCK2	1794	NM_004946	31377467	GAAUGAGUAUCGCUCCGUU
Plate 1	G07	M-012695-01	D-012695-01	DOCK3	1795	NM_004947	54400756	GAAGAUAGGCUGCACUGUU
Plate 1	G07	M-012695-01	D-012695-02	DOCK3	1795	NM_004947	54400756	CGAGAUCACUGGCGAGUAU
Plate 1	G07	M-012695-01	D-012695-03	DOCK3	1795	NM_004947	54400756	UGACGCCCAUUCCAGAUUA
Plate 1	G07	M-012695-01	D-012695-04	DOCK3	1795	NM_004947	54400756	GACCUGUGAUGGACACGUA
Plate 1	G08	M-017968-01	D-017968-01	DOCK4	9732	NM_014705	92091571	CAAAGGGUCUGGAGCAUUA
Plate 1	G08	M-017968-01	D-017968-03	DOCK4	9732	NM_014705	92091571	UAAGAGAGCUGAUGCUUGA
Plate 1	G08	M-017968-01	D-017968-04	DOCK4	9732	NM_014705	92091571	GGAAAUAGAUGUGAUAGUG
Plate 1	G08	M-017968-01	D-017968-17	DOCK4	9732	NM_014705	92091571	CCUCUUAUAUGACGAGCUA
Plate 1	G09	M-018931-01	D-018931-01	DOCK5	80005	NM_024940	117553585	AGAACUAUCUAAUUCGUUG
Plate 1	G09	M-018931-01	D-018931-02	DOCK5	80005	NM_024940	117553585	GUAACGGGAUGCCCAAGGA
Plate 1	G09	M-018931-01	D-018931-03	DOCK5	80005	NM_024940	117553585	GAGUGGCAGUGAUGGAUAU
Plate 1	G09	M-018931-01	D-018931-04	DOCK5	80005	NM_024940	117553585	UAUCAUACAUGGGAAGGUG
Plate 1	G10	M-031950-01	D-031950-01	DOCK6	57572	NM_020812	157426886	UCACGUAUGUGGAACCGUA
Plate 1	G10	M-031950-01	D-031950-02	DOCK6	57572	NM_020812	157426886	CGACAGAACUUCGAGAUCG
Plate 1	G10	M-031950-01	D-031950-03	DOCK6	57572	NM_020812	157426886	CGGUGGAGAUGUAUAUUGA
Plate 1	G10	M-031950-01	D-031950-17	DOCK6	57572	NM_020812	157426886	GGUCAGCAGCAGUGCCGUA
Plate 1	G11	M-031725-01	D-031725-01	DOCK7	85440	NM_033407	54112428	GAUCGAAGUUGUAAUCGUA
Plate 1	G11	M-031725-01	D-031725-02	DOCK7	85440	NM_033407	54112428	GAGGACAGCUCGGUACGUA
Plate 1	G11	M-031725-01	D-031725-03	DOCK7	85440	NM_033407	54112428	GGCAUGAAAUGGGUAGAUA
Plate 1	G11	M-031725-01	D-031725-04	DOCK7	85440	NM_033407	54112428	UAACCUAGGUCAAGCAUCU
Plate 1	H02	M-026106-01	D-026106-02	DOCK8	81704	NM_203447	44889959	GAUCAGAGCCUCAUUAGGA
Plate 1	H02	M-026106-01	D-026106-03	DOCK8	81704	NM_203447	44889959	GGAAAUACGUCCAGUACCA
Plate 1	H02	M-026106-01	D-026106-04	DOCK8	81704	NM_203447	44889959	CCGCUAAGCUCACAGUAAA
Plate 1	H02	M-026106-01	D-026106-17	DOCK8	81704	NM_203447	44889959	GGCCAAUGAUCGAGCGGAA
Plate 1	H03	M-014040-00	D-014040-01	DOCK9	23348	NM_015296	24308028	GUAAACGAACGUCUGAUUA
Plate 1	H03	M-014040-00	D-014040-02	DOCK9	23348	NM_015296	24308028	ACUCAGAAGUUUCGAGAUA
Plate 1	H03	M-014040-00	D-014040-03	DOCK9	23348	NM_015296	24308028	CAGCUUGACUACUCAUUAA
Plate 1	H03	M-014040-00	D-014040-04	DOCK9	23348	NM_015296	24308028	CGGCAUUGCUUCUCCAUAU

Plate 1	H04	M-023079-01	D-023079-01	DOCK10	55619	NM_014689	154146188	CCAGAUAACUCCUACAUUA
Plate 1	H04	M-023079-01	D-023079-02	DOCK10	55619	NM_014689	154146188	GCAGUAAGAUCAGUAUUUA
Plate 1	H04	M-023079-01	D-023079-03	DOCK10	55619	NM_014689	154146188	GAUAGCAACUCAUUACUAA
Plate 1	H04	M-023079-01	D-023079-04	DOCK10	55619	NM_014689	154146188	CAAUAUAGCUACGGAGGUU
Plate 1	H05	M-015696-01	D-015696-01	DOCK11	139818	NM_144658	145699122	UAAAUGAGCGGCUAAUUAA
Plate 1	H05	M-015696-01	D-015696-02	DOCK11	139818	NM_144658	145699122	GAUCAACACCGACAGUUUA
Plate 1	H05	M-015696-01	D-015696-03	DOCK11	139818	NM_144658	145699122	CGACAGAGUUCUACAAGGA
Plate 1	H05	M-015696-01	D-015696-04	DOCK11	139818	NM_144658	145699122	CGAAACAGAUCAGGAGUAA
Plate 1	H06	M-006450-00	D-006450-01	ECT2	1894	NM_018098	21735571	GAUAAAGGAUGAUCUUGAA
Plate 1	H06	M-006450-00	D-006450-02	ECT2	1894	NM_018098	21735571	GCACUCACCUUGUAGUUGA
Plate 1	H06	M-006450-00	D-006450-03	ECT2	1894	NM_018098	21735571	GAAGGGCUCUUAUGACAUC
Plate 1	H06	M-006450-00	D-006450-04	ECT2	1894	NM_018098	21735571	CAGAGGAGAUUAAGACUAU
Plate 1	H07	M-024733-01	D-024733-01	LOC345930	345930	NM_001077706	118150677	GCACAGAGCAUCGGAAUAU
Plate 1	H07	M-024733-01	D-024733-02	LOC345930	345930	NM_001077706	118150677	GGUAUGACCAACAUUCUAA
Plate 1	H07	M-024733-01	D-024733-03	LOC345930	345930	NM_001077706	118150677	GUACCCAUCCCGAAGAUUU
Plate 1	H07	M-024733-01	D-024733-04	LOC345930	345930	NM_001077706	118150677	GUAAGAAGGAGUUAUUCAA
Plate 1	H08	M-014168-01	D-014168-05	ALS2	57679	NM_020919	40316934	UCAGACGACUUCAUAAUUA
Plate 1	H08	M-014168-01	D-014168-06	ALS2	57679	NM_020919	40316934	GAGACUACAUUGAAGGUUA
Plate 1	H08	M-014168-01	D-014168-07	ALS2	57679	NM_020919	40316934	GAGAGUGGCUGCUACUUAU
Plate 1	H08	M-014168-01	D-014168-08	ALS2	57679	NM_020919	40316934	GCAAAGAAGUAAUCCAUCU
Plate 1	H09	M-027177-02	D-027177-02	OBSCN	84033	NM_052843	58331252	GGAAGGACAUACACUCUCA
Plate 1	H09	M-027177-02	D-027177-03	OBSCN	84033	NM_052843	58331252	CAGGAGAGAUCCAAUUUGU
Plate 1	H09	M-027177-02	D-027177-05	OBSCN	84033	NM_052843	58331252	GCAGACAGCGACACCUAUA
Plate 1	H09	M-027177-02	D-027177-06	OBSCN	84033	NM_052843	58331252	AGACAUACCGCGAAGAUGA
Plate 1	H10	M-032927-01	D-032927-21	FLJ41603	389337	NM_001001669	83715965	AGUUCAAACAGGCGCUUUA
Plate 1	H10	M-032927-01	D-032927-22	FLJ41603	389337	NM_001001669	83715965	GAAAUUUAAGCAACGGCUA
Plate 1	H10	M-032927-01	D-032927-23	FLJ41603	389337	NM_001001669	83715965	CCAUGGAUUUAUCGGUGUA
Plate 1	H10	M-032927-01	D-032927-24	FLJ41603	389337	NM_001001669	83715965	ACUUCAGGCCGCACGAAUA
Plate 1	H11	M-014170-00	D-014170-01	NOPE	57722	NM_020962	19882240	CAACACAGAUUAUGAGUUC
Plate 1	H11	M-014170-00	D-014170-02	NOPE	57722	NM_020962	19882240	AAACAAGGUGUAUCGAGUA
Plate 1	H11	M-014170-00	D-014170-03	NOPE	57722	NM_020962	19882240	GAUCUCUGGCUACAAACUA
Plate 1	H11	M-014170-00	D-014170-04	NOPE	57722	NM_020962	19882240	UAGAAUACGGUUUGGGAAA

Appendix 15: ONTARGETPlus RhoGEF/GAP and Rho GTPase siRNA catalogue numbers and sequences

LP_15876								
G-CUSTOM-199705								
Plate	**Well**	**Pool Catalog Number**	**Duplex Catalog Number**	**Gene Symbol**	**GENE ID**	**Gene Accession**	**GI Number**	**Sequence**
Plate 1	B02	L-003860-00	J-003860-10	RHOA	387	NM_001664	50593005	CGACAGCCCUGAUAGUUUA
Plate 1	B02	L-003860-00	J-003860-11	RHOA	387	NM_001664	50593005	GACCAAAGAUGGAGUGAGA
Plate 1	B02	L-003860-00	J-003860-12	RHOA	387	NM_001664	50593005	GCAGAGAUAUGGCAAACAG
Plate 1	B02	L-003860-00	J-003860-13	RHOA	387	NM_001664	50593005	GGAAUGAUGAGCACACAAG
Plate 1	B03	L-008395-00	J-008395-11	RHOB	388	NM_004040	42716309	GCAUCCAAGCCUACGACUA
Plate 1	B03	L-008395-00	J-008395-12	RHOB	388	NM_004040	42716309	CAGAACGGCUGCAUCAACU
Plate 1	B03	L-008395-00	J-008395-13	RHOB	388	NM_004040	42716309	CGACGAGCAUGUCCGCACA
Plate 1	B03	L-008395-00	J-008395-14	RHOB	388	NM_004040	42716309	AAGCACUUCUGUCCCAAUG
Plate 1	B04	L-008555-00	J-008555-05	RHOC	389	NM_175744	34222243	GAAAGAAGCUGGUGAUCGU
Plate 1	B04	L-008555-00	J-008555-06	RHOC	389	NM_175744	34222243	GAACUAUAUUGCGGACAUU
Plate 1	B04	L-008555-00	J-008555-07	RHOC	389	NM_175744	34222243	GGACAUGGCGAACCGGAUC
Plate 1	B04	L-008555-00	J-008555-08	RHOC	389	NM_175744	34222243	CUACGUCCCUACUGUCUUU
Plate 1	B05	L-003560-00	J-003560-14	RAC1	5879	NM_006908	38505163	GUGAUUUCAUAGCGAGUUU
Plate 1	B05	L-003560-00	J-003560-15	RAC1	5879	NM_006908	38505163	GUAGUUCUCAGAUGCGUAA
Plate 1	B05	L-003560-00	J-003560-16	RAC1	5879	NM_006908	38505163	AUGAAAGUGUCACGGGUAA
Plate 1	B05	L-003560-00	J-003560-17	RAC1	5879	NM_006908	38505163	GAACUGCUAUUUCCUCUAA
Plate 1	B06	L-007741-00	J-007741-09	RAC2	5880	NM_002872	27881480	UGACAACUAUUCAGCCAAU
Plate 1	B06	L-007741-00	J-007741-10	RAC2	5880	NM_002872	27881480	CCAAGGAGAUUGACUCGGU
Plate 1	B06	L-007741-00	J-007741-11	RAC2	5880	NM_002872	27881480	CCAAGUGGUUCCCAGAAGU
Plate 1	B06	L-007741-00	J-007741-12	RAC2	5880	NM_002872	27881480	UGAAAACCGUGUUCGACGA
Plate 1	B07	L-008836-00	J-008836-06	RAC3	5881	NM_005052	38683861	AAACUGACGUCUUUCUGAU

Plate 1	B07	L-008836-00	J-008836-07	RAC3	5881	NM_005052	38683861	ACAAGAAGCUGGCACCCAU
Plate 1	B07	L-008836-00	J-008836-08	RAC3	5881	NM_005052	38683861	GAAGACAUGCUUGCUGAUC
Plate 1	B07	L-008836-00	J-008836-09	RAC3	5881	NM_005052	38683861	CGUGAUGGUGGACGGGAAA
Plate 1	B08	L-008995-00	J-008995-05	RHOG	391	NM_001665	46249392	CUACACAACUAACGCUUUC
Plate 1	B08	L-008995-00	J-008995-06	RHOG	391	NM_001665	46249392	CCAGUCCGCCGUCCUAUGA
Plate 1	B08	L-008995-00	J-008995-07	RHOG	391	NM_001665	46249392	GCUGUGCGCUACCUCGAAU
Plate 1	B08	L-008995-00	J-008995-08	RHOG	391	NM_001665	46249392	GAGUAUGACCGCCUCCGUA
Plate 1	B09	L-005057-00	J-005057-05	CDC42	998	NM_044472	16357471	CGGAAUAUGUACCGACUGU
Plate 1	B09	L-005057-00	J-005057-06	CDC42	998	NM_044472	16357471	GCAGUCACAGUUAUGAUUG
Plate 1	B09	L-005057-00	J-005057-07	CDC42	998	NM_044472	16357471	GAUGACCCCUCUACUAUUG
Plate 1	B09	L-005057-00	J-005057-08	CDC42	998	NM_044472	16357471	CUGCAGGGCAAGAGGAUUA
Plate 1	B10	L-010367-00	J-010367-05	RHOJ	57381	NM_020663	29171294	UCAAUUAUCUGAGGUUGUC
Plate 1	B10	L-010367-00	J-010367-06	RHOJ	57381	NM_020663	29171294	UCAUAGGGACCCAGAUUGA
Plate 1	B10	L-010367-00	J-010367-07	RHOJ	57381	NM_020663	29171294	UCAGAAAGGUCUCAAAGCG
Plate 1	B10	L-010367-00	J-010367-08	RHOJ	57381	NM_020663	29171294	AGAAACCUCUCACUUACGA
Plate 1	B11	L-009943-00	J-009943-05	RHOQ	23433	NM_012249	50263041	CACCUAGAAUGUAAGUUAA
Plate 1	B11	L-009943-00	J-009943-06	RHOQ	23433	NM_012249	50263041	GCAGUUGGUCCCUAAGUGA
Plate 1	B11	L-009943-00	J-009943-07	RHOQ	23433	NM_012249	50263041	GAGCGACAACUUAUAUACA
Plate 1	B11	L-009943-00	J-009943-08	RHOQ	23433	NM_012249	50263041	GUAAUAAGGUCAUAACUGC
Plate 1	C02	L-008929-00	J-008929-05	RND1	27289	NM_014470	21314660	GGAUCUCCCUACUACGAUA
Plate 1	C02	L-008929-00	J-008929-06	RND1	27289	NM_014470	21314660	GAGCUUAGUCUCUGGGAUA
Plate 1	C02	L-008929-00	J-008929-07	RND1	27289	NM_014470	21314660	AGACAGACCUGCGAACAGA
Plate 1	C02	L-008929-00	J-008929-08	RND1	27289	NM_014470	21314660	CAGAAGAGCCCUGUCCGAA
Plate 1	C03	L-009727-00	J-009727-05	RND2	8153	NM_005440	66472870	GCGAUCCGCUCAGCUGUCA

Plate 1	C03	L-009727-00	J-009727-06	RND2	8153	NM_005440	66472870	CGACAUUAGCCGACCAGAA
Plate 1	C03	L-009727-00	J-009727-07	RND2	8153	NM_005440	66472870	ACGCCUAUCCCGGGAGUUA
Plate 1	C03	L-009727-00	J-009727-08	RND2	8153	NM_005440	66472870	ACACAAGGAUCGAGCCAAA
Plate 1	C04	L-007794-00	J-007794-06	RND3	390	NM_005168	56676394	CUACAGUGUUUGAGAAUUA
Plate 1	C04	L-007794-00	J-007794-07	RND3	390	NM_005168	56676394	UAGUAGAGCUCUCCAAUCA
Plate 1	C04	L-007794-00	J-007794-08	RND3	390	NM_005168	56676394	CAGCAAAUCUAUCAUGGAU
Plate 1	C04	L-007794-00	J-007794-09	RND3	390	NM_005168	56676394	GCGGACAGAUGUUAGUACA
Plate 1	C05	L-009882-00	J-009882-05	RHOU	58480	NM_021205	45827773	CAUCGUCGCUGGCAUUCAA
Plate 1	C05	L-009882-00	J-009882-06	RHOU	58480	NM_021205	45827773	AAGCAGGACUCCAGAUAAA
Plate 1	C05	L-009882-00	J-009882-07	RHOU	58480	NM_021205	45827773	GUACUGCUGUUUCGUAUGA
Plate 1	C05	L-009882-00	J-009882-08	RHOU	58480	NM_021205	45827773	GAACGUCAGUGAGAAAUGG
Plate 1	C06	L-006374-00	J-006374-05	RHOV	171177	NM_133639	20070359	GGACGAUGUCAACGUACUA
Plate 1	C06	L-006374-00	J-006374-06	RHOV	171177	NM_133639	20070359	GUAUUUGACUCGGCUAUUC
Plate 1	C06	L-006374-00	J-006374-07	RHOV	171177	NM_133639	20070359	GCUCAGCCUUGACGCAGAA
Plate 1	C06	L-006374-00	J-006374-08	RHOV	171177	NM_133639	20070359	GAAACUGAAUGCCAAAGGU
Plate 1	C07	L-008940-00	J-008940-05	RHOD	29984	NM_014578	17738304	CGGCUCGGCUCCAUGACAA
Plate 1	C07	L-008940-00	J-008940-06	RHOD	29984	NM_014578	17738304	CCACGGUGUUUGAGCGGUA
Plate 1	C07	L-008940-00	J-008940-07	RHOD	29984	NM_014578	17738304	GCAAGAAGGUACCCAUCAU
Plate 1	C07	L-008940-00	J-008940-08	RHOD	29984	NM_014578	17738304	GAUUGGAGCCUGUGACCUA
Plate 1	C08	L-008316-00	J-008316-05	RHOF	54509	NM_019034	38016956	CAUCGGUGUUCGAGAAGUA
Plate 1	C08	L-008316-00	J-008316-06	RHOF	54509	NM_019034	38016956	GCAAGACAGACCUGAGGAA
Plate 1	C08	L-008316-00	J-008316-07	RHOF	54509	NM_019034	38016956	UCCCUGAGGUCACGCAUUU
Plate 1	C08	L-008316-00	J-008316-08	RHOF	54509	NM_019034	38016956	UGAAGAAGGCGCAACGGCA
Plate 1	C09	L-008804-00	J-008804-05	RHOH	399	NM_004310	45827772	GAGUACAGCAGGUGUUUGA

Plate 1	C09	L-008804-00	J-008804-06	RHOH	399	NM_004310	45827772	AACCAUAACUCAUUCCUGA
Plate 1	C09	L-008804-00	J-008804-07	RHOH	399	NM_004310	45827772	GGACACAGCCGGCAAUGAC
Plate 1	C09	L-008804-00	J-008804-08	RHOH	399	NM_004310	45827772	GAACUGCCGUCAACCAGGC
Plate 1	C10	L-009389-00	J-009389-05	RHOBTB1	9886	NM_001032380	75905818	GAACUUGGCUUACCAUACU
Plate 1	C10	L-009389-00	J-009389-06	RHOBTB1	9886	NM_001032380	75905818	GGACGUGACAUUUAAAUUG
Plate 1	C10	L-009389-00	J-009389-07	RHOBTB1	9886	NM_001032380	75905818	GAACACCCGUUAUCCUUGU
Plate 1	C10	L-009389-00	J-009389-08	RHOBTB1	9886	NM_001032380	75905818	GACAGACGCUUUGCAUAUG
Plate 1	C11	L-009252-00	J-009252-05	RHOBTB2	23221	NM_015178	14165285	GACCGUCGCUUUGCUUAUG
Plate 1	C11	L-009252-00	J-009252-06	RHOBTB2	23221	NM_015178	14165285	CAUCCGAGCUGCACUCAUC
Plate 1	C11	L-009252-00	J-009252-07	RHOBTB2	23221	NM_015178	14165285	GGUAAGACCAGGCUCAUCU
Plate 1	C11	L-009252-00	J-009252-08	RHOBTB2	23221	NM_015178	14165285	CAGAAGAUCCUCUCACCUA
Plate 1	D02	L-009654-00	J-009654-05	ARHGEF18	23370	NM_015318	41327768	UCAGGGCGCUUGAAAGAUA
Plate 1	D02	L-009654-00	J-009654-06	ARHGEF18	23370	NM_015318	41327768	GCAGUGACCGGAAUUAUGU
Plate 1	D02	L-009654-00	J-009654-07	ARHGEF18	23370	NM_015318	41327768	CACAACGCAUAACCAAAUA
Plate 1	D02	L-009654-00	J-009654-08	ARHGEF18	23370	NM_015318	41327768	GGACGCAACUCGGACCAAU
Plate 1	D03	L-024506-00	J-024506-05	ARHGEF28	64283	XM_371755	51464955	CAAGUAAUCUACAGUCGAA
Plate 1	D03	L-024506-00	J-024506-06	ARHGEF28	64283	XM_371755	51464955	CAUAAAGACUUACGCAAAG
Plate 1	D03	L-024506-00	J-024506-07	ARHGEF28	64283	XM_371755	51464955	GGCUUGAGAUCCUAAAUAA
Plate 1	D03	L-024506-00	J-024506-08	ARHGEF28	64283	XM_371755	51464955	GAAGAUAUAAAGCGUGUCA
Plate 1	D04	L-009883-00	J-009883-06	ARHGEF2	9181	NM_004723	15011973	GAAUUAAGAUGGAGUUGCA
Plate 1	D04	L-009883-00	J-009883-07	ARHGEF2	9181	NM_004723	15011973	GUGCGGAGCAGAUGUGUAA
Plate 1	D04	L-009883-00	J-009883-08	ARHGEF2	9181	NM_004723	15011973	GAAGGUAGCAGCCGUCUGU
Plate 1	D04	L-009883-00	J-009883-09	ARHGEF2	9181	NM_004723	15011973	CCACGGAACUGGCAUUACU
Plate 1	D05	L-008868-00	J-008868-06	AKAP13	11214	NM_144767	31563332	UGGAUGAGCUGAUCAGUAU

Plate 1	D05	L-008868-00	J-008868-07	AKAP13	11214	NM_144767	31563332	ACACAUAGCCCUAGAGUUC
Plate 1	D05	L-008868-00	J-008868-08	AKAP13	11214	NM_144767	31563332	GGUCAAACGGCAAGAAGUA
Plate 1	D05	L-008868-00	J-008868-09	AKAP13	11214	NM_144767	31563332	GAUGAGCAGUUCAGUUGUU
Plate 1	D06	L-013243-00	J-013243-05	ARHGEF3	50650	NM_019555	9506400	CCAAGAAGCCGCCUGGUAA
Plate 1	D06	L-013243-00	J-013243-06	ARHGEF3	50650	NM_019555	9506400	UGCCUCAGCUCCUAUGAUA
Plate 1	D06	L-013243-00	J-013243-07	ARHGEF3	50650	NM_019555	9506400	UUAAAGCGCUUCAGUCAAA
Plate 1	D06	L-013243-00	J-013243-08	ARHGEF3	50650	NM_019555	9506400	CAAUGACACUUUCAACAAA
Plate 1	D07	L-008480-00	J-008480-05	ARHGEF12	23365	NM_015313	7662087	GAUCAAAUCUCGUCAGAAA
Plate 1	D07	L-008480-00	J-008480-06	ARHGEF12	23365	NM_015313	7662087	GAAAUGAGACCUCUGUUAU
Plate 1	D07	L-008480-00	J-008480-07	ARHGEF12	23365	NM_015313	7662087	GGACAUAUGCCCUUUAGAA
Plate 1	D07	L-008480-00	J-008480-08	ARHGEF12	23365	NM_015313	7662087	GGCAACAUUUCCCAAGAUA
Plate 1	D08	L-009421-00	J-009421-05	ARHGEF1	9138	NM_198977	39777603	UGACGUGGCGGGUGACUAA
Plate 1	D08	L-009421-00	J-009421-06	ARHGEF1	9138	NM_198977	39777603	AAACUGGUGUGCUCUCAUC
Plate 1	D08	L-009421-00	J-009421-07	ARHGEF1	9138	NM_198977	39777603	CCACGGCCCUUCGGAAAGU
Plate 1	D08	L-009421-00	J-009421-08	ARHGEF1	9138	NM_198977	39777603	UAUACGAGCUGGUGGCACA
Plate 1	D09	L-003915-00	J-003915-06	NET1	10276	NM_005863	19923326	GGAGGAUGCUAUAUUGAUA
Plate 1	D09	L-003915-00	J-003915-07	NET1	10276	NM_005863	19923326	GAGUCUCCCUUCAGUCGAA
Plate 1	D09	L-003915-00	J-003915-08	NET1	10276	NM_005863	19923326	UCACGUCCUUGGCAAAUUU
Plate 1	D09	L-003915-00	J-003915-09	NET1	10276	NM_005863	19923326	UUGGUGAUCUGGACUCUUA
Plate 1	D10	L-010360-00	J-010360-05	ARHGEF11	9826	NM_014784	38026914	GCAAGUGGCUGCACAGUUC
Plate 1	D10	L-010360-00	J-010360-06	ARHGEF11	9826	NM_014784	38026914	UCAACAGGCUCAAGGAUAU
Plate 1	D10	L-010360-00	J-010360-07	ARHGEF11	9826	NM_014784	38026914	UCUAUGAGCUGGUUGCAUU
Plate 1	D10	L-010360-00	J-010360-08	ARHGEF11	9826	NM_014784	38026914	GGAACUCGGUACUGUCAGA
Plate 1	D11	L-008365-00	J-008365-05	ITSN1	6453	NM_001001132	47717124	GAUAUCAGAUGUCGAUUGA

Plate 1	D11	L-008365-00	J-008365-06	ITSN1	6453	NM_001001132	47717124	GAACGAAAGAUCAUAGAAU
Plate 1	D11	L-008365-00	J-008365-07	ITSN1	6453	NM_001001132	47717124	CGACAAGGCCGGAGUCUUC
Plate 1	D11	L-008365-00	J-008365-08	ITSN1	6453	NM_001001132	47717124	GCACAGAUAUGGGCACUAG
Plate 1	E02	L-009841-00	J-009841-05	ITSN2	50618	NM_147152	22325382	GAUCAAACGUGACAAGUUG
Plate 1	E02	L-009841-00	J-009841-06	ITSN2	50618	NM_147152	22325382	CCAAACAUGUGGGCUAUUA
Plate 1	E02	L-009841-00	J-009841-07	ITSN2	50618	NM_147152	22325382	CCUCAUGGGUCAUCUUAUA
Plate 1	E02	L-009841-00	J-009841-08	ITSN2	50618	NM_147152	22325382	GGUGAAUUAUAGAGCAUUA
Plate 1	E03	L-009833-00	J-009833-05	ARHGEF26	26084	NM_015595	21361486	CAAAUGGCCUUGCCGCUAA
Plate 1	E03	L-009833-00	J-009833-06	ARHGEF26	26084	NM_015595	21361486	UUGGAGAUCUUGAUACGAA
Plate 1	E03	L-009833-00	J-009833-07	ARHGEF26	26084	NM_015595	21361486	AGAGUGAGGUCGAUAACGA
Plate 1	E03	L-009833-00	J-009833-08	ARHGEF26	26084	NM_015595	21361486	GAGAUAACAUGUCAAGCUA
Plate 1	E04	L-032365-02	J-032365-18	ARHGEF35	445328	NM_001003702	51172609	AUAGAGGAAUUCAGCAUUA
Plate 1	E04	L-032365-02	J-032365-19	ARHGEF35	445328	NM_001003702	51172609	AGUGGGAGCAGGAGGAUAU
Plate 1	E04	L-032365-02	J-032365-20	ARHGEF35	445328	NM_001003702	51172609	GGAGGAUGUUUGUGCCGAU
Plate 1	E04	L-032365-02	J-032365-21	ARHGEF35	445328	NM_001003702	51172609	AAUUUGUUGUGGCGAGUUU
Plate 1	E05	L-005093-00	J-005093-05	ARHGEF5	7984	NM_001002861	50959183	CCUGGUAGCUCAAGGAUCU
Plate 1	E05	L-005093-00	J-005093-06	ARHGEF5	7984	NM_001002861	50959183	GAAUCCAUCUCAAAUCUAG
Plate 1	E05	L-005093-00	J-005093-07	ARHGEF5	7984	NM_001002861	50959183	CGAGAGAACCUUUGAGAAG
Plate 1	E05	L-005093-00	J-005093-08	ARHGEF5	7984	NM_001002861	50959183	CCACAGAGUCUCCCGCCUA
Plate 1	E06	L-009354-01	J-009354-09	NGEF	25791	NM_019850	29789101	GAGACAACCCCGAACGGAA
Plate 1	E06	L-009354-01	J-009354-10	NGEF	25791	NM_019850	29789101	AUGGAGAACGAGCGGAUAA
Plate 1	E06	L-009354-01	J-009354-11	NGEF	25791	NM_019850	29789101	GGACCAAGUUUGUUUCGUU
Plate 1	E06	L-009354-01	J-009354-12	NGEF	25791	NM_019850	29789101	GAAAAUGAGCCGCACGGAA
Plate 1	E07	L-008370-01	J-008370-11	ARHGEF19	128272	NM_153213	40255148	CGGGAGAAUAAGCGAGUCA

Plate 1	E07	L-008370-01	J-008370-12	ARHGEF19	128272	NM_153213	40255148	GUCAAGAGCACCAGCGAGA
Plate 1	E07	L-008370-01	J-008370-13	ARHGEF19	128272	NM_153213	40255148	AAUGGAGGCUCGAAGUGUA
Plate 1	E07	L-008370-01	J-008370-14	ARHGEF19	128272	NM_153213	40255148	GUACCAGCGUGAAGAGGUC
Plate 1	E08	L-010234-00	J-010234-05	ARHGEF16	27237	NM_014448	15011976	CCAACGAGGUCUACCAACA
Plate 1	E08	L-010234-00	J-010234-06	ARHGEF16	27237	NM_014448	15011976	GCGGAGAGCUGUUCUUAGU
Plate 1	E08	L-010234-00	J-010234-07	ARHGEF16	27237	NM_014448	15011976	CGGCCAACGUGCUACCUUU
Plate 1	E08	L-010234-00	J-010234-08	ARHGEF16	27237	NM_014448	15011976	GAUACGCUCUGCCUCAAGA
Plate 1	E09	L-009731-00	J-009731-05	ARHGEF15	22899	NM_173728	32307165	GCAAGAUCAUCGAGCGUUG
Plate 1	E09	L-009731-00	J-009731-06	ARHGEF15	22899	NM_173728	32307165	GCAUGAAGCAGACUGAAGA
Plate 1	E09	L-009731-00	J-009731-07	ARHGEF15	22899	NM_173728	32307165	GGUUACAGGUUCUGGACUA
Plate 1	E09	L-009731-00	J-009731-08	ARHGEF15	22899	NM_173728	32307165	GAACGGUGCUCCAGAUGCU
Plate 1	E10	L-009323-00	J-009323-05	RASGRF1	5923	NM_153815	24797100	AAGCAAAGGUAACGCAAUA
Plate 1	E10	L-009323-00	J-009323-06	RASGRF1	5923	NM_153815	24797100	GAGAGAGGAGUCAGAUAUU
Plate 1	E10	L-009323-00	J-009323-07	RASGRF1	5923	NM_153815	24797100	CGAGUCUUCUCUCCGAAUA
Plate 1	E10	L-009323-00	J-009323-08	RASGRF1	5923	NM_153815	24797100	GGACCAAUCUUUUGUAAUG
Plate 1	E11	L-024516-00	J-024516-07	RASGRF2	5924	NM_006909	38505169	CGAAAGAACUCCUUACAUU
Plate 1	E11	L-024516-00	J-024516-08	RASGRF2	5924	NM_006909	38505169	UGACAAAGACCUUAUCAUA
Plate 1	E11	L-024516-00	J-024516-09	RASGRF2	5924	NM_006909	38505169	UAUAUGAGCUGUCACUAAA
Plate 1	E11	L-024516-00	J-024516-10	RASGRF2	5924	NM_006909	38505169	UAGCUGAUCUGUUUGAUAU
Plate 1	F02	L-013460-00	J-013460-05	ARHGEF10	9639	NM_014629	62548863	CGAGUGAAUUUGAAAGUUA
Plate 1	F02	L-013460-00	J-013460-06	ARHGEF10	9639	NM_014629	62548863	CGAUGAAAGUCAACCCAUA
Plate 1	F02	L-013460-00	J-013460-07	ARHGEF10	9639	NM_014629	62548863	CUUAUAACCCUGAACCUUA
Plate 1	F02	L-013460-00	J-013460-08	ARHGEF10	9639	NM_014629	62548863	GGAAGCCGAUACCUCAUUC
Plate 1	F03	L-017096-01	J-017096-09	ARHGEF10L	55160	NM_001011722	74136546	GGAUGGCCGUGAUGCGCAA

Plate 1	F03	L-017096-01	J-017096-10	ARHGEF10L	55160	NM_001011722	74136546	AGGUCAGCGUUUCGGACAU
Plate 1	F03	L-017096-01	J-017096-11	ARHGEF10L	55160	NM_001011722	74136546	GAAGAGUUCCCGUCGCAUU
Plate 1	F03	L-017096-01	J-017096-12	ARHGEF10L	55160	NM_001011722	74136546	GGAACCUGCUCUACGAGGA
Plate 1	F04	L-009751-00	J-009751-06	ARHGEF17	9828	NM_014786	21361457	AGUGAUGGGUUAAAUCUAA
Plate 1	F04	L-009751-00	J-009751-07	ARHGEF17	9828	NM_014786	21361457	AUGGAGAGCUUGUGGUCUA
Plate 1	F04	L-009751-00	J-009751-08	ARHGEF17	9828	NM_014786	21361457	AUUGAGGGAUGGAGGAUUU
Plate 1	F04	L-009751-00	J-009751-09	ARHGEF17	9828	NM_014786	21361457	GGAAGUCCCUGUCAAAUCC
Plate 1	F05	L-005194-00	J-005194-06	SOS1	6654	NM_005633	15529995	AACAGAAGCUGAUCGCAUA
Plate 1	F05	L-005194-00	J-005194-07	SOS1	6654	NM_005633	15529995	GGCAGAAAUUCGACAAUAU
Plate 1	F05	L-005194-00	J-005194-08	SOS1	6654	NM_005633	15529995	GGAUAUGUUUCAUCAAGAU
Plate 1	F05	L-005194-00	J-005194-09	SOS1	6654	NM_005633	15529995	UAGUAGCAGUCUUAGAAUA
Plate 1	F06	L-005195-00	J-005195-06	SOS2	6655	NM_006939	39930603	GGAGUAAGCCAUAAUAUUA
Plate 1	F06	L-005195-00	J-005195-07	SOS2	6655	NM_006939	39930603	ACAAGUCACUAGAAAUUGA
Plate 1	F06	L-005195-00	J-005195-08	SOS2	6655	NM_006939	39930603	GGAAUAUGUCCAACCAGUA
Plate 1	F06	L-005195-00	J-005195-09	SOS2	6655	NM_006939	39930603	UACUCUAGAUCGAAUGUUA
Plate 1	F07	L-008519-00	J-008519-06	FARP1	10160	NM_001001715	48928037	CAGGAAAACUCGUGUCCAU
Plate 1	F07	L-008519-00	J-008519-07	FARP1	10160	NM_001001715	48928037	CAGGAGGCAUUUGAAGUUC
Plate 1	F07	L-008519-00	J-008519-08	FARP1	10160	NM_001001715	48928037	CCGGAAAAUUCGGGGAUCA
Plate 1	F07	L-008519-00	J-008519-09	FARP1	10160	NM_001001715	48928037	CUUGGAACGUGGACAGAAG
Plate 1	F08	L-009237-00	J-009237-06	FARP2	9855	NM_014808	7662309	CGAAAUUGCUCGAAAGUUG
Plate 1	F08	L-009237-00	J-009237-07	FARP2	9855	NM_014808	7662309	GGAUUUGGCUUGAACCUAU
Plate 1	F08	L-009237-00	J-009237-08	FARP2	9855	NM_014808	7662309	CCAGGACACAUUAGAAUUU
Plate 1	F08	L-009237-00	J-009237-09	FARP2	9855	NM_014808	7662309	GGAACAUGCGCCAGUUAAA
Plate 1	F09	L-009612-00	J-009612-06	FGD1	2245	NM_004463	24797152	GGACCACUCAAGACCGAUA

Plate 1	F09	L-009612-00	J-009612-07	FGD1	2245	NM_004463	24797152	CCCAAGAGGUUGACAGUGA
Plate 1	F09	L-009612-00	J-009612-08	FGD1	2245	NM_004463	24797152	UCUCAAGGACUAUCUGUUA
Plate 1	F09	L-009612-00	J-009612-09	FGD1	2245	NM_004463	24797152	AUAAGCUGCUGAAGGUAUA
Plate 1	F10	L-008431-01	J-008431-09	FGD2	221472	NM_173558	34222232	UGAAGUACCACCACCGAUU
Plate 1	F10	L-008431-01	J-008431-10	FGD2	221472	NM_173558	34222232	GGGCCGAACUGAAAUACGA
Plate 1	F10	L-008431-01	J-008431-11	FGD2	221472	NM_173558	34222232	GCAGAGAAUUCCACGUUAC
Plate 1	F10	L-008431-01	J-008431-12	FGD2	221472	NM_173558	34222232	CCAUUGACCAAAUCGAGAA
Plate 1	F11	L-010371-02	J-010371-10	FGD3	89846	NM_033086	134133264	UCUAAGACCAGACGUGACA
Plate 1	F11	L-010371-02	J-010371-11	FGD3	89846	NM_033086	134133264	CGUGUGAGCUGAAUCGUGA
Plate 1	F11	L-010371-02	J-010371-12	FGD3	89846	NM_033086	134133264	GCUCGAGCCCAGAAAACUA
Plate 1	F11	L-010371-02	J-010371-18	FGD3	89846	NM_033086	134133264	GCAGGAGGUAUGCGGGAAC
Plate 1	G02	L-007123-00	J-007123-05	FGD4	121512	NM_139241	21245127	GAACCUAAAUGCUCCUAGA
Plate 1	G02	L-007123-00	J-007123-06	FGD4	121512	NM_139241	21245127	CAAGAUGGAUCCGAGAUAA
Plate 1	G02	L-007123-00	J-007123-07	FGD4	121512	NM_139241	21245127	GAAGUGACAAUGUGUAUGA
Plate 1	G02	L-007123-00	J-007123-08	FGD4	121512	NM_139241	21245127	CAACCGACUUGACCUCUUA
Plate 1	G03	L-028077-01	J-028077-09	FGD5	152273	NM_152536	50080161	GUGAAGAGGCCACGGGUGU
Plate 1	G03	L-028077-01	J-028077-10	FGD5	152273	NM_152536	50080161	GUGCAGACCAGGACGCAGA
Plate 1	G03	L-028077-01	J-028077-11	FGD5	152273	NM_152536	50080161	GAUGGAAUCCUGUGGACUA
Plate 1	G03	L-028077-01	J-028077-12	FGD5	152273	NM_152536	50080161	GGAAGAUGCGAGUGUGUUA
Plate 1	G04	L-026895-00	J-026895-05	FGD6	55785	NM_018351	55742696	GAAGGGACCGGUUUUAUAA
Plate 1	G04	L-026895-00	J-026895-06	FGD6	55785	NM_018351	55742696	GAAUUCCGAGUCUAAAGUA
Plate 1	G04	L-026895-00	J-026895-07	FGD6	55785	NM_018351	55742696	CUAAGCAGCUCAAAUUAAC
Plate 1	G04	L-026895-00	J-026895-08	FGD6	55785	NM_018351	55742696	GCUCGUCUGUUACGCCAAA
Plate 1	G05	L-005047-00	J-005047-05	TRIO	7204	NM_007118	45439358	GUAAAGAAGUGAAAGAUUC

Plate 1	G05	L-005047-00	J-005047-06	TRIO	7204	NM_007118	45439358	CGACCUAUCCGUAGCAUUA
Plate 1	G05	L-005047-00	J-005047-07	TRIO	7204	NM_007118	45439358	GGAAUACAACCACGAAGAA
Plate 1	G05	L-005047-00	J-005047-08	TRIO	7204	NM_007118	45439358	AGAACAGGGUAUUGCAUUA
Plate 1	G06	L-004121-01	J-004121-09	ARHGEF25	115557	NM_133483	19311007	CCCAAGCGCUGCAACGAUA
Plate 1	G06	L-004121-01	J-004121-10	ARHGEF25	115557	NM_133483	19311007	AGGGUGGGAUCCAGCGCUA
Plate 1	G06	L-004121-01	J-004121-11	ARHGEF25	115557	NM_133483	19311007	AGAAAAUGUACGUGGACGA
Plate 1	G06	L-004121-01	J-004121-12	ARHGEF25	115557	NM_133483	19311007	GGCAGAUUGUGGAGGGUUA
Plate 1	G07	L-003904-00	J-003904-06	MCF2	4168	NM_005369	19923309	GAACUGGGCAAGAUGAUAA
Plate 1	G07	L-003904-00	J-003904-07	MCF2	4168	NM_005369	19923309	UAACAGAACGGGAUAAGUU
Plate 1	G07	L-003904-00	J-003904-08	MCF2	4168	NM_005369	19923309	GAAGAAGGCACUCGAUGCA
Plate 1	G07	L-003904-00	J-003904-09	MCF2	4168	NM_005369	19923309	GAGCUCAGUUAGUGAUUUG
Plate 1	G08	L-009313-01	J-009313-09	MCF2L2	23101	NM_015078	31742504	CUGAAUGUCCGGACGAUAU
Plate 1	G08	L-009313-01	J-009313-10	MCF2L2	23101	NM_015078	31742504	UGAACGACAUUGCGACAUU
Plate 1	G08	L-009313-01	J-009313-11	MCF2L2	23101	NM_015078	31742504	UGAGAUUGCCAGUCGAAAU
Plate 1	G08	L-009313-01	J-009313-12	MCF2L2	23101	NM_015078	31742504	UCUCUGACCUUCACGGCUA
Plate 1	G09	L-010098-01	J-010098-09	MCF2L	23263	NM_024979	27777654	GAACAAGCACUACGCGGUA
Plate 1	G09	L-010098-01	J-010098-10	MCF2L	23263	NM_024979	27777654	CAGCAUCUUUCCCGGCAAA
Plate 1	G09	L-010098-01	J-010098-11	MCF2L	23263	NM_024979	27777654	UUACACGGUUACAUCGAUA
Plate 1	G09	L-010098-01	J-010098-12	MCF2L	23263	NM_024979	27777654	UCAUGGAGCACGUGCGAAA
Plate 1	G10	L-010063-01	J-010063-09	PREX1	57580	NM_020820	34452731	AAGAUGGGACAGCGGAUUA
Plate 1	G10	L-010063-01	J-010063-10	PREX1	57580	NM_020820	34452731	CCACGGACAUCAUGCGGAA
Plate 1	G10	L-010063-01	J-010063-11	PREX1	57580	NM_020820	34452731	ACGUCAUGAUUGCGGAGAA
Plate 1	G10	L-010063-01	J-010063-12	PREX1	57580	NM_020820	34452731	CCUUUAAGCAGCUGGACGA
Plate 1	G11	L-014602-00	J-014602-05	PREX2	80243	NM_025170	47578116	GAAGCGGACUCCACGGAAA

Plate 1	G11	L-014602-00	J-014602-06	PREX2	80243	NM_025170	47578116	GAACACCUAUGUCAGAGAA
Plate 1	G11	L-014602-00	J-014602-07	PREX2	80243	NM_025170	47578116	CAAGAUACCUGGGUCAUGA
Plate 1	G11	L-014602-00	J-014602-08	PREX2	80243	NM_025170	47578116	GAAGCGAAUUUGUGUCAUG
Plate 2	B02	L-003935-00	J-003935-06	VAV1	7409	NM_005428	7108366	CGACAAAGCUCUACUCAUC
Plate 2	B02	L-003935-00	J-003935-07	VAV1	7409	NM_005428	7108366	GCAGCGAGUUCUCAAAUAU
Plate 2	B02	L-003935-00	J-003935-08	VAV1	7409	NM_005428	7108366	GCCAUCAGCAUUAAAUAUA
Plate 2	B02	L-003935-00	J-003935-09	VAV1	7409	NM_005428	7108366	UCAAAUACAAGGAGAGGUU
Plate 2	B03	L-005199-00	J-005199-05	VAV2	7410	NM_003371	40549447	CUGAAAGUCUGCCACGAUA
Plate 2	B03	L-005199-00	J-005199-06	VAV2	7410	NM_003371	40549447	UGGCAGCUGUCUUCAUUAA
Plate 2	B03	L-005199-00	J-005199-07	VAV2	7410	NM_003371	40549447	GUGGGAGGGUCGUCUGGUA
Plate 2	B03	L-005199-00	J-005199-08	VAV2	7410	NM_003371	40549447	GCCGCUGGCUCAUCGAUUG
Plate 2	B04	L-010178-00	J-010178-06	VAV3	10451	NM_006113	21614495	GAAACAUUAUCACGACUUU
Plate 2	B04	L-010178-00	J-010178-07	VAV3	10451	NM_006113	21614495	GCAAUUAGCAUUAAGUACA
Plate 2	B04	L-010178-00	J-010178-08	VAV3	10451	NM_006113	21614495	AGUACAAGAUAGCCAAUAA
Plate 2	B04	L-010178-00	J-010178-09	VAV3	10451	NM_006113	21614495	AGACCGAACUUAUUAAUAG
Plate 2	B05	L-015006-00	J-015006-05	ARHGEF39	84904	NM_001031728	72534741	CGUCGUAGCUUUGGCUGAA
Plate 2	B05	L-015006-00	J-015006-06	ARHGEF39	84904	NM_001031728	72534741	CAACAGCCCUGACCAUCAA
Plate 2	B05	L-015006-00	J-015006-07	ARHGEF39	84904	NM_001031728	72534741	GGAGCUCUAUAACCAAUUU
Plate 2	B05	L-015006-00	J-015006-08	ARHGEF39	84904	NM_001031728	72534741	AAAUAAAGGUUUCCGGAGG
Plate 2	B06	L-003932-00	J-003932-05	TIAM1	7074	NM_003253	4507500	GCAGGCUACUGUCGGAAUU
Plate 2	B06	L-003932-00	J-003932-06	TIAM1	7074	NM_003253	4507500	GUAUAAAGAUGGUUCCAAA
Plate 2	B06	L-003932-00	J-003932-07	TIAM1	7074	NM_003253	4507500	GAACCGAAGCUGUAAAGAA
Plate 2	B06	L-003932-00	J-003932-08	TIAM1	7074	NM_003253	4507500	CAAAUUAGCCAUAGCAACA
Plate 2	B07	L-008434-00	J-008434-09	TIAM2	26230	NM_001010927	73695942	GAACUUCAGGCGUCACAUA

Plate 2	B07	L-008434-00	J-008434-10	TIAM2	26230	NM_001010927	73695942	CGACCUAAAUUCUGUUCUA
Plate 2	B07	L-008434-00	J-008434-11	TIAM2	26230	NM_001010927	73695942	GAGCACUUCUCCCGGGAAA
Plate 2	B07	L-008434-00	J-008434-12	TIAM2	26230	NM_001010927	73695942	GUGUAAGGAUCGCCUGGUA
Plate 2	B08	L-010231-00	J-010231-05	ARHGEF6	9459	NM_004840	47078220	GAGGAUGUCUUAUAUCUUA
Plate 2	B08	L-010231-00	J-010231-06	ARHGEF6	9459	NM_004840	47078220	GGACGUUCCUCUUCUCUUA
Plate 2	B08	L-010231-00	J-010231-07	ARHGEF6	9459	NM_004840	47078220	GAGGAGGAAUAUGUGAUUA
Plate 2	B08	L-010231-00	J-010231-08	ARHGEF6	9459	NM_004840	47078220	GGACAUCAUUUACGUCACA
Plate 2	B09	L-009616-00	J-009616-05	ARHGEF7	8874	NM_003899	22027526	GAGCAUGAUUGAGCGGAUA
Plate 2	B09	L-009616-00	J-009616-06	ARHGEF7	8874	NM_003899	22027526	UGAAUGUCCUCACGGAACA
Plate 2	B09	L-009616-00	J-009616-07	ARHGEF7	8874	NM_003899	22027526	GGACGAGCUUUCCUUCUCA
Plate 2	B09	L-009616-00	J-009616-08	ARHGEF7	8874	NM_003899	22027526	GGAGGAUUAUCAUACAGAU
Plate 2	B10	L-024745-01	J-024745-09	PLEKHG1	57480	NM_001029884	71274147	GACAAGGCCUAGAGAACGA
Plate 2	B10	L-024745-01	J-024745-10	PLEKHG1	57480	NM_001029884	71274147	CGGAAAGGGAUCAGCGCUA
Plate 2	B10	L-024745-01	J-024745-11	PLEKHG1	57480	NM_001029884	71274147	GAAGAGAGAUGACACGUUU
Plate 2	B10	L-024745-01	J-024745-12	PLEKHG1	57480	NM_001029884	71274147	GGAUGUAUAUAACGAGGAA
Plate 2	B11	L-023690-00	J-023690-05	PLEKHG2	64857	NM_022835	45237196	CCUCAUAGAUGCCCAUGUU
Plate 2	B11	L-023690-00	J-023690-06	PLEKHG2	64857	NM_022835	45237196	AGCGAGAGCCCAACCAAUA
Plate 2	B11	L-023690-00	J-023690-07	PLEKHG2	64857	NM_022835	45237196	UGACAGCGGUUGCCUGGUA
Plate 2	B11	L-023690-00	J-023690-08	PLEKHG2	64857	NM_022835	45237196	CCUAGUCUCUCUGACAUUU
Plate 2	C02	L-022051-01	J-022051-10	PLEKHG3	26030	NM_015549	55749620	GCGUCAUUGCGGAGCGAUU
Plate 2	C02	L-022051-01	J-022051-11	PLEKHG3	26030	NM_015549	55749620	CUGCAGAGUGCCAGCCGAA
Plate 2	C02	L-022051-01	J-022051-12	PLEKHG3	26030	NM_015549	55749620	CCUAUUAUCCCAAUCGGUA
Plate 2	C02	L-022051-01	J-022051-13	PLEKHG3	26030	NM_015549	55749620	UCGUGGAGACAGAGCGCAU
Plate 2	C03	L-022573-01	J-022573-09	PLEKHG4	25894	NM_015432	70912385	GGACAAGGCUGACGAGCUA

Plate 2	C03	L-022573-01	J-022573-10	PLEKHG4	25894	NM_015432	70912385	ACAACAAGGAGGUGCGCAU
Plate 2	C03	L-022573-01	J-022573-11	PLEKHG4	25894	NM_015432	70912385	CCAGACUACAGGACGGCAA
Plate 2	C03	L-022573-01	J-022573-12	PLEKHG4	25894	NM_015432	70912385	GAAUAAGCCUCGCUCCGAU
Plate 2	C04	L-013873-01	J-013873-09	PLEKHG5	57449	NM_020631	38373681	GCAAGAACAUGUCGGAGUU
Plate 2	C04	L-013873-01	J-013873-10	PLEKHG5	57449	NM_020631	38373681	CUGCUUAACUCCACGCUCA
Plate 2	C04	L-013873-01	J-013873-11	PLEKHG5	57449	NM_020631	38373681	UGGCCCAGCUCUACCGAAU
Plate 2	C04	L-013873-01	J-013873-12	PLEKHG5	57449	NM_020631	38373681	GGAGGAGACACACGGAUGA
Plate 2	C05	L-031878-01	J-031878-09	PLEKHG4B	153478	NM_052909	76253939	CCAGGAAGUCGCCGAGUUA
Plate 2	C05	L-031878-01	J-031878-10	PLEKHG4B	153478	NM_052909	76253939	CGGGAUGAGUUUAUCGUUU
Plate 2	C05	L-031878-01	J-031878-11	PLEKHG4B	153478	NM_052909	76253939	GAAGAGGCCCACCGAGUUA
Plate 2	C05	L-031878-01	J-031878-12	PLEKHG4B	153478	NM_052909	76253939	GGGAAAACAGUAAGCGAGA
Plate 2	C06	L-020318-02	J-020318-06	PLEKHG6	55200	NM_018173	222080065	GACCAUGGCUUACGCCCGA
Plate 2	C06	L-020318-02	J-020318-07	PLEKHG6	55200	NM_018173	222080065	GCUGAGACCCUGUUUGGAA
Plate 2	C06	L-020318-02	J-020318-08	PLEKHG6	55200	NM_018173	222080065	GGAAUGUGGUGGUGGAAAC
Plate 2	C06	L-020318-02	J-020318-17	PLEKHG6	55200	NM_018173	222080065	GAGAAGAACCUGCGCCCAU
Plate 2	C07	L-032389-01	J-032389-09	PLEKHG7	440107	NM_001004330	51972239	UUACAAGCCCAAACGGAAA
Plate 2	C07	L-032389-01	J-032389-10	PLEKHG7	440107	NM_001004330	51972239	ACAAAGUAUUUCCGAGGGA
Plate 2	C07	L-032389-01	J-032389-11	PLEKHG7	440107	NM_001004330	51972239	UGAAAGGCAGUUUGAAUAA
Plate 2	C07	L-032389-01	J-032389-12	PLEKHG7	440107	NM_001004330	51972239	GUUCUUAGGGUCAGAUUAU
Plate 2	C08	L-015469-01	J-015469-09	SPATA13	221178	NM_153023	23308552	CCACACAGGAACACGGUGA
Plate 2	C08	L-015469-01	J-015469-10	SPATA13	221178	NM_153023	23308552	GUACCAUGCUCUAAAGCGA
Plate 2	C08	L-015469-01	J-015469-11	SPATA13	221178	NM_153023	23308552	CUGCAACCUCAGCGUGAAA
Plate 2	C08	L-015469-01	J-015469-12	SPATA13	221178	NM_153023	23308552	GGACCAACGUCAUCCGGGA
Plate 2	C09	L-008235-00	J-008235-05	ARHGEF4	50649	NM_015320	15011978	UGUCUGCGCUGACGAAGUG

Plate 2	C09	L-008235-00	J-008235-06	ARHGEF4	50649	NM_015320	15011978	GCUCAGAACUCAUCUACUC
Plate 2	C09	L-008235-00	J-008235-07	ARHGEF4	50649	NM_015320	15011978	CAACGGGACUGAACCACAU
Plate 2	C09	L-008235-00	J-008235-08	ARHGEF4	50649	NM_015320	15011978	CAGCGAAUGUUCUUUCUCU
Plate 2	C10	L-020314-00	J-020314-05	ARHGEF9	23229	NM_015185	7662107	CAAGAUGGAUUCUGGAUAU
Plate 2	C10	L-020314-00	J-020314-06	ARHGEF9	23229	NM_015185	7662107	UGGCUGAGCUCCUAAAGUA
Plate 2	C10	L-020314-00	J-020314-07	ARHGEF9	23229	NM_015185	7662107	CAAGCGACGUUUAGAGAAU
Plate 2	C10	L-020314-00	J-020314-08	ARHGEF9	23229	NM_015185	7662107	GAUCUGCAAGUAUCCCUUA
Plate 2	C11	L-017817-01	J-017817-09	DEF6	50619	NM_022047	31542500	GGAGAUAAGCGUCCGGUCA
Plate 2	C11	L-017817-01	J-017817-10	DEF6	50619	NM_022047	31542500	ACGUAUGAGAUGAGCGCCU
Plate 2	C11	L-017817-01	J-017817-11	DEF6	50619	NM_022047	31542500	AGGAGGAGCAGGAGCGCUA
Plate 2	C11	L-017817-01	J-017817-12	DEF6	50619	NM_022047	31542500	GAGAAGGAACUGGGCCGAA
Plate 2	D02	L-010323-01	J-010323-09	SWAP70	23075	NM_015055	93102363	CAGGAGAGCUUUACGCUAA
Plate 2	D02	L-010323-01	J-010323-10	SWAP70	23075	NM_015055	93102363	GCAUAGUGUUACCGAUUUA
Plate 2	D02	L-010323-01	J-010323-11	SWAP70	23075	NM_015055	93102363	AGGAUUAAUUCGACUGAUA
Plate 2	D02	L-010323-01	J-010323-12	SWAP70	23075	NM_015055	93102363	CCGAGUAUGUGCUGUUAAA
Plate 2	D03	L-011253-00	J-011253-05	DOCK1	1793	NM_001380	50345995	GUACCGAGGUUACACGUUA
Plate 2	D03	L-011253-00	J-011253-06	DOCK1	1793	NM_001380	50345995	GAAAGUCGAUGGUGGUGAA
Plate 2	D03	L-011253-00	J-011253-07	DOCK1	1793	NM_001380	50345995	UAAAUGAGCAGCUGUACAA
Plate 2	D03	L-011253-00	J-011253-08	DOCK1	1793	NM_001380	50345995	GGCCCAAGCCUGACUAUUU
Plate 2	D04	L-019915-00	J-019915-05	DOCK2	1794	NM_004946	31377467	GGUCUUUGAUGCGAAGUUA
Plate 2	D04	L-019915-00	J-019915-06	DOCK2	1794	NM_004946	31377467	CUACAUUACUCUCUUACAA
Plate 2	D04	L-019915-00	J-019915-07	DOCK2	1794	NM_004946	31377467	GGUACAAGCUUGGUCAGAA
Plate 2	D04	L-019915-00	J-019915-08	DOCK2	1794	NM_004946	31377467	CAAGGUGGCUGUCCCUAUU
Plate 2	D05	L-012695-00	J-012695-05	DOCK3	1795	NM_004947	54400756	CGAGAUCACUGGCGAGUAU

Plate 2	D05	L-012695-00	J-012695-06	DOCK3	1795	NM_004947	54400756	GAGAAUAGCACGUUUAAUA
Plate 2	D05	L-012695-00	J-012695-07	DOCK3	1795	NM_004947	54400756	CAGGAGGCCUUCUUUGAUA
Plate 2	D05	L-012695-00	J-012695-08	DOCK3	1795	NM_004947	54400756	UGACGCCCAUUCCAGAUUA
Plate 2	D06	L-017968-01	J-017968-09	DOCK4	9732	NM_014705	92091571	CCUCUUAUAUGACGAGCUA
Plate 2	D06	L-017968-01	J-017968-10	DOCK4	9732	NM_014705	92091571	ACGAUAUUGUCAAACGAUA
Plate 2	D06	L-017968-01	J-017968-11	DOCK4	9732	NM_014705	92091571	GGAGAAAAUUGCACGAUUA
Plate 2	D06	L-017968-01	J-017968-12	DOCK4	9732	NM_014705	92091571	GCCAAGAACAUGUCGGAUA
Plate 2	D07	L-018931-00	J-018931-05	DOCK5	80005	NM_024940	45439361	GAGGAGAGAUUGUUAAGUU
Plate 2	D07	L-018931-00	J-018931-06	DOCK5	80005	NM_024940	45439361	GAACAUUAAACACAACCUA
Plate 2	D07	L-018931-00	J-018931-07	DOCK5	80005	NM_024940	45439361	GCAAAUUCAUUCAAAGCAU
Plate 2	D07	L-018931-00	J-018931-08	DOCK5	80005	NM_024940	45439361	GGGUUGCGAUCUAUAACUA
Plate 2	D08	L-031950-00	J-031950-05	DOCK6	57572	NM_020812	40217610	CGGUGGAGAUGUAUAUUGA
Plate 2	D08	L-031950-00	J-031950-06	DOCK6	57572	NM_020812	40217610	UCAAGGACCGGGUGACCUA
Plate 2	D08	L-031950-00	J-031950-07	DOCK6	57572	NM_020812	40217610	GAUCUUGGCUCUGUAUGAU
Plate 2	D08	L-031950-00	J-031950-08	DOCK6	57572	NM_020812	40217610	GAACUCGGACUCCAUGAAG
Plate 2	D09	L-031725-00	J-031725-05	DOCK7	85440	NM_033407	54112428	GAUCGAAGUUGUAAUCGUA
Plate 2	D09	L-031725-00	J-031725-06	DOCK7	85440	NM_033407	54112428	UCUCGAAGCCUUAGUAAUA
Plate 2	D09	L-031725-00	J-031725-07	DOCK7	85440	NM_033407	54112428	CGACUCUGCUUUAAAGAUU
Plate 2	D09	L-031725-00	J-031725-08	DOCK7	85440	NM_033407	54112428	UAACCAAACUUGCAGAGAU
Plate 2	D10	L-026106-00	J-026106-05	DOCK8	81704	NM_203447	44889959	GAUCAGAGCCUCAUUAGGA
Plate 2	D10	L-026106-00	J-026106-06	DOCK8	81704	NM_203447	44889959	GGAAAUACGUCCAGUACCA
Plate 2	D10	L-026106-00	J-026106-07	DOCK8	81704	NM_203447	44889959	CAACGCAGCUCAACAGGAU
Plate 2	D10	L-026106-00	J-026106-08	DOCK8	81704	NM_203447	44889959	CCGCUAAGCUCACAGUAAA
Plate 2	D11	L-014040-01	J-014040-09	DOCK9	23348	NM_015296	24308028	CGGUCAAGCCUUAGCGGUA

Plate 2	D11	L-014040-01	J-014040-10	DOCK9	23348	NM_015296	24308028	UCUGGAAAGCCGAGCGCUA
Plate 2	D11	L-014040-01	J-014040-11	DOCK9	23348	NM_015296	24308028	GCACAAUGGUUCACGGGAU
Plate 2	D11	L-014040-01	J-014040-12	DOCK9	23348	NM_015296	24308028	AGGAAGAAGUCGCGGUUAA
Plate 2	E02	L-023079-00	J-023079-05	DOCK10	55619	NM_014689	58037090	GGACCUGACUAAGCGUAUA
Plate 2	E02	L-023079-00	J-023079-06	DOCK10	55619	NM_014689	58037090	CAAUAUAGCUACGGAGGUU
Plate 2	E02	L-023079-00	J-023079-07	DOCK10	55619	NM_014689	58037090	CAACAUUCGCUUGCAAUUA
Plate 2	E02	L-023079-00	J-023079-08	DOCK10	55619	NM_014689	58037090	CCAGACAGCUAUCAAACAU
Plate 2	E03	L-015696-01	J-015696-09	DOCK11	139818	NM_144658	40068508	GAACUAAAUGAGCGGCUAA
Plate 2	E03	L-015696-01	J-015696-10	DOCK11	139818	NM_144658	40068508	CCAGAGAUUUCCCGAGACA
Plate 2	E03	L-015696-01	J-015696-11	DOCK11	139818	NM_144658	40068508	UGGAAAAUAUACAGCGAUU
Plate 2	E03	L-015696-01	J-015696-12	DOCK11	139818	NM_144658	40068508	CGAAACAGAUCAGGAGUAA
Plate 2	E04	L-006450-00	J-006450-05	ECT2	1894	NM_018098	21735571	GCACUCACCUUGUAGUUGA
Plate 2	E04	L-006450-00	J-006450-06	ECT2	1894	NM_018098	21735571	CAGAGGAGAUUAAGACUAU
Plate 2	E04	L-006450-00	J-006450-07	ECT2	1894	NM_018098	21735571	UAACAGCAAUCGCAAACGA
Plate 2	E04	L-006450-00	J-006450-08	ECT2	1894	NM_018098	21735571	GUAAUGAGUCGUCUUUCUA
Plate 2	E05	L-024733-01	J-024733-09	ECT2L	345930	XM_941136	88999490	GUAUAUGAACACAGCGUAA
Plate 2	E05	L-024733-01	J-024733-10	ECT2L	345930	XM_941136	88999490	GGCACAGAGCAUCGGAAUA
Plate 2	E05	L-024733-01	J-024733-11	ECT2L	345930	XM_941136	88999490	UGGGAGAAAUAGUCACGAA
Plate 2	E05	L-024733-01	J-024733-12	ECT2L	345930	XM_941136	88999490	CGUAAGAAGGAGUUAUUCA
Plate 2	E06	L-014168-00	J-014168-09	ALS2	57679	NM_020919	40316934	GAAUGUGUCCUUCGACUAA
Plate 2	E06	L-014168-00	J-014168-10	ALS2	57679	NM_020919	40316934	GAAUUUAGGCUCUGAGGUA
Plate 2	E06	L-014168-00	J-014168-11	ALS2	57679	NM_020919	40316934	CGAGUUAGCUACUACAGAA
Plate 2	E06	L-014168-00	J-014168-12	ALS2	57679	NM_020919	40316934	GAUUCCAGCUUCUUGCUAA
Plate 2	E07	L-027177-00	J-027177-07	OBSCN	84033	NM_052843	58331252	GAUGUGAGCUGCAGAUUCA

Plate 2	E07	L-027177-00	J-027177-08	OBSCN	84033	NM_052843	58331252	CCAAGGUGGUGUUUGCUAA
Plate 2	E07	L-027177-00	J-027177-09	OBSCN	84033	NM_052843	58331252	GCAGACAGCGACACCUAUA
Plate 2	E07	L-027177-00	J-027177-10	OBSCN	84033	NM_052843	58331252	GAUGGAGAGUUCCGUGAUU
Plate 2	E08	L-032927-01	J-032927-05	ARHGEF37	389337	NM_001001669	83715965	GAAAUUUAAGCAACGGCUA
Plate 2	E08	L-032927-01	J-032927-06	ARHGEF37	389337	NM_001001669	83715965	ACUUCAGGCCGCACGAAUA
Plate 2	E08	L-032927-01	J-032927-07	ARHGEF37	389337	NM_001001669	83715965	CCAUGGAUUUAUCGGUGUA
Plate 2	E08	L-032927-01	J-032927-08	ARHGEF37	389337	NM_001001669	83715965	AGUUCAAACAGGCGCUUUA
Plate 2	E09	L-014170-01	J-014170-09	IGDCC4	57722	NM_020962	19882240	CAAACAAGGUGUAUCGAGU
Plate 2	E09	L-014170-01	J-014170-10	IGDCC4	57722	NM_020962	19882240	GUGAAAGACAUACGAGACA
Plate 2	E09	L-014170-01	J-014170-11	IGDCC4	57722	NM_020962	19882240	CCUUAUGGGUGGCGGUGUU
Plate 2	E09	L-014170-01	J-014170-12	IGDCC4	57722	NM_020962	19882240	GAUCACAUAGGAUGCGAUA
Plate 2	E10	L-020676-00	J-020676-05	ARHGEF38	54848	NM_017700	8923172	GUGGAUAGCUUGUUUAGCA
Plate 2	E10	L-020676-00	J-020676-06	ARHGEF38	54848	NM_017700	8923172	GAACCGGCCAUGCAAGUAA
Plate 2	E10	L-020676-00	J-020676-07	ARHGEF38	54848	NM_017700	8923172	UAUCCAGUCCUUAAAGUAA
Plate 2	E10	L-020676-00	J-020676-08	ARHGEF38	54848	NM_017700	8923172	AUAGUAUACUGGAGUCCUA
Plate 2	E11	L-030269-01	J-030269-09	ARHGEF40	55701	NM_018071	50843836	GCUCAUCUGUCCACGAUUU
Plate 2	E11	L-030269-01	J-030269-10	ARHGEF40	55701	NM_018071	50843836	CGGAUGGAGCGCAAGCGAA
Plate 2	E11	L-030269-01	J-030269-11	ARHGEF40	55701	NM_018071	50843836	GAAGCGAGCUGCAGGUCGA
Plate 2	E11	L-030269-01	J-030269-12	ARHGEF40	55701	NM_018071	50843836	CGAGACACGCUGAACACAA
Plate 2	F02	L-026304-01	J-026304-09	DNMBP	23268	NM_015221	39930350	GCAGAGAACGAAUGCGGUA
Plate 2	F02	L-026304-01	J-026304-10	DNMBP	23268	NM_015221	39930350	AAGAAAUCCAACCGAGUUA
Plate 2	F02	L-026304-01	J-026304-11	DNMBP	23268	NM_015221	39930350	GAUGAAGCCUGGUCCGCAA
Plate 2	F02	L-026304-01	J-026304-12	DNMBP	23268	NM_015221	39930350	UAGCUGAGGUUAACGGGAA
Plate 2	F03	L-013854-01	J-013854-09	ARFGEF3	57221	NM_020340	38569486	UGGAAGAACUUGAUCGAUA

Plate 2	F03	L-013854-01	J-013854-10	ARFGEF3	57221	NM_020340	38569486	GAUACUGAAUGCCGUGAAA
Plate 2	F03	L-013854-01	J-013854-11	ARFGEF3	57221	NM_020340	38569486	UCACAAUGCUGACCGAUAU
Plate 2	F03	L-013854-01	J-013854-12	ARFGEF3	57221	NM_020340	38569486	CUAGAUGACACAAACGAUA
Plate 2	F04	L-008650-00	J-008650-05	RACGAP1	29127	NM_013277	21361396	UAAAUGAGAUUGAGCAAAG
Plate 2	F04	L-008650-00	J-008650-06	RACGAP1	29127	NM_013277	21361396	GCGAAGUGCUCUGGAUGUU
Plate 2	F04	L-008650-00	J-008650-07	RACGAP1	29127	NM_013277	21361396	CCACAGACACCAGAUAUUA
Plate 2	F04	L-008650-00	J-008650-08	RACGAP1	29127	NM_013277	21361396	GAAGUCACAUCUGCCUGUU
Plate 2	F05	L-009266-00	J-009266-05	RALBP1	10928	NM_006788	46358409	GAUCAGCCCUACUAAGUUU
Plate 2	F05	L-009266-00	J-009266-06	RALBP1	10928	NM_006788	46358409	GAAGUGAGACUGAGGAGUA
Plate 2	F05	L-009266-00	J-009266-07	RALBP1	10928	NM_006788	46358409	AAAGAGGACUGAAGGCUAU
Plate 2	F05	L-009266-00	J-009266-08	RALBP1	10928	NM_006788	46358409	GAGCAUGGCAGCGGGCUUA
Plate 2	F06	L-026514-01	J-026514-09	ARHGAP20	57569	NM_020809	51479147	AUACUUAGGACAACGAAAU
Plate 2	F06	L-026514-01	J-026514-10	ARHGAP20	57569	NM_020809	51479147	CCAAAGAGCUACUUCGUGA
Plate 2	F06	L-026514-01	J-026514-11	ARHGAP20	57569	NM_020809	51479147	CGGCAUAAGUCUUUGCAAA
Plate 2	F06	L-026514-01	J-026514-12	ARHGAP20	57569	NM_020809	51479147	GAUUACCAGUUGUGGGUCA
Plate 2	F07	L-021122-00	J-021122-05	ARHGAP11A	9824	NM_199357	40788017	AUUACAGGCUGCAGUAGUA
Plate 2	F07	L-021122-00	J-021122-06	ARHGAP11A	9824	NM_199357	40788017	GGUAUCAGUUCACAUCGAU
Plate 2	F07	L-021122-00	J-021122-07	ARHGAP11A	9824	NM_199357	40788017	GAUCGCAGGAGACAUGAAA
Plate 2	F07	L-021122-00	J-021122-08	ARHGAP11A	9824	NM_199357	40788017	AAGCGUACAUUGCCAGUAG
Plate 2	F08	L-035016-00	J-035016-01	ARHGAP11B	89839	NM_001039841	89886349	GGAUCUGUGAUUCGCCUAA
Plate 2	F08	L-035016-00	J-035016-02	ARHGAP11B	89839	NM_001039841	89886349	AGAACAUAUUCAUACCGAA
Plate 2	F08	L-035016-00	J-035016-03	ARHGAP11B	89839	NM_001039841	89886349	GAGAAAGAGAAGACAACGU
Plate 2	F08	L-035016-00	J-035016-04	ARHGAP11B	89839	NM_001039841	89886349	GUAUUAAGGUGAAGGGUGU
Plate 2	F09	L-008611-00	J-008611-05	ABR	29	NM_001092	38679953	CAAGUGGGAUGAGGAGUUU

Plate 2	F09	L-008611-00	J-008611-06	ABR	29	NM_001092	38679953	GCAAUCAGCCAACCUGUAC
Plate 2	F09	L-008611-00	J-008611-07	ABR	29	NM_001092	38679953	GCGAAGAGAUCUACAUUAA
Plate 2	F09	L-008611-00	J-008611-08	ABR	29	NM_001092	38679953	GCAAUAAAGACGACGAUGA
Plate 2	F10	L-003875-00	J-003875-15	BCR	613	NM_021574	82546844	GCAGAUGGCUCGUUCGGAA
Plate 2	F10	L-003875-00	J-003875-16	BCR	613	NM_021574	82546844	GCAAAACGCAGCAGUAUGA
Plate 2	F10	L-003875-00	J-003875-17	BCR	613	NM_021574	82546844	ACCAAGAACUCUCUGGAAA
Plate 2	F10	L-003875-00	J-003875-18	BCR	613	NM_021574	82546844	CGAGUGAGCUGGACUUGGA
Plate 2	F11	L-010251-01	J-010251-09	CHN1	1123	NM_001025201	68533256	CCACCUGCUCACUGCGAAA
Plate 2	F11	L-010251-01	J-010251-10	CHN1	1123	NM_001025201	68533256	CUCCAGAACUAGACGCCAU
Plate 2	F11	L-010251-01	J-010251-11	CHN1	1123	NM_001025201	68533256	CCGGAUGAGCAAUUGGAAA
Plate 2	F11	L-010251-01	J-010251-12	CHN1	1123	NM_001025201	68533256	GCAUAUAACCAGAUUAAAG
Plate 2	G02	L-003791-01	J-003791-13	CHN2	1124	NM_001039936	91106927	GACAUAUGCAUUCGGGAAA
Plate 2	G02	L-003791-01	J-003791-14	CHN2	1124	NM_001039936	91106927	GGUCAUAGUCUUUUCGUAU
Plate 2	G02	L-003791-01	J-003791-15	CHN2	1124	NM_001039936	91106927	ACUUUAAGGUCCACACGUU
Plate 2	G02	L-003791-01	J-003791-16	CHN2	1124	NM_001039936	91106927	CAGAAUAACUGUCAACGUU
Plate 2	G03	L-008426-00	J-008426-05	ARHGAP26	23092	NM_015071	32189359	GCACUACUGUACAUAUCAA
Plate 2	G03	L-008426-00	J-008426-06	ARHGAP26	23092	NM_015071	32189359	CAAGGGCUGUAUCGAAUUG
Plate 2	G03	L-008426-00	J-008426-07	ARHGAP26	23092	NM_015071	32189359	GAACGGAUACGGAUGAUUG
Plate 2	G03	L-008426-00	J-008426-08	ARHGAP26	23092	NM_015071	32189359	GGAGAAACGUCACUUUGGA
Plate 2	G04	L-009444-00	J-009444-05	OPHN1	4983	NM_002547	4505506	GAAAUGGGCUUUAGGAAUA
Plate 2	G04	L-009444-00	J-009444-06	OPHN1	4983	NM_002547	4505506	CAACAUGGGAGUAAUCUUU
Plate 2	G04	L-009444-00	J-009444-07	OPHN1	4983	NM_002547	4505506	CUAGUGAUUUGCUGAUUAA
Plate 2	G04	L-009444-00	J-009444-08	OPHN1	4983	NM_002547	4505506	GUAUAUAAGCUACCAGAAA
Plate 2	G05	L-009382-01	J-009382-09	ARHGAP10	79658	NM_024605	50843947	UGAACUGUCUCUCGAGUAU

Plate 2	G05	L-009382-01	J-009382-10	ARHGAP10	79658	NM_024605	50843947	ACUAUUGCAUGUAUCGAAA
Plate 2	G05	L-009382-01	J-009382-11	ARHGAP10	79658	NM_024605	50843947	AGUUUGAGUUUAUCGGUGA
Plate 2	G05	L-009382-01	J-009382-12	ARHGAP10	79658	NM_024605	50843947	CGUUGAAACACGAGGUAUA
Plate 2	G06	L-004775-01	J-004775-09	ARHGAP21	57584	NM_020824	50345878	GAAAAUAGCAGAUCGGUUA
Plate 2	G06	L-004775-01	J-004775-10	ARHGAP21	57584	NM_020824	50345878	GAUGAUAAAUGGCGAGAUU
Plate 2	G06	L-004775-01	J-004775-11	ARHGAP21	57584	NM_020824	50345878	GGAUCUAAUUAGUCGAAGA
Plate 2	G06	L-004775-01	J-004775-12	ARHGAP21	57584	NM_020824	50345878	GCACAGAGAUGCUACCGAA
Plate 2	G07	L-009238-01	J-009238-09	ARHGAP44	9912	NM_014859	50233869	ACUCCUAAGCCGCGACAGA
Plate 2	G07	L-009238-01	J-009238-10	ARHGAP44	9912	NM_014859	50233869	GGGGAUUAGGGGAGUGAGA
Plate 2	G07	L-009238-01	J-009238-11	ARHGAP44	9912	NM_014859	50233869	UAUCCAAGCUGUCAGAAUA
Plate 2	G07	L-009238-01	J-009238-12	ARHGAP44	9912	NM_014859	50233869	CCACAGUGUCGCUGCAAAU
Plate 2	G08	L-008335-02	J-008335-09	ARHGAP17	55114	NM_018054	54860104	AGUAAGAAGCAGUGCGUUA
Plate 2	G08	L-008335-02	J-008335-10	ARHGAP17	55114	NM_018054	54860104	CAAGAUAAGUGGGCGGAAA
Plate 2	G08	L-008335-02	J-008335-11	ARHGAP17	55114	NM_018054	54860104	GCAUUAGCAGUCUUAGAAA
Plate 2	G08	L-008335-02	J-008335-12	ARHGAP17	55114	NM_018054	54860104	GGUGGAAUUUAAUGUAUCA
Plate 2	G09	L-009546-01	J-009546-09	SH3BP1	23616	NM_018957	85815828	UGGAGAUUCAGGCCGAUUA
Plate 2	G09	L-009546-01	J-009546-10	SH3BP1	23616	NM_018957	85815828	GAGGGAGAACCACGGCCAA
Plate 2	G09	L-009546-01	J-009546-11	SH3BP1	23616	NM_018957	85815828	UCCAGAAGCUCGUGUCCGA
Plate 2	G09	L-009546-01	J-009546-12	SH3BP1	23616	NM_018957	85815828	GCCCAGUCUCUUUGAGUAA
Plate 2	G10	L-009580-00	J-009580-05	ARHGAP5	394	NM_001173	71834860	GUACGAAUUUGCAACCAUA
Plate 2	G10	L-009580-00	J-009580-06	ARHGAP5	394	NM_001173	71834860	GCUGAUACAACCACAAUUA
Plate 2	G10	L-009580-00	J-009580-07	ARHGAP5	394	NM_001173	71834860	GAUCAUGGCCGCUUAAGAU
Plate 2	G10	L-009580-00	J-009580-08	ARHGAP5	394	NM_001173	71834860	GGAAUCAGUUAAACACAAU
Plate 2	G11	L-004158-00	J-004158-06	ARHGAP35	2909	NM_004491	25121939	CUACUCAUAUGUACGAUAA

Plate 2	G11	L-004158-00	J-004158-07	ARHGAP35	2909	NM_004491	25121939	UCAGCGAGAUCCAAUGUAA
Plate 2	G11	L-004158-00	J-004158-08	ARHGAP35	2909	NM_004491	25121939	GAGGGCGAGUGGUCAAUAA
Plate 2	G11	L-004158-00	J-004158-09	ARHGAP35	2909	NM_004491	25121939	GAAAUUGACGGAAGGUUCA
Plate 3	B02	L-009302-01	J-009302-13	ARAP2	116984	NM_139182	21264593	GGACGAUAAACUUCGAAAU
Plate 3	B02	L-009302-01	J-009302-14	ARAP2	116984	NM_139182	21264593	CUAAGGAGCUCUACCCAUA
Plate 3	B02	L-009302-01	J-009302-15	ARAP2	116984	NM_139182	21264593	GUAAGAAGACAUUGGGUUA
Plate 3	B02	L-009302-01	J-009302-16	ARAP2	116984	NM_139182	21264593	GCAAAUUUGUCUAUGCUUA
Plate 3	B03	L-009136-00	J-009136-05	ARAP1	116985	NM_015242	21264595	GGAGUGGCCUAUUAAGAGU
Plate 3	B03	L-009136-00	J-009136-06	ARAP1	116985	NM_015242	21264595	UAACAAGGACGCUUACUCU
Plate 3	B03	L-009136-00	J-009136-07	ARAP1	116985	NM_015242	21264595	CCGCAGGGAUCUUACAUCU
Plate 3	B03	L-009136-00	J-009136-08	ARAP1	116985	NM_015242	21264595	GAUCACCUGCGAUACUUUG
Plate 3	B04	L-007052-00	J-007052-05	ARAP3	64411	NM_022481	58331234	GUAAUGAGAUAGUACAGUU
Plate 3	B04	L-007052-00	J-007052-06	ARAP3	64411	NM_022481	58331234	GCAGAAAUGUGCGGCUCUA
Plate 3	B04	L-007052-00	J-007052-07	ARAP3	64411	NM_022481	58331234	ACACGGGAGUGGACAGUGA
Plate 3	B04	L-007052-00	J-007052-08	ARAP3	64411	NM_022481	58331234	GAACGGGAGUGGCCUUUGG
Plate 3	B05	L-009535-00	J-009535-05	MYO9B	4650	NM_004145	33356169	CCAAGUACGUGAAGAUGUA
Plate 3	B05	L-009535-00	J-009535-06	MYO9B	4650	NM_004145	33356169	GCUCUCAGGUCGACUCUAA
Plate 3	B05	L-009535-00	J-009535-07	MYO9B	4650	NM_004145	33356169	CAGGGAAGGUGAAAUAUCA
Plate 3	B05	L-009535-00	J-009535-08	MYO9B	4650	NM_004145	33356169	UGAAACCCUUCUAGUCGUA
Plate 3	B06	L-006539-01	J-006539-09	MYO9A	4649	NM_006901	5902011	GAACAUACAUUACGGAUAU
Plate 3	B06	L-006539-01	J-006539-10	MYO9A	4649	NM_006901	5902011	CUCCAAAGGCUAAGCGCAA
Plate 3	B06	L-006539-01	J-006539-11	MYO9A	4649	NM_006901	5902011	AAACAAUGGCUUCGAGAUU
Plate 3	B06	L-006539-01	J-006539-12	MYO9A	4649	NM_006901	5902011	GCGUAUUCGUCGAGGAAAC
Plate 3	B07	L-008966-00	J-008966-05	ARHGAP1	392	NM_004308	19923243	GCCAAGUGCUCAAAUAUGA

Plate 3	B07	L-008966-00	J-008966-06	ARHGAP1	392	NM_004308	19923243	GGCGGAAGAUCAUUGUGUU
Plate 3	B07	L-008966-00	J-008966-07	ARHGAP1	392	NM_004308	19923243	UAACCUGGCUGUUGUUUUC
Plate 3	B07	L-008966-00	J-008966-08	ARHGAP1	392	NM_004308	19923243	GGGAAGUGCAGCAGAAGUA
Plate 3	B08	L-009427-00	J-009427-07	ARHGAP8	23779	NM_181335	66346659	GGUCAUCCCUCCCGAAGUU
Plate 3	B08	L-009427-00	J-009427-08	ARHGAP8	23779	NM_181335	66346659	CAGAAGACGUCUCUAGUGU
Plate 3	B08	L-009427-00	J-009427-09	ARHGAP8	23779	NM_181335	66346659	GCACGAGUCACCCGUUCUA
Plate 3	B08	L-009427-00	J-009427-10	ARHGAP8	23779	NM_181335	66346659	UAACCUGGCCUGUGUCUUC
Plate 3	B09	L-010254-01	J-010254-09	STARD8	9754	NM_014725	31543658	AUCCAGAACCUGCGUCAAA
Plate 3	B09	L-010254-01	J-010254-10	STARD8	9754	NM_014725	31543658	GACAUGACGAUUUGGCAUA
Plate 3	B09	L-010254-01	J-010254-11	STARD8	9754	NM_014725	31543658	GCUUAUGGUAGUGGGCUAA
Plate 3	B09	L-010254-01	J-010254-12	STARD8	9754	NM_014725	31543658	CCACUUUCCUCCAGAUCUA
Plate 3	B10	L-010256-00	J-010256-05	STARD13	90627	NM_052851	16445030	GGAUGAAAGUUCCCGACUA
Plate 3	B10	L-010256-00	J-010256-06	STARD13	90627	NM_052851	16445030	GUUAAUUGGAGGACCGGUA
Plate 3	B10	L-010256-00	J-010256-07	STARD13	90627	NM_052851	16445030	GCUUAUGAUGUGGCGGAUA
Plate 3	B10	L-010256-00	J-010256-08	STARD13	90627	NM_052851	16445030	GUACAGACAACCCGGUCAU
Plate 3	B11	L-003628-00	J-003628-06	ARHGAP4	393	NM_001666	41327157	GGGAUGUGCUUGAUUCCUU
Plate 3	B11	L-003628-00	J-003628-07	ARHGAP4	393	NM_001666	41327157	CUACCUGCAUGACGUCUUG
Plate 3	B11	L-003628-00	J-003628-08	ARHGAP4	393	NM_001666	41327157	AGAAGACGUACCAGGCAUA
Plate 3	B11	L-003628-00	J-003628-09	ARHGAP4	393	NM_001666	41327157	CGCAAGAGCUCCCUCAAGA
Plate 3	C02	L-026974-00	J-026974-05	SRGAP1	57522	NM_020762	44917603	GAACGAAUAUCUCCUAACA
Plate 3	C02	L-026974-00	J-026974-06	SRGAP1	57522	NM_020762	44917603	GCAGAUAAGUGAGGAUUCU
Plate 3	C02	L-026974-00	J-026974-07	SRGAP1	57522	NM_020762	44917603	CAUGAGGGCUUAGACAUUA
Plate 3	C02	L-026974-00	J-026974-08	SRGAP1	57522	NM_020762	44917603	UUAACGAUCUGAUUUCUUG
Plate 3	C03	L-021531-02	J-021531-11	SRGAP2	23380	NM_001042758	112363095	CCACACGAGCGAUGACGAA

Plate 3	C03	L-021531-02	J-021531-13	SRGAP2	23380	NM_001042758	112363095	GCACAAUGGCAUCGACGGA
Plate 3	C03	L-021531-02	J-021531-22	SRGAP2	23380	NM_001042758	112363095	CUGCUUUACCAGCGGGCUU
Plate 3	C03	L-021531-02	J-021531-23	SRGAP2	23380	NM_001042758	112363095	GGGUCAUGUAGCCGAUAUU
Plate 3	C04	L-014175-00	J-014175-05	SRGAP3	9901	NM_001033116	75677371	GAACUGCUCAUGCGUUAUC
Plate 3	C04	L-014175-00	J-014175-06	SRGAP3	9901	NM_001033116	75677371	GGACCUAUCUCUCAGCUGA
Plate 3	C04	L-014175-00	J-014175-07	SRGAP3	9901	NM_001033116	75677371	CAACGCAGCUAUAAGCAAA
Plate 3	C04	L-014175-00	J-014175-08	SRGAP3	9901	NM_001033116	75677371	GAGGAGAAGCAGUUCAAUA
Plate 3	C05	L-008277-00	J-008277-05	ARHGAP29	9411	NM_004815	38016931	ACACACAAGUUUCGCAAAU
Plate 3	C05	L-008277-00	J-008277-06	ARHGAP29	9411	NM_004815	38016931	UGAACGAGCUACAUCAUUU
Plate 3	C05	L-008277-00	J-008277-07	ARHGAP29	9411	NM_004815	38016931	UAGCAUAGGUGUUGUUGAU
Plate 3	C05	L-008277-00	J-008277-08	ARHGAP29	9411	NM_004815	38016931	UCAUAUACGUCUAGAGGAA
Plate 3	C06	L-021160-01	J-021160-09	GMIP	51291	NM_016573	91208436	CGAGUGUCCUCAAGCGAUU
Plate 3	C06	L-021160-01	J-021160-10	GMIP	51291	NM_016573	91208436	GUGCCAGGCUUUCGAGAAU
Plate 3	C06	L-021160-01	J-021160-11	GMIP	51291	NM_016573	91208436	GGCCACACCUACCGAGAUU
Plate 3	C06	L-021160-01	J-021160-12	GMIP	51291	NM_016573	91208436	CAGGGUGGCUGCACGAUUU
Plate 3	C07	L-014713-01	J-014713-09	ARHGAP24	83478	NM_001025616	71043935	CGAAAUGCCGAGCGAGCAA
Plate 3	C07	L-014713-01	J-014713-10	ARHGAP24	83478	NM_001025616	71043935	AGAGCUUAGAACAGCGAAA
Plate 3	C07	L-014713-01	J-014713-11	ARHGAP24	83478	NM_001025616	71043935	GUGUUAAGGAAUUAGCAAA
Plate 3	C07	L-014713-01	J-014713-12	ARHGAP24	83478	NM_001025616	71043935	CGAGAGAGGAAACACAAUA
Plate 3	C08	L-021175-01	J-021175-09	ARHGAP25	9938	NM_014882	55770896	AAGCAGAGGUCCAUCGUGA
Plate 3	C08	L-021175-01	J-021175-10	ARHGAP25	9938	NM_014882	55770896	GGAAAAUGCAAUCUCGUAA
Plate 3	C08	L-021175-01	J-021175-11	ARHGAP25	9938	NM_014882	55770896	GGACUUCCACCUACGAUAA
Plate 3	C08	L-021175-01	J-021175-12	ARHGAP25	9938	NM_014882	55770896	CCACUGAAGACCUCCGAAU
Plate 3	C09	L-019080-01	J-019080-09	ARHGAP22	58504	NM_021226	34013589	CAGUCCACCACGAGCGGAA

Plate 3	C09	L-019080-01	J-019080-10	ARHGAP22	58504	NM_021226	34013589	GGUCAGAAGGGGACGGUAC
Plate 3	C09	L-019080-01	J-019080-11	ARHGAP22	58504	NM_021226	34013589	CCACAGAAAUGGAGGGCGC
Plate 3	C09	L-019080-01	J-019080-12	ARHGAP22	58504	NM_021226	34013589	GCGGAGGGAUCUUUGGGCA
Plate 3	C10	L-003021-00	J-003021-09	PIK3R2	5296	NM_005027	48976048	GCGCCCAGCUUAAGGUCUA
Plate 3	C10	L-003021-00	J-003021-10	PIK3R2	5296	NM_005027	48976048	GGAACGCACUUGGUACGUG
Plate 3	C10	L-003021-00	J-003021-11	PIK3R2	5296	NM_005027	48976048	GGACAAGAGCCGCGAGUAU
Plate 3	C10	L-003021-00	J-003021-12	PIK3R2	5296	NM_005027	48976048	GGAAAGGCGGGAACAAUAA
Plate 3	C11	L-003020-00	J-003020-14	PIK3R1	5295	NM_181504	32455251	AGUAAAGCAUUGUGUCAUA
Plate 3	C11	L-003020-00	J-003020-15	PIK3R1	5295	NM_181504	32455251	CCAACAACGGUAUGAAUAA
Plate 3	C11	L-003020-00	J-003020-16	PIK3R1	5295	NM_181504	32455251	GACGAGAGACCAAUACUUG
Plate 3	C11	L-003020-00	J-003020-17	PIK3R1	5295	NM_181504	32455251	UAUUGAAGCUGUAGGGAAA
Plate 3	D02	L-010026-00	J-010026-07	OCRL	4952	NM_001587	21396492	GAACGAAGGUACCGGAAAG
Plate 3	D02	L-010026-00	J-010026-08	OCRL	4952	NM_001587	21396492	CGAAGAAGACUAAGGCUUU
Plate 3	D02	L-010026-00	J-010026-09	OCRL	4952	NM_001587	21396492	GCGGGAGGGUCUCAUCAAA
Plate 3	D02	L-010026-00	J-010026-10	OCRL	4952	NM_001587	21396492	GAAAGGAUCAGUGUCGAUA
Plate 3	D03	L-021811-00	J-021811-09	INPP5B	3633	NM_005540	52138518	GGACAAGGCUCAUAUUUUA
Plate 3	D03	L-021811-00	J-021811-10	INPP5B	3633	NM_005540	52138518	GAAGAGGAUUACACCUAUA
Plate 3	D03	L-021811-00	J-021811-11	INPP5B	3633	NM_005540	52138518	GGAGGAACCAGGACUAUAA
Plate 3	D03	L-021811-00	J-021811-12	INPP5B	3633	NM_005540	52138518	CAACUCGGGUGAAGACAAA
Plate 3	D04	L-010047-01	J-010047-09	ARHGAP9	64333	NM_032496	14210509	AGGACAAGAAGGUCGGUUA
Plate 3	D04	L-010047-01	J-010047-10	ARHGAP9	64333	NM_032496	14210509	GGGUGGUGUUAACGGGUAA
Plate 3	D04	L-010047-01	J-010047-11	ARHGAP9	64333	NM_032496	14210509	GCAACAAACUAAAGCGGCU
Plate 3	D04	L-010047-01	J-010047-12	ARHGAP9	64333	NM_032496	14210509	CGAAAGACCAACUCCGACU
Plate 3	D05	L-008729-01	J-008729-09	ARHGAP12	94134	NM_018287	26986533	GAACAGGUCUUAUUCGUGA

Plate 3	D05	L-008729-01	J-008729-10	ARHGAP12	94134	NM_018287	26986533	CCAAAUAACUCCACGAAAA
Plate 3	D05	L-008729-01	J-008729-11	ARHGAP12	94134	NM_018287	26986533	UGAAGGAGGUCACGCGCAA
Plate 3	D05	L-008729-01	J-008729-12	ARHGAP12	94134	NM_018287	26986533	GGGAAUUGCCAAAGUAUAA
Plate 3	D06	L-018019-02	J-018019-09	ARHGAP15	55843	NM_018460	188497641	CAUCACAGUGCUUCCGAUA
Plate 3	D06	L-018019-02	J-018019-10	ARHGAP15	55843	NM_018460	188497641	CAGUAAGAUCUUCGGCUCA
Plate 3	D06	L-018019-02	J-018019-12	ARHGAP15	55843	NM_018460	188497641	AGUUUGUGGAAGCGAUCAA
Plate 3	D06	L-018019-02	J-018019-18	ARHGAP15	55843	NM_018460	188497641	GAUGGAAUAUAUCGAGUUA
Plate 3	D07	L-008213-00	J-008213-05	ARHGAP32	9743	NM_014715	29469070	GAGCAUAUCUGAGCCAAUU
Plate 3	D07	L-008213-00	J-008213-06	ARHGAP32	9743	NM_014715	29469070	GAUAAGGCCUAUUUCCAAA
Plate 3	D07	L-008213-00	J-008213-07	ARHGAP32	9743	NM_014715	29469070	GGAGAGGACCGCUUCUAUA
Plate 3	D07	L-008213-00	J-008213-08	ARHGAP32	9743	NM_014715	29469070	GGUAGUAGCCAAUGUCAGA
Plate 3	D08	L-023577-01	J-023577-09	ARHGAP31	57514	NM_020754	55742785	GGGAAAUUUCAAUCGAACA
Plate 3	D08	L-023577-01	J-023577-10	ARHGAP31	57514	NM_020754	55742785	UCACCAAGCAGGAGGGCGA
Plate 3	D08	L-023577-01	J-023577-11	ARHGAP31	57514	NM_020754	55742785	GGAUGUAACCCAUUCAGUA
Plate 3	D08	L-023577-01	J-023577-12	ARHGAP31	57514	NM_020754	55742785	CCUCAGCGGAGAUCAGUAA
Plate 3	D09	L-009225-01	J-009225-09	ARHGAP33	115703	NM_052948	23510412	CCCAUGUGAUCAAACGGUA
Plate 3	D09	L-009225-01	J-009225-10	ARHGAP33	115703	NM_052948	23510412	GGUGUUUGGCUGCGAUCUU
Plate 3	D09	L-009225-01	J-009225-11	ARHGAP33	115703	NM_052948	23510412	CCGCAUGGCGAGACACAGU
Plate 3	D09	L-009225-01	J-009225-12	ARHGAP33	115703	NM_052948	23510412	CGGCAUGCUUGGCCAAUCA
Plate 3	D10	L-015856-01	J-015856-09	SYDE1	85360	NM_033025	42475969	GCGCCUUACUUGCGACCCA
Plate 3	D10	L-015856-01	J-015856-10	SYDE1	85360	NM_033025	42475969	CGGGACCAGUCGCGUGUAU
Plate 3	D10	L-015856-01	J-015856-11	SYDE1	85360	NM_033025	42475969	CCUCAAGGAUUAUCUUCGA
Plate 3	D10	L-015856-01	J-015856-12	SYDE1	85360	NM_033025	42475969	CCGGUGACUUCGAAGACGA
Plate 3	D11	L-021617-02	J-021617-09	SYDE2	84144	NM_032184	149274654	GAGGAAUGUUAUAAGCCGA

Plate 3	D11	L-021617-02	J-021617-10	SYDE2	84144	NM_032184	149274654	AGCCGAAAGCUAAGCGUUA
Plate 3	D11	L-021617-02	J-021617-12	SYDE2	84144	NM_032184	149274654	CGAACAUGCAGGUGAUAUU
Plate 3	D11	L-021617-02	J-021617-19	SYDE2	84144	NM_032184	149274654	UUUAAAACCACCUCGGAUA
Plate 3	E02	L-013830-00	J-013830-05	DEPDC1B	55789	NM_018369	23510330	GUACAAGCGUCACAGUAUU
Plate 3	E02	L-013830-00	J-013830-06	DEPDC1B	55789	NM_018369	23510330	CGAAGUUCAUCAUCCAUAA
Plate 3	E02	L-013830-00	J-013830-07	DEPDC1B	55789	NM_018369	23510330	GUACUGGGUUUGUUACAGA
Plate 3	E02	L-013830-00	J-013830-08	DEPDC1B	55789	NM_018369	23510330	GCGUGUGGCUCAUCUACGA
Plate 3	E03	L-021125-00	J-021125-09	DEPDC1	55635	NM_017779	41282232	CGUAUGAUUUCCCGAAUGA
Plate 3	E03	L-021125-00	J-021125-10	DEPDC1	55635	NM_017779	41282232	CAUCGAUGCUCUACAGUUA
Plate 3	E03	L-021125-00	J-021125-11	DEPDC1	55635	NM_017779	41282232	CCAAAGUUCCGUAGUCUAA
Plate 3	E03	L-021125-00	J-021125-12	DEPDC1	55635	NM_017779	41282232	GGAAUGAAGUUACCACAUC
Plate 3	E04	L-020738-01	J-020738-09	FAM13B	51306	NM_016603	7706136	UCAAAUAGUGUUACGGCAA
Plate 3	E04	L-020738-01	J-020738-10	FAM13B	51306	NM_016603	7706136	GCCUAUGGGACUUCAGUUA
Plate 3	E04	L-020738-01	J-020738-11	FAM13B	51306	NM_016603	7706136	AGAAAUAGUGAGCAGGAUA
Plate 3	E04	L-020738-01	J-020738-12	FAM13B	51306	NM_016603	7706136	CAAAGUGUGGUGUGUAAUA
Plate 3	E05	L-020516-00	J-020516-05	FAM13A	10144	NM_001015045	62865868	CGUCAGAAAUCCAGUACUA
Plate 3	E05	L-020516-00	J-020516-06	FAM13A	10144	NM_001015045	62865868	GGGCGAAACUGCUUCCUUC
Plate 3	E05	L-020516-00	J-020516-07	FAM13A	10144	NM_001015045	62865868	GAACUGGACCUGAUGAUUU
Plate 3	E05	L-020516-00	J-020516-08	FAM13A	10144	NM_001015045	62865868	GGAGACAACUUAAAGAAUC
Plate 3	E06	L-032590-01	J-032590-09	ARHGAP39	80728	NM_025251	58331178	GCAUGCAGAGAGAGCGCUA
Plate 3	E06	L-032590-01	J-032590-10	ARHGAP39	80728	NM_025251	58331178	UAUGAGAUUUACCGGGAUU
Plate 3	E06	L-032590-01	J-032590-11	ARHGAP39	80728	NM_025251	58331178	CCUCGGAGACGGACAUCGA
Plate 3	E06	L-032590-01	J-032590-12	ARHGAP39	80728	NM_025251	58331178	GCGGGUCAGCUCCGAGAAA
Plate 3	E07	L-018322-02	J-018322-17	ARHGAP19	84986	NM_032900	67906813	CGUAAUUUGCUGAAGUUAU

Plate 3	E07	L-018322-02	J-018322-18	ARHGAP19	84986	NM_032900	67906813	CUAAGAUGCACAAGCGUUU
Plate 3	E07	L-018322-02	J-018322-19	ARHGAP19	84986	NM_032900	67906813	UAAUAGAAGCUGUGAUCGA
Plate 3	E07	L-018322-02	J-018322-20	ARHGAP19	84986	NM_032900	67906813	UCAUGUCUCUCAAGCGAAA
Plate 3	E08	L-008711-01	J-008711-09	TAGAP	117289	NM_138810	23199968	GCAAGAACUCUGAGGUGAA
Plate 3	E08	L-008711-01	J-008711-10	TAGAP	117289	NM_138810	23199968	GAAUCGAGGCCCUGAAACA
Plate 3	E08	L-008711-01	J-008711-11	TAGAP	117289	NM_138810	23199968	UGUCAUUUGAAGCCCAGAA
Plate 3	E08	L-008711-01	J-008711-12	TAGAP	117289	NM_138810	23199968	ACAUGCUCACCCUGGAGAA
Plate 3	E09	L-023893-00	J-023893-05	HMHA1	23526	NM_012292	47834347	GAGCGGACGUCAUCCAGUG
Plate 3	E09	L-023893-00	J-023893-06	HMHA1	23526	NM_012292	47834347	GAGCUGAGGUAGUCGUCCA
Plate 3	E09	L-023893-00	J-023893-07	HMHA1	23526	NM_012292	47834347	GGGAAAGGCAGCCGGAAUU
Plate 3	E09	L-023893-00	J-023893-08	HMHA1	23526	NM_012292	47834347	CCAAGAACAUGGCCAAGUA
Plate 3	E10	L-031016-01	J-031016-13	ARHGAP28	79822	NM_030672	59710110	CAGUAAUGUUGAAAGCGUU
Plate 3	E10	L-031016-01	J-031016-14	ARHGAP28	79822	NM_030672	59710110	CGGAAGGAGUCAUACGGGU
Plate 3	E10	L-031016-01	J-031016-15	ARHGAP28	79822	NM_030672	59710110	UGUCAUUUGAAGUGUCUUA
Plate 3	E10	L-031016-01	J-031016-16	ARHGAP28	79822	NM_030672	59710110	GCCUAAUGCUUAAGUACCA
Plate 3	E11	L-015110-01	J-015110-09	ARHGAP18	93663	NM_033515	39932588	GAAAAUGGCUUAUGACCGA
Plate 3	E11	L-015110-01	J-015110-10	ARHGAP18	93663	NM_033515	39932588	GGGAGUGAUUCGAGUGCAA
Plate 3	E11	L-015110-01	J-015110-11	ARHGAP18	93663	NM_033515	39932588	AGAUAUGGCCAGUACACUA
Plate 3	E11	L-015110-01	J-015110-12	ARHGAP18	93663	NM_033515	39932588	AAGCAAGAUAAGAGUACAA
Plate 3	F02	L-024189-02	J-024189-09	ARHGAP40	343578	NM_001164431	256574757	AGAGGACAGUGGCGGGAAU
Plate 3	F02	L-024189-02	J-024189-10	ARHGAP40	343578	NM_001164431	256574757	GAGAAUGGCGACUCCGGUA
Plate 3	F02	L-024189-02	J-024189-12	ARHGAP40	343578	NM_001164431	256574757	UCAAAAGGUUCAUCCGGAA
Plate 3	F02	L-024189-02	J-024189-17	ARHGAP40	343578	NM_001164431	256574757	CCACCUAAACCCUGCGAGU
Plate 3	F03	L-026507-01	J-026507-09	ARHGAP42	143872	XM_370651	89034272	GUAUCCAUGGUAACGAAUA

Plate 3	F03	L-026507-01	J-026507-10	ARHGAP42	143872	XM_370651	89034272	UCUCAUGACUGUCUCAAAU
Plate 3	F03	L-026507-01	J-026507-11	ARHGAP42	143872	XM_370651	89034272	GGUCAAAGUAUCACUACAC
Plate 3	F03	L-026507-01	J-026507-12	ARHGAP42	143872	XM_370651	89034272	CGUAGCAAUUGUAGAGUUU
Plate 3	F04	L-027281-01	J-027281-09	ARHGAP27	201176	NM_199282	40548321	CUACUGUGCGUGUGCGAUA
Plate 3	F04	L-027281-01	J-027281-10	ARHGAP27	201176	NM_199282	40548321	GCAUGUCGGUGCAGAGCGU
Plate 3	F04	L-027281-01	J-027281-11	ARHGAP27	201176	NM_199282	40548321	CGGCACAAGCUCCGCAAGU
Plate 3	F04	L-027281-01	J-027281-12	ARHGAP27	201176	NM_199282	40548321	AGGGAAAGCGGCUCCGGAA
Plate 3	F05	L-023061-01	J-023061-09	ARHGAP23	57636	XM_290799	89041496	CCACAGGCAUUUACCGAGU
Plate 3	F05	L-023061-01	J-023061-10	ARHGAP23	57636	XM_290799	89041496	CCGUCAACCGCAAGCGCAA
Plate 3	F05	L-023061-01	J-023061-11	ARHGAP23	57636	XM_290799	89041496	UCAAGUCCUUCUUCCGAAA
Plate 3	F05	L-023061-01	J-023061-12	ARHGAP23	57636	XM_290799	89041496	CCCACAUGCCUGACCGCUA
Plate 3	F06	L-009130-01	J-009130-09	ARHGAP30	257106	NM_181720	71040095	CCAUACUAUCAUCGAGAUU
Plate 3	F06	L-009130-01	J-009130-10	ARHGAP30	257106	NM_181720	71040095	GGCCAUGAGACUAAGCGUA
Plate 3	F06	L-009130-01	J-009130-11	ARHGAP30	257106	NM_181720	71040095	AAUUUGAGUCAGAGCGGAA
Plate 3	F06	L-009130-01	J-009130-12	ARHGAP30	257106	NM_181720	71040095	GUGGAGAGUGGGUGGCGAU
Plate 3	F07	L-009304-00	J-009304-05	ARHGAP6	395	NM_013422	7382477	CAUCAUCGCUGUUGUGCAA
Plate 3	F07	L-009304-00	J-009304-06	ARHGAP6	395	NM_013422	7382477	CGGAGAAGCUUUACAGAGU
Plate 3	F07	L-009304-00	J-009304-07	ARHGAP6	395	NM_013422	7382477	GGAAUUUGACCGUGGGAUU
Plate 3	F07	L-009304-00	J-009304-08	ARHGAP6	395	NM_013422	7382477	GUACACAGCUUUCAUCAAC
Plate 3	F08	L-008446-01	J-008446-09	ARHGAP36	158763	NM_144967	40255079	GAUCCAGAGUGCACGCAUA
Plate 3	F08	L-008446-01	J-008446-10	ARHGAP36	158763	NM_144967	40255079	GAGGCAUGCUAGAACGUUA
Plate 3	F08	L-008446-01	J-008446-11	ARHGAP36	158763	NM_144967	40255079	GGACGAAGAUGGUAUCGAU
Plate 3	F08	L-008446-01	J-008446-12	ARHGAP36	158763	NM_144967	40255079	AAGAGGUCCUGGUGAACGA

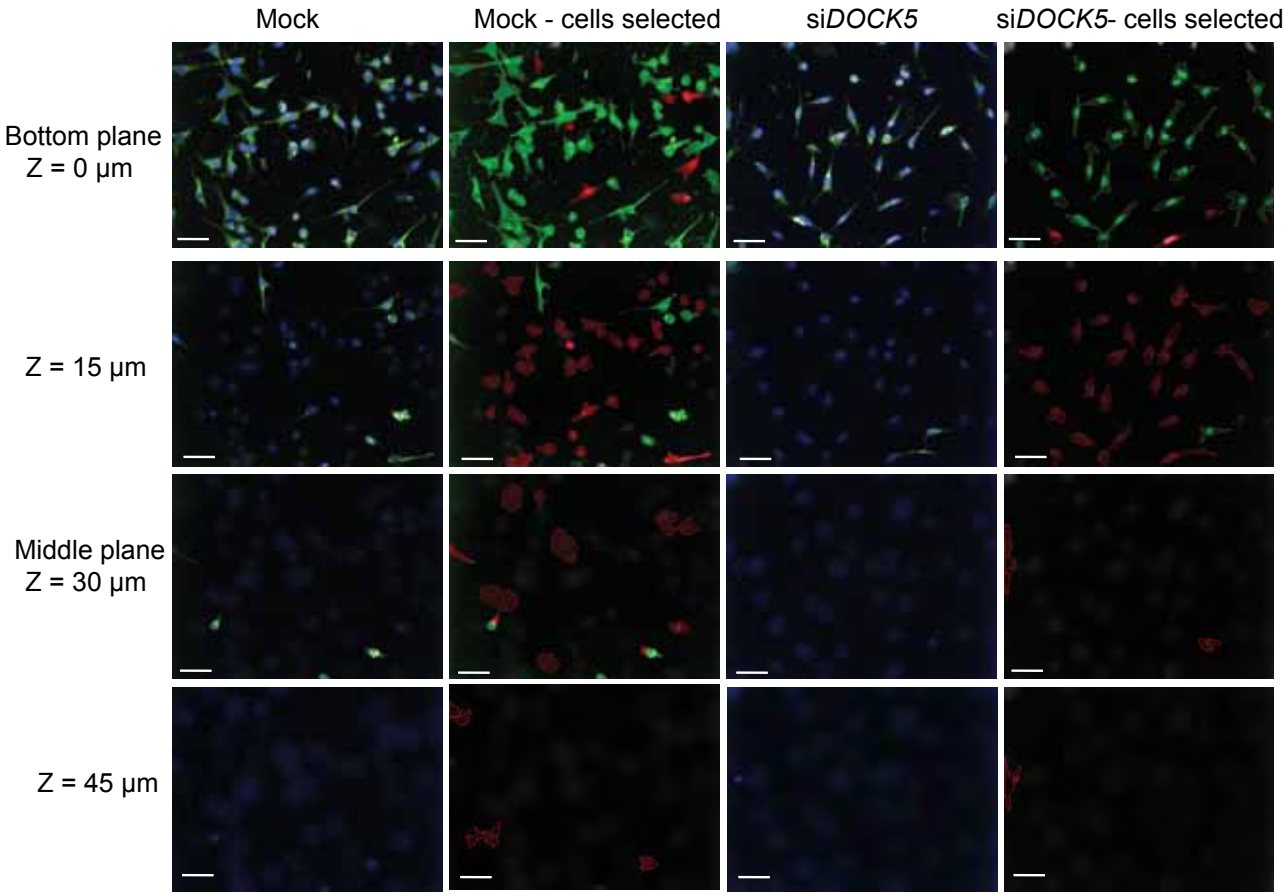

Appendix 16: Automated segmentation for Collagen Invasion Quantification. Images for mock and si*DOCK5* transfected cells shown at planes quantified: bottom plane 0µm and middle plane 30µm. As well as intermediate planes 15µm, and 45µm. Cells selected indicate cells that the software has identified to be in that particular plane (green) following a filtering process. Those that are not considered to be in that plane are in red. Shows that cells which are counted in middle plane are not spanning other planes. Scale bar 50µm.